Modélisation des effets de fluides externes et internes sur le comportement dynamique des dirigeables flexibles

Robin Le Mestre

INSTITUT POLYTECHNIQUE DE PARIS

NNT : 2022IPPAE008

Thèse de doctorat

ENSTA IP PARIS

Modeling of external and internal fluid effects on the dynamic behavior of a flexible airship

Thèse de doctorat de l'Institut Polytechnique de Paris
préparée à École nationale supérieure de techniques avancées

École doctorale n°626 École doctorale de l'Institut Polytechnique de Paris (EDIPP)
Spécialité de doctorat: Mécanique des fluides et des solides, acoustique

Thèse présentée et soutenue à l'ONERA Châtillon, le 16/06/2022, par

ROBIN LE MESTRE

Composition du Jury :

Roger Ohayon Professeur émérite, Conservatoire National des Arts et Métiers (Laboratoire de Mécanique des Structures et des Systèmes Couplés)	Président
Anne-Virginie Salsac directrice de recherche CNRS, Université de Technologie de Compiègne (laboratoire Biomécanique et Bioingénierie)	Rapporteur
Jean Lerbet Professeur, Université d'Évry (Laboratoire de Mathématiques et Modélisation d'Évry)	Rapporteur
Alban Leroyer Maitre de conférence, École Centrale de Nantes (Laboratoire de recherche en Hydrodynamique, Énergétique et Environnement Atmosphérique)	Examinateur
Olivier Doaré Professeur, ENSTA Paris (Institut des Sciences de la Mécanique et Applications Industrielles)	Directeur de thèse
Jean-Sébastien Schotté Ingénieur de recherche, ONERA Châtillon (Département Aérodynamique, Aéroélasticité, Acoustique)	Co-directeur de thèse

Résumé en français

Cette thèse de doctorat porte sur la modélisation et la simulation des interactions fluide-structure entre un dirigeable souple, un écoulement externe et un gaz porteur interne. Du fait de leur grande taille, les dirigeables évoluent dans des écoulements dont le nombre de Reynolds est très élevé, ce qui permet de négliger les effets visqueux et ainsi considèrer que le fluide est potentiel. L'écoulement potentiel est résolu sur un maillage de l'interface fluide-structure grâce à la Méthode des Éléments de Frontière. Cette dernière est basée sur la représentation intégrale qui permet de calculer le potentiel de vitesse à l'interface uniquement en fonction de variables définies à l'interface et non pas dans tout le domaine fluide grâce à des fonctions adéquates appelées fonctions de Green. Ainsi, la méthode des éléments de frontière s'appuie sur un maillage surfacique de l'interface fluide-structure. Le travail des efforts de pression associé à l'écoulement est obtenu par la Méthode des Eléments Finis. Les équations du fluide sont exprimées dans un formalisme Arbitrairement Lagrangien-Eulérien consistant dans cette étude à suivre les mouvements des points matériels de l'interface dans la description du problème fluide. Afin de se ramener à des calculs sur un maillage de référence invariant, on considère de grands mouvements d'ensemble (rotations et translations) auxquels s'ajoutent de petits mouvements de corps rigides et de petites déformations par rapport auxquels le problème fluide est linéarisé. Cela conduit en pratique à différencier les opérateurs de la Méthode des Éléments de Frontière pour caractériser la cinématique du fluide ainsi que les opérateurs de la Méthode des Eléments Finis pour déterminer les efforts associés exercés sur l'interface fluide-structure, ceci afin de prendre en compte les perturbations dans le domaine fluide liées aux mouvements de l'interface. La linéarisation permet d'exprimer les efforts du fluide à l'aide d'opérateurs de masse, gyroscopique et de raideur ajoutés, proportionnels respectivement à l'accélération, la vitesse et les déplacements de l'interface. On montre que l'opérateur de masse ajoutée du fluide est indépendant des vitesse de corps rigide de la structure à l'ordre zéro conformément à la littérature, tandis que les opérateurs gyroscopiques et de raideur du fluide sont respectivement linéaires et quadratiques par rapport aux mouvements de corps rigide à l'ordre zéro. Cette dernière propriété permet prédire presque instantanément les fluctuations des opérateurs du fluide lorsque les mouvements de corps rigide à l'ordre zéro varient plutôt que de devoir les recalculer. Un modèle simplifié d'ailerons basé sur la théorie de Theodorsen quasi-statique est utilisé afin qe le modèle prenne en compte leur portance.

La partie structure du problème est modélisée à partir de la Méthode des Eléments Finis appliquée à une membrane. Celle-ci est précontrainte par la pression statique du fluide interne et de l'écoulement externe, dont les effets varient en fonction de la vitesse. Le modèle fluide-structure ainsi obtenu est utilisé pour étudier la stabilité d'un tel système couplé fluide-structure sur un cas test de dirigeable. Les opérateurs fluide-structure permettent d'obtenir les valeurs propres du système pour diverses vitesses du dirigeable. Le problème fluide-structure est coûteux à résoudre car les matrices de la Méthode des Éléments de Frontière sont pleines, et pour réduire la taille du problème, celui-ci est projeté sur une base réduite des modes de la structure dans le vide. On constate qu'en l'absence d'ailerons, le système fluide-structure est instable dès que la vitesse d'écoulement n'est pas nulle à cause du moment de Munk conformément à la littérature. La présence d'ailerons à la queue de l'appareil permet de le stabiliser jusqu'à une vitesse critique à partir de laquelle advient une divergence par flottement.

Enfin, la masse ajoutée obtenue par le modèle d'écoulement potentiel est comparée avec des résultats expérimentaux obtenus à partir d'une maquette rigide oscillant en rotation dans une cuve de fluide au repos. En faisant varier la fréquence d'oscillation de la maquette, la densité et la viscosité du fluide, on a pu caractériser, en fonction du nombre de Stokes, l'ordre de grandeur des efforts visqueux relativement aux efforts inertiels du fluide prédits pour un fluide potentiel.

Remerciements

Je tiens à remercier très chaleureusement Olivier Doaré et Jean-Sébastien Schotté pour avoir encadré ces travaux de doctorat avec beaucoup de rigueur, d'énergie et d'humanité à la fois.

Je remercie vivement les membres du jury qui ont porté un vif intérêt à ces travaux et l'ont beaucoup enrichi de leurs commentaires et remarques au cours des discussions lors de la soutenance.

Je remercie tous les collègues de laboratoire pour avoir su rendre une atmosphère de travail aussi agréable au cours de ces quatre années. Je remercie les stagiaires, doctorants et post-doctorants avec qui les pauses café furent agréables et réconfortantes. Je remercie les nombreux permanents de l'ENSTA qui, malgré leur charge de travail, ont si souvent donné de leur temps pour m'aider à avancer dans ce projet.

Je remercie ma compagne, mes colocataires et mes amis pour leur soutien moral indéfectible et tous les beaux moments partagés ensemble.

Enfin, je remercie ma mère et mon frère du fond du coeur, et je dédie ce manuscrit à mon père.

Contents

Chapter I

Introduction

I.1 Context of the study

Context

Airships are a mean of aerial locomotion for which the lift required to raise it into the air is provided by an internal carrier gas lighter than air: hydrogen or helium. Thanks to this, the lift is done at a lower energy cost than an airplane or helicopter whose lift is aerodynamic. Moreover, this allows the airship to make hovering flights without using energy. However, this is at the expense of controllability: large volumes of carrier gas are required, which makes the airships imposing and low-profiled. Consequently, the maneuverability of airships is very tedious, hence the need for accurate dynamic models to predict and improve their control.

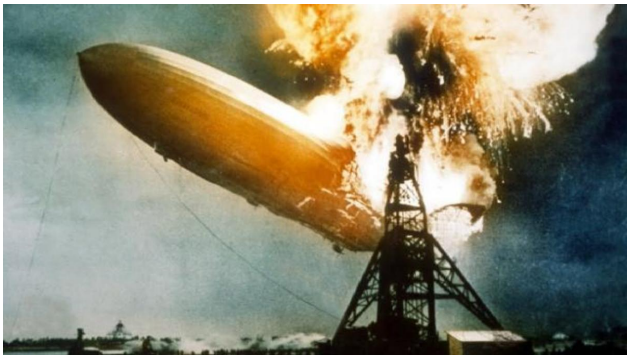

Figure I.1: Hidenburg disaster, 1937.

Airships were the first flying structure in history. However, the Hidenburg disaster which took place in 1937[1], consisting of the destruction of the airship during its docking as pictured in Figure I.1, has led to a sharp decline in interest in these devices. Nonetheless, a recent resurgence of demand is arising, with several contexts considered:

- Heavy load transport with projects such as the LCA-60T Flying Whales project[2] (funded by the Office National des Forets), forecasted to carry 60 ton loads. One can also mention the NATAC shuttle project by Voliris[3] and the Airlander 10 project by Hybrid Air Vehicles[4], two projects of airships slightly heavier than air but whose streamlined shape of the hull allows to ensure the necessary lift.
- Passenger transport for tourism with the Dirisolar DS1500 project[5].
- Stratospheric missions with the Stratobus project conducted by Thales Alenia Space[6], which will enable to perform missions of observation, telecommunication or others at an altitude of around 20km above the ground.

Contrarily to airships such as the Hidenburg filled with Hydrogen, a highly flamable gas, most recent airship project rely on helium as a lifting gas which is non-flammable. It is interesting to mention as well that both HAV and Voliris airships are hybrid airships, which means that they

[1] Hidenburg disaster Wikipedia page: https://en.wikipedia.org/wiki/Hindenburg_disaster
[2] Flying Whales company website: https://www.flying-whales.com
[3] Voliris company website: https://voliris.com
[4] Hybrid Air Vehicles company website: https://www.hybridairvehicles.com
[5] Dirisolar company website: http://dirisolar.com/Projets
[6] Thales Alenia Space communications about the Stratobus project: https://www.thalesgroup.com/en/taxonomy/term/7436

Figure I.2: Overview of current flexible airship projects. Top left: heavy lift NATAC project by Voliris, top right: heavy lift Airlander 10 project by Hybrid Air Vehicles, bottom: stratospheric missions Stratobus project by Thales Alenia Space.

are slightly heavier than air, which is compensated by the profiled shape of the hull enabling to generate lift (Manikandan and Pant, 2021), see Figure I.2.

There are three types of airships. Rigid airships consist of a rigid skeletonon on which the envelope is attached, containing non-pressurized carrier gas balloons. Semi-rigid airships have a rigid keel to support the airship envelope, but their shape is maintained by the internal pressure of the carrier gas. Finally, flexible airships have no keel nor skeleton, and the integrity of the membrane is ensured solely by the internal pressure. It is this solution which is retained for the great majority of the projects of recent airships (Li et al., 2011).

As an example, the current projects of airships are based on the following archetypes: Flying Whales and Dirisolar are rigid airships, while Stratobus, Airlander 10 and Voliris are flexible airship (see Figure I.2).

Overall scientific bottleneck

Although the internal pressure ensures the geometric integrity of the hull of non-rigid airships, it is necessary to ensure that the flexibility does not induce instabilities leading to the rupture or loss of control of the airships. Moreover, one should keep in mind that airships have much less experienced data than aircrafts which have been intensively studied over the past decades, and consequently the associated dynamic models are not as advanced and trustworthy.

Under these circumstances, the design of airships taking into account their flexible behavior in nominal or unfavorable flight conditions remains a scientific bottleneck for aeronautical engineers (Li et al., 2011). This is due to the lack of accurate models taking into account the interaction between the elastic membrane and the surrounding fluids, which justifies the research presented through this manuscript, consisting of the implementation of a model of the internal lifting gas and

the external flow effects on the dynamic behavior of a flexible airship.

The rest of chapter I presents in section I.2 an overview of the state of the art in the field of airship aerodynamics, rigid or flexible, stationary or dynamic. A key element of this work being the Boundary Element Method (BEM), a brief presentation of the associated state of the art is then presented, both concerning its application to potential flows, but also with respect to the works on its geometric differentiation, which is a key point of this research. Following this rather global overview of the literature, the section I.3 presents in more detail some classical results from the literature. First, a reminder of the equations associated with incompressible potential flows in an Eulerian formalism is given. Then, the integral representation associated with the velocity potential is presented, which is a key element for the implementation of the BEM, allowing to "condense" the kinematic equations of the fluid at the fluid-structure interface.

In chapter II, the objective is to introduce an original model of the fluid forces based on a Newtonian approach (contrary to the literature mainly focused on Lagrange equations). In order to take into account the moving interface in a practical way, the integral representation of the fluid velocity potential is expressed according to an Arbitrary Lagrangian-Eulerian (ALE) formalism, drawing inspiration from studies such as (Pfister, 2019; Mavaleix-Marchessoux, 2020). The fluid variables (velocity potential, pressure and virtual power), which depend on the large rigid body motions of the interface (large translations and large rotations), are then linearized with respect to the small elastic and rigid body displacements of the interface. The consideration of linearized forces due to small deformations in the context of large rotations of the structure is an aspect that is, to the author's knowledge, an original contribution of the thesis and was cited as a scientific lock in the work of (Li et al., 2009). The linearized forces can then be expressed in terms of fluid mass, gyroscopic and stiffness operators, respectively linear with the acceleration, velocity and displacements of the interface, in a similar fashion to (Li et al., 2009). It is shown in the manuscript that these three operators are respectively independent, linear and quadratic with regard to the six rigid body motions of the structure, allowing to decompose the calculation of these operators associated to any rigid body motion depending on contributions from each translation and rotation. Finally, it is shown that, contrary to the Newtonian approach introduced in this manuscript, the prediction of linear fluctuations of the fluid forces on the interface using an approach via Lagrange's equations would require the computation of the second order fluctuations of the geometric variables as well as of the velocity potential, thus justifying the use of the Newtonian approach in this study.

In Chapter III, the objective is to introduce and validate a numerical method to predict the fluid operators put into equations in Chapter II. A numerical implementation of the linearized BEM based on the theoretical model introduced in Chapter II is presented. The computation of the linearized BEM operators taking into account the deformations of the structure is, to the author's knowledge, an originality of this work. In order to accelerate their numerical computation, the Hierarchical Matrix Method has been implemented on the usual BEM operators, then adapted to the case of the linearized BEM operators introduced in this study. The fluid forces can thus be computed using a Finite Element Method (FEM)-BEM coupling. The classical BEM operators have been validated by comparing the associated solution with analytical solutions linked to an ellipsoid. The linearized FEM-BEM operators have been validated by comparing the linear fluctuation results predicted by the model with the nonlinear fluctuation results obtained using the finite difference method with mesh deformation. The numerical solution of the potential fluid associated with a stationary flow around an airship is then qualitatively compared with a RANS simulation.

In Chapter IV, the effects of internal and external fluids on the flexibility of an airship are studied. For this purpose, a dynamic model of the structure is presented, taking into account

non-linear effects associated with the internal pressure as well as dynamic elastic deformations around the prestressed state. The associated operators are calculated numerically using the FEM. Thanks to the monolithic equation obtained by coupling the FEM operators of the structure and the FEM-BEM operators of the fluid, the associated eigenvalues can be calculated as a function of the flow velocity, which allows to predict the risks of instabilities of the airship by divergence or flutting. The stabilizing effect of the fins are then introduced numerically and the new associated eigenvalues are studied.

Finally, in Chapter V, the added mass results obtained from potential flow theory are compared with experimental results acquired from rotating oscillations of an ellipsoidal model in a pool of water at rest. First, a model allowing to obtain an order of magnitude of the viscous forces of the fluid as a function of the frequency, density and viscosity of the fluid, or more generally as a function of the Stokes number which takes into account these three parameters, is introduced. In this section, the equation of the fluid stresses is dimensionless, enabling to put forward similarities between flows with equivalent non-dimensional parameters. The experimental setup allows to verify the relationship between the fluid forces and the Stokes number and to verify experimentally whether or not the predicted similitude is observed.

Each chapter will be followed by a small conclusion as well as associated perspectives. Then, a general conclusion of the thesis work will be presented, which will first put forward the scientific bottlenecks unlocked thanks to this manuscript, then to what extent this approach concurs or stands out from the state of the art, and then give possible perspectives in order to deepen the modeling of the effects of the internal and external fluids on the dynamics of the flexible airships. Following this are the appendices, and finally the list of sources cited throughout this manuscript.

I.2 State of the art

Before presenting in detail the model on which this study will be based, this section gives an overview of the state of the art, first in the field of airships, whether rigid or flexible, in a stationary or dynamic framework. Then, important works of the literature associated with potential flows solved using an integral representation, as is the case for BEM, are presented.

I.2.1 Airships aerodynamics

This section is largely based on the comprehensive literary review compiled by (Li et al., 2011), to which the reader may refer for more exhaustive information on the field, but it is also supplemented by studies from the last decade.

Stationary rigid airships

Numerous studies were focused on the hovering of rigid airships, either experimentally in wind tunnels (Jones and Bell, 1929; Freeman and Wheatley, 1932; Funk et al., 2003) or more recently from CFD (Jakobi et al., 2000; Lutz et al., 2002; Kale et al., 2005) amongst other studies listed by (Li et al., 2011). Lutz et al. (2002) based themselves on a coupling of the Panel Method and were able to compare their results with wind tunnel experiments on the Lotte airship. More recently, Carbone et al. (2020) compared Reynolds Averaged Navier-Stokes (RANS) simulations around an ellipsoidal shape with wind tunnel measurements, showing a good agreement between the two methods.

Dynamics of rigid airships

The prediction of the unsteady forces of the flow around a rigid airship is critical because these forces are involved in many situations: during maneuvers when the airship is rotating, taking off, landing, or in the presence of gusts.

Unlike the field of aviation where the phenomenon of added mass is often negligible, the inertia of the fluid surrounding airships is of the same order of magnitude as the inertia of the structure itself due to the lightness of airships (Li et al., 2011).

The study of Thomasson and Woolsey (2013) based on Lagrange's equations shows how the 6×6 rigid matrix of added mass associated with the effects of inertia according to rotations and translations allows to calculate the effects of inertia of an inhomogeneous, unsteady flow on a rigid structure in motion in the framework of potential flows. This added mass matrix depends only on the properties of the geometry of the structure and the density of the fluid. The resulting forces then depend on both the acceleration and velocity of the structure. The calculation of the rigid added mass operator of airships can be done using the BEM, which is well mastered by the airship scientific community (Li et al., 2011).

Carbone et al. (2019) predicted numerically the added mass of airships near obstacles. They developed a BEM code to calculate the added mass. The structure as well as the obstacles are meshed. This BEM code was applied to structures in an infinite fluid domain or near walls in order to validate the numerical results. Then the influence of more complex obstacle shapes such as mountains on the added mass was studied. The limitations of this study are that the model does not take into account the fluid effects other than the added mass.

In order to predict the unsteady forces of the flow, Li and Nahon (2007) solved the nonlinear forces of a perfect fluid flow around a rigid ellipsoid based on the works of Thomasson (2000). They used Lagrange's equations associated with the velocity potential of the fluid, solved analytically around an approximation of the airship shape as an ellipsoid. The dynamic model thus takes into account the potential forces of the fluid, to which are added in particular the effects of lift of the fins and turbulence at the tail of the airship. These different forces are taken into account by distinct models. They were thus able to simulate the behavior of an airship and compare these simulations with experimental flight tests. The non-linear model was also linearized to study the stability of the airship. This made it possible to validate their model by comparison with CFD calculations and experimental results. The stability analysis showed that the flow almost always has a stabilizing effect on a rigid airship. The limitations of this study are that the effects of potential flow and the lift of the fins were taken into account by separate methods and not by a single homogeneous model. Moreover flexibility is not considered in this study, but will be in a later published article discussed below.

Airships are particularly sensitive to gusts because of their large size. Thus, Reynolds Average Navier Stokes (RANS) simulations were used by Carbone et al. (2020) to predict gust forces on a non-profiled ellispoïd body. (Carbone, 2020) also computed a slice model to predict gust forces at lower cost than RANS simulations, and compared the RANS results with the slice model. This allowed for the characterization of the lift and pitching moment forces generated by a gust, in agreement with the results of Kanoria et al. (2015). This also validated the suitability of the slice-based model to predict the efforts of a gust at a lower cost. The limitations of this study of gust forces come from the fact that a non-profiled body was considered, in the absence of fins used for airships.

Flexible stationary airships

The deflection of airships under aerodynamic loads was already investigated in the eighties by Hunt (1982). The approach consisted in coupling a FE model of a tethered aerostat with aerodynamic loads of the external flow obtained by interpolating pressure data from wind tunnel tests. This approach allowed for a rough prediction of the stress concentration zones to verify if the structural elements appeared to be correctly dimensioned.

The development of more powerful computational tools helped to improve the accuracy of the methods used to study the deflection of airships. Bessert and Frederich (2005) used the Panel Method on a three-dimensional mesh to predict the deformations of an airship under the effect of a stationary flow. The mesh includes the hull, the fins and a wake surface behind their trailing edge. The Panel Method allows to obtain the fluid forces for a much lower cost compared to RANS simulations for example. The counterpart is that the turbulent effects are not taken into account. The non-linear deformations of the structure are calculated using FEM. The results are compared to those obtained for linear deformations. This allowed the calculation of the nonlinear deformations associated with the flow for various angles of attack. The associated lift coefficient was also obtained. An extension of the model to dynamics was made by calculating the derivatives of the forces according to the rigid body movements of the airship around the deformed position. The study allowed to highlight the strongly non-linear character of the deformations due to the flow by the important difference of lift between the linear and non-linear structure models. Finally, the stability analysis allowed them to show that the flexibility effects tended to stabilize the structure. The limitations of this study come from the fact that the dynamic effects are taken into account only by deriving from the rigid body motions, and not from the elastic motions. Moreover, since the Panel Method is based on potential flow theory, turbulence effects are not taken into account.

El Omari et al. (2004) used a different approach: they also assumed an inviscid flow, however the fluid was solved using the Mixed Element Volume discretization, requiring to mesh a large volume of fluid contrarily to the approach of Bessert and Frederich (2005). Consistently with the literature (Amiryants et al., 2002; Bessert and Frederich, 2005), their study highlighted the predominance of the first bending mode in the flexible behavior of the airship. The static flexible solution was determined more precisely by Liu et al. (2010) and Wu et al. (2015) using Reynolds-Averaged Navier-Stokes (RANS) methods. Moreover, Wu et al. (2015) were able to compare their numerical results with a wind tunnel experiment, showing good comparison with respect to the global deformations of the model.

However, the cost of RANS calculations is prohibitive for large dynamic fluid-structure coupled problems such as airships (Li et al., 2011) (especially if the flexibility of the structure comes into play) , hence the need for simplified approaches such as those presented in the following section.

Dynamics of flexible airships

In order to study the linear stability of a tethered aerostat, Lambert and Nahon (2003) used finite differences to obtain the linear fluctuations of aerodynamic forces as a function of the aerostat movements.

Airships altitude and pitch can be controlled through the inflation or deflation of internal balloons containing gas called the ballonets. These inflated structure are not rigid, and therefore have their own dynamical behaviour which has been studied by Maekawa and Saito (2004) using a cylindrical tank analytical model to predict the influence of the ballonets on the dynamics of

the airships, enabling to predict specific operating conditions where ballonet slosh may become an important design issue. More complete coupling methods between elastic structures and free surface liquids have been used for stability analysis in the litterature such as Ohayon (2004) but have not been applied to airship ballonet dynamics yet.

Based on some simplification hypothesis, Destuynder and Santi (2006) derived an analytic dynamic aeroelastic model of an airship in a flow, leading to a formulation of the fluid forces based on aerodynamical mass, damping and stiffness operators.

In their study, Amiryants et al. (2002) predicted the effects of a flow on the stability of a flexible airship. They have simplified the geometry into two surfaces obtained by projection of the volume according to a horizontal and a vertical plane. These two surfaces were meshed and used to predict the fluid forces using the Panel Method in order to take into account the effects of fluid circulation around the hull and the fins. The dynamics of the structure were calculated using the FEM. An equivalent beam model was compared to the full structure model. The response of the flexible airship to the gust was studied, and a stability analysis was performed. Their study showed that beam models can accurately capture the dynamics of the structure. The motions of the structure were projected onto the rigid body motions and the first bending modes of the structure. This allowed the authors to perform a stability analysis for various flow velocities. This study made it possible to predict the appearance of a flutter instability at a critical speed. In particular, they observed that the flutter involves the first bending mode. The limitations of this study come from the fact that the internal fluid was not taken into account in the dynamics of the airship. In addition, the movements of large rotation of the structure were not be taken into account. Finally, the approximation of the shape of the structure by projection of the volume according to vertical and horizontal surfaces is not very realistic for the hull which is not very profiled.

In their studies, Bennaceur et al. (2006); Bennaceur (2009) studied flexible airships in a perfect, potential fluid. They considered rigid-body movements and bending modes by approximating the fluid-structure interface as a cylinder deformed as a cosine function, and solved in cylindrical coordinates the ideal fluid dynamical equations based on Lagrange's equations. This approximated model helped them to compute the trajectories of a flexible airship and compare it with rigid airship results to estimate the effects of flexibility. Azouz et al. (2012); Chaabani (2014) carried on these works: the potential flow solution around an airship with an unconventional shape was found analytically using Lamé's functions based on a sphero-conal approximation of the shape of the airship. In this work, the coupling between the deformations of the airship and its large rotations has been partially taken into account.

Li et al. (2009) extended their rigid airship model commented above to the case of flexible airship motions. They projected the elastic motions according to the first bending modes of the airship computed with a beam model: According to Amiryants et al. (2002), the airship deformations were correctly predicted with this model. They calculated the linear fluctuations of the fluid forces by combining the forces of the fins and the turbulent forces at the tail of the airship with the potential forces of the flow. Those fluctuations were predicted using the linearized Lagrangian equations, coupled with the thin profile approximation which consists in neglecting some three-dimensional effects of the flow due to the elongation of the structure. The resulting model was then used to characterize the gust response of flexible airships and determine the influence of the structure's flexibility on it. Finally, a stability analysis of the flexible airship was carried out. The stability analysis done for various longitudinal flow velocities revealed a risk of flutter by coupling of the first bending mode with the pitching mode of the structure, consistent with the results of Amiryants et al. (2002). The limitations of this study come from the fact that the internal fluid and the

associated prestressing effects were not taken into account. Moreover, the potential flow forces were integrated around an ellipsoidal interface and not around a real airship shape. Contrary to the study of Bessert and Frederich (2005), the prediction of the lift forces of the fins and the potential forces around the airship were not taken into account from a single and unified model. Moreover, the fluid forces were linearized around an order zero longitudinal translation speed: order zero diving movements or large rotations could not be taken into account.

Now that the state of the art on airship aeroelasticity has been presented, the following section will look at the coupling between structures and potential flows solved using an integral representation, as is the case with the BEM in the work presented later in this manuscript. Then, some studies in the literature that have used geometric differentiation of the BEM in various contexts are presented.

I.2.2 Boundary Element methods for potential flows

As presented in more detail in Chapter III, the BEM is a numerical calculation method based on an integral representation, which has the advantage of solving a numerical problem whose unknowns are localized only on an interface. Thus, in the case of an airship for example, the flow will be solved using a surface mesh of the fluid-structure interface, and not from a volume mesh of the fluid as is the case with methods such as Finite Volume Method. According to Morino and Gennaretti (1992), Boundary Element Methods can be classified into two categories, "direct methods" and "indirect methods". Indirect methods allow to compute a solution based on fundamental solutions of the Laplace equation such as sources, doublets or vortices. Such methods have been used in the airship literature, as for instance the study of Amiryants et al. (2002) based on the Doublet Lattice Method to model unsteady potential flows around profiled bodies supposed to be infinitely thin. Let us also mention the study of Bessert and Frederich (2005) based on the Panel Method which takes into account the thickness of the profiles. The direct methods are based on the direct resolution of the unknowns of the problem, such as the velocity potential, the acceleration potential or the pressure distribution. As this work is based on these methods, the associated literature is presented with more details in the following section.

Direct BEM for potential flows

The resolution of potential flows using the BEM has been used in recent problems of fluid-structure interaction. For example, we can mention the work of Veron et al. (2016) who studied the dynamical interaction of flexible pipes with an external fluid and an internal flow. More recently, the behavior of submarines subjected to underwater explosions has been simulated by Mavaleix-Marchessoux (2020). These last two studies have both used partitioned approaches: the fluid-structure problem is separated into two sub-problems, one fluid and one structure. Each of these sub-problems is solved in turn with as input the deformation or pressure field obtained by solving the complementary sub-problem. The pressure or deformation field obtained is used as data to solve the other sub-problem again, iterating until convergence.

In the work of Morino and Gennaretti (1992), the BEM is used in an aeronautical context, for planes as well as helicopter rotors. Unlike Veron et al. (2016); Mavaleix-Marchessoux (2020), their model includes a wake sheet that takes into account circulations generated by profiled bodies.

Now that we have presented works involving the BEM associated with potential flows to solve fluid-structure interaction problems in different industrial contexts, illustrating the pertinence of

the method in different fields of study, the following section will present, in a non-exhaustive way, studies that have focused on the domain differentiation of the BEM.

Domain differentiation of boundary integral equations

As mentionned by Bonnet (1999), the first derivative of the integral representation on which the BEM is based plays a crucial role in various physical problems. Amongst those, we might consider the study of Potthast (1994) who used domain differentiation of the BEM operators in the domain of acoustics, or Costabel and Le Louër (2012) in the field of electromagnetic scattering. Nishimura and Kobayashi (1991) used this method in order to detect cracks and Mukherjee and Chandra (1991) for design sensitivity purposes in nonlinear solid mechanics.

However, to the author's knowledge, domain differentiation has not yet been introduced in the framework of potential, incompressible flows as is done in this manuscript.

I.3 Problem overview and general equations

With a view to predicting how the fluid affects the structure trajectory, we are seeking for an explicit expression of its work with respect to the interface movements. The Euler equations for an incompressible, irrotational flow are thus reminded to the reader in this section. The integral representation is introduced so as to condense the kinematic equations of the flow at the interface, enabling to reduce the dimension of the fluid unknowns, both for the external and internal fluid cases. The combination of the Euler equations and the integral representation is a well posed problem, making it possible to to obtain an implicit expression of the work of the fluid with respect to the interface movements. The equations developed in section I.3.1 have already been intensively studied in the litterature: see for example Lamb (1918), Newman (2018), and Katz and Plotkin (2001) for the Euler equations of potential flows and Bonnet (1999), Posrikidis (2002) or Hackbusch (1995) for integral equations. These equation are introduced as a preamble in this introductory chapter.

I.3.1 Euler equations for inviscid, incompressible flows

The equations for an incompressible potential flow have been intensively studied in the litterature (Katz and Plotkin, 2001; Newman, 2018; Nitikitpaiboon and Bathe, 1993; Morand and Ohayon, 1995; Li et al., 2009; Veron et al., 2016; Mavaleix-Marchessoux, 2020), and this section introduces them with the aim of modeling the work of the fluid on the fluid-structure interface.

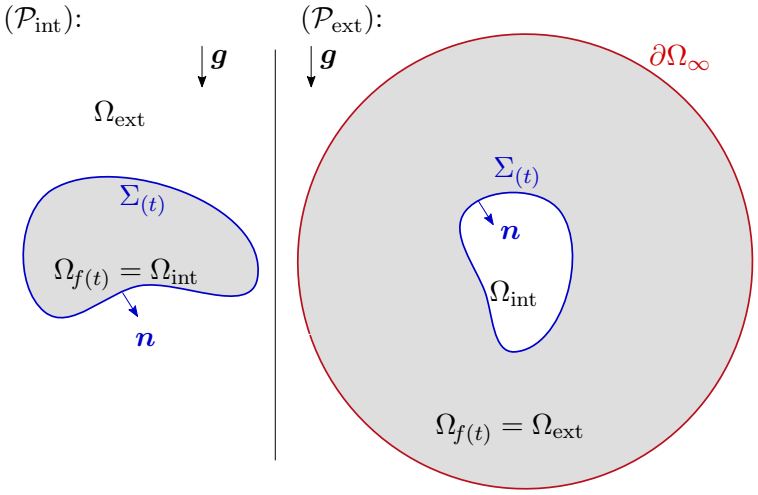

Figure I.3: Geometry of the internal fluid problem $(\mathcal{P}_{\text{int}})$ and the external fluid problem $(\mathcal{P}_{\text{ext}})$.

In the following manuscript, the vectors will be in bold notation and the order 2 tensors will be double-struck. Let us consider a fluid-structure interface $\Sigma_{(t)}$ that moves in a potential fluid at rest in the domain $\Omega_{f(t)}$, as sketched in figure I.3. In this section, two distinct problems will be dealt with: the internal problem $(\mathcal{P}_{\text{int}})$ where the fluid fills an enclosed domain Ω_{int} which is associated with the lifting gas for airship, and the external problem $(\mathcal{P}_{\text{ext}})$ where the fluid at rest is in the unbounded domain Ω_{ext}. The unit normal $\boldsymbol{n}$ at the interface $\Sigma_{(t)}$ is arbitrarily set to be outward the fluid domain, hence toward Ω_{ext} for $(\mathcal{P}_{\text{int}})$ and toward Ω_{int} for $(\mathcal{P}_{\text{ext}})$, enabling to apply the divergence theorem consistently. The time is denoted t and the spatial coordinates are denoted $\boldsymbol{x}$. With a view to having a coherent coupling between the weak formulation of the structure model in chapter III, the aim of this chapter is to calculate the virtual power of the fluid $\delta\mathcal{P}_f(\delta\boldsymbol{v})$ associated

with a virtual, infinitesimal displacement $\delta\boldsymbol{v}$ of the interface $\Sigma_{(t)}$ separating the solid and fluid domain. The velocity $\boldsymbol{v}$ of a structural material point of position $\boldsymbol{x}$ at the interface is defined as:

$$\boldsymbol{v}(\boldsymbol{x},t) = \frac{\partial \boldsymbol{x}}{\partial t}, \quad \boldsymbol{x} \in \Sigma_{(t)}. \tag{I.1}$$

We define the characteristic length L, velocity V and frequency Ω of the structure as well as their dimensionless counterparts $\boldsymbol{v}^*$, t^* and $\boldsymbol{x}^*$ such that:

$$\boldsymbol{v}^* = \frac{\boldsymbol{v}}{V} \sim 1 \quad \text{on } \Sigma_{(t)} \tag{I.2a}$$

$$\frac{\partial \boldsymbol{v}^*}{\partial t^*} = \frac{1}{V\Omega}\frac{\partial \boldsymbol{v}}{\partial t} \sim 1 \quad \text{on } \Sigma_{(t)} \tag{I.2b}$$

$$\boldsymbol{x}^* - \boldsymbol{y}^* = \frac{\boldsymbol{x}-\boldsymbol{y}}{L} \sim 1, \quad \forall \boldsymbol{x},\boldsymbol{y} \in {\Sigma_{(t)}}^2, \tag{I.2c}$$

where the notation $a \sim b$ means "a has the same order of magnitude as b". At the scale of airships, the velocity of the structure is much lower than that of the sound in air c, and the Mach number M_a verifies

$$M_a = \frac{V}{c} < 0.3. \tag{I.3}$$

The flow can be hence be considered as incompressible:

$$\boldsymbol{\nabla}\rho_f = \boldsymbol{0} \quad \text{in } \Omega_{f(t)}. \tag{I.4}$$

This property makes the conservation of mass equation equivalent to the conservation of volume equation, which writes as a function of the velocity of the fluid $\boldsymbol{u}$:

$$\boldsymbol{\nabla}\cdot\boldsymbol{u} = 0 \quad \text{in } \Omega_{f(t)}. \tag{I.5}$$

Remark

In the very case of airships, the incompressibility of the flow is not verified during the ascent phase, where the elevation of the structure in the sky causes the density of the atmosphere to vary. However, the hypothesis is valid when considering maneuvers around a nominal operating altitude (Li and Nahon, 2007).

For the internal problem $(\mathcal{P}_{\text{int}})$, one might note that the incompressibility condition of the fluid implies a restriction on the flux at the boundaries which can be obtained using the divergence theorem, recalling the $\Sigma_{(t)}$ encloses $\Omega_{f(t)} = \Omega_{\text{int}}$:

$$\begin{aligned} \boldsymbol{\nabla}\cdot\boldsymbol{u} = 0 \quad \text{on } \Omega_{f(t)} &\Rightarrow \int_{\Omega_{f(t)}} \boldsymbol{\nabla}\cdot\boldsymbol{u}\,\mathrm{d}\Omega = 0 \\ &\Rightarrow \int_{\Sigma_{(t)}} \boldsymbol{u}\cdot\boldsymbol{n}\,\mathrm{d}\Sigma_{(t)} = 0 \quad \text{for } (\mathcal{P}_{\text{int}}). \end{aligned} \tag{I.6}$$

Equation (I.6) ensures that the net flux in the internal incompressible fluid domain is equal to zero. However, this condition does not apply to the external problem ($\mathcal{P}_{\text{ext}}$), because a non nil net flux at the interface $\Sigma_{(t)}$ can be compensated by fluid fluxes remotely on the unbounded fluid domain. The thermal effects in the fluid region are neglected in this manuscript: the flow is considered adiabatic. For an adiabatic flow with uniform and constant density, the relationship between the velocity of the fluid $\boldsymbol{u}$ and the pressure p is given by the momentum equation for incompressible fluids as part of the Navier-Stokes equations:

$$\rho_f \left(\frac{\partial \boldsymbol{u}}{\partial t} + \nabla \boldsymbol{u}\, \boldsymbol{u} \right) = -\boldsymbol{\nabla} p + \rho_f \boldsymbol{g} + \mu_f \Delta \boldsymbol{u} \quad \text{in } \Omega_{f(t)}. \tag{I.7}$$

In the above equation, μ_f is the dynamic viscosity of the fluid and $\boldsymbol{g}$ is the oriented acceleration of gravity. Furthermore, the continuity of velocity at the fluid-structure interface reads:

$$\boldsymbol{u} = \boldsymbol{v} \quad \text{on } \Sigma_{(t)}. \tag{I.8}$$

In a fluid at rest, the velocity of the flow is imposed by the structure movements. Therefore, one can deduce from equation (I.8) and its time derivative that the velocitiy and the acceleration of the fluid and of the structure are of the same order of magnitude:

$$\boldsymbol{u}^* = \frac{\boldsymbol{u}}{V} \sim 1 \qquad \text{in } \Omega_{f(t)} \tag{I.9a}$$

$$\frac{\partial \boldsymbol{u}^*}{\partial t^*} = \frac{1}{V\Omega} \frac{\partial \boldsymbol{u}}{\partial t} \sim 1 \qquad \text{in } \Omega_{f(t)}. \tag{I.9b}$$

The dimensionless pressure p^* is introduced as well, even though no information enables to ensure of its order of magnitude at this stage of the model development:

$$p^* = \frac{p}{\rho_f V^2} \quad \text{in } \Omega_{f(t)}. \tag{I.10}$$

Further considerations on the order of magnitude of p^* are given later in equation (I.18), under the assumption that the characteristic spatial variations of the flow are of the order of the structure length L, one verifies:

$$\nabla^* \boldsymbol{u}^* = \frac{L}{V} \nabla \boldsymbol{u} \sim 1 \qquad \text{in } \Omega_{f(t)} \tag{I.11a}$$

$$\Delta^* \boldsymbol{u}^* = \frac{L^2}{V} \Delta \boldsymbol{u} \sim 1 \qquad \text{in } \Omega_{f(t)}. \tag{I.11b}$$

Finally, the Reynolds $\mathcal{R}_{\text{e}}$, Stokes $\mathcal{S}_t$ and Froude $\mathcal{F}_r$ numbers are introduced, noting g the amplitude of gravity acceleration:

$$\mathcal{R}_e = \frac{\rho_f V L}{\mu_f} \tag{I.12a}$$

$$\mathcal{S}_t = \frac{\rho_f \Omega L^2}{\mu_f} \tag{I.12b}$$

$$\mathcal{F}_r = \frac{\sqrt{\rho_f g}}{V}. \tag{I.12c}$$

The ratio between the advective acceleration ($\nabla \boldsymbol{u}\, \boldsymbol{u}$) and the viscous effects is quantified by $\mathcal{R}_e$, $\mathcal{S}_t$ quantifies the ratio between the local acceleration ($\partial \boldsymbol{u}/\partial t$) and the viscous effects, and $\mathcal{F}_r$ is a ratio between inertial and gravity effects. By combining equations (I.7) and (I.12), the momentum equation can be rewritten under the non-dimensional form:

$$\mathcal{S}_t \frac{\partial \boldsymbol{u}^*}{\partial t^*} + \mathcal{R}_e \nabla^* \boldsymbol{u}^*\, \boldsymbol{u}^* = -\mathcal{R}_e \boldsymbol{\nabla}^* p^* + \mathcal{R}_e \mathcal{F}_r^{-2} \boldsymbol{e}_g + \Delta^* \boldsymbol{u}^* \quad \text{in } \Omega_{f(t)}. \tag{I.13}$$

The unit vector $\boldsymbol{e}_g = \boldsymbol{g}/g$ is is the direction of the gravity acceleration. In this thesis, either the Reynolds number or the Stokes number are supposed to be much larger than unit:

$$\max(\mathcal{R}_e, \mathcal{S}_t) \gg 1, \tag{I.14}$$

meaning that the viscous terms $\Delta^* \boldsymbol{u}^*$ plays a negligible role in the momentum equation (I.13) compared to the inertial terms (either from the local acceleration $\partial \boldsymbol{u}/\partial t$ for $\mathcal{S}_t \gg 1$ or from the convective acceleration $\nabla \boldsymbol{u}\boldsymbol{u}$ for $\mathcal{R}_e \gg 1$). Consequently, we consider the model of an inviscid fluid (since the thermal effects are neglected as well, it might be referred to as an ideal fluid), leading to the Euler equation for the conservation of momentum:

$$\mathcal{S}_t \mathcal{R}_e^{-1} \frac{\partial \boldsymbol{u}^*}{\partial t^*} + \nabla^* \boldsymbol{u}^*\, \boldsymbol{u}^* = -\boldsymbol{\nabla}^* p^* + \mathcal{F}_r^{-2} \boldsymbol{e}_g \quad \text{in } \Omega_{f(t)}. \tag{I.15}$$

The reduced velocity $\mathcal{U}_r$, commonly used in the field of aerodynamics (Katz and Plotkin, 2001), is introduced as the ratio between the velocity of the structure and the characteristic velocity ΩL:

$$\mathcal{U}_r = \frac{V}{\Omega L}, \tag{I.16}$$

From (I.15) and (I.16) can be deduced the magnitude of the pressure spatial variations, noting that $\mathcal{U}_r = \mathcal{R}_e \mathcal{S}_t^{-1}$:

$$\boldsymbol{\nabla}^* p^* \sim \max\left(1, \mathcal{U}_r^{-1}, \mathcal{F}_r^{-2}\right) \quad \text{in } \Omega_{f(t)}. \tag{I.17}$$

An expression with dimensions equivalent to the above equation can be obtained by multiplying it by :

$$p(\boldsymbol{x}) - p(\boldsymbol{y}) \sim \begin{cases} \rho_f V^2 & \text{if } \mathcal{U}_r \gg 1 \,\&\, \mathcal{F}_r^2 \gg 1 \\ \rho_f \Omega V L & \text{if } \mathcal{U}_r \ll 1 \,\&\, \mathcal{U}_r \ll \mathcal{F}_r^2 \\ \rho_f g L & \text{if } \mathcal{F}_r^2 \ll 1 \,\&\, \mathcal{F}_r^2 \ll \mathcal{U}_r \end{cases} \quad \forall \boldsymbol{x}, \boldsymbol{y} \in \Sigma_{(t)}. \tag{I.18}$$

The two first line of equation (I.18) concern the case where gravity effects are negligible. The first line traduces that the pressure effects of a stationary flow around a structure are of the order of $\rho_f V^2$, referred to as dynamic pressure effects. When the structure undergoes large accelerations, the pressure forces are of the order of $\rho_f \Omega V$ as shown in the second line. The term ΩV is the acceleration amplitude of the structure, and the resulting pressure will cause an added mass effect because of the inertia of the fluid surrounding the structure (Lamb, 1918). The predominance of aforementioned effects is given by the parameter $\mathcal{U}_r$: for large reduced velocity, the dynamic pressure effects will dominate while added mass effects dominate at small reduced velocity. For an immobile structure, the pressure is of the order of $\rho_f g L$ as is shown in the third line.

The Euler equation for the conservation of momentum (I.15) can be rewritten with dimensional variables:

$$\rho_f \left(\frac{\partial \boldsymbol{u}}{\partial t} + \nabla \boldsymbol{u}\, \boldsymbol{u} \right) = -\boldsymbol{\nabla} p + \rho_f \boldsymbol{g} \quad \text{in } \Omega_{f(t)}. \tag{I.19}$$

For an inviscid fluid, the continuity of the velocity (I.8) is replaced by the continuity of the normal velocity, the absence of strain forces enabling the fluid to freely slide tangentially to the interface:

$$\boldsymbol{u} \cdot \boldsymbol{n} = \boldsymbol{v} \cdot \boldsymbol{n} \quad \text{on } \Sigma_{(t)}. \tag{I.20}$$

By combining the no slip condition (I.20) with the incompressibility condition for the internal problem (I.6), one gets the following restriction for the movements of the interface on the internal problem:

$$\int_{\Sigma_{(t)}} \boldsymbol{v} \cdot \boldsymbol{n}\, \mathrm{d}\Sigma_{(t)} = 0 \quad \text{for } (\mathcal{P}_{\text{int}}), \tag{I.21}$$

which means that $\boldsymbol{v}$ must be part of the kinematically admissible $\mathcal{K}^{\mathcal{A}}_{\text{isoV}}$ fields(where isoV stands for iso volume since the volume enclosed by the interface is conserved) for the internal problem :

$$\boldsymbol{v} \in \mathcal{K}^{\mathcal{A}}_{\text{isoV}} = \left\{ \boldsymbol{v} \in \mathcal{C}^1 \left(\Sigma_{(t)}, \mathbb{R}^3 \right) \;\middle|\; \int_{\Sigma} \boldsymbol{v} \cdot \boldsymbol{n}\, \mathrm{d}\Sigma = 0 \right\}. \tag{I.22}$$

where $\mathcal{C}^1$ is the space of continuous functions with continuous derivatives. Before using the equations above to obtain the expression of the virtual pressure, the magnitude of viscous strains at either large Reynolds or large Stokes are investigated in the following section.

On the inviscid fluid hypothesis

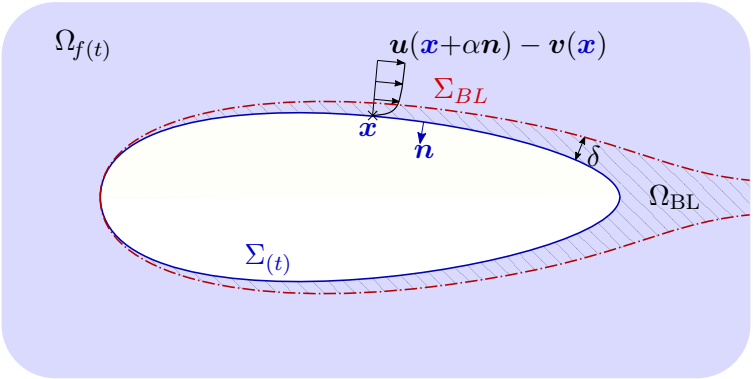

Figure I.4: Laminar boundary layer developing around an interface (in the case of a structure moving toward the left of the figure). $\boldsymbol{u}(\boldsymbol{x}+\alpha\boldsymbol{n}) - \boldsymbol{v}(\boldsymbol{x})$ gives the velocity profile of the flow relative to the interface velocity. The boundary layer $\Omega_{\text{BL}} \subset \Omega_{f(t)}$ of thickness δ is enclosed between the interface $\Sigma_{(t)}$ and its edge Σ_{BL}.

It is important to mention that, close to the fluid-structure interface, there is a boundary layer region Ω_{BL} where the fluid velocity develops, with $\boldsymbol{u} = \boldsymbol{0}$ at the interface $\Sigma_{(t)}$. This boundary layer

is studied in the following paragraphs. First, the case of a stationnary flows boundary layer, hence with $\mathcal{U}_r \gg 1$, is investigated since it is more documented than the case of unstationnary flows in the literature. The normal velocity being almost constant in the boundary layer (Schobeiri, 2010; Darrozès and François, 1982), one can deduce that the condition (I.20) is verified at the edge of the boundary layer Σ_{BL}, and not at the fluid-structure interface $\Sigma_{(t)}$. Moreover, in the region Ω_{BL}, the hypothesis on the order of magnitude $\Delta^*\boldsymbol{u}^*$ from equation (I.11) related to L is not verified since the magnitude of the boundary layer thickness δ intervenes too. Hence, it would make more sense to solve the velocity of the fluid with the boundary condition on Σ_{BL} instead of $\Sigma_{(t)}$, and use the Euler equation (I.19) only in the fluid domain $\Omega_{f(t)} \backslash \Omega_{\mathrm{BL}}$. However, if we consider a laminar, attached boundary layer, the velocity of the fluid develops in this boundary layer of thickness δ (the definition of the latter is arbitrary and can vary from one approach to another). As Schobeiri (2010) explains with the help of a flat plate model, one can estimate the relative thickness δ/L of the boundary layer as:

$$\frac{\delta}{L} \sim \mathcal{R}_e^{-\frac{1}{2}}. \tag{I.23}$$

Therefore, if we consider a large enough Reynolds number $\mathcal{R}_e^2 \gg 1$, the difference between the geometry of the fluid domains $\Omega_{f(t)}$ and Ω_{BL} delimited by $\Sigma_{(t)}$ and Σ_{BL} becomes negligible relatively to the size of the structure. Consequently, using the boundary condition (I.20) on $\Sigma_{(t)}$ instead of Σ_{BL} and the momentum equation (I.19) on $\Omega_{f(t)}$ instead of $\Omega_{f(t)} \backslash \Omega_{\mathrm{BL}}$ is expected to give accurate results for attached laminar boundary layers at high Reynolds. Solving this problem means that the velocity can be obtained at the outer surface Σ_{BL} of the boundary layer and not at the fluid-structure interface, which means the pressure obtained with the Euler equation will be known on Σ_{BL} but not on $\Sigma_{(t)}$. However, in a laminar attached boundary layer, the normal fluctuations of the pressure are negligible. Therefore, calculating the pressure p on the edge of the boundary layer Σ_{BL} will allow to predict with good precision the pressure at the fluid structure interface $\Sigma_{(t)}$ (Darrozès and François, 1982). The viscous forces have been neglected as well in the conservation of momentum equation (I.19), which also needs to be justified. The fluid stress tensor writes as:

$$\boldsymbol{\sigma}_f = -p\mathbb{1} + \boldsymbol{\sigma}_\mu, \tag{I.24}$$

where $\boldsymbol{\sigma}_\mu$ is a skew-symmetric tensor accounting for the viscous stresses. According to (Schobeiri, 2010), the amplitude of $\boldsymbol{\sigma}_\mu$ can be estimated for an attached laminar boundary layer as:

$$\boldsymbol{\sigma}_\mu \sim \rho_f V^2 \mathcal{R}_e^{-\frac{1}{2}}. \tag{I.25}$$

By combining the pressure and viscous stresses amplitudes from equations (I.10), (I.17) and (I.25), we obtain the ratio between the viscous and the pressure stresses:

$$\frac{\boldsymbol{\sigma}_\mu}{p} \sim \frac{\mathcal{R}_e^{-\frac{1}{2}}}{\max(1, \mathcal{U}_r, \mathcal{F}r^{-2})} < \mathcal{R}_e^{-\frac{1}{2}}, \tag{I.26}$$

which means that viscous strain effects might be neglected for high Reynolds, stationary laminar flows. As mentionned previously, equation (I.26) is valid for stationnary flows $\mathcal{U}_r \gg 1$. For unsteady laminar flows, a similar result can be obtained by using the magnitude of the viscous effects of a laminar flow on an flat plate oscillating tangentially, as shown by Doaré (2020):

$$\varpi_\mu \sim \rho_f \Omega L^2 \mathcal{S}_t^{-\frac{1}{2}}. \tag{I.27}$$

More details can be found about the above equation in Chapter IV where the viscous effects on oscillating structures are investigated experimentally. As a consequence, the ratio between viscous and pressure stresses becomes

$$\frac{\varpi_\mu}{p} = \frac{\mathcal{S}_t^{-\frac{1}{2}}}{\max(1, \mathcal{U}_r, \mathcal{F}_r^{-2})} < \mathcal{S}_t^{-\frac{1}{2}}. \tag{I.28}$$

As for steady viscous effects at large Reynolds laminar flows, the unsteady viscous strains at large Stokes laminar flows can be neglected.

Since most of the boundary layer around airships is turbulent, similar results can be obtained using Schlichting and Kestin (1961) results:

$$\frac{\delta}{L} \sim \mathcal{R}_e^{-\frac{1}{5}} \tag{I.29a}$$

$$\varpi_\mu \sim \rho_f V^2 \mathcal{R}_e^{-\frac{1}{5}}. \tag{I.29b}$$

The Euler equations for the fluid described in this section will allow a coherent mathematical coupling between the fluid forces and the structure dynamics, expressed with a weak formulation as well in chapter III. Because the viscous forces have been neglected, there is no tangential forces applied by the fluid on the interface, only a normal pressure force. Now that the conservation of mass (I.5), momentum (I.19) and continuity of normal velocity at the interface (I.20) have been determined, we will focus on the particular case of irrotational flows. As a consequence the weak form of the force exerted by an incompressible, inviscid flow associated with a virtual velocity $\delta\boldsymbol{v}$ of the interface is given by:

$$\delta\mathcal{P}_f = \int_{\Sigma_{(t)}} p\boldsymbol{n} \cdot \delta\boldsymbol{v} \, \mathrm{d}\Sigma, \tag{I.30}$$

where the viscous strains ϖ_μ have been neglected for reasons mentioned in the study of the boundary layer.

Potential flow

Another assumption is made about the flow: it is supposed to be irrotational. According to the Lagrange theorem, if a volume of ideal flow particles is irrotational at a given time, this volume of fluid particles will remain irrotational at any time (Darrozès and François, 1982). However, the hypothesis that the structure causes no vorticity in the fluid is quite strong. Regarding the case of airships, Lutz et al. (2002) observed experimentally that important vorticity phenomena occur around the fins, which is to be expected since they generate lift by creating a circulation on the surrounding fluid. Therefore, we expect the results obtained with the irrotational hypothesis to be inaccurate around the fins region, which is the reason why section IV.3 introduces the superposition of circulation effects and irrotational effects. Moreover, Lutz et al. (2002) highlighted that, at non zero angles of attack, turbulent phenomena are occurring at the rear of the airship, which will not be captured either by the irrotational model. As Li and Nahon (2007) has mentioned and put into

practice, it is possible to superimpose the circulation and turbulent effects at the fins and rear of the airship on top of the irrotational solution. According to the Helmoltz-Hodge theorem (Shaw, 1922), any sufficiently smooth, rapidly decaying vector field in three dimensions can be expressed as the superposition of an irrotational and a divergence free contributions. Therefore, the velocity $\boldsymbol{u}$ can be resolved into the sum of a potential flow $\boldsymbol{\nabla}\phi$ and a rotational flow $\boldsymbol{\nabla} \wedge \boldsymbol{\Gamma}$:

$$\boldsymbol{u} = \boldsymbol{\nabla}\phi + \boldsymbol{\nabla} \wedge \Gamma \quad \text{in } \Omega_{f(t)}. \tag{I.31}$$

The potential velocity $\boldsymbol{\nabla}\phi$ of the flow is irrotational by property of the curl: $\boldsymbol{\nabla} \wedge \boldsymbol{\nabla}\phi = \boldsymbol{0}$. The rotational velocity associated to $\boldsymbol{\Gamma}$ is divergence free by property of the divergence: $\boldsymbol{\nabla}.(\boldsymbol{\nabla} \wedge \boldsymbol{\Gamma}) = 0$. Because the velocity of the flow $\boldsymbol{u}$ depends on the spatial derivatives of the scalar potential ϕ and the vector potential $\boldsymbol{\Gamma}$, both of these are defined up to a spatial constant. This manuscript will not venture into the introduction of corrections to take into account the rear turbulence. We suppose that the flow is irrotational, that is:

$$\boldsymbol{\nabla} \wedge \boldsymbol{u} = \boldsymbol{0} \quad \text{in } \Omega_{f(t)}. \tag{I.32}$$

Newman demonstrated that the rotational contribution $\boldsymbol{\nabla} \wedge \boldsymbol{\Gamma}$ is nil for an irrotational flow in a connex domain (Newman, 2018), hence we can write $\boldsymbol{u}$ as a potential flow:

$$\boldsymbol{u} = \boldsymbol{\nabla}\phi \quad \text{in } \Omega_{f(t)}. \tag{I.33}$$

This means that the fluid problem can now be determined by solving a scalar field $\phi(\boldsymbol{x}, t) \in \mathcal{C}^2(\Omega_{f(t)} \times \mathbb{R}^+, \mathbb{R})$ (two times differentiable and continuous scalar function) instead of a vector field $\boldsymbol{u}(\boldsymbol{x}, t) \in \mathcal{C}^1(\Omega_f \times \mathbb{R}^+, \mathbb{R})$ (differentiable and continuous vector function), thus reducing the dimension of the fluid kinematic unkowns from three to one. We now want to rewrite the Euler equations (I.5), (I.19) and (I.20) shown in previous section for a potential flow. The conservation of mass (I.5) becomes combined with (I.33):

$$\Delta\phi = 0 \quad \text{in } \Omega_{f(t)}, \tag{I.34}$$

which means that the potential ϕ is the solution of a Laplace equation. The boundary no-slip condition (I.20) becomes when combined with (I.33):

$$\partial_{\boldsymbol{n}}\phi = \boldsymbol{v} \cdot \boldsymbol{n} \quad \text{on } \Sigma_{(t)}, \tag{I.35}$$

where $\partial_{\boldsymbol{n}}$ stands for the normal derivation $\boldsymbol{n} \cdot \boldsymbol{\nabla}$. Laplace's equation is thus associated with a Neumann condition for the flux at the interface. However, such problems does not have unique solutions because they are defined only with derivatives of the potential. It is much more convenient to impose the uniqueness of the solution (to ensure good conditioning of the numerical operators amongst other advantages), by adding a new arbitrary equation ensuring the uniqueness of the solution without affecting the physics of the fluid. The distance r is introduced as:

$$r = \|\boldsymbol{x} - \boldsymbol{y}\|, \tag{I.36}$$

and the uniqueness condition writes

$$\phi = o(1), \quad r \to \infty \qquad \forall (\boldsymbol{x}, \boldsymbol{y}) \quad \text{in } \Sigma_{(t)} \times \Omega_{f(t)} \text{ for } (\mathcal{P}_{\text{ext}}) \tag{I.37a}$$

$$\phi(\boldsymbol{x}_{\text{ref}}) = 0, \qquad \boldsymbol{x}_{\text{ref}} \in \Sigma_{(t)} \text{ for } (\mathcal{P}_{\text{int}}) \tag{I.37b}$$

The artificial zero-value conditions (I.37a) and (I.37b) are not related to the physics of the fluid problem, but are rather mathematical tricks to prevent the velocity potential to vary up to an homogeneous constant, which wouldn't affect the velocity which is defined with the gradient of the velocity potential. The second line associated with the interior problem would also work with any $\boldsymbol{x}_{\text{ref}} \in \Omega_{f(t)}$, but since the velocity potential will be condensed at the interface $\Sigma_{(t)}$ in section I.3.2, it is much more convenient to manipulate a condition that is at the interface as well. It can therefore be noticed that for a pure fluid problem the velocity of a potential flow has the advantage of being resolvable without taking into account the pressure of the fluid. According to Folland (2020), the exterior Laplace problem $(\mathcal{P}_{\text{ext}})$ with Neumann boundary condition associated with equations (I.34), (I.35), (I.37a) and (I.37b) is well posed, and its unique solution can be written as the sum of single layer and double layer potentials (associated respectively with the Green function G and its normal derivative $\partial_{\boldsymbol{n}} G$ (whose expressions are given later in the manuscript in I.3.2). This means that the velocity potential, its temporal and its spatial derivatives verify remotely from the structure:

$$\text{for } (\mathcal{P}_{\text{ext}}) : \quad \begin{cases} \phi & = \mathcal{O}\left(r^{-1}\right) \\ \boldsymbol{\nabla}\phi \cdot \boldsymbol{n} & = \mathcal{O}\left(r^{-2}\right) \\ \frac{\partial \phi}{\partial t} & = \mathcal{O}\left(r^{-1}\right) \end{cases} \quad \forall \boldsymbol{x} \in \Sigma_{(t)},\, \boldsymbol{y} \in \mathbb{R}^3,\, r \to \infty. \tag{I.38}$$

where $a = \mathcal{O}(b)$ means that a is of the same order as b at the neighborhood of a point (which might be infinity, as is the case above). In order to calculate the forces of the fluid, the pressure can be obtained as a function of the potential. To obtain the expression of the pressure, one might first use the property obtained with vector calculus identity and the irrotationality of the flow (I.32):

$$\nabla \boldsymbol{u}\, \boldsymbol{u} = \frac{1}{2}\boldsymbol{\nabla}\boldsymbol{u}^2 + (\boldsymbol{\nabla} \wedge \boldsymbol{u}) \wedge \boldsymbol{u} = \frac{1}{2}\boldsymbol{\nabla}\boldsymbol{u}^2, \tag{I.39}$$

enabling to get the convenient form of the momentum conservation by combining equations (I.19), (I.33) and (I.39):

$$\frac{\partial \boldsymbol{\nabla}\phi}{\partial t} + \frac{1}{2}\boldsymbol{\nabla}(\boldsymbol{u}^2) = -\frac{\boldsymbol{\nabla} p}{\rho_f} + \boldsymbol{g}\cdot \tag{I.40}$$

The unsteady Bernoulli equation for potential flows (Newman, 2018) can be deduced from the equation above with spatial integration, recalling the homogeneous density of the fluid (I.4):

$$\frac{p}{\rho_f} + \frac{1}{2}\boldsymbol{u}^2 + \dot{\phi} - \boldsymbol{g}\cdot\boldsymbol{x} = \frac{\pi}{\rho_f}, \tag{I.41}$$

π being an homogeneous pressure appearing with the spatial integration. With a view to expressing π for the external problem $(\mathcal{P}_{\text{ext}})$, the fixed reference point $\bar{\boldsymbol{x}}_{\text{c}}$ is introduced. The pressure of the fluid at the altitude of $\bar{\boldsymbol{x}}_{\text{c}}$ but infinitely remote from the structure can be expressed, recalling the decay of the potential and its gradient from (I.38),

$$\begin{aligned}\frac{\pi}{\rho_f} &= \frac{p}{\rho_f} + \frac{1}{2}\boldsymbol{u}^2 + \dot{\phi} - \boldsymbol{g}\cdot\boldsymbol{x} \\ &= \frac{p}{\rho_f} + \boldsymbol{g}\cdot\bar{\boldsymbol{x}}_{\mathrm{c}} \quad \text{for } \boldsymbol{x}\to\infty,\, \boldsymbol{x}\cdot\boldsymbol{e}_g = \bar{\boldsymbol{x}}_{\mathrm{c}}.\boldsymbol{e}_z,\, (\mathcal{P}_{\mathrm{ext}}).\end{aligned} \tag{I.42}$$

We suppose that the pressure p at a given altitude $\boldsymbol{x}\cdot\boldsymbol{e}_g = \bar{\boldsymbol{x}}_{\mathrm{c}}\cdot\boldsymbol{e}_g$ is known remotely from the structure:

$$p(\boldsymbol{x}) = p_{\mathrm{c}}^{\infty} \quad \text{for } \boldsymbol{x}\to\infty,\, \boldsymbol{x}\cdot\boldsymbol{e}_g = \bar{\boldsymbol{x}}_{\mathrm{c}}\cdot\boldsymbol{e}_g,\, (\mathcal{P}_{\mathrm{ext}}), \tag{I.43}$$

enabling to obtain the expression of the pressure for the external problem:

$$\begin{aligned}&\frac{\pi}{\rho_f} = p_{\mathrm{c}}^{\infty} + g\bar{\boldsymbol{x}}_{\mathrm{c}}\cdot\boldsymbol{e}_z \quad \text{for } \boldsymbol{x}\to\infty \\ \Leftrightarrow\ &\frac{p}{\rho_f} = \frac{p_{\mathrm{c}}^{\infty}}{\rho_f} - \frac{1}{2}\boldsymbol{u}^2 - \dot{\phi} + \boldsymbol{g}\cdot(\boldsymbol{x}-\bar{\boldsymbol{x}}_c).\end{aligned} \tag{I.44}$$

In order to lighten the equations, the following notation ψ_{c} is introduced:

$$\psi_{\mathrm{c}} = \begin{cases} \frac{p_{\mathrm{c}}^{\infty}}{\rho_f} & \text{for } (\mathcal{P}_{\mathrm{ext}}) \\ \frac{\pi}{\rho_f} + \boldsymbol{g}\cdot\bar{\boldsymbol{x}}_{\mathrm{c}} & \text{for } (\mathcal{P}_{\mathrm{int}}) \end{cases} \tag{I.45}$$

Consequently, the Bernoulli equation for potential flows can be rewritten by combining equations (I.41) and (I.45):

$$\frac{p}{\rho_f} = \psi_{\mathrm{c}} - \dot{\phi} - \frac{1}{2}\boldsymbol{u}^2 + \boldsymbol{g}\cdot(\boldsymbol{x}-\bar{\boldsymbol{x}}_{\mathrm{c}}) \quad \text{for } (\mathcal{P}_{\mathrm{int}})\,\&\,(\mathcal{P}_{\mathrm{ext}}). \tag{I.46}$$

The term ψ_{c} is referred to as the homogeneous aerostatic pressure, the term involving $\boldsymbol{g}$ is the aerostatic gradient of pressure, and the remaining terms are related to the dynamic pressure which depends on the velocity and acceleration of the interface, see Figure I.5. By combining equations (I.30) and (I.46), we can therefore obtain the weak expression of the fluid forces on the interface in an Eulerian framework:

$$\delta\mathcal{P}_f = \rho_f \int_{\Sigma_{(t)}} \left(\psi_{\mathrm{c}} - \dot{\phi} - \frac{1}{2}\boldsymbol{u}^2 - \boldsymbol{g}\cdot(\boldsymbol{x}-\bar{\boldsymbol{x}}_{\mathrm{c}})\right)\delta\boldsymbol{v}\cdot\boldsymbol{n}\,\mathrm{d}\Sigma \tag{I.47}$$

Regarding the work of the fluid for the internal problem $(\mathcal{P}_{\mathrm{int}})$, if we choose virtual displacements $\delta\boldsymbol{v}$ compatible with the incompressibility condition (I.6), we obtain from equations (I.22) and (I.30):

$$\int_{\Sigma_{(t)}} \psi_{\mathrm{c}}\delta\boldsymbol{v}\cdot\boldsymbol{n}\,\mathrm{d}\Sigma = \psi_{\mathrm{c}}\int_{\Sigma_{(t)}} \delta\boldsymbol{v}\cdot\boldsymbol{n}\,\mathrm{d}\Sigma = 0 \quad \text{for } \delta\boldsymbol{v}\in\mathcal{K}^{\mathcal{A}}_{\mathrm{isoV}}. \tag{I.48}$$

Therefore the internal problem is independent of the constant ψ_{c}. Note: if we were to impose the incompressibility condition for the exterior problem as well (e.g considering a thin shell with displacements homogeneous through its thickness separating both fluid domain,), i.e for $\delta\boldsymbol{v}\in\mathcal{K}^{\mathcal{A}}_{\mathrm{isoV}}$ for $(\mathcal{P}_{\mathrm{ext}})$), then the term p_{c} would vanish over the integral, which means the work of the external fluid would become independent from the pressure conditions at infinity.

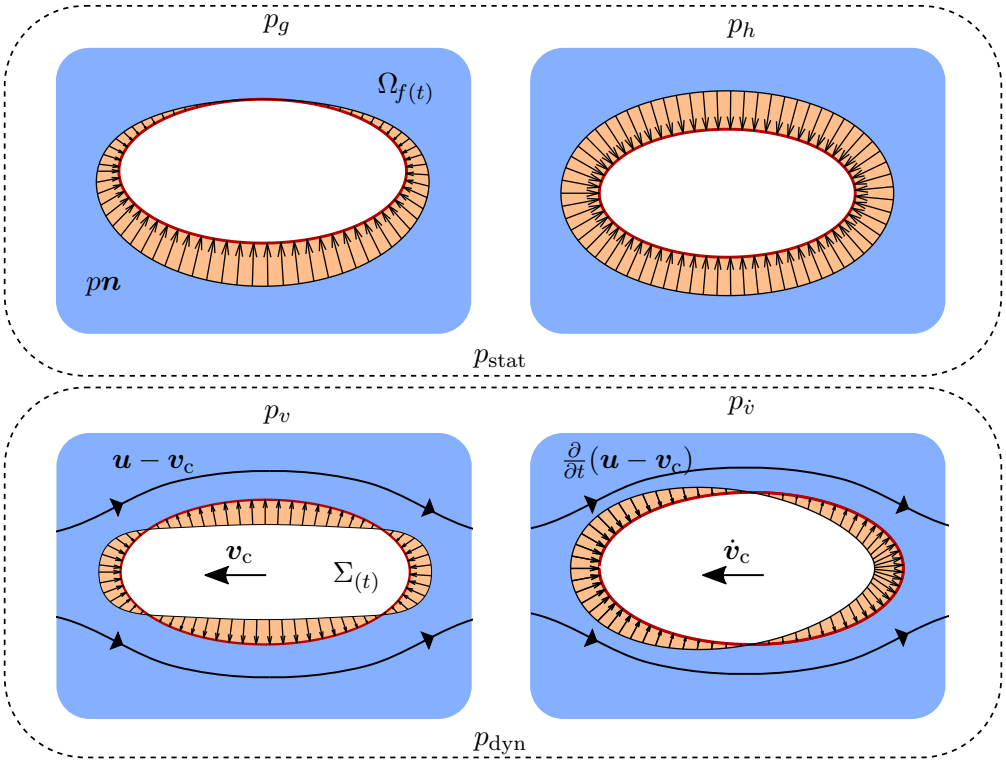

Figure I.5: Examples of pressure acting on the interface projected on the normal direction. Top right: aerostatic gradient of pressure caused by gravity on a structure at rest, top right: homogeneous aerostatic pressure acting on a structure at rest in a flow with negligible gravity effects, bottom left: dynamic pressure acting on an ellipsoid with a stationnary longitudinal motion, bottom right dynamic pressure acting on a structure at rest but with a longitudinal acceleration, at the very time the structure starts accelerating, causing added mass effects.

Remark

For the internal problem, restraining the virtual velocity of the structure to kinematically admissible movements is convenient here to simplify the expression of the virtual power in equation (I.48) while enabling to explore with the virtual velocity all the movements the system can possibly evolve into (Morand and Ohayon, 1995).

The equations for the fluid have been presented, with two distinct problems: a kinematic problem ($\mathcal{F}_{\mathcal{K}}$) associated with the velocity and velocity potential of the flow through the fluid domain: equations (I.33) to (I.35), (I.37a) and (I.37b), and a dynamic problem associated with the virtual work of the fluid on the fluid-structure interface (I.47). The latter one only depends on fluid variables defined at the interface whereas the fluid kinematic problem is set in the whole fluid domain.

I.3.2 Integral representation of the velocity potential

The calculation of ϕ could be achieved by introducing a weak formulation (Morand and Ohayon, 1992) associated to the local equations (I.34) and (I.35) in order to use the FEM. However this approach would have inconveniences in this particular case. It would require to solve the potential at every node of the fluid mesh, which is very costly. Moreover, because the domain is infinite, it would

have to be artificially truncated by meshing only a part of it, introducing artificial confinement effects. Finally, the ALE formulation is convenient to manage the coupling of the structure with the flow, but it requires the introduction of a mesh displacement within the fluid domain when used with the FEM (Pfister et al., 2019), which is not the case with the BEM used in this work as the mesh displacement at the interface is the same as the structure displacement. As a solution, we will use here an integral equation.

For that purpose, the Green's function G associated with Laplace's equation (I.34) in a three-dimension space (Bonnet, 1999) is defined as:

$$\forall \boldsymbol{x}, \boldsymbol{y} \in \mathbb{R}^3 \times \mathbb{R}^3 :$$

$$G(\boldsymbol{x}-\boldsymbol{y}) = -\frac{1}{4\pi \left\|\boldsymbol{x}-\boldsymbol{y}\right\|}, \qquad \text{solution of :} \tag{I.49a}$$

$$\Delta_{\boldsymbol{x}} G(\boldsymbol{x}-\boldsymbol{y}) = \delta(\boldsymbol{x}-\boldsymbol{y}), \qquad \text{with the property :} \tag{I.49b}$$

$$\boldsymbol{\nabla}_{\boldsymbol{x}} G(\boldsymbol{x}-\boldsymbol{y}) = \frac{\boldsymbol{x}-\boldsymbol{y}}{4\pi \left\|\boldsymbol{x}-\boldsymbol{y}\right\|^3} \tag{I.49c}$$

where δ denotes the Dirac distribution. The integral representation will be obtained using Green's second identity on an arbitrary domain Ω and its enclosing boundary $\partial\Omega$ which will be specified later to suit the internal or external problem (recalling that $\boldsymbol{n}$ is oriented outward the fluid domain):

$$\int_{\Omega} \Delta G\left(\boldsymbol{x}-\boldsymbol{y}\right)\phi\left(\boldsymbol{x}\right) - \Delta\phi\left(\boldsymbol{x}\right) G\left(\boldsymbol{x}-\boldsymbol{y}\right) \,\mathrm{d}\Omega = \oint_{\partial\Omega} \partial_{\boldsymbol{n}} G\left(\boldsymbol{x}-\boldsymbol{y}\right)\phi\left(\boldsymbol{x}\right) - \partial_{\boldsymbol{n}}\phi\left(\boldsymbol{x}-\boldsymbol{y}\right) G\left(\boldsymbol{x}-\boldsymbol{y}\right) \,\mathrm{d}\partial\Omega. \tag{I.50}$$

In the above equation, it is implicit that the spatial derivations, the normal and the small elements of volume or area are relative to the coordinate $\boldsymbol{x}$ which is the integration variable. By combining equations (I.34), (I.49) and (I.50) we obtain the following relation:

$$\int_{\Omega} \delta\left(\boldsymbol{x}-\boldsymbol{y}\right)\phi\left(\boldsymbol{x}\right) \,\mathrm{d}\Omega = \oint_{\partial\Omega} \partial_{\boldsymbol{n}} G\left(\boldsymbol{x}-\boldsymbol{y}\right)\phi\left(\boldsymbol{x}\right) - \partial_{\boldsymbol{n}}\phi\left(\boldsymbol{x}-\boldsymbol{y}\right) G\left(\boldsymbol{x}-\boldsymbol{y}\right) \,\mathrm{d}\partial\Omega, \tag{I.51}$$

which is the main equation leading to the integral representation. Because of the term $\delta(\boldsymbol{x}-\boldsymbol{y})$, the integrand in the above equation is singular when $\boldsymbol{x} \to \boldsymbol{y}$. In order to deal mathematically with this singularity, the ball Ω_ε and its enclosing sphere $\Sigma_\varepsilon(\boldsymbol{y})$ of infinitesimal radius noted[7] ε and centered around $\boldsymbol{y} \in \mathbb{R}^3$ is introduced. The normal $\boldsymbol{n}$ on Σ_ε is arbitrarily oriented toward the center of the sphere. In this section, the internal and external problems will be dealt with separately since the practical determination of the integral equation slightly differs for each case.

Internal problem

We first focus on the internal problem ($\mathcal{P}_{\text{int}}$) where the fluid is enclosed by $\Sigma_{(t)}$ in the domain $\Omega_{f(t)} = \Omega_{\text{int}}$. In order to deal with the singularity in $\boldsymbol{x}-\boldsymbol{y} = \boldsymbol{0}$, we take into consideration the fluid domain without the ball Ω_ε around $\boldsymbol{y}$:

[7] There is no risk of confusion with the dimensionless amplitude of the displacements noted ε too in section II.2 since the infinitesimal sphere is only referred to in this very section of the thesis.

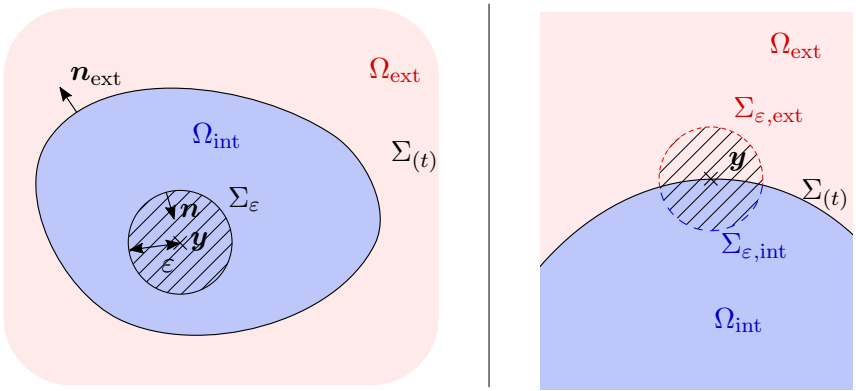

Figure I.6: Left: external and internal domains Ω_{ext}, Ω_{int} and excluded domain Ω_ε enclosed by the sphere Σ_ε. The unit normal $\boldsymbol{n}_{\text{ext}}$ on $\Sigma_{(t)}$ is oriented toward the external domain, and $\boldsymbol{n}$ is always oriented towards the center of the sphere $\boldsymbol{y}$ on Σ_ε. Right: sphere Σ_ε split into an external and an internal portions of sphere when $\boldsymbol{y}$ is on the interface $\Sigma_{(t)}$.

$$\Omega = \Omega_{\text{int}} \backslash \Omega_\varepsilon \quad \text{for } (\mathcal{P}_{\text{int}}). \tag{I.52}$$

The associated boundary is the sum of the interface Σ from which has been excluded the intersection with Ω_ε and the internal portion of sphere $\Sigma_{\varepsilon\text{int}} = \Sigma_\varepsilon \cap \Omega_{\text{int}}$ (see figure I.6):

$$\partial\Omega = (\Sigma_{(t)} \backslash \Omega_\varepsilon) \cup \Sigma_{\varepsilon\text{int}} \quad \text{for } (\mathcal{P}_{\text{int}}). \tag{I.53}$$

For $\boldsymbol{y} \in \Sigma_{(t)}$, Σ_ε is a portion of sphere. For $\boldsymbol{y} \in \Omega_{\text{int}} \backslash \Sigma_{(t)}$ we consider that ε is taken sufficiently small such that $\Omega_\varepsilon \subset \Omega_{\text{int}}$ and $\Sigma_{\varepsilon\text{int}} = \Sigma_\varepsilon$, and for $\boldsymbol{y} \in \Omega_{\text{ext}} \backslash \Sigma_{(t)}$ we take ε sufficiently small such that $\Omega_\varepsilon \cap \Omega_{\text{int}} = \emptyset$ and $\Sigma_{\varepsilon\text{int}} = \emptyset$. Equation (I.51) can be combined with equations (I.52) and (I.53) for the internal problem:

$$\int_{\Omega_{\text{int}} \backslash \Omega_\varepsilon} \delta(\boldsymbol{x}-\boldsymbol{y})\, \phi(\boldsymbol{x})\, \mathrm{d}\Omega = \oint_{(\Sigma_{(t)} \backslash \Omega_\varepsilon) \cup \Sigma_{\varepsilon\text{int}}} \partial_{\boldsymbol{n}} G(\boldsymbol{x}-\boldsymbol{y})\, \phi(\boldsymbol{x}) - \partial_{\boldsymbol{n}} \phi(\boldsymbol{x}-\boldsymbol{y})\, G(\boldsymbol{x}-\boldsymbol{y})\, \mathrm{d}\Sigma \quad \text{for } (\mathcal{P}_{\text{int}}). \tag{I.54}$$

Because we have chosen accordingly the integration domain Ω, we have the property:

$$\delta(\boldsymbol{x}-\boldsymbol{y}) = 0 \quad \text{for } \boldsymbol{x} \in \Omega_{\text{int}} \backslash \Omega_\varepsilon. \tag{I.55}$$

By combining equations (I.54) and (I.55) the dirac distribution vanishes, leading to the equation below by splitting the integrals on $\Sigma \backslash \Omega_\varepsilon$ and $\Sigma_{\varepsilon\text{int}}$:

$$\begin{aligned} \int_{\Sigma_{(t)} \backslash \Omega_\varepsilon} \partial_{\boldsymbol{n}} G(\boldsymbol{x}-\boldsymbol{y}) \phi(\boldsymbol{x}) - \partial_{\boldsymbol{n}} \phi(\boldsymbol{x})\, G(\boldsymbol{x}-\boldsymbol{y})\, \mathrm{d}\Sigma = \ldots \\ - \int_{\Sigma_{\varepsilon\text{int}}} \partial_{\boldsymbol{n}} G(\boldsymbol{x}-\boldsymbol{y})\, \phi(\boldsymbol{x}) - \partial_{\boldsymbol{n}} \phi(\boldsymbol{x})\, G(\boldsymbol{x}-\boldsymbol{y})\, \mathrm{d}\Sigma \quad \text{for } (\mathcal{P}_{\text{int}}). \end{aligned} \tag{I.56}$$

One should note that, for $\varepsilon > 0$, both integrands of the above equation are well-defined contrarily to (I.51). However, the associated solution is not convenient to obtain because ϕ and its gradient are unknown on Σ_ε. To overcome this issue, we use $\varepsilon \to 0$, so that an alternative expression of the right integral can be obtained. First, one should note the property on Σ_ε:

$$\boldsymbol{y} = \boldsymbol{x} + \varepsilon \boldsymbol{n} \quad \text{for } \boldsymbol{x} \in \Sigma_\varepsilon \Rightarrow \left\{ \begin{array}{ll} G & = -\frac{1}{4\pi\varepsilon} \\ \partial_{\boldsymbol{n}} G & = -\frac{1}{4\pi\varepsilon^2}. \end{array} \right. \quad \text{for } \boldsymbol{x} \in \Sigma_\varepsilon. \tag{I.57}$$

Moreover, the following Taylor expansions will come in handy for later developments, recalling that $\phi \in C^2(\Omega_{f(t)} \times \mathbb{R}^+, \mathbb{R})$ is twice differentiable:

$$\phi(\boldsymbol{y}) = \phi(\boldsymbol{x} + \varepsilon \boldsymbol{n}) = \phi(\boldsymbol{x}) + \varepsilon \partial_{\boldsymbol{n}} \phi(\boldsymbol{y}) + \mathcal{O}\left(\varepsilon^2\right) \tag{I.58a}$$

$$\partial_{\boldsymbol{n}} \phi(\boldsymbol{x}) = \partial_{\boldsymbol{n}} \phi(\boldsymbol{y} - \varepsilon \boldsymbol{n}) = \partial_{\boldsymbol{n}} \phi(\boldsymbol{y}) + \mathcal{O}(\varepsilon). \tag{I.58b}$$

We first show how the right integrand on $\Sigma_{\varepsilon \text{int}}$ from equation (I.56) is negligible for $\varepsilon \to 0$, recalling that the small element of surface on $\Sigma_{\varepsilon \text{int}}$ verifies $\mathrm{d}\Sigma = \mathcal{O}\left(\varepsilon^2\right)$:

$$\int_{\Sigma_{\varepsilon \text{int}}} \partial_{\boldsymbol{n}} \phi(\boldsymbol{x})\, G(\boldsymbol{x} - \boldsymbol{y}) = -\frac{1}{4\pi\varepsilon} \int \left(\partial_{\boldsymbol{n}} \phi(\boldsymbol{y}) + \mathcal{O}(\varepsilon)\right) \mathrm{d}\Sigma = \mathcal{O}\left(\varepsilon^{-1}\varepsilon^2\right) = \mathcal{O}(\varepsilon) \quad \text{for } (\mathcal{P}_{\text{int}}). \tag{I.59}$$

The second left integrand on $\Sigma_{\varepsilon \text{int}}$ from equation (I.56) can be simplified as well thanks to the following formula:

$$\begin{aligned} &\text{for } (\mathcal{P}_{\text{int}}): \\ \int_{\Sigma_{\varepsilon \text{int}}} \partial_{\boldsymbol{n}} G(\boldsymbol{x} - \boldsymbol{y})\, \phi(\boldsymbol{x})\, \mathrm{d}\Sigma &= \int_{\Sigma_{\varepsilon \text{int}}} \partial_{\boldsymbol{n}} G(\boldsymbol{x} - \boldsymbol{y})\, \phi(\boldsymbol{y})\, \mathrm{d}\Sigma + \int_{\Sigma_{\varepsilon \text{int}}} \partial_{\boldsymbol{n}} G(\boldsymbol{x} - \boldsymbol{y}) \left(\phi(\boldsymbol{x}) - \phi(\boldsymbol{y})\right) \mathrm{d}\Sigma \\ &= \int_{\Sigma_{\varepsilon \text{int}}} \partial_{\boldsymbol{n}} G(\boldsymbol{x} - \boldsymbol{y})\, \phi(\boldsymbol{y})\, \mathrm{d}\Sigma + \int_{\Sigma_{\varepsilon \text{int}}} \partial_{\boldsymbol{n}} G(\boldsymbol{x} - \boldsymbol{y}) \left(-\varepsilon \partial_{\boldsymbol{n}} \phi(\boldsymbol{y})\right) \mathrm{d}\Sigma \\ &= \int_{\Sigma_{\varepsilon \text{int}}} \partial_{\boldsymbol{n}} G(\boldsymbol{x} - \boldsymbol{y})\, \phi(\boldsymbol{y})\, \mathrm{d}\Sigma + \mathcal{O}(\varepsilon) \\ &= -\frac{\phi(\boldsymbol{y})}{4\pi\varepsilon^2} \int_{\Sigma_{\varepsilon \text{int}}} \mathrm{d}\Sigma + \mathcal{O}(\varepsilon). \end{aligned} \tag{I.60}$$

Therefore, by noting the area of $\Sigma_{\varepsilon \text{int}}$

$$\|\Sigma_{\varepsilon \text{int}}\| := \int_{\Sigma_{\varepsilon \text{int}}} \mathrm{d}\Sigma, \tag{I.61}$$

we obtain the following relation by combining equations (I.56), (I.59) and (I.60) and noting that $\varepsilon \to 0 \Rightarrow \Sigma_{(t)} \backslash \Omega_\varepsilon \to \Sigma_{(t)}$:

$$\int_{\Sigma_{(t)}} \partial_{\boldsymbol{n}} G(\boldsymbol{x} - \boldsymbol{y})\, \phi(\boldsymbol{x}) - \partial_{\boldsymbol{n}} \phi(\boldsymbol{x})\, G(\boldsymbol{x} - \boldsymbol{y})\, \mathrm{d}\Sigma = \frac{\phi(\boldsymbol{y})}{4\pi\varepsilon^2} \|\Sigma_{\varepsilon \text{int}}\| \quad \text{for } (\mathcal{P}_{\text{int}}), \varepsilon \to 0. \tag{I.62}$$

The integral above, though it is strongly singular because of the term $\boldsymbol{\nabla} G \cdot \boldsymbol{n}$, is defined in the sense of the Cauchy principal value (Hackbusch, 1995). In order to obtain the aforementioned area, one can inject the arbitrary homogeneous solution of the problem $\phi(\boldsymbol{x}) = 1$ into (I.62), leading to the relation:

$$\int_{\Sigma_{(t)}} \partial_{\boldsymbol{n}} G\left(\boldsymbol{x}-\boldsymbol{y}\right) \mathrm{d}\Sigma = \frac{1}{4\pi\varepsilon^2} \left\|\Sigma_{\varepsilon \mathrm{int}}\right\| \quad \text{for } (\mathcal{P}_{\mathrm{int}}),\ \varepsilon \to 0. \tag{I.63}$$

Considering the above equation, the area of $\Sigma_{\varepsilon \mathrm{int}}$ can be calculated as:

$$\left\|\Sigma_{\varepsilon \mathrm{int}}\right\| = 4\pi\varepsilon^2 \int_{\Sigma_{(t)}} \partial_{\boldsymbol{n}} G\left(\boldsymbol{x}-\boldsymbol{y}\right) \mathrm{d}\Sigma \quad \text{for } (\mathcal{P}_{\mathrm{int}}). \tag{I.64}$$

In order to calculate the potential associated with the external problem, the above equation comes in handy. Moreover, it is convenient for later when dealing with $(\mathcal{P}_{\mathrm{ext}})$ to express $\left\|\Sigma_{\varepsilon \mathrm{int}}\right\|$ in a way that is common for both problems $(\mathcal{P}_{\mathrm{int}})$ and $(\mathcal{P}_{\mathrm{ext}})$, which is done by using the external normal $\boldsymbol{n}_{\mathrm{ext}}$ (see figure I.6), noting that $\boldsymbol{n} = \boldsymbol{n}_{\mathrm{ext}}$ for $(\mathcal{P}_{\mathrm{int}})$:

$$\left\|\Sigma_{\varepsilon \mathrm{int}}\right\| = 4\pi\varepsilon^2 \int_{\Sigma_{(t)}} \frac{\partial G\left(\boldsymbol{x}-\boldsymbol{y}\right)}{\partial \boldsymbol{n}_{\mathrm{ext}}} \mathrm{d}\Sigma \quad \text{for } (\mathcal{P}_{\mathrm{int}}) \ \& \ (\mathcal{P}_{\mathrm{ext}}), \tag{I.65}$$

where $\partial / \partial \boldsymbol{n}_{\mathrm{ext}}$ is the spatial derivation in the direction of $\boldsymbol{n}_{\mathrm{ext}}$. By combining (I.62) and (I.64), we obtain the integral representation, where the $\varepsilon \to 0$ contributions vanish:

$$\int_{\Sigma_{(t)}} \partial_{\boldsymbol{n}} G\left(\boldsymbol{x}-\boldsymbol{y}\right) \phi\left(\boldsymbol{x}\right) - \partial_{\boldsymbol{n}} \phi\left(\boldsymbol{x}\right) G\left(\boldsymbol{x}-\boldsymbol{y}\right) \mathrm{d}\Sigma = \phi(\boldsymbol{y}) \int_{\Sigma_{(t)}} \partial_{\boldsymbol{n}} G\left(\boldsymbol{x}-\boldsymbol{y}\right) \mathrm{d}\Sigma \quad \text{for } (\mathcal{P}_{\mathrm{int}}). \tag{I.66}$$

It is more convenient to group the integrands of the above equation as follows:

$$\int_{\Sigma_{(t)}} \partial_{\boldsymbol{n}} G\left(\boldsymbol{x}-\boldsymbol{y}\right) \left(\phi\left(\boldsymbol{x}\right) - \phi\left(\boldsymbol{y}\right)\right) \mathrm{d}\Sigma = \int_{\Sigma_{(t)}} \partial_{\boldsymbol{n}} \phi\left(\boldsymbol{x}\right) G\left(\boldsymbol{x}-\boldsymbol{y}\right) \mathrm{d}\Sigma \quad \text{for } (\mathcal{P}_{\mathrm{int}}). \tag{I.67}$$

Finally, by replacing the normal derivative of ϕ at the interface using the boundary condition (I.35), the above equation becomes:

$$\int_{\Sigma_{(t)}} \partial_{\boldsymbol{n}} G\left(\boldsymbol{x}-\boldsymbol{y}\right) \left(\phi\left(\boldsymbol{x}\right) - \phi\left(\boldsymbol{y}\right)\right) \mathrm{d}\Sigma = \int_{\Sigma_{(t)}} G\left(\boldsymbol{x}-\boldsymbol{y}\right) \boldsymbol{v} \cdot \boldsymbol{n} \, \mathrm{d}\Sigma \quad \text{for } (\mathcal{P}_{\mathrm{int}}). \tag{I.68}$$

This equation is the integral representation of the potential ϕ for the internal problem $(\mathcal{P}_{\mathrm{int}})$. It enables to calculate the potential ϕ at any point in space knowing its value and normal derivative on the interface Σ. To solve the potential at the interface as a function of the interface normal velocity using the BEM, the integral equation is obtained by expressing the integral representation for any $\boldsymbol{y} \in \Sigma_{(t)}$.

Remark

The solid angle ϑ for the internal fluid is defined as

$$\vartheta = \lim_{\varepsilon \to 0} \frac{\|\Sigma_{\varepsilon \text{int}}\|}{4\pi\varepsilon^2}. \tag{I.69}$$

It is proportional to the fluid volume enclosed by an infinitesimal sphere centered around a point $\boldsymbol{y}$, as shown on a few examples in Figure III.1. It is common practice in the literature (Mavaleix-Marchessoux, 2020; Veron et al., 2016; Carbone et al., 2019) to set its value to

$$\vartheta = \frac{1}{2}. \tag{I.70}$$

It is actually the case for locally smooth surfaces, but it is however inaccurate at the nodes of a mesh which constitute a geometry singularity or when the geometry of the interface is singular as presented on examples in Figure III.1. In this thesis, the choice to use the relation (I.64) instead of (I.70) is justified by two main reasons. First, as just mentioned, it enables to take into account the singularities of the geometry and the mesh. Secondly, it also enables to regularize the double layer term $\overline{\partial_n G}$ from equation (I.62), which becomes less singular in equation (I.68) since the term $\phi(\boldsymbol{x}) - \phi(\boldsymbol{y})$ tends to 0 for $\boldsymbol{x} \to \boldsymbol{y}$, thus reducing by an order the singularity of the integrand. The advantages of this method are quantified in Chapter II, see Figure III.2.

External problem

We now focus on obtaining the integral representation of the potential associated with the external problem. For this purpose, we choose:

$$\left\{ \begin{array}{ll} \Omega & = \Omega_{\text{ext}} \backslash \Omega_\varepsilon \\ \Sigma_{\varepsilon\text{ext}} & = \Sigma_\varepsilon \cup \Omega_{\text{ext}} = \Sigma_\varepsilon \backslash \Sigma_{\varepsilon\text{int}} \\ \partial\Omega & = (\Sigma \backslash \Omega_\varepsilon) \cup \Sigma_{\varepsilon\text{ext}} \cup \partial\Omega_\infty \end{array} \right. \quad \text{for } (\mathcal{P}_{\text{ext}}). \tag{I.71}$$

The main difference between the above equation and the one associated with $(\mathcal{P}_{\text{int}})$ comes from the fact that the supposedly infinite fluid domain $\Omega_{f(t)}$ is artificially bounded by a border $\partial\Omega_\infty$ (see figure I.3) which is however supposed to be infinitely remote from the structure. By combining equations (I.51) and (I.71), we obtain:

$$\int_{\Omega_{\text{ext}} \backslash \Omega_\varepsilon} \delta(\boldsymbol{x} - \boldsymbol{y})\, \phi(\boldsymbol{x})\, \mathrm{d}\Omega = \int_{(\Sigma \backslash \Omega_\varepsilon) \cup \Sigma_{\varepsilon\text{ext}} \cup \partial\Omega_\infty} \partial_{\boldsymbol{n}} G(\boldsymbol{x} - \boldsymbol{y})\, \phi(\boldsymbol{x}) - \partial_{\boldsymbol{n}} \phi(\boldsymbol{x})\, G(\boldsymbol{x} - \boldsymbol{y})\, \mathrm{d}\partial\Omega. \tag{I.72}$$

First, let us consider the left term of the integrand at the right of equation (I.72), on the infinitely remote boundary $\partial\Omega_\infty$. We know that a small element of area scales as $\mathrm{d}\Sigma_{(t)} = \mathcal{O}\left(r^2\right)$ on $\partial\Omega_\infty$. Moreover, one can deduce from equations (I.49a) and (I.49c) that $\partial_{\boldsymbol{n}} G = \mathcal{O}\left(r^{-2}\right)$ on $\partial\Omega_\infty$ and $G = \mathcal{O}\left(r^{-1}\right)$ on $\partial\Omega_\infty$. The order of magnitude of ϕ remotely from the structure is known as well from (I.38). Consequently, one can obtain the order of magnitude of the integrand on $\partial\Omega_\infty$:

$$\begin{array}{ll} \partial_{\boldsymbol{n}} G(\boldsymbol{x} - \boldsymbol{y}) \phi(\boldsymbol{x})\, \mathrm{d}\Sigma & = \mathcal{O}\left(r^{-2} r^{-1} r^2\right) = \mathcal{O}\left(r^{-1}\right) \\ \partial_{\boldsymbol{n}} \phi(\boldsymbol{x}) G(\boldsymbol{x} - \boldsymbol{y})\, \mathrm{d}\Sigma & = \mathcal{O}\left(r^{-2} r^{-1} r^2\right) = \mathcal{O}\left(r^{-1}\right) \end{array} \quad \text{on } \partial\Omega_\infty \quad \text{for } (\mathcal{P}_{\text{ext}}). \tag{I.73}$$

Therefore, when considering an infinitely remote boundary $\partial\Omega_\infty$ with $r \to \infty$, the integral terms on $\partial\Omega_\infty$ from equation (I.72) vanish, leading to the equation:

$$\int_{\Omega_{\text{ext}} \backslash \Omega_\varepsilon} \delta(\boldsymbol{x} - \boldsymbol{y})\, \phi(\boldsymbol{x})\, \mathrm{d}\Omega = \int_{(\Sigma \backslash \Omega_\varepsilon) \cup \Sigma_{\varepsilon\text{ext}}} \partial_{\boldsymbol{n}} G(\boldsymbol{x} - \boldsymbol{y})\, \phi(\boldsymbol{x}) - \partial_{\boldsymbol{n}} \phi(\boldsymbol{x})\, G(\boldsymbol{x} - \boldsymbol{y})\, \mathrm{d}\partial\Omega. \tag{I.74}$$

With developments analogous to those done for the internal problem $(\mathcal{P}_{\text{int}})$ in equations (I.54 - I.62), equation (I.74) becomes:

$$\int_{\Sigma_{(t)}} \partial_{\boldsymbol{n}} G\left(\boldsymbol{x}-\boldsymbol{y}\right) \phi\left(\boldsymbol{x}\right) - \partial_{\boldsymbol{n}} \phi\left(\boldsymbol{x}\right) G\left(\boldsymbol{x}-\boldsymbol{y}\right) \, \mathrm{d}\Sigma = \frac{\phi(\boldsymbol{y})}{4\pi\varepsilon^2} \left\|\Sigma_{\varepsilon\text{ext}}\right\|. \tag{I.75}$$

In order to obtain the area $\|\Sigma_{\varepsilon\text{ext}}\|$, we might use (I.65), which gives combined to the properties $\|\Sigma_{\varepsilon\text{ext}}\| + \|\Sigma_{\varepsilon\text{int}}\| = \|\Sigma_{\varepsilon}\|$ and $\|\Sigma_{\varepsilon}\| = 4\pi\varepsilon^2$:

$$\begin{aligned} \left\|\Sigma_{\varepsilon\text{ext}}\right\| &= 4\pi\varepsilon^2 \left(1 - \int_{\Sigma_{(t)}} \frac{\partial G\left(\boldsymbol{x}-\boldsymbol{y}\right)}{\partial \boldsymbol{n}_{\text{ext}}} \, \mathrm{d}\Sigma\right) \quad \text{for } (\mathcal{P}_{\text{int}}) \ \& \ (\mathcal{P}_{\text{ext}}) \\ &= 4\pi\varepsilon^2 \left(1 + \int_{\Sigma_{(t)}} \partial_{\boldsymbol{n}} G\left(\boldsymbol{x}-\boldsymbol{y}\right) \, \mathrm{d}\Sigma\right) \quad \text{for } (\mathcal{P}_{\text{ext}}). \end{aligned} \tag{I.76}$$

The last line of the above equation is obtained recalling that, for the external problem, the normal of the interface pointing outward the fluid domain verifies: $\boldsymbol{n} = -\boldsymbol{n}_{\text{ext}}$ for $(\mathcal{P}_{\text{ext}})$. Consequently, one gets by combining equations (I.75) and (I.76) the integral representation:

$$-\phi(\boldsymbol{y}) + \int_{\Sigma_{(t)}} \partial_{\boldsymbol{n}} G\left(\boldsymbol{x}-\boldsymbol{y}\right) \left(\phi\left(\boldsymbol{x}\right) - \phi\left(\boldsymbol{y}\right)\right) \mathrm{d}\Sigma = \int_{\Sigma_{(t)}} \partial_{\boldsymbol{n}} \phi\left(\boldsymbol{x}\right) G\left(\boldsymbol{x}-\boldsymbol{y}\right) \, \mathrm{d}\Sigma \quad \text{for } (\mathcal{P}_{\text{ext}}). \tag{I.77}$$

The integral equation for the external problem can therefore be obtained by taking $\boldsymbol{y} \in \Sigma_{(t)}$ and using the boundary condition (I.35):

$$-\phi(\boldsymbol{y}) + \int_{\Sigma_{(t)}} \partial_{\boldsymbol{n}} G\left(\boldsymbol{x}-\boldsymbol{y}\right) \left(\phi\left(\boldsymbol{x}\right) - \phi\left(\boldsymbol{y}\right)\right) \mathrm{d}\Sigma = \int_{\Sigma_{(t)}} G\left(\boldsymbol{x}-\boldsymbol{y}\right) \boldsymbol{v}\cdot\boldsymbol{n} \, \mathrm{d}\Sigma \quad \forall \boldsymbol{y} \in \Sigma_{(t)} \quad \text{for } (\mathcal{P}_{\text{ext}}). \tag{I.78}$$

For a more condensed form, and with a view to highlighting the linearity of the equations, we introduce the operators $\mathcal{H}$ and $\mathcal{G}$ associated respectively with the single and double layer terms:

$$\begin{aligned} &\mathcal{H}\colon \mathcal{C}^2(\Omega_{f(t)},\mathbb{R}) \times \Sigma_{(t)} \times \mathbb{R}^+ \longrightarrow \mathbb{R} \\ &\qquad \phi, \boldsymbol{y}, t \longmapsto \kappa\phi(\boldsymbol{y}) + \int_{\Sigma_{(t)}} \partial_{\boldsymbol{n}} G\left(\boldsymbol{x}-\boldsymbol{y}\right) \left(\phi\left(\boldsymbol{x}\right) - \phi\left(\boldsymbol{y}\right)\right) \mathrm{d}\Sigma, \quad \kappa = \begin{cases} -1 & \text{for } (\mathcal{P}_{\text{ext}}) \\ 0 & \text{for } (\mathcal{P}_{\text{int}}) \end{cases} \end{aligned} \tag{I.79a}$$

$$\begin{aligned} &\mathcal{G}\colon \mathcal{C}^1(\Sigma_{(t)},\mathbb{R}^2) \times \Sigma_{(t)} \times \mathbb{R}^+ \longrightarrow \mathbb{R} \\ &\qquad \boldsymbol{v}, \boldsymbol{y}, t \longmapsto \int_{\Sigma_{(t)}} G\left(\boldsymbol{x}-\boldsymbol{y}\right) \boldsymbol{v}\left(\boldsymbol{x}\right)\cdot\boldsymbol{n} \, \mathrm{d}\Sigma \end{aligned} \tag{I.79b}$$

Operators $\mathcal{H}$ and $\mathcal{G}$ are linear with ϕ and $\boldsymbol{v}$ respectively. By combining equations (I.68), (I.75) and (I.79) the integral equation writes for both $(\mathcal{P}_{\text{int}})$ and $(\mathcal{P}_{\text{ext}})$:

$$\mathcal{H}(\phi, \boldsymbol{y}, t) = \mathcal{G}(\boldsymbol{v}, \boldsymbol{y}, t) \quad \forall \{\boldsymbol{y}, t\} \in \Sigma_{(t)} \times \mathbb{R}^+. \tag{I.80}$$

A way to obtain the velocity potential ϕ at the interface is thus to solve the integral equation (I.80). Then, the value of the velocity potential might be found anywhere outside of the boundary using either (I.68) or (I.77).

The most relevant equations introduced in sections I.3.1 and I.3.2 are summarized below, thus showing in a concise set of equation the equations involved in the calculation of the fluid forces.

Overview of the kinematic and dynamic potential flow equations in an Eulerian framework.

The fluid problem can be split into kinematic and dynamic equations. The kinematic equation of the fluid ($\mathcal{F}_\mathcal{K}$) (equation (I.34)) associated with the incompressibility and the kinematic interface condition ($\mathcal{I}_\mathcal{K}$) (equation (I.35)) associated with the continuity of the normal velocity lead to the integral equation (I.80) allowing to solve the flow potential ϕ depending on its value and normal derivative at the interface:

$$\left.\begin{array}{lllll} (\mathcal{F}_\mathcal{K}): & \Delta\phi & = 0 & \text{in } \Omega_{f(t)} \\ (\mathcal{I}_\mathcal{K}): & \partial_{\boldsymbol{n}}\phi & = \boldsymbol{v}\cdot\boldsymbol{n} & \text{on } \Sigma_{(t)} \end{array}\right\} \quad \mathcal{H}(\phi) = \mathcal{G}(\boldsymbol{v}) \quad \text{on } \Omega_{f(t)}$$

The restriction of the latter equation on $\Sigma_{(t)}$, called integral equation, enables to solve the potential ϕ at the interface as a function of its velocity $\boldsymbol{v}$. The potential solution ϕ enables to obtain the virtual power $\delta\mathcal{P}_f$ of the fluid on the interface through ($\mathcal{F}_\mathcal{D}$) the fluid dynamic equation (I.47):

$$(\mathcal{F}_\mathcal{D}): \quad \delta\mathcal{P}_f = \int_{\Sigma_{(t)}} p\boldsymbol{n}\cdot\delta\boldsymbol{v}\,\mathrm{d}\Sigma_{(t)}, \quad \delta\boldsymbol{v}\in\mathcal{K}^\mathcal{A}$$

Once these have been obtained, the coupling of the interface dynamic condition ($\mathcal{I}_\mathcal{D}$) with a structure weak equation ($\mathcal{S}$) enabling to link the virtual power $\delta\mathcal{P}_s$ of the structure to the displacement field $\boldsymbol{v}$:

$$\begin{array}{lll} (\mathcal{I}_\mathcal{D}): & \delta\mathcal{P}_s & = \delta\mathcal{P}_f \\ (\mathcal{S}): & \delta\mathcal{P}_s & = f(\delta\boldsymbol{v}). \end{array}$$

The structure equation ($\mathcal{S}$) will be dealt with later in this thesis, in Chapter III. It cannot be separated into a kinematic and a dynamic equation since both are interdependent.

In this section, the fluid problem as been modeled by superimposing a kinematic problem, which only involves fluid variables at the fluid-structure interface thanks to the integral representation, and a dynamic transmission condition set on the interface as well.

The integral equation (I.80) can be solved with a numerical approximation using the BEM, and the dynamic transmission condition can be conveniently approached using the FEM, both of these method being introduced in the next chapter. However, the Eulerian description used for these equations implies to express the variables relatively to a fixed point of space, which is hardly consistent with the movements of the boundaries of the fluid problem.

These fluid equations having been introduced, it is important to recall what are the scientific obstacles and what are those that this thesis aims to overcome. These obstacles are resumed below through the lens of two studies on flexible airships fluid-structure interaction:

Li and Nahon (2007); Li et al. (2009)

- Pros:

  - Monolithic equation.
  - Dynamic effects taken into account through added mass, gyroscopic and stiffness fluid loads.
  -

- Remaining obstacles
  - Order zero quasi-steady movements can only take into account translation velocity but not rotation velocity.
  - Calculation of the fluid operators using slender body theory approximation valid for very elongated structures, and only taking into account "cantilever" movements of the structure (curvilinear model from the fluid and structure point of view).
  - Fluid operators integrated over an interface approximated as an ellipsoid.
  - Flow around the fins calculated independently from the flow around the hull which might not capture some coupling between both.
  - As demonstrated in Chapter II, second order derivatives are required to derive the whole linear potential forces.
  - no mention made of pre-stress effects

Bessert and Frederich (2005):

- Pros:
  - Potential flow around the hull and the fin calculated simultaneously, taking into account the vortex sheet behing the trailing edge
  - Non linear coupling between the flow and the structure deformations
  - Flow and structure modeled with surface elements (no curvilinear assumption), adaptable to any shape of the airship
- Cons:
  - Iterative, partitioned approach.
  - Stationnary calculations.
  - Rotation speed of the airship not taken into account.

Mavaleix-Marchessoux (2020) (flexible submarine):

- Pros:
  - Potential flow around hull and fin calculated simultaneously
  - Flow and structure modeled with surface elements (no curvilinear assumption), adaptable to any shape of the interface
  - Dynamic calculations with unsteady, non-homogeneous ambient flow
- Cons:
  - Iterative, partitioned approach

– Circulation effects induced by the fins not taken into account

The list above highlights the pros and cons of two approaches from the literature. Bessert and Frederich (2005) models the non-linear deformations of an airship induced by the flow around it by taking into account both the hull, the fins and the circulation effects they induce. However their approach only enables to tackle stationary problems. In order to study time-dependent maneuvers, their approach would require to be extended to dynamic effects. Moreover, even though partitioned approach are efficient for solving non-linear problems, they are not best suited for performing stability analysis as the derivative of the forces with respect to the interface movements does not arise naturally. Mavaleix-Marchessoux (2020) has extended a very similar method for the study of submarines subjected to underwater explosions, however his model didn't include circulation effects from the fin, which play a crucial role on the stability of airships and are therefore a critical part of airship dynamics modeling. On the other hand, Li et al. (2009) have been able to solve the dynamic fluid-structure effects of flexible airships using less accurate models than Bessert as listed above but he has been able to predict the linear fluctuations of the efforts which is convenient for carrying stability analysis. However, neither Bessert nor Li have modeled maneuvers of airships with rotations. Given the statement above, this thesis aims to overcome some of the scientific obstacles that still prevent a good tackling of flexible airships behavior:

- A formulation of the linearized flow efforts (under the form of added mass, gyroscopic and stiffness effects) on the airship has been introduced in chapters II with an associated numerical resolution in Chapter II similarly to what has been done by Li et al. (2009), but with the following advantages:
  - Order zero steady maneuvers of the airship can be considered including rotation effects.
  - They model allows to solve the problem using any associated mesh, enabling not to use slender body assumption nor integrate over an approximated hull as an ellipsoid.
  - Contrarily to Lagrange's equations, the Newton approach enables to predict the whole linear potential forces fluctuations without having to calculate second order derivatives which are very costly.
- The following obstacles are not tackled in this manuscript:
  - As done by Li et al. (2009), the effects of the fin have been calculated separatedly from the hull aerodynamic effects. The method of Bessert and Frederich (2005) tackling both circulation around the fins and hull effects at the same times seems much more physically correct to the author. However, the new method that is introduced in chapters II and III seem promising and in adequation with a possible extension to introduce a vortex sheet behind the fins as done by Bessert and Frederich (2005). Such a future developpement would therefore enable to predict harmoniously the dynamic fluctuations of the aerodynamics effects linked both to the hull and the circulation around the fins.
  - Unlike what Mavaleix-Marchessoux (2020) has done, this thesis doesn't venture into the effects of unsteady or inhomogeneous flows on airship aerodynamics. However, the method introduced in this manuscript is quite adapted for future extension taking into account those external effects. Such an extension could be possible with the following procedure: first, extend the method presented in appendix ... to unsteady, inhomogeneous flows. Once this has been done, it might be coupled to the great motions of an elastic airship introduced in Chapter II.

Chapter II

Derivation of the integral equation for a potential flow around a free elastic structure on a fixed reference domain

Introduction

In view of the important role of fluid forces on airships trajectories (Cook et al., 2000), it is of high importance to predict those efforts for various flight conditions airships might evolve in. Li et al. (2011) mentioned that we still lack a formalism to take into account the coupling of large structure rotations and small elastic deformations with the surrounding fluids. This chapter introduces a linearized integral equation of the velocity potential depending on the structure large rigid body motions coupled with small elastic deformations in a fluid at rest, which is an original contribution with regards to the literature. It will be used to find a numerical approximation of the fluid velocity field with the BEM in chapter III. A weak formulation of the fluid forces is introduced as a function of the velocity potential interface position, velocity and acceleration. The associated operators are solved numerically in chapter III as well, allowing to couple the fluid behavior with the structure dynamics in chapter IV.

II.1 Modeling the fluid coherently with moving boundaries using the Arbitrary-Lagrangian-Eulerian (ALE) description

The fluid model introduced in the previous section has two drawbacks. First, it is based on an Eulerian framework. It is hence inconvenient to implement for an interaction problem whose boundaries are in motion, and it is tricky to couple with the structure model since the latter is described with a Lagrangian description. Secondly, it involves time-dependent domains, which means that the numerical solution will be based on a variable mesh, implying recalculations on an updated mesh at each time step. The ALE description of the fluid equations presented in this section overcomes those two drawbacks. It consists in observing the fluid behavior from the point of view of the moving interface material points, enabling to introduce a time-independent reference interface suited for a coherent coupling with the Lagrangian description of the structure. The ALE

formalism has been used for a long time to deal with fluid-structure interaction problems (e.g. (Nitikitpaiboon and Bathe, 1993)) and does not constitute in itself an originality of this study. However, this thesis differs from other works in the literature in the use of ALE to compute the linear fluctuations of the potential fluid operators associated with an integral equation (and thus with the BEM). For example, Mavaleix-Marchessoux (2020) used ALE to compute the nonlinear fluctuations of the fluid forces using a partitioned BEM approach, while Pfister et al. (2019) used ALE to compute the linear fluctuations of the weak form of the fluid equations discretized with the FEM.

II.1.1 Comparison of Eulerian, Lagrangian and ALE frameworks for fluid problems with mobile boundaries

With a view to finding out which description is better suited for the present fluid-structure interaction problem, the Eulerian, Lagrangian and ALE descriptions are exhibited and compared in this section.

In this manuscript, three different kinds of descriptions are used: Lagrangian, Eulerian and Arbitrary-Lagrangian-Eulerian frameworks. Each one corresponds to a particular way of looking at the material particles, either with a fix or mobile point of view. Before developing the fluid and structure equations, a brief explanation on the pros and cons of these descriptions is given. Which description is used will determine how the spatial coordinates evolve with time when studying fluid or solid matter.

- In a Lagrangian framework, the spatial coordinates used to study the matter behavior follow the material point to which it is associated. Hence, the Lagrangian formalism is associated to a reference state with an initial material repartition. When the material points undergo displacements, it is however still referred to with spatial coordinate on the reference configuration. This formalism is widely used in the domain of structural mechanics, for which it is very convenient to follow each particle movement, which remains most of the time of limited amplitude. However, many fluid problems are impractical to study with such a formalism because, most of the time, fluid particles are not constrained spatially, which means they are likely to flow far away from the interest zone, making it hard and inconvenient to follow them during their travel, though some exceptions exist (Bennett et al., 2006).

- In an Eulerian framework, the matter is studied through fixed spatial coordinates. It means that, even though the material point move, the point of view associated with a spatial coordinate does not change. Hence, instead of following the particle through its displacement like a Lagrangian formalism, the flux of material points is observed on a fixed spatial coordinates, and the particles observed at two distinct times at a given spatial coordinate are almost never the same. When studying a fluid in a time dependent domain, Eulerian framework has a disadvantage: if an interface is moving, then some points of space that are part of the fluid domain at one time might be outside of the fluid domain at another time, which means it will be inconsistent to calculate the fluid solution. Moreover, one should note that there exists a method to study the linear fluctuations of the fluid loads based on an Eulerian framework (Fernández and Le Tallec, 2003), based on a reference interface. However, the author of the present manuscript could not adapt this linearized formulation to the case of potential flows. Therefore, another solution would be to use an observation point that is able to move in order to remain in the fluid domain when the boundaries are deformed, without having to follow the large movements of the fluid particles, which is the case with an ALE description.

- Finally, in an Arbitrary-Lagrangian-Eulerian framework, the material zone associated with a spatial coordinate is neither the exact same geometric zone where material particles are observed flowing, nor the coordinates of the material point after it moved from the reference configuration. Instead, it consists in observing the flow of material particles through a zone whose position varies with time, but not necessarily following the movement of the particles observed. For examples of studies based on the ALE, see (Nitikitpaiboon and Bathe, 1993; Pfister et al., 2019; Mavaleix-Marchessoux, 2020). The next section will give more in details on how the Arbitrary-Lagrangian-Eulerian framework is used in the very case studied in this manuscript.

Given that the ALE description is well suited for modeling the fluid-structure interaction, the following sections will introduce the model associated with such a description.

II.1.2 Kinematics of the structure on a reference domain

The ALE description is based on a point of view following the movements of a solid material particle at the interface. With this in mind, this section will give a more complete description of the interface motion based on a decomposition comprised of rigid body movements and elastic deformations, before introducing the ALE description in the following section. This decomposition of the movements introduces the fictitious domains associated with the undeformed and the undisplaced interfaces, which are not mandatory for the ALE description (Mavaleix-Marchessoux, 2020) but will come in handy for the linearization in section II.2. The different domains are sketched in Figure II.1.

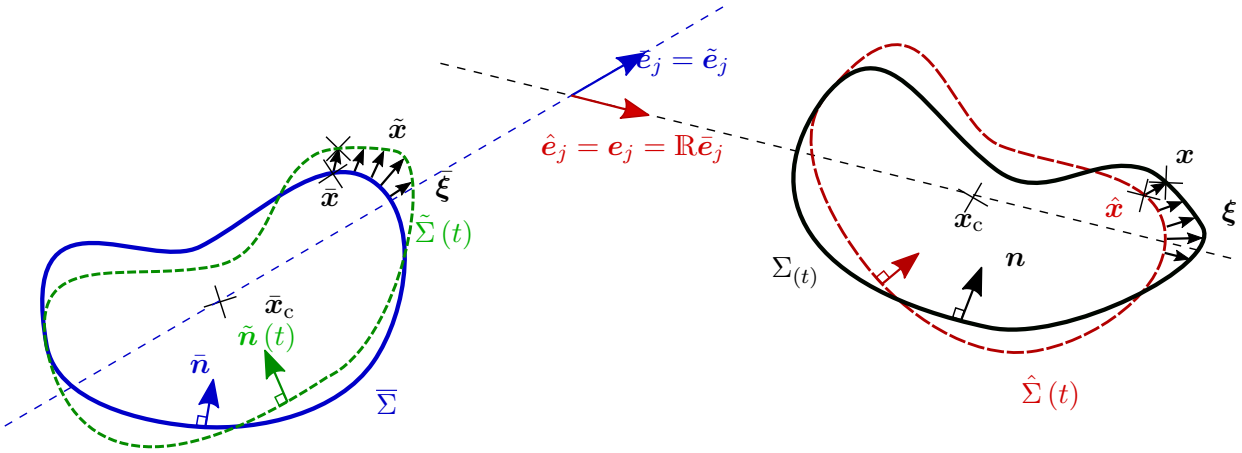

Figure II.1: Different mathematical domains used in the study: the physical domain $\Sigma_{(t)}$, the fictitous undeformed domain with rigid body motion $\hat{\Sigma}(t)$, the fictitous reference, time independent domain $\overline{\Sigma}$ and the fictitious deformed domain with no rigid body motions $\tilde{\Sigma}$. The two first are in a frame rotated by the rotation matrix $\mathbb{R}$ relatively to the reference frame.

A reference point $\boldsymbol{x}_c$ associated with the structure is introduced around which the rotations of the interface are expressed. In this manuscript, $\boldsymbol{x}_c$ has been arbitrarily fixed as the center of volume enclosed by the interface:

$$\boldsymbol{x}_c = \frac{\int_{\Omega_{\text{int}}} \boldsymbol{x}\, \mathrm{d}\Omega}{\mathcal{V}(\Omega_{\text{int}})}, \quad \mathcal{V}(\Omega_{\text{int}}) = \int_{\Omega_{\text{int}}} \mathrm{d}\Omega. \tag{II.1}$$

A reference domain associated with a fixed reference interface $\overline{\Sigma}$, whose spatial coordinates are noted $\bar{\boldsymbol{x}}$ and associated with a reference point $\bar{\boldsymbol{x}}_{\mathrm{c}}$, is introduced:

$$\overline{\Sigma} = \left\{ \bar{\boldsymbol{x}} \right\}. \tag{II.2}$$

The vectors from the reference domain are referred to using a bar notation. The reference point $\bar{\boldsymbol{x}}_{\mathrm{c}}$ is introduced with respect to the internal domain $\bar{\Omega}_{\mathrm{int}}$ bounded by $\overline{\Sigma}$:

$$\bar{\boldsymbol{x}}_{\mathrm{c}} = \frac{\int_{\bar{\Omega}_{\mathrm{int}}} \bar{\boldsymbol{x}} \, \mathrm{d}\Omega}{\mathcal{V}(\bar{\Omega}_{\mathrm{int}})}, \quad \mathcal{V}(\bar{\Omega}_{\mathrm{int}}) = \int_{\bar{\Omega}_{\mathrm{int}}} \mathrm{d}\Omega. \tag{II.3}$$

The deformations $\bar{\boldsymbol{\xi}}$ of the reference interface $\overline{\Sigma}$ are introduced as well as the fictitious deformed interface $\tilde{\Sigma}$:

$$\tilde{\Sigma}\,(t) = \left\{ \tilde{\boldsymbol{x}} \quad | \quad \tilde{\boldsymbol{x}} = \bar{\boldsymbol{x}} + \bar{\boldsymbol{\xi}}(\bar{\boldsymbol{x}}, t),\, \bar{\boldsymbol{x}} \in \overline{\Sigma} \right\}. \tag{II.4}$$

The physical domain $\Sigma_{(t)}$ associated with a reference point $\boldsymbol{x}_{\mathrm{c}}$ is obtained by applying a combination of deformations and rigid body motions to the reference interface $\overline{\Sigma}$, or equivalently by applying rigid body motions to the deformed interface $\tilde{\Sigma}\,(t)$. The rigid body motions are defined with the translation of the reference point $\bar{\boldsymbol{d}}_{\mathrm{c}}$ and with the rotation operator $\mathbb{R}$, a 3×3 orthogonal direct matrix, verifying the following property:

$$\mathbb{R}^{-1} = \mathbb{R}^{\mathrm{T}}, \tag{II.5}$$

as shown by Shabana (2003). The rotation $\mathbb{R} \in \mathrm{SO}(3)$ from the reference to the physical interface verifies:

$$\forall \boldsymbol{x} \in \Sigma_{(t)}, \exists\, \bar{\boldsymbol{x}} \in \overline{\Sigma},\, \boldsymbol{x} - \boldsymbol{x}_{\mathrm{c}} = \mathbb{R}(\bar{\boldsymbol{x}} + \bar{\boldsymbol{\xi}} - \bar{\boldsymbol{x}}_{\mathrm{c}}). \tag{II.6}$$

Complementary, the translation $\boldsymbol{d}_{\mathrm{c}}$ verifies:

$$\boldsymbol{x}_{\mathrm{c}} = \bar{\boldsymbol{x}}_{\mathrm{c}} + \boldsymbol{d}_{\mathrm{c}}. \tag{II.7}$$

The physical interface can consequently be defined by combining (II.4), (II.6) and (II.7):

$$\Sigma_{(t)} = \left\{ \boldsymbol{x} \quad | \quad \boldsymbol{x} = \bar{\boldsymbol{x}}_{\mathrm{c}} + \mathbb{R}(\bar{\boldsymbol{d}}_{\mathrm{c}}(t) + \bar{\boldsymbol{x}} + \bar{\boldsymbol{\xi}}(\bar{\boldsymbol{x}}, t) - \bar{\boldsymbol{x}}_{\mathrm{c}}),\, \bar{\boldsymbol{x}} \in \overline{\Sigma} \right\}. \tag{II.8}$$

The boundary condition (I.35) requires to determine the interface velocity, which is obtained by temporal derivation, combining equations (II.6) to (II.8):

$$\begin{aligned} \boldsymbol{v} = \dot{\boldsymbol{x}} &= \frac{\partial}{\partial t} \left(\bar{\boldsymbol{x}}_{\mathrm{c}} + \boldsymbol{d}_{\mathrm{c}}(t) + \mathbb{R}(\bar{\boldsymbol{x}} + \bar{\boldsymbol{\xi}}(\bar{\boldsymbol{x}}, t) - \bar{\boldsymbol{x}}_{\mathrm{c}}) \right) \\ &= \dot{\boldsymbol{d}}_{\mathrm{c}} + \dot{\mathbb{R}} \left(\bar{\boldsymbol{x}} + \bar{\boldsymbol{\xi}}(\bar{\boldsymbol{x}}, t) - \bar{\boldsymbol{x}}_{\mathrm{c}} \right) + \mathbb{R}\dot{\bar{\boldsymbol{\xi}}} = \dot{\boldsymbol{d}}_{\mathrm{c}} + \dot{\mathbb{R}}\mathbb{R}^{-1} \left(\boldsymbol{x} - \boldsymbol{x}_{\mathrm{c}} \right) + \mathbb{R}\dot{\bar{\boldsymbol{\xi}}}. \end{aligned} \tag{II.9}$$

The translation velocity $\boldsymbol{v}_{\mathrm{c}}$ and the rotation velocity $\boldsymbol{\omega}$ of the structure are introduced:

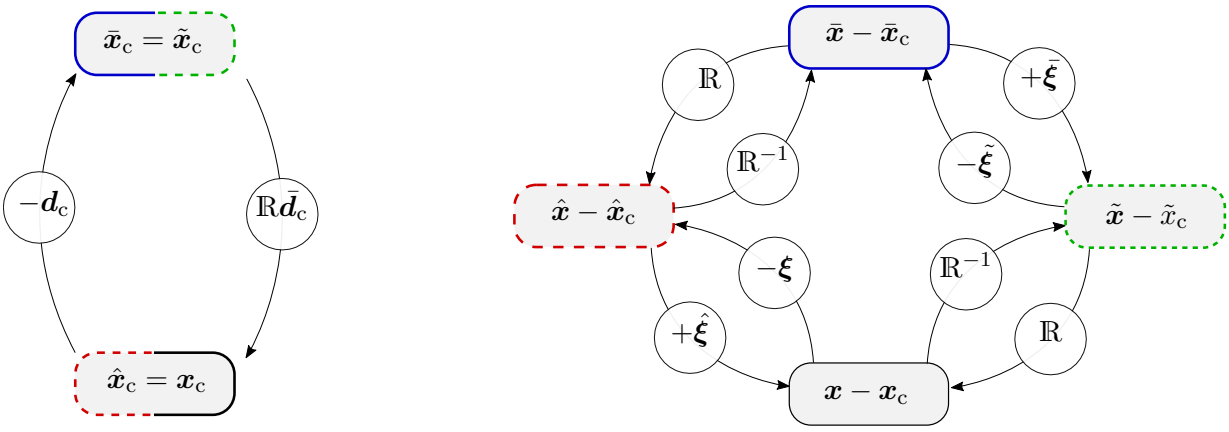

Figure II.2: Linear relationship between each domain: reference domain $\overline{\Sigma}$, undeformed domain $\hat{\Sigma}(t)$, deformed domain without rigid body motions $\tilde{\Sigma}(t)$ and physical domain $\Sigma_{(t)}$. As an example, the relation between $\bar{\boldsymbol{x}}_c$ and $\boldsymbol{x}_c$ reads $\boldsymbol{x}_c = \bar{\boldsymbol{x}}_c + \boldsymbol{d}_c$ and the relation between $\hat{\boldsymbol{x}} - \hat{\boldsymbol{x}}_c$ and $\bar{\boldsymbol{x}} - \bar{\boldsymbol{x}}_c$ reads $\hat{\boldsymbol{x}} - \hat{\boldsymbol{x}}_c = \mathbb{R}(\bar{\boldsymbol{x}} - \bar{\boldsymbol{x}}_c)$

$$\boldsymbol{v}_c := \dot{\boldsymbol{d}}_c \tag{II.10a}$$

$$\boldsymbol{\omega}_\wedge := \dot{\mathbb{R}}\mathbb{R}^{-1}, \tag{II.10b}$$

where the notation $\boldsymbol{a}_\wedge$ stands for the operator associated with the cross product:

$$\boldsymbol{a}_\wedge \boldsymbol{b} = \boldsymbol{a} \wedge \boldsymbol{b} \quad \forall \boldsymbol{a}, \boldsymbol{b} \in \mathbb{R}^3. \tag{II.11}$$

With a view to ensuring the existence of $\boldsymbol{\omega}$ as it has been defined in equation (II.10b), one might notice the skew-symmetry[1] of the term $\dot{\mathbb{R}}\mathbb{R}^{-1}$. By combining equations (II.9) and (II.10a) we obtain:

$$\boldsymbol{v} = \boldsymbol{v}_c + \boldsymbol{\omega} \wedge (\boldsymbol{x} - \boldsymbol{x}_c) + \mathbb{R}\dot{\tilde{\boldsymbol{\xi}}}. \tag{II.12}$$

The translation velocity and the rotation velocity are more convenient to manipulate on the reference interface, since they are the velocities relative to the pilot's point of view:

$$\bar{\boldsymbol{v}}_c = \mathbb{R}^{-1}\boldsymbol{v}_c \tag{II.13a}$$

$$\bar{\boldsymbol{\omega}} = \mathbb{R}^{-1}\boldsymbol{\omega}. \tag{II.13b}$$

By property of the rotation applied to a cross product

$$(\mathbb{R}\boldsymbol{a}) \wedge (\mathbb{R}\boldsymbol{b}) = \mathbb{R}(\boldsymbol{a} \wedge \boldsymbol{b}) \quad \forall \boldsymbol{a}, \boldsymbol{b} \in \mathbb{R}^3, \tag{II.14}$$

[1] $\mathbb{R}\mathbb{R}^{\mathrm{T}} = \mathbb{R}\mathbb{R}^{-1} = \mathbb{1} \Leftrightarrow \frac{\partial \mathbb{R}\mathbb{R}^{\mathrm{T}}}{\partial t} = 0 \Leftrightarrow \dot{\mathbb{R}}\mathbb{R}^{\mathrm{T}} + \mathbb{R}\dot{\mathbb{R}}^{\mathrm{T}} = 0 \Leftrightarrow \dot{\mathbb{R}}\mathbb{R}^{\mathrm{T}} = -\left(\dot{\mathbb{R}}\mathbb{R}^{\mathrm{T}}\right)^{\mathrm{T}} \Leftrightarrow \dot{\mathbb{R}}\mathbb{R}^{-1} = -\left(\dot{\mathbb{R}}\mathbb{R}^{-1}\right)^{\mathrm{T}}$ which demonstrates the skew-symmetry mentioned. Writing the non nil coefficients of $\boldsymbol{\omega}_\wedge$ such that $\boldsymbol{\omega}_\wedge \boldsymbol{a} = \boldsymbol{\omega} \wedge \boldsymbol{a}$ shows that any skew-symmetric matrix can be associated with the cross product of a unique vector, hence proving the existence of $\boldsymbol{\omega}$ as defined in (II.10b).

the term in $\boldsymbol{\omega}$ from equation (II.12) can be expressed by combining with equation (II.8):

$$\boldsymbol{\omega} \wedge (\boldsymbol{x} - \boldsymbol{x}_{\mathrm{c}}) = (\mathbb{R}\bar{\boldsymbol{\omega}}) \wedge \left(\mathbb{R}(\bar{\boldsymbol{x}} + \bar{\boldsymbol{\xi}} - \bar{\boldsymbol{x}}_{\mathrm{c}})\right) = \mathbb{R}\left(\boldsymbol{\omega} \wedge (\bar{\boldsymbol{x}} + \bar{\boldsymbol{\xi}} - \bar{\boldsymbol{x}}_{\mathrm{c}})\right) \tag{II.15}$$

leading to the expression of the interface velocity on the reference configuration by combining equations (II.12), (II.13) and (II.15):

$$\boldsymbol{v} = \mathbb{R}\left(\bar{\boldsymbol{v}}_{\mathrm{c}} + \bar{\boldsymbol{\omega}} \wedge (\bar{\boldsymbol{x}} + \bar{\boldsymbol{\xi}} - \bar{\boldsymbol{x}}_{\mathrm{c}}) + \dot{\bar{\boldsymbol{\xi}}}\right). \tag{II.16}$$

For control and guidance purposes, it is convenient to decompose the rigid body movements (composed of translations and rotations) and their time derivative from the reference interface (hence from the pilot's point of view), while the position is convenient to manipulate on the earth referential (hence using $\boldsymbol{d}_{\mathrm{c}}$). Such decomposition can be obtained by introducing the rigid body movements distributor $\overline{\mathbb{Q}}$ and the associated general coordinates of the rigid body velocity $\bar{\boldsymbol{\nu}}$ on the reference interface as:

$$\boldsymbol{v} = \mathbb{R}\left(\overline{\mathbb{Q}}\bar{\boldsymbol{\nu}} + \bar{\boldsymbol{\omega}} \wedge \bar{\boldsymbol{\xi}} + \dot{\bar{\boldsymbol{\xi}}}\right) \tag{II.17a}$$

$$\bar{\boldsymbol{\nu}} := (\bar{\boldsymbol{v}} \cdot \bar{\boldsymbol{e}}_x, .., \bar{\boldsymbol{v}} \cdot \bar{\boldsymbol{e}}_z, \bar{\boldsymbol{\omega}} \cdot \bar{\boldsymbol{e}}_x, .., \bar{\boldsymbol{\omega}} \cdot \bar{\boldsymbol{e}}_z)^{\mathrm{T}} \tag{II.17b}$$

$$\overline{\mathbb{Q}} := [\overline{\mathbb{Q}}_v, \overline{\mathbb{Q}}_\omega] \tag{II.17c}$$

$$\overline{\mathbb{Q}}_v = [\overline{\mathbb{Q}}_1, \overline{\mathbb{Q}}_2, \overline{\mathbb{Q}}_3] := [\bar{\boldsymbol{e}}_x, \bar{\boldsymbol{e}}_y, \bar{\boldsymbol{e}}_z] \tag{II.17d}$$

$$\overline{\mathbb{Q}}_\omega = [\overline{\mathbb{Q}}_4, \overline{\mathbb{Q}}_5, \overline{\mathbb{Q}}_6] := [\bar{\boldsymbol{e}}_x \wedge (\bar{\boldsymbol{x}} - \bar{\boldsymbol{x}}_{\mathrm{c}}), \bar{\boldsymbol{e}}_y \wedge (\bar{\boldsymbol{x}} - \bar{\boldsymbol{x}}_{\mathrm{c}}), \bar{\boldsymbol{e}}_z \wedge (\bar{\boldsymbol{x}} - \bar{\boldsymbol{x}}_{\mathrm{c}})]. \tag{II.17e}$$

$\bar{\boldsymbol{x}}_{\mathrm{c}}$ might be associated with any point of space, however some choices are more judicious than others.

The movements of the structure have been described in the above section. Among the resulting fictitious domains presented, the reference time independent domain is of great importance: the ALE formulation introduced in the section below is based on it.

II.1.3 Integral equation on a fixed reference domain

With the help of description of the interface kinematics, the ALE formulation of the fluid equations based on the reference interface is presented in this section. The equations lead to an expression of the fluid variables based on a time-independent domain.

The mapping function $\mathcal{Z}$ is introduced, conveniently connecting both physical and reference interfaces:

$$\begin{aligned} \mathcal{Z} \colon \overline{\Sigma} \times \mathbb{R}^+ &\longrightarrow \Sigma_{(t)} \times \mathbb{R}^+ \\ \bar{\boldsymbol{x}}, t &\longmapsto \boldsymbol{x}, t \end{aligned} \tag{II.18}$$

In order to obtain a formulation based on a fixed interface, the fluid variables on $\overline{\Sigma}$ are introduced as:

$$\bar{\phi}\colon \overline{\Sigma} \times \mathbb{R}^+ \longrightarrow \mathbb{R} \qquad \bar{\boldsymbol{x}}, t \longmapsto \phi(\mathcal{Z}(\bar{\boldsymbol{x}}, t)) \tag{II.19a}$$

$$\bar{\boldsymbol{u}}\colon \overline{\Sigma} \times \mathbb{R}^+ \longrightarrow \mathbb{R} \qquad \bar{\boldsymbol{x}}, t \longmapsto \mathbb{R}^{-1}\boldsymbol{u}(\mathcal{Z}(\bar{\boldsymbol{x}}, t)) \tag{II.19b}$$

$$\bar{p}\colon \overline{\Sigma} \times \mathbb{R}^+ \longrightarrow \mathbb{R} \qquad \bar{\boldsymbol{x}}, t \longmapsto p(\mathcal{Z}(\bar{\boldsymbol{x}}, t)) \tag{II.19c}$$

Since the scalars are not affected by the rotations of the domain, $\bar{\phi}$ and $\bar{p}$ are equal to their counterparts on the physical interface, whereas $\bar{\boldsymbol{u}}$ undergoes a rotation to match its physical counterpart. Because the integral equation has reduced the solution space dimension by one, those three variables do not need to be defined outside of the reference interface. With a view to expressing the integral equation (I.80) on a fixed interface, one needs to determine the value of $\boldsymbol{n}$ based on variables defined on $\overline{\Sigma}$. This is achieved by first introducing the gradient $\overline{\boldsymbol{\nabla}}$ on the reference interface:

$$\overline{\boldsymbol{\nabla}} a := \frac{\partial a}{\partial \boldsymbol{x}} \quad \forall a \in \mathcal{C}(\overline{\Sigma}, \mathbb{R}), \tag{II.20}$$

as well as $\overline{\boldsymbol{\nabla}}_{\mathrm{t}}$ its tangent counterpart:

$$\overline{\boldsymbol{\nabla}}_{\mathrm{t}} := (\mathbb{1} - \bar{\boldsymbol{n}} \otimes \bar{\boldsymbol{n}})\overline{\boldsymbol{\nabla}}. \tag{II.21}$$

With the help of the tangent gradient on the reference interface above, one can introduce the tangent gradient tensor $\overline{\nabla}_{\mathrm{t}}$ on the reference interface as:

$$\overline{\nabla}_{\mathrm{t}}^{\mathrm{T}} := (\mathbb{1} - \bar{\boldsymbol{n}} \otimes \bar{\boldsymbol{n}})\, \overline{\nabla}^{\mathrm{T}}. \tag{II.22}$$

The surface deformation gradient $\overline{\mathbb{F}}_{\mathrm{t}}$ and the surface deformation operator $\bar{\mathbb{\Phi}}_{\mathrm{t}}$ are finally defined as:

$$\overline{\mathbb{F}}_{\mathrm{t}}\colon \overline{\Sigma} \times \mathbb{R}^+ \longrightarrow \mathbb{R}^3 \otimes \mathbb{R}^3 \qquad \bar{\boldsymbol{x}}, t \longmapsto \mathbb{1} + \overline{\nabla}_{\mathrm{t}}\bar{\boldsymbol{\xi}}(\bar{\boldsymbol{x}}, t) \tag{II.23}$$

$$\bar{\mathbb{\Phi}}_{\mathrm{t}}\colon \overline{\Sigma} \times \mathbb{R}^+ \longrightarrow \mathbb{R}^3 \otimes \mathbb{R}^3 \qquad \bar{\boldsymbol{x}}, t \longmapsto \det\left(\overline{\mathbb{F}}_{\mathrm{t}}(\bar{\boldsymbol{x}}, t)\right) \overline{\mathbb{F}}_{\mathrm{t}}{}^{-\mathrm{T}}(\bar{\boldsymbol{x}}, t) \tag{II.24}$$

Nanson's formula (Holmes, 2009), demonstrated in section A.1, gives an expression of the normal fluctuation:

$$\tilde{\boldsymbol{n}}\, \mathrm{d}\tilde{\Sigma}\,(t) = \bar{\mathbb{\Phi}}_{\mathrm{t}}^{\mathrm{T}} \bar{\boldsymbol{n}}\, \mathrm{d}\overline{\Sigma} \tag{II.25}$$

The value of the normal $\boldsymbol{n}$ on the physical domain can be deduced from $\tilde{\boldsymbol{n}}$ by applying the rotation operator:

$$\boldsymbol{n}\, \mathrm{d}\Sigma = \mathbb{R}\left(\bar{\mathbb{\Phi}}_{\mathrm{t}}^{\mathrm{T}} \bar{\boldsymbol{n}}\right)\, \mathrm{d}\overline{\Sigma} \tag{II.26}$$

One might notice the nuance between $\bar{\boldsymbol{u}}$ which is obtained by rotating $\boldsymbol{u}$ with the operator $\mathbb{R}^{-1}$, whereas $\bar{\boldsymbol{n}}$ is not equal to $\boldsymbol{n}$ rotated by $\mathbb{R}^{-1}$: the rotation linking $\bar{\boldsymbol{n}}$ to $\boldsymbol{n}$ is the sum of the global rigid body rotation and the local rotation of the interface normal due to its elastic deformation. Keeping in mind the objective to express the integral equation on the reference interface, the counterparts of the Green function and its spatial derivative are defined as:

$$\begin{aligned} \overline{\partial_n G}(\bar{\boldsymbol{x}}, \bar{\boldsymbol{y}}, \bar{\boldsymbol{\xi}}) &:= \partial_{\boldsymbol{n}} G(\boldsymbol{x} - \boldsymbol{y}) \\ \overline{\boldsymbol{G_n}}(\bar{\boldsymbol{x}}, \bar{\boldsymbol{y}}, \bar{\boldsymbol{\xi}}) &:= G(\boldsymbol{x} - \boldsymbol{y}) \boldsymbol{n}(\boldsymbol{x}). \end{aligned} \tag{II.27}$$

As shown in equation (A.26d), the expressions of $\overline{\partial_n G}$ and $\overline{\boldsymbol{G_n}}$ do not vary with either the translation $\boldsymbol{d}_{\mathrm{c}}$ or the rotation $\mathbb{R}$ of the interface. This is due to the fact that the fluid domain is invariant by rotation or translation in the very case of this thesis, because the fluid domain is supposed to be unbounded (on the contrary to the example displayed in Figure II.3).

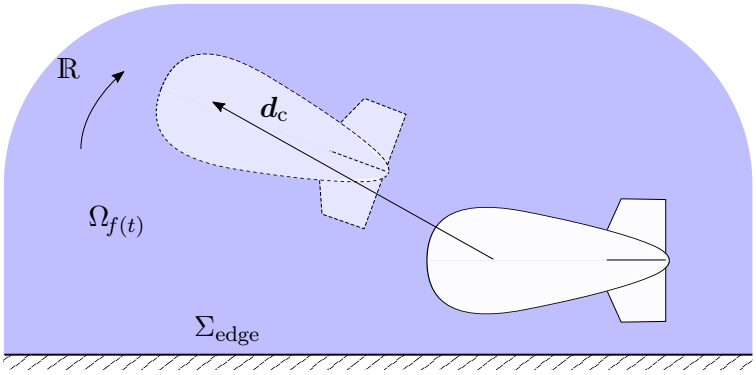

Figure II.3: Case of a fluid domain not invariant with either the rotation $\mathbb{R}$ or the rigid displacement $\boldsymbol{d}_{\mathrm{c}}$ of an interface because of the edge Σ_{edge} of the fluid domain at the bottom. The two structures show configurations of the interface at different times.

Remark

In practice, there are cases where airships evolve in environments where the fluid domain cannot be considered invariant by translation or rotation. For example, when studying the landing or take-off of airships, the relative distance and orientation between the airship and the ground indeed does affect the fluid domain. Another example is the case of airships evolving close to hills as studied by Carbone et al. (2019). As a consequence, when studying the dynamics of airships evolving in bounded fluid domains, extra care must be put into taking into account the boundaries of the fluid domain. For example, this can be done by meshing a finite part of the boundaries of the fluid domain that is large enough with respect to the airship dimensions in order to avoid important domain truncature effects. This method increases greatly the size of the BEM problems manipulated (Carbone et al., 2019). The image method allows to simulate the proximity of an infinite pane wall next to an airship by virtually removing the plane wall and adding a virtual frontier of the fluid domain defined as the reflection of the interface with respect to the plane wall (Carbone et al., 2019). Finally, a special Green function G (that depends on the position and orientation of the interface relatively to the fluid domain boundaries) verifying the no-slip boundary conditions at the edge of the fluid domains might be calculated and then used for the integral equation to naturally take into account the border effects on the fluid (Mavaleix-Marchessoux, 2020).

The single and double layer operators are defined on $\overline{\Sigma}$ as

$$\overline{\mathcal{H}}\colon \mathrm{C}^2(\overline{\Sigma}\times\mathbb{R}^+,\mathbb{R})\times\overline{\Sigma}\longrightarrow\mathbb{R}$$
$$\bar{\phi},\bar{\boldsymbol{y}}\longmapsto\kappa\bar{\phi}(\bar{\boldsymbol{y}})+\int_{\overline{\Sigma}}\overline{\partial_n G}(\bar{\boldsymbol{x}},\bar{\boldsymbol{y}})\left(\bar{\phi}\left(\bar{\boldsymbol{y}}\right)-\bar{\phi}\left(\bar{\boldsymbol{x}}\right)\right)\mathrm{d}\overline{\Sigma}(\bar{\boldsymbol{x}}),\quad \kappa=\begin{cases}1 & \text{for } (\mathcal{P}_{\text{ext}})\\ 0 & \text{for } (\mathcal{P}_{\text{int}})\end{cases} \tag{II.28a}$$

$$\overline{\mathcal{G}}\colon \mathrm{C}^1(\overline{\Sigma}\times\mathbb{R}^+,\mathbb{R}^+)\times\overline{\Sigma}\longrightarrow\mathbb{R}$$
$$\bar{\boldsymbol{v}},\bar{\boldsymbol{y}}\longmapsto\int_{\overline{\Sigma}}\overline{\boldsymbol{G_n}}(\bar{\boldsymbol{x}},\bar{\boldsymbol{y}}).\bar{\boldsymbol{v}}\,\mathrm{d}\overline{\Sigma}(\bar{\boldsymbol{x}}) \tag{II.28b}$$

recalling that κ is either equal to 1 for the external problem $(\mathcal{P}_{\text{ext}})$ or to 0 for the internal problem $(\mathcal{P}_{\text{int}})$ as defined in equation (I.79). The operators verify

$$\overline{\mathcal{H}}(\bar{\phi},\bar{\boldsymbol{y}},\bar{\boldsymbol{\xi}})=\mathcal{H}(\phi,\boldsymbol{y}) \tag{II.29a}$$
$$\overline{\mathcal{G}}(\bar{\boldsymbol{v}},\bar{\boldsymbol{y}},\bar{\boldsymbol{\xi}})=\mathcal{G}(\boldsymbol{v},\boldsymbol{y}). \tag{II.29b}$$

$\overline{\mathcal{H}}$ and $\overline{\mathcal{G}}$ are linear with the velocity potential $\bar{\phi}$ and the structure velocity $\bar{\boldsymbol{v}}$ respectively. The integral representation (I.80) can therefore be rewritten on the reference interface:

$$\overline{\mathcal{H}}(\bar{\phi},\bar{\boldsymbol{y}})=\overline{\mathcal{G}}(\bar{\boldsymbol{v}},\bar{\boldsymbol{y}})\quad\forall\bar{\boldsymbol{y}}\in\overline{\Sigma}. \tag{II.30}$$

It can be seen that the expression above is independent of the relative position $\boldsymbol{d}_{\text{c}}$ and the angular position $\mathbb{R}$ due to the invariance of the fluid by translation and rotation, which shows that the kinematic problem is invariant as well by translation and rotation. The velocity associated to the solution $\bar{\phi}$ of the equation above can be obtained as:

$$\bar{\boldsymbol{u}}=\mathbb{R}^{-1}\left(\boldsymbol{\nabla}\phi\right)=\left(\mathbb{1}+\overline{\nabla}\bar{\boldsymbol{\xi}}\right)^{-\mathrm{T}}\overline{\boldsymbol{\nabla}}\bar{\phi}, \tag{II.31}$$

which will be useful to obtain an expression of the pressure on the reference interface in the following section.

Now that the definition of the Green's function and its derivative on the surface of the reference configuration made it possible to write the integral equation on this fixed surface independent of the deformations and rigid body motions(provided that $\overline{\mathcal{H}}$ and $\overline{\mathcal{G}}$ now depend on the deformations $\bar{\boldsymbol{\xi}}$), the next section will focus on the expression of the pressure and virtual power on the reference interface.

II.1.4 Formulation of the fluid work on a reference interface

The objective in this section is to express all the terms from equation (I.30) on the reference interface to calculate the virtual power of fluid $\delta\mathcal{P}_f$.

The time derivative of ϕ needs to be rewritten with respect to the reference interface. With this in mind, by applying the chain rule and recalling that $\bar{\boldsymbol{x}}$ is defined on a time-independent interface we obtain:

$$\frac{\mathrm{d}\bar{\phi}}{\mathrm{d}t} = \frac{\partial\bar{\phi}}{\partial t} + \frac{\partial\bar{\phi}}{\partial\bar{\boldsymbol{x}}}\cdot\frac{\partial\bar{\boldsymbol{x}}}{\partial t} = \dot{\bar{\phi}} \tag{II.32a}$$

$$\frac{\mathrm{d}\phi}{\mathrm{d}t} = \frac{\partial\phi}{\partial t} + \frac{\partial\phi}{\partial\boldsymbol{x}}\cdot\frac{\partial\boldsymbol{x}}{\partial t} = \dot{\phi} + \boldsymbol{\nabla}\phi\cdot\boldsymbol{v} = \dot{\phi} + \boldsymbol{v}\cdot\boldsymbol{u}, \tag{II.32b}$$

where the last line is obtained recalling that the velocity $\boldsymbol{v}$ of the interface $\Sigma_{(t)}$ writes as $\frac{\partial\boldsymbol{x}}{\partial t} = \boldsymbol{v}$ for $\boldsymbol{x}\in\Sigma_{(t)}$. Since by definition $\phi = \bar{\phi}$, the total fluctuation with time for both must be equal:

$$\frac{\mathrm{d}\phi}{\mathrm{d}t} = \frac{\mathrm{d}\bar{\phi}}{\mathrm{d}t}, \tag{II.33}$$

which gives combined with equations (II.32a) and (II.32b):

$$\dot{\phi} + \boldsymbol{v}\cdot\boldsymbol{u} = \dot{\bar{\phi}}. \tag{II.34}$$

Using the conservation of the scalar product with rotations property

$$(\mathbb{R}\boldsymbol{a})\cdot(\mathbb{R}\boldsymbol{b}) = \boldsymbol{a}\cdot\boldsymbol{b} \quad \forall\boldsymbol{a},\boldsymbol{b}\in\mathbb{R}^3, \tag{II.35}$$

the partial time derivative of the potential on the physical domain can be expressed with respect to the reference interface as

$$\dot{\phi}(\boldsymbol{x}) = \dot{\bar{\phi}} - \bar{\boldsymbol{v}}\cdot\bar{\boldsymbol{u}} \quad \text{for } \boldsymbol{x}\in\Sigma_{(t)}. \tag{II.36}$$

Using equation (II.35), the quadratic velocity term involved in the pressure equation (I.46) becomes

$$\boldsymbol{u}^2 = \bar{\boldsymbol{u}}^2. \tag{II.37}$$

The aerostatic terms of pressure depend on the relative position $\boldsymbol{x}-\bar{\boldsymbol{x}}_{\mathrm{c}}$ which is expressed on the reference interface thanks to equation (II.8):

$$\boldsymbol{x} - \bar{\boldsymbol{x}}_{\mathrm{c}} = \mathbb{R}(\bar{\boldsymbol{x}} + \bar{\boldsymbol{\xi}} - \bar{\boldsymbol{x}}_{\mathrm{c}}) + \boldsymbol{d}_{\mathrm{c}}. \tag{II.38}$$

Therefore, by using equation (II.26) the pressure at the interface can be expressed on the reference interface as

$$\frac{\bar{p}}{\rho_f} = \psi_{\mathrm{c}} - \dot{\bar{\phi}} + \bar{\boldsymbol{v}}\cdot\bar{\boldsymbol{u}} - \frac{1}{2}\bar{\boldsymbol{u}}^2 - \boldsymbol{g}\cdot\mathbb{R}(\bar{\boldsymbol{x}} - \bar{\boldsymbol{x}}_{\mathrm{c}} + \bar{\boldsymbol{\xi}} + \bar{\boldsymbol{d}}_{\mathrm{c}}). \tag{II.39}$$

In order to calculate the virtual power of the fluid, we introduce the virtual velocity $\delta\bar{\boldsymbol{v}} = \mathbb{R}^{-1}\delta\boldsymbol{v}$ of the interface that will be used to calculate the virtual power later in section II.1.4. Similarly to the physical velocity, the virtual velocity can be decomposed as a unique sum of rigid body and elastic motion as:

$$\delta\boldsymbol{v} = \delta\boldsymbol{v}_{\mathrm{c}} + \delta\boldsymbol{\omega}\wedge(\boldsymbol{x}-\boldsymbol{x}_{\mathrm{c}}) + \delta\dot{\boldsymbol{\xi}}. \tag{II.40}$$

The equivalent virtual velocity is obtained on the reference interface with a rotation:

$$\delta\bar{\boldsymbol{v}} = \mathbb{R}^{-1}\delta\boldsymbol{v} \quad = \delta\bar{\boldsymbol{v}}_{\mathrm{c}} + \delta\bar{\boldsymbol{\omega}}\wedge(\bar{\boldsymbol{x}}-\bar{\boldsymbol{x}}_{\mathrm{c}}) + \delta\bar{\boldsymbol{\omega}}\wedge\bar{\boldsymbol{\xi}} + \delta\dot{\bar{\boldsymbol{\xi}}}. \tag{II.41}$$

In the expression above, the virtual terms $\delta\dot{\bar{\boldsymbol{\xi}}}$, $\delta\bar{\boldsymbol{v}}$ and $\delta\bar{\boldsymbol{\omega}}$ enable to respectively to obtain the elastic generalized forces, the forces and the moments exerted by the fluid on the structure. The normal component of the virtual velocity can be expressed on the reference interface as:

$$\begin{aligned}\delta\boldsymbol{v}\cdot\boldsymbol{n}\,\mathrm{d}\Sigma &= (\mathbb{R}\delta\bar{\boldsymbol{v}})\cdot(\mathbb{R}(\bar{\Phi}_{\mathrm{t}}^{\mathrm{T}}\bar{\boldsymbol{n}}))\,\mathrm{d}\overline{\Sigma}\\ &= \delta\bar{\boldsymbol{v}}\cdot(\bar{\Phi}_{\mathrm{t}}^{\mathrm{T}}\bar{\boldsymbol{n}})\,\mathrm{d}\overline{\Sigma}.\end{aligned}$$

Finally, one can thus write the virtual power of the fluid on the interface by combining equations (I.30), (II.36), (II.37) and (II.42):

$$\delta\mathcal{P}_f = \rho_f\int_{\overline{\Sigma}}\left[\psi_{\mathrm{c}} - \dot{\bar{\phi}} + \bar{\boldsymbol{v}}\cdot\bar{\boldsymbol{u}} - \frac{1}{2}\bar{\boldsymbol{u}}^2 + \boldsymbol{g}\cdot\left(\mathbb{R}(\bar{\boldsymbol{x}}-\bar{\boldsymbol{x}}_{\mathrm{c}}+\bar{\boldsymbol{\xi}})+\boldsymbol{d}_{\mathrm{c}}\right)\right]\delta\bar{\boldsymbol{v}}\cdot(\bar{\Phi}_{\mathrm{t}}^{\mathrm{T}}\bar{\boldsymbol{n}})\,\mathrm{d}\overline{\Sigma}. \tag{II.42}$$

In this section, the ALE framework led to equations conveniently linking the force of the flow on a moving structure which was not the case with the Eulerian framework from section I.3.1. The main equations giving the force of the flow are summarized in the following paragraph.

Overview of the kinematic and dynamic potential flow equations in an ALE framework.

The movements of the structure can be split into rigid body motions described through translation $\boldsymbol{d}_{\mathrm{c}}$ and rotation $\mathbb{R}$ with equation (II.8) connecting the reference and time dependent interfaces $\overline{\Sigma}$ and $\Sigma_{(t)}$:

$$\boldsymbol{x} = \boldsymbol{d}_{\mathrm{c}} + \mathbb{R}(\bar{\boldsymbol{x}} + \bar{\boldsymbol{\xi}} - \bar{\boldsymbol{x}}_{\mathrm{c}}).$$

The kinematics of the structure are described in equation (II.16) with a decomposition into rigid body and elastic movements:

$$\begin{aligned}\bar{\boldsymbol{v}} &= \bar{\boldsymbol{v}}_{\mathrm{c}} + \bar{\boldsymbol{\omega}}\wedge(\bar{\boldsymbol{x}}+\bar{\boldsymbol{\xi}}-\bar{\boldsymbol{x}}_{\mathrm{c}}) + \dot{\bar{\boldsymbol{\xi}}}\\ &= \overline{\mathbb{Q}}\bar{\boldsymbol{\nu}} + \bar{\boldsymbol{\omega}}\wedge\bar{\boldsymbol{\xi}} + \dot{\bar{\boldsymbol{\xi}}}.\end{aligned}$$

The fluid problem can be split into kinematic and dynamic equations. The equation of the fluid ($\mathcal{F}_{\mathcal{K}}$) and the kinematic interface condition ($\mathcal{I}_{\mathcal{K}}$) lead to the integral equation (II.30) allowing to solve the flow potential ϕ depending on its value and normal derivative at the reference interface:

$$\left.\begin{array}{lllll}(\mathcal{F}_{\mathcal{K}}): & \Delta\phi & = 0 & \text{in } \Omega_{f(t)}\\ (\mathcal{I}_{\mathcal{K}}): & \partial_{\boldsymbol{n}}\phi & = \boldsymbol{v}\cdot\boldsymbol{n} & \text{on } \Sigma_{(t)}\end{array}\right\}\quad \overline{\mathcal{H}}(\bar{\phi},\bar{\boldsymbol{y}}) = \overline{\mathcal{G}}(\bar{\boldsymbol{v}},\bar{\boldsymbol{y}})\quad \forall\{\bar{\boldsymbol{y}},t\}\in\overline{\Sigma}\times\mathbb{R}^+.$$

The latter equation on $\overline{\Sigma}$ is the integral equation on the reference domain and enables to solve the potential $\bar{\phi}$ at the interface as a function of its velocity $\bar{\boldsymbol{v}}$. The potential solution $\bar{\phi}$ enables to obtain the virtual power $\delta\mathcal{P}_f$ of the fluid on the interface through ($\mathcal{F}_{\mathcal{D}}$), the fluid dynamic equation (II.42):

$$(\mathcal{F}_{\mathcal{D}}):\quad \delta\mathcal{P}_f = \int_{\overline{\Sigma}}\bar{p}(\bar{\Phi}_{\mathrm{t}}^{\mathrm{T}}\bar{\boldsymbol{n}}).\delta\bar{\boldsymbol{v}}\,\mathrm{d}\overline{\Sigma}.$$

One can show that the virtual movements $\delta\bar{\boldsymbol{v}}$ kinematically admissible can be decomposed similarly to the movements of the structure as in equation (II.41):

$$\delta\bar{\boldsymbol{v}} = \overline{\mathbb{Q}}\delta\bar{\boldsymbol{\nu}} + \delta\bar{\boldsymbol{\omega}} \wedge \bar{\boldsymbol{\xi}} + \delta\dot{\bar{\boldsymbol{\xi}}}.$$

Once these have been obtained, the coupling of the interface dynamic condition ($\mathcal{I}_{\mathcal{D}}$) with a structure weak equation ($\mathcal{S}$) links the virtual power $\delta\mathcal{P}_s$ of the structure with the help of the structure stiffness and mass operators detailed in Chapter III.

The ALE description introduced in this section leads to a new model where the fluid variables are expressed on a time-independent reference domain. However, the expression of the operators from equation (I.79) has a nonlinear dependence with the displacements of the interface, which results in the necessity to recalculate them at each deformation step of the structure as done by Mavaleix-Marchessoux (2020); Veron et al. (2016). This is a costly procedure. To avoid such recalculations, the next section introduces an original linearization method to perform calculations based on reference, time-independent operators in the case of small perturbations of the system.

II.2 Introduction of the linearized ALE integral equation for a potential flow around a flexible structure

The objective of this section is to introduce a fluid model whose operators does not have to be recalculated when the interface moves. It is obtained by calculating the linear perturbation of the fluid solution for small movements of the structure around a zero order solution.

II.2.1 Linearization of the flow perturbations for small elastic movements of the structure

In the context of flexible airships dynamics, it is usual to assume that the deformations of the interface are small with respect to the structure size (Li et al., 2009; Azouz et al., 2012; Li et al., 2011), which is the case as well for submarines or bubbles as an examples (Mavaleix-Marchessoux, 2020; Miloh and Galper, 1993). In agreement with this hypothesis, the linear perturbations of the virtual power of the flow induced by small movements of the structure are addressed in this section. This approach will enable both stability analysis by linearizing all the kinematics of the structure (hence with both order zero and one rigid body movements as well), and guidance or trajectories determination by linearizing only the elastic deformations while keeping only the rigid body movements at order zero. For the first application, the order zero rigid body movements are a given of the problem, around which the deformations and rigid body small perturbations are studied. In the second case, both rigid body movements and elastic are unknown and need to be solved.

The small perturbations hypothesis is satisfied under the conditions

$$\varepsilon = \max_{(\bar{\boldsymbol{x}}\in\overline{\Sigma},t\in\mathbb{R}^+)} \left(\frac{\|\boldsymbol{\xi}\|}{L}, \overline{\nabla}_{\mathrm{t}}\bar{\boldsymbol{\xi}}, \frac{1}{V}\left\|\dot{\bar{\boldsymbol{\xi}}}\right\| \right) \ll 1 \tag{II.43}$$

and (II.43) enables to write the order of magnitude recalling the structure characteristic length L and velocity V introduced in Chapter I:

$$\bar{\boldsymbol{\xi}} \sim \varepsilon L \tag{II.44a}$$
$$\overline{\nabla}_{\mathrm{t}}\bar{\boldsymbol{\xi}} \sim \varepsilon \tag{II.44b}$$
$$\dot{\bar{\boldsymbol{\xi}}} \sim \varepsilon V. \tag{II.44c}$$

The above expressions encourage us to introduce a new variable $\bar{\boldsymbol{\xi}}'$ with the same order of magnitude as L such that:

$$\bar{\boldsymbol{\xi}} = \varepsilon\bar{\boldsymbol{\xi}}', \qquad \frac{\bar{\boldsymbol{\xi}}'}{L} \sim \overline{\nabla}_{\mathrm{t}}\bar{\boldsymbol{\xi}}' \sim 1 \tag{II.45a}$$
$$\dot{\bar{\boldsymbol{\xi}}} = \varepsilon\dot{\bar{\boldsymbol{\xi}}}', \qquad \frac{1}{V}\dot{\bar{\boldsymbol{\xi}}}' \sim 1. \tag{II.45b}$$

Thanks to this new deformation variable $\bar{\boldsymbol{\xi}}'$, the small perturbations of the velocity potential, the pressure and finally the virtual power of the fluid on the structure will be calculated. However, the variables aforementioned depend on other kinematics variables than the deformations $\bar{\boldsymbol{\xi}}, \partial\bar{\boldsymbol{\xi}}/\partial t$, which is why these other kinematic variables are linearized first. But before doing so, it is convenient to have in mind their characteristic amplitude. As rotation does not modify the magnitude:

$$\mathbb{R} \sim 1, \tag{II.46}$$

one can deduce from equation (II.12) that

$$\frac{\bar{\boldsymbol{v}}}{V} \sim 1 \tag{II.47a}$$
$$\frac{L}{V}\bar{\boldsymbol{\omega}} \sim 1 \tag{II.47b}$$

Finally, we arbitrarily impose that the order of magnitude of the structure translations is comparable to the characteristic size of the structure

$$\frac{\bar{\boldsymbol{d}}_{\mathrm{c}}}{L} \sim 1. \tag{II.48}$$

In view of the orders of magnitude of the parameters aforementioned, the small perturbations $\mathbb{R}'$, $\bar{\boldsymbol{d}}'_{\mathrm{c}}$, $\bar{\boldsymbol{v}}'_{\mathrm{c}}$ and $\bar{\boldsymbol{\omega}}'$ of these kinematic parameters is introduced as

$$\mathbb{R} = \mathbb{R}^o + \mathbb{R}', \qquad \mathbb{R}^o \sim \mathbb{R}' \sim 1 \tag{II.49a}$$
$$\boldsymbol{d}_{\mathrm{c}} = \boldsymbol{d}^o_{\mathrm{c}} + \varepsilon\boldsymbol{d}'_{\mathrm{c}}, \qquad \frac{\boldsymbol{d}^o_{\mathrm{c}}}{L} \sim \frac{\boldsymbol{d}'_{\mathrm{c}}}{L} \sim 1 \tag{II.49b}$$
$$\bar{\boldsymbol{v}}_{\mathrm{c}} = \bar{\boldsymbol{v}}^o_{\mathrm{c}} + \varepsilon\bar{\boldsymbol{v}}'_{\mathrm{c}}, \qquad \frac{\bar{\boldsymbol{v}}^o_{\mathrm{c}}}{V} \sim \frac{\bar{\boldsymbol{v}}'_{\mathrm{c}}}{V} \sim 1 \tag{II.49c}$$
$$\bar{\boldsymbol{\omega}} = \bar{\boldsymbol{\omega}}^o + \varepsilon\bar{\boldsymbol{\omega}}', \qquad \frac{L}{V}\bar{\boldsymbol{\omega}}^o \sim \frac{L}{V}\bar{\boldsymbol{\omega}}' \sim 1. \tag{II.49d}$$

The operator $\mathbb{R}'$ is the small perturbation of the rotation operator $\mathbb{R}$, but it is not itself a rotation operator. It is a 3×3 matrix. However, it is shown in A.4 that the operator $\mathbb{R}'\mathbb{R}^{o\mathrm{T}}$ is a skew-symmetric matrix, and can consequently be described with only three independent perturbation coefficients. As mentioned before, any skew symmetric 3×3 matrix is associated with a unique cross product operator, which enables to introduce the vector $\boldsymbol{\theta}'$:

$$\boldsymbol{\theta}'_{\wedge} := \mathbb{R}'\mathbb{R}^{o\mathrm{T}} \tag{II.50}$$

Since using a rotation vector $\boldsymbol{\theta}'$ is less cumbersome than a rotation operator $\mathbb{R}'$, the small angular perturbations will be expressed with respect to the former in the equations to come. Introducing small perturbations of rigid body motions $\boldsymbol{d}'_{\mathrm{c}}$, $\boldsymbol{\theta}'$,$\bar{\boldsymbol{v}}'_{\mathrm{c}}$ and $\bar{\boldsymbol{\omega}}'$ can be useful for stability analysis. However, in order to compute the trajectory of a structure from temporal simulations, these perturbations of rigid body motions can be imposed as nil, since the zero-order solution becomes an unknown of the problem and no longer a given.

Linearized kinematics

Now that the perturbations of the interface kinematics of the structure have been introduced, we are interested in the consequences of these perturbations on the velocity potential, which is the first step toward obtaining the perturbations of the virtual power of the fluid. We expect the small movements of the structure defined by equation (II.43) to produce fluctuations on the velocity potential described at first order as

$$\bar{\phi} = \bar{\phi}^o + \varepsilon\bar{\phi}' + \mathcal{O}\left(\varepsilon^2\right), \quad \frac{\bar{\phi}^o}{VL} \sim \frac{\bar{\phi}'}{VL} \sim 1. \tag{II.51}$$

The fluctuations of $\bar{\phi}$ can be obtained with the integral equation on the reference interface, which thus need to be linearized first. The latter involves the normal fluctuations which are obtained using the linearized Nanson formula thanks to the small strains hypothesis $\overline{\nabla}_{\mathrm{t}}\bar{\boldsymbol{\xi}} \ll 1$ from equation (II.43) (Bonnet, 1999). Its calculation, whose details are given in section A.1, leads to the expression

$$\bar{\Phi}_{\mathrm{t}}^{\mathrm{T}}\bar{\boldsymbol{n}}\,\mathrm{d}\overline{\Sigma} = \bar{\boldsymbol{n}} + \varepsilon\bar{\boldsymbol{\tau}}'\,\mathrm{d}\overline{\Sigma}. \tag{II.52}$$

As mentioned in section A.1, the variable $\bar{\boldsymbol{\tau}}'$ we have introduced is linear with respect to the structure deformations $\bar{\boldsymbol{\xi}}'$, and contains information both on the normal rotation and the surface dilatation at first order. The Green function and its spatial derivative are obtained using a first order Taylor expansion (see section A.2 for details on the calculation and their expression), which leads to

$$\overline{\boldsymbol{G_n}} = \overline{\boldsymbol{G_n}}^o(\bar{\boldsymbol{x}}, \bar{\boldsymbol{y}}) + \varepsilon\overline{\boldsymbol{G_n}}'(\bar{\boldsymbol{x}}, \bar{\boldsymbol{y}}; \bar{\boldsymbol{\xi}}') + \mathcal{O}\left(\varepsilon^2\right), \tag{II.53a}$$

$$\overline{\partial_n G} = \overline{\partial_n G}^o(\bar{\boldsymbol{x}}, \bar{\boldsymbol{y}}) + \varepsilon\overline{\partial_n G}'(\bar{\boldsymbol{x}}, \bar{\boldsymbol{y}}; \bar{\boldsymbol{\xi}}') + \mathcal{O}\left(\varepsilon^2\right). \tag{II.53b}$$

The zero and first order of the operators $\mathcal{H}$ and $\mathcal{G}$ can consequently be obtained as follow, reminding the definition of κ from equation (I.79):

$$\overline{\mathcal{H}}^o\colon \mathrm{C}^2(\overline{\Sigma}\times\mathbb{R}^+,\mathbb{R})\times\overline{\Sigma}\longrightarrow\mathbb{R}$$
$$\bar{\phi},\bar{\boldsymbol{y}}\longmapsto\kappa\bar{\phi}(\bar{\boldsymbol{y}})+\int_{\overline{\Sigma}}\overline{\partial_n G}^o(\bar{\boldsymbol{x}},\bar{\boldsymbol{y}})\left(\bar{\phi}\left(\bar{\boldsymbol{y}}\right)-\bar{\phi}\left(\bar{\boldsymbol{x}}\right)\right)\,\mathrm{d}\overline{\Sigma}(\bar{\boldsymbol{x}}) \tag{II.54a}$$

$$\overline{\mathcal{H}}'\colon \mathrm{C}^2(\overline{\Sigma}\times\mathbb{R}^+,\mathbb{R})\times\overline{\Sigma}\times\mathrm{C}(\overline{\Sigma}\times\mathbb{R}^+,\mathbb{R}^3)\longrightarrow\mathbb{R}$$
$$\bar{\phi},\bar{\boldsymbol{y}};\bar{\boldsymbol{\xi}}\longmapsto\kappa\bar{\phi}(\bar{\boldsymbol{y}})+\int_{\overline{\Sigma}}\overline{\partial_n G}'(\bar{\boldsymbol{x}},\bar{\boldsymbol{y}};\bar{\boldsymbol{\xi}})\left(\bar{\phi}\left(\bar{\boldsymbol{y}}\right)-\bar{\phi}\left(\bar{\boldsymbol{x}}\right)\right)\,\mathrm{d}\overline{\Sigma}(\bar{\boldsymbol{x}})' \tag{II.54b}$$

$$\overline{\mathcal{G}}^o\colon \mathrm{C}^1(\overline{\Sigma}\times\mathbb{R}^+,\mathbb{R}^3)\times\overline{\Sigma}\longrightarrow\mathbb{R}$$
$$\bar{\boldsymbol{v}},\bar{\boldsymbol{y}}\longmapsto\int_{\overline{\Sigma}}\overline{\boldsymbol{G_n}}^o(\bar{\boldsymbol{x}},\bar{\boldsymbol{y}}).\bar{\boldsymbol{v}}\,\mathrm{d}\overline{\Sigma}(\bar{\boldsymbol{x}})\,' \tag{II.54c}$$

$$\overline{\mathcal{G}}'\colon \mathrm{C}^1(\overline{\Sigma}\times\mathbb{R}^+,\mathbb{R}^3)\times\overline{\Sigma}\times\mathrm{C}(\overline{\Sigma}\times\mathbb{R}^+,\mathbb{R}^3)\longrightarrow\mathbb{R}$$
$$\bar{\boldsymbol{v}},\bar{\boldsymbol{y}};\bar{\boldsymbol{\xi}}\longmapsto\int_{\overline{\Sigma}}\overline{\boldsymbol{G_n}}'(\bar{\boldsymbol{x}},\bar{\boldsymbol{y}};\bar{\boldsymbol{\xi}}).\bar{\boldsymbol{v}}\,\mathrm{d}\overline{\Sigma}(\bar{\boldsymbol{x}})\,' \tag{II.54d}$$

By combining equations (I.79), (II.52) and (II.53), one can obtain the first order development of the single and double layer operators

$$\overline{\mathcal{H}}(\bar{\phi},\bar{\boldsymbol{y}})=\overline{\mathcal{H}}^o(\bar{\phi},\bar{\boldsymbol{y}})+\varepsilon\overline{\mathcal{H}}'(\bar{\phi},\bar{\boldsymbol{y}};\bar{\boldsymbol{\xi}}')+\mathcal{O}\left(\varepsilon^2\right) \tag{II.55a}$$
$$\overline{\mathcal{G}}(\bar{\boldsymbol{u}},\bar{\boldsymbol{y}})=\overline{\mathcal{G}}^o(\bar{\boldsymbol{u}},\bar{\boldsymbol{y}})+\varepsilon\overline{\mathcal{G}}'(\bar{\boldsymbol{u}},\bar{\boldsymbol{y}};\bar{\boldsymbol{\xi}}')+\mathcal{O}\left(\varepsilon^2\right) \tag{II.55b}$$

Because of the linear properties of $\mathcal{H}$ and $\mathcal{G}$ with respect to variables $\bar{\phi}$ and $\bar{\boldsymbol{u}}$, we have the same linearity properties for $\mathcal{H}^o$, $\mathcal{G}^o$, $\mathcal{H}'$ and $\mathcal{G}'$. The integral equation (II.30) takes the interface velocity as an argument, which therefore needs to be expanded at first order as:

$$\bar{\boldsymbol{v}}=\bar{\boldsymbol{v}}^o+\bar{\boldsymbol{v}}' \tag{II.56a}$$
$$\text{with } \bar{\boldsymbol{v}}^o=\bar{\boldsymbol{v}}^o_{\mathrm{c}}+\bar{\boldsymbol{\omega}}^o\wedge(\bar{\boldsymbol{x}}-\bar{\boldsymbol{x}}_{\mathrm{c}})=\overline{\mathbb{Q}}\bar{\boldsymbol{\nu}}^o \tag{II.56b}$$
$$\tag{II.56c}$$
$$\text{and } \bar{\boldsymbol{v}}'=\bar{\boldsymbol{v}}'_{\mathrm{c}}+\bar{\boldsymbol{\omega}}'\wedge(\bar{\boldsymbol{x}}-\bar{\boldsymbol{x}}_{\mathrm{c}})+\bar{\boldsymbol{\omega}}^o\wedge\bar{\boldsymbol{\xi}}'+\dot{\bar{\boldsymbol{\xi}}}'=\overline{\mathbb{Q}}\bar{\boldsymbol{\nu}}'+\boldsymbol{\omega}^o\wedge\bar{\boldsymbol{\xi}}'+\dot{\bar{\boldsymbol{\xi}}}'. \tag{II.56d}$$

Combining equations (II.51), (II.55) and (II.56) enables to obtain the integral equation associated with the zero order and first order perturbations of the velocity potential

$$\mathcal{H}^o(\bar{\phi}^o,\bar{\boldsymbol{y}})+\varepsilon\mathcal{H}'(\bar{\phi}^o,\bar{\boldsymbol{y}})+\varepsilon\mathcal{H}^o(\bar{\phi}',\bar{\boldsymbol{y}})+\mathcal{O}\left(\varepsilon^2\right)=\mathcal{G}^o(\bar{\boldsymbol{v}}^o,\bar{\boldsymbol{y}})+\varepsilon\mathcal{G}'(\bar{\boldsymbol{v}}^o,\bar{\boldsymbol{y}})+\varepsilon\mathcal{G}^o(\bar{\boldsymbol{v}}',\bar{\boldsymbol{y}})+\mathcal{O}\left(\varepsilon^2\right),$$

which leads to the following equations:

$$\overline{\mathcal{H}}^o(\bar{\phi}^o,\bar{\boldsymbol{y}})=\overline{\mathcal{G}}^o(\bar{\boldsymbol{v}}^o,\bar{\boldsymbol{y}}) \tag{II.57a}$$
$$\overline{\mathcal{H}}^o(\bar{\phi}',\bar{\boldsymbol{y}})=\overline{\mathcal{G}}^o(\bar{\boldsymbol{v}}',\bar{\boldsymbol{y}})+\overline{\mathcal{G}}'(\bar{\boldsymbol{v}}^o,\bar{\boldsymbol{y}};\bar{\boldsymbol{\xi}}')-\overline{\mathcal{H}}'(\bar{\phi}^o,\bar{\boldsymbol{y}};\bar{\boldsymbol{\xi}}'). \tag{II.57b}$$

Noting how the first order integral equation involves the linear fluctuations of both the displacement $\bar{\boldsymbol{\xi}}'$ of the interface and its velocity, given by (II.56d), the velocity potential functions Φ_v and Φ_d associated with the velocity and displacement boundary conditions are respectively:

$$\begin{aligned}
&\Phi_v \colon \mathrm{C}(\overline{\Sigma}\times\mathbb{R}^+,\mathbb{R}^3) \longrightarrow \mathrm{C}(\overline{\Sigma}\times\mathbb{R}^+,\mathbb{R}) \\
&\qquad\qquad \bar{\boldsymbol{u}} \longmapsto \bar{\phi} \quad | \quad \left\{\overline{\mathcal{H}}^o(\bar{\phi},\bar{\boldsymbol{y}}) = \overline{\mathcal{G}}^o(\bar{\boldsymbol{u}},\bar{\boldsymbol{y}}) \quad \forall \bar{\boldsymbol{y}} \in \overline{\Sigma}\right\}
\end{aligned} \tag{II.58a}$$

$$\begin{aligned}
&\Phi_d \colon \mathbb{R}^6 \times \mathrm{C}(\overline{\Sigma}\times\mathbb{R}^+,\mathbb{R}^3) \longrightarrow \mathrm{C}(\overline{\Sigma}\times\mathbb{R}^+,\mathbb{R}) \\
&\qquad\qquad \bar{\boldsymbol{\nu}};\bar{\boldsymbol{\xi}} \longmapsto \bar{\phi} \quad | \quad \left\{ \begin{array}{ll} \mathcal{H}^o(\bar{\phi},\bar{\boldsymbol{y}}) & = \overline{\mathcal{G}}^o([\mathbb{O},\mathbb{1}]\bar{\boldsymbol{\nu}}\wedge\bar{\boldsymbol{\xi}},\bar{\boldsymbol{y}}) + \overline{\mathcal{G}}'(\overline{\mathbb{Q}}\bar{\boldsymbol{\nu}},\bar{\boldsymbol{y}};\bar{\boldsymbol{\xi}})... \\ & \quad -\overline{\mathcal{H}}'(\Phi_v(\overline{\mathbb{Q}}\bar{\boldsymbol{\nu}}),\bar{\boldsymbol{y}};\bar{\boldsymbol{\xi}})) \quad \forall \bar{\boldsymbol{y}} \in \overline{\Sigma} \end{array} \right\}
\end{aligned} \tag{II.58b}$$

By combining equations (II.55), (II.58a) and (II.58b) comes the linearity of Φ_v and Φ_v. The expression of the velocity potential at orders zero and one becomes:

$$\bar{\phi}^o = \Phi_v(\bar{\boldsymbol{v}}^o) \tag{II.59a}$$

$$\bar{\phi}' = \Phi_v\left(\overline{\mathbb{Q}}\bar{\boldsymbol{\nu}}' + \dot{\bar{\boldsymbol{\xi}}}'\right) + \Phi_d(\bar{\boldsymbol{\nu}}^o;\bar{\boldsymbol{\xi}}'). \tag{II.59b}$$

The above equation enables to understand what causes the velocity potential to fluctuate. First, the term $\Phi_v\left(\bar{\boldsymbol{v}}'\right)$ shows how the velocity of the interface is transmitted to the surrounding fluid. $\Phi_d(\bar{\boldsymbol{\nu}}^o,\bar{\boldsymbol{\xi}}')$ relates to the linear fluctuations of the velocity potential due to the variations of the domain geometry. As the interface shape changes, the flow has to reconfigurate around it, which is taken into account by the terms expression equation (II.58b). Moreover, because the interface is rotating, the deformation of the interface might influence its velocity by making the material points closer or farther from the rotation axis, which is taken into account by the term $\overline{\mathcal{G}}^o([\mathbb{O},\mathbb{1}]\bar{\boldsymbol{\nu}}\wedge\bar{\boldsymbol{\xi}},\bar{\boldsymbol{y}})$ from equation (II.58b). With a view to condensing the equations, making it more comfortable to manipulate them, the potential vectors, sometimes referred to as Kirchhoff potentials in the literature, are introduced (Thomasson and Woolsey, 2013):

$$\bar{\boldsymbol{\Psi}}(\bar{\boldsymbol{x}}) = \begin{pmatrix} \bar{\boldsymbol{\varphi}}(\bar{\boldsymbol{x}}) \\ \bar{\boldsymbol{\chi}}(\bar{\boldsymbol{x}}) \end{pmatrix}, \tag{II.60a}$$

$$\text{with } \bar{\boldsymbol{\varphi}}(\bar{\boldsymbol{x}}) = \begin{pmatrix} \Phi_v(\overline{\mathbb{Q}}_1) \\ \Phi_v(\overline{\mathbb{Q}}_2) \\ \Phi_v(\overline{\mathbb{Q}}_3) \end{pmatrix} \tag{II.60b}$$

$$\text{and } \bar{\boldsymbol{\chi}}(\bar{\boldsymbol{x}}) = \begin{pmatrix} \Phi_v(\overline{\mathbb{Q}}_4) \\ \Phi_v(\overline{\mathbb{Q}}_5) \\ \Phi_v(\overline{\mathbb{Q}}_6) \end{pmatrix} \tag{II.60c}$$

(II.60d)

where $\overline{\mathbb{Q}}_i$ is the i^{h} component of $\overline{\mathbb{Q}}$ as shown in equation (II.17). We then obtain a condensed expression of the potential and its fluctuations, conveniently highlighting the space and time dependence of each term:

$$\bar{\phi}^o(\bar{\boldsymbol{x}},t) = \bar{\boldsymbol{\varphi}}(\bar{\boldsymbol{x}})\cdot\bar{\boldsymbol{v}}_{\mathrm{c}}^o(t) + \bar{\boldsymbol{\chi}}(\bar{\boldsymbol{x}})\cdot\bar{\boldsymbol{\omega}}^o(t) = \bar{\boldsymbol{\Psi}}(\bar{\boldsymbol{x}})\cdot\bar{\boldsymbol{\nu}}^o(t) \tag{II.61a}$$

$$\bar{\phi}'(\bar{\boldsymbol{x}},t) = \bar{\boldsymbol{\Psi}}(\bar{\boldsymbol{x}})\cdot\bar{\boldsymbol{\nu}}'(t) + \Phi_v\left(\dot{\bar{\boldsymbol{\xi}}}'(\bar{\boldsymbol{x}},t)\right) + \Phi_d(\bar{\boldsymbol{\nu}}^o(t);\bar{\boldsymbol{\xi}}'(\bar{\boldsymbol{x}},t)) \tag{II.61b}$$

Now that the fluid velocity potential is determined, we can obtain the fluid velocity $\bar{\boldsymbol{u}}$ with

$$\bar{\boldsymbol{u}} = \bar{\boldsymbol{u}}^o + \varepsilon \bar{\boldsymbol{u}}', \quad \frac{\bar{\boldsymbol{u}}^o}{V} \sim \frac{\bar{\boldsymbol{u}}'}{V} \sim 1. \tag{II.62}$$

Using the gradient $\overline{\boldsymbol{\nabla}}\bar{\phi}$ is tricky since $\bar{\phi}$ is only calculated at the interface, making it inconvenient to calculate its normal derivative. However, it is still possible to calculate $\boldsymbol{u}$ only using the surface gradient of the velocity potential. For that purpose, the normal and tangential components of a vector at the interface are introduced:

$$\bar{\boldsymbol{a}}_{\mathrm{n}} := (\bar{\boldsymbol{n}} \otimes \bar{\boldsymbol{n}})\bar{\boldsymbol{a}} \tag{II.63a}$$
$$\bar{\boldsymbol{a}}_{\mathrm{t}} := \bar{\boldsymbol{a}} - \bar{\boldsymbol{a}}_{\mathrm{n}}. \tag{II.63b}$$

where $\otimes$ is the tensor product[2]. The order zero and one velocity calculations are detailed in equation A.31, leading to the following expression at order zero where the perturbations are neglected:

$$\bar{\boldsymbol{u}}^o = \bar{\boldsymbol{u}}^o_{\mathrm{t}} + \bar{\boldsymbol{u}}^o_{\mathrm{n}} \tag{II.64a}$$
$$\bar{\boldsymbol{u}}^o_{\mathrm{n}} = \bar{\boldsymbol{v}}^o_{\mathrm{n}} \tag{II.64b}$$
$$\bar{\boldsymbol{u}}^o_{\mathrm{t}} = (\overline{\boldsymbol{\nabla}}\bar{\phi}^o)_{\mathrm{t}} = \overline{\boldsymbol{\nabla}}_{\mathrm{t}}\bar{\phi}^o. \tag{II.64c}$$

The equivalent expression at first order is:

$$\bar{\boldsymbol{u}}' = \bar{\boldsymbol{u}}'_{\mathrm{t}} + \bar{\boldsymbol{u}}'_{\mathrm{n}} \tag{II.65a}$$
$$\bar{\boldsymbol{u}}'_{\mathrm{n}} = \bar{\boldsymbol{v}}'_{\mathrm{n}} + (\bar{\boldsymbol{v}}^o - \bar{\boldsymbol{u}}^o) \cdot \left(\overline{\nabla}_{\mathrm{t}}^{\mathrm{T}} \bar{\boldsymbol{\xi}}' \, \bar{\boldsymbol{n}}\right) \bar{\boldsymbol{n}} \tag{II.65b}$$
$$\bar{\boldsymbol{u}}'_{\mathrm{t}} = \overline{\boldsymbol{\nabla}}_{\mathrm{t}}\bar{\phi}' - \overline{\nabla}_{\mathrm{t}}^{\mathrm{T}} \bar{\boldsymbol{\xi}}' \, \bar{\boldsymbol{u}}^o. \tag{II.65c}$$

The expressions above enable to calculate the velocity at order zero and its first order perturbations with only spatial derivations of the velocity potential $\bar{\phi}$ tangential to the reference interface, which are convenient to calculate, contrarily to the normal derivative. This decomposition will come in handy for the numerical implementation. In a similar way to the velocity potential perturbations, the velocity perturbations can be seen as the linear fluctuations with respect to both deformations amplitude and velocity at the interface. This decomposition is denoted with the following functions:

$$\begin{aligned} \boldsymbol{\mathcal{U}}_v \colon \mathrm{C}^1(\overline{\Sigma} \times \mathbb{R}^+, \mathbb{R}^2) &\longrightarrow C^1(\overline{\Sigma} \times \mathbb{R}^+, \mathbb{R}^2) \\ \bar{\boldsymbol{v}} &\longmapsto \overline{\boldsymbol{\nabla}}_{\mathrm{t}}\Phi_v(\bar{\boldsymbol{v}}) + \bar{\boldsymbol{n}} \otimes \bar{\boldsymbol{n}} \;\; \bar{\boldsymbol{v}} \end{aligned} \tag{II.66a}$$

$$\begin{aligned} \boldsymbol{\mathcal{U}}_d \colon \mathbb{R}^6 \times C^2(\overline{\Sigma} \times \mathbb{R}^+, \mathbb{R}) &\longrightarrow \mathrm{C}^1(\overline{\Sigma} \times \mathbb{R}^+, \mathbb{R}^2) \\ \bar{\boldsymbol{\nu}}; \bar{\boldsymbol{\xi}} &\longmapsto \overline{\boldsymbol{\nabla}}_{\mathrm{t}}\Phi_d(\bar{\boldsymbol{\nu}}; \bar{\boldsymbol{\xi}}) - \overline{\nabla}_{\mathrm{t}}\bar{\boldsymbol{\xi}} \, \boldsymbol{\mathcal{U}}_v(\overline{\mathbb{Q}}\bar{\boldsymbol{\nu}}) + \left(\overline{\mathbb{Q}}\bar{\boldsymbol{\nu}} - \boldsymbol{\mathcal{U}}_v(\overline{\mathbb{Q}}\bar{\boldsymbol{\nu}})\right) \cdot \left(\overline{\nabla}_{\mathrm{t}}^{\mathrm{T}}\bar{\boldsymbol{\xi}} \, \bar{\boldsymbol{n}}\right) \bar{\boldsymbol{n}} \end{aligned} \tag{II.66b}$$

One should note the linearity of the functions above with respect to $\bar{\boldsymbol{v}}$, $\bar{\boldsymbol{\nu}}$ and $\bar{\boldsymbol{\xi}}$. With a view to obtaining an expression highlighting the linearity of the velocity field with respect to the order zero solution, a new formulation of the velocity is obtained by combining equations (II.64) to (II.66):

[2]The tensor product is defined as $(\boldsymbol{a} \otimes \boldsymbol{b})\boldsymbol{c} = \boldsymbol{a}(\boldsymbol{b} \cdot \boldsymbol{c}) \quad \forall \boldsymbol{a}, \boldsymbol{b}, \boldsymbol{c} \in \mathbb{R}^3$

$$\bar{\boldsymbol{u}}^o = \boldsymbol{\mathcal{U}}_v(\bar{\boldsymbol{v}}^o) = \boldsymbol{\mathcal{U}}_v(\overline{\mathbb{Q}}\bar{\boldsymbol{\nu}}^o) \tag{II.67a}$$

$$\bar{\boldsymbol{u}}' = \boldsymbol{\mathcal{U}}_v(\bar{\boldsymbol{v}}') + \boldsymbol{\mathcal{U}}_d(\bar{\boldsymbol{\nu}}^o; \bar{\boldsymbol{\xi}}') = \boldsymbol{\mathcal{U}}_v(\overline{\mathbb{Q}}\bar{\boldsymbol{\nu}}' + \dot{\bar{\boldsymbol{\xi}}}') + \boldsymbol{\mathcal{U}}_d(\bar{\boldsymbol{\nu}}^o, \bar{\boldsymbol{\xi}}'). \tag{II.67b}$$

Similarly to the potential fluctuations expressed with fixed vector potentials in (II.61), the fluid velocity fluctuations can be obtained with time-independent reference velocity fluctuations using the linear properties of the operators:

$$\bar{\boldsymbol{u}}' = \boldsymbol{\mathcal{U}}_v\left(\dot{\bar{\boldsymbol{\xi}}}'\right) + \left[\boldsymbol{\mathcal{U}}_v(\overline{\mathbb{Q}}_1), .., \boldsymbol{\mathcal{U}}_v(\overline{\mathbb{Q}}_6)\right]\bar{\boldsymbol{\nu}}'(t) + \left[\boldsymbol{\mathcal{U}}_d(\overline{\mathbb{Q}}_1; \bar{\boldsymbol{\xi}}'), .., \boldsymbol{\mathcal{U}}_d(\overline{\mathbb{Q}}_6; \bar{\boldsymbol{\xi}}')\right] \cdot \bar{\boldsymbol{\nu}}^o(t). \tag{II.68}$$

Now that the velocity perturbations of the flow have been characterized, we can move on to the determination of the force done by the fluid perturbations.

Linearized dynamics

With a view to expressing the linearized fluid forces, the order zero and one pressure expressions are determined from equations (II.39), (II.51) and (II.62):

$$\frac{\bar{p}^o}{\rho} = \psi_{\mathrm{c}} - \dot{\bar{\phi}}^o + \bar{\boldsymbol{v}}^o \cdot \bar{\boldsymbol{u}}^o - \frac{1}{2}(\bar{\boldsymbol{u}}^o)^2 - \boldsymbol{g} \cdot [\mathbb{R}^o(\bar{\boldsymbol{x}} - \bar{\boldsymbol{x}}_{\mathrm{c}}) + \boldsymbol{d}^o_{\mathrm{c}}] \tag{II.69a}$$

$$\frac{\bar{p}'}{\rho_f} = -\dot{\bar{\phi}}' + (\bar{\boldsymbol{v}}^o - \bar{\boldsymbol{u}}^o) \cdot \bar{\boldsymbol{u}}' + \bar{\boldsymbol{u}}^o \cdot \bar{\boldsymbol{v}}' - \boldsymbol{g} \cdot [\mathbb{R}'(\bar{\boldsymbol{x}} - \bar{\boldsymbol{x}}_{\mathrm{c}}) + \mathbb{R}^o\bar{\boldsymbol{\xi}}' + \boldsymbol{d}'_{\mathrm{c}}]. \tag{II.69b}$$

By multiplying equation (II.50) by $\mathbb{R}^o$ at the right one gets the expression of the angular array $\boldsymbol{\theta}'$ as a function of the rotation operators:

$$\mathbb{R}' = \boldsymbol{\theta}'_{\wedge}\mathbb{R}^o, \tag{II.70}$$

leading to a new expression of the pressure perturbations:

$$\frac{\bar{p}'}{\rho_f} = -\dot{\bar{\phi}}' + (\bar{\boldsymbol{v}}^o - \bar{\boldsymbol{u}}^o) \cdot \bar{\boldsymbol{u}}' + \bar{\boldsymbol{u}}^o \cdot \bar{\boldsymbol{v}}' + \boldsymbol{g} \cdot \left[\boldsymbol{\theta}' \wedge (\mathbb{R}^o(\bar{\boldsymbol{x}} - \bar{\boldsymbol{x}}_{\mathrm{c}})) + \mathbb{R}^o\bar{\boldsymbol{\xi}}' + \boldsymbol{d}'_{\mathrm{c}}\right] \tag{II.71}$$

The pressure expression above can be split into contribution of various physical nature. The terms quadratic in velocity (both velocities of the fluid and the interface) are referred to as dynamic pressure. It is worth noticing that d'Alembert's paradox (Newman, 2018) ensures that the dynamic pressure of an external fluid does not exert any force on a closed interface. The terms with a factor g are linked to gravity forces, and the terms proportional to $\dot{\phi}$ generate a phenomenon called the added mass, which is due to the inertia of the fluid accelerated via the fluid structure interface. This decomposition can be shown introducing the functions

$$\begin{aligned} \mathcal{P}^o_v \colon \mathbb{R}^6 \times \mathbb{R}^6 &\longrightarrow \mathrm{C}^1(\overline{\Sigma} \times \mathbb{R}^+, \mathbb{R}) \\ \bar{\boldsymbol{\nu}}_a, \bar{\boldsymbol{\nu}}_b &\longmapsto \left(\overline{\mathbb{Q}}\bar{\boldsymbol{\nu}}_a - \frac{1}{2}\boldsymbol{\mathcal{U}}_v(\overline{\mathbb{Q}}\bar{\boldsymbol{\nu}}_a)\right) \cdot \boldsymbol{\mathcal{U}}_v(\overline{\mathbb{Q}}\bar{\boldsymbol{\nu}}_b) \end{aligned} \tag{II.72a}$$

$$\begin{aligned} \mathcal{P}^o_g \colon \mathrm{SO}(3) \times \mathbb{R}^3 &\longrightarrow \mathrm{C}^1(\overline{\Sigma} \times \mathbb{R}^+, \mathbb{R}) \\ \mathbb{R}, \boldsymbol{d}_{\mathrm{c}} &\longmapsto \boldsymbol{g} \cdot (\mathbb{R}(\bar{\boldsymbol{x}} - \bar{\boldsymbol{x}}_{\mathrm{c}}) + \boldsymbol{d}_{\mathrm{c}}) \end{aligned} \tag{II.72b}$$

with $\mathcal{P}_v$ a bilinear function with respect to $\bar{\boldsymbol{\nu}}_a$ and $\bar{\boldsymbol{\nu}}_b$. One obtains by combining equations (II.69a) and (II.72) the condensed expression of the pressure at order zero, recalling from equation (II.56c) that $\bar{\boldsymbol{v}}^o = \overline{\mathbb{Q}}\bar{\boldsymbol{\nu}}^o$:

$$\frac{\bar{p}^o}{\rho_f} = \psi_{\mathrm{c}} + \mathcal{P}_v^o(\bar{\boldsymbol{\nu}}^o, \bar{\boldsymbol{\nu}}^o) - \bar{\boldsymbol{\Psi}}.\dot{\bar{\boldsymbol{\nu}}}^o + \mathcal{P}_g^o\left(\mathbb{R}^o, \boldsymbol{d}_{\mathrm{c}}^o\right). \tag{II.73}$$

The above equations highlight the previously mentioned quadratic dependence of the dynamic pressure with respect to the structure velocity, and the linear dependence of the added mass effects with the acceleration of the structure. In a similar way, one can group the pressure perturbations with various contributions

$$\begin{aligned}\mathcal{P}'_{v;\xi}\colon \mathbb{R}^6 \times \mathbb{R}^6 \times \mathrm{C}(\overline{\Sigma} \times \mathbb{R}^+, \mathbb{R}^3) &\longrightarrow \mathrm{C}^1(\overline{\Sigma} \times \mathbb{R}^+, \mathbb{R}) \\ \bar{\boldsymbol{\nu}}_a, \bar{\boldsymbol{\nu}}_b; \bar{\boldsymbol{\xi}}' &\longmapsto \left(\overline{\mathbb{Q}}\bar{\boldsymbol{\nu}}_a - \boldsymbol{\mathcal{U}}_v\left(\overline{\mathbb{Q}}\bar{\boldsymbol{\nu}}_a\right)\right) \cdot \boldsymbol{\mathcal{U}}_d(\bar{\boldsymbol{\nu}}_b; \bar{\boldsymbol{\xi}}') + \boldsymbol{\mathcal{U}}_v(\overline{\mathbb{Q}}\bar{\boldsymbol{\nu}}_a) \cdot [\mathbb{0}, \mathbb{1}]\bar{\boldsymbol{\nu}}_b \wedge \bar{\boldsymbol{\xi}}'\end{aligned} \tag{II.74a}$$

$$\begin{aligned}\mathcal{P}'_{v;v}\colon \mathbb{R}^6 \times \mathbb{R}^6 \times \mathrm{C}(\overline{\Sigma} \times \mathbb{R}^+, \mathbb{R}^3) &\longrightarrow \mathrm{C}^1(\overline{\Sigma} \times \mathbb{R}^+, \mathbb{R}) \\ \bar{\boldsymbol{\nu}}^o, \begin{pmatrix}\bar{\boldsymbol{\nu}}' \\ \dot{\bar{\boldsymbol{\xi}}}'\end{pmatrix} &\longmapsto \mathcal{P}'_{v;v}\left(\bar{\boldsymbol{\nu}}^o, \begin{pmatrix}\bar{\boldsymbol{\nu}}' \\ \dot{\bar{\boldsymbol{\xi}}}'\end{pmatrix}\right)\end{aligned}$$

$$\mathcal{P}'_{v;v}\left(\bar{\boldsymbol{\nu}}^o, \begin{pmatrix}\bar{\boldsymbol{\nu}}' \\ \dot{\bar{\boldsymbol{\xi}}}'\end{pmatrix}\right) = -\Phi_d(\bar{\boldsymbol{\nu}}^o; \dot{\bar{\boldsymbol{\xi}}}') + \left(\overline{\mathbb{Q}}\bar{\boldsymbol{\nu}}^o - \boldsymbol{\mathcal{U}}_v\left(\overline{\mathbb{Q}}\bar{\boldsymbol{\nu}}^o\right)\right) \cdot \boldsymbol{\mathcal{U}}_v(\overline{\mathbb{Q}}\bar{\boldsymbol{\nu}}' + \dot{\bar{\boldsymbol{\xi}}}') + \boldsymbol{\mathcal{U}}_v(\overline{\mathbb{Q}}\bar{\boldsymbol{\nu}}^o) \cdot \left(\overline{\mathbb{Q}}\bar{\boldsymbol{\nu}}' + \dot{\bar{\boldsymbol{\xi}}}'\right), \tag{II.74b}$$

$$\begin{aligned}\mathcal{P}'_{\dot{v};\xi}\colon \mathbb{R}^6 \times \mathrm{C}(\overline{\Sigma} \times \mathbb{R}^+, \mathbb{R}^3 &\longrightarrow \mathrm{C}^1(\overline{\Sigma} \times \mathbb{R}^+, \mathbb{R}) \\ \dot{\bar{\boldsymbol{\nu}}}, \bar{\boldsymbol{\xi}}' &\longmapsto -\Phi_d(\dot{\bar{\boldsymbol{\nu}}}, \bar{\boldsymbol{\xi}}')\end{aligned} \tag{II.74c}$$

$$\begin{aligned}\mathcal{P}'_g\colon \mathrm{SO}(3) \times \mathbb{R}^6 \times \mathrm{C}^1(\overline{\Sigma} \times \mathbb{R}^+, \mathbb{R}^3 &\longrightarrow \mathrm{C}^1(\overline{\Sigma} \times \mathbb{R}^+, \mathbb{R}) \\ \mathbb{R}^o, \begin{pmatrix}\boldsymbol{d}_{\mathrm{c}} \\ \boldsymbol{\theta} \\ \bar{\boldsymbol{\xi}}\end{pmatrix} &\longmapsto \boldsymbol{g} \cdot \left[\boldsymbol{\theta} \wedge \mathbb{R}^o\left(\bar{\boldsymbol{x}} - \bar{\boldsymbol{x}}_{\mathrm{c}}\right) + \mathbb{R}^o\bar{\boldsymbol{\xi}} + \boldsymbol{d}_{\mathrm{c}}\right]'\end{aligned} \tag{II.74d}$$

where $\mathcal{P}'_{v;\xi}$ is a trilinear operator and $\mathcal{P}'_{v;v}$ and $\mathcal{P}'_{\dot{v};\xi}$ are bilinear operators. However one should note that p'_g is not linear with respect to the rotation $\mathbb{R}^o$. The expression for the pressure perturbations becomes:

$$\frac{\bar{p}'}{\rho_f} = \mathcal{P}'_{v;\xi}(\bar{\boldsymbol{\nu}}^o, \bar{\boldsymbol{\nu}}^o, \bar{\boldsymbol{\xi}}') + \mathcal{P}'_{v;v}\left(\bar{\boldsymbol{\nu}}^o, \begin{pmatrix}\bar{\boldsymbol{\nu}}' \\ \dot{\bar{\boldsymbol{\xi}}}'\end{pmatrix}\right) + \mathcal{P}'_{\dot{v},\xi}\left(\dot{\bar{\boldsymbol{\nu}}}^o, \bar{\boldsymbol{\xi}}'\right) - \Phi_v\left(\dot{\bar{\boldsymbol{v}}}'\right) - \Phi_d\left(\bar{\boldsymbol{\nu}}^o; \dot{\bar{\boldsymbol{\xi}}}'\right) + \mathcal{P}'_g\left(\mathbb{R}^o, \begin{pmatrix}\boldsymbol{d}'_{\mathrm{c}} \\ \boldsymbol{\theta}' \\ \bar{\boldsymbol{\xi}}'\end{pmatrix}\right) \tag{II.75}$$

In the above equations, the terms $\mathcal{P}'_{v;\xi}$ is associated with the dynamic pressure perturbations due to interface geometry deformations. As the geometry of the interface changes, the fluid has to reconfigure, therefore perturbing the flow velocity as well as the dynamic pressure. The term $\mathcal{P}'_{v;v}$ is associated with the perturbations of the dynamic pressure occurring when the interface velocity incurs changes in the the velocity of the surrounding flow, thus perturbing the dynamic pressure. The term $\mathcal{P}'_{\dot{v}}$ dictates how the added mass effects associated with the acceleration of the structure at order zero vary with respect to the interface geometry. The added mass associated with the small

accelerations of the interface is described with Φ_v, whereas the changes in direction and amplitude of the aerostatic pressure due to the elevation and rotations of the interface are described by $\mathcal{P}'_g$. Because of the invariance of the kinematic problem by translation and rotation, the pressure term $\mathcal{P}'_{v,\xi}$ does not depend on the variables $\boldsymbol{d}'_c, \bar{\boldsymbol{\theta}}'$. On the other hand, as the gravitational force is oriented, the term $\mathcal{P}'_g$ is dependent on these two variables. In order to calculate the virtual power associated with the pressure of the fluid, the linearization of the virtual displacements is developed as:

$$\delta\bar{\boldsymbol{v}} = \delta\bar{\boldsymbol{v}}^o + \varepsilon\delta\bar{\boldsymbol{v}}', \qquad \delta\bar{\boldsymbol{v}}^o \sim \delta\bar{\boldsymbol{v}}' \tag{II.76a}$$

$$\delta\bar{\boldsymbol{v}}^o = \delta\bar{\boldsymbol{v}}_c + \delta\bar{\boldsymbol{\omega}} \wedge (\bar{\boldsymbol{x}} - \bar{\boldsymbol{x}}_c) + \delta\dot{\bar{\boldsymbol{\xi}}} \tag{II.76b}$$

$$\delta\bar{\boldsymbol{v}}' = \delta\bar{\boldsymbol{\omega}} \wedge \bar{\boldsymbol{\xi}}'. \tag{II.76c}$$

One should note that the first order perturbations of the virtual velocity field play an important role in order to obtain the correct value of the moment exerted by the fluid on the interface, since the deformation of the interface can influence the lever arm associated with the moment exerted by the pressure forces. As a consequence, the virtual power of the fluid can be expressed at order zero as

$$\delta\mathcal{P}_f^o = \rho_f \int_{\overline{\Sigma}} \bar{p}^o \delta\bar{\boldsymbol{v}}^o \cdot \bar{\boldsymbol{n}} \, \mathrm{d}\overline{\Sigma}, \tag{II.77}$$

and its perturbations are expressed as

$$\delta\mathcal{P}'_f = \rho_f \int_{\overline{\Sigma}} \bar{p}^o (\delta\bar{\boldsymbol{v}}^o \cdot \bar{\boldsymbol{\tau}}' + \delta\bar{\boldsymbol{v}}' \cdot \bar{\boldsymbol{n}}) + \bar{p}' \delta\bar{\boldsymbol{v}}^o \cdot \bar{\boldsymbol{n}} \, \mathrm{d}\overline{\Sigma}. \tag{II.78}$$

Now that an explicit expression of the perturbation of the fluid forces has been obtained with equation (II.78), we are interested in an expression of these perturbations under the form of mass, gyroscopic and stiffness loads from the flow, with a view to carrying out stability analysis in chapter IV.

II.2.2 Expression of the fluid forces on the interface acting as mass, gyroscopic and stiffness loads

This section introduces, under specific hypothesis which are detailed below, an expression of the fluid action as mass, gyroscopic and stiffness loads of the fluid on the interface. Furthermore, the zeroth, first or second order properties of these operators with the order zero kinematic parameters introduced in (II.49) are studied.

The translation vector, the rotation vector and the elastic deformations are grouped within a single global variable:

$$\mathbf{X} = \begin{pmatrix} \boldsymbol{d}'_c \\ \boldsymbol{\theta}' \\ \bar{\boldsymbol{\xi}}' \end{pmatrix}, \quad \mathbf{X} \in \mathbb{R}^6 \times \mathcal{C}(\overline{\Sigma}, \mathbb{R}^3). \tag{II.79}$$

The global perturbations of position $\mathbf{X}$ can be derived one or two times with respect to time, giving the following expressions:

$$\overline{\mathbf{V}} = \begin{pmatrix} \bar{\boldsymbol{\nu}}' \\ \dot{\bar{\boldsymbol{\xi}}}' \end{pmatrix} \tag{II.80a}$$

$$\dot{\overline{\mathbf{V}}} = \begin{pmatrix} \dot{\bar{\boldsymbol{\nu}}}' \\ \ddot{\bar{\boldsymbol{\xi}}}' \end{pmatrix} \tag{II.80b}$$

The virtual movements of the interface can be expressed with respect to the virtual global perturbations referred to as $\delta\overline{\mathbf{V}}$:

$$\delta\overline{\mathbf{V}} = \begin{pmatrix} \delta\bar{\boldsymbol{v}}_{\mathrm{c}} \\ \delta\bar{\boldsymbol{\omega}} \\ \delta\dot{\bar{\boldsymbol{\xi}}} \end{pmatrix}. \tag{II.81}$$

The added mass operator is introduced:

$$\mathrm{M}^f\left(\dot{\overline{\mathbf{V}}}, \delta\overline{\mathbf{V}}\right) = \int_{\overline{\Sigma}} \Phi_v(\dot{\bar{\boldsymbol{v}}}')\, \bar{\boldsymbol{n}} \cdot \delta\bar{\boldsymbol{v}}^o \,\mathrm{d}\overline{\Sigma}. \tag{II.82}$$

Similarly to the added mass, the gyroscopic operator is introduced, name associated with velocity-dependent conservative loads (by analogy with the gyroscopic effects of rotating structures) according to the load zoology established by Ziegler (1977):

$$\mathrm{G}^f(\bar{\boldsymbol{\nu}}^o, \overline{\mathbf{V}}, \delta\overline{\mathbf{V}}) = -\int_{\overline{\Sigma}} \left(p'_{v;v}(\bar{\boldsymbol{\nu}}^o, \bar{\boldsymbol{v}}') - \Phi_d(\bar{\boldsymbol{\nu}}^o, \dot{\bar{\boldsymbol{\xi}}}')\right) \bar{\boldsymbol{n}} \cdot \delta\bar{\boldsymbol{v}}^o \,\mathrm{d}\overline{\Sigma}. \tag{II.83}$$

The demonstration of the conservative aspect of the above loads is shown in Appendix D.2 and follows from the antisymmetry of the G^f operator demonstrated in section B via the Lagrange equations. Finally, the added stiffness operator is introduced:

$$\mathrm{K}^f{}_v\left(\bar{\boldsymbol{\nu}}^o, \bar{\boldsymbol{\nu}}^o, \mathbf{X}, \delta\overline{\mathbf{V}}\right) = -\int_{\overline{\Sigma}} \left[\mathcal{p}_v^o(\bar{\boldsymbol{\nu}}, \bar{\boldsymbol{\nu}}) \left(\bar{\boldsymbol{\tau}}'(\bar{\boldsymbol{\xi}}') \cdot \delta\bar{\boldsymbol{v}}^o + \bar{\boldsymbol{n}} \cdot \delta\bar{\boldsymbol{v}}'\right) + \mathcal{p}'_{v;\xi}(\bar{\boldsymbol{\nu}}, \bar{\boldsymbol{\nu}}, \bar{\boldsymbol{\xi}}')\bar{\boldsymbol{n}} \cdot \delta\bar{\boldsymbol{v}}^o \,\mathrm{d}\overline{\Sigma}\right. \tag{II.84a}$$

$$\mathrm{K}^f{}_{,\dot{v}}\left(\dot{\bar{\boldsymbol{\nu}}}^o, \mathbf{X}, \delta\overline{\mathbf{V}}\right) = -\int_{\overline{\Sigma}} -\bar{\boldsymbol{\Psi}} \cdot \dot{\bar{\boldsymbol{\nu}}}^o, \left(\bar{\boldsymbol{\tau}}'(\bar{\boldsymbol{\xi}}') \cdot \delta\bar{\boldsymbol{v}}^o + \bar{\boldsymbol{n}} \cdot \delta\bar{\boldsymbol{v}}'\right) + \mathcal{p}'_{\dot{v}}(\dot{\bar{\boldsymbol{\nu}}}^o, \bar{\boldsymbol{\xi}}')\bar{\boldsymbol{n}} \cdot \delta\bar{\boldsymbol{v}}^o \,\mathrm{d}\overline{\Sigma} \tag{II.84b}$$

$$\mathrm{K}^f{}_{,g}\left(\mathbb{R}^o, \boldsymbol{d}_{\mathrm{c}}^o, \mathbf{X}, \delta\overline{\mathbf{V}}\right) = \int_{\overline{\Sigma}} \mathcal{p}_g^o(\mathbb{R}^o, \boldsymbol{d}_{\mathrm{c}}^o) \left(\bar{\boldsymbol{\tau}}'(\bar{\boldsymbol{\xi}}') \cdot \delta\bar{\boldsymbol{v}}^o + \bar{\boldsymbol{n}} \cdot \delta\bar{\boldsymbol{v}}'\right) + \mathcal{p}'_g(\mathbb{R}^o, \mathbf{X})\bar{\boldsymbol{n}} \cdot \delta\bar{\boldsymbol{v}}^o \,\mathrm{d}\overline{\Sigma}. \tag{II.84c}$$

$$\mathrm{K}^f{}_{,\mathrm{h}}(\mathbf{X}, \delta\overline{\mathbf{V}}) = \int_{\overline{\Sigma}} \psi_{\mathrm{c}} \left(\bar{\boldsymbol{\tau}}' \cdot \delta\bar{\boldsymbol{v}}^o + \bar{\boldsymbol{n}} \cdot \delta\bar{\boldsymbol{v}}'\right) \,\mathrm{d}\overline{\Sigma} \tag{II.84d}$$

Remark

The stiffness operator associated with the dynamic pressure contains the follower force stiffness:

$$\mathrm{K}^f{}_{,\mathrm{fol}} = \int_{\overline{\Sigma}} \mathcal{p}_v^o \bar{\boldsymbol{\tau}}'.\delta\bar{\boldsymbol{v}}^o. \tag{II.85}$$

It is referred to as a follower force since the efforts applied by the pressure at order zero follow the fluctuating direction of the interface normal. This follower force is associated with a constant order

zero pressure because of the linearization that decouples pressure fluctuations and normal fluctuations at first order. In practice, the pressure efforts follow the interface normal but vary in amplitude at the same time because of the fluid reconfiguration leading to dynamic pressure variations. The follower force stiffness is not conservative by itself, but the overall stiffness of the fluid is conservative because of the fluid hypotheses of a potential flow without vortex shedding.

$$\begin{aligned}-\frac{\delta\mathcal{P}_f'}{\rho_f} =&\mathrm{M}^f\left(\dot{\overline{\mathbf{V}}},\delta\overline{\mathbf{V}}\right)+\mathrm{G}^f\left(\bar{\boldsymbol{\nu}}^o,\overline{\mathbf{V}},\delta\overline{\mathbf{V}}\right)+\mathrm{K}^f{}_v\left(\bar{\boldsymbol{\nu}}^o,\bar{\boldsymbol{\nu}}^o,\mathbf{X},\delta\overline{\mathbf{V}}\right)+\mathrm{K}^f{}_{,\dot{v}}\left(\dot{\bar{\boldsymbol{\nu}}}^o,\mathbf{X},\delta\overline{\mathbf{V}}\right)\ldots\\ &+\mathrm{K}^f{}_{,g}\left(\mathbb{R}^o,\boldsymbol{d}_{\mathrm{c}}^o,\mathbf{X},\delta\overline{\mathbf{V}}\right)+\mathrm{K}^f{}_{,\mathrm{h}}\left(\mathbf{X},\delta\overline{\mathbf{V}}\right).\end{aligned} \tag{II.86}$$

Because of the linear properties of the operators, it is possible to decompose them as follows:

$$\begin{aligned}\mathrm{K}^f{}_v\left(\bar{\boldsymbol{\nu}}^o,\bar{\boldsymbol{\nu}}^o,\mathbf{X},\delta\overline{\mathbf{V}}\right)&=\left(\bar{\boldsymbol{\nu}}^o\otimes\bar{\boldsymbol{\nu}}^o\right):\mathbb{K}_v^{f*}\left(\bar{\boldsymbol{\xi}}',\delta\overline{\mathbf{V}}\right)\bar{\boldsymbol{\nu}}^o\\ \mathrm{K}^f{}_{,\dot{v}}\left(\dot{\bar{\boldsymbol{\nu}}}^o,\mathbf{X},\delta\overline{\mathbf{V}}\right)&=\mathbf{K}_{f,\dot{v}}^*\left(\bar{\boldsymbol{\xi}}',\delta\overline{\mathbf{V}}\right)\cdot\dot{\bar{\boldsymbol{\nu}}}^o\\ \mathrm{G}^f\left(\bar{\boldsymbol{\nu}}^o,\overline{\mathbf{V}},\delta\overline{\mathbf{V}}\right)&=\mathbf{G}^{f*}\left(\overline{\mathbf{V}},\delta\overline{\mathbf{V}}\right)\cdot\boldsymbol{\nu}^o\\ \text{with }\left(\mathbb{K}_v^{f*}\left(\bar{\boldsymbol{\xi}}',\delta\bar{\boldsymbol{\xi}}\right)\right)_{i,j}&=\mathrm{K}^f{}_v\left(\overline{\mathbb{Q}}_i,\overline{\mathbb{Q}}_j,\begin{pmatrix}\bar{\boldsymbol{\nu}}=\mathbf{0}\\ \bar{\boldsymbol{\xi}}'\end{pmatrix},\delta\overline{\mathbf{V}}\right)\\ \left(\mathbf{K}_{f,\dot{v}}^*\left(\overline{\mathbf{V}},\delta\overline{\mathbf{V}}\right)\right)_i&=\mathrm{K}^f{}_{,\dot{v}}\left(\overline{\mathbb{Q}}_i,\overline{\mathbf{V}},\delta\overline{\mathbf{V}}\right)\\ \left(\mathbf{G}^{f*}\left(\overline{\mathbf{V}},\delta\overline{\mathbf{V}}\right)\right)_i&=\mathrm{G}^f\left(\overline{\mathbb{Q}}_i,\overline{\mathbf{V}},\delta\overline{\mathbf{V}}\right)\end{aligned} \tag{II.87}$$

The results above highlight how the gyroscopic operator associated with a given order zero rigid body velocity of an interface can in fact be calculated as the sum of six elementary operators, each being associated with a given rigid body motion of space. The same goes for the stiffness operator, except that because of the quadratic dependence, it is the sum of thirty-six elementary operators. The interest of this result can be illustrated with the example of a structure that is considered to move with any translation in a plane $\boldsymbol{e}_x,\boldsymbol{e}_y$. As a consequence, any velocity $\bar{\boldsymbol{v}}_{\mathrm{c}}^o$ on that plane will result in operators that can be calculated based on two elementary operators for the gyroscopic effects, and four elementary operators for the stiffness effects. As a consequence, instead of calculating new operators for each $\bar{\boldsymbol{v}}_{\mathrm{c}}^o$, a better strategy might be to calculate the elementary operators of the plane once, enabling to obtain the operators associated with any $\bar{\boldsymbol{v}}_{\mathrm{c}}^o$ with a simple projection.

II.2.3 Simplification of terms for isochoric problems

The study of an incompressible fluid enclosed by a boundary leads to specific properties, some of which are detailed in this section, in particular the fact that a fluid internal to a membrane without rotations is associated with zero gyroscopic and stiffness operators.

The equivalent of the incompressibility condition (I.6) at orders zero and one can be obtained by developing the terms:

$$\text{for }(\mathcal{P}_{\mathrm{int}}):$$

$$\int_{\overline{\Sigma}}\bar{\boldsymbol{v}}^o\cdot\bar{\boldsymbol{n}}\,\mathrm{d}\overline{\Sigma}=0 \tag{II.88a}$$

$$\int_{\overline{\Sigma}}\bar{\boldsymbol{v}}'\cdot\bar{\boldsymbol{n}}+\bar{\boldsymbol{v}}^o\cdot\bar{\boldsymbol{\tau}}'\,\mathrm{d}\overline{\Sigma}=0. \tag{II.88b}$$

If we chose a virtual power compatible with the constraints of the problem, i.e that meets a condition equivalent to (II.88).

$$\text{for } (\mathcal{P}_{\text{int}}):$$

$$\int_{\overline{\Sigma}} \delta\bar{\boldsymbol{v}}^o \cdot \bar{\boldsymbol{n}} \, \mathrm{d}\overline{\Sigma} = 0 \tag{II.89a}$$

$$\int_{\overline{\Sigma}} \delta\bar{\boldsymbol{v}}' \cdot \bar{\boldsymbol{n}} + \delta\bar{\boldsymbol{v}}^o \cdot \bar{\boldsymbol{\tau}}' \, \mathrm{d}\overline{\Sigma} = 0. \tag{II.89b}$$

For the internal problem , the velocity of an interface in translation $\boldsymbol{v}_{\text{c}}$ is transmitted homogeneously to the contained fluid no matter its shape, consequently the variations of velocity and dynamic pressure with respect to the interface deformations $\bar{\boldsymbol{\xi}}$ are nil:

$$\text{for } (\mathcal{P}_{\text{int}}): \quad \boldsymbol{\mathcal{U}}_d \left(\begin{pmatrix} \bar{\boldsymbol{v}}_{\text{c}}^o \\ \mathbf{0} \end{pmatrix}, \bar{\boldsymbol{\xi}}' \right) = \mathbf{0} \tag{II.90a}$$

$$\mathcal{P}'_{v;\xi} \left(\begin{pmatrix} \bar{\boldsymbol{v}}_{\text{c}}^o \\ \mathbf{0} \end{pmatrix}, \begin{pmatrix} \bar{\boldsymbol{v}}_{\text{c}}^o \\ \mathbf{0} \end{pmatrix}, \bar{\boldsymbol{\xi}}' \right) = 0 \tag{II.90b}$$

Moreover, without rotations the dynamic pressure at order zero is homogeneous, and therefore:

$$\int_{\overline{\Sigma}} \mathcal{P}_v^o \left(\bar{\boldsymbol{\tau}}'.\delta\bar{\boldsymbol{v}}^o + \bar{\boldsymbol{n}}.\delta\bar{\boldsymbol{v}}' \right) \, \mathrm{d}\overline{\Sigma} = \mathcal{P}_v^o \int_{\overline{\Sigma}} \left(\bar{\boldsymbol{\tau}}'.\delta\bar{\boldsymbol{v}}^o + \bar{\boldsymbol{n}}.\delta\bar{\boldsymbol{v}}' \right) \, \mathrm{d}\overline{\Sigma}. \tag{II.91}$$

By combining equations (II.89) and (II.91), the above expression becomes nil, since an homogeneous pressure does not work on movements compatible with the incomprehensibility condition:

$$\int_{\overline{\Sigma}} \mathcal{P}_v^o \left(\bar{\boldsymbol{\tau}}'.\delta\bar{\boldsymbol{v}}^o + \bar{\boldsymbol{n}}.\delta\bar{\boldsymbol{v}}' \right) \, \mathrm{d}\overline{\Sigma} = 0. \tag{II.92}$$

As a consequence of equations (II.90) and (II.92), the stiffness operator associated with the dynamic pressure for the internal problem with no rotation at order zero is nil:

$$\mathrm{K}^f{}_v \left(\begin{pmatrix} \bar{\boldsymbol{v}}_{\text{c}}^o \\ \mathbf{0} \end{pmatrix}, \begin{pmatrix} \bar{\boldsymbol{v}}_{\text{c}}^o \\ \mathbf{0} \end{pmatrix}, \mathbf{X}, \delta\overline{\mathbf{V}} \right) = 0 \quad \text{for } (\mathcal{P}_{\text{int}}). \tag{II.93}$$

II.3 Summary of the kinematic and dynamic linearized potential flow equations

II.3.1 Rigid body motions coupled with elastic deformations fluid loads

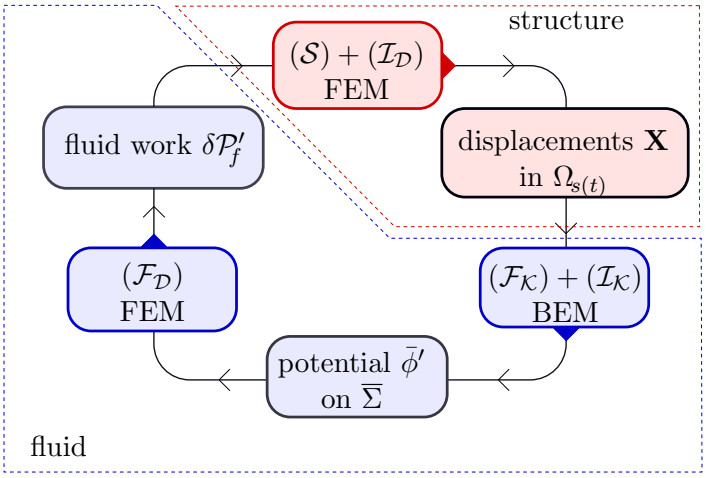

Figure II.4: Fluid-structure interaction diagram.

As described in Figure II.4, the equations are split into a fluid kinematic behaviour $(\mathcal{F}_\mathcal{K})$, a fluid dynamic relation $(\mathcal{F}_\mathcal{D})$, conditions of kinematic and dynamic compatibility at the interface $(\mathcal{I}_\mathcal{K})$ and $(\mathcal{I}_\mathcal{D})$ respectively, and a solid equation $(\mathcal{S})$ (which cannot be split into kinematic and dynamic independent relations since both are intricately linked). The main associated equations are summarized below.

Summary of the main equations

The movements of the structure can be split into rigid body motions described through translation $\boldsymbol{d}_\mathrm{c}$ and rotation $\mathbb{R}$ and elastic motions at order zero and one, as described by equations (II.45b) and (II.49):

$$\boldsymbol{x} = \boldsymbol{d}_\mathrm{c}^o + \boldsymbol{d}'_\mathrm{c} + \mathbb{R}^o(\bar{\boldsymbol{x}} + \bar{\boldsymbol{\xi}}' - \bar{\boldsymbol{x}}_\mathrm{c}) + \mathbb{R}'(\bar{\boldsymbol{x}} - \bar{\boldsymbol{x}}_\mathrm{c}) + \mathcal{O}\left(\varepsilon^2\right).$$

The kinematics of the structure are described with a decomposition into rigid body and elastic movements by equation (II.49):

$$\bar{\boldsymbol{v}}^o = \overline{\mathbb{Q}}\bar{\boldsymbol{\nu}}^o$$
$$\bar{\boldsymbol{v}}' = \overline{\mathbb{Q}}\bar{\boldsymbol{\nu}}' + \bar{\boldsymbol{\omega}}^o \wedge \bar{\boldsymbol{\xi}}' + \dot{\bar{\boldsymbol{\xi}}}'$$

The fluid problem can be split into kinematic and dynamic equations. The kinematic equation of the flow $(\mathcal{F}_\mathcal{K})$ and the kinematic interface condition $(\mathcal{I}_\mathcal{K})$ lead to the integral equations (II.57a) and (II.57b) allowing to solve the flow potential $\bar{\phi}^o$ and $\bar{\phi}'$ depending on the interface velocity and time-independent integral operators:

$$
\begin{aligned}
(\mathcal{F}_\mathcal{K})^o + (\mathcal{I}_\mathcal{K})^o : &\quad \mathcal{H}^o(\bar{\phi}^o, \bar{\boldsymbol{y}}) = \mathcal{G}^o(\bar{\boldsymbol{v}}^o, \bar{\boldsymbol{y}}) \\
(\mathcal{F}_\mathcal{K})' + (\mathcal{I}_\mathcal{K})' : &\quad \mathcal{H}^o(\bar{\phi}', \bar{\boldsymbol{y}}) = \mathcal{G}^o(\bar{\boldsymbol{v}}', \bar{\boldsymbol{y}}) + \mathcal{G}'(\bar{\boldsymbol{v}}^o, \bar{\boldsymbol{y}}; \bar{\boldsymbol{\xi}}') - \mathcal{H}'(\bar{\phi}^o, \bar{\boldsymbol{y}}; \bar{\boldsymbol{\xi}}').
\end{aligned}
$$

As a consequence, the potential at order zero and one can be expressed introducing the operators Φ_v and Φ_d as well as the Kirchhoff potential $\bar{\boldsymbol{\Psi}}$, see equation (II.59):

$$
\begin{aligned}
(\mathcal{F}_\mathcal{K})^o + (\mathcal{I}_\mathcal{K})^o : &\quad \bar{\phi}^o = \Phi_v(\bar{\boldsymbol{v}}^o) = \bar{\boldsymbol{\Psi}} \cdot \bar{\boldsymbol{\nu}}^o \\
(\mathcal{F}_\mathcal{K})' + (\mathcal{I}_\mathcal{K})' : &\quad \bar{\phi}' = \Phi_v(\bar{\boldsymbol{v}}') + \Phi_d(\bar{\boldsymbol{\nu}}^o; \bar{\boldsymbol{\xi}}') = \bar{\boldsymbol{\Psi}} \cdot \bar{\boldsymbol{\nu}}' + \Phi_v\left(\dot{\bar{\boldsymbol{\xi}}}'\right) + \Phi_d(\bar{\boldsymbol{\nu}}^o; \bar{\boldsymbol{\xi}}')
\end{aligned}
$$

The potential solution $\bar{\phi}$ enables to obtain the pressure $\bar{p}$ at both orders zero and one, from which the virtual power $\delta\mathcal{P}_f$ of the fluid on the interface at orders zero and one can be calculated through $(\mathcal{F}_\mathcal{D})$ the fluid dynamic equations (II.77) and (II.78):

$$
\begin{aligned}
(\mathcal{F}_\mathcal{D})^o : &\quad \delta\mathcal{P}_f^o = \int_{\overline{\Sigma}} \bar{p}^o \bar{\boldsymbol{n}}.\delta\bar{\boldsymbol{v}}^o \, \mathrm{d}\overline{\Sigma}, && \delta\bar{\boldsymbol{v}}^o = \overline{\mathbb{Q}}\delta\bar{\boldsymbol{\nu}}^o + \delta\dot{\bar{\boldsymbol{\xi}}} \\
(\mathcal{F}_\mathcal{D})' : &\quad \delta\mathcal{P}_f' = \int_{\overline{\Sigma}} \bar{p}' \bar{\boldsymbol{n}}.\delta\bar{\boldsymbol{v}}^o + \bar{p}^o(\bar{\boldsymbol{\tau}}'.\delta\bar{\boldsymbol{v}}^o + \bar{\boldsymbol{n}}.\delta\bar{\boldsymbol{v}}') \, \mathrm{d}\overline{\Sigma}, && \delta\bar{\boldsymbol{v}}' = \delta\bar{\boldsymbol{\omega}} \wedge \bar{\boldsymbol{\xi}}'.
\end{aligned}
$$

It is convenient to encompass the small perturbations of the the rigid-body and elastic movements of the structure in a generalized coordinates vectors $\mathbf{X}$ and $\overline{\mathbf{V}}$ defined in (II.79):

$$
\mathbf{X} = \begin{pmatrix} \boldsymbol{d}_\mathrm{c}' \\ \boldsymbol{\theta}' \\ \bar{\boldsymbol{\xi}}' \end{pmatrix}, \quad \overline{\mathbf{V}} = \begin{pmatrix} \bar{\boldsymbol{\nu}}' \\ \dot{\bar{\boldsymbol{\xi}}}' \end{pmatrix}.
$$

Equations (II.86) and (II.82) to (II.84a) show that the virtual power of the flow can be expressed linearly to the generalized coordinates and their time derivatives through added stiffness, gyroscopic and mass operators as:

$$
\begin{aligned}
-\frac{\delta\mathcal{P}_f'}{\rho_f} =& \mathrm{M}^f\left(\dot{\overline{\mathbf{V}}}, \delta\overline{\mathbf{V}}\right) + \mathrm{G}^f\left(\bar{\boldsymbol{\nu}}^o, \mathbf{X}, \delta\overline{\mathbf{V}}\right) + \mathrm{K}^f{}_v\left(\bar{\boldsymbol{\nu}}^o \otimes \bar{\boldsymbol{\nu}}^o, \mathbf{X}, \delta\overline{\mathbf{V}}\right) ... \\
&+ \mathrm{K}^f{}_{,\dot{v}}\left(\dot{\bar{\boldsymbol{\nu}}}^o, \mathbf{X}, \delta\overline{\mathbf{V}}\right) + \mathrm{K}^f{}_{,g}\left(\mathbb{R}^o, \bar{\boldsymbol{d}}_\mathrm{c}^o, \mathbb{R}', \mathbf{X}, \delta\overline{\mathbf{V}}\right) + \mathrm{K}^f{}_{,\mathrm{h}}.
\end{aligned}
$$

In the case where there are no accelerations at order zero and the gravity terms are neglected, the formulation becomes independent of the relative position $\boldsymbol{d}_\mathrm{c}$, $\boldsymbol{\theta}$ of the interface:

$$
-\frac{\delta\mathcal{P}_f'}{\rho_f} = \mathrm{M}^f\left(\dot{\overline{\mathbf{V}}}, \delta\overline{\mathbf{V}}\right) + \mathrm{G}^f\left(\bar{\boldsymbol{\nu}}^o, \mathbf{X}, \delta\overline{\mathbf{V}}\right) + \mathrm{K}^f{}_v\left(\bar{\boldsymbol{\nu}}^o \otimes \bar{\boldsymbol{\nu}}^o, \mathbf{X}, \delta\overline{\mathbf{V}}\right)
$$

Once these have been obtained, the coupling of the interface dynamic condition $(\mathcal{I}_\mathcal{D})$ with a structure weak equation $(\mathcal{S})$ enables to link the virtual power $\delta\mathcal{P}_s$ of the structure with the help of the structure stiffness and mass operators detailed in Chapter III.

The results presented above describe the main lines of the analytical developments developed during this chapter, which is focused on the mathematical aspects of the model introduced in this

manuscript. An implementation of this theory on a simplified case will be implemented in Chapter IV in order to study the stability of a membrane structure in a potential flow.

II.3.2 Elastic fluid loads

In chapters III and IV, the loads of the fluids associated with and projected on the elastic movements in the absence of gravity forces and order zero accelerations will be used, hence the perturbations of the rigid body movements will be considered as nil. Consequently, we present in this section the associated fluid loads perturbations as:

$$\begin{aligned}\frac{\delta\mathcal{P}_f'}{\rho_f}(\bar{\boldsymbol{\nu}}'=\mathbf{0},\bar{\boldsymbol{\xi}},\delta\bar{\boldsymbol{x}}=\delta\bar{\boldsymbol{\xi}}) &= -\mathrm{M}^f_{\xi\xi}(\ddot{\bar{\boldsymbol{\xi}}}',\delta\dot{\bar{\boldsymbol{\xi}}}) - \mathrm{G}^f_{\xi\xi}(\bar{\boldsymbol{\nu}}^o,\dot{\bar{\boldsymbol{\xi}}}',\delta\dot{\bar{\boldsymbol{\xi}}}) - \mathrm{K}^f{}_{v,\xi\xi}(\bar{\boldsymbol{\nu}}^o,\bar{\boldsymbol{\nu}}^o,\bar{\boldsymbol{\xi}}',\delta\dot{\bar{\boldsymbol{\xi}}})\\ &= -\mathrm{M}^f_{\xi\xi}(\ddot{\bar{\boldsymbol{\xi}}}',\delta\dot{\bar{\boldsymbol{\xi}}}) - \bar{\boldsymbol{\nu}}^o\cdot\mathbf{G}^f_{\xi\xi}{}^*(\dot{\bar{\boldsymbol{\xi}}}',\delta\dot{\bar{\boldsymbol{\xi}}}) - \bar{\boldsymbol{\nu}}^o\otimes\bar{\boldsymbol{\nu}}^o : \mathbb{K}^{f*}_{v,\xi\xi}(\bar{\boldsymbol{\xi}}',\delta\dot{\bar{\boldsymbol{\xi}}}).\end{aligned} \tag{II.94}$$

In the equation above, the operators with an index $_{\xi\xi}$ describe the elastic loads projected on the virtual elastic velocity field $\delta\dot{\bar{\boldsymbol{\xi}}}$ as a function of the elastic movements $\bar{\boldsymbol{\xi}}'$ and its time derivatives. Because the fluid is potential and there is no vortex shedding, the fluid loads are conservative, which means that the stiffness and mass operators are symmetric and the gyroscopic operator is skew-symmetric. It is demonstrated in Appendix D.2 how symmetric added mass and stiffness loads derive from a potential, and how the virtual power of skew-symmetric gyroscopic loads is always nil. However, the Newtonian approach used in this manuscript is not convenient to demonstrate the (skew-)symmetry of these operators, even though the symmetry of the added mass operator is demonstrated by Rangette (1990) based on a Newtonian approach. The Lagrange equations presented later in section II.4 allows us to demonstrate the (skew-)symmetry properties of the operators at the price of manipulating second order derivatives. However, as illustrated with the example of rigid-body motions in Appendix D.5, the operators can lose the aforementioned (skew-)symmetry properties when rotations are involved, thus making the reference frame non-Galilean.

II.3.3 Loads of an ambient flow on a structure without large displacements

The results developed previously can be used to calculate the fluid loads associated with a structure with large rigid body motions and small elastic deformations in a potential fluid at rest. However, this thesis work started by studying the loads associated with an interface with small elastic deformations and rigid body motions set to zero, immersed in an homogeneous, stationary ambient flow field $\boldsymbol{u}_\infty$. The associated equations are not presented in this manuscript to avoid cumbersome calculations, however the detailed expressions associated can be found in Le Mestre et al. (2022) (this paper has been included in Appendix F of this manuscript). The associated results are however very similar. In particular, we find an added mass independent of the ambient flow $\boldsymbol{u}_\infty$, a linear gyroscopic operator in $\boldsymbol{u}_\infty$ and in $\dot{\bar{\boldsymbol{\xi}}}$, and a stiffness operator quadratic in $\boldsymbol{u}_\infty$ and linear in $\bar{\boldsymbol{\xi}}$. This shows the similar roles between the ambient flow $\boldsymbol{u}_\infty$ from Le Mestre et al. (2022) and the translational velocity $\bar{\boldsymbol{v}}^o$ of this manuscript. It is the model associated with an ambient flow that will be used for the stability analysis in Chapter IV. Moreover, this approach opens the perspective to study the impact of gusts (instationary flows $\boldsymbol{u}_\infty(t)$) on the airship stability.

Figure II.5 presents a non-exhaustive list of loads that arise in structural dynamics[3]. Instationary loads are not dealt with in this manuscript. In the case of airship, they would however arise

[3] $\mathrm{d}W = \delta\mathcal{P}_f(\delta\dot{\bar{\boldsymbol{\xi}}} = \mathrm{d}\bar{\boldsymbol{\xi}})$, see equation (D.17a), and $\mathrm{d}V = \frac{\partial V}{\partial\bar{\boldsymbol{\xi}}}\,\mathrm{d}\bar{\boldsymbol{\xi}}$

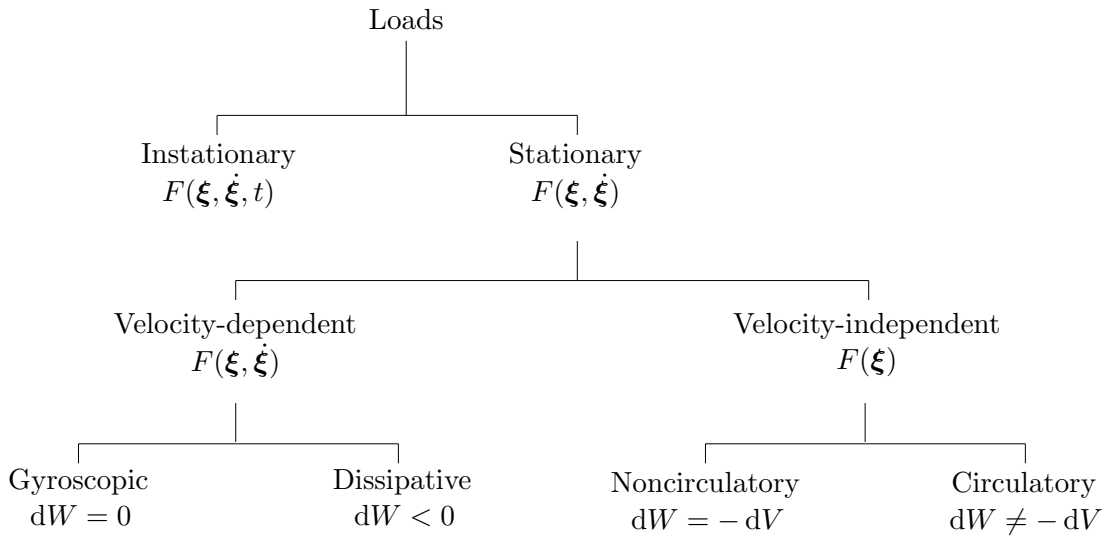

Figure II.5: Loads classification adapted from Ziegler (1977). The loads F are characterized based on the associated work W and possibly its relation to a force potential V

when airship are facing wind gusts for instance, which could be taking into account the ambient flow model with instationary flow $\boldsymbol{u}_\infty(t)$. Added mass loads are applied through the operator M^f. As mentionned by Morand and Ohayon (1992), the added mass operator is positive. It is not strictly positive since tangential accelerations of the interface such that $\ddot{\boldsymbol{\xi}}.\bar{\boldsymbol{n}} = 0$ don't generate any acceleration of the surrounding flow, and are therefore associated with a nil added mass. Gyroscopic loads are applied to the structure by the full-potential flow through the operator G^f and are conservative. Since G^f is skew-symmetric, it is not definite nor positive with respect to real vectors. As explained by Ziegler (1977), gyroscopic effects tend to stabilize the structure. Noncirculatory loads are applied as well through the operator K^f and are conservative as well. The stiffness operator K^f is not necessarily positive: due to the translational invariance of the problem, the fluid stiffness associated with translational movements is zero, and it was found that the fluid stiffness associated with an ellipsoidal membrane in its first bending mode is negative. Nongyroscopic terms are applied through the damping operator of the fins D_{fins}. These can be either dissipative or non-dissipative, which can destabilize the system. Circulatory forces are applied through the stiffness operator of the fins, which stabilize the system.

II.4 Comparison of the present model with different approaches from the literature

In this section, we compare the expression of the added stiffness, gyroscopic and mass operators of the flow obtained in this thesis thanks to a linearization of the ALE action of the flow on the interface obtained with a Newtonian approach, with the expression obtained by Li et al. (2009) obtained by linearization of the Lagrange equations derived from the kinetic energy of the fluid. It means that instead of using the forces of the fluid, their approach is rather based on the derivation of the energy with respect to the interface movements.

The expression of the fluid operators detailed in Appendix B, equation (B.24) which is rewritten below for the convenience of the reader, and is valid with no rotations $\boldsymbol{\omega}^o = \mathbf{0}$ and for small elastic perturbations:

$$\mathrm{K}_{f,v}(\bar{\boldsymbol{\xi}}', \delta\dot{\bar{\boldsymbol{\xi}}}) = -\delta\dot{\bar{\boldsymbol{\xi}}}^{\mathrm{T}}(\mathbb{L}_k + \mathbb{L}_k^{\mathrm{T}})\bar{\boldsymbol{\xi}}'$$
$$\mathrm{G}^f(\dot{\bar{\boldsymbol{\xi}}}', \delta\dot{\bar{\boldsymbol{\xi}}}) = \delta\dot{\bar{\boldsymbol{\xi}}}^{\mathrm{T}}(\mathbb{L}_g^{\mathrm{T}} - \mathbb{L}_g)\dot{\bar{\boldsymbol{\xi}}}'$$
$$\mathrm{M}^f(\ddot{\bar{\boldsymbol{\xi}}}', \delta\dot{\bar{\boldsymbol{\xi}}}) = \delta\dot{\bar{\boldsymbol{\xi}}}^{\mathrm{T}}(\mathbb{L}_m + \mathbb{L}_m^{\mathrm{T}})\ddot{\bar{\boldsymbol{\xi}}}'.$$

Even though the operators above have been obtained using a different approach than the Newtonian approach used in this thesis, they describe the same physics and are consequently expected to be the same operators. One can see the Lagrangian mechanics have the advantage of putting forward the symmetry of the mass and stiffness elastic operators associated with an order zero translation velocity, as well as the skew-symmetry of the elastic gyroscopic operator (for an order zero translation velocity). It should be noted that Rangette (1990) has been able to demonstrate the symmetry of the added mass operator via the Newtonian approach, but from the point of view of the author of this manuscript a similar demonstration for the gyroscopic and stiffness operators would likely be difficult and tedious. However, as already mentioned in Appendix B, the computation of the stiffness and gyroscopic operators from the Lagrange equation requires the determination of the second order derivative of the oriented surface and of the velocity potential, which is prohibitively expansive to calculate. Furthermore, as will be shown in Chapter IV, the second order derivatives involved in the added stiffness play a non-negligible role in the fluid-structure interaction of flexible airships. The Newtonian approach represents this effect without requiring the computation of the second order derivatives. This shows that the Newtonian approach is better suited for the computation of small perturbations of the forces of a potential flow associated with elastic deformations than the Lagrange equations used by Li et al. (2009) for example.

II.5 Conclusion

During the course of this chapter, the following work has been done:

1. The Eulerian description of the fluid equations presented in Chapter I is not adapted to interfaces in motion. For this reason, we have introduced a formulation of the integral equations of the potential fluid consistent with the interface motions thanks to an Arbitrary-Lagrangian-Eulerian approach.

2. From the ALE expression of the fluid equations, a linearization has been performed in order to express the forces at the fluid-structure interface on a time independent reference interface, despite the rotations and elastic deformations of the structure. In particular, an expression of the fluid velocity potential was obtained from a linear integral equation based on a reference domain, which in the context of incompressible potential flows is an originality of this study to the author's knowledge.

3. An expression of linearized fluid forces involving mass, stiffness and gyroscopic operators of the fluid has been shown, similar to the studies of Destuynder and Santi (2006) or Li et al. (2011) for example, although having a different expression due to the different approaches chosen. It has been demonstrated that the gyroscopic operator is linear with the translational and rotational velocities of the structure at zero order. Similarly, the fluid stiffness operator has been shown to be quadratic with the rigid body motions at zero order, which allows the expression of these operators to be decomposed according to

the basis of the six rigid body motions.

4. The expression of the linearized fluid forces from Lagrange equations used by Li et al. (2011); Chaabani (2014) has the advantage of showing the symmetry properties of the fluid operators associated with the conservative aspect of the non-viscous irrotational flows, unlike the Newtonian approach introduced in this work. However, an originality of this study, to the best of the author's knowledge, was to demonstrate in Appendix B that the expression of the linear fluctuations of the fluid forces requires to compute the fluctuations of the geometry and of the velocity potential at order two, contrary to the Newtonian approach used in this manuscript. This demonstration thus highlights the interest of the Newtonian approach.

Thus, now that an expression for the linear fluctuations of the fluid forces has been obtained based on a time independent reference interface, we will want to determine the forces of the fluid on the interface as a function of the movements of the latter. Thus, obtaining a numerical approximation of the mass, stiffness and gyroscopic operators of the fluid from a reference mesh is the objective of the next chapter.

II.6 Perspectives

The model presented in this chapter is based on strong hypothesis, including potential flow. In order to improve the accurracy, one could:

1. Take into account a surface of discontinuity of the potential behind the wake to model the vortex sheet associated with the Kutta condition at the trailing edge (Morino and Gennaretti, 1992).

2. Add corrections at the rear of the airship where turbulence is not negligible (Lutz et al., 2002) with models like those presented by Li and Nahon (2007).

   Moreover, the range of flight conditions could be more complete:

3. By considering unsteady and inhomogeneous ambient flow effects from the results of Le Mestre et al. (2022) to study how turbulence, gusts and other specific winds that might affects the airship trajectory

4. By taking into account the coupling between an ambient flow with structure large rigid body motions and small deformations

5. By taking into account obstacles (ground, montains), it is possible to use the image method (meshing of a mirror structure) like in (Carbone et al., 2019), to mesh the ground like in (Carbone et al., 2019) or even use an adapted Green function allowing to use only the structure mesh: the information of the obstacles is contained in the Green function.

Chapter III

Coupled FEM-BEM implementation of the linearized potential flow operators on a fixed reference mesh

Introduction

In this chapter, the linearized potential flow operators from chapter II are approximated numerically using both BEM and FEM methods, allowing a coherent coupling of the fluid effects with the structure dynamic operators based on FEM and which will be introduced in the next chapter. Once the numerical implementation is done, the results obtained are compared with various test case taken from the literature to validate the method and quantify its limits.

Based on the integral equation over the reference interface, the BEM is used to calculate the quasi-steady velocity potential around a given interface as well as its perturbations for small movements of the interface in section III.1. Since, to the knowledge of the author, the calculation of the spatial derivatives of the BEM operators associated with a potential flow constitute an original contribution, its implementation is documented with particular attention. The linear fluctuations of the fluid forces over the interface are then approximated in section III.2 with the help of FEM. In the aim of validating the numerical operators, section III.3 quantifies the error associated with the numerical and linear approximations based on two test cases. Finally, the results obtained with the present method are compared with other numerical or experimental approaches from the literature, enabling to compare the implementation complexity and the accuracy of those methods.

III.1 Numerical approximation of the quasi-steady and perturbed potential flows with the Boundary Element Method (BEM)

In order to obtain the FEM-BEM operators for fluid forces, it is first necessary to calculate the BEM operators enabling to get the velocity potential linear fluctuations at the interface, which is the aim of this section. The condensed form of the velocity potential integral equation introduced in the previous chapter and given by equations (II.57a) and (II.57b) is suited for implementing the BEM which will enable to find a numerical solution of the velocity potential on the mesh of the

fluid-structure interface.

III.1.1 Presentation of the BEM and its application for the steady-state velocity potential

With the aim of determining the linear fluctuations of the velocity potential, a prerequisite is to calculate an order zero solution. In order to do so, the BEM is introduced, similarly to (Bonnet, 1999; Veron et al., 2016; Mavaleix-Marchessoux, 2020). It is then applied to the case of the quasi-steady solution fluid operators.

In this section, the reference interface $\overline{\Sigma}$ is discretized as a mesh $\overline{\Sigma}_N$ made up of planar triangle elements whose vertices are associated with nodes. For example, an arbitrary vector $\{\bar{a}\}$ associated with a continuous field $\bar{a}$ is defined as:

$$\{\bar{a}\} = \left\{ \begin{array}{c} \bar{a}(\bar{\boldsymbol{x}}_1) \\ \vdots \\ \bar{a}(\bar{\boldsymbol{x}}_N) \end{array} \right\} \in \mathbb{R}^N \quad \forall \bar{a} \in \mathrm{C}(\overline{\Sigma} \times \mathbb{R}^+, \mathbb{R}) \tag{III.1a}$$

$$\{\bar{\boldsymbol{a}}\} = \left\{ \begin{array}{c} \{\bar{\boldsymbol{a}}.\bar{\boldsymbol{e}}_1\} \\ \{\bar{\boldsymbol{a}}.\bar{\boldsymbol{e}}_2\} \\ \{\bar{\boldsymbol{a}}.\bar{\boldsymbol{e}}_3\} \end{array} \right\} \in \mathbb{R}^{3N} \quad \forall \bar{\boldsymbol{a}} \in \mathrm{C}(\overline{\Sigma} \times \mathbb{R}^+, \mathbb{R}^3) \tag{III.1b}$$

(III.1c)

The values of the variables in the mesh elements are obtained via a linear interpolation from their values at nodes. The linear interpolation matrix $[\mathrm{N}(\bar{\boldsymbol{x}})]$ of size $3 \times N$ enables to obtain the value of $\bar{a}$ at any point of the reference interface mesh as a function of its discrete counterpart $\{\bar{a}\}$:

$$\bar{a}(\bar{\boldsymbol{x}}) = [\mathrm{N}(\bar{\boldsymbol{x}})]\,\{\bar{a}\}, \quad \bar{\boldsymbol{x}} \in \overline{\Sigma}_N. \tag{III.2}$$

This work only used triangular meshes because it is the most convenient elements to implement, however the method can be expanded to quadrangular elements (Bonnet, 1999). In order to obtain an approximation of the potential $\bar{\phi}^o$, our objective is to solve a discrete equivalent of the integral equation at order zero (II.57a). Thus, the BEM operators [H] and [G] of respective sizes $N \times N$ and $N \times 3N$ are computed using the collocation method such that they approximate the continuous operators at order zero, $\mathcal{G}^o$ and $\mathcal{H}^o$, of the integral equation (III.3):

$$\mathcal{G}^o(\bar{\boldsymbol{v}}, \bar{\boldsymbol{y}}_i, t) \simeq \sum_j [\mathrm{G}]_{ij} \{\bar{\boldsymbol{v}}\}_j \simeq \int_{\overline{\Sigma}_N} \overline{\boldsymbol{G_n}}^o(\bar{\boldsymbol{x}}, \bar{\boldsymbol{y}}_i) \cdot \bar{\boldsymbol{v}}\, \mathrm{d}\overline{\Sigma}(\bar{\boldsymbol{x}}) \tag{III.3a}$$

$$\mathcal{H}^o(\bar{\phi}, \bar{\boldsymbol{y}}_i, t) \simeq \sum_j [\mathrm{H}]_{ij} \{\bar{\phi}\}_j \simeq \int_{\overline{\Sigma}_N} \overline{\partial_n G}^o(\bar{\boldsymbol{x}}, \bar{\boldsymbol{y}}_i)(\bar{\phi}(\bar{\boldsymbol{x}}) - \bar{\phi}(\bar{\boldsymbol{y}}_i))\, \mathrm{d}\overline{\Sigma}(\bar{\boldsymbol{x}}). \tag{III.3b}$$

The collocation method consists in writing the integral equation at each node $\bar{\boldsymbol{y}}_i$ of the interface $\overline{\Sigma}_N$ to obtain a square matrix system whose unknowns are the values of the function at the interface nodes. The integration is then calculated using Gaussian weights, the value of $\bar{\boldsymbol{x}}$, $\bar{\boldsymbol{v}}$ and $\bar{\phi}(\bar{\boldsymbol{x}})$ being obtained on each of the three Gauss points using the linear interpolation matrix $[\mathrm{N}(\bar{\boldsymbol{x}})]$. Because of the non-linearity of the terms $\overline{\boldsymbol{G_n}}^o$ and $\overline{\partial_n G}^o$, the integration with Gaussian weigths is not exact, hence the $\simeq$ sign in equations (III.3). The finer the mesh, the better the discrete equation (III.3)

approximates its continuous counterparts, since the triangles become more coincident with the real surface that has been meshed, and the linear interpolations over the small triangles can approximate more closely non linear fluctuations of the physical variables. However, when $\bar{\boldsymbol{x}}$ is located in the same triangle as $\bar{\boldsymbol{y}}_i$, the norm $\|\boldsymbol{x} - \boldsymbol{y}_i\|$ is nil at $\bar{\boldsymbol{x}} = \bar{\boldsymbol{y}}_i$, which means the integral over the triangle is improper and its value has to be calculated carefully. For the double layer term

$$\overline{\partial_n G}^{\,o} = \frac{(\bar{\boldsymbol{x}} - \bar{\boldsymbol{y}}_i) \cdot \bar{\boldsymbol{n}}}{\|\bar{\boldsymbol{x}} - \bar{\boldsymbol{y}}_i\|^3},$$

the planar shape of the triangles implies that any vector connecting two points of a same triangle is included in the triangle (see Figure III.3), and is consequently perpendicular to the triangle normal, hence:

$$(\bar{\boldsymbol{x}} - \bar{\boldsymbol{y}}_i) \cdot \bar{\boldsymbol{n}} = 0 \quad \text{for } \bar{\boldsymbol{x}}, \bar{\boldsymbol{y}}_i \text{ in the same triangle.} \tag{III.4}$$

Consequently, the term $\overline{\partial_n G}^{\,o}$ is trivial to integrate in that case. Though equation (III.4) simplifies the implementation of the BEM by preventing the calculation of highly singular terms, Posrikidis (2002) mentions that this triangle mesh approximation causes a discretization error of the order of $\delta\kappa/4\pi$, where δ is the perimeter of the triangle and κ the mean curvature of the real surface $\overline{\Sigma}$. On the contrary, the term $\overline{\boldsymbol{G_n}}^{\,o}$ does not cancel for $\bar{\boldsymbol{x}} \to \bar{\boldsymbol{y}}_i$ and the integral has to be calculated carefully: its implementation was done using a Lachat-Watson transformation as detailed by Fischnaller and Thöbin (2009).

Once [G] and [H] have been calculated, the order zero integral equation can be approximated numerically as:

$$[\mathrm{H}] \left\{\bar{\phi}^o\right\} = [\mathrm{G}] \left\{\bar{\boldsymbol{v}}^o\right\}. \tag{III.5}$$

Remark

It is possible to reduce the calculation and storage cost of the operator [G] by an order of three by applying this operator directly to the normal velocity $\{\bar{\boldsymbol{v}} \cdot \bar{\boldsymbol{n}}\}$, hence using the new definition:

$$\sum_j [\mathrm{G}]_{ij} \{\bar{\boldsymbol{v}} \cdot \bar{\boldsymbol{n}}\}_j = \int_{\overline{\Sigma}} \overline{\boldsymbol{G_n}}^{o}(\bar{\boldsymbol{x}} - \bar{\boldsymbol{y}}_i)\bar{\boldsymbol{v}}(\bar{\boldsymbol{x}}) \cdot \bar{\boldsymbol{n}}\, \mathrm{d}\overline{\Sigma}(\bar{\boldsymbol{x}}),$$

as done by Veron et al. (2016); Mavaleix-Marchessoux (2020). However, since the normal of the surface is well defined on the triangles but not at the nodes of the mesh, this would imply to use an interpolated value of $\bar{\boldsymbol{n}}$ at the nodes. Therefore, the advantage of less expansive calculation would be at the price of lower accuracy. This storage reduction method could be considered for fine mesh calculations, which is not the case in this thesis, leading to the choice of a larger to store but more precise BEM operator. An equivalent implementation using the reducing storage method mentioned here is nonetheless presented in Appendix E in case this approach is of interest to the reader.

By inverting the linear system (III.5), the value of the potential at the nodes ϕ^o is obtained:

$$\left\{\bar{\phi}^o\right\} = [\mathrm{H}]^{-1} [\mathrm{G}] \left\{\bar{\boldsymbol{v}}^o\right\}. \tag{III.6}$$

One should be cautious with the equation above, as it is valid only if [H] is invertible. For the external problem, the existence and uniqueness of the solution mentionned in Chapter I ensures the

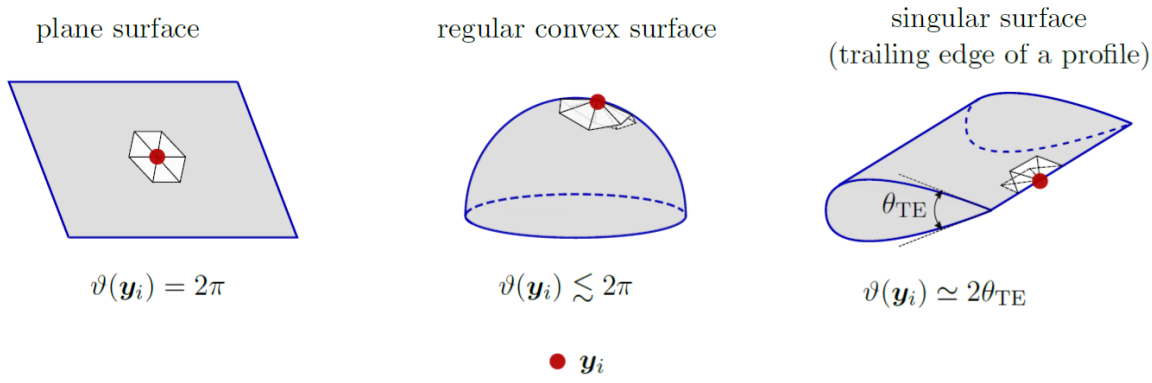

Figure III.1: Value of the solid angle ϑ associated with the mesh of surfaces with various geometry regularity. The mesh of a plane surface is smooth, the mesh of a regular convex surface (here a sphere) is slightly singular at the node, while the mesh of a profile is strongly singular at the trailing edge. The symbol $\lesssim$ stands for "slightly less than". For a regular concave surface, one would get $\vartheta(\boldsymbol{y}_i) \gtrsim 2\pi$.

invertibility of [H], which is however not the case for the internal problem. The source of singularity of the double layer operator [H] is the non uniqueness of the associated solution. One might recall that the uniqueness of the potential has been ensured mathematically thanks to equation (I.37a). For the external case, this relation $\phi \to 0$ at infinity is automatically taken into account by the BEM for the integral at infinity has been set to zero. However, for the internal case, the condition $\bar{\phi}(\bar{\boldsymbol{x}}_{\mathrm{ref}})$ has to be set manually. In practice, this can be done by arbitrarily setting the velocity on the first node to be nil (arbitrarily, because the value could as well be set as nil at any node of the mesh):

$$\bar{\phi}^o(\bar{\boldsymbol{x}}_1) = 0 \quad \text{for } (\mathcal{P}_{\mathrm{int}}), \tag{III.7}$$

thus ensuring the uniqueness of the solution. As a consequence, the BEM linear equation can be written as follows:

$$\begin{bmatrix} [\mathrm{H}_{11}] & [\mathrm{H}_{12}] \\ [\mathrm{H}_{21}] & [\mathrm{H}_{22}] \end{bmatrix} \begin{Bmatrix} 0 \\ \{\bar{\phi}_2^o\} \end{Bmatrix} = \begin{bmatrix} [\mathrm{G}_{1\cdot}] \\ [\mathrm{G}_{2\cdot}] \end{bmatrix} \{\bar{\boldsymbol{v}}^o\}, \tag{III.8}$$

where the index $[\mathrm{H}]_{11}$ is the top left coefficient of the operator [H], $[\mathrm{H}_{12}]$ contains the first row of the matrix and all its columns except the first and so on for $[\mathrm{H}_{12}]$ and $[\mathrm{H}_{22}]$.The vector $\{\bar{\phi}_2^o\}$ contains all the elements of the array excepted the first, and finally $[\mathrm{G}_{1\cdot}]$ is the first row of the operator while $[\mathrm{G}_{2\cdot}]$ is complementary to the latter. The linear set of equations from (III.8) is ill-posed because there is one more equation than there are unknowns. Consequently, its first row might be removed, enabling to solve the problem with the following equation:

$$\{\bar{\phi}^o\} = \begin{Bmatrix} 0 \\ [\mathrm{H}_{22}]^{-1} [\mathrm{G}_{2\cdot}] \{\bar{\boldsymbol{v}}^o\} \end{Bmatrix} \quad \text{for } (\mathcal{P}_{\mathrm{int}}). \tag{III.9}$$

One might notice that the non-singularity of the equation above is ensured by the fact that the rigid body motions are compatible with the incompressible condition for the internal fluid (I.21). As mentioned in section II.2, the order zero velocity depends on 6 independent parameters, that are

the three translations and rotations in space. This can be put forward by introducing the discrete equivalent $\left[\overline{\mathbb{Q}}\right]$ of the distributor $\overline{\mathbb{Q}}$ from equation (II.17) such that:

$$\left[\overline{\mathbb{Q}}\right]\{\bar{\boldsymbol{\nu}}^o\} = \{\bar{\boldsymbol{v}}^o\}\,. \tag{III.10}$$

Therefore, the order zero solution becomes:

$$\left\{\bar{\phi}^o\right\} = \begin{cases} [\mathrm{H}]^{-1}\,[\mathrm{G}]\left[\overline{\mathbb{Q}}\right]\{\bar{\boldsymbol{\nu}}^o\} & \text{for } (\mathcal{P}_{\text{ext}}) \\ \begin{Bmatrix} 0 \\ [\mathrm{H}_{22}]^{-1}\,[\mathrm{G}_{2\cdot}]\left[\overline{\mathbb{Q}}\right]\{\bar{\boldsymbol{\nu}}^o\} \end{Bmatrix} & \text{for } (\mathcal{P}_{\text{int}}). \end{cases} \tag{III.11}$$

This expression can be simplified by introducing the matrix $[\Phi_v]$, the discrete equivalent of the function Φ_v from equation (II.58a):

$$[\Phi_v] = \begin{cases} [\mathrm{H}]^{-1}\,[\mathrm{G}] & \text{for } (\mathcal{P}_{\text{ext}}) \\ \begin{bmatrix} 0\ldots 0 \\ [\mathrm{H}_{22}]^{-1}\,[\mathrm{G}]_{2\cdot} \end{bmatrix} & \text{for } (\mathcal{P}_{\text{int}}) \end{cases} \tag{III.12}$$

$$\left\{\bar{\phi}^o\right\} = [\Phi_v]\left[\overline{\mathbb{Q}}\right]\{\bar{\boldsymbol{\nu}}^o\}\,.$$

Calculating the matrix operator $[\Phi_v]$ is costly because of the matrix inversion required, even more so recalling that the BEM matrix [H] is full. Thus, the matrix $[\Phi_v]$ will rarely be calculated explicitly in practice (except for coarse meshes) and the solving of equation (III.11) will be carried out using a GMRes algorithm described by Saad and Schultz (1986).

In order to validate the implementation of the BEM procedure at order zero, a simple test case is presented. It consists of an ellipsoid of revolution (also referred to as spheroid). Its semi-axes are of length L and $L/\mathcal{A}_r$ respectively, $\mathcal{A}_r$ being the aspect ratio of the ellipsoid. For this test-case, an aspect ratio of $\mathcal{A}_r = 3$ has been used. Since all the physical parameters of the problem have been reduced, a unitary length $L = 1$ has been used for the mesh. The ellipsoid has a uniform longitudinal translation velocity of amplitude V. An analytic expression of the resulting potential at the interface can be obtained from (Lamb, 1932), leading to the following expression:

$$\bar{\phi}^*(\bar{\boldsymbol{x}}) = -k_1\bar{x}^* \quad \text{for } \bar{\boldsymbol{x}} \in \overline{\Sigma}, \tag{III.13}$$

where $\bar{x}^*$ is a reduced longitudinal coordinate $\bar{x}^* = \bar{\boldsymbol{x}}.\bar{\boldsymbol{e}}_x/L$ and k_1 is a non dimensional geometric parameter function of the aspect ratio which expression (C.2a) can be found in Appendix C.

In order to validate the quasi-steady BEM procedure, the analytic potential solution is compared to numerical results. The vector $\left\{\bar{\phi}^*_{\text{BEM}}\right\}$ has been obtained with the BEM for various mesh fineness in order to study the convergence of the method. The numerical results are presented in Figure III.2, where the error has been defined relatively to the exact solution $\bar{\phi}^*$ with the $L^2(\overline{\Sigma}_N)$ error:

$$\text{err}\left(\bar{\phi}^*_{\text{BEM}}\right) = \frac{\left\|\bar{\phi}^*_{\text{BEM}} - \bar{\phi}^*\right\|_{L^2(\overline{\Sigma}_N)}}{\left\|\bar{\phi}^*\right\|_{L^2(\overline{\Sigma}_N)}}, \tag{III.14}$$

where the $L^2(\overline{\Sigma}_N)$ norm of an arbitrary scalar vector a is defined as:

$$\|a\|_{L^2(\overline{\Sigma}_N)} = \sqrt{\int_{\overline{\Sigma}_N} a(\bar{\boldsymbol{x}})^2\,\mathrm{d}\overline{\Sigma}}, \quad \text{with } a(\bar{\boldsymbol{x}}) = [\mathrm{N}(\bar{\boldsymbol{x}})]\,\{a\}\,. \tag{III.15}$$

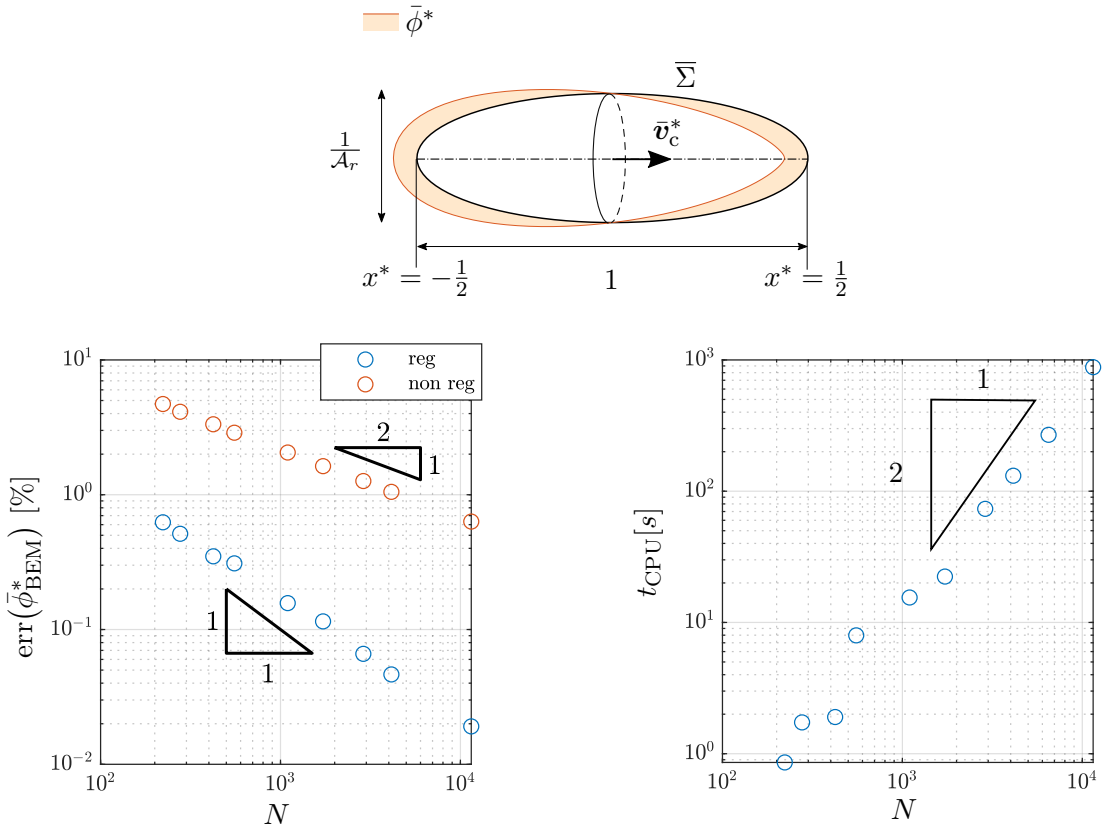

Figure III.2: Top: Side view of a spheroid of aspect ratio $\mathcal{A}_r = 3$, with the the potential solution $\bar{\phi}$ associated with a reduced longitudinal velocity $\bar{\boldsymbol{v}}_c^* = \bar{\boldsymbol{e}}_x$. Bottom left: relative error of the numerical solution $\left\{\bar{\phi}^*_{\mathrm{BEM}}\right\}$ compared to its theoretical value as a function of the number of nodes. The orange markers with a slope of $\mathcal{O}\left(N^{-1/2}\right)$ are associated with the non regularized double layer matrix [H] from equation (III.16) whereas the blue markers with a slope of $\mathcal{O}\left(N^{-1}\right)$ are obtained using the regularized double layer matrix from equation (III.3b). Bottom right: CPU time t_{CPU} used to calculate the BEM operator [H] depending on the number of nodes N.

Moreover, with a view to highlight the interest of the regularization of the matrix operator [H] rather than using the simplified expression (I.70) leading to the simplified, non regularized operator $\left[\mathrm{H}_{1/2}\right]$

$$\sum_j \left[\mathrm{H}_{1/2}\right]_{ij} \left\{\bar{\phi}\right\}_j \simeq \frac{1}{2}\bar{\phi}(\bar{\boldsymbol{y}}_i) - \int_{\overline{\Sigma}_N} \overline{\partial_n G}^o(\bar{\boldsymbol{x}}, \bar{\boldsymbol{y}}_i)\bar{\phi}(\bar{\boldsymbol{y}}_i)\, \mathrm{d}\overline{\Sigma}(\bar{\boldsymbol{x}}), \tag{III.16}$$

both results with and without regularization are displayed in Figure III.2 right. The regularized method converges significantly faster in $\mathcal{O}\left(N^{-1}\right)$ versus $\mathcal{O}\left(N^{-1/2}\right)$ for the non regularized method. The convergence of the BEM when refining the mesh seems therefore to have been verified.

Now that the order zero fluid operators have been implemented, the coupling with the fluid operator from section III.2.1 and the pre-stress solid operators from section IV.1.1 will enable to obtain an order zero solution in section IV.2.1.

III.1.2 Numerical calculation of the velocity potential perturbations

With the aim of solving the fluid-structure linear fluctuations, one needs to characterize the fluid force fluctuations, which requires first to get the linear fluctuations of the velocity potential. This section introduces the linearized operators which enable to predict the linear fluctuations of the quasi-steady BEM operators from section III.1.1. The latter helps obtaining the numerical operator connecting the velocity potential perturbations with the structure displacements and velocity, recalling that the order one equation of the fluid and the associated BEM linearized operators enable to overcome the time dependency of the BEM operators for non-linear problems.

With a view to calculating the potential perturbations $\left\{\bar{\phi}'\right\}$, we are looking for a numerical approximation of equation (II.57b). This is done by introducing a discrete equivalent of the involved operators similarly to the order zero numerical procedure:

$$\mathcal{G}'(\bar{\boldsymbol{v}}, \bar{\boldsymbol{y}}_i; \bar{\boldsymbol{\xi}}') \simeq \sum_j \left[\mathrm{G}'(\bar{\boldsymbol{v}})\right]_{ij} \left\{\bar{\boldsymbol{\xi}}'\right\}_j \simeq \int_{\overline{\Sigma}_N} \overline{\boldsymbol{G_n}}'(\bar{\boldsymbol{x}}, \bar{\boldsymbol{y}}_i; \bar{\boldsymbol{\xi}}').\bar{\boldsymbol{v}}\, \mathrm{d}\overline{\Sigma}(\bar{\boldsymbol{x}}) \quad \simeq \tag{III.17a}$$

$$\mathcal{H}'(\bar{\phi}^o, \bar{\boldsymbol{y}}_i; \bar{\boldsymbol{\xi}}') \simeq \sum_j \left[\mathrm{H}'(\bar{\phi}^o)\right]_{ij} \left\{\bar{\boldsymbol{\xi}}'\right\}_j \simeq \int_{\overline{\Sigma}_N} \overline{\partial_n G}'(\bar{\boldsymbol{x}}, \bar{\boldsymbol{y}}_i; \bar{\boldsymbol{\xi}}') \left(\bar{\phi}^o(\bar{\boldsymbol{x}}) - \bar{\phi}^o(\bar{\boldsymbol{y}}_i)\right) \mathrm{d}\overline{\Sigma}(\bar{\boldsymbol{x}}) \quad \simeq . \tag{III.17b}$$

As shown in equation (A.26d), the double layer linearized term is strongly singular for $\bar{\boldsymbol{x}} \to \bar{\boldsymbol{y}}$, and as a consequence one might expect that difficulties could arise integrating it. However, for the same reason that the scalar product $(\bar{\boldsymbol{x}} - \bar{\boldsymbol{y}}) \cdot \bar{\boldsymbol{n}}$ is nil at order zero, the term $\overline{\partial_n G}'$ vanishes when $\bar{\boldsymbol{x}}$ and $\bar{\boldsymbol{y}}$ are in the same triangle: the rotated normal associated with the deformed triangle will remain perpendicular to the deformed vector $\bar{\boldsymbol{x}} + \bar{\boldsymbol{\xi}}'(\bar{\boldsymbol{x}}) - (\bar{\boldsymbol{y}} + \bar{\boldsymbol{\xi}}'(\bar{\boldsymbol{y}}))$ as demonstrated in section A.5 (see Figure III.3). This ensures that the double layer term at order one $\overline{\partial_n G}'$ vanishes when both $\bar{\boldsymbol{x}}$ and $\bar{\boldsymbol{y}}$ are on the same triangle. Consequently, the order one integral equation becomes, by combining equations (II.57b) and (III.17):

$$[\mathrm{H}]\left\{\bar{\phi}'\right\} = [\mathrm{G}]\left\{\bar{\boldsymbol{v}}'\right\} + \left(\left[\mathrm{G}'(\bar{\boldsymbol{v}}^o)\right] - \left[\mathrm{H}'(\bar{\phi}^o)\right]\right)\left\{\bar{\boldsymbol{\xi}}'\right\}. \tag{III.18}$$

Since the BEM operators are affected by the displacements of the interface in the three directions of space $\left\{\bar{\boldsymbol{\xi}}\right\}$, their size is of $N \times 3N$. In practice, the two perturbation matrices H' and G' in the right parenthesis of the above equations are calculated at once and stored as a unique matrix, enabling to optimize the computation time and only requiring half of the storage. Similarly to the

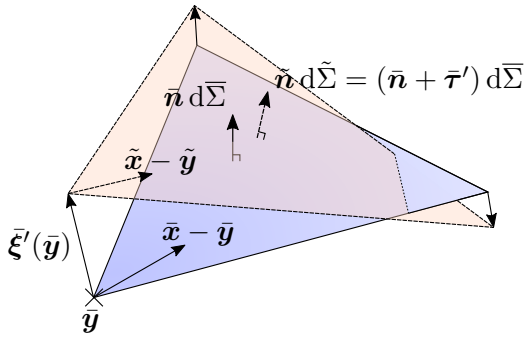

Figure III.3: Reference triangle (blue) and linear perturbation of its geometry (orange) with linear interpolation of the displacements.

order zero solution associated with the internal problem, the order one solution for the internal problem has to be treated with extra care to take into account the singularity of the problem:

$$\left\{\bar{\phi}'\right\} = [\mathrm{H}]^{-1}\left([\mathrm{G}]\left\{\bar{\boldsymbol{v}}'\right\} + \left(\left[\mathrm{G}'(\bar{\boldsymbol{v}}^o)\right] - \left[\mathrm{H}'(\bar{\phi}^o)\right]\right)\left\{\bar{\boldsymbol{\xi}}'\right\}\right) \qquad \text{for } (\mathcal{P}_{\text{ext}}) \qquad \text{(III.19a)}$$

$$\left\{\bar{\phi}'\right\} = \left\{\begin{array}{c} 0 \\ [\mathrm{H}_{22}]^{-1}\left([\mathrm{G}_{2.}]\left\{\bar{\boldsymbol{v}}'\right\} + \left([\mathrm{G}'_{2.}(\bar{\boldsymbol{v}}^o)] - \left[\mathrm{H}'_{2.}(\bar{\phi}^o)\right]\right)\left\{\bar{\boldsymbol{\xi}}'\right\}\right) \end{array}\right\} \qquad \text{for } (\mathcal{P}_{\text{int}}) \qquad \text{(III.19b)}$$

Keeping in mind that the velocity fluctuations $\bar{\boldsymbol{v}}'$ are not only due to the elastic and rigid body velocities, but as well to the coupling between the order zero rotation speed and the elastic displacements, the vector product matrix $[\bar{\boldsymbol{\omega}}^o_\wedge]$ is introduced such that:

$$\left\{\bar{\boldsymbol{v}}'\right\} = \left\{\dot{\bar{\boldsymbol{\xi}}}'\right\} + \left[\,\overline{\mathbb{Q}}\,\right]\left\{\bar{\boldsymbol{\nu}}'\right\} + [\bar{\boldsymbol{\omega}}^o_\wedge]\left\{\bar{\boldsymbol{\xi}}'\right\} \qquad \text{(III.20a)}$$

$$\text{with } [\bar{\boldsymbol{\omega}}^o_\wedge]\left\{\bar{\boldsymbol{\xi}}'\right\} = \left\{\bar{\boldsymbol{\omega}}^o \wedge \bar{\boldsymbol{\xi}}'\right\}. \qquad \text{(III.20b)}$$

The discrete integral equation (III.18) can be rewritten by introducing the matrix operator $[\Phi_d]$, counterpart of the continuous operator Φ_d defined in equation (II.58b), associated with the potential perturbations induced by the interface geometry fluctuations:

$$[\Phi_d] = \left\{\begin{array}{ll} [\mathrm{H}]^{-1}\left([\mathrm{G}'(\bar{\boldsymbol{u}}^o)] - \left[\mathrm{H}'(\bar{\phi}^o)\right] + [\mathrm{G}]\,[\bar{\boldsymbol{\omega}}^o_\wedge]\right) & \text{for } (\mathcal{P}_{\text{ext}}) \\ \begin{bmatrix} 0 & \dots & 0 \\ [\mathrm{H}_{22}]^{-1}\left([\mathrm{G}'_{2.}(\bar{\boldsymbol{u}}^o)] - \left[\mathrm{H}'_{2.}(\bar{\phi}^o)\right] + [G]_{2.}\,[\bar{\boldsymbol{\omega}}^o_\wedge]\right) \end{bmatrix} & \text{for } (\mathcal{P}_{\text{int}}) \end{array}\right. \qquad \text{(III.21)}$$

As a consequence, the fluctuations of the potential can be expressed linearly with the velocity and displacements of the structure as:

$$\left\{\bar{\phi}'\right\} = [\Phi_v]\left(\left\{\dot{\bar{\boldsymbol{\xi}}}'\right\} + \left[\,\overline{\mathbb{Q}}\,\right]\left\{\bar{\boldsymbol{\nu}}'\right\}\right) + [\Phi_d]\left\{\bar{\boldsymbol{\xi}}'\right\} \qquad \text{(III.22)}$$

The operator equivalent for the Kirchoff potential $[\Psi]$ can be introduced as

$$[\Psi] = [\Phi_v] \left[\overline{\mathbb{Q}} \right], \tag{III.23}$$

enabling to obtain an equation consistent with (II.61b):

$$\left\{ \bar{\phi}' \right\} = [\Phi_v] \left\{ \dot{\bar{\boldsymbol{\xi}}}' \right\} + [\Psi] \left\{ \bar{\boldsymbol{\nu}}' \right\} + [\Phi_d] \left\{ \bar{\boldsymbol{\xi}}' \right\}. \tag{III.24}$$

Despite the BEM operators can now be calculated to approximate the integral equation, their $\mathcal{O}\left(N^2\right)$ complexity constitutes a limitation in practice (Bonnet, 1999). The time of calculation and the storage increases rapidly as the mesh gets finer, making it hard to solve problems with $N \gtrsim 10^4$. A more efficient way of calculating and storing those operators would enable to solve problems with finer meshes in an effort to get more accurate results, which is the aim of the next section.

III.1.3 Storage and computing time optimization of the BEM with H-matrices

The BEM operators implemented in the above sections are not only costly to calculate, but to store as well. The H-matrix approximation enables to store only the coefficients of the BEM operators containing the most information relatively to a given criterion explained later, while the rest of the matrix associated with more marginal contributions will be stored using low rank approximations. This method is well suited to improve both calculation time and storage costs for BEM problems with many degrees of freedom, and it enables to perform parallel computing unlike the classical BEM method. The implementation of H-matrices is detailed in this section.

Because of their N^2 non nil coefficients, the BEM matrices implemented in the above sections are not only time consuming to compute, but also expensive to store. Thus, the computational costs quicly become prohibitive in the case of calculations on refined meshes. In order to overcome this drawback of the BEM, acceleration methods have been developed in the literature to speed up the computation and reduce the storage costs. The Fast Multipole Method (FMM) allows to approximate a BEM matrix-vector product using multipole expansions. Although this process reduces the computational costs for single matrix-vector products, it does not stores the BEM operators, making it necessary to calculate new approximations for each matrix-vector product of a same matrix. In this thesis, we have chosen to compute the BEM operators as well as their derivative based on a reference mesh, in order to reuse them in the current configuration. It is therefore convenient to store these operators to be able to apply them to multiple vectors, which is referred to as multiple right-hand side problems (Simoncini and Gallopoulos, 1995). As an example, in the case studied in Chapter IV, where a modal projection is used, the BEM operators have to be applied to each vector constituting the reduced basis. A method well adapted to speed up the BEM while allowing to store the associated matrices is the Hierarchical matrix (H-matrix) method (Chaillat et al., 2017).

In order to reduce the cost of computation and storage, the H-matrix method has been implemented and specifically extended for the very case of the linearized single and double layer BEM matrices $\left[\mathrm{H}'(\bar{\phi}^o)\right]$ and $[\mathrm{G}'(\bar{\boldsymbol{u}}^o)]$.

The method first consists in clustering the interface, before decomposing the BEM matrix into full rank blocks and low rank approximated blocks, enabling to reduce its computing cost. The clustering of the interface is done by first subdividing it into two sub-regions of equivalent size (see domains (1.1) and (1.2) in Figure III.4). The two sub-regions obtained are each subdivided into

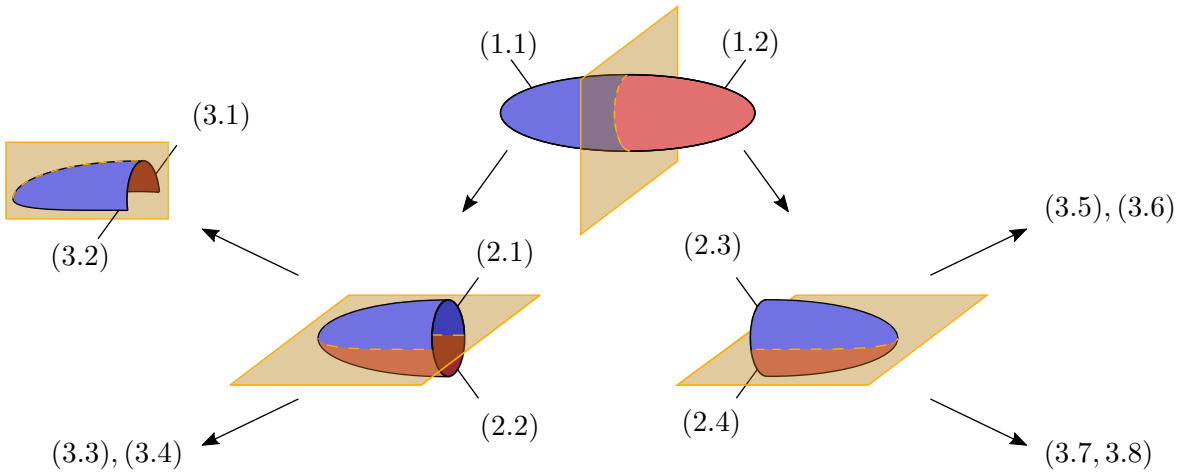

Figure III.4: Successive subdivisions of an ellipsoidal interface for the H-mat implementation.

two sub-regions again (domains (2.1) to (2.4)), and so on until each sub-region reaches a given size. The regions are no longer subdivided when their number of nodes is less than a criterion n_{leaf} called "leaf number". Once the clustering has been done (hence when the smallest regions have reached leaf level), the BEM matrix is decomposed into full blocks and low-rank blocks: depending on how close or far apart they are from each other, based on an arbitrary criterion called the admissibility condition, the sub-regions are classified separately. If two sub-regions are close to each other, then the interface motions in the former region will have a strong impact on the fluid behavior in the latter region. As a consequence, these interactions are too important and cannot be approximated in the BEM matrix. The coefficients of the latter associated with these sub-regions will have to be computed in the classical way (full block), which is costly in terms of storage as mentioned previously. On the other hand, if two regions are considered to be far apart, then interface movements in one will have a limited influence on the fluid behavior in the second. For example, local displacements at the nose of the airship are likely to have little effects on the flow at its tail. The interactions between these two distant regions in the BEM operator can then be approximated using a low rank approximation (low rank block). The calculation of low rank blocks implemented in our code by S. Chaillat (Chaillat et al., 2017) is based on the Adaptative Cross Approximation (ACA) Bebendorf and Rjasanow (2003). This algorithm allows to compute the approximation $[\mathrm{M}_k]$ (of rank k) of a matrix $[\mathrm{M}]$ written as the sum of products of vectors:

$$[\mathrm{M}_k] = \sum_{i=1}^{k} \boldsymbol{a}_i \boldsymbol{b}_i^{\mathrm{T}}, \qquad \text{with } \boldsymbol{a}_i, \boldsymbol{b}_i \in \mathbb{R}^m, \tag{III.25}$$

where m is the size of $[\mathrm{M}]$. The value of the rank k depends on an admissibility criterion ε_{ACA} such that:

$$\frac{\|[\mathrm{M}_k] - [\mathrm{M}]\|_{\text{fro}}}{\|[\mathrm{M}]\|_{\text{fro}}} \leq \varepsilon_{\text{ACA}}, \tag{III.26}$$

where $\|\|_{\text{fro}}$ is the Frobenius norm[1] of a matrix. As equation (III.25) shows, the storage cost of the approximation block is in $[\mathrm{M}_k] = \mathcal{O}(2km)$ instead of the initial cost $[\mathrm{M}] = \mathcal{O}(m^2)$. As a

[1]The Frobenius norm of a matrix $\mathbb{A} \in \mathbb{R}^n \otimes \mathbb{R}^n$ with $n \in \mathbb{N}$ is defined as $\|\mathbb{A}\|_{\text{fro}} = \sqrt{\text{trace}(\mathbb{A}\mathbb{A}^{\mathrm{T}})}$

consequence, the ACA algorithm enables to compress the matrix [M] when its rank is lower than the size N of the matrix. Further explanations on the clustering and the low rank approximations can be found in either (Chaillat et al., 2017; Mavaleix-Marchessoux, 2020). Moreover, the H-matrix method is well suited for parallel computing, since each block can be computed independently from the others, unlike the classical BEM method which requires to compute the whole operator at once. As a consequence, by splitting the calculation of the operators with the H-matrix method to different cores, a significant gain of time has been obtained.

In the framework of this thesis, the implementation of the clustering in the code as been done by Stéphanie Chaillat (Chaillat et al., 2017), as well as the approximation of the matrix [H] using low rank blocks, which was then adapted to the operator [G]. One of the challenges of the current work has therefore been to extend the H-matrix method and code to the linearized BEM operators [G′] and [H′] that were introduced in this thesis.

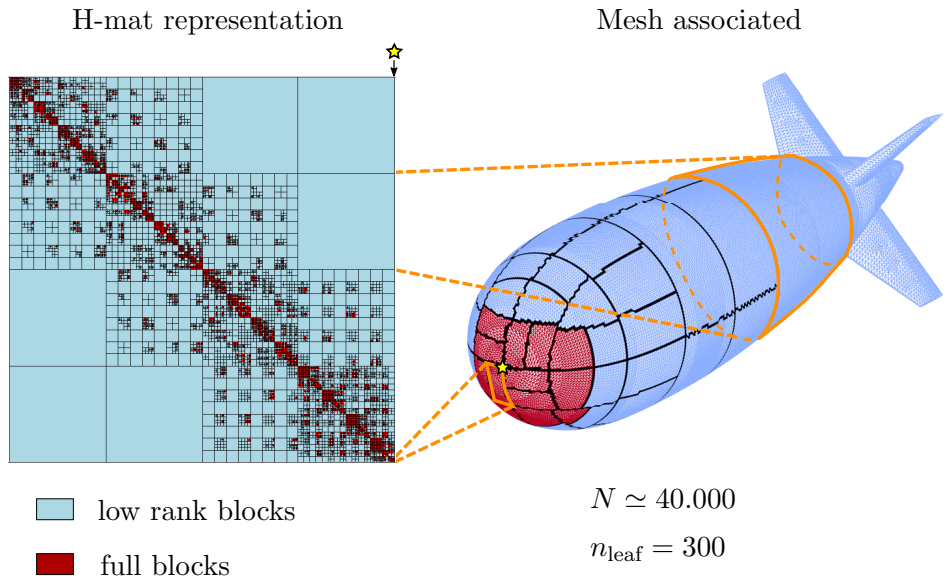

Figure III.5: On the left: H-matrix representation with low rank blocks (blue) and full blocks (red). Left: associated interface mesh. The full and low rank regions on the mesh are associated with the interactions with the node marked with a star, at the node of the structure. The dashed orange lines link the coefficients of the column associated with the node marked with a star, and their counterpart on the physical mesh.

An example is given in Figure III.5. On the left, one can see the hierarchical representation associated with the matrix, where each red square is associated with a full block and each blue square stands for a low-rank approximation. One might notice that the degrees of freedom have been rearranged by sub-regions. The proximity of the matrix diagonal is very dense with full matrices: this is due to the fact that the associated lines and columns in this zone are much more likely to be spatially close to each other since the nodes have been rearranged by sub-regions. On the contrary, as one gets farther from the diagonal, the coefficients associated with the lines and columns become much more likely to be remote from each other. Consequently, their interaction tends to be accurately enough approximated using low rank blocks. The relatively small size of the full rank blocks is due to the high ratio between the number of nodes of the mesh N and the size of the full blocks n_{leaf}. The gain of space is illustrated in Figure III.6, showing at the left the already mentioned quadratic cost of storage of the full BEM operators, compared to a the storage cost of

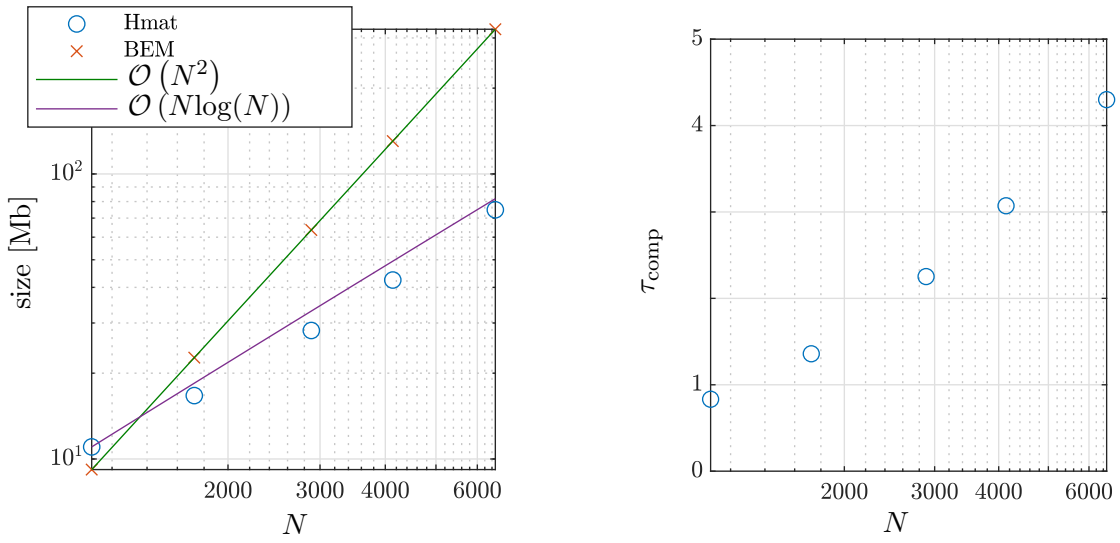

Figure III.6: Left: storage size of the full BEM and Hmat operators for varying number of nodes. Right: the compression rate τ_{comp} is the ratio between the storage cost of the full BEM operator and its H-matrix counterpart. Results obtained for $n_{\text{leaf}}/N = \text{cte}$.

the H-matrix with the trend $N\log(N)$ predicted theoretically by Chaillat et al. (2017).

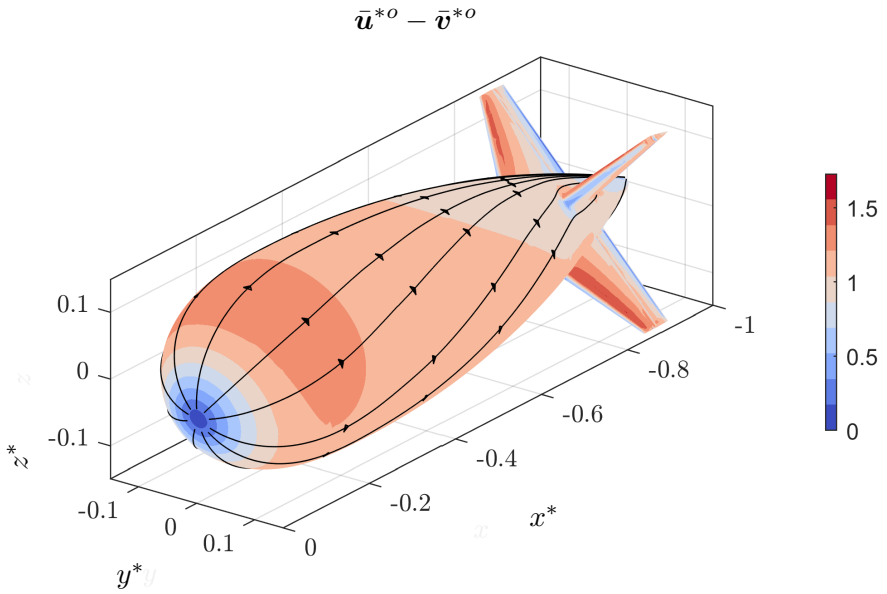

Figure III.7: Order zero relative flow velocity around an airship with a translation at an angle of attack of $\alpha = 10°$. $\bar{\boldsymbol{u}}^{*o}$ and $\bar{\boldsymbol{v}}^{*o}$ are respectively the flow and interface velocity normalized by the characteristic structure speed. The structure has a forward motion $\bar{\boldsymbol{v}}^{*o} = \boldsymbol{e}_x$. The coordinates x^*,y^* and z^* are normalized by the characteristic length L. The black curves are associated with the streamlines, with the arrowheads denoting the direction of the relative flow.

The relative flow velocity $\bar{\boldsymbol{u}} - \bar{\boldsymbol{v}}$ being tangential to the interface to meet the non penetration of the fluid condition, the velocity associated with the potential at order zero can be obtained by

calculating the surface gradient of the potential $\bar{\phi}^o$ on the reference mesh, which is done in practice using the surface gradient of the interpolation matrix $[\mathrm{N}(\bar{\boldsymbol{x}})]$. The relative velocity obtained on a representative airship geometry with $N \sim 10^4$ in a translation with a angle of attack of $10°$ relatively to the longitudinal axis is plotted in Figure III.7. The streamlines were obtained by seeding around the stagnation point. As expected, there is a stagnation point slightly below the nose of the airship due to the angle of attack, and the flow is accelerated to compensate for the obstacle that is the structure in the regions where $\|\bar{\boldsymbol{u}}^{*o} - \bar{\boldsymbol{v}}^{*o}\| > 1$, helping to have confidence in the physical sense of the BEM solution.

The H-matrix method coupled with the BEM operators associated with the quasi-steady and the perturbation problems enabled to obtain a numerical explicit relation between the discretized velocity potential and the displacements and velocity at the nodes of the mesh. As a consequence, it is now possible to use this expression of the velocity potential and its time derivative to obtain an explicit expression of the virtual power of the fluid with respect to the mesh movements. Next section aims at calculating the operator connecting the virtual power of the fluid with the velocity potential and the velocity of the structure.

III.2 Integration of the fluid loads on the interface

Once the discrete operators for the velocity potential have been calculated, the next step toward a monolithic fluid-structure coupled model is to calculate the virtual power of the fluid loads. The FEM enables to do so conveniently.

III.2.1 Implementation of the FEM operators associated with the fluid loads on the interface

In order to integrate the virtual power of the fluid pressure on the interface as a function of the velocity potential, the interface displacements and their time derivatives, this section introduces the required FEM operators.

For the rest of the chapter, gravity effects as well as order zero accelerations effects (term $\dot{\boldsymbol{\nu}}^o$) are not considered. Unlike the kinematic problem which required to take into account the whole fluid domain (which one might recall is the reason why the BEM was used, enabling to reduce the unknowns dimension by one, from the fluid volume to the interface), the virtual power of the fluid only involves fluid variables at the interface: it is therefore already a problem based at the interface. Consequently, the FEM allows to integrate those efforts conveniently. With a view to approximate the virtual power of the fluid as a function of $\bar{\phi}$, $\bar{\boldsymbol{\xi}}$, $\bar{\boldsymbol{v}}$ and their time derivatives, the following discretized bilinear operators are introduced:

$$
\begin{aligned}
\{\delta\bar{\boldsymbol{v}}\}^{\mathrm{T}}\left[\mathrm{P_a}\right]\left\{\dot{\bar{\phi}}'\right\} &\simeq \int_{\overline{\Sigma}_N} \dot{\bar{\phi}}'\bar{\boldsymbol{n}}\cdot\delta\bar{\boldsymbol{v}}\ \mathrm{d}\overline{\Sigma},\\
\{\delta\bar{\boldsymbol{v}}\}^{\mathrm{T}}\left[\mathrm{P_b}(\bar{\boldsymbol{u}}^o)\right]\left\{\bar{\phi}'\right\} &\simeq \int_{\overline{\Sigma}_N} \bar{\boldsymbol{u}}^o\cdot\overline{\boldsymbol{\nabla}}_{\mathrm{t}}\bar{\phi}'\,\bar{\boldsymbol{n}}\cdot\delta\bar{\boldsymbol{v}}\ \mathrm{d}\overline{\Sigma},\\
\{\delta\bar{\boldsymbol{v}}\}^{\mathrm{T}}\left[\mathrm{P_c}(\bar{\boldsymbol{u}}^o)\right]\left\{\dot{\bar{\boldsymbol{\xi}}}'\right\} &\simeq \int_{\overline{\Sigma}_N} -\dot{\bar{\boldsymbol{\xi}}}'\cdot\bar{\boldsymbol{u}}^o\,\bar{\boldsymbol{n}}\cdot\delta\bar{\boldsymbol{v}}\ \mathrm{d}\overline{\Sigma}.\\
\{\delta\bar{\boldsymbol{v}}\}^{\mathrm{T}}\left[\mathrm{P_d}(\bar{\boldsymbol{u}}^o-\bar{\boldsymbol{v}}^o,\bar{\boldsymbol{u}}^o)\right]\left\{\bar{\boldsymbol{\xi}}'\right\} &\simeq \int_{\overline{\Sigma}_N} -(\bar{\boldsymbol{u}}^o-\bar{\boldsymbol{v}}^o)\cdot\left(\left[\overline{\nabla}_{\mathrm{t}}^{\mathrm{T}}\bar{\boldsymbol{\xi}}'\right]\bar{\boldsymbol{u}}^o\right)\bar{\boldsymbol{n}}\cdot\delta\bar{\boldsymbol{v}}\ \mathrm{d}\overline{\Sigma},\\
\{\delta\bar{\boldsymbol{v}}\}^{\mathrm{T}}\left[\mathrm{P_e}(\bar{p}^o_{\mathrm{dyn}})\right]\left\{\bar{\boldsymbol{\xi}}'\right\} &\simeq \int_{\overline{\Sigma}_N} \bar{p}^o_{\mathrm{dyn}}\bar{\boldsymbol{\tau}}'(\bar{\boldsymbol{\xi}}')\cdot\delta\bar{\boldsymbol{v}},\\
\{\delta\bar{\boldsymbol{v}}\}^{\mathrm{T}}\left[\mathrm{P_f}(\bar{\boldsymbol{u}}^o,\bar{\boldsymbol{\omega}}^o)\right]\left\{\bar{\boldsymbol{\xi}}'\right\} &\simeq \int_{\overline{\Sigma}_N} -\bar{\boldsymbol{u}}^o\cdot(\bar{\boldsymbol{\omega}}^o\wedge\bar{\boldsymbol{\xi}}')\delta\bar{\boldsymbol{v}},\\
\{\delta\bar{\boldsymbol{\nu}}\}^{\mathrm{T}}\left[\mathrm{P_g}(\bar{p}^o_{\mathrm{dyn}})\right]\left\{\bar{\boldsymbol{\xi}}'\right\} &\simeq \int_{\overline{\Sigma}_N} \bar{p}^o_{\mathrm{dyn}}\bar{\boldsymbol{n}}\cdot(\delta\bar{\boldsymbol{\omega}}\wedge\bar{\boldsymbol{\xi}}')\,\mathrm{d}\overline{\Sigma}.
\end{aligned}
\tag{III.27}
$$

In the equation above, the variables $\bar{\phi}', \bar{\boldsymbol{\xi}}'$ and their time derivatives and $\delta\bar{\boldsymbol{v}}$ on $\overline{\Sigma}_N$ are obtained using the interpolation matrix. The velocity $\bar{\boldsymbol{u}}^o$ is obtained on each element using $\bar{\phi}^o$ and the surface gradient of the interpolation matrix $[\mathrm{N}(\bar{\boldsymbol{x}}]$ As will be shown in section III.3, the operator $[\mathrm{P_g}]$ associated with the linear fluctuations of the virtual rotations $\delta\bar{\boldsymbol{\omega}}$ plays a crucial role for the prediction of the moment. As the virtual displacements of the interface can be expressed as

$$
\{\delta\bar{\boldsymbol{v}}^o\} = \left[\left[\overline{\mathbb{Q}}\right],[\mathbb{1}]\right]\left\{\delta\overline{\mathbf{V}}\right\}. \tag{III.28}
$$

Therefore, the virtual power associated with the dynamic pressure can be expressed by combining equations (II.75), (II.78) and (III.27):

$$
\begin{aligned}
\delta\mathcal{P}'_f = &-\left\{\delta\overline{\mathbf{V}}\right\}^{\mathrm{T}}\left[\left[\overline{\mathbb{Q}}\right],[\mathbb{1}]\right]^{\mathrm{T}}\Big[\left[\mathrm{P_a}\right]\left\{\dot{\bar{\phi}}'\right\}+\left[\mathrm{P_b}(\bar{\boldsymbol{u}}^o)\right]\left\{\bar{\phi}'\right\}...\\
&+\left[\mathrm{P_c}(\bar{\boldsymbol{u}}^o)\right]\left(\left[\overline{\mathbb{Q}}\right]\left\{\bar{\boldsymbol{\nu}}'\right\}+\left\{\dot{\bar{\boldsymbol{\xi}}}'\right\}+\left[\bar{\boldsymbol{\omega}}^o_{\wedge}\right]\left\{\bar{\boldsymbol{\xi}}'\right\}\right)...\\
&+\left(\left[\mathrm{P_d}(\bar{\boldsymbol{u}}^o-\bar{\boldsymbol{v}}^o,\bar{\boldsymbol{u}}^o)\right]+\left[\mathrm{P_e}(\bar{p}^o_{\mathrm{dyn}})\right]+\left[\mathrm{P_f}(\bar{\boldsymbol{u}}^o,\bar{\boldsymbol{\omega}}^o)\right]\right)\left\{\bar{\boldsymbol{\xi}}'\right\}\Big]-\left\{\delta\bar{\boldsymbol{\nu}}\right\}^{\mathrm{T}}\left[\mathrm{P_g}(\bar{p}^o_{\mathrm{dyn}})\right]\left\{\bar{\boldsymbol{\xi}}'\right\}
\end{aligned}
\tag{III.29}
$$

III.2.2 Resulting mixed FEM-BEM fluid operators

In this section, further considerations about the properties of the fluid operators are given.

Elastic movements only

We first focus on the case where only elastic perturbations are involved and rigid body perturbations are nil, since the associated operators will have an important role in Chapter IV. The elastic fluid forces can be written as follows for $\bar{\boldsymbol{v}}'=\mathbf{0}$ and $\bar{\boldsymbol{\omega}}'=\mathbf{0}$, from (III.29) with $\bar{\boldsymbol{\nu}}'=\mathbf{0}$:

$$\delta\mathcal{P}_f'(\delta\dot{\underline{\xi}}) = \left\{\delta\dot{\underline{\xi}}\right\}^{\mathrm{T}} \left(\left[\mathrm{M}_{\xi\xi}^f\right] \left\{\ddot{\underline{\xi}}'\right\} + \left[\mathrm{G}_{\xi\xi}^f\right] \left\{\dot{\underline{\xi}}'\right\} + \left[\mathrm{K}_{\xi\xi}^f\right] \left\{\underline{\xi}'\right\} \right), \tag{III.30}$$

$$\left[\mathrm{M}_{\xi\xi}^f\right] = \left[\mathrm{P_a}\right] \left[\Phi_v\right] \tag{III.31}$$

$$\left[\mathrm{G}_{\xi\xi}^f\right] = \left[\mathrm{P_a}\right] \left[\Phi_d(\bar{\boldsymbol{u}}^o)\right] + \left[\mathrm{P_b}(\bar{\boldsymbol{u}}^o)\right] \left[\Phi_v\right] + \left[\mathrm{P_c}(\bar{\boldsymbol{u}}^o)\right] \tag{III.32}$$

$$\left[\mathrm{K}_{\xi\xi}^f\right] = \left[\mathrm{P_b}(\bar{\boldsymbol{u}}^o)\right] \left[\Phi_d(\bar{\boldsymbol{u}}^o)\right] + \left[\mathrm{P_c}(\bar{\boldsymbol{u}}^o)\right] \left[\bar{\boldsymbol{\omega}}_\wedge^o\right] + \left[\mathrm{P_d}(\bar{\boldsymbol{u}}^o - \bar{\boldsymbol{v}}^o, \bar{\boldsymbol{u}}^o)\right] + \left[\mathrm{P_e}(\bar{p}_{\mathrm{dyn}}^o)\right] + \left[\mathrm{P_f}(\bar{\boldsymbol{u}}^o, \bar{\boldsymbol{\omega}}^o)\right] \tag{III.33}$$

As mentioned in Chapter II, we expect the mass and stiffness operators $\left[\mathrm{M}^f\right]$ and $\left[\mathrm{K}^f\right]$ to be symmetric and the gyroscopic operator $\left[\mathrm{G}^f\right]$ to be skew-symmetric. However, because of the Newtonian formulation used, the expressions obtained are not obviously symmetric and this property is not necessarily verified exactly by the matrices obtained after discretization. The numerical error on this theoretical property of (skew-)symmetry has been observed in Appendix D.2 with relations (D.22), showing good agreement with the expected properties with relatively low errors. On the other hand, the operators expressed using Lagrange's equations, which are presented later in section III.4.2, naturally verify these properties. However, Rangette (1990) demonstrated that a posteriori symmetrization of the added mass operator $\left[\mathrm{M}_{\xi\xi}^f\right]$ minimizes the maximum prediction error of the added mass efforts. This demonstration is presented in Appendix D.1.

Remark

The symmetrized Newtonian operator $\left[\mathrm{M}^f\right]$ is equal to the added mass operator's expression based on Lagrange's equation, as shown by equation (B.27).

One can then naturally extend this result to the added stiffness operator $\left[\mathrm{K}_{\xi\xi}^f\right]$, whose a posteriori symmetrization thus allows to minimize the maximum error on the prediction of the associated loads. As part of this work, the demonstration has also been extended to the antisymmetrization of the gyroscopic operator $\left[\mathrm{G}_{\xi\xi}^f\right]$ in Appendix D.1, which had not yet been proved in the literature to the author's knowledge.

Let us remark that it is possible as well to implement the BEM based on a variational formulation of the integral representation (Rangette, 1990): this approach would ensure the symmetry of the added mass matrix at the expense of more integrations. For this reason, the collocation method used to implement the BEM in this article seems to be an acceptable compromise between accuracy and numerical effort. However, the (skew-)symmetry of the fluid operators has been numerically evaluated in section III.2.2.

Elastic movements coupled with rigid body perturbations

In this section, we investigate how the rigid body perturbations affect the fluid operators.

$$\left[\mathrm{M}^f\right] = \left[\left[\,\overline{\mathbb{Q}}\,\right], \left[\mathbb{1}\right]\right]^{\mathrm{T}} \left[\mathrm{P_a}\right] \left[\Phi_v\right] \left[\left[\,\overline{\mathbb{Q}}\,\right], \left[\mathbb{1}\right]\right] \tag{III.34}$$

The added mass operator above is symmetric just like the purely elastic added mass operator $\left[\mathrm{M}_{\xi\xi}^f\right]$. The gyroscopic operator writes as:

$$
\begin{aligned}
\left[\mathrm{G}^f\right] &= \begin{bmatrix} \left[\overline{\mathbb{Q}}\right]^{\mathrm{T}} \left[\mathrm{G}^f_{\xi\nu}\right] & \left[\mathrm{G}^f_{\xi\nu}\right] \\ \left[\overline{\mathbb{Q}}\right]^{\mathrm{T}} \left[\mathrm{G}^f_{\xi\xi}\right] & \left[\mathrm{G}^f_{\xi\xi}\right] \end{bmatrix} \\
\left[\mathrm{G}^f_{\xi\nu}\right] &= \left[\mathrm{P_b}(\bar{\boldsymbol{u}}^o)\right]\left[\Phi_v\right] + \left[\mathrm{P_c}(\bar{\boldsymbol{u}}^o)\right] \\
\left[{\mathrm{G}^f}_{\xi\xi}\right] &= \left[\mathrm{P_a}\right]\left[\Phi_d(\bar{\boldsymbol{u}}^o)\right] + \left[{\mathrm{G}^f}_{\xi\nu}\right]
\end{aligned}
\tag{III.35}
$$

One should note that $\left[\mathrm{G}^f\right]$ loses its skew-symmetry, since:

$$
\left[{\mathrm{G}^f}_{\xi\nu}\right] \neq \left[{\mathrm{G}^f}_{\xi\xi}\right]\left[\overline{\mathbb{Q}}\right], \tag{III.36}
$$

and consequently:

$$
\left[{\mathrm{G}^f}_{\xi\nu}\right] \neq -\left[{\mathrm{G}^f}_{\nu\xi}\right]^{\mathrm{T}}, \tag{III.37}
$$

The fluid stiffness associated with the dynamic pressure can be computed as:

$$
\left[\mathrm{K}^f\right] = \left[\left[\overline{\mathbb{Q}}\right], [\mathbb{1}]\right]^{\mathrm{T}} \left(\left[\mathrm{P_b}(\bar{\boldsymbol{u}}^o\right]\left[\Phi_d\right] + \left[\mathrm{P_c}(\bar{\boldsymbol{u}}^o)\right]\left[\bar{\boldsymbol{\omega}}^o_{\wedge}\right] + \left[\mathrm{P_d}(\bar{\boldsymbol{u}}^o - \bar{\boldsymbol{v}}^o, \bar{\boldsymbol{u}}^o)\right] + \left[\mathrm{P_e}(\bar{p}^o_{\mathrm{dyn}})\right] + \left[\mathrm{P_g}(\bar{\boldsymbol{u}}^o, \bar{\boldsymbol{\omega}}^o)\right]\right) - \left[[\mathbb{O}], \left[\overline{\mathbb{Q}}_{\omega}\right], [\mathbb{O}\right.
\tag{III.38}
$$

which can be rewritten under the condensed form:

$$
\begin{aligned}
\left[\mathrm{K}^f\right] &= \begin{bmatrix} [\mathbb{O}] & [\mathbb{O}] & [\mathbb{O}] \\ [\mathbb{O}] & [\mathbb{O}] & \left[{\mathrm{K}^f}_{\omega\xi}\right] \\ [\mathbb{O}] & [\mathbb{O}] & \left[{\mathrm{K}^f}_{,\xi\xi}\right] \end{bmatrix} \\
\left[\mathrm{K}^f_{\omega\xi}\right] &= \left[\overline{\mathbb{Q}}_{\omega}\right]^{\mathrm{T}} \left[\mathrm{P_g}(\bar{p}^o_{\mathrm{dyn}})\right] \\
\left[\mathrm{K}^f_{\xi\xi}\right] &= \left[\mathrm{P_b}(\bar{\boldsymbol{u}}^o\right]\left[\Phi_d\right] + \left[\mathrm{P_c}(\bar{\boldsymbol{u}}^o)\right]\left[\bar{\boldsymbol{\omega}}^o_{\wedge}\right] + \left[\mathrm{P_d}(\bar{\boldsymbol{u}}^o - \bar{\boldsymbol{v}}^o, \bar{\boldsymbol{u}}^o)\right] + \left[\mathrm{P_e}(\bar{\boldsymbol{u}}^o, \bar{\boldsymbol{\omega}}^o)\right] + \left[\mathrm{P_f}(\bar{p}^o_{\mathrm{dyn}})\right]
\end{aligned}
\tag{III.39}
$$

Therefore, the stiffness operator K^f_v loses its symmetry when rigid body perturbations are considered. Let us remark that both the gyroscopic and stiffness fluid operators lose their (skew-)symmetry properties because of the introduction of rotations.

Having calculated the added mass, gyroscopic and stiffness matrices of the fluid enables to predict the linear fluctuations of the fluid virtual power on the interface. We now want to validate the model, which is the sake of the following section.

III.2.3 Validation of the mixed FEM-BEM approach

In order to validate the mixed FEM-BEM approach enabling to determine the loads of the fluid, two test cases are looked at.

III.2.4 Longitudinal added mass test case

The first one is the prediction of the longitudinal added mass ${\mathrm{M}^f}_{xx}$. The longitudinal added mass is defined as the longitudinal force of the fluid caused by an unit longitudinal acceleration of the structure, resulting in a virtual inertia added by the surrounding fluid on the structure. With the definition just mentioned, ${\mathrm{M}^f}_{xx}$ can be computed from equation (III.24) as:

$$\mathrm{M}^f_{xx} = \{\boldsymbol{e}_x\}^{\mathrm{T}} \left[\mathrm{M}^f_{\xi\xi}\right] \{\boldsymbol{e}_x\} \tag{III.40}$$

The results of $\mathrm{M}^f{}_{xx}$ can be compared to its analytical expression given by Lamb (1932) in the case of a revolution ellipsoid of major axis $\boldsymbol{e}_x$ and presented in equation (C.6a) of this manuscript.

The second test case compares the numerical value of the computed Munk's moment with its analytical expression found in Lamb (1932) as well and in equation (C.8). The Munk moment, known for its destabilizing effects on airships (Li et al., 2011), results from a potential flow around an ellipsoid translating in a direction distinct from its symmetry axis. The Munk moment is directed perpendicularly to the translation velocity and the symmetry axis of the ellipsoid. The reduced Munk moment is calculated as:

$$M^*_{\mathrm{Munk}} = \frac{M_{\mathrm{Munk}}}{\rho_f L^3 V^2}. \tag{III.41}$$

For an ellipsoid translating with an angle of attack α as pictured in figure III.8, its expression becomes:

$$M^*_{\mathrm{Munk}} = \sin(2\alpha) g(\mathcal{A}_r), \tag{III.42}$$

with $g(\mathcal{A}_r)$ a function of the aspect ratio of the ellipsoid which expression is given in equation (C.8). It is positive when the longitudinal axis is longer than the radial axis of the revolution ellipsoid, causing the Munk moment to destabilize elongated ellipsoids, at all angles of attack different from either $\alpha = n\pi$, $n \in \mathbb{N}$ (translation aligned with the major axis) which is an unsteady equilibrium position or from $\alpha = n\pi + \pi/2$, $n \in \mathbb{N}$ (translation normal to the major axis) which is a stable equilibrium position. In the case of a sphere (hence $Ar = 1$), $g(\mathcal{A}_r = 1) = 0$ because a potential flow does not exert any moment on a sphere. The Munk moment is determined numerically by integrating the order zero pressure over the mesh, projected onto the rotation movement among $\boldsymbol{e}_y$ (see figure III.8), recalling the rotation distributor $\overline{\mathbb{Q}}_5 = \bar{\boldsymbol{e}}_y \wedge (\bar{\boldsymbol{x}} - \bar{\boldsymbol{x}}_{\mathrm{c}})$:

$$M_{\mathrm{Munk}} = \int_{\overline{\Sigma}_N} \bar{p}^o \boldsymbol{e}_z \overline{\mathbb{Q}}_5 \cdot \bar{\boldsymbol{n}} \, \mathrm{d}\overline{\Sigma}. \tag{III.43}$$

The comparison between the numerical and theoretical longitudinal added mass is presented at the left of Figure III.8. The error associated with the mixed FEM-BEM procedure is roughly 2.5 times larger than the error associated with the FEM integration based on the exact potential solution, no matter the fineness of the mesh. This means that, for added mass calculations, the numerical error induced by the BEM and by the FEM is of the same orders. Coherently with Figure III.2 and Figure III.9, the global error evolves in N^{-1} for the mixed FEM-BEM procedure. The error on the Munk moment plotted at the bottom right of Figure III.8 shows that the error is in $\mathcal{O}\left(N^{-1}\right)$ for either FEM-BEM and FEM-analytic approaches.

Let us remark that unlike the BEM operators which increases in $\mathcal{O}\left(N^2\right)$ (see Figure III.2), the time required to compute FEM does not vary much in comparison, which means that, due to their sparse structure, the FEM operators calculation time is going to be negligible compared to the time required for the BEM operators. The sparsity of the FEM also means that their storage cost is in $\mathcal{O}\left(N\right)$ against a cost in $\mathcal{O}\left(N^2\right)$ for the BEM problem, which means that the BEM is much more limiting than the FEM for the storage as well.

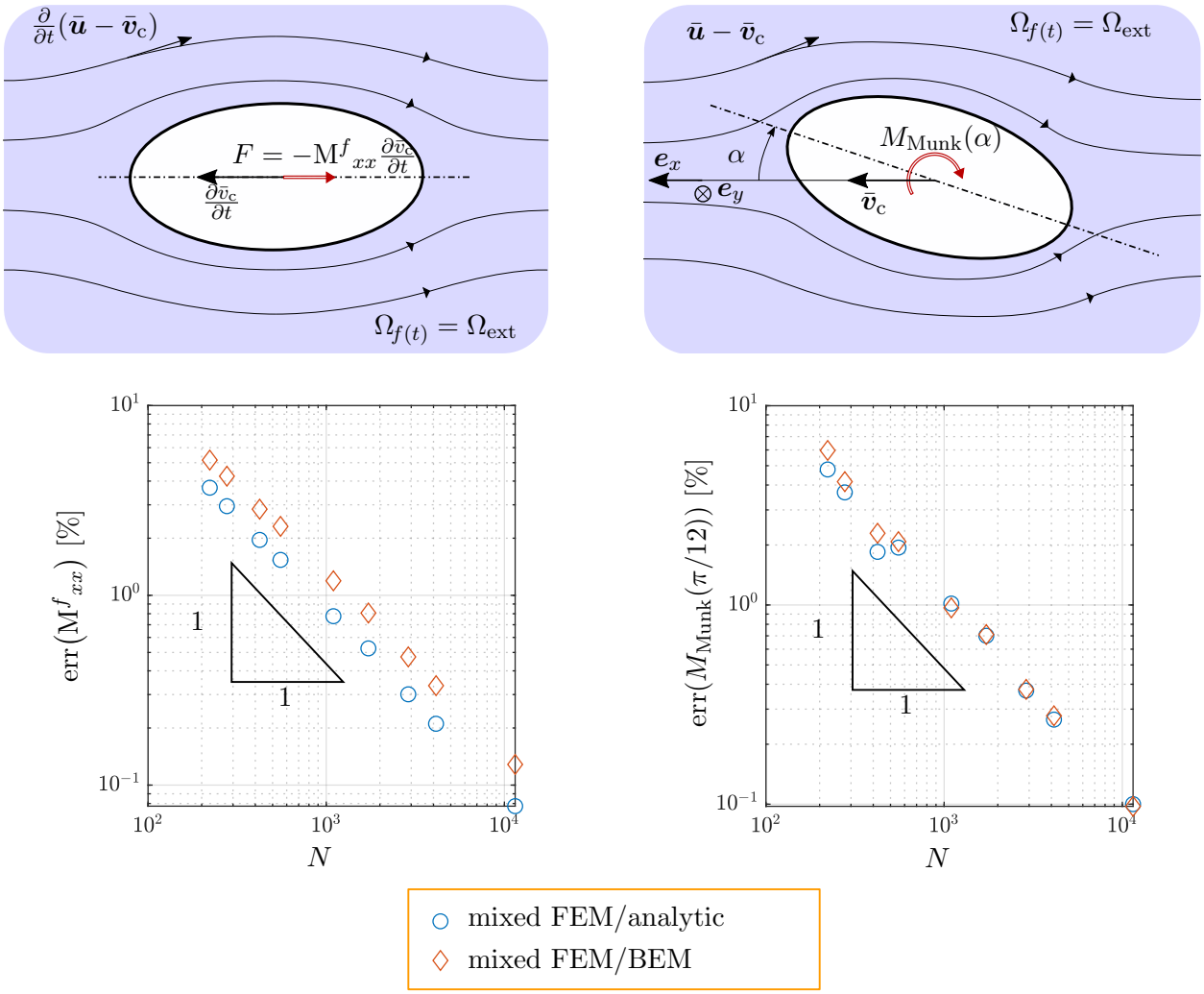

Figure III.8: Top left: Structure with longitudinal acceleration in a potential flow. The streamlines are associated with the acceleration of the flow relative to the structure and the red vector is associated with the added mass force of the fluid, opposed to the acceleration of the structure. Top right: Munk moment $M_{\text{Munk}}(\alpha)$ exerted by a steady external flow around a revolution ellipsoid with an angle of attack α. The streamlines are associated with the velocity of the flow relative to the structure. Bottom left: convergence of the numerically predicted longitudinal added mass $\mathrm{M}^f{}_{xx}$. The orange diamond markers are associated with the mixed FEM-BEM, while the blue circles were obtained by integrating the analytic expression of the potential instead of calculating it with the BEM for comparison. Bottom right: convergence of the numerically predicted Munk moment associated with an angle of attack $\alpha = \pi/12$, using either a mixed FEM-BEM solution or integrating the virtual power with FEM from the analytic expression of ϕ.

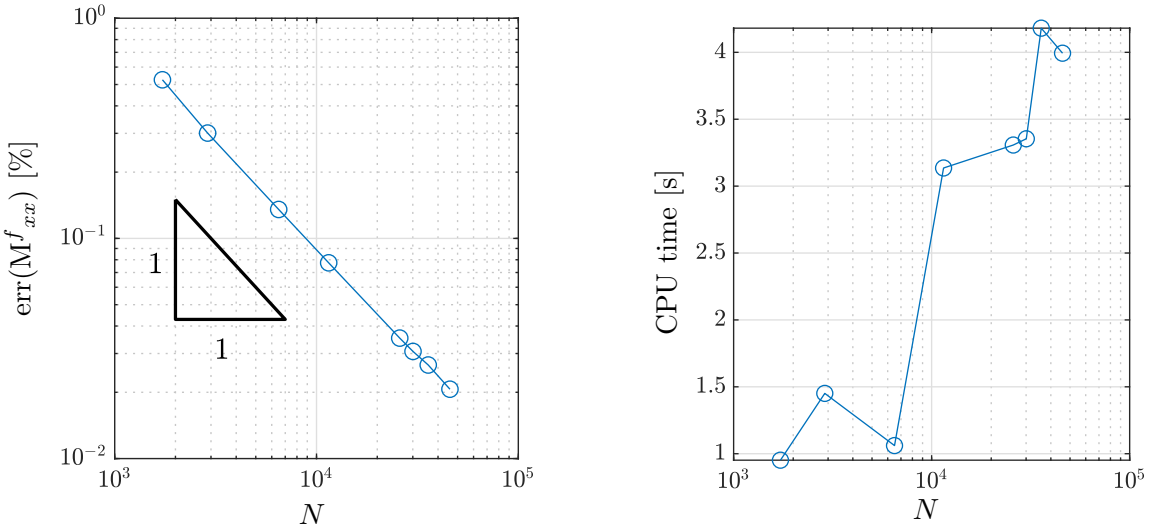

Figure III.9: FEM error on the numerical longitudinal translation added mass coefficient $\{\bar{e}_x\}^{\mathrm{T}} \left[\mathrm{M}^f\right] \{\bar{e}_x\}$ compared with the analytical predicted value at the left. At the right, CPU time required to compute the FEM operator $[\mathrm{P_a}]$ required to determine $\left[\mathrm{M}^f\right]$.

Once both the velocity potential and the virtual power of the fluid have been calculated, their coupling enables to obtain an explicit expression of the fluid forces in the form of added mass, gyroscopic and stiffness matrices.

III.3 Validation of the model linearization

In this section, the error associated with the present linearization method is quantified, investigating the consequences of the asymptotic detailed in section II.2. In order to do so, the perturbations of the forces obtained with the linear model are compared with the force perturbations obtained using finite differences with non linear calculations for various small amplitudes of deformation or velocity. In order to validate the linearization, the relative error between the linear and the non-linear perturbation must be in $\mathcal{O}\left(\varepsilon^2\right)$, meaning that all the linear terms in $\mathcal{O}\left(\varepsilon\right)$ are well captured.

The results are obtained on a mesh with $N \sim 3000$ of an arbitrary ellipsoid of semi axis 0.5, 0.2 and 0.1. The deformation perturbations imposed are arbitrarily set as:

$$\bar{\boldsymbol{\xi}}'^{*} = \dot{\bar{\boldsymbol{\xi}}}'^{*} = \left\{ \begin{array}{c} \cos 2\pi x^{*} \\ x^{*}y^{*} \\ z^{*2} \end{array} \right\}. \tag{III.44}$$

The complex expression of $\bar{\boldsymbol{\xi}}'$ and its time derivative as well as the different semi axis of the ellipsoidal mesh enable to ensure that the couplings involve all the fluid BEM and FEM operators. The same results where obtained for each possible coupling of order zero non nil movements (either $\bar{\boldsymbol{v}}^o_{\mathrm{c}}$ or $\bar{\boldsymbol{\omega}}^o$) with small perturbations in position, velocity or acceleration for the external problem, as reported in table III.1. For the sake of clarity, the operators concerned have been included: stiffness K^f associated with deformations, G^f associated with velocities and M^f associated with accelerations. In this table, the columns associated with acceleration terms are not associated with order zero velocities $\bar{\boldsymbol{v}}^o$ or $\bar{\boldsymbol{\omega}}^o$ since added mass loads are independent of the velocity of the structure at order zero. Two examples of the convergence are given in Figure III.10: the one on the left validates the fluctuations of the fluid forces for a structure with large rotation and small deformations, and the one on the right validates the fluid forces perturbations for the coupling between large and small rotations. One should note that the linearization of the virtual velocity field $\delta\bar{\boldsymbol{v}}' = \delta\bar{\boldsymbol{\omega}}^o \wedge \bar{\boldsymbol{\xi}}'$ is required to obtain a good prediction of the associated moment: without coding it, the prediction is not in $\mathcal{O}\left(\varepsilon^2\right)$ anymore. Due to time constraints, the stiffness and gyroscopic internal fluid operators have not yet been validated. Even though their analytic expression was double checked, it has not been test proofed like the external problem operators and should be implemented with particular care if used in future studies. The small perturbations in $\dot{\bar{\boldsymbol{\xi}}}'$ where computed using the order zero dynamic pressure associated with large displacement velocities, which was not introduced in Chapter II for conciseness purposes, but whose expression is given here to enable the validation of the linear perturbations of the dynamic pressure:

$$p^o_{\mathrm{dyn}}(\bar{\boldsymbol{x}}) = -\dot{\bar{\phi}}^o - \frac{1}{2}(\bar{\boldsymbol{u}}^o)^2 + \bar{\boldsymbol{v}}^o \cdot \bar{\boldsymbol{u}}^o. \tag{III.45}$$

When there is an order zero velocity, the time derivative of $\bar{\phi}^o$ has a much more complicated expression that can be found by deriving equation (II.57a) with respect to time:

$$\frac{\mathrm{d}}{\mathrm{d}t}\mathcal{H}^o(\bar{\phi}^o) = \frac{\mathrm{d}}{\mathrm{d}t}\mathcal{G}^o(\bar{\boldsymbol{v}}^o). \tag{III.46}$$

The expression above can be developed using the chain rule as:

$$\frac{\partial \mathcal{H}^o}{\partial \bar{\boldsymbol{\xi}}^o}\left(\bar{\phi}^o, \frac{\partial \bar{\boldsymbol{\xi}}^o}{\partial t}\right) + \mathcal{H}^o\left(\frac{\partial \bar{\phi}^o}{\partial t}\right) = \frac{\partial \mathcal{G}^o}{\partial \bar{\boldsymbol{\xi}}^o}\left(\bar{\boldsymbol{v}}^o, \frac{\partial \bar{\boldsymbol{\xi}}^o}{\partial t}\right) + \mathcal{G}^o\left(\frac{\partial \bar{\boldsymbol{v}}^o}{\partial t}\right). \tag{III.47}$$

Movements	order zero perturbations	$\bar{\boldsymbol{v}}^o$				$\bar{\boldsymbol{\omega}}^o$				–
		$\bar{\boldsymbol{\xi}}'$	$\bar{\boldsymbol{v}}'$	$\bar{\boldsymbol{\omega}}'$	$\dot{\bar{\boldsymbol{\xi}}}'$	$\bar{\boldsymbol{\xi}}'$	$\bar{\boldsymbol{v}}'$	$\bar{\boldsymbol{\omega}}'$	$\dot{\bar{\boldsymbol{\xi}}}'$	$\frac{\partial^2\bar{\boldsymbol{\xi}}'}{\partial t^2}, \frac{\partial\bar{\boldsymbol{v}}'}{\partial t}, \frac{\partial\bar{\boldsymbol{\omega}}'}{\partial t}$
Operator		K^f	G^f			K^f	G^f			M^f
Problem	$(\mathcal{P}_{\text{ext}})$	✓	✓	✓	✓	✓	✓	✓	✓	✓
	$(\mathcal{P}_{\text{int}})$	✗	✗	✗	✗	✗	✗	✗	✗	✓

Table III.1: Validation of the virtual power fluctuations and the associated matrices $\left[\mathrm{K}^f\right]$, $\left[\mathrm{G}^f\right]$ and $\left[\mathrm{M}^f\right]$.

The expression of the temporal fluctuations of the operators above can conveniently be obtained using the expression of their perturbation:

$$\mathcal{H}^o\left(\frac{\partial\bar{\phi}^o}{\partial t}\right) = \mathcal{G}^o\left(\frac{\partial\bar{\boldsymbol{v}}^o}{\partial t}\right) + \mathcal{G}'\left(\bar{\boldsymbol{v}}^o; \frac{\partial\bar{\boldsymbol{\xi}}^o}{\partial t}\right) - \mathcal{H}'\left(\bar{\phi}^o; \frac{\partial\bar{\boldsymbol{\xi}}^o}{\partial t}\right) \tag{III.48}$$

The order zero time derivative of the potential associated with large deformation velocity can therefore be determined numerically as:

$$\left\{\frac{\partial\bar{\phi}^o}{\partial t}\right\} = [\mathrm{H}]^{-1}\left([\mathrm{G}]\left\{\frac{\partial\bar{\boldsymbol{v}}^o}{\partial t}\right\} + \left(\left[\mathrm{G}'(\bar{\boldsymbol{v}}^o)\right] - \left[\mathrm{H}'(\bar{\phi}^o)\right]\right)\left\{\frac{\partial\bar{\boldsymbol{\xi}}^o}{\partial t}\right\}\right). \tag{III.49}$$

With the expression above, the linear perturbations of the fluid efforts with respect to the deformation velocity could therefore be validated by comparing them with the non linear perturbations for small amplitude velocities ($\varepsilon \ll 1$).

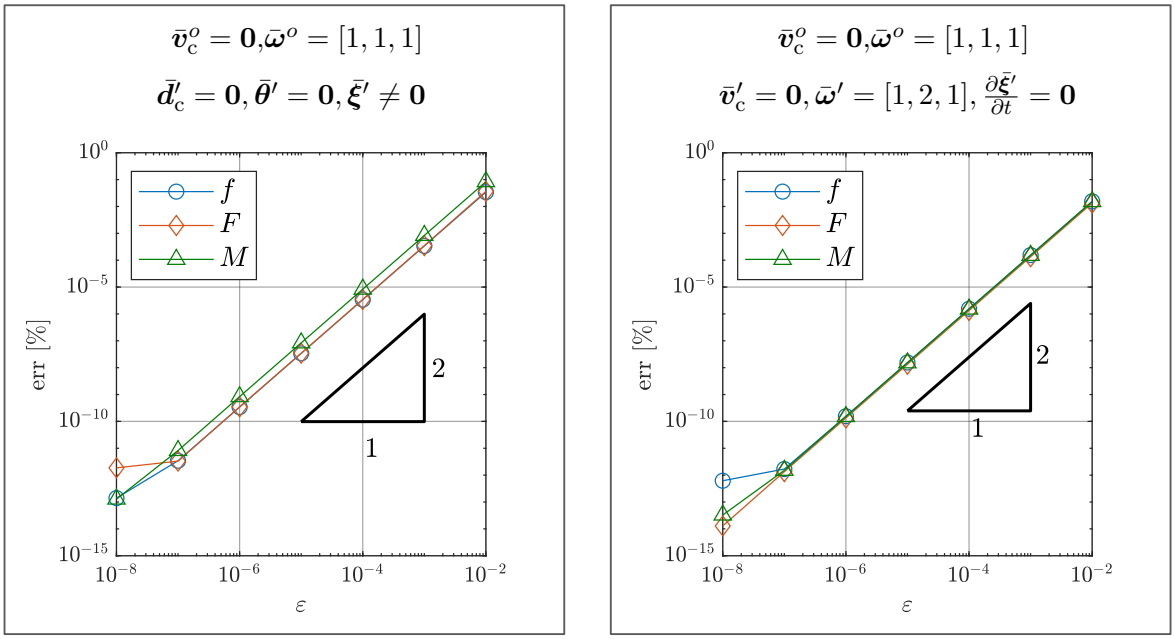

Figure III.10: Error of the linear perturbations of virtual power prediction compared to non linear perturbations. The forces f, F and M are associated with the elastic deformations, the translations and the rotations respectively.

Now that the convergence of the model with respect to the linear and numerical approximations has been verified, it is of great interest to study how the present method compares with existing methods from the literature, both in terms of implementation and accuracy.

III.4 Comparison of the present method with methods from the literature

The aim of this section is to gain insight on the advantages and drawbacks of the present method and its hypotheses by comparing its results with models inspired by the literature.

III.4.1 Comparison of the steady BEM solution with RANS simulations

In order to further verify if the results obtained for a potential flow solved with the BEM enable to capture well the fluid forces around an interface, this section compares results obtained from the quasi-steady order zero solution presented in this article with RANS simulations.

In this section, the pressure obtained with the BEM is compared to the results obtained on the same problem solved with a RANS simulation, which allows to take into account the effects of turbulence on the contrary to the potential flow model which the BEM is based on. The comparison of the dynamic pressure repartition between the BEM and the RANS method is presented in Figure III.11 on a vertical slice $y = 0$ of the interface including both the symmetry axis of the structure and the velocity vector of the ambient flow $\boldsymbol{u}_\infty$. The BEM is calculated on a $N = 5713$ surface mesh. The RANS method was obtained for a compressible flow with a Spalart-Allmaras turbulence model at $\mathcal{R}_e = 2,2.10^6$. For visualization purposes, the pressure, which is supposed to be constant over the elements, has been interpolated linearly for both methods, hence the relative smoothness of both curves. For a quasi-steady case, the dynamic pressure is defined as:

$$p_{dyn} = -\frac{1}{2}\bar{\boldsymbol{u}}^2 + \bar{\boldsymbol{v}} \cdot \bar{\boldsymbol{u}}. \tag{III.50}$$

Because the static pressure is straightforward to obtain, its value has been removed to compare only the dynamic pressure which is much more challenging to predict. Since the RANS mesh is singular on the symmetry axis of the mesh, the fluid perceives the front and rear of the interface as a hole very locally, hence the pressure local spikes of the RANS results at an altitude $z = 0$ associated with the axis of symmetry. Except for this artifact, one can see that the BEM and RANS pressure repartition are similar on most of the interface slice presented here, exception made of two zones. On the top rear of the interface, the BEM dynamic pressure is overpredicted (recalling that with the projection of p_{dyn} in Figure III.11, a curve closer to the interface means a higher pressure). This means that the RANS predicted pressure will create a suction force on the top of the interface which is not captured by the BEM. It is due to the fact that, because of the angle of attack, the flow past the interface creates a lift (caused by the suction on the top of the interface) toward $z > 0$. Because of the d'Alembert paradox, the potential model used for the BEM cannot predict any lift on the structure as mentioned by Li et al. (2011), hence this first divergence between the two methods. The second difference between these methods is that the BEM predicts a stationary point at the rear of the structure (a nil dynamic pressure associated with a nil velocity), whereas the RANS calculation does not predict a stationary point. This is due to turbulent effects causing the fluid to stall locally at the rear of the structure. Because turbulence effects cannot taken into account with the potential flow hypothesis, BEM is not able to predict the stall phenomenon. Apart from these two regions, both method give very similar pressure predictions. Let us also remark

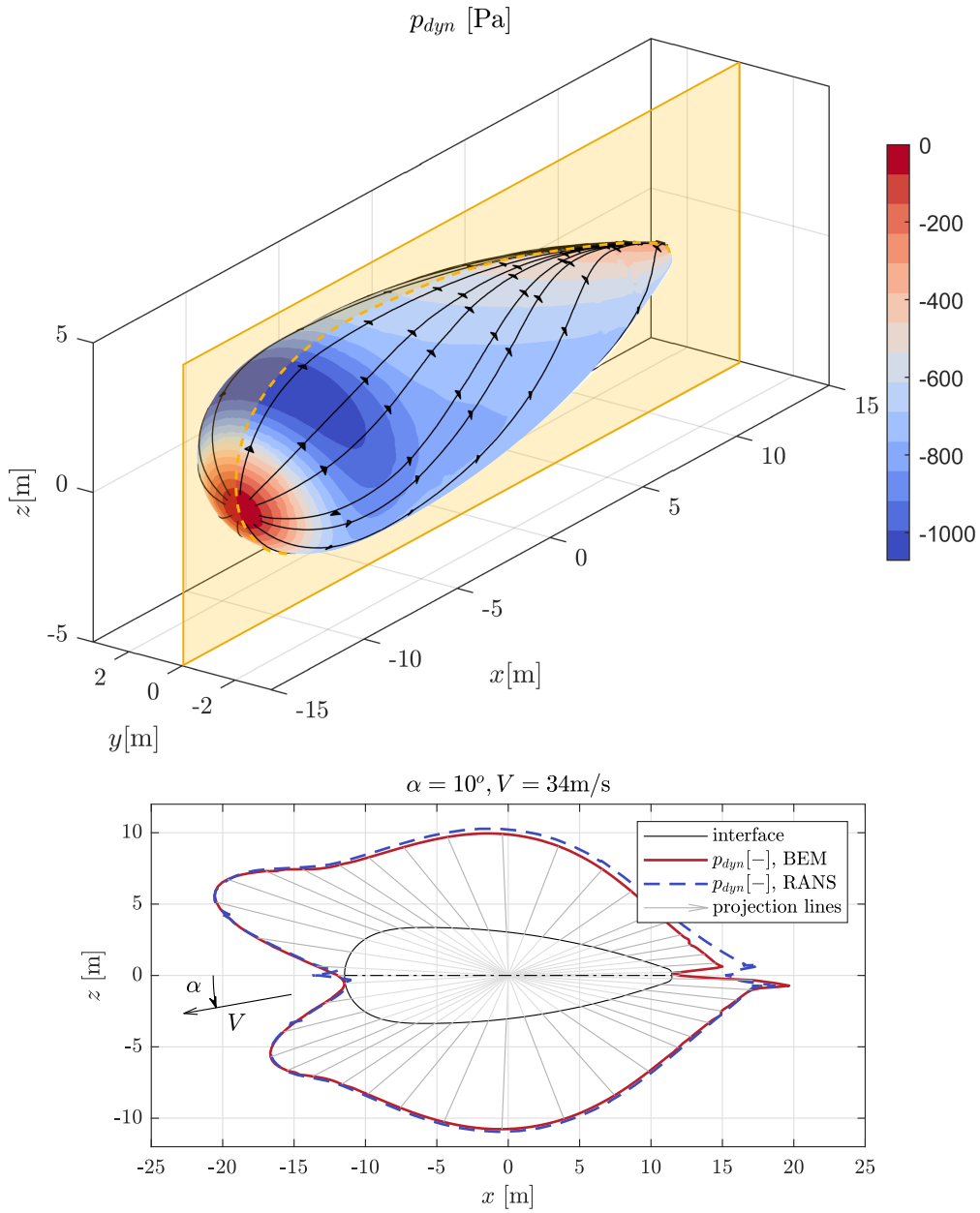

Figure III.11: Dynamic pressure associated with the steady ambient flow around a generic airship shape with a symmetry axis. The structure translation velocity has an angle of attack α of 10° relatively to the longitudinal axis. Top: non-dimensional dynamic pressure field p^*_{dyn} repartition obtained with the BEM. The black curves show the streamlines associated with the velocity of the fluid relative to the structure's. The arrows show the relative flow direction. The orange plane $y = 0$ is used to visualize the pressure repartition on the bottom graph on a slice shown with orange dots on the upper figure. Bottom: comparison of the pressure amplitude obtained with RANS and BEM, projected among a radial direction represented by the light grey lines. When the pressure curve is coincident with the interface, it signifies that there is no dynamic pressure at this point. If the pressure curve is outside the airship domain, it signifies the the dynamic pressure is negative.

that the fluctuation spikes of pressure that appear on the blue curves appart from the symmetry axis ($[x, z] \simeq \{[-20, 5], [-15, -3], [16, 1], [16, -1]\}$ are artifacts due to the linear interpolation of the pressure field between different mesh zones and therefore do not describe with fidelity the RANS numerical results. Further comparisons between potential flow theory and experimental measurements can be found in (Clarke, 2009). In that study, the pressure repartition around a non-axisymetric ellipsoid of aspect ratio $\mathcal{A}_r = 3.5$ obtained with an analytic potential method is compared with both RANS simulations at $\mathcal{R}_e \sim 5.10^7$ and experimental measurements at $\mathcal{R}_e \sim 10^6$. This study leads to similar comparisons: the potential pressure repartition compares well exception made of the rear of the body where stall occurs. Because the interface from Figure III.11 is more profiled than the $\mathcal{A}_r = 3.5$ ellipsoid, the associated stall region is less important in the results presented in this section than in (Clarke, 2009), leading to a better prediction of the pressure by the potential at the rear than in the case of 4.2:2:1 ellipsoid.

The results presented in this section confirms statements that had been made in the literature (Li et al., 2011): at sufficiently low angles of attack, the potential flow hypothesis enables to capture quite well the pressure fluctuations of the flow, even thought it cannot capture the lift caused by the circulation induced on the flow in practice, and it is not able to predict turbulent effects at the rear of the body. Moreover, as the RANS simulations are associated with a compressible fluid, these results tend to validate the hypothesis that the compressibility of the fluid plays a negligible role at the scale of airships, as one would expect for a Mach number of 0.1.

III.4.2 Quantification of the numerical errors with Lagrangian mechanics

We now want to study how Lagrange's equations, used by Li et al. (2009); Azouz et al. (2012), affect the results compared to a Newtonian approach as in the present study.

Lagrangian mechanics, a distinct framework from Newtonian mechanics presented in II.4, has the advantage, among others, to naturally display the symmetry or skew-symmetry properties of the fluid mass, gyroscopic and stiffness operators. However, it comes at the price of having to calculate second order derivatives with respect to the structure movements for the added stiffness. This section investigates how numerical results with Newtonian and Lagrangian mechanics compare, and to what extent the second order derivatives contribute to the added stiffness of the fluid.

The aim of this section is to quantify and compare the error associated with linearized models based on Newton and Lagrange dynamical equations. Due to time constraints, only the quasi-steady fluctuations have been investigated in this manuscript: as a consequence, the gyroscopic and added mass effects from both approaches were not compared, and only the added stiffness effects were investigated. The error associated with linear perturbations has to be associated with a criterion. In this section, two criteria are used to investigate the accuracy of the methods. The first criterion relates to the virtual power fluctuation associated either with the Newton approach or its equivalent Lagrangian approach. The second criterion compares the fluctuations of the fluid kinetic energy. In order to quantify the accuracy of each method, the methodology is the following: the criterion (either virtual power or energy) is first calculated on a reference mesh. Then, the first order fluctuations of the fluid efforts associated with a reference arbitrary movement are determined. Finally, the reference mesh undergoes a displacement associated with the reference movement, with a sufficiently small amplitude in order to ensure quadratic and other higher order terms to have negligible effects. A new quasi-steady solution (and the associated criterion perturbation) can therefore be calculated on this new mesh. As a consequence, the exact perturbation calculated with finite difference based on the reference mesh and the deformed mesh can be compared with

the first order prediction.

The first criterion studied is the virtual power of the flow associated with a virtual velocity $\delta\dot{\bar{\boldsymbol{\xi}}}$. The linear perturbations of the normal and the velocity potential associated with the perturbation $\delta\dot{\bar{\boldsymbol{\xi}}}$ are noted $\bar{\boldsymbol{\tau}}'(\delta\dot{\bar{\boldsymbol{\xi}}})$ and $\bar{\phi}'(\delta\dot{\bar{\boldsymbol{\xi}}})$ are obtained using equations (A.13) and (II.61b) applied to a quasi-steady virtual motion:

$$\bar{\boldsymbol{\tau}}'(\delta\dot{\bar{\boldsymbol{\xi}}}) = (\overline{\boldsymbol{\nabla}}_{\mathrm{t}} \cdot \delta\dot{\bar{\boldsymbol{\xi}}} - \overline{\nabla}_{\mathrm{t}}^{\mathrm{T}} \delta\dot{\bar{\boldsymbol{\xi}}})\bar{\boldsymbol{n}} \tag{III.51a}$$

$$\bar{\phi}'(\delta\dot{\bar{\boldsymbol{\xi}}}) = \Phi_d(\bar{\boldsymbol{\nu}}^o; \delta\dot{\bar{\boldsymbol{\xi}}}). \tag{III.51b}$$

One can express the order zero virtual force associated with the virtual velocity field $\delta\dot{\bar{\boldsymbol{\xi}}}$ using either equation (II.77) or (B.21) for the Newtonian and Lagrangian expression of the virtual force respectively:

$$\delta\mathcal{P}^o_{f,\mathrm{New}}(\delta\dot{\bar{\boldsymbol{\xi}}}) = \int_{\overline{\Sigma}} \bar{p}^o \bar{\boldsymbol{n}} \cdot \delta\dot{\bar{\boldsymbol{\xi}}} \, \mathrm{d}\overline{\Sigma} \tag{III.52}$$

$$\delta\mathcal{P}^o_{f,\mathrm{Lag}}(\delta\dot{\bar{\boldsymbol{\xi}}}) = \frac{1}{2} \int_{\overline{\Sigma}} \bar{\boldsymbol{v}}^o \cdot \left(\bar{\phi}^o \bar{\boldsymbol{\tau}}(\delta\dot{\bar{\boldsymbol{\xi}}}) + \bar{\phi}'(\delta\dot{\bar{\boldsymbol{\xi}}}) \bar{\boldsymbol{n}} \right) \mathrm{d}\overline{\Sigma}, \tag{III.53}$$

where the indexes $_{\mathrm{New}}$ and $_{\mathrm{Lag}}$ stand for the Newtonian and Lagrangian approaches respectively. This expression will be used to determine numerically the quasi-steady virtual force on the reference mesh and on the deformed mesh. The expression of the force fluctuations for both approaches is given by equation (II.78) and the added stiffness expression from equation (B.24) (the expression of $\mathbb{L}_k$ can be found in equation (B.14)):

$$\delta\mathcal{P}'_{f,\mathrm{New}}(\bar{\boldsymbol{\xi}}', \delta\dot{\bar{\boldsymbol{\xi}}}) = \int_{\overline{\Sigma}} \left(\bar{p}^o \bar{\boldsymbol{\tau}}'(\bar{\boldsymbol{\xi}}') + \bar{p}' \bar{\boldsymbol{n}} \right) \cdot \delta\dot{\bar{\boldsymbol{\xi}}} \, \mathrm{d}\overline{\Sigma} \tag{III.54a}$$

$$\delta\mathcal{P}'_{f,\mathrm{Lag}}(\bar{\boldsymbol{\xi}}', \delta\dot{\bar{\boldsymbol{\xi}}}) = \frac{1}{2} \delta\dot{\bar{\boldsymbol{\xi}}}^{\mathrm{T}} (\mathbb{L}_k + \mathbb{L}_k^{\mathrm{T}}) \bar{\boldsymbol{\xi}}', \tag{III.54b}$$

where the expression of the efforts with Lagrange's equation was obtained neglecting the gyroscopic and added mass terms because of the quasi-steady hypothesis, and the velocity fluctuations from equation (II.78) have been neglected for the same reason.

In order to further compare the accuracy of both models, it is possible as well to compare the fluctuations of energy associated with the small, quasi-steady elastic perturbations. For this purpose, the quasi-steady energy can be calculated as in equation (B.3):

$$\mathcal{L} = \frac{1}{2} \int_{\Sigma} \bar{\phi} \bar{\boldsymbol{v}} \cdot \boldsymbol{n} \, \mathrm{d}\Sigma. \tag{III.55}$$

Because the force is equal to the derivative of the energy with respect to the quasi-steady movements, the force perturbations can be calculated as the second derivative of the energy. This enables to calculate the force fluctuations with a different approach based on the energy (similar to Lagrange equations) and not on virtual power (like the Newton approach). The second order

derivative is calculated using finite differences. For this purpose, the energy is calculated on the reference mesh, and then on two deformed mesh with different displacement amplitudes. The energy fluctuation can therefore be approximated with finite differences:

$$\delta\mathcal{P}_f' = \frac{\partial^2 \mathcal{L}}{\partial q_j^2} = \frac{\mathcal{L}(-\varepsilon) + \mathcal{L}(\varepsilon) - 2\mathcal{L}^o}{\varepsilon^2}. \tag{III.56}$$

where $\mathcal{L}(\varepsilon)$ and $\mathcal{L}(-\varepsilon)$ are obtained by applying small elastic deformations to the mesh with two opposite amplitudes, and $\mathcal{L}^o$ is calculated on the reference mesh. Comparing the force fluctuations with those two different methods (either the first derivative of the force from the variational equation or the second derivative of the kinetic energy) enables eventual bias (hence comparing the force fluctuations predicted by the Newton and Lagrange approaches with the force fluctuations from the variational approach calculated with finite differences might advantage the Newton approach while comparing with the second derivative of the energy might advantage Lagrange's approach).

The results obtained from both approaches are compared on the mesh of a 3.5:1 aspect ratio prolate ellipsoid. The calculations are based on the movement $\bar{\boldsymbol{\xi}}'$ of the first bending mode of an homogeneous equivalent cantilever beam (banana-shaped mode), see Figure III.12, left. The virtual velocity used for this test case is the same as the deformations. The results obtained numerically are summarized in table III.2. The values of the virtual forces have been non-dimensionalized by the structure characteristic parameters. Each line is associated on a different method to calculate the force perturbations. The first line has been calculated with the Newton method $\delta\mathcal{P}_{f,\text{New}}$ as described in this thesis, the second line has been calculated using Lagrange's equations as described in Appendix B. It is important to note that latter expression has the disadvantage of depending on the second order derivative of the normal and of the velocity potential with respect to the structure deformations. These two values have been approximated using finite differences method. Finally, the last line is based on a Lagrange's equations approximated by neglecting the second order deformations aforementioned (where the index $^{\text{f.o}}$ stands for "first order"), as done by Li et al. (2009) for example. Considering the results displayed in table III.2, one can see that the second order derivatives terms in Lagrange's linearized equations play an important role (at least for the arbitrary bending mode considered here), as neglecting those second order derivatives leads to an underestimation of the force fluctuations of more than 20%. On the contrary, one can see that the prediction using the complete Lagrange equations (including the second order derivatives) seem to converge well, as it predicts the force fluctuations with an error of less than 1% when compared either with the Newtonian force derivative or with the kinetic energy second derivative. However, one should note that this convergence comes at a high price as already mentioned earlier: the second order derivatives of the normal and more especially of the potential with respect to the interface deformation are very costly to calculate. Regarding the Newtonian approach, one can see that it predicts with very good accuracy the force fluctuations with an error almost equal to zero, whereas the relative error, when comparing with the second order derivative of the kinetic energy, is a little lower than 2%.

The results presented in this section enabled to further validate the approach developed in this manuscript and how it enables to predict the linear fluctuations of the forces of the fluid. But more importantly, it has highlighted how the linearized Lagrange equations require to take into account the second order derivatives of the geometry and the velocity potential in order to predict well the load fluctuations. As these second order derivatives are very costly to calculate relatively to the first order derivatives, this section puts forward how the Newton approach seem better suited than Lagrange's equation for the prediction of the linear perturbations of the fluid forces on the

	value [-]	$\mathrm{err}\left(\frac{\partial^2 \mathcal{L}}{\partial q^2}\right)$	$\mathrm{err}\left(\frac{\partial \delta \mathcal{P}_f^o}{\partial q}\right)$
$\delta \mathcal{P}_{f,\mathrm{New}}$	2.82	1.73%	3×10^{-7}%
$\delta \mathcal{P}_{f,\mathrm{Lag}}$	2.85	0.88%	−0.87%
$\delta \mathcal{P}^{\mathrm{f.o}}_{f,\mathrm{Lag}}$	3.48	−21.2%	−23.3%

Table III.2: Error associated with the prediction of the fluid efforts fluctuations based on a Newtonian approach, Lagrange's equations or Lagrange's equations without second order derivatives.

interface.

III.4.3 Comparison with results obtained from the slender body theory

The perturbations of the velocity potential can be calculated with different approaches. Li et al. (2009) have used the slender body approximation which simplifies the calculation of the velocity potential perturbations associated with transverse flexible movements of slender structures. In this section, we show how the simplifying hypothesis of the slender body theory causes a less accurate prediction of the perturbations than the approach proposed here.

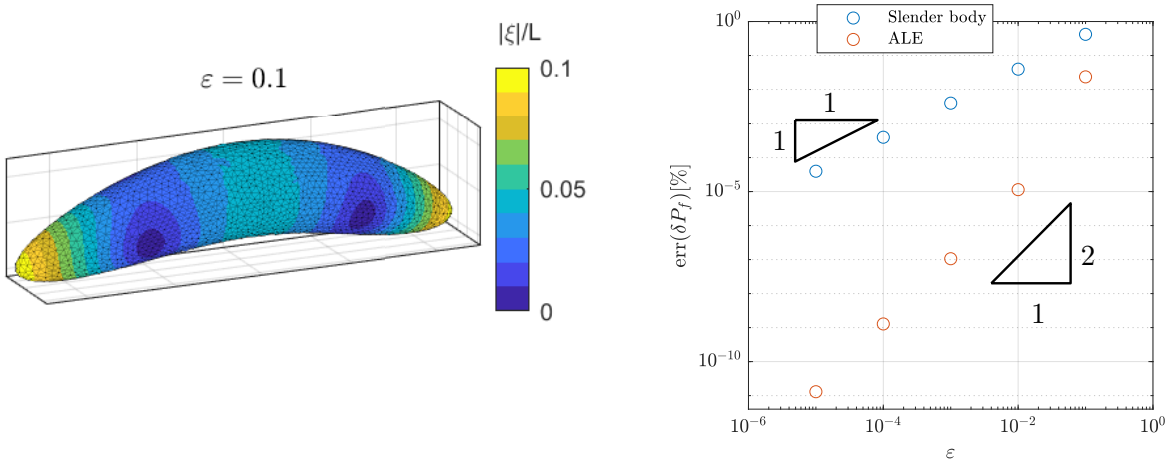

Figure III.12: Left: shape of the deformed ellipsoidal fluid-structure interface for $\varepsilon = 0.1$. Right: error of the linear models for the prediction of the fluid force perturbations, associated with velocity potential perturbations using the ALE method introduced in this manuscript (red dots) or using the slender body approximation (blue dots), as a function of the deformation amplitude.

In order to compare both velocity potential calculation approaches (the ALE approach presented in this manuscript and the slender body theory detailed in (Paidoussis, 1998)), an ellipsoidal mesh has been deformed among the first mode of a free-free cantilever as in the section above, and the results obtained from both linearized models have been compared with non linear perturbations based on finite differences by deforming the mesh. The error associated with both models can be seen in Figure III.12. It shows how the prediction of the perturbations of the velocity potential based on the ALE enable to obtain a prediction of the fluid loads perturbations with an order of

$\mathcal{O}\left(\varepsilon^2\right)$ hence quadratic with the deformations amplitude. It means that the linear perturbations are well predicted, whereas higher order terms in $\mathcal{O}\left(\varepsilon^2\right)$ are not predicted as expected for a linear approach. On the other hand, even though the slender body theory enables to predict reasonably the fluid forces perturbations (error below 1%), it appears that the error associated is in $\mathcal{O}\left(\varepsilon\right)$ which signifies that part of the linear perturbations are not well predicted.

III.5 Conclusion

Through this chapter, the following works have been presented:

1. A BEM code has been implemented. It includes the classical operators of the method, but also their derivative with respect to the geometry of the structure, allowing to compute the velocity potential at zero order as well as at the first order based on a mesh of the reference interface. Moreover, the FEM operators allow to calculate the fluctuations of the fluid forces based on the velocity potential. Thus, the mixed FEM-BEM made it possible to calculate the mass, stiffness and gyroscopic operators of the fluid.
2. Results from Rangette (1990) demonstrating the better prediction of the fluid forces by the symmetric part of the mass operator than by the complete numerical operator, were naturally extended to the fluid stiffness operator because of its symmetry, but also to the better prediction of the fluid forces using the skew-symmetric part of the numerical gyroscopic operator.
3. The H-matrix method, which allows to reduce the storage cost and the computation time linked to the BEM and enables parrallel computing, has been implemented on the classical operators similarly to Chaillat et al. (2017). It was then adapted to linearized BEM operators as well.
4. The BEM and FEM operators have been validated by comparison with analytical results linked to stationary flow or to the added mass associated with an ellipsoid. The potential flow hypothesis was critically studied by comparison with RANS simulations around airship bodies without fins. This confirmed the ability of the potential flow model to capture the fluid pressure forces, except for the effects of lift and separation at the tail of the airship, consistent with the literature (Clarke, 2009).
5. The linear prediction of the potential flow forces has been validated by comparison with non-linear results obtained through finite differences via mesh deformation. The same method was used to highlight how both the slender body theory and the use of Lagrange's equations without second order derivatives as used by Li et al. (2009) are not able to predict the entirety of the first order fluctuations of the fluid forces.

Now that the fluid forces can be obtained via the fluid operators computed using a mixed FEM-BEM approach. The next chapter will thus introduce the numerical computation of the dynamic operators of the structure in order to be able to couple them to the fluid operators and thus characterize the dynamics of the fluid-structure interaction problem.

III.6 Perspectives

In order to go deeper into the work presented in this chapter, the perspectives outlined below provide interesting avenues to explore:

- The computation and the numerical implementation of the gradient of the integral representation associated with the velocity potential has not been implemented because it would have introduced hypersingular operators. However, this approach would allow to compute directly the velocity $\boldsymbol{u}$ at the nodes of the mesh rather than to obtain it by means of a spatial derivative of the velocity potential ϕ, this numerical gradient being constant on the elements of the mesh and not defined at the nodes .
- Little information on the performance of the codes is given in the manuscript because it would not be relevant since they were developed in a non-compiled language (Matlab), but in order to apply them to industrial cases with fast response times (the method having been thought to be efficient: fixed mesh, projection on the modes, etc.), it would be necessary to develop this method on a compiled code.
- It would be interesting to extend the numerical method to unsteady and inhomogeneous ambient flows based on the extension of the theoretical model proposed in the perspectives in section II.6.
- In this chapter, numerical calculations have been compared with analytical results of perfect fluid flows as well as with RANS simulations of turbulent fluid in the framework of a finless hull. However, the comparison of these results with experimental results or flight tests for example would be a further validation of the method.

Chapter IV

Fluid-structure stability analysis of a free flexible airship

Introduction

The aim of this chapter is to study the stability of flexible airships immersed in flows. It is achieved by coupling the structure dynamical operators, which are introduced in this chapter, with the fluid operators presented in chapter III. A parametric exploration enables to characterize the stability of the airship for various structural properties and under multiple flight conditions.

The chapter is organized as follows. In section IV.1, the weak form of the structure dynamical equation is presented, associated with large rigid body motion and small elastic deformations. The pre-stressing effects of the internal gas are presented as well, and the linearized FEM numerical operators are shown. In section IV.2, the monolithic equation resulting from the coupling of the fluid and structure operators is studied. The associated eigenvalue equation is also obtained and the method to solve it is shown. The stabilizing effects of the fins are introduced in section IV.3. The stability is studied for various forward flight velocities.

IV.1 FEM computation of the dynamics of a free elastic structure under external loads

IV.1.1 Computation of the structure dynamic operators with FEM

In this section, we introduce the mass and stiffness operators of the membrane prestressed by an internal pressure and the dynamic pressure due to an external flow, in order to couple them with the fluid operators. Due to time constraints, we consider here only the case with order zero translation velocity (no rotations of order zero), and only elastic perturbations of order one (rotations or translations of order one are not considered).

In this section, four configurations are considered: natural $\grave{\bullet}$, inflated by the internal overpressure with no external flow $\breve{\Sigma}$, steady deformed by the external flow $\bar{\bullet}$ and the current configuration $\Sigma_{(t)}$, see Figure IV.1. . The stress tensor $\boldsymbol{\sigma}$ is linked to the displacement $\boldsymbol{\xi}$ of the structure by the

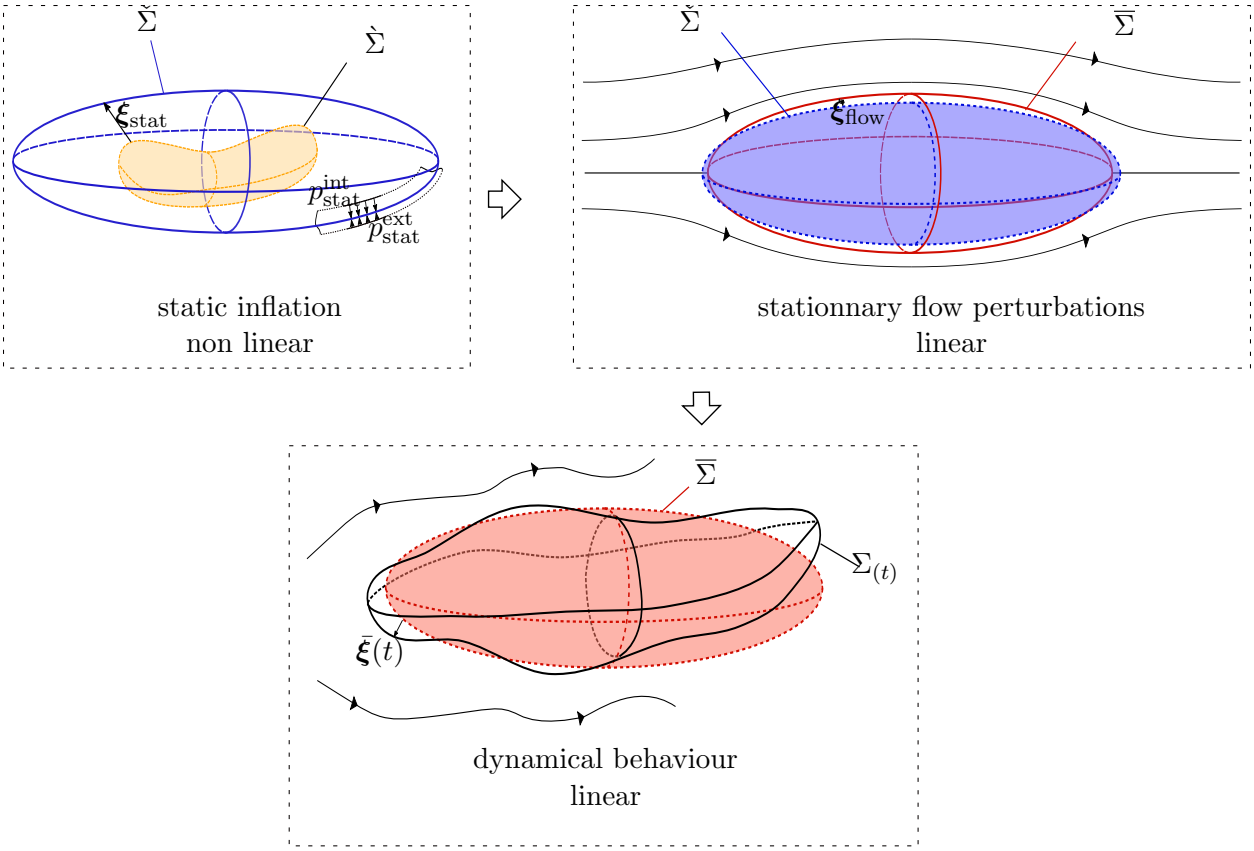

Figure IV.1: Stress-free membrane $\grave{\Sigma}$, inflated interface $\breve{\Sigma}$ by internal and external static pressure and steady deformed interface $\overline{\Sigma}$ by the external dynamic pressure. The instantaneous interface $\Sigma_{(t)}$ results from small deformations of the steady deformed interface $\overline{\Sigma}$ as described in details in Chapter II.

structure equation ($\mathcal{S}$):

$$\boldsymbol{\nabla} \cdot \boldsymbol{\sigma} = \rho_s \ddot{\boldsymbol{\xi}} \quad \text{on } \Omega_{s(t)}, \tag{IV.1}$$

and to the fluid stress tensor $\boldsymbol{\sigma}_f$ with the dynamic condition at the interface ($\mathcal{I}_{\mathcal{D}}$) for an ideal fluid:

$$\boldsymbol{\sigma}\boldsymbol{n} = \boldsymbol{\sigma}_f \boldsymbol{n} \quad \text{on } \Sigma_{(t)}. \tag{IV.2}$$

By combining equations (IV.1) and (IV.2), one can obtain the weak form of the structure equation using the Green identity:

$$\int_{\Omega_{s(t)}} \boldsymbol{\sigma} : \nabla \delta\boldsymbol{\xi} \, \mathrm{d}\Omega + \int_{\Omega_{s(t)}} \rho_s \ddot{\boldsymbol{\xi}} \cdot \delta\boldsymbol{\xi} \, \mathrm{d}\Omega = \int_{\Sigma_{(t)}} (\boldsymbol{\sigma}_f \boldsymbol{n}) \cdot \delta\boldsymbol{\xi} \, \mathrm{d}\Sigma \quad \forall \delta\boldsymbol{\xi}. \tag{IV.3}$$

The equation above is written on the instantaneous, time-dependent solid domain $\Omega_{f(t)}$. It is more convenient to use a formulation based on a time-independent domain in order to perform

calculations based on a single, time-independent mesh. In order to obtain such a formulation, the calculations are based on a reference configuration called the stress-free domain, which is the spatial shape of the solid domain when no external forces are applied on it as shown with the orange interface in the top left of Figure IV.1. In order to transfer the calculations from the time-dependent domain to the stress-free domain, we introduce the first Piola-Kirchoff stress tensor $\mathbb{P}$, $\mathfrak{E}$ the symmetrical part of the gradient of the displacements and $\mathfrak{E}^Q$ a quadratic expression of the gradient of the displacements (both symmetric), $\mathbb{S}$ the second Piola stress tensor (which is symmetric), $\mathbb{F}$ the deformation gradient, $\mathbb{E}$ the Green-Lagrange strain tensor (which is symmetric as well) and C the elasticity tensor (see (Bonet and Wood, 1997)):

$$\grave{\mathbb{P}} = \grave{\mathbb{F}}\grave{\mathbb{S}} \tag{IV.4}$$

$$\grave{\mathbb{F}} = \mathbb{1} + \grave{\nabla}\grave{\boldsymbol{\xi}} \tag{IV.5}$$

$$\grave{\mathbb{S}} = \mathrm{C}\grave{\mathbb{E}} \tag{IV.6}$$

$$\grave{\mathbb{E}} = \frac{1}{2}\left(\grave{\mathbb{F}}^{\mathrm{T}}\grave{\mathbb{F}} - \mathbb{1}\right) = \grave{\mathfrak{E}}(\grave{\boldsymbol{\xi}}) + \grave{\mathfrak{E}}^Q(\grave{\boldsymbol{\xi}}, \grave{\boldsymbol{\xi}}) \tag{IV.7}$$

$$\grave{\mathfrak{E}}(\grave{\boldsymbol{\xi}}) = \frac{1}{2}\left(\grave{\nabla}\grave{\boldsymbol{\xi}} + \grave{\nabla}^{\mathrm{T}}\grave{\boldsymbol{\xi}}\right) \tag{IV.8}$$

$$\grave{\mathfrak{E}}^Q(\grave{\boldsymbol{\xi}}^a, \grave{\boldsymbol{\xi}}^b) = \frac{1}{4}\left(\grave{\nabla}^{\mathrm{T}}\grave{\boldsymbol{\xi}}^a\,\grave{\nabla}\grave{\boldsymbol{\xi}}^b + \grave{\nabla}\grave{\boldsymbol{\xi}}^b\,\grave{\nabla}^{\mathrm{T}}\grave{\boldsymbol{\xi}}^a\right) \tag{IV.9}$$

The tensors introduced above enable to express the integrands from the weak equation of the structure (IV.3) on the stress-free domain:

$$\boldsymbol{\sigma} : \nabla\delta\boldsymbol{\xi}\,\mathrm{d}\Omega = \grave{\mathbb{P}} : \grave{\nabla}\delta\boldsymbol{\xi}\,\mathrm{d}\grave{\Omega} \tag{IV.10}$$

$$\rho_s\,\mathrm{d}\Omega = \grave{\rho}_s\,\mathrm{d}\grave{\Omega} \tag{IV.11}$$

$$\boldsymbol{\varpi}_f\boldsymbol{n}\,\mathrm{d}\Sigma = -\grave{p}\,\grave{\mathbb{\Phi}}_{\mathrm{t}}^{\mathrm{T}}\grave{\boldsymbol{n}}\,\mathrm{d}\grave{\Sigma} \tag{IV.12}$$

Which gives the following non-linear equation:

$$\int_{\grave{\Omega}_s} \grave{\mathbb{P}}(\grave{\boldsymbol{\xi}}) : \grave{\nabla}(\delta\boldsymbol{\xi})\,\mathrm{d}\grave{\Omega} + \int_{\grave{\Omega}_s} \grave{\rho}_s\ddot{\grave{\boldsymbol{\xi}}}\cdot\delta\boldsymbol{\xi}\,\mathrm{d}\grave{\Omega} = -\int_{\grave{\Sigma}} \grave{p}\left(\grave{\boldsymbol{\xi}}, \dot{\grave{\boldsymbol{\xi}}}, \ddot{\grave{\boldsymbol{\xi}}}\right)\left(\grave{\mathbb{\Phi}}_{\mathrm{t}}^{\mathrm{T}}(\grave{\boldsymbol{\xi}})\,\grave{\boldsymbol{n}}\right)\cdot\delta\boldsymbol{\xi}\ \mathrm{d}\grave{\Sigma} \quad \forall\delta\boldsymbol{\xi}. \tag{IV.13}$$

The equation above gives the non-linear dynamical equation of a structure coupled with a surrounding fluid. However, the objective for this study is to analyze the perturbations induced by the flow, which is why the dynamical equation will be developed at orders zero and one in the next section.

IV.1.2 Linearization of the structure equations

The objective of this section is to study the linearized dynamic equation associated with the small perturbations $\bar{\boldsymbol{\xi}}'$ around the reference interface $\overline{\Sigma}$, similarly to the fluid equation developed in Chapter II. To do this, we first calculate the inflation of the membrane due to the internal fluid overpressure leading from the natural $\grave{\Sigma}$ state to the prestressed no-flow $\breve{\Sigma}$ state (see Figure IV.1).

Then we will study the linear perturbations of the membrane due to the external stationary flow at zero order leading to the shape of the $\overline{\Sigma}$ interface, and to what extent these perturbations can be considered as small. Finally we will focus on the linearized dynamics of the structure around this state.

In this section, we only consider translations for rigid-body motions at order zero which don't affect the internal pressure. Actually, the internal pressure depends on order zero rotations but not on order zero translations. If one were to develop the same equations generalized to take into account order zero rotations, this would be possible by considering internal pressure varying with the order zero solution. The dynamical, non-linear structure problem described in equation (IV.13) is very hard to solve. However, with the help of simplifying hypothesis, it will become possible to split this problem into simpler sub-problems. First, the static, non-linear problem associated with the inflation of the membrane by the internal and external static pressures. Second, the linearized problem associated with the stationary order zero flow around the membrane. Third, the linear, dynamic perturbations problem associated with small movements of the membrane.

The first step is the inflation of the membrane thanks to the homogeneous steady pressure of the internal gas $p^{\text{int}}_{\text{stat}}$ and the external gas $p^{\text{ext}}_{\text{stat}}$ in the absence of movements translation velocity of the structure as described in Figure IV.1 (top left). When the structure with no translation velocity is inflated by the internal pressure, it results in a large displacement $\check{\boldsymbol{\xi}}^{\text{stat}}$ from the natural configuration $\grave{\Sigma}$ to the inflate at rest membrane $\check{\Sigma}$. This can be written as

$$\check{\boldsymbol{x}} = \grave{\boldsymbol{x}} + \grave{\boldsymbol{\xi}}^{\text{stat}}, \quad \grave{\boldsymbol{x}} \in \grave{\Sigma}, \check{\boldsymbol{x}} \in \check{\Sigma}, \tag{IV.14}$$

with $\grave{\boldsymbol{\xi}}^{\text{stat}} \sim L$. The displacements $\grave{\boldsymbol{\xi}}^{\text{stat}}$ are solved with equation (IV.13) from which the dynamic terms depending on the acceleration and the pressure terms associated with the fluid flow have been removed:

$$\int_{\grave{\Omega}_s} \grave{\mathbb{P}}(\grave{\boldsymbol{\xi}}^{\text{stat}}) : \grave{\nabla}(\delta\boldsymbol{\xi})\, \mathrm{d}\grave{\Omega} = -\int_{\grave{\Sigma}^{\text{int}} \cap \grave{\sigma}^{\text{ext}}} p_{\text{stat}} \left(\grave{\Phi}_{\text{t}}^{\text{T}}(\grave{\boldsymbol{\xi}})\, \grave{\boldsymbol{n}} \right) \cdot \delta\boldsymbol{\xi}\ \mathrm{d}\grave{\Sigma} \quad \forall \delta\boldsymbol{\xi}. \tag{IV.15}$$

In the equation above, Σ^{int} and Σ^{ext} are the interfaces of the structure with the internal and the external flow respectively. Once the inflated membrane at rest $\check{\Sigma}$ has been solved, the next step is to determine how the stationary flow associated with the order zero translation velocity of the structure will affect the shape of the membrane. When the structure undergoes a transnational velocity $\boldsymbol{v}_{\text{c}}^{o}$, this results in a stationary flow of the fluid particles resulting in a pressure p_{flow} on the external fluid-structure interface. As mentioned previously, the internal pressure of the membrane is not affected by a stationary translation velocity of the structure.

To calculate the structure deformations, the method consists in first calculating the steady-deformed large deformations of the structure and then calculate the small time-dependent perturbations around this state. The non-linear equations associated with the steady deformed displacements $\grave{\boldsymbol{\xi}}^{o}$ are:

$$\grave{\boldsymbol{\xi}}(\grave{\boldsymbol{x}}, t) = \grave{\boldsymbol{\xi}}^{o}(\grave{\boldsymbol{x}}) + \varepsilon \grave{\boldsymbol{\xi}}'(\grave{\boldsymbol{x}}, t). \tag{IV.16}$$

Hence the equation at order zero becomes

$$\int_{\grave{\Omega}_s} \grave{\mathbb{P}}(\grave{\boldsymbol{\xi}}^o) : \grave{\varepsilon}(\delta\boldsymbol{\xi})\,\mathrm{d}\grave{\Omega} + \int_{\grave{\Sigma}} \grave{p}(\grave{\boldsymbol{\xi}}^o)\left(\grave{\Phi}_{\mathrm{t}}^{\mathrm{T}}(\grave{\boldsymbol{\xi}}^o)\,\grave{\boldsymbol{n}}\right)\cdot\delta\boldsymbol{\xi}\;\mathrm{d}\grave{\Sigma} = 0 \quad \forall\delta\boldsymbol{\xi}. \tag{IV.17}$$

We have the following property, since $\bar{\boldsymbol{x}} = \grave{\boldsymbol{x}} + \grave{\boldsymbol{\xi}}^o$:

$$\int_{\grave{\Sigma}} \grave{p}(\grave{\boldsymbol{\xi}}^o)\left(\grave{\Phi}_{\mathrm{t}}^{\mathrm{T}}(\grave{\boldsymbol{\xi}}^o)\,\grave{\boldsymbol{n}}\right)\cdot\delta\boldsymbol{\xi}\;\mathrm{d}\grave{\Sigma} = \int_{\overline{\Sigma}} \bar{p}^o(\bar{\boldsymbol{\xi}}^o)\bar{\boldsymbol{n}}\cdot\delta\bar{\boldsymbol{\xi}}\,\mathrm{d}\overline{\Sigma} = \delta\mathcal{P}_f^o(\delta\bar{\boldsymbol{\xi}}). \tag{IV.18}$$

Therefore, the order zero equation becomes

$$\int_{\grave{\Omega}_s} \grave{\mathbb{P}}(\grave{\boldsymbol{\xi}}^o) : \grave{\nabla}\delta\boldsymbol{\xi}\,\mathrm{d}\grave{\Omega} = \delta\mathcal{P}_f^o(\delta\bar{\boldsymbol{\xi}}) \quad \forall\delta\boldsymbol{\xi}. \tag{IV.19}$$

By developing the structure terms in the equation above, we obtain the following order zero equation:

$$\int_{\grave{\Omega}_s} \left(\mathbb{1} + \grave{\nabla}^{\mathrm{T}}\grave{\boldsymbol{\xi}}^o\right)\mathrm{C}\left(\grave{\varepsilon}(\grave{\boldsymbol{\xi}}^o) + \grave{\varepsilon}^Q(\grave{\boldsymbol{\xi}}^o,\grave{\boldsymbol{\xi}}^o)\right) : \grave{\nabla}\delta\boldsymbol{\xi}\,\mathrm{d}\grave{\Omega} = \delta\mathcal{P}_f^o(\delta\bar{\boldsymbol{\xi}}) \quad \forall\delta\boldsymbol{\xi}. \tag{IV.20}$$

By keeping only the first order terms of the dynamic equation, we get:

$$\int_{\grave{\Omega}_s} \grave{\mathbb{P}}'\left(\bar{\boldsymbol{\xi}}^o;\bar{\boldsymbol{\xi}}'\right) : \grave{\nabla}\delta\boldsymbol{\xi}\,\mathrm{d}\grave{\Omega} + \int_{\grave{\Omega}_s} \grave{\rho}_s\ddot{\grave{\boldsymbol{\xi}}}'\cdot\delta\boldsymbol{\xi}\,\mathrm{d}\grave{\Omega} = \delta\mathcal{P}_f'(\delta\boldsymbol{\xi}) \quad \forall\delta\boldsymbol{\xi}, \tag{IV.21}$$

where

$$\mathbb{P}'\left(\bar{\boldsymbol{\xi}}^o;\bar{\boldsymbol{\xi}}'\right) = \grave{\nabla}\grave{\boldsymbol{\xi}}'\grave{\mathbb{S}}^o\left(\grave{\boldsymbol{\xi}}^o\right) + \mathrm{C}\mathbb{E}'\left(\bar{\boldsymbol{\xi}}^o;\bar{\boldsymbol{\xi}}'\right) \tag{IV.22}$$

$$\mathbb{E}'\left(\bar{\boldsymbol{\xi}}^o;\bar{\boldsymbol{\xi}}'\right) = \frac{1}{2}\left(\grave{\nabla}^{\mathrm{T}}\grave{\boldsymbol{\xi}}^o\,\grave{\nabla}\grave{\boldsymbol{\xi}}' + \grave{\nabla}^{\mathrm{T}}\grave{\boldsymbol{\xi}}'\grave{\nabla}\grave{\boldsymbol{\xi}}^o + \grave{\nabla}^{\mathrm{T}}\grave{\boldsymbol{\xi}}' + \grave{\nabla}\grave{\boldsymbol{\xi}}'\right) \tag{IV.23}$$

$$= \grave{\varepsilon}\left(\grave{\boldsymbol{\xi}}'\right) + 2\grave{\varepsilon}^Q\left(\grave{\boldsymbol{\xi}}^o,\grave{\boldsymbol{\xi}}'\right). \tag{IV.24}$$

Hence the first order equation becomes:

$$\int_{\grave{\Omega}_s} \left(\grave{\nabla}\grave{\boldsymbol{\xi}}'\grave{\mathbb{S}}^o + \mathrm{C}\left(\grave{\varepsilon}(\grave{\boldsymbol{\xi}}') + 2\grave{\varepsilon}^Q(\grave{\boldsymbol{\xi}}^o,\grave{\boldsymbol{\xi}}')\right)\right) : \grave{\nabla}\delta\boldsymbol{\xi}\,\mathrm{d}\grave{\Omega} + \int_{\grave{\Omega}_s} \grave{\rho}_s\ddot{\grave{\boldsymbol{\xi}}}'\cdot\delta\boldsymbol{\xi}\,\mathrm{d}\grave{\Omega} = \delta\mathcal{P}_f'(\delta\boldsymbol{\xi}) \quad \forall\delta\boldsymbol{\xi}. \tag{IV.25}$$

The following structure operators are introduced:

$$\mathrm{K}_{\mathrm{el}}^s(\grave{\boldsymbol{\xi}}',\delta\boldsymbol{\xi}) = \int_{\grave{\Omega}_s} \mathrm{C}\grave{\varepsilon}(\grave{\boldsymbol{\xi}}') : \grave{\nabla}\delta\boldsymbol{\xi}\,\mathrm{d}\grave{\Omega} \tag{IV.26}$$

$$\mathrm{K}_{\mathrm{geo}}^s(\grave{\boldsymbol{\xi}}^o,\grave{\boldsymbol{\xi}}',\delta\boldsymbol{\xi}) = \int_{\grave{\Omega}_s} \grave{\nabla}\grave{\boldsymbol{\xi}}'\grave{\mathbb{S}}^o : \grave{\nabla}\delta\boldsymbol{\xi}\,\mathrm{d}\grave{\Omega} \tag{IV.27}$$

$$\mathrm{K}_{\mathrm{Q,L}}^s(\grave{\boldsymbol{\xi}}^o,\grave{\boldsymbol{\xi}}',\delta\boldsymbol{\xi}) = \int_{\grave{\Omega}_s} 2\mathrm{C}\grave{\varepsilon}^Q(\grave{\boldsymbol{\xi}}^o,\grave{\boldsymbol{\xi}}') : \grave{\nabla}\delta\boldsymbol{\xi}\,\mathrm{d}\grave{\Omega} \tag{IV.28}$$

$$\mathrm{M}^s\left(\ddot{\grave{\boldsymbol{\xi}}}',\delta\boldsymbol{\xi}\right) = \int_{\grave{\Omega}_s} \grave{\rho}_s\ddot{\grave{\boldsymbol{\xi}}}'\cdot\delta\boldsymbol{\xi}\,\mathrm{d}\grave{\Omega}, \tag{IV.29}$$

and we get the fluid-structure equation:

$$\mathrm{M}^s\left(\ddot{\boldsymbol{\xi}}', \delta\boldsymbol{\xi}\right) + \mathrm{K}^s_{\mathrm{el}}(\dot{\boldsymbol{\xi}}', \delta\boldsymbol{\xi}) + \left(\mathrm{K}^s_{\mathrm{geo}} + \mathrm{K}^s_{\mathrm{Q,L}}\right)(\dot{\boldsymbol{\xi}}^o, \dot{\boldsymbol{\xi}}', \delta\boldsymbol{\xi}) = \delta\mathcal{P}'_f(\delta\xi). \tag{IV.30}$$

Equation (IV.30) enables to calculate the structure mass and stiffness, which enables to obtain the linear fluid-structure dynamical equation when completed by the fluid mass, gyroscopic and stiffness operators introduced in Chapter II. As a consequence, the linearized dynamical behaviour of the fluid-structure problem can be obtained based on the resolution of the problem at order zero that has to be previously solved. In the case of inflated membranes, most of the time the elastic stiffness operator $\mathrm{K}^s_{\mathrm{el}}$ plays a negligible role since the pre-stress effects from the internal overpressure are dominant. A bottleneck of this method comes from the fact that the order zero solution varies with the order zero velocity of the structure, which means that for each value of the order zero velocity of the structure that has to be explored, a new order zero solution has to be computed which is very costly and time consuming. As a consequence, the parametric space exploration, which consists in studying the dynamic behavior for a velocity amplitude V with varying values, becomes much harder and longer to perform. In order to avoid this constraint, a linearization of the order zero solution has been performed based on the hypothesis that the quasi-steady order zero dynamic pressure p^o is very small relatively to the static internal and external pressures $p^{\mathrm{int}}_{\mathrm{stat}}$ and $p^{\mathrm{ext}}_{\mathrm{stat}}$. For the sake of simplicity, we suppose that the internal and the external pressures have the same order of magnitude. The associated hypothesis is introduced using a small parameter δ defined as:

$$\epsilon = \frac{\rho_f V^2}{p^{\mathrm{int}}_{\mathrm{stat}}} \ll 1. \tag{IV.31}$$

As a consequence, the order zero pressure can be linearized as:

$$p^o = p_{\mathrm{stat}} + \epsilon p'_{\mathrm{dyn}} \tag{IV.32}$$

$$\frac{p_{\mathrm{stat}}}{p_{\mathrm{int}}} \sim \frac{p'_{\mathrm{dyn}}}{p_{\mathrm{int}}} \sim 1. \tag{IV.33}$$

As a consequence, the structure equation (IV.19) can be rewritten as:

$$\int_{\grave{\Omega}_s} \grave{\mathbb{P}}(\dot{\boldsymbol{\xi}}^o) : \grave{\nabla}\delta\boldsymbol{\xi}\,\mathrm{d}\grave{\Omega} = \int_{\grave{\Sigma}} \grave{p}_{\mathrm{stat}}\left(\grave{\Phi}^{\mathrm{T}}_{\mathrm{t}}\left(\dot{\boldsymbol{\xi}}^o\right)\dot{\boldsymbol{n}}\right)\cdot\delta\boldsymbol{\xi}\,\mathrm{d}\grave{\Sigma} + \epsilon\int_{\grave{\Sigma}} \grave{p}'_{\mathrm{dyn}}\left(\grave{\Phi}^{\mathrm{T}}_{\mathrm{t}}\left(\dot{\boldsymbol{\xi}}^o\right)\dot{\boldsymbol{n}}\right)\cdot\delta\boldsymbol{\xi}\,\mathrm{d}\grave{\Sigma} \quad \forall\delta\boldsymbol{\xi}. \tag{IV.34}$$

From the expression above, it seems natural for infinitesimal values of ϵ to linearize the order zero displacements as:

$$\dot{\boldsymbol{\xi}}^o = \dot{\boldsymbol{\xi}}_{\mathrm{stat}} + \epsilon\dot{\boldsymbol{\xi}}'_{\mathrm{dyn}} \tag{IV.35a}$$

$$\frac{\dot{\boldsymbol{\xi}}_{\mathrm{stat}}}{L} \sim \frac{\dot{\boldsymbol{\xi}}'_{\mathrm{dyn}}}{L} \sim 1. \tag{IV.35b}$$

As a consequence, the fluid operators can be expanded with respect to the small parameter ϵ using calculations that are not included in this manuscript due to time constraints:

$$\mathrm{K}^s_{\mathrm{geo}}\left(\grave{\boldsymbol{\xi}}^o, \grave{\boldsymbol{\xi}}', \delta\boldsymbol{\xi}\right) = \mathrm{K}^s_{\mathrm{geo}}\left(\grave{\boldsymbol{\xi}}_{\mathrm{stat}}, \grave{\boldsymbol{\xi}}', \delta\boldsymbol{\xi}\right) + \epsilon\delta\mathrm{K}^s_{\mathrm{geo}}\left(p'_{\mathrm{dyn}}, \grave{\boldsymbol{\xi}}', \delta\boldsymbol{\xi}\right) + \mathcal{O}\left(\epsilon^2\right) \tag{IV.36}$$

$$\mathrm{K}^s_{\mathrm{Q,L}}\left(\grave{\boldsymbol{\xi}}^o, \grave{\boldsymbol{\xi}}', \delta\boldsymbol{\xi}\right) = \mathrm{K}^s_{\mathrm{Q,L}}\left(\grave{\boldsymbol{\xi}}_{\mathrm{stat}}, \grave{\boldsymbol{\xi}}', \delta\boldsymbol{\xi}\right) + \epsilon\delta\mathrm{K}^s_{\mathrm{Q,L}}\left(p'_{\mathrm{dyn}}, \grave{\boldsymbol{\xi}}', \delta\boldsymbol{\xi}\right) + \mathcal{O}\left(\epsilon^2\right) \tag{IV.37}$$

$$\frac{\delta\mathrm{K}^s_{\mathrm{geo}}}{p^{\mathrm{int}}_{\mathrm{stat}}} \sim \frac{\delta\mathrm{K}^s_{\mathrm{Q,L}}}{p^{\mathrm{int}}_{\mathrm{stat}}} \sim 1. \tag{IV.38}$$

The analytic expression of the fluctuations $\delta\mathrm{K}^s_{\mathrm{geo}}\left(p'_{\mathrm{dyn}}, \grave{\boldsymbol{\xi}}', \delta\boldsymbol{\xi}\right)$ are not detailed here, however they will be calculated using the finite differences based on a variation of V in section IV.2. Similarly, the fluid operators can be written as:

$$\mathrm{K}^f(\bar{\boldsymbol{\xi}}', \delta\bar{\boldsymbol{v}}) = \epsilon\mathrm{K}^{f*}(\grave{\boldsymbol{\xi}}_{\mathrm{stat}}, \bar{\boldsymbol{\xi}}', \delta\bar{\boldsymbol{v}}) + \mathcal{O}\left(\epsilon^2\right) \tag{IV.39}$$

$$\mathrm{G}^f(\dot{\bar{\boldsymbol{\xi}}}', \delta\bar{\boldsymbol{v}}) = \mathcal{U}_r^{-1}(\epsilon\mathrm{G}^{f*}(\grave{\boldsymbol{\xi}}_{\mathrm{stat}}, \dot{\bar{\boldsymbol{\xi}}}', \delta\bar{\boldsymbol{v}}) + \mathcal{O}\left(\epsilon^2\right)) \tag{IV.40}$$

$$\mathrm{M}^f(\ddot{\bar{\boldsymbol{\xi}}}', \delta\bar{\boldsymbol{v}}) = \mathrm{M}^f(\grave{\boldsymbol{\xi}}_{\mathrm{stat}}, \ddot{\bar{\boldsymbol{\xi}}}', \delta\bar{\boldsymbol{v}}) + \epsilon\delta\mathrm{M}^{f*}(\grave{\boldsymbol{\xi}}_{\mathrm{stat}}, p'_{\mathrm{dyn}}, \delta\bar{\boldsymbol{v}}) + \mathcal{O}\left(\epsilon^2\right)) \tag{IV.41}$$

$$\frac{\mathrm{K}^{f*}(\grave{\boldsymbol{\xi}}_{\mathrm{stat}}, \bar{\boldsymbol{\xi}}', \delta\bar{\boldsymbol{v}})}{p^{\mathrm{stat}}_{\mathrm{int}}L^2} \sim \frac{\mathrm{G}^{f*}(\grave{\boldsymbol{\xi}}_{\mathrm{stat}}, \dot{\bar{\boldsymbol{\xi}}}', \delta\bar{\boldsymbol{v}})}{p^{\mathrm{stat}}_{\mathrm{int}}L^2} \sim \frac{\mathrm{M}^f(\grave{\boldsymbol{\xi}}_{\mathrm{stat}}, \ddot{\bar{\boldsymbol{\xi}}}', \delta\bar{\boldsymbol{v}})}{\rho_f\Omega^2L^4} \sim \frac{\delta\mathrm{M}^{f*}(\grave{\boldsymbol{\xi}}_{\mathrm{stat}}, \ddot{\bar{\boldsymbol{\xi}}}', \delta\bar{\boldsymbol{v}})}{\rho_f\Omega^2L^4} \sim 1. \tag{IV.42}$$

The expression of the operators $\mathrm{K}^{f*}(\grave{\boldsymbol{\xi}}_{\mathrm{stat}}, \bar{\boldsymbol{\xi}}', \delta\bar{\boldsymbol{v}})$, $\mathrm{G}^{f*}(\grave{\boldsymbol{\xi}}_{\mathrm{stat}}, \dot{\bar{\boldsymbol{\xi}}}', \delta\bar{\boldsymbol{v}})$ and $\mathrm{M}^f(\grave{\boldsymbol{\xi}}_{\mathrm{stat}}, \ddot{\bar{\boldsymbol{\xi}}}', \delta\bar{\boldsymbol{v}})$ is the same as detailed in Chapter II. One can see from the equation above that for $\epsilon \ll 1$, the fluctuations of the fluid stiffness and gyroscopic operators due to the change of shape $\boldsymbol{\xi}'_{\mathrm{dyn}}$ (associated with the fluctuations of the dynamic pressure $\rho_f V^2$) are negligible, whereas the added mass operator fluctuates at order ϵ due to these change of shape.

Remark

In the cases studied in this thesis, the prestress stiffness of the inflated membrane is much more important than the elastic stiffness: the internal pressure is what gives the structural rigidity of the structure whereas the elastic efforts are negligible because of the thinness of the membrane. As a consequence, the internal parameter p_{int} dictates the membrane rigidity (similarly to the Young modulus dictating the rigidity of an elastic solid in the absence of prestresses). As a consequence, it appears that the small parameter ϵ is the ratio between a dynamic pressure and a stiffness parameter: it is consequently a Cauchy number (De Langre, 2008). Actually, as shown in equation (IV.35a), the displacements caused by the structure can be considered negligible when ϵ is small, and can be considered important when $\epsilon \sim 1$.

Remark

In the literature, the stiffness term $\mathrm{K}^s_{\mathrm{Q,L}}$ is sometimes neglected, as in (Combescure, 2000). In this thesis, the implementation of this elastic term couldn't be implemented due to time constraints. As a consequence, it would be interesting to check how such contributions would affect the inflated structure behavior.

IV.1.3 Discretization of the incompressibility condition

Though the rigid body movements naturally respect the fluid incomprehensibility condition, one has to ensure that the elastic deformations are isovolume. The incompressibility condition can be

discretized as follows:

$$\{1\}^{\mathrm{T}} \left[\mathrm{P_a}\right]^{\mathrm{T}} \left\{\bar{\boldsymbol{\xi}}'\right\} = 0, \tag{IV.43}$$

where $\{1\}$ is a discretized scalar field which value is 1 at each node. Therefore, the incompressibility condition can be imposed by using the homogeneous pressure π from equations (I.45) and (I.46) as an additional unknown, thus adding an equation and an unknown to the initial system:

$$\begin{bmatrix} \left[\mathrm{M}^s\right] + \left[\mathrm{M}^f\right] & 0 \\ 0 & 0 \end{bmatrix} \begin{Bmatrix} \left\{\ddot{\bar{\boldsymbol{\xi}}}'\right\} \\ \pi \end{Bmatrix} + \begin{bmatrix} \left[\mathrm{K}^s\right] & \left[\mathrm{P_a}\right]\{1\} \\ \{1\}^{\mathrm{T}} \left[\mathrm{P_a}\right]^{\mathrm{T}} & 0 \end{bmatrix} \begin{Bmatrix} \left\{\bar{\boldsymbol{\xi}}'\right\} \\ \pi \end{Bmatrix} = \delta \mathcal{P}_f^o \tag{IV.44}$$

We then see that π plays the role of a Lagrange multiplier.

IV.2 Stability analysis of a free elastic structure coupled to an irrotational flow

IV.2.1 Determination of the quasi-steady fluid-structure solution

L (ellipsoid major axis)	10 m
D (ellipsoid minor axis)	2 m
e (membrane thickness)	1 mm
ρ_s (solid density)	8000 kg m^{-3}
ν (Poisson's ratio)	0.25
E (Young's modulus)	2×10^9Pa
Δp (internal overpressure)	7000Pa
β (internal fluid compressibility)	0
N (number of mesh nodes)	3037
g (gravity acceleration)	0 ms^{-2}

Table IV.1: Parameters used for the description of the structure and its internal fluid.

In this section, the method presented above is implemented as a test case, consisting of an ellipsoidal inflated membrane in a uniform flow, whose eigenvalues and eigenmodes are computed. Due to time constraints, this section has been implemented using the method from Le Mestre et al. (2022) which can be found in Appendix F based on a structure with small elastic movements in a homogeneous ambient flow rather than the one detailed in Chapter II with a structure with great rigid body motions coupled to small rigid body motions and elastic displacements in a fluid at rest. The results are expected to be similar, however the projection of the movements differs from both methods as a small rotation in the ambient flow method doesn't impact the kinematics of other variables since they are expressed in the earth referential, whereas a small rotation impacts the structure movements with the method introduced in this thesis as the kinematic variables have been expressed mostly in the structure rotated referential. The prolate ellipsoid has an aspect ratio of $5:1$, characterized by the aspect ratio number $\mathcal{A}_r$:

$$\mathcal{A}_r = \frac{L}{D} = 5. \tag{IV.45}$$

It is also referred to as slenderness number by De Langre (2008). In order to characterize the structure, operators $[\mathrm{K}^s]$ and $[\mathrm{M}^s]$ from equation (II.94) are calculated using the Finite Element analysis program NASTRAN. For that purpose, a membrane finite element linear model has been used, inflated by an incompressible fluid. Its parameters are described in table IV.1. The fluid operators $\left[\mathrm{K}^f\right]$, $\left[\mathrm{G}^f\right]$ and $\left[\mathrm{M}^f\right]$ are calculated using the method presented in Chapter III. Since they are theoretically expected to be (skew-)symmetric, the fluid operators have been (skew-)symmetrized manually once calculated to ensure the physical properties associated with the potential flow. Both fluid and solid operators are calculated on the same conforming surface mesh as shown in Figure IV.2. In the case of a thin shell, as shown in figure IV.2 (b), the movements of the structure are considered homogeneous through its thickness. Moreover, both internal and external fluid-structure interfaces coincide with the mean surface of the shell. As a consequence, the incompressibility condition of the internal fluid on the internal fluid-structure interface constrains the displacements of the external fluid-structure interface as well.

We suppose that the reference interface coincides with the fluid-structure quasi steady solution.

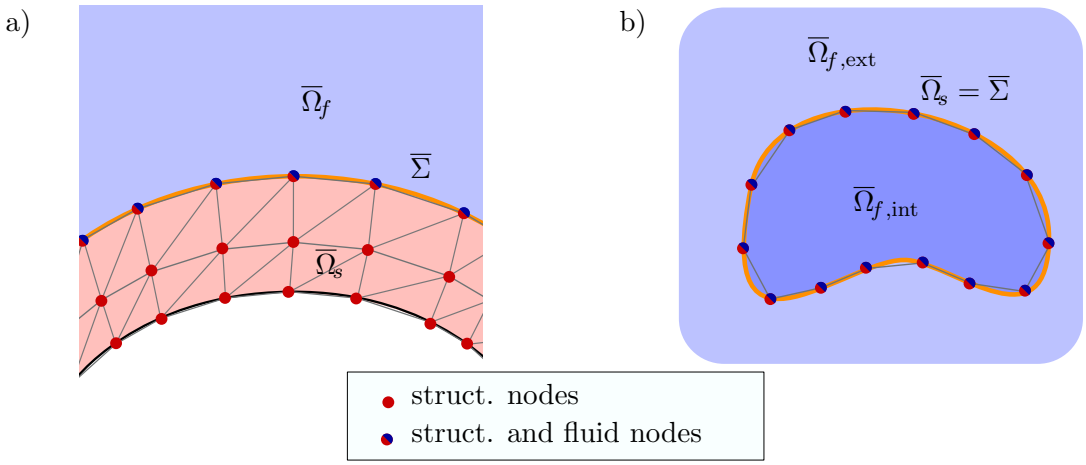

Figure IV.2: Planar view of conformal meshing strategies for a) a tridimensional structure domain and its fluid-structure interface, and b) a thin shell interacting with both external and internal fluids. The red dots denote structure nodes,red and blue dots denote nodes belonging to both fluid and structure, grey lines depict the borders of the mesh elements. The orange line is the reference fluid-structure interface. In the case of a thin shell, the structure domain is associated to its mean plane, which is also approximated as the fluid-structure interface for the thickness is supposed to be negligible.

For the sake of simplicity, we calculate in this study the dynamics of the structure as an invariant shape $\overline{\Sigma}$ assuming that the structure quasi-steady state with the value and direction of V doesn't drastically change. This hypothesis enables us to perform calculations based on the same reference configuration. As a consequence, the structure operators are only computed once, and are associated with a quasi steady state with no ambient flow (homogeneous external pressure field) used as the reference configuration. The coupled model was obtained by grouping the fluid and solid operators as described in equation (IV.30). After characterizing the fluid-structure operators, the objective of this section is to calculate the associated eigenvalues. For this purpose, the displacement $\boldsymbol{\xi}$ is looked for as the product of a function of space $\boldsymbol{q}$ and a function of time:

$$\boldsymbol{\xi}(\boldsymbol{x}, t) = \boldsymbol{q}(\boldsymbol{x}) \ \exp(\lambda t), \tag{IV.46}$$

where λ can be complex. In the following, all the variables are written on the reference configuration and the bar notation $\overline{(\bullet)}$ is not used since there is no risk of confusion. The solution in the form of equation (IV.46) is introduced in equation (IV.30), which gives:

$$\left[\left([\mathrm{M}^s] + \left[\mathrm{M}^f\right] \right) \lambda^2 + \left[\mathrm{G}^f\right] \lambda + [\mathrm{K}^s] + \left[\mathrm{K}^f\right] \right] \boldsymbol{q} \exp(\lambda t) = 0. \tag{IV.47}$$

However, because the fluid operators are dense (as a consequence of condensing the fluid equations on the interface with the integral representation (Bonnet, 1999)), solving such a problem requires a large amount of memory. To overcome this issue, the size of the problem is reduced by projecting the unknown displacements $\boldsymbol{\xi}$ of the structure on a reduced basis. The basis chosen here contains the six rigid body motions (three translations and three infinitesimal rotations), and is completed with two structural modes obtained with a modal calculation from NASTRAN as well, one of which can be seen on Figure III.12 left. The other one has not been plotted, but it has a similar shape

oriented differently since these banana-shaped flexible modes are orthogonal. They have the same *in vacuo* frequency and only differ by a rotation among the symmetry axis of their direction. According to Li et al. (2009), these banana modes are expected to be the lowest frequency elastic modes emerging for high aspect ratio flexible airships. The displacement field is therefore projected on a reduced basis $\mathbb{Q}_{\mathrm{rb}}$:

$$\boldsymbol{\xi}(\boldsymbol{x},t) = \mathbb{Q}_{\mathrm{rb}}(\boldsymbol{x})\boldsymbol{q}_{\mathrm{rb}}\exp(\lambda t), \tag{IV.48a}$$

$$\boldsymbol{q}_{\mathrm{rb}} = \begin{pmatrix} \boldsymbol{d} \\ \boldsymbol{\theta} \\ q_{\mathrm{rb}7} \\ q_{\mathrm{rb}8} \end{pmatrix}. \tag{IV.48b}$$

The reduced basis projector $\mathbb{Q}_{\mathrm{rb}}$ is an eight-columns concatenation of the rigid body movement matrix $\mathbb{Q}$ defined in (II.17) for the first six columns, and the mode shape functions of the banana modes for the two last columns. The volume center displacement is given by $\boldsymbol{d}$, the structure rotation is given by $\boldsymbol{\theta}$ and the amplitudes of the elastic modes are given by the modal coefficients $q_{\mathrm{rb}7}$ and $q_{\mathrm{rb}8}$. The displacements are therefore characterized by the new generalized coordinates vector $\boldsymbol{q}_{\mathrm{rb}}$ of the fluid-structure problem and the associated eigenvalue λ. Equation (IV.47) is quadratic with respect to λ, however it is much more convenient to determine eigenvalues associated with linear eigen equations. For that purpose, the equation is shifted into the state space, thus reducing its order in λ from quadratic to linear, which gives by projecting on the $\mathbb{Q}_{\mathrm{rb}}$ basis:

$$[\mathrm{A}] = \begin{bmatrix} [\mathrm{K}^s]_{\mathrm{rb}} + \left[\mathrm{K}^f\right]_{\mathrm{rb}} & 0 \\ 0 & [\mathrm{M}^s]_{\mathrm{rb}} + \left[\mathrm{M}^f\right]_{\mathrm{rb}} \end{bmatrix}, \tag{IV.49a}$$

$$[\mathrm{B}] = \begin{bmatrix} -\left[\mathrm{G}^f\right]_{\mathrm{rb}} & -\left([\mathrm{M}^s]_{\mathrm{rb}} + \left[\mathrm{M}^f\right]_{\mathrm{rb}}\right) \\ \left([\mathrm{M}^s]_{\mathrm{rb}} + \left[\mathrm{M}^f\right]_{\mathrm{rb}}\right) & 0 \end{bmatrix}, \tag{IV.49b}$$

$$[\bullet]_{\mathrm{rb}} = \mathbb{Q}_{\mathrm{rb}}^{\mathrm{T}}\,[\bullet]\,\mathbb{Q}_{\mathrm{rb}}, \tag{IV.49c}$$

$$[\mathrm{A}]\begin{pmatrix} \boldsymbol{q}_{\mathrm{rb}} \\ \lambda\boldsymbol{q}_{\mathrm{rb}} \end{pmatrix} = \lambda\,[\mathrm{B}]\begin{pmatrix} \boldsymbol{q}_{\mathrm{rb}} \\ \lambda\boldsymbol{q}_{\mathrm{rb}} \end{pmatrix}. \tag{IV.49d}$$

Equation (IV.49d) consists of a system of sixteen equations since the dynamic equations have been projected on the modal basis (of size eight) with the help of a left-multiplication by $\mathbb{Q}_{\mathrm{rb}}^{\mathrm{T}}$. One might note that, because of the symmetry of $\mathrm{K}^s, \mathrm{M}^s, \mathrm{K}^f$ and M^f and the skew-symmetry of G^f, the matrices [A] and [B] are symmetric and skew-symmetric respectively. This eigenvalue equation is solved using MATLAB for a flow velocity $\boldsymbol{u}_\infty$ colinear to the structure axis.

Remark

It is possible to use symmetric and skew-symmetric alternative forms of [A] and [B]:

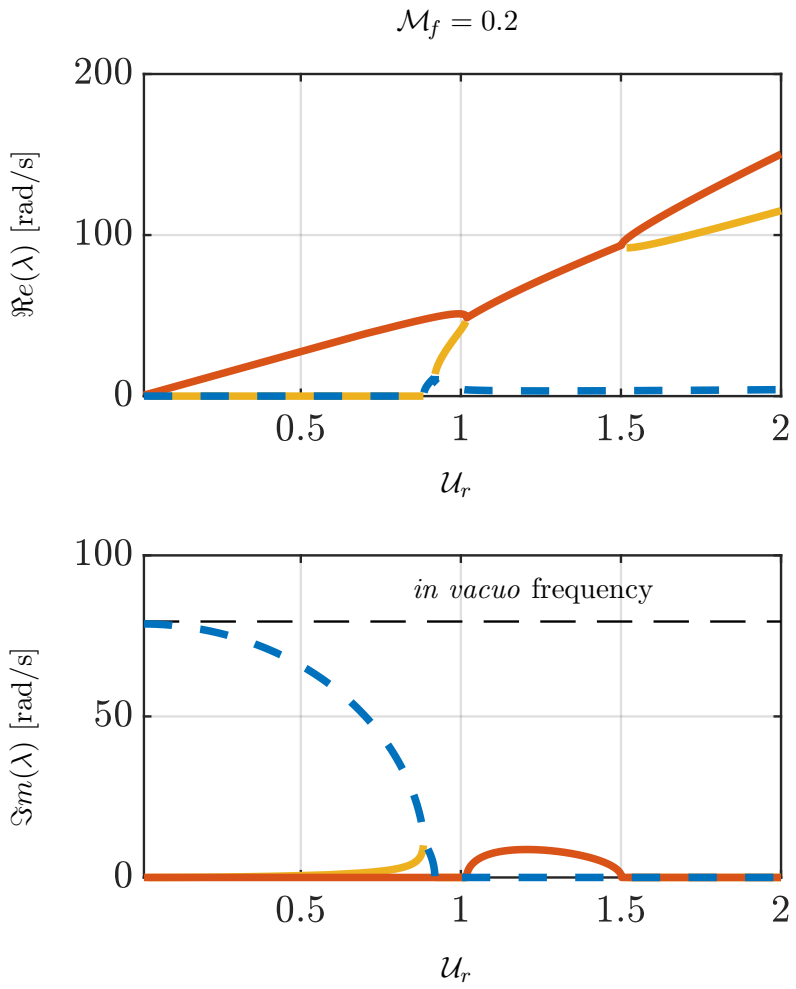

Figure IV.3: Evolution of the real part of the modes (top) associated with the growth rate and their imaginary part (bottom) associated with the circular frequency as a function of the reduced velocity $\mathcal{U}_r$. The mass ratio is $\mathcal{M}_f = 0.2$. Each color stands for an identified mode using a Modal Assurance Criterion. Only the modes with positive frequency, positive growth rate and strictly positive absolute value have been plotted. The black horizontal dashed line shows the frequency of the banana mode in the absence of fluid.

$$[\mathrm{A}] = \begin{pmatrix} \left[\mathrm{G}^f\right]_{\mathrm{rb}} & \left[\mathrm{M}^f\right]_{\mathrm{rb}} + [\mathrm{M}^s]_{\mathrm{rb}} \\ -\left[\mathrm{M}^f\right]_{\mathrm{rb}} - [\mathrm{M}^s]_{\mathrm{rb}} & [0] \end{pmatrix}$$

$$[\mathrm{B}] = \begin{pmatrix} [\mathrm{K}^s]_{\mathrm{rb}} + \left[\mathrm{K}^f\right]_{\mathrm{rb}} & [0] \\ [0] & \left[\mathrm{M}^f\right]_{\mathrm{rb}} + [\mathrm{M}^s]_{\mathrm{rb}} \end{pmatrix}.$$

However, when this form is used in Matlab, the eigenvalues algorithm doesn't converge using the matrixes introduced in this remark on the contrary to the form from equation (IV.49a).

Remark

The quasi-steady linear fluctuations of the potential associated with the displacement for each mode are calculated here by introducing the differentiation of the BEM equation as presented in chapters II and III. However, those quasi-steady perturbations could be obtained as well using the finite differences method. In practice, such a result would be obtained by solving, for each mode, the quasi-steady order zero problem associated with a mesh deformed among the mode with an arbitrary infinitesimal amplitude to ensure the fluctuations are linear. As a consequence, the linear, quasi-steady potential fluctuations for each mode could be obtained by calculating the fluctuations of the potential between the undeformed and the deformed mesh, divided by the displacement amplitude. In the example presented above, it would mean calculating a new order zero solution associated with each mode instead of linearizing the BEM operators and projecting them on each mode afterwards.

However, the finite differences method have some major drawbacks in practice:

- The necessity to calculate the fluctuations for several amplitude of each mode in order to ensure that the associated perturbations are well approached linearly: if not, the amplitude of deformation need to be more adapted.
- According to Bonnet (1999) in chapter 12, the finite-difference estimation of gradients is mathematically ill-posed, which leads to inaccuracies.
- Even though the calculation of the BEM operators perturbations is a costly process, once is has been calculated it can be applied to any chosen deformation to obtain the associated perturbation using matrix-vector products. With the finite-difference, each new deformation that has to be considered requires the recalculation of new BEM operators on the deformed configuration which is very costly when considering multiple modes of displacements.

Because of these three reasons, the choice to derive analytically the integral equation was preferred over finite-difference estimations.

A range of fluid velocities V and densities ρ_f are investigated. The results are plotted with respect to the reduced velocity $\mathcal{U}_r$ introduced in equation (I.16) and the mass ratio $\mathcal{M}_f$ defined as:

$$\mathcal{M}_f = \frac{\rho_f}{\rho_s \frac{e}{D}}. \tag{IV.50}$$

The reduced velocity $\mathcal{U}_r$ determines the ratio between the flow velocity and the velocity required for a fluid particle to travel across the structure during a characteristic period. The value of the characteristic frequency Ω is chosen as the frequency *in vacuo* of the elastic modes. The mass ratio compares the order of magnitude between the added mass of the fluid and the membrane mass, D being the diameter of the ellipsoid (hence $D = L/5$ for a 5:1 prolate). The particular dependence of the operators on V is taken advantage of: they are calculated at an arbitrary velocity, and their value can be recalculated for each $\mathcal{U}_r$ with a scalar multiplication, recalling that the fluid mass operator doesn't vary with V, the fluid gyroscopic operator is linear with V and the fluid stiffness operator is linear with V^2, as shown in Chapter II. Similarly, by looking at equation (I.47) one can deduce that the fluid operators are linear with the fluid density ρ_f. The results are presented in Figure IV.3 for a mass ratio of $\mathcal{M}_f = 0.2$. The order zero solution is an unstable equilibrium position as soon as there is a flow. Indeed, for $\mathcal{U}_r \in]0, 1]$, the system has a mode with a nil frequency $\Im m(\lambda) = 0$ and a positive growth rate $\Re e(\lambda) > 0$ (plotted in blue in Figure IV.3): it is a divergence mode. At an arbitrary value $\mathcal{U}_r = 0.3$ in this region, the modal decomposition of this unstable mode $\boldsymbol{q}_{\text{rb}}$ is shown in Figure IV.4 with blue bars. It appears that the generalized coordinates

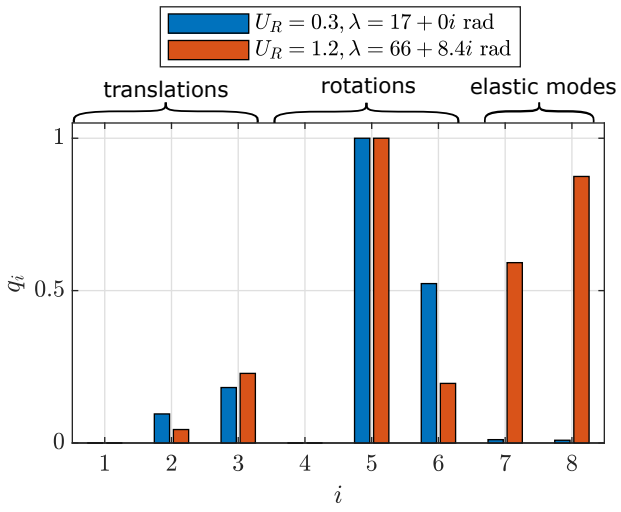

Figure IV.4: Generalised coordinates of a static unsteady mode (blue) and a flutter mode (orange) for two different values of $\mathcal{U}_r$, with $\mathcal{M}_f = 0.2$.

contributing to the instability are the rotations and translations perpendicular to the axis of $\boldsymbol{u}_\infty$, while translation and rotation in the axis of the structure and flexible deformations are not involved in the instability. The latter is triggered by the mechanical moment displayed in figure III.8 top right: a small variation of $\boldsymbol{\theta}^1$ induces a moment in the same direction on the structure, leading to an exponentially growing drift. The moment responsible for this drift is known by airship engineers as the Munk moment. The contribution of the translations displayed in Figure IV.4 results from the appearance of a force perpendicular to the ambient flow when the structure rotates. In the region $\mathcal{U}_r \in]0, 1]$ of Figure IV.3, the frequency of the elastic mode (dashed blue line) decreases with the reduced velocity until it vanishes. If the flow velocity increases past this point, another static unstable mode appears (yellow line), with a growth rate increasing with $\mathcal{U}_r$. When the flow reaches the critical velocity $\mathcal{U}_r \simeq 1.04$, the growth rate of the two unstable modes become equal, and we see the apparition of a mode associated to strictly positive frequency and growth rate, resulting in exponentially growing oscillations of the structure. This instability is referred to as flutter (Pfister et al., 2019). The orange bars from Figure IV.4 show the generalized coordinates of this flutter mode. It appears that unlike the static unstable mode below the critical velocity (plotted with blue bars in the same figure) this instability results from the coupling of rigid body movements with elastic deformations of the structure. Around $\mathcal{U}_r = 1.53$, the flutter mode splits into two static unstable modes. We see as well that for a mass ratio of $\mathcal{M}_f$ =0.2 the added mass has a small influence on the dynamics. Indeed, for $\mathcal{U}_r = 0$ (hence when the fluid stiffness or gyroscopic loads vanish), the frequency of the elastic mode (dashed blue line in Figure IV.3) is almost the same as the frequency of the structure *in vacuo* (dashed horizontal black line). Figure IV.6 is inspired by Paidoussis (1998) and shows how the flutter instability is triggered by coupling of two divergent modes.

Figure IV.5 shows the evolution of the eigenvalues for a range of values of mass ratio $\mathcal{M}_f$. As expected, for larger values of the fluid density, the frequency of the immersed elastic mode in a fluid at rest decreases. The second graph of Figure IV.5 displays the evolution of the eigenvalues

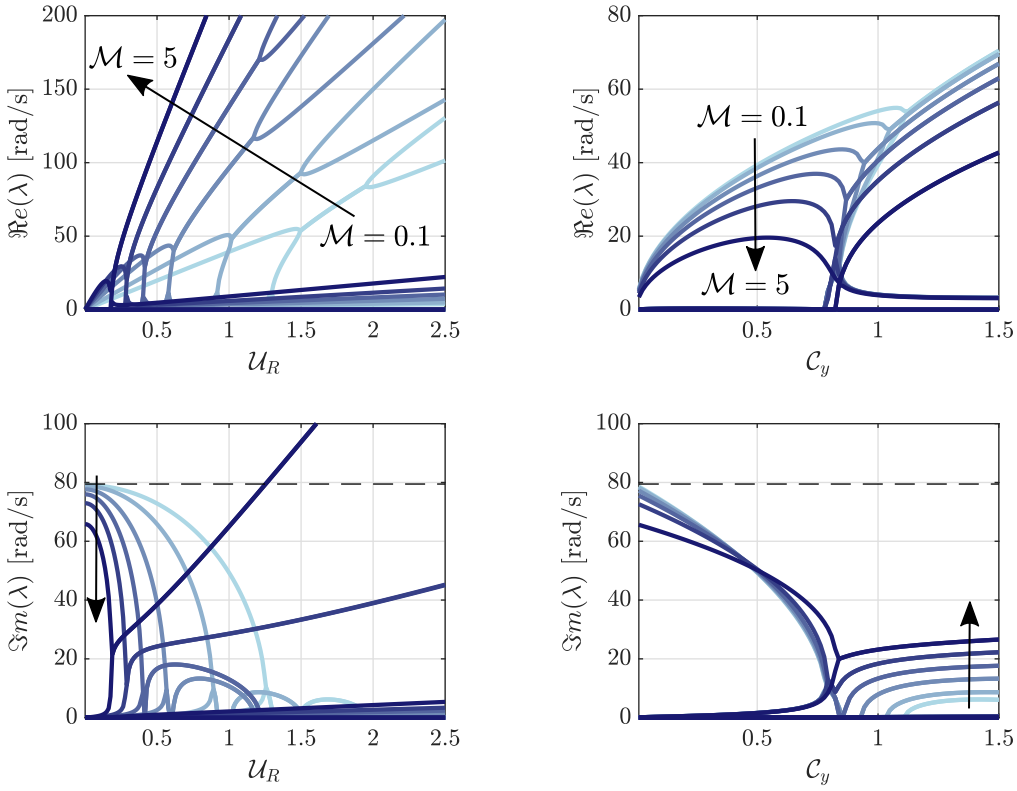

Figure IV.5: Real part (growth rate, top) and imaginary part (frequency, bottom) of the eigenvalues as a function of the reduced velocity $\mathcal{U}_r$ (left) and the Cauchy number $\mathcal{C}_y$ (right). Curves are for $\mathcal{M}_f$ =0.1, 0.2, 0.5, 1, 2 and 5. The dashed horizontal line is the *in vacuo* frequency of the structure.

with respect to the Cauchy number $\mathcal{C}_y$, defined as the ratio between the magnitude of the fluid load and the solid flexible stiffness De Langre (2008):

$$\mathcal{C}_y = \frac{\rho_f V^2 D}{\rho_s e L D \Omega^2} = \mathcal{M}_f \mathcal{U}_r^2 \mathcal{A}_r. \tag{IV.51}$$

The numerator quantifies the order of magnitude of the fluid force by multiplying the characteristic dynamic pressure $\rho_f V^2$ with the characteristic surface of the structure LD. The denominator quantifies the characteristic flexible stiffness of the structure, obtained by multiplying its characteristic mass $\rho_s e L$ by the square of the characteristic flexible frequency Ω^2. Figure IV.7 shows the type of instability of the system (static divergence or flutter) as a function of the parameters $\mathcal{C}_y$ and $\mathcal{M}_f$. The dashed line represents the value of $\mathcal{C}_y$ at which the flexible mode frequency vanishes. Hence when the dashed blue line from Figure IV.3 associated with the imaginary part reaches the horizontal axis, which happens when the fluid and solid stiffness of the flexible mode cancel each other at a constant $\mathcal{C}_y$. If $\mathcal{M}_f$ becomes large enough ($\mathcal{M}_f \simeq 2$) the dotted line reaches the flutter zone (red), and for higher values of $\mathcal{M}_f$ the dotted line disappears. This can be observed on Figure IV.5: for $\mathcal{M}_f = 5$, the imaginary part of the flexible mode doesn't vanish anymore when $\mathcal{C}_y$

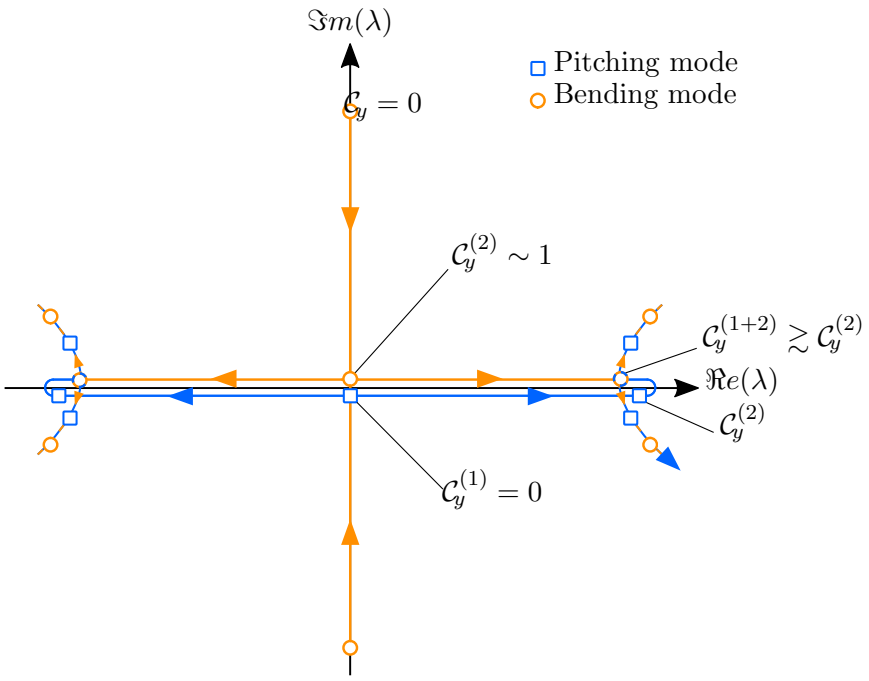

Figure IV.6: Simplified Argand diagram of the mechanism of pitching divergence (blue squares) and bending divergence (orange circles) coupling into a post-divergence (or Païdoussis) coupled-mode flutter. For the sake of visualization, the eigenvalues are not completely aligned with the real axis even when they are nil. $\mathcal{C}_y^{(1)} = 0$ is the critical Cauchy number at which the pitching mode becomes divergent. As the Cauchy number increases, the total stiffness associated with the bending mode decreases which causes its pulsation to come closer to the real axis. At $\mathcal{C}_y^{(2)} \sim 1$, the total stiffness becomes nil, which triggers a divergence of the bending mode. At $\mathcal{C}_y^{(1+2)}$, the growth rate of the pitching and bending modes becomes equal, triggering the post-divergence coupled-mode flutter.

increases. We can see as well that for $\mathcal{M}_f \geq \mathcal{O}\left(10^4\right)$ the $\mathcal{C}_y$ value at which flutter arises reaches a plateau. The value $\mathcal{M}_f$ at which flutter occurs at high $\mathcal{C}_y$ reaches a plateau as well at $\mathcal{M}_f^{lim} \simeq 1.72$, which was observed by plotting the same map for higher values of $\mathcal{C}_y$.

Important remark

As discussed in this section, the model introduced in this thesis predicts a risk of flutter around $\mathcal{C}_y \sim 1$. However, one should recall that the results presented here are based on the hypothesis that the quasi-steady order zero dynamic pressure induces small deformations of the membrane. However, noting from equation (IV.31) that we have in fact $\epsilon \sim \mathcal{C}_y$, at $\mathcal{C}_y \sim 1$ (where $\mathcal{C}_y$ is the ratio between the order zero dynamic pressure and the structure stiffness), one might expect large deformations induced by the dynamic pressure, which means that the linear fluctuations covered by the model might not be viable any more. Therefore, an interesting perspective could be to verify how the dynamic pressure affects the displacements of the structure around $\mathcal{C}_y \sim 1$, and whether or not the linear model still matches well the non-linear results.

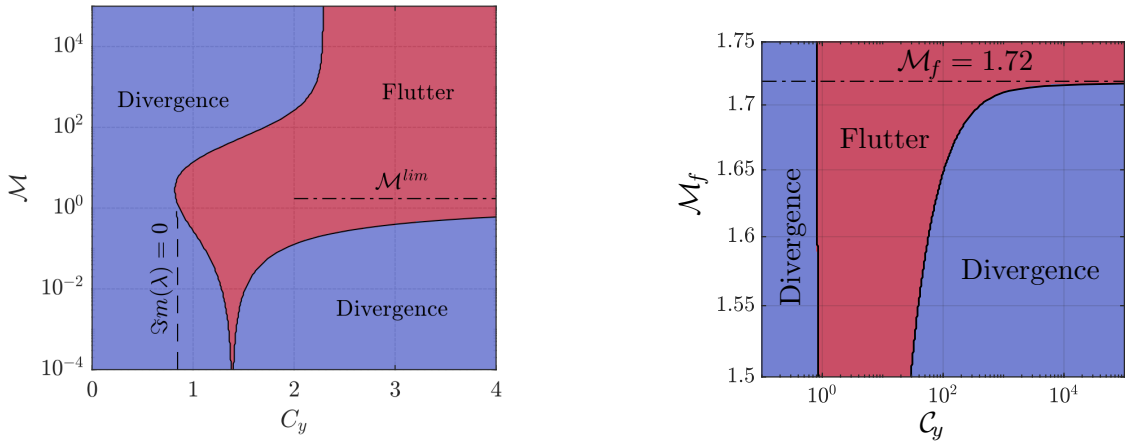

Figure IV.7: Instability map predicted by the linear model: divergence (static) or flutter (dynamic), for $\mathcal{M}_f \in [10^{-4}, 10^6]$ and $\mathcal{C}_y \in [0, 4]$. The dashed vertical line is associated with the $\mathcal{C}_y$ at which the flexible mode frequency becomes nil and the dot line, and the horizontal dashed dotted line is associated with the value $\mathcal{M}_f^{lim} = 1.72$ for which no divergence occur for $\mathcal{C}_y \gg 1$.

IV.2.2 Comparison of the eigenvalues obtained with different methods

As already explained in Chapter II, the method introduced in this thesis differs from various approaches from the literature. The objective of this section is to quantify the error linked with various simplifications used in the literature.

For this purpose, let us recall that the slender body model consists of an approximation of the normal rotations using the rotation of the center line of the hull. As a consequence, the potential perturbations can be calculated by considering the fluctuations of the normal while neglecting the rest of geometrical perturbations (e.g displacements or dilatation of the interface). Thus, the perturbations of the potential can be calculated using two methods: ϕ_{ALE} refers to the present method taking into account the whole linearized geometry perturbations, whereas ϕ_{slen} only takes into account the normal perturbations obtained with the slender body assumption. In practice, the slender body theory is implemented by using the following approximations:

$$\text{Slender body hypothesis :} \tag{IV.52}$$

$$\overline{\partial_n G}' \approx 0 \tag{IV.53}$$

$$\overline{\boldsymbol{G_n}}' \approx G^o \boldsymbol{n}' \tag{IV.54}$$

$$\mathrm{d}\Sigma' \approx 0, \tag{IV.55}$$

which means that the the fluctuations of the Green's function and the dilatation of the interface are not taken into account by the method: the only geometrical perturbations considered are the normal rotations, which have to be calculated based on the approximated curvilinear movement of the centerline of the hull for each mode as done by Li et al. (2009).

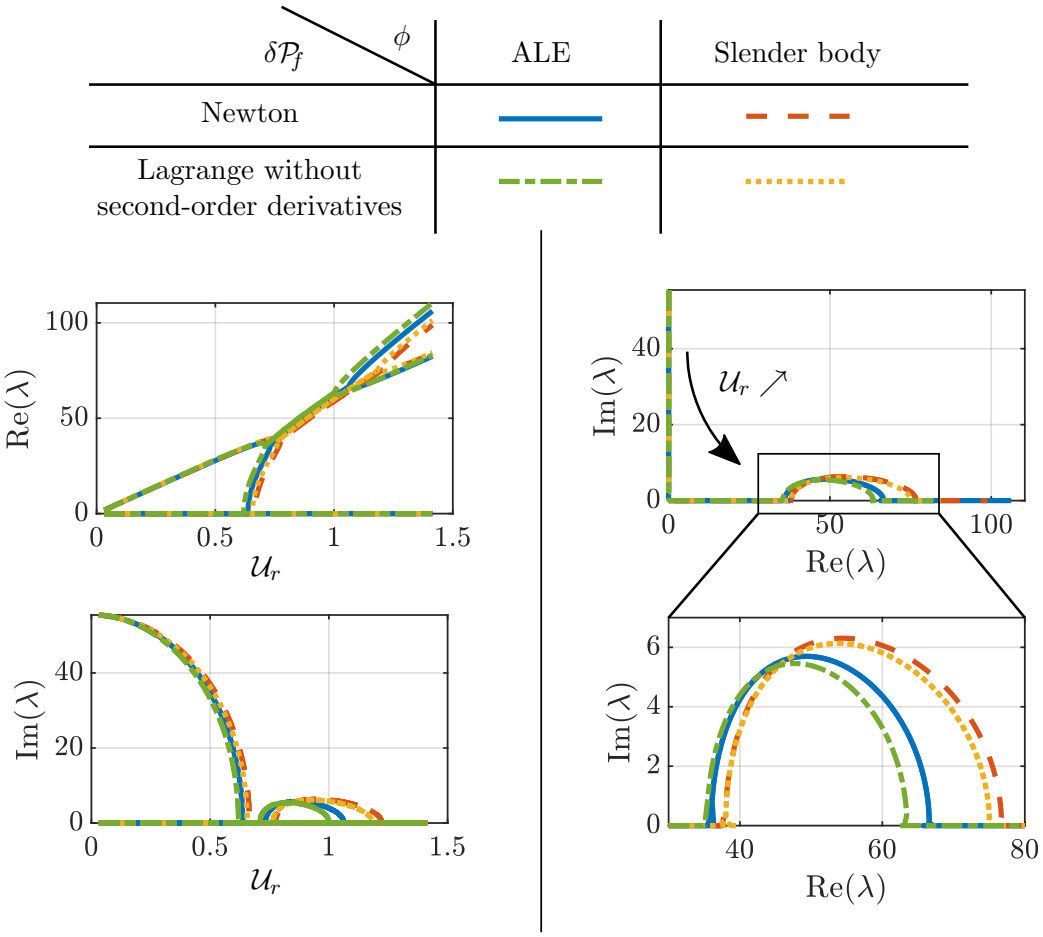

Figure IV.8: Top: legend used to differentiate the methods used to calculate the potential ϕ and the forces $\delta\mathcal{P}_f$. Bottom: Instabilities predicted by four different methods for calculating the added stiffness operator. In blue, the ALE method is the one presented in this thesis. In orange, the slender body method approximates the perturbations of the potential by considering the small rotations of the hull's centerline. In yellow, the slender body method is coupled to the stiffness calculations associated with the Lagrange equations neglecting second order derivatives. In green, the ALE method for predicting the velocity potential perturbations is coupled with the Lagrange equations neglecting second order derivatives.Top and bottom left: real and imaginary parts of the eigenvalues respectively, as a function of the reduced velocity $\mathcal{U}_r$. Top right: evolution of the eigenvalues in the real, imaginary plane. The eigenvalues goes from left to right of the graph as $\mathcal{U}_r$ increases (see the increase of the real part with respect to $\mathcal{U}_r$ in the top left graph). Bottom right: zoom on the flutter region.

Remark

In order to study the fluid-structure interaction of submarines with underwater explosions, Mavaleix-Marchessoux (2020) used a partitioned approach coupling the FEM operators of the structure with a BEM procedure for the fluid. Regarding the BEM procedure, an hypothesis used by him was that

for small elastic deformations relatively to a small criterion ε, the fluctuations of the BEM operators could be neglected, and therefore the only varying geometrical object under this hypothesis remained the normal of the mesh, which is similar to the hypothesis described by equation (IV.52) excepted that the fluctuation of the normal was taken into account naturally by refreshing the mesh at each time step. As a consequence, the results presented in this section might help considering the interest of such hypothesis used in the literature.

On top of those two different manners to calculate the potential fluctuations, two distinct approaches to calculate the added stiffness can be used. The first approach used in this section is a calculation based on the Newtonian formulation of the forces, leading to the expression of the added stiffness as introduced in this thesis. The second approach is inspired by the works of Li et al. (2009). It consists of calculating the added stiffness based on Lagrange's equation and neglecting the second order contributions from equation (B.24) as done by Li et al. (2009) since it is particularly inconvenient to calculate. The approach based on Lagrange equation can be used with both predictions of the potential ϕ_{ALE} and ϕ_{slen}. The results are presented in Figure IV.8. The blue curve, associated with a Newtonian ALE approach is the reference one based on the method introduced in this thesis, while the other curves are based on approximations detailed above. One can see how the Newtonian approach and the approximated Lagrangian approach yield very similar results, as shown by the proximity of the blue and green curves and the similarity of the yellow and orange curves. In order to quantify the relative error associated with the approximated Lagrangian approach compared to the Newtonian approach, the critical velocity at which flutter appears are compared: it is underestimated by 3% when using ϕ_{ALE}. The slender body gives accurate results in the case of an elongated $\mathcal{A}_r = 5$ ellipsoid. Even though the curves associated with ϕ_{ALE} and ϕ_{Slen} do not coincide exactly, the critical velocity is over-predicted by only $2,7\%$ using the slender body theory with a Newtonian approach (orange curve compared to blue curve).

Finally, since integrating over an ellipsoidal interface enables to solve more conveniently the potential solution using appropriate analytic simplifications, Li et al. (2009) performed stability analysis on an airship hull based on an equivalent ellipsoidal interface. In order to see if this approximation yields good results, a calculation has been performed to compare the stability criteria obtained by the method introduced in this thesis with the coupling of the slender body approach with a simplified Lagrange formalism on an equivalent ellipsoid. The equivalent ellipsoid was set to have the same length and the same volume (thus the same aerostatic lift generated by the internal lifting gas) than the airship hull. The movements of the airship hull and the equivalent ellipsoidal interface were set out to be equivalent about the centerline, see Figure IV.9. The center line modes of deformations were arbitrarily set as the plane rigid body motion completed by the first elastic mode of an equivalent curvilinear free-free homogeneous beam. The results obtained for both methods are presented in Figure IV.9. One can see that both methods yield similar results, even though the critical velocity is underestimated by 6.6% using the approximated calculations on an equivalent ellipsoid. Moreover, one should note that some errors might compensate each other: the slender body theory lead to an overestimation of the critical velocity as shown in Figure IV.8, whereas the approximated Lagrange equations and the ellipsoidal approximation of the geometry seem to underestimate the critical velocity as shown in Figures IV.8 and IV.9. Similar computations were performed to compare the instability trigger for an airship hull and an ellipsoidal hull (both shown in Figure IV.9) with equivalent internal volume, both computed with the method from this article. It was found out that the critical velocity for the ellipsoid is 6.2% lower than that of the streamlined hull, which means that with an equivalent volume, the streamlined body is more stable than the bluff ellipsoidal body with respect to the flutter instability. As a consequence, one might expect that the predictions made by Li et al. (2009) lead to accurate results but with an overprediction of

the risk of unstability (associated with an underprediction of the critical velocity). The calculations mentioned here were performed only by comparing different approaches in the calculation of the stiffness, however the different approaches to calculate the gyroscopic operators where not compared as only the Newtonian approach has been used due to time constraints. As already mentionned in Chapter III, the added mass operator is the same based on the Lagrange's equation or on the Newton approach with a posteriori symetrization of the operator.

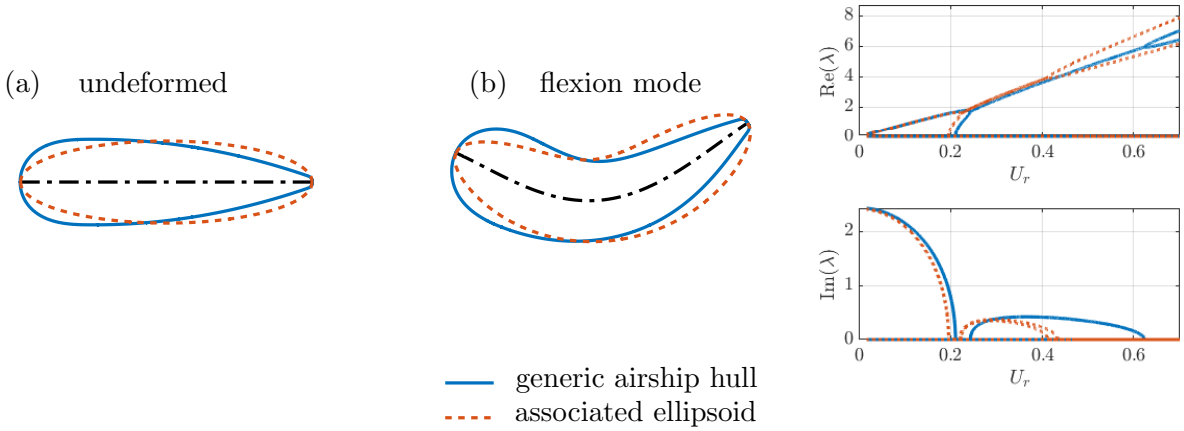

Figure IV.9: Left: (a): Cross-section of a characteristic axisymmetric membrane of an airship in blue, and the ellipsoid with same length and volume in dashed orange line. Both have the same center line displayed with a black dash-dot line. (b): same cross section showing the deformed structure with respect to the flexible elastic mode. Right: stability analysis of both configurations, with the real part of the eigenvalues at the top and the imaginary part at the bottom for a varying reduced velocity $\mathcal{U}_r$. The airship eigenvalues have been obtained with the method introduced in this thesis, whereas the eigenvalues of the equivalent ellipsoid have been obtained using a method similar to Li et al. (2009).

IV.3 Effect of fins inclusion

IV.3.1 Quasi-steady efforts of a flow on a 2D fin

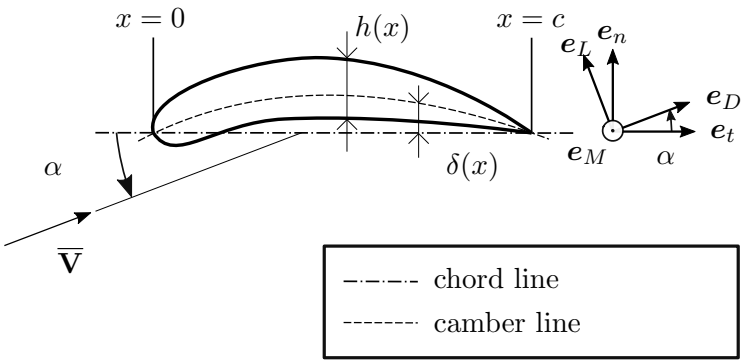

Figure IV.10: Two-dimensional fin at an angle of attack, chord and camber lines.

We consider an homogeneous ambient flow going past a thin fin with infinite length in the $\boldsymbol{e}_y$ direction as shown in Figure IV.10. The chord line is defined as the straight line going from the leading edge to the trailing edge of the profile. For a straight fin, the camber line coincide with the chord line. We suppose that the chord line is oriented among $\boldsymbol{e}_x$. The thickness of the foil among the normal direction $\boldsymbol{e}_n$ is noted h and the vertical distance between the chord line and the camber line is δ. The distance from the leading edge to the trailing edge is noted the chord length C, and its direction is associated with the tangential vector $\boldsymbol{e}_t$. The spanwidth of the fin is noted W. The angle of attack is defined as the angle between the chord line and the ambient flow direction:

$$\alpha = \operatorname{acos}\left(\frac{\boldsymbol{V}.\boldsymbol{e}_t}{V}\right) \quad \text{with } V = \|\boldsymbol{V}\|\,. \tag{IV.56}$$

In practice, the ambient flow velocity will be taken equal to zero and the fin will have a non zero velocity, which is however equivalent to the case presented in Figure IV.10 by a change of Galilean referential (hence placing ourselves in a fixed referential relatively to the fin). In addition to the relative flow velocity $\boldsymbol{V}$, the fin can have a velocity along $\boldsymbol{e}_t$ and $\boldsymbol{e}_n$, referred to as $\dot{z}$ and $\dot{x}$ respectively. Moreover, the fin can have pitching motions around its quarter chord at $x = c/4$, resulting in an angular velocity $\dot{\alpha}$ of the angle of attack. In this thesis, the loads on the fins are predicted under a certain set of hypotheses, required to refer to the thin airfoil theory:

- Small angle of attack : $\alpha \ll 1$ (IV.57)

- Small relative plunging velocity : $\frac{\dot{z}}{V} \ll 1$ (IV.58)

- negligible longitudinal velocitiy : $\frac{\dot{x}}{C\alpha} \ll 1$ (IV.59)

- negligible pitching velocity : $\frac{c\dot{\alpha}}{C\alpha} \ll 1$ (IV.60)

- negligible thickness : $\frac{h}{c} \ll 1$ (IV.61)

- negligible camber : $\frac{\delta}{c\alpha} \ll 1$ (IV.62)

- Inviscid fluid : $\mathcal{R}_e^{\text{fin}} = \frac{\rho_f V C}{\mu} \gg 1$ (IV.63)

- rigid airfoil : $\frac{\partial}{\partial t}\{c, \delta, h\} = 0$ (IV.64)

- high aspect ratio : $\frac{C}{W} \ll 1$ (IV.65)

- Kutta condition: the flow particles flowing on top and bottom of the foil separate from the interface at the sharp trailing edge. On the opposite to Chapter I, this condition will induce a circulation of the flow, which can however still be described by a velocity potential that will have a discontinuity behind the trailing edge (Katz and Plotkin, 2001).

- Quasi-steady vortex sheet: the Kutta condition leads to the apparition of a vortex sheet behind the airfoil trailing edge (Katz and Plotkin, 2001). In this thesis, we make the assumption that this vortex sheet spreads infinitely in the same direction as $\boldsymbol{V}$ (see Figure IV.12 as an example). We make the assumption that the fin movements are slow enough so that the vortex sheet remains plane. In practice, oscillations of the fin might lead to change of shape of the vortex sheet, but the oscillations of the fin are supposed to remain relatively small which justifies the fact that we neglect the vortex sheet geometry perturbations.

- Quasi-steady circulatory effects: we suppose that the shed vortices result in in-phase loads on the airfoil, which is valid for relatively low frequency oscillations of the airfoil compared to the characteristic time required for the fluid particles to cross the chord length.

Finally, we will suppose that the camber line is a parabolic arc:

$$\delta = 4\delta_{\max}\frac{x}{C}\left(1 - \frac{x}{C}\right). \tag{IV.66}$$

The flow induces a force $\boldsymbol{F}$ and a moment $\boldsymbol{M}(x = 0)$ on the foil. Katz and Plotkin (2001) gives an approximation of these efforts under the hypothesis abovementionned for a quasi steady flow ($\dot{\alpha} = 0$, $\dot{x} = \dot{z} = 0$), which can be described using the lift force F_L, the drag force F_D and the leading edge pitching moment M_0:

(IV.67a)

$$\boldsymbol{F}.\boldsymbol{e}_D = F_D = 0 \tag{IV.67b}$$

$$\boldsymbol{F}.\boldsymbol{e}_L = F_L = \rho V^2 \pi C W \left(\alpha + 2\frac{\delta_{\max}}{C}\right) \tag{IV.67c}$$

$$\boldsymbol{M}(x=0).\boldsymbol{e}_M = M_0 = \rho V^2 \pi \frac{C^2 W}{4}\left(\alpha + \frac{4\delta_{\max}}{C}\right). \tag{IV.67d}$$

Because of the negligible camber hypothesis, the lift and moment expressions become:

$$F_L = \rho V^2 \pi C W \alpha \tag{IV.68}$$

$$M_0 = \rho V^2 \pi \frac{C^2 W \alpha}{4}. \tag{IV.69}$$

One can note that for an ideal flow where skin friction is neglected, no drag forces are predicted. The lift force L is caused by the sharp trailing edge, which induces a circulation in the surrounding fluid because of the Kutta condition. This circulation causes a lift. As we arbitrarily set the pitching rotation movements of the foil to be around the quarter-chord $x = c/4$, the pitching moment from equation (IV.68) is expressed at the quarter-chord as well using equations (IV.67):

$$M\left(x = \frac{C}{4}\right).\boldsymbol{e}_y = M_{1/4} = M_0 + F_L\frac{C}{4} = 0. \tag{IV.70}$$

As one can see from the equation above, the advantage of describing pitching motions relatively to the quarter chord comes from the fact that the flow past a non-cambered airfoil will create no moment around the quarter-chord: the quarter-chord is consequently referred to as the aerodynamic center of the airfoil.

By combining equations (IV.67c) and (IV.70), one gets the expression of the force and moment acting on the airfoil:

$$F_L = \rho V^2 \pi C \left(\alpha - \frac{\dot{z}}{V}\right) \tag{IV.71a}$$

$$M_{1/4} = 0. \tag{IV.71b}$$

The force applied by the flow on a two-dimensional airfoil in plunging and slow pitching motion in an ideal fluid has been given by equation (IV.71). In order to model the forces applied by the flow on the three-dimensional fins of a structure, this thesis is based on additional simplifying hypotheses for the convenience of modeling.

First, the three-dimensional effects of the flow around the fin are neglected. This means for example that the wingtip vortices will be ignored in the model. A first step toward taking into account three-dimensional effects could be done by using the lifting-line theory as explained in Katz and Plotkin (2001), which could conveniently be implemented to enhance the model presented in this thesis. Because three-dimensional effects tend to decrease the lift predicted by two-dimensional

approximations, one should bear in mind that the two-dimensional flow hypothesis around the fins will lead to an overestimation of the lift effects.

For the second hypothesis, the flow perturbations induced by the hull are ignored, which means that we consider a relative velocity of the ambient flow around the foil to be equal to $\boldsymbol{V} = -\bar{\boldsymbol{v}}$.

Finally, the fin will be arbitrary supposed to be attached to the hull at its quart-chord position at a longitudinal position x_{fin} (see Figure IV.11). In order to approximate the movements of the fins caused by the displacements of the hull, the movements of the fins will be supposed to follow the centerline of the hull (see Figure IV.11). First, the centerline transverse deformation associated with each mode $\bar{\boldsymbol{\xi}}'$ is approximated as the polynomial expression of order n with respect to the longitudinal coordinate x that best fits the transverse deformations $(\mathbb{1} - \boldsymbol{e}_x \otimes \boldsymbol{e}_x)\bar{\boldsymbol{\xi}}'$ associated with the mode. In practice, an order of $n = 5$ has been used since it allows us to capture well enough the transverse displacements ${\xi_{\text{c.l}}}'$ of the centerline for the reduced basis used in this thesis. Once the centerline transverse displacements have been obtained, the plunging motion h' of the airfoil is defined as the transverse displacement at the fixation point of the fin, and the angle of attack fluctuations are defined as the longitudinal derivative of the centerline transverse displacements at the fixation point of the fin:

$$h' = \xi'_{\text{c.l}}(x_{\text{fin}}) \tag{IV.72a}$$

$$\alpha' = \frac{\partial \xi_{\text{c.l}}}{\partial x}. \tag{IV.72b}$$

Once the angle of attack and plunging motion perturbations are known for each mode, the work of the fluid associated with the fins can be determined as:

$$\delta\mathcal{P}_{\text{fin}} = M\delta\alpha + F_L(\alpha, \dot{h})\delta h, \tag{IV.73}$$

where the virtual angle of attack and pluging motion $\delta\alpha$ and δh are deduced from $\delta\bar{\boldsymbol{\xi}}$ in the same way than α' and h' were obtained from $\bar{\boldsymbol{\xi}}'$. Since the moment remains nil according to equation (IV.71), one gets the following expression of the virtual power of the fluid associated with the circulation around the fin:

$$\delta\mathcal{P}_{\text{fin}} = \pi\rho \left\|\bar{\boldsymbol{v}}\right\|^2 \pi CW \left(\alpha - \frac{\dot{z}}{\left\|\bar{\boldsymbol{v}}\right\|}\right). \tag{IV.74}$$

The expression above can be written at order zero as:

$$\delta\mathcal{P}_{\text{fin}} = \pi\rho_f \left\|\bar{\boldsymbol{v}}^o\right\|^2 \pi CW \left(\alpha^o - \frac{\dot{z}^o}{\left\|\bar{\boldsymbol{v}}\right\|}\right). \tag{IV.75}$$

Because we made the small angle of attack assumption $\alpha \ll 1$, one can consider that the order zero velocity is mostly in the longitudinal direction:

$$\bar{\boldsymbol{v}}^o = \boldsymbol{e}_x \otimes \boldsymbol{e}_x \bar{\boldsymbol{v}}^o + \mathcal{O}(\alpha)). \tag{IV.76}$$

As a consequence, the norm of the velocity can be expressed as:

$$\bar{\boldsymbol{v}}^2 = (\bar{\boldsymbol{v}}^o)^2 + 2\bar{\boldsymbol{v}}^o.\bar{\boldsymbol{v}}' + \mathcal{O}\left(\varepsilon^2\right) = (\bar{\boldsymbol{v}}^o)^2 + 2\left\|\bar{\boldsymbol{v}}^o\right\| \boldsymbol{e}_x.\bar{\boldsymbol{v}}' + \mathcal{O}(\alpha) + \mathcal{O}\left(\varepsilon^2\right). \tag{IV.77}$$

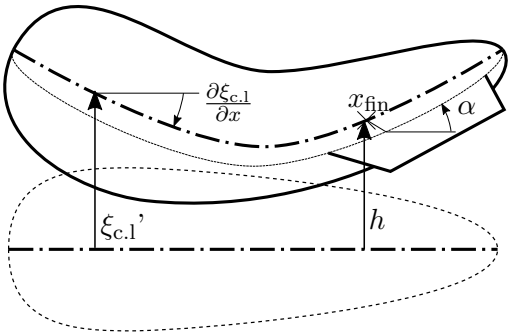

Figure IV.11: Displacement of an airship (the initial position being visualized with dashed line).

Because of the negligible longitudinal velocity of the fin hypothesis, the term $\boldsymbol{e}_x.\bar{\boldsymbol{v}}' = \mathcal{O}\left(\alpha^2\right)$ can be neglected and therefore the expression becomes:

$$\bar{\boldsymbol{v}}^2 = (\bar{\boldsymbol{v}}^o)^2 + \mathcal{O}\left(\varepsilon^2\right) + \mathcal{O}\left(\alpha^2\right) \sim V^2. \tag{IV.78}$$

The following expression of the virtual power can consequently be obtained at orders zero and one:

$$\delta\mathcal{P}^o_{\text{fin}} = \pi\rho_f V^2 CW\alpha^o \tag{IV.79a}$$

$$\delta\mathcal{P}'_{\text{fin}} = \pi\rho_f CW\left(V^2\alpha'(\bar{\boldsymbol{\xi}}') - V\dot{h}'\left(\dot{\bar{\boldsymbol{\xi}}}'\right)\right). \tag{IV.79b}$$

As one can see from the expression above, the modelisation of the circulation effects induced by the fins leads to the emergence of additional stiffness and damping.

Remark

In the model presented in this section, the lift has been calculated only considering the circulation effects of the two-dimensional flow around fins that has been isolated from the rest of the fluid-structure interface. Therefore, both three dimensional effects at the tip of the fin and hull-fin flow interaction effects aren't taken into account. A better grasp of the physics associated with the aforementioned phenomena could be obtained by using a vortex sheet Σ_{wake} as shown in FigureIV.12. The implementation of the vortex sheet would first require to create an associated mesh. As a first approximation, a straight vortex sheet propagated in the direction of the relative flow is commonly used (Bessert and Frederich, 2005; Katz and Plotkin, 2001). The vortex sheet separates locally the fluid domain into two zones Σ^+_{wake} and Σ^-_{wake} (even though they still belong to the same global fluid domain). Each point of the vortex sheet is therefore associated with two distinct velocity potential value: one ϕ^+ above the sheet (on Σ^+_{wake}) and one ϕ^- below (on Σ^-_{wake}). The associated potential solution might then be obtained by using an integral equation now based on $\Sigma \cup \Sigma^+_{\text{wake}} \cup \Sigma^-_{\text{wake}}$ instead of just Σ. However, the associated BEM should be implemented with extra care, as taking into consideration infinitely thin walls requires adaptations of the method described in Chapter I, such as the introduction specific operators as described by Gennaretti et al. (1997).

The fins are characterized by a chord of length C and a span of W. They relate to each other with the fins aspect ratio $\mathcal{A}^{\text{fin}}_r$ and to the structure characteristic surface with the surface ratio $\mathcal{S}^{\text{fin}}_r$:

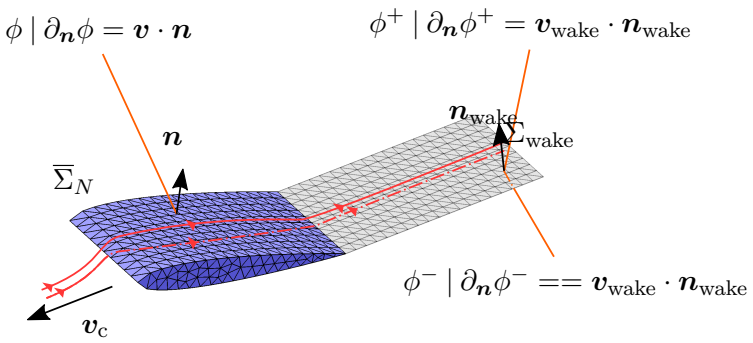

Figure IV.12: In blue: coarse mesh Σ_N of a NACA0012 airfoil . In grey: generated mesh of a vortex sheet Σ_{wake} extending from the trailing edge in the direction of the flow relative to the structure. The potential field has a discontinuity at the vortex sheet, hence the two field ϕ^+ and ϕ^- associated with the upper and lower part of the vortex sheet: each node of the vortex sheet is associated with two distinct potential unknowns. The fluid can't flow through the vortex sheet, hence the associated normal gradient condition on the associated mesh.

$$\mathcal{A}_r^{\text{fin}} = \frac{C}{W} \tag{IV.80}$$

$$\mathcal{S}_r^{\text{fin}} = \frac{CW}{LD}. \tag{IV.81}$$

Moreover, in order to take into account three dimensional effects, a correction coefficient was used to roughly take into account the vortices at the tip of the fin. Using the Lifting Line theory based on the approximation of a constant chord airfoil (Katz and Plotkin, 2001), the three dimensional lift was calculated as:

$$F_L^{3D} = f F_L^{2D} \tag{IV.82a}$$

$$f = \frac{1}{1 + 2\mathcal{A}_r^{\text{fin}}}. \tag{IV.82b}$$

According to the expression above, the lower the aspect ratio of the airfoil $\mathcal{A}_r^{\text{fin}}$, the greater the losses of lift due to three dimensional effects. As expected, the two dimensional model predicts with more accuracy the lift of high aspect ratio airfoils since it is closer to the two-dimensional case. According to equation (IV.79b), the higher the surface ratio $\mathcal{S}_r^{\text{fin}}$, the greater the fin surface CW, and consequently the greater the lift force predicted. Thus, greater stabilization effects from the fins (enabling balance the instability associated with the Munk moment) are expected at higher surface ratio $\mathcal{S}_r^{\text{fin}}$. This can be observed in FigureIV.14. When the surface of the fins is negligible relatively to the airship hull characteristic surface, the structure is unstable as if there were no fins. When the surface of the fins increases, the flutter instability around $\mathcal{C}_y \simeq 1$ eventually disappears. A flutter instability then appears at low $\mathcal{C}_y$. Finally, once the fins have reach a sufficient area, the structure becomes stable at low speeds, but with a risk of flutter if a critical velocity is reached. The higher the fins area, the higher the stability and the critical velocity associated with flutter.

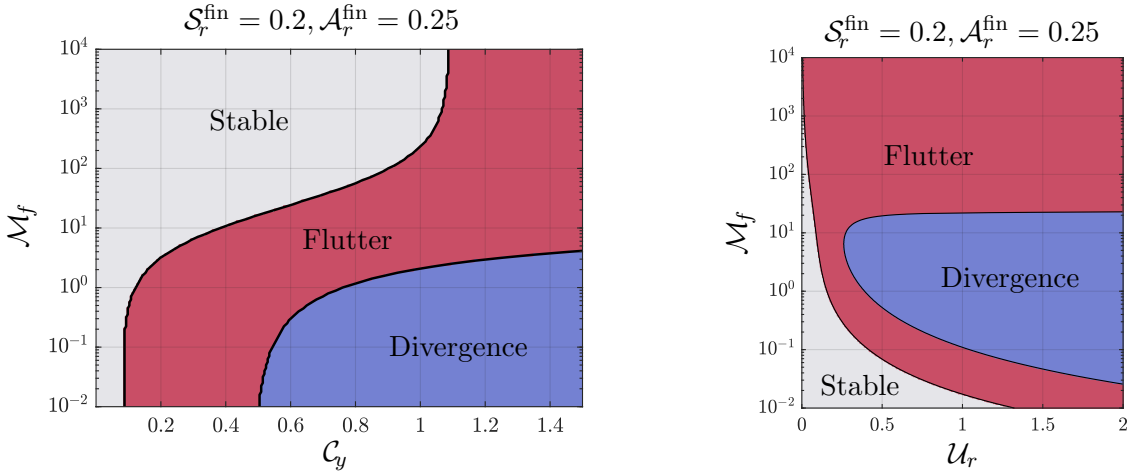

Figure IV.13

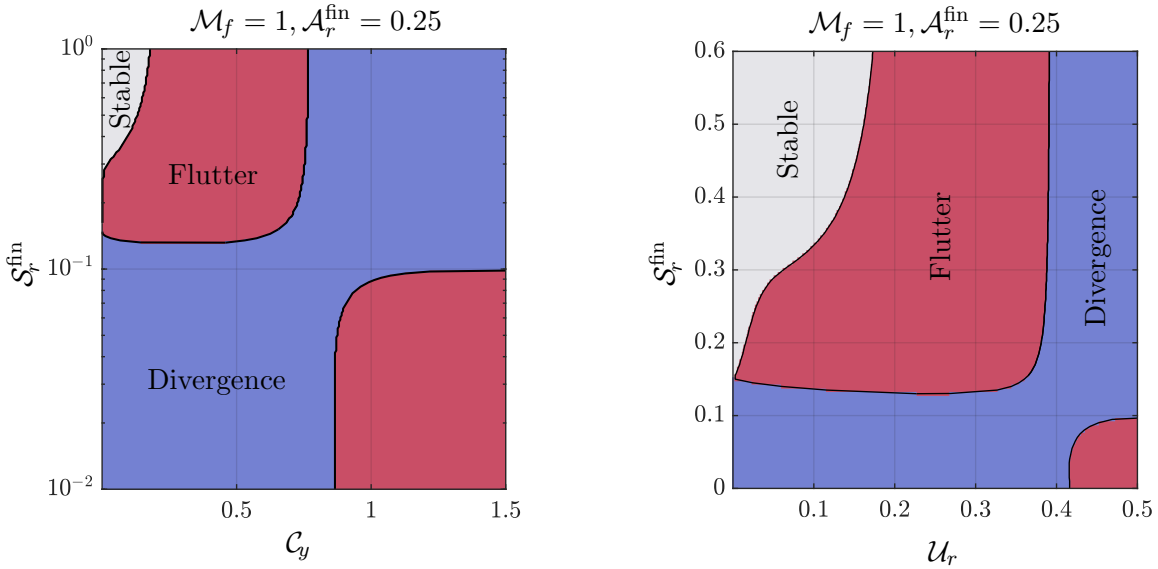

Figure IV.14: Left: Zones of instability of an ellipsoid as a function of the Cauchy number $\mathcal{C}_y$ and the reduced fins area $\mathcal{S}_r^{\text{fin}}$, for a mass number $\mathcal{M}_f = 1$ and a fin aspect ratio of $\mathcal{A}_r^{\text{fin}} = 0.25$. As the chord length is fixed by the parameter $\mathcal{A}_r^{\text{fin}}$, the variations of $\mathcal{S}_r^{\text{fin}}$ result in a variation of the fins span W. Right: equivalent map with the reduced velocity $\mathcal{U}_r$ variable in place of the Cauchy number $\mathcal{C}_y$.

The results presented in this section are based on a simplified model to take into account the fins reaction. Though the accuracy of these results could be improved (see propositions in the seciton above or a recap of the possible improvements in the perspectives section below), this straightforward analysis enables to understand the physical phenomena involved in the stabilization of the system.

IV.4 Conclusion

Through this chapter, the following work has been done:

1. A dynamic model of a hyperelastic structure prestressed by an internal fluid and subjected to external forces has been presented. This part does not constitute an originality of the thesis, one can find for instance a similar approach by Hoareau (2019). We note however that the pre-stressing effects of the internal fluid on the dynamics of flexible airships has not been done to the authors' knowledge (except by Bessert2005, but their analysis uses a flexible deformation at zero order and then focuses on the stability with respect to small rigid body movements only).
2. A linear fluid-structure dynamic equation has been proposed by coupling the prestressed hyperelastic structure with the external and internal fluid forces. The resulting formulation involves external flow independent fluid and structure mass operators, a linear fluid gyroscopic operator with zero-order structure rigid body motions $\bar{\boldsymbol{\nu}}^o$, and quadratic fluid and structure stiffness operators with rigid body motions $\bar{\boldsymbol{\nu}}^o \otimes \bar{\boldsymbol{\nu}}^o$.
3. The stability of an inflated ellipsoidal membrane in ambient flow has been studied as a function of flow velocity, and the results have been compared to physical phenomena from the literature. As expected, the absence of fins leads to an instability of the structure in the flow whatever its non-zero velocity.
4. A very simple fin model has been introduced and the associated stabilizing effects have been studied.

One of the main objectives of the manuscript was to obtain and study a complete dynamic model of a pre-inflated airship in large rigid body motions and small deformations interacting with an internal lifting gas and an external flow. During this chapter, a model allowing to couple a structure in large translational movements with internal and external fluids was introduced, with the perspective of adapting this model with rotational movements. Since the fluid forces have been modeled in this study using the hypothesis of a potential flow, the potential and viscous effects associated with the oscillations of a model in a fluid are investigated experimentally in the next chapter to determine whether it is consistent to neglect the viscous effects.

IV.5 Perspectives

- The developments from Chapters II and III give the required tools to take into account the effects of the internal fluid on the dynamics of the structure. In this Chapter, due

to time constraints, only the stationnary, pre-stressing effects of the internal fluid on the stiffness of the membrane have been studied, and it would be an interesting perspective to study how the added mass of the internal fluid affects the dynamics.

- It would be of high interest to calculate the structure trajectory and see the influence of its flexibility on the trajectories without ambient flow, with an homogeneous ambient flow or with unhomogeneous, unsteady ambient flow.
- Calculate the whole F/S modes without projecting on the structure *in vacuo* modes, see if the resulting modes is close to *in vacuo* modal base by comparing the eigenvalues. Use of the main fluid-structure modes obtained as a new reduced base to project the problem onto.
- Studying the effects of the pre-stress stiffness $\mathrm{K}^{s}_{\mathrm{Q,L}}$ on the dynamics of the fluid-structure problem would be an interesting possibility to explore.
- Take into account the effects of the fins at zero and first orders using a vortex sheet mesh as prescribed by (Gennaretti et al., 1997). The new mesh would originate at the trailing edge and propagates in the direction of the flow as displayed in Figure IV.12.
- For more complex fluid models with $\mathrm{G}^{f}(\Omega)$ and $\mathrm{K}^{f}(\Omega)$ for example: nonlinear eigenvalue equation, which would be costly to solve, hence making the parametric study much more expansive. This drawback could be compensated by using better strategies for parametric exploration, such as tracking the stability front in the $\mathcal{M}_f$,$\mathcal{U}_r$ space for example.
- The structure considered for the stability analysis consists of an ellipsoïdal membrane of homogeneous properties (thickness, Young modulus,...). In order to get closer to nominal airship conditions, an interesting perspective would be to use more complex airship models with realistic geometry and materials.
- For practical reason, the non-linear calculation of the inflated displacements $\grave{\boldsymbol{\xi}}_{\mathrm{stat}}$ of a free-free structure has not yet been implemented, and the test prestress effects of the test case have been calculated linearly for in the scope of this thesis. Consequently, it would be an interesting perspective to study how the non-linear inflation of the membrane might affect the results presented in this section.

Chapter V

Experimental analysis of the fluid forces exerted on an oscillating rigid ellipsoid

Introduction

The results presented in the previous chapters are obtained using potential flow theory, which is based on strong hypothesis, as explained in section I.3.1. Consequently, the aim of this chapter is to determine experimentally to which extent the potential model enables to predict the fluid forces in the case of a structure vibrating in a fluid at rest. For this purpose, the viscous effects which are not predicted by potential flows are investigated experimentally for various relevant dimensionless flow numbers: the Stokes number and the relative displacement amplitude.

In section V.1, the loads exerted on a plate vibrating transversely in a viscous flow are studied, with a particular focus on their relationship with the Stokes number, and to what extent those loads differ from those predicted by the potential theory of chapter I. In order to verify these predictions, an experimental setup is presented in section V.2, consisting of an oscillating rigid structure rotating in a fluid at rest. For parametric exploration purposes, the frequency and amplitude of vibration can vary, as well as the dynamic viscosity and density of the fluid. Damping and added mass coefficients are obtained experimentally from torque and acceleration measurements. In section V.3, those coefficients are obtained for various experimental parameters, enabling to study how viscous effects scale, and how it compares to theoretical results. Finally, considerations are drawn on the orders of magnitude of fluid viscous effects for airships, which associated Stokes number are higher than those explored experimentally.

V.1 Modeling of the viscous laminar effects in a quiescent fluid

The aim of this chapter is to study dynamical boundary layer effects. More especially, we are interested in how they scale with the relevant dimensionless numbers, and consequently in what role they are expected to play at the scale of airship dynamics, to check to what extent the potential flow hypothesis is valid. Stationary effects of the boundary layer have already been compared to potential flow results in Chapter III by comparing with RANS simulations: in this chapter, the

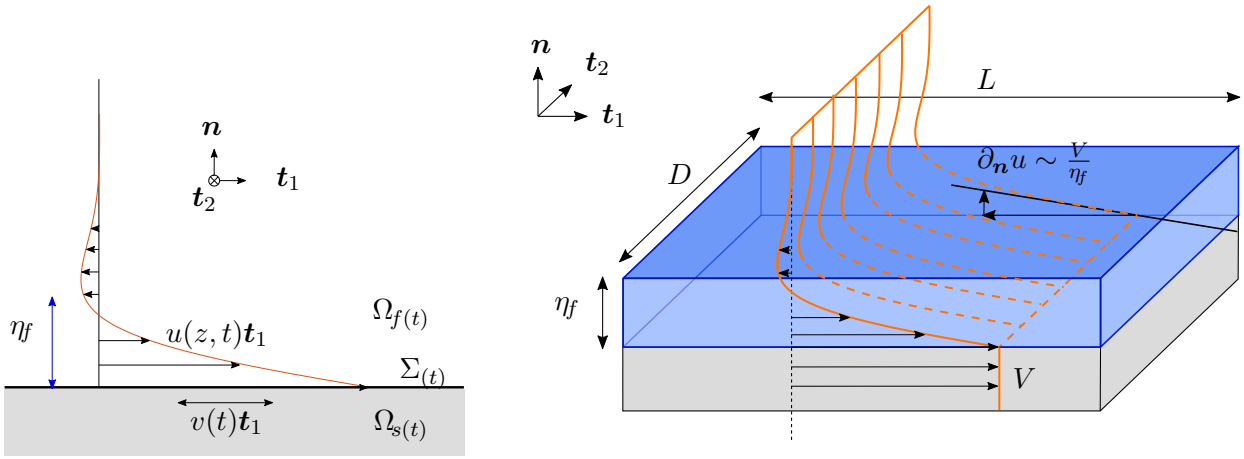

Figure V.1: Left: infinite plane plate with transverse harmonic vibrations in a laminar fluid at rest, and the resulting velocity profile in the fluid domain. Right: three dimensional view of the solution, the fluid velocity profile is displayed in orange and the boundary layer volume is displayed in blue.

boundary layer effects are studied experimentally in the case of unsteady movements of the interface. The present study focuses on rigid body rotational movement, and the extension of the experimental process to elastic movements would therefore be an interesting perspectives for carrying further this work.

V.1.1 Laminar boundary layer effects on a solid vibrating in a fluid at rest

In the context of this chapter, gravity effects will be neglected. In this section, the viscous loads of a laminar fluid at rest in contact with an infinite plate with transverse vibrations are studied. As shown in Figure V.1, the plate is placed in the tangential plane $\{\boldsymbol{t}_1, \boldsymbol{t}_2\}$ and vibrates along the $\boldsymbol{t}_1$ direction. The velocity obeys

$$\boldsymbol{v} = v(t)\boldsymbol{t}_1 \quad \text{with } v(t) = V\cos(\omega t). \tag{V.1}$$

The induced flow is supposed to be laminar: turbulence effects are neglected. The boundary condition verifies the continuity of velocity introduced in equation (I.8), and the velocity amplitude of the fluid at rest has to vanish remotely from the wall:

$$u(z = 0, t) = v(t) \tag{V.2a}$$
$$u(z \to \infty, t) \to 0. \tag{V.2b}$$

The fluid behavior in the domain $\Omega_{f(t)}$ is described by the Navier-Stokes equation (I.7). The expression of the fluid velocity is based on the characteristic boundary layer thickness η_f defined as (De Langre, 2001):

$$u(z,t) = V \exp\left(-\frac{z}{2\eta_f}\right) \sin\left(\Omega t - \frac{z}{2\eta_f}\right) \quad \text{in } \Omega_{f(t)} \tag{V.3a}$$

$$\text{with } \eta_f = \sqrt{\frac{\mu_f}{2\rho_f \Omega}}. \tag{V.3b}$$

The boundary layer thickness η_f may have various definitions, and accordingly different values (Schobeiri, 2010), all with roughly the same order of magnitude: the boundary layer thickens when the dynamic viscosity μ_f increases, and and gets thinner when the density ρ_f and the frequency Ω increase, because of competition between viscous and inertial effects. The choice for the expression (V.3b) of η_f enables here to be coherent with the equivalent volume of fluid accelerated in the boundary layer as will appear later in the boundary layer added mass expression (V.8). For the rest of this chapter, unless otherwise stated, we suppose that the characteristic length of the structure studied is much larger than the characteristic length of the boundary layer:

$$\frac{\eta_f}{L} \sim \mathcal{S}_t^{-\frac{1}{2}} \ll 1. \tag{V.4}$$

The resulting stresses at the interface are expressed as (Doaré, 2020):

$$\boldsymbol{\sigma}_f \cdot \boldsymbol{n} = -p_{\text{stat}} \boldsymbol{n} - \left(\rho_f \, \eta_f \, \dot{v}(t) + \frac{\mu_f}{\eta_f} v(t)\right) \boldsymbol{t}_1 \quad \text{on } \Sigma_{(t)}. \tag{V.5}$$

In the expression above, there is no dependency on the dynamic pressure p_{flow} because the movements of the plate are tangential. Considering the expression above, the resistive viscous stresses from the laminar flow include two contributions.

- The first contribution is proportional to the boundary layer thickness and to the acceleration of the interface $\dot{v}$. If these stresses are integrated over a characteristic surface of length L and width D, the associated force can be seen as the inertia added by the fluid enclosed in the box of length L, width D and thickness η_f as shown in Figure V.1 right.

- The second contribution, in phase and proportional with the interface velocity v, is related to the shear inside the boundary layer. The rate of shear $\partial_{\boldsymbol{n}} u$ is of the order of the ratio between the interface velocity and the boundary layer thickness (see Figure V.1 right).

Based on the physical considerations introduced in this section for an infinite flat plate in transverse oscillations, the next section will study how the problem can be expressed with dimensionless parameters using the similitude principle. This will enable to check if the latter principle can be verified experimentally.

V.1.2 Scaling of the inertia and damping effects of the fluid

In this section, we study how the added mass and damping coefficients evolve with the Stokes number and the displacement number.

Let us first consider the pressure effects outside of the boundary layer. As described in Chapter I, the dynamic pressure can be decomposed into an added mass contribution $p_{\dot{v}}$ and a velocity convection contribution p_v:

$$p_{\text{flow}} = p_{\dot{v}}(\dot{v}) + p_v(v). \tag{V.6}$$

By using dimensional analysis, the added mass and convection contributions of the pressure can be written as (cf Chapter I):

$$p_{\text{flow}} = \rho_f \Omega L V p^*_{\dot{v}}(\dot{v}^*) + \rho_f V^2 p^*_v(v^*), \quad p^*_{\dot{v}} \sim p^*_v \sim 1. \tag{V.7a}$$
$$v = V v^*, \quad v^* \sim 1 \tag{V.7b}$$
$$\dot{v} = \Omega V \dot{v}^*, \quad \dot{v}^* \sim 1 \tag{V.7c}$$

Noting from equation (V.1) that $\dot{v} \sim \Omega V$, the shear stresses on an oscillating solid write as:

$$\boldsymbol{\varpi}_\mu = \rho_f \eta_f \Omega V \left(\boldsymbol{\varpi}^*_{\mu,\dot{v}}(\dot{v}^*) + \boldsymbol{\varpi}^*_{\mu,v}(v^*) \right), \quad \boldsymbol{\varpi}^*_{\mu,\dot{v}} \sim \boldsymbol{\varpi}^*_{\mu,v} \sim 1. \tag{V.8}$$

In the equation above, the dimensionless unit viscous terms are respectively the added mass viscous stress $\boldsymbol{\varpi}^*_{\mu,\text{am}}$ which is linear with the acceleration $\dot{v}^*$ and the shear stress $\boldsymbol{\varpi}^*_{\mu,\text{shear}}$ linear with the velocity v^*. Both added mass and added damping viscous terms have the same order of magnitude but their phase differs by $\pi/2$ for harmonic motions. As a consequence, the fluid stresses can be rewritten as:

$$\frac{\boldsymbol{\varpi} \cdot \boldsymbol{n}}{\rho_f \Omega L V} = -(p^*_{\dot{v}} + \mathcal{U}_r p^*_v)\boldsymbol{n} + \mathcal{S}_t^{-\frac{1}{2}} \left(\boldsymbol{\varpi}^*_{\mu,\dot{v}}(\dot{v}^*) + \boldsymbol{\varpi}^*_{\mu,v}(v^*) \right) \boldsymbol{n}. \tag{V.9}$$

As already mentioned previously, the predominance of the convective or added mass forces depends on the relative velocity of the interface $\mathcal{U}_r$. When the thin boundary layer hypothesis is met, one expects the ratio between amplitude of the viscous effects and the fluid inertia effects to scale as $\mathcal{S}_t^{-1/2}$. Recalling from Chapter I that for the case of stationary flows, the latter ratio is of the order of $\mathcal{R}_e^{-1/2}$, to a certain extent the Stokes number is to oscillating flows what the Reynolds number is to stationary flows.

As the experimental setup aims to study the fluid forces acting on an ellipsoid with harmonic rotations around its diameter, the associated equations will be further developed for this very case. The objective is to determine the moment exerted by the fluid on the rotation axis of the structure. In order to do so, the angular amplitude Θ, the rotation speed ω and its dimensionless counterpart ω^* are introduced, and the virtual movements associated with an infinitesimal rotation $\delta\omega$ among the axis $\boldsymbol{e}_z$ are considered:

$$\omega = \Omega \Theta \omega^* \tag{V.10a}$$
$$\dot{\omega} = \Omega^2 \Theta \dot{\omega}^* \tag{V.10b}$$
$$\delta \boldsymbol{v} = \delta\omega \boldsymbol{e}_z \wedge \boldsymbol{x} = L \delta \boldsymbol{v}^* \tag{V.10c}$$
$$\omega^* \sim \dot{\omega}^* \sim \delta \boldsymbol{x}^* \sim 1. \tag{V.10d}$$

One should note that the angular amplitude scales as the dimensionless displacements ξ/L since the order of magnitude of the displacements of the ellipsoid tip is ΘL. The characteristic velocity of the fluid is of the order of the angular velocity multiplied by the characteristic structure length:

$$V = \Omega L \Theta. \tag{V.11}$$

As a consequence, the reduced velocity is here equal to the angular amplitude:

$$\mathcal{U}_r = \frac{V}{\Omega L} = \Theta. \tag{V.12}$$

As the experiment focuses on the fluid effects resulting from rotation of the interface, the mass and added mass effects might be refered to as "inertia" in the following sections. Because of the above equation, the virtual power associated with the torque τ_f exerted on the axis writes as:

$$\begin{aligned}\tau_f &= \delta\mathcal{P}_f(\omega, \dot{\omega}, \delta\omega = 1) \\ &= \rho_f \Omega^2 L^3 \Theta \int_{\overline{\Sigma}} \Big[-\left(p_{\dot{v}}^*(\dot{\omega}) + \mathcal{U}_r p_v^*(\omega)\right) \boldsymbol{n} + \mathcal{S}_t^{-\frac{1}{2}} \left(\boldsymbol{\varpi}_{\mu,\mathrm{am}}^*(\dot{\omega}^*) + \boldsymbol{\varpi}_{\mu,\mathrm{shear}}^*(\omega^*)\right) \boldsymbol{n} \Big] \cdot \delta\boldsymbol{v}^* \, \mathrm{d}\overline{\Sigma}. \end{aligned} \tag{V.13}$$

In the equation above, the arguments of the pressure and viscous stress contributions have been switched from v to ω (or their respective time-derivative). The rotation speed and the velocity are related by the distance from the material point to the rotation axis. In order to non-dimensionalize the latter equation, the stresses of the flow are integrated on the dimensionless interface $\overline{\Sigma}^*$ such that:

$$\text{for } \bar{\boldsymbol{x}} \in \overline{\Sigma}, \quad \bar{\boldsymbol{x}}^* = \frac{\bar{\boldsymbol{x}}}{L} \in \overline{\Sigma}. \tag{V.14}$$

As a consequence of the equation above, a small element of area meets the property $\mathrm{d}\overline{\Sigma}^* = L^2 \, \mathrm{d}\overline{\Sigma}$, enabling to write the dimensionless moment of the fluid ${\tau_f}^*$ as:

$${\tau_f}^* = \frac{\tau_f}{\rho_f \Omega^2 L^5 \Theta} = \tau_{f^*_{p,\dot{v}}}(\mathcal{A}_r) + \mathcal{U}_r \tau_{f^*_{p,v}}(\mathcal{A}_r) + \mathcal{S}_t^{-\frac{1}{2}} \tau_{f^*_{\mu}}(\mathcal{A}_r) \tag{V.15}$$

$$\tau_{f^*_{p,\dot{v}}}(\mathcal{A}_r) = \int_{\overline{\Sigma}^*} -p_{\dot{v}}^*(\dot{\omega}^*) \boldsymbol{n} \cdot \delta\boldsymbol{v}^* \, \mathrm{d}\overline{\Sigma}^*. \tag{V.16}$$

$$\tau_{f^*_{p,v}}(\mathcal{A}_r) = \int_{\overline{\Sigma}^*} -p_v^*(\omega^*) \boldsymbol{n} \cdot \delta\boldsymbol{v}^* \, \mathrm{d}\overline{\Sigma}^*. \tag{V.17}$$

$$\tau_{f^*_{\mu}}(\mathcal{A}_r) = \int_{\overline{\Sigma}^*} \left(\boldsymbol{\varpi}_{\mu,\mathrm{am}}^*(\dot{\omega}^*) + \boldsymbol{\varpi}_{\mu,\mathrm{shear}}^*(\omega^*)\right) \boldsymbol{n} \cdot \delta\boldsymbol{v}^* \, \mathrm{d}\overline{\Sigma}^* \tag{V.18}$$

$$\tau_{f^*_{p,\dot{v}}}(\mathcal{A}_r) \sim \tau_{f^*_{p,v}}(\mathcal{A}_r) \sim \tau_{f^*_{\mu}}(\mathcal{A}_r) \sim 1 \tag{V.19}$$

The above equation enables us to solve the problem on a reference mesh. As the geometry of the interface is set as an ellipsoid, the only geometry variable of the reference mesh $\overline{\Sigma}^*$ is its aspect ratio $\mathcal{A}_r$. As a consequence, the expression of the dimensionless moment above only depends on two independent parameters with the exception of angular velocity and acceleration: the ellipsoid aspect ratio $\mathcal{A}_r$ and the Stokes number $\mathcal{S}_t$. The loads of a potential flow on a rotating ellipsoid can be found in Lamb (1932):

$$\tau_{f^*_{p,\dot{v}}}(\mathcal{A}_r) = -\mathrm{I}^*_{\rho_f}(\mathcal{A}_r)\dot{\omega}^* \text{ with } \mathrm{I}^*_{\rho_f} \sim 1 \tag{V.20a}$$

$$\tau_{f^*_{p,v}}(\mathcal{A}_r) = 0, \tag{V.20b}$$

The analytic expression of $\mathrm{I}^*_{\rho_f}(\mathcal{A}_r)$ is given in equation (C.6c), with $\mathrm{I}^*_{\rho_f}(\mathcal{A}_r) = \mathrm{I}_y/(\rho_f L^5)$. Since the convective pressure forces ${\tau_f}^*_{p,v}$ are nil, one expects the loads ${\tau_f}^*$ to be of the order of unity no matter the reduced velocity $\mathcal{U}_r$: ${\tau_f}^* \sim 1$ (see equation (V.15)). By judging the expression of the solution for the case of a thin plate in transverse vibrations (V.5), we make the hypothesis that the viscous forces of the boundary layer write as:

$$ {\tau_f}^*_{\mu}(\mathcal{A}_r) = -\mathrm{I}^*_{\mu_f}(\mathcal{A}_r)\dot{\omega}^* - \mathrm{D}^*_{\mu_f}(\mathcal{A}_r)\omega^*. \tag{V.21} $$

The expressions introduced above can be summarized according to the expression:

$$ {\tau_f}^*(\omega^*, \delta\omega) = -\left(\mathrm{I}^*_{\rho_f}(\mathcal{A}_r) + \mathcal{S}_t^{-\frac{1}{2}}\mathrm{I}^*_{\mu_f}(\mathcal{A}_r)\right)\dot{\omega}^* - \mathcal{S}_t^{-\frac{1}{2}}\mathrm{D}^*_{\mu_f}(\mathcal{A}_r)\omega^*, \tag{V.22} $$

where the analytic expression of the inviscid fluid added inertia $\mathrm{I}^*_{\rho_f}$ is known unlike the viscous terms $\mathrm{I}^*_{\mu_f}$ and $\mathrm{D}^*_{\mu_f}$, and all the terms in this equation with a * index are of the order of unity. The expression with dimensions of the equation above can be obtained by multiplying by $\rho_f\Omega^2 L^3\Theta$. In the literature, similar developments were performed based on the laminar flow around a infinite cylinder oscillating in a fluid at rest by Wang (1968). The analytic expression of the fluid forces on the flow, referred to as Stokes-Wang solution (Rashid et al., 2011), writes as:

$$ {\tau_f}^* = -\left(\mathrm{M}^*_{\rho_f} + \mathcal{S}_t^{-\frac{1}{2}}\mathrm{M}^*_{\mu_f 1/2} + \mathcal{S}_t^{-\frac{3}{2}}\mathrm{M}^*_{\mu_f 3/2}\right)\dot{v}^* + \left(\mathcal{S}_t^{-\frac{1}{2}}\mathrm{D}_{\mu_f 1/2} + \mathcal{S}_t^{-1}\mathrm{D}_{\mu_f 1} + \mathcal{S}_t^{-\frac{3}{2}}\mathrm{D}_{\mu_f 3/2}\right)v^*, \tag{V.23} $$

where all the coefficients above with a star exponent * are of the order of unity. Since the equation above describes a cylinder with translation oscillations, the added mass and damping expressions differ in the case of a rotating ellipsoid.

The experimental setup will aim to measure the fluid forces and compare the added mass and damping with the small Stokes predictions derived above.

V.2 Experimental setup

In order to compare the model of the potential and boundary layer moments introduced in equation (V.22) acting on an ellipsoid with rotational vibrations in a fluid with reality, an experiment is now proposed. The main purpose is to find whether or not the analytic expression of the added mass on a rotating ellipsoid is validated with experiments, and if the boundary layer added mass and damping scale in $\mathcal{S}_t^{-1/2}$ as predicted by the model.

Kinematics An arbitrary aspect ratio of $\mathcal{A}_r = 2$ has been 3D-printed. It has been fixed on a rotation axis using two bearings. The axis of the ellipsoid undergoes oscillating rotations thanks to a crank-rod system as shown in Figure V.2. A first crank is driven at a constant rotation speed by a motor. This crank drives the oscillating movement of a connecting rod, which in turn drives a second larger crank. Thanks to this mechanism, the constant rotation of the motor causes the second crank to undergo periodic angular oscillations. The angular amplitude of these oscillations depends, among other geometrical parameters, on the length ratio between the two cranks. The

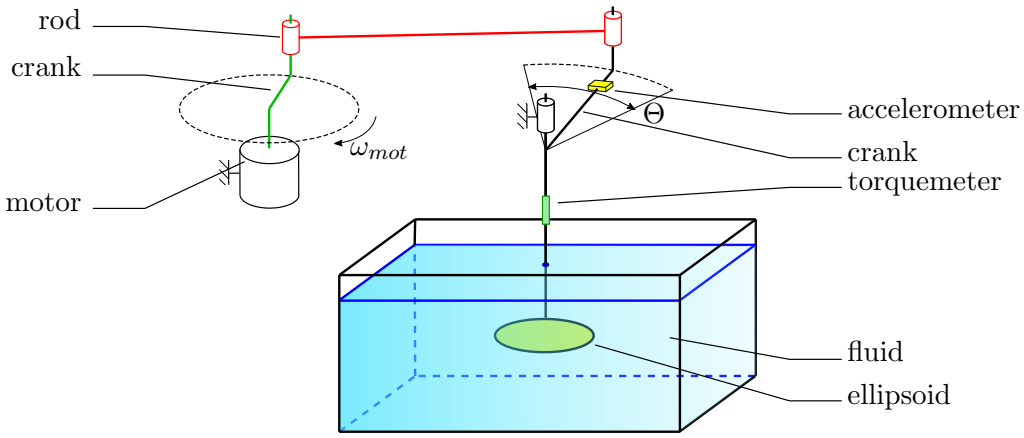

Figure V.2: Schematic view of the experimental setup. The crank-rod system converting the homogeneous rotations of the motor into oscilating rotations of the axis is shown with a kinematic diagram. The dashed lines represent the circular path of the tip of motor crank and the arc-shaped path of tip of the crank connected to the model axis.

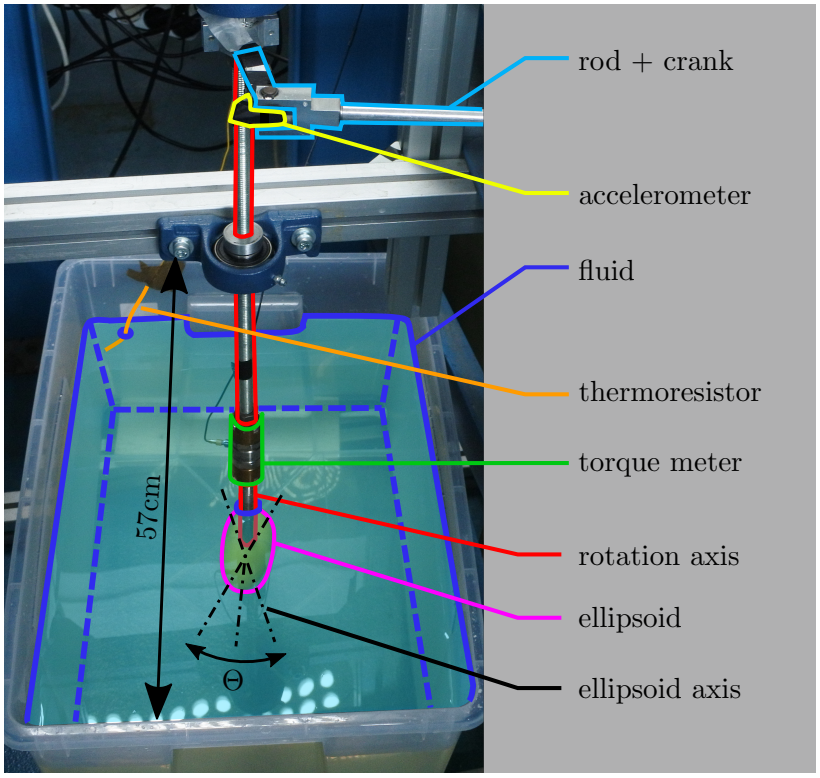

Figure V.3: Picture of the setup with highlights of the main elements.

oscillations of the second crank are then transmitted to the axis of the ellipsoid [1]. It is important to note that such a mechanism has the disadvantage of creating non-harmonic movements of the second crank. In order to have oscillations as close as possible to purely harmonic motion, the movements of rotations have been predicted using a geometric closure to find a geometric configuration resulting in a signal close to purely harmonic by adapting the distance between the axes of the motor and the ellipsoid.

Measurements Keeping in mind that the objective is to verify if the torque exerted by the fluid on the ellipsoid depends on the angular velocity and acceleration as predicted by equation (V.22), we want to be able to determine the three aforementioned variables: torque of the fluid on the ellipsoid, angular velocity and acceleration. In order to measure indirectly the torque exerted by the fluid on the ellipsoid, a torque-meter has been fixed between two parts of the rotation axis. This enables to get the torque exerted by the whole system composed of the bottom axis, the ellipsoid and its surrounding fluid on the torque-meter. How the purely fluid torque can be isolated from the torque measured (hence remove the forces of inertia from the ellipsoid and its axis) will be explained later in this section. In order to measure the angular acceleration, an accelerometer is placed on the crank of the ellipsoid axis. Because of its distance from the center of rotation, the measured acceleration can be directly linked to the angular acceleration by dividing it by its distance from the rotation axis. Either torque or acceleration measurements enable to obtain the frequency of the signal oscillations thanks to a Fast Fourier Transform (FFT). By dividing the measured angular acceleration amplitude by the frequency, one expects to obtain the angular velocity amplitude.

Now that the basic principles of the measurements have been exposed, the following parts will be devoted to the methodology in more detail to analyze the measurements and extract the physical quantities of interest for this study. First, the following time-constant variables are measured without motion of the ellipsoid: the length of the ellipsoid L, its aspect ratio $\mathcal{A}_r$[2] and the radius R between the rotation axis and the accelerometer have been measured with a meter, and the angular amplitude Θ using a protractor. The density of the fluid ρ_f has been measured using a graduated test tube, a beaker and a balance. The viscosity of the fluid μ_f has been measured using a viscometer. Once these have been measured, the motor can be started for the ellipsoid to oscillate, and the torque τ and acceleration α signals are measured over time. In practice, the temporal signal of the torque and acceleration is never used as is. It is more convenient to obtain their amplitudes $|\tau|$ and $|\alpha|$ and the associated frequency Ω using an FFT of the signal:

$$\alpha(\Omega) = |\alpha| \mathrm{e}^{\mathrm{i}(\Omega t + \phi_\alpha)} \tag{V.24a}$$

$$\tau(\Omega) = |\tau| \mathrm{e}^{\mathrm{i}(\Omega t + \phi_\tau)} \tag{V.24b}$$

Moreover, as will be explained later in this manuscript with further details, an interesting measure is the transfer function H between the torque τ and the acceleration α. Since the angular acceleration $\dot{\omega}$ is equal to the acceleration α divided by the accelerometer eccentricity R, the transfer function can be defined as follows:

[1] See the followinglink to see a video of the experimental setup

[2] those two parameters have been measured to make sure the dimensions required to the 3D printer have been respected

$$H(\Omega) = \frac{\tau}{\dot{\omega}} = \frac{|\tau|}{|\dot{\omega}|} \mathrm{e}^{\mathrm{i}(\phi_\tau - \phi_\omega)} = \frac{|\tau| R}{|\alpha|} \mathrm{e}^{\mathrm{i}(\phi_\tau - \phi_\alpha)}. \tag{V.25}$$

This transfer function will enable to obtain the amplitude ratio $|\tau|/|\alpha|$ between the two signals as well as their phase shift $\phi_\tau - \phi_\alpha$, which will come in handy when needing to separate acceleration and velocity related phenomena since both variables are out of phase by $\pi/2$. In order to use the measurements listed above, the torque τ acting on the torquemeter is the sum of all the fluid forces and the inertia forces due to all the solid parts below the torque sensor:

$$\tau = \tau_f + \tau_s. \tag{V.26}$$

The quantities of interest that have to be studied here are included in τ_f, while τ_s is equal to the angular acceleration multiplied by the total rotating inertia I_s:

$$\tau_s = \mathrm{I}_s \, \dot{\omega}. \tag{V.27}$$

Instead of performing a calculation of this inertia based on the moving components, we chose to first perform measurements with the ellipsoid in a fluid of negligible density $\mathcal{M}_f \ll 1$, enabling to have negligible fluid loads and isolate the structure loads:

$$\mathrm{I}_s = \Re e \left(H(\mathcal{M}_f \ll 1) \right). \tag{V.28}$$

In practice, when the ellipsoid is surrounded by air, one can consider that the fluid effects are negligible, with an inertia ratio between the fluid and solid effects estimated around

$$\frac{\mathrm{I}_f(\mathcal{M}_f \ll 1)}{\mathrm{I}_s} \sim 10^{-3}.$$

One should note that, in equation (V.2), both acceleration and torque signals are supposed to be in phase when the fluid effects are negligible since there are no damping effects from the solid, only inertia effects. Thus, either taking the real part or the amplitude of H would work since its imaginary part is negligible. Before measuring experimentally the inertia of the ellipsoid and its axis, the measurement chain had to be calibrated, especially at low frequencies ($\sim$ 2Hz) where the accelerometer and the torque meter where out of their nominal working conditions, inducing some errors on the amplitude and phase of the signals. In order to calibrate the setup, the transfer function between the raw signals of torque and accelerations H_{raw} has been measured for a model with a known inertia $\mathrm{I}_s^{\mathrm{cal}}$. The calibration model is a cylinder inertia whose inertia $\mathrm{I}_s^{\mathrm{cal}}$ has been previously obtained by measuring its mass, length and diameter. The calibrated transfer function H was then obtained by calculating, for various frequencies Ω, the complex correction C such that:

$$H(\Omega) = C(\Omega) H_{\mathrm{raw}}(\Omega) \tag{V.29a}$$

$$C(\Omega) = |C|(\Omega) \, \mathrm{e}^{\mathrm{i}\phi_C(\Omega)}. \tag{V.29b}$$

For each frequency Ω, the phase correction ϕ_C is calculated such that the imaginary part of H becomes zero as expected for a structure in a fluid with negligible density, and the amplitude

correction $|C[$ is calculated such that the amplitude $|H|$ of the transfer function matches the known inertia M^s of the cylinder:

$$C(\Omega) = \frac{H(\Omega)}{H_{\mathrm{raw}}(\Omega)} = \frac{\mathrm{I}_s}{H_{\mathrm{raw}}(\Omega)} \tag{V.30}$$

Once the solid inertia has been measured using the transfer function H for an ellipsoid without fluid, its contribution can be removed from the transfer function H obtained with measurements in dense flows to isolate the fluid contributions of the torque on the ellipsoid, which is the quantity we are interested in:

$$\tau_f = \tau - \mathrm{I}_s\,\dot{\omega}. \tag{V.31}$$

Now that we are able to extract the fluid contributions from the transfer function between the torquemeter and accelerometer, we are interested in identifying the added inertia $\mathrm{I}^*_{\rho_f}, \mathrm{I}^*_{\mu_f}$ and damping $\mathrm{D}^*_{\mu_f}$ coefficients expressed in equation (V.22). The fluid forces might be expressed as a function of the dimensionless angular velocity and acceleration using equation (V.22). The angular velocity is obtained by integrating the angular acceleration:

$$\omega^* = \frac{\dot{\omega}^*}{\mathrm{i}} = -\mathrm{i}\dot{\omega}^*. \tag{V.32}$$

Therefore, one gets by combining equations (V.22) and (V.32):

$$\left(\mathrm{I}^*_{\rho_f}(\mathcal{A}_r) + \mathcal{S}_t^{-\frac{1}{2}}\mathrm{I}^*_{\mu_f}(\mathcal{A}_r) - \mathrm{i}\mathcal{S}_t^{-\frac{1}{2}}\mathrm{D}^*_{\mu_f}(\mathcal{A}_r)\right)\dot{\omega}^* = -{\tau_f}^*. \tag{V.33}$$

The above equation can be reformulated using quantities measurable by the experimental device:

$$\mathrm{I}^*_{\rho_f}(\mathcal{A}_r) + \mathcal{S}_t^{-\frac{1}{2}}\mathrm{I}^*_{\mu_f}(\mathcal{A}_r) - \mathrm{i}\mathcal{S}_t^{-\frac{1}{2}}\mathrm{D}^*_{\mu_f}(\mathcal{A}_r) = -\frac{{\tau_f}^*}{\dot{\omega}^*} = -\frac{\Omega^2\Theta}{\rho_f L^5\Omega^2\Theta}\frac{\tau - \tau_f}{\dot{\omega}} \tag{V.34}$$

$$= -\frac{H - \mathrm{I}_s}{\rho_f L^5}. \tag{V.35}$$

As expected, the dimensionless added mass expression is reduced by a quantity $\rho_f L^5$ that has the dimension of an inertia. Since the added mass and damping coefficients are real numbers, one can identify experimentally the following dimensionless coefficients:

$$\mathrm{M}^{f*}(\mathcal{A}_r, \mathcal{S}_t) = \mathrm{I}^*_{\rho_f}(\mathcal{A}_r) + \mathcal{S}_t^{-\frac{1}{2}}\mathrm{I}^*_{\mu_f}(\mathcal{A}_r)$$

$$= -\frac{\Re e(H) - \mathrm{M}^s}{\rho_f L^5} \tag{V.36a}$$

$$\mathrm{I}^\dagger_{\mu_f}(\mathcal{A}_r, \mathcal{S}_t) = \mathcal{S}_t^{-\frac{1}{2}}\mathrm{I}^*_{\mu_f} = \mathrm{I}^*_f - \mathrm{I}^*_{\rho_f} \tag{V.36b}$$

$$\mathrm{D}^\dagger_{\mu_f}(\mathcal{A}_r, \mathcal{S}_t) = \mathcal{S}_t^{-\frac{1}{2}}\mathrm{D}^*_{\mu_f}(\mathcal{A}_r)$$

$$= \frac{\Im m\,(H)}{\rho_f L^5} \tag{V.36c}$$

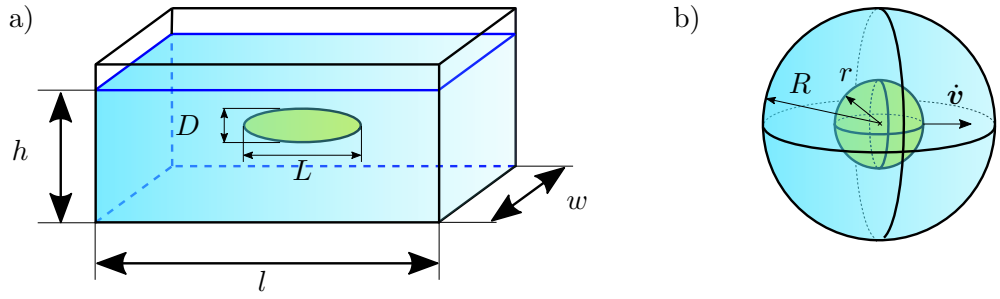

Figure V.4: a) Dimensions of the ellipsoid and the fluid domain. b) Sphere accelerating in a spherical container filled with fluid.

The first line (V.36a) of the above equations enables us to identify experimentally the total added mass of the fluid surrounding the ellipsoid, including the potential added mass and the added mass of the boundary layer. The second line (V.36b) is used to determine the added mass due to boundary layer effects. It is obtained by calculating the difference between the total measured added mass of the fluid and the value of the potential added mass obtained via its analytic expression (V.20a) as a function of its aspect ratio $\mathcal{A}_r$. The third line (V.36c) enables to determine the damping due to the shear stresses in the boundary layer. In order to check if the similitude principle is respected, the three aforementioned coefficients (fluid added mass, boundary layer added mass and boundary layer shear stress), are measured for different parameters. The parameters explored are the following:

- The frequency Ω of the motor can be controlled. In this study, it varies roughly from 2 to 6 Hz (or 13 to 35 rad/s, see Figure V.7).

- The angular amplitude Θ can vary by changing the length of the motor crank. In this thesis, the explored range is $\Delta\Theta \simeq [\pi/30; \pi/4] = [6^o, 45^o]$.

- The viscosity μ_f of the fluid can vary. The fluid used is a mixture of water and glucose syrup, the viscosity of the latter being roughly two orders of magnitude higher than that of water. The concentration of glucose syrup can vary from 0 to 1, thus increasing the viscosity of the mixture.

- The density ρ_f of the fluid varies slightly too with the concentration of glucose syrup, as the latter is lighter than water.

As a result of the fluctuations of the four aforementioned parameters, the two dimensionless parameters fluctuating are the Stokes number $\mathcal{S}_t$ and the angular amplitude Θ (or equivalently the Stokes number $\mathcal{S}_t$ and the Reynolds number $\mathcal{R}_e$, as for a structure with harmonic angular oscillations we have $\mathcal{R}_e = \Theta\mathcal{S}_t$). The viscosity and the density of the fluid are obtained thanks to a characterization of the latter prior to the experiments. Using a viscometer, the viscosity variations were measured at different temperatures of the fluid and especially at different concentrations of glucose syrup. Before starting each measurement, the concentration of glucose syrup is measured with a graduated cylinder, a beaker and a balance, and a thermoresistance is immersed in the water to measure its temperature.

Both torque and acceleration signals are amplified, then plugged to an analog low-pass filter to cut out high frequency noise and and prevent aliasing. The filtered signals are then send to an acquisition card controlled via Matlab. The sampling frequency is 40Hz which was deemed sufficient since the largest oscillation frequency of the model is less than 6 Hz ($\gtrsim$ 7 samples per period). For each measurement, the acquisition time was set to 10 seconds to capture between

20 and 50 periods of the signal depending on the oscillation frequency. The resulting amplitude and phase of the transfer functions is consequently an average over all the periods of the signal performed by the FFT. One should recall that the model developed to obtain equation (V.22) is based on the infinite fluid domain hypothesis. In practice, one has to restrain to finite length water tanks for technical reasons. In the case of this experiment, the dimensions of the water domain (length l, width w and height h) are $[l, w, h] = [56, 39, 23]$ cm, which becomes reduced by the ellipsoid characteristic length L: $[l^*, w^*, h^*] = [5.6, 3.9, 2.3]$. According to Doaré (2020), the finite length of the domain increases the added mass effects predicted by the infinite fluid domain hypothesis. The three-dimensional added mass correction factor associated with the ratio between the added mass in the basin $\mathrm{M}^*_{\rho_f}$ and the added mass $\mathrm{M}^*_{f,\infty}$ associated with an infinite domain is defined as:

$$C_{3D}(\mathcal{A}_r, l^*, w^*, h^*) = \frac{\mathrm{I}^*_{\rho_f}(\mathcal{A}_r)}{\mathrm{I}^*_{\rho_f,\infty}(\mathcal{A}_r)} - 1 > 0. \tag{V.37}$$

The coefficient C_{3D} is necessarily larger than zero because confinement effects constrain the movements of the fluid particles, making the energy required to displace them more important.

However, an approximation of the order of magnitude of the confinements effects can be obtained considering analogous systems. The confinements effects on the added mass of a sphere of radius r in translation at the center of a spherical container of radius R are of (Lamb, 1932):

$$C_{3D}^{\text{sphere}}\left(\alpha = \frac{r}{R}\right) = 3\frac{\alpha}{1-\alpha}. \tag{V.38}$$

The associated confinement effects would be of $C_{3D}^{\text{sphere}} = 0.6\%, 1.7\%$ and 3.1% for confinement ratios of $\alpha = \frac{D}{w}, \frac{L}{l}$ and $\frac{D}{h}$ respectively. Consequently, the expected confinement effects are of $\simeq 1\%$.

In addition to the confinement effects due to the finite dimensions of the water tank, it is important to note that the fluid domain has a free surface. The latter could be eliminated by using, for example, a perforated cover fixed at the water level that would let the rotation axis of the model enter the fluid. The addition of such an improvement to the experimental device would be an interesting prospect. In the absence of a cover, it is necessary to determine the natural frequency of the tank sloshing frequency to ensure that the model's rotations do not transmit a significant amount of energy to the free surface modes, which could affect the fluid forces exerted on the structure and render the infinite domain hypothesis and the expression (V.22) unrepresentative of the phenomena at stakes in the fluid domain. According to Morand and Ohayon (1992), the lowest sloshing frequency $\Omega_{\text{min}}^{\text{slosh}}$ of a rectangular tank of length l filled with an ideal fluid of height h can be expressed as:

$$\Omega_{\text{min}}^{\text{slosh}} = \pi\frac{g}{l}\tanh\left(\pi\frac{h}{l}\right). \tag{V.39}$$

In the case of the basin used for our experiments, the associated frequency is of $\Omega_{\text{min}}^{\text{slosh}} = 47$ rad/s, which is 35% above the highest frequency of the model used ($\Omega_{\text{max}} \sim 35$ rad/s as shown in Figure V.7). Therefore, the free surface is not expected to resonate in the range of frequencies explored for the model. This was verified as well with naked eye throughout the experiments by observing the movements of the free surface. At the highest frequencies $\Omega \sim 35$ [rad/s], surface waves localized around the axis of rotation of the model were perceived, but their amplitude seemed negligible.

Before moving toward the analysis of the experimental results, a summary of the experimental process is presented below:

Recap of the experimental process

(i) Mechanism development:
Drives an ellipsoidal model in rotational vibrations in air or in a fluid, in a quasi-harmonic motion.

(ii) Implementation of the measurement chain:
Accelerometer and torquemeter are connected to an amplifier, then to a low pass filter. The resulting signal is sent to an acquisition card whose temporal measurements will be exploited by Maltab.

(iii) Calibration:
In order to compensate for the deviation of the sensors whose nominal frequency is higher than that of the measurements carried out, a correction of the amplitude and the phase of the transfer function between torque and acceleration is obtained for each frequency with the help of a model whose inertia in air is known. The inertia of the ellipsoid and its axis is then measured. The viscosity of the fluid is measured for varying glucose syrup concentration and temperature to obtain abacuses.

The three steps listed above only have to be done once, on the contrary to the two following steps which have to be repeated for each frequency Ω, angular amplitude Θ and glucose syrup concentration.

(1) Measurement of viscosity and density of the fluid:
The concentration of glucose syrup and the temperature of the fluid in which the model will vibrate are measured. Thus, with the help of abacuses obtained prior to the data acquisition with the help of a viscometer, one can determine its viscosity and its density.

(2) Measurement of quantities of interest:
The transfer function between torque and acceleration measured from the model vibrating in the fluid is calculated. Its real part is used to obtain the added mass effects of the fluid at the structure and boundary layer scales, and its imaginary part is used to obtain the added damping effects due to shear effects in the boundary layer.

Once enough data has been collected with the two steps above, the next step is

(iv) Plotting of graphs and physical discussion:
The added mass and damping effects are studied for the varying dimensionless coefficients $\mathcal{S}_t$ and Θ. See next section V.3.

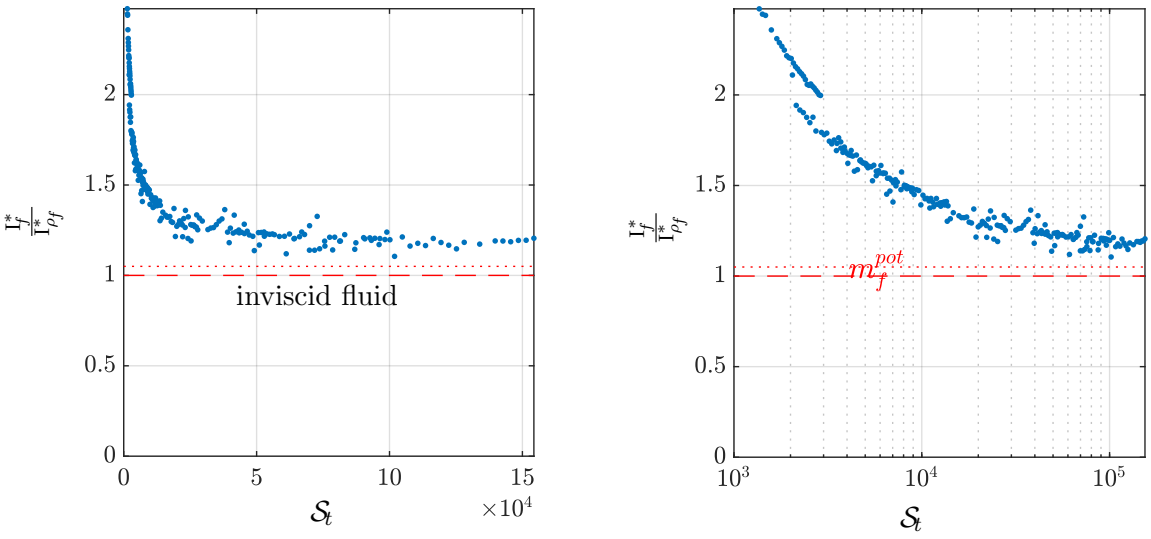

Figure V.5: Ratio between the measured added mass I_f^* and its theoretical value $I_{\rho_f}^*$ based on potential flow theory from equation (V.20a), with a linear or logarithmic scale of $\mathcal{S}_t$ for the left and right graphs respectively. The dashed line is the theoretical value, and the dotted line shows the 1.05 value, hence a value 5% higher than the potential prediction.

V.3 Results of added mass and added damping

In this section, the results obtained after running the experimental process for an explored range of parameters are presented. The graphs presented are accompanied by physical discussions about the shape of the curves obtained and to what extent it is consistent with the model presented in section V.1.

The measurements of the dimensionless added mass as a function of the Stokes number $\mathcal{S}_t$ are presented in Figure V.5. At the left, the added mass is plotted against a linear scale of the Stokes number, which squeezes the points together at low Stokes numbers $\mathcal{S}_t \sim 10^3$. For this reason, the added mass is plotted against a logarithmic scale of $\mathcal{S}_t$ at the right. The added mass has been divided by the theoretical value for a potential fluid toward which the added mass of the viscous fluid is supposed to tend to for $\mathcal{S}_t \to \infty$). The measurements show that the added mass seems to be underestimated theoretically relatively to the experimental results. This difference is probably linked to an inaccuracy in the calibration of the measurement chain. However, as expected, the lower the Stokes number, the thicker the boundary layer, and consequently the higher the associated added mass. The uncertainties associated with the measurements from Figure V.6 are shown in Figure G.2.

In the experiment, the Stokes number $\mathcal{S}_t = \Omega L/\nu_f$ varies with the frequency Ω and the kinematic viscosity $\nu_f = \mu_f/\rho_f$. The variations of the viscous added mass and the viscous damping have been plotted as a function of those two variables in Figure V.7. The experiment explores a range of frequency between $\Omega^{\min} = 13$ rad/s and $\Omega^{\max} \sim 35$ rad/s. Lower frequencies could not be reached as the drift of the sensors was too high and the error induced could not be reasonably compensated anymore using calibrations on a given solid inertia. Higher frequencies could have been reached but would have resulted in higher risks of damage to the experimental setup. The kinematic

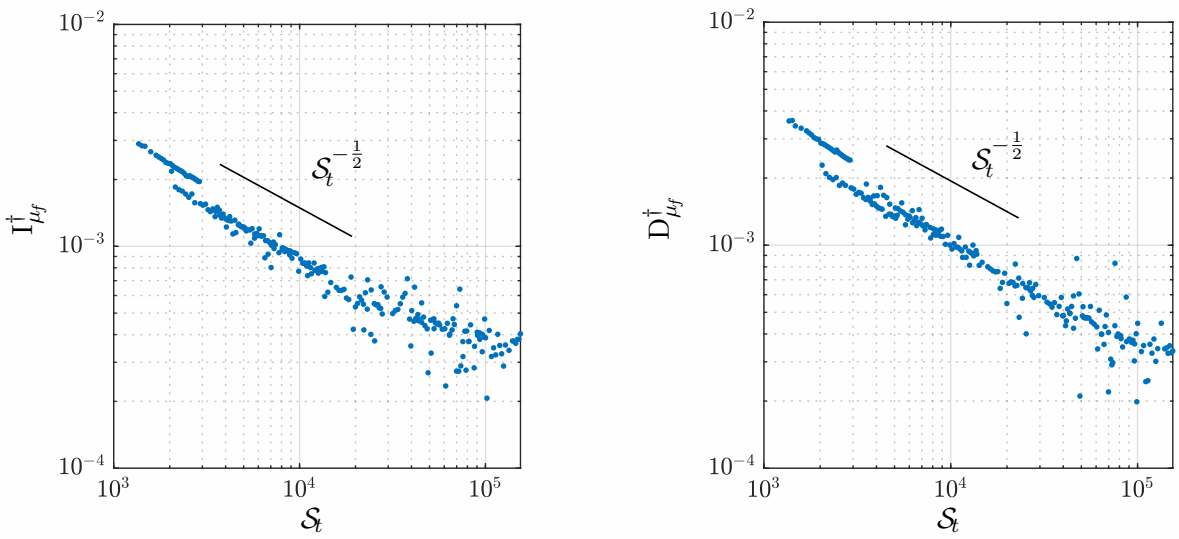

Figure V.6: Boundary layer added mass $\mathrm{I}^{\dagger}_{\mu_f}$ (left) and added damping $\mathrm{D}^{\dagger}_{\mu_f}$ (right) plotted against the Stokes number. Both axis are on a logarithmic scale.

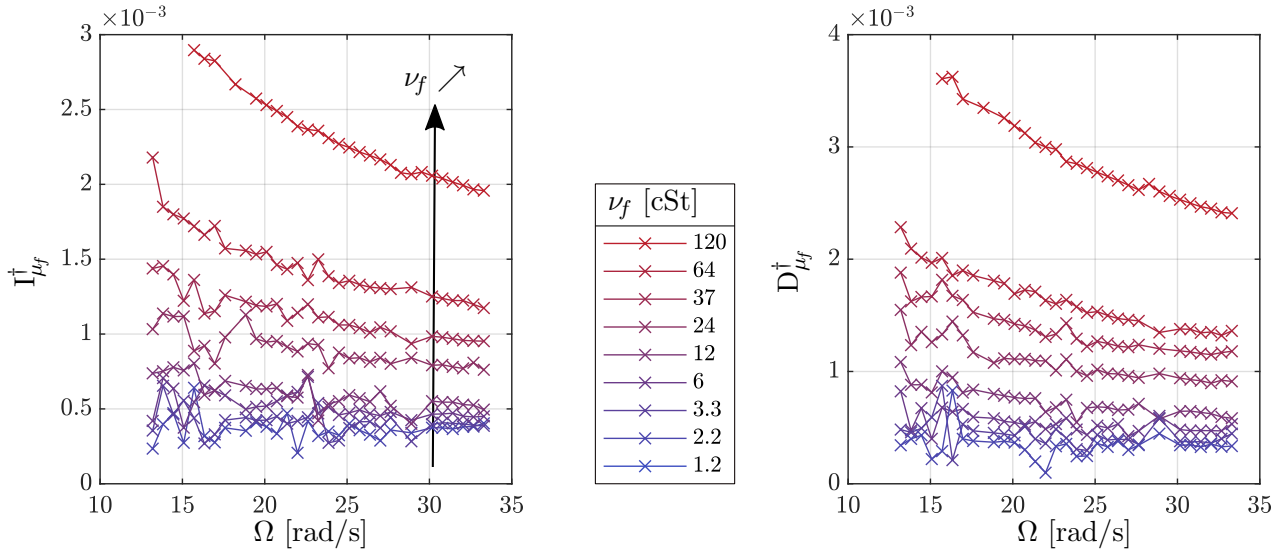

Figure V.7: Boundary layer added mass (left) and damping (right) as a function of the frequency. The color scheme indicates the concentration of glucose syrup, from 0 (pure water) in blue to 1 (pure glucose) in red. The kinematic viscosity $\nu_f = \mu_f/\rho_f$ varies with the glucose syrup concentration from 1.2 centiStokes (cSt) with water to 120 cSt with pure glucose syrup.

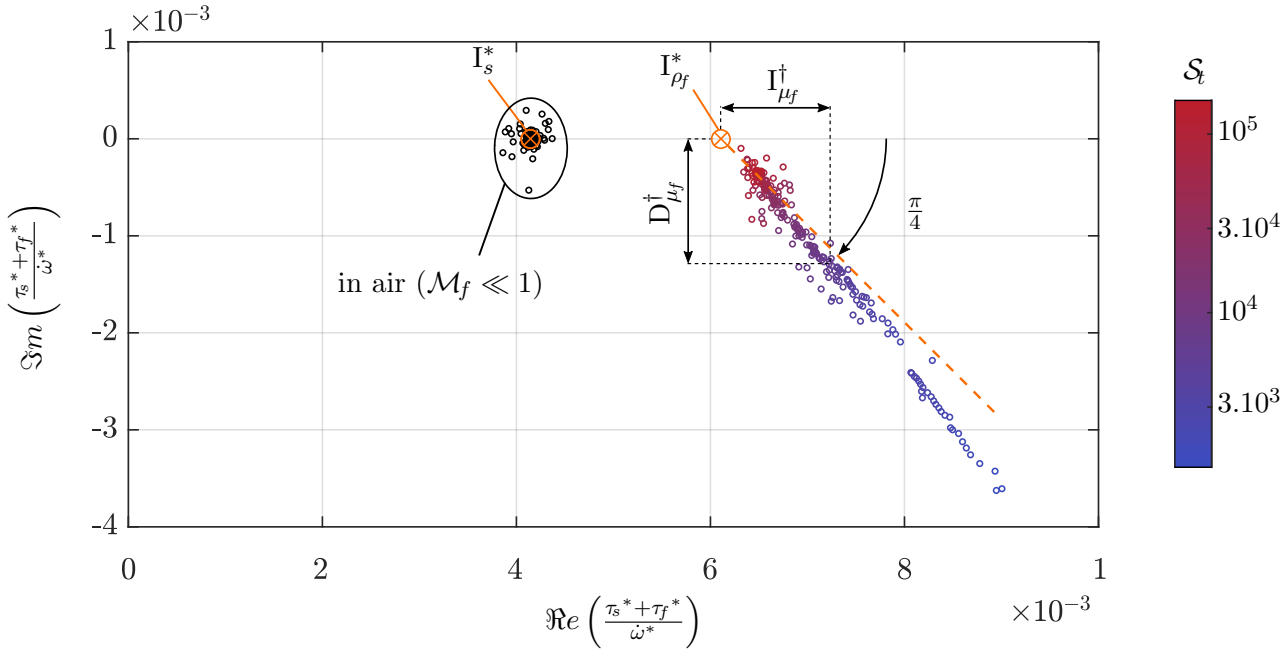

Figure V.8: Evolution of the dimensionless transfer function between the measured torque and angular acceleration in the complex plane, with the model either in air (black dots) or in a water-glucose mixing. Results are plotted along orthonormal axes. The color of the latter indicates the associated Stokes number. The orange crosses indicate both the measured dimensionless mass of the ellipsoid and its axis and the theoretical value of the added mass predicted by the potential theory (Lamb, 1932). Although the force measurements in air (black dots) do not contain any information about the physical behavior of the fluid, they have been plotted to give an overview of the dispersion of the acquisition chain measurements as the model frequency varies. The horizontal and vertical double arrows going from the potential added mass $\mathrm{I}_{\rho_f}^*$ to an arbitrary point of a measured transfer function are associated with the dimensionless boundary layer added mass $\mathrm{I}_{\mu_f}^\dagger$ and damping $\mathrm{D}_{\mu_f}^\dagger$ associated with the measure respectively. The orange dashed line with a 45^o angle is associated with the theoretical aspect of the curve from equation (V.22).

viscosity of the glucose syrup being approximately 100 times that of water, the kinematic viscosity is explored through two orders of magnitude. This gives a ratio of 270 between the maximum and minimum explored values of the explored Stokes number. As shown in figure V.5, the Stokes number varies roughly from $\mathcal{S}_t \sim 3.10^3$ to $\mathcal{S}_t \sim 10^5$. According to equation (V.3b), this means that the ratio between the boundary layer thickness and the length of the model varies roughly from $\eta_f/L \sim 1‰$(for $\mathcal{S}_t \sim 10^5$) to $\eta_f/L \sim 1\%$ (for $\mathcal{S}_t \sim 10^3$). As for an ellipsoid of length L and aspect ratio 2, the smallest radius of curvature is $r = L/8$ at the tip. As a consequence, the ratio between the boundary layer thickness and the minimal radius of curvature is around $\eta_f/r \sim 1\%$ for $\mathcal{S}_t \sim 10^5$ and $\eta_f/r \sim 10\%$ for $\mathcal{S}_t \sim 10^3$. Hence, the thin boundary layer assumption is rather respected in the whole range of measurements, except at the tip of the ellipsoid for $\mathcal{S}_t \lesssim 10^4$. As mentioned in equation (V.3b), decreasing the frequency Ω and increasing the kinematic viscosity ν_f increases the boundary layer thickness, which results in higher boundary layer added mass and damping as verified in Figure V.7. In order to verify the predicted amplitude of the boundary layer added mass and damping in $\mathcal{S}_t^{-1/2}$, these parameters have been plotted with respect to the Stokes number in Figure V.6. The trend of both curves is in agreement with the predicted evolution of $\mathcal{S}_t^{-1/2}$. It is interesting to notice how the measurements are much more dispersed at higher Stokes. This is due to multiple factors. First, the fact that the boundary layer becomes much more smaller in this region, and consequently the associated effects become more negligible in front of the added mass effect, and are therefore harder to capture as their order of magnitude gets closer and closer to the measurement noise. Second, as the Stokes number gets higher, turbulence effects become more important, which might be a reason as well for the more chaotic results at high Stokes compared to more laminar regions. One might note as well that for $\mathcal{S}_t \sim 10^3$, the added damping seems to offset from the rest of the curve in the same way as for the added mass. In order to gain insight on the orders of magnitude of the fluid and solid forces acting on the torquemeter in the conducted experiments, the transfer function between the torque exerted by the fluid and solid system on the torquemeter and the angular acceleration has been plotted in Figure V.8. On this graph, the values on the real axis are in phase with the acceleration, which is the reason why the measured solid mass I_s^* and the analytical potential added mass I_f^* are located on it. Looking at the fluid forces plotted with color varying from blue to red when $\mathcal{S}_t$ increases, it appears clearly that for high Stokes the added damping and the boundary layer added mass becomes negligible in comparison with the inviscid added mass. The orange dashed line at 45^o with the horizontal shows the theoretical evolution of the fluid forces for varying Stokes as predicted by equation (V.22), since both boundary layer added mass and added damping are supposed to evolve in $\mathcal{S}_t^{-1/2}$. Though the measurement are in agreement with this prediction at high Stokes, it seems like the added damping $\mathrm{D}_{\mu_f}^\dagger$ increases slightly faster than the boundary layer added mass $\mathrm{I}_{\mu_f}^\dagger$ when the Stokes number $\mathcal{S}_t$ decreases. A possible explanation for this might come from the fact that, at higher orders, the damping evolves in $\mathcal{S}_t^{-1}$ whereas the added mass evolves in $\mathcal{S}_t^{-3/2}$ like in the predictions of the Stokes-Wang equation (V.23). Another possible explanation might come from a sensor drift not well compensated by the calibrations. One should note that the measurements for the pure glucose syrup, which were associated to an offset at $\mathcal{S}_t \sim 10^3$ (see Figure V.6) do not seem to have an offset in the complex plane shown in Figure V.8. As a consequence, it probably means that the added mass and damping coefficients $\mathrm{I}_{\mu_f}^\dagger$ and $\mathrm{D}_{\mu_f}^\dagger$ are well predicted since they are aligned with the rest of the curve in Figure V.8. Therefore, the most convincing explanation regarding the offset in Figure V.6 is that the Stokes number associated with pure glucose syrup has not been well measured. Since the evolution with respect to the frequency Ω with the pure glucose syrup ($\nu_f = 120$ cSt) in Figure V.7 seems to have a coherent shape, the error in the Stokes number is likely to come from the viscosity measurements. It is interesting to note as well that, for each

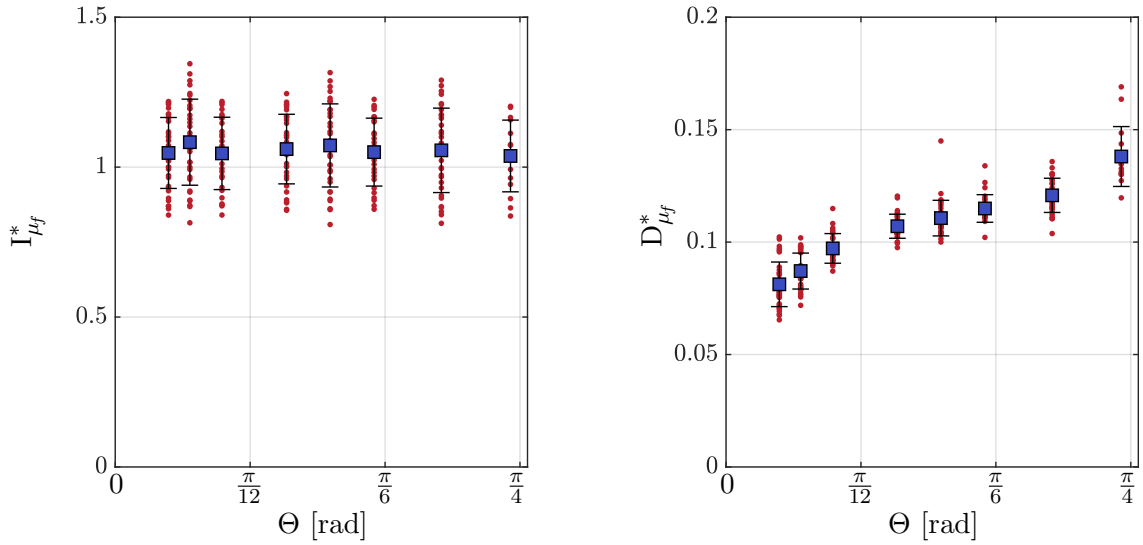

Figure V.9: Dimensionless mass coefficient $I^*_{\mu_f}$ (left) and damping coefficient $D^*_{\mu_f}$ (right) of the boundary layer as a function of the angular amplitude Θ. Each red dot is an individual measurement. The blue squares and the error bar are associated respectively with the mean value and the standard deviation of the measurements for each value of angular amplitude.

glucose syrup concentration, the Stokes number associated with the highest frequencies is of the same order than Stokes number with lower glucose concentration (hence lower viscosity) and lower frequency, and the resulting added mass and damping coefficients match, which tends to show how various viscosity and frequencies might lead to similar added mass effects if the Stokes number remains the same as predicted by the similitude principle.

So far, the angular amplitude of the model has been mentioned very little, and for good reason since it is not supposed to influence the non dimensional boundary layer added mass and added damping coefficients from equation (V.22). In order to check if this is consistent with the experimental setup, the angular amplitude has been modified by changing the size of the motor crank. In this series of experiments, the fluid forces were measured only in pure water, but with the same frequency range as previously: $\Omega \in [13, 35]$ rad/s. The boundary layer added mass and damping coefficients have been plotted in Figure V.9. For each angular amplitude Θ, the spread of the points is due to variations in the Stokes number (or equivalently due to frequency fluctuations as the length L and the viscosity ν_f are fixed here). As mentioned before, these variations are due either to measurement noise which is quite high in the case of water (because of the relatively small boundary layer effects we are trying to capture), or to variations in the fluid forces due to turbulence (which is quite higher in water than in the glucose syrup because of higher Stokes number). Actually, equation (V.22) based on negligible turbulence predicts that the boundary layer added mass coefficient $M^*_{\mu_f}$ does not vary with the Stokes number. It can be seen on the graph on the left that, as expected, the boundary layer does not vary significantly as the angular amplitude varies. However, this is not the case for the added damping, which seems to increase as the angular amplitude increases as well.

V.3.1 Conclusion on viscous results at airship scale

Table V.1 gives the Stokes number associated with two airships, Ω being taken as the lowest elastic natural frequency documented in (Inamoto et al., 2003) and (Li et al., 2009). It appears that the Stokes number at the scale of airships $\mathcal{S}_t \sim 10^7$ is two orders higher than the highest Stokes reached with the experimental setup $\mathcal{S}_t \sim 10^5$.

	Skyship 500 (Li et al., 2009)	Stratospheric platform airship (Inamoto et al., 2003)
L [m]	50	25
Ω [Hz]	0.04	0.1
$\mathcal{S}_t$ [-]	3×10^7	2.4×10^7

Table V.1: Stokes numbers associated with nominal use of two airships.

V.4 Conclusion

In this chapter, the following work has been done:

1. An experimental setup has been introduced, with the aim of measuring the fluid loads on an ellipsoid with rotation oscillations. It enabled to compare the measurements of added mass and damping from the fluid with theoretical predictions based on an infinite flat plate in transverse oscillations model.
2. The prediction of the added mass effect based on the potential
3. The experimental campaign enabled to verify that, for large Stokes numbers, the fluid forces other than the potential added mass are negligible. For lower Stokes number, the boundary layer added mass and damping effects were measured with a trend in $\mathcal{S}_t^{-1/2}$ coherent with the theoretical model predictions.
4. As expected, it was found out that the angular amplitude didn't affect the added mass coefficients, which was not the case for the added damping however. However, for larger angular amplitudes than those explored in this study, the vortex shedding might interact with the structure as observed by Sarpkaya (1977), thus affecting the added mass coefficient.

V.5 Perspectives

In order to further develop the study presented in this chapter, the following work could be considered:

- According to Vashy-Buckingham, the viscous and potential coefficients of the fluid loads $I^*_{\rho_f}$, $I^*_{\mu_f}$ and $D^*_{\mu_f}$ on a rotation ellipsoid dépendent de the independent dimensionless parameters $\mathcal{A}_r$, $\mathcal{S}_t$ and Θ. Their dependence on the parameters $\mathcal{S}_t$ and Θ has been studied during this chapter, but not the influence of the aspect ratio $\mathcal{A}_r$. Thus, making new measurements on model with more or less elongation would allow to better understand the influence of this parameter on the fluid forces.

- In order to approach the conditions of use of airships, the experiments should be reproduced for higher Stokes numbers. This could be done by either increasing the dimensions L of the model (which would imply using a larger fluid basin as well), by increasing the maximal frequency Ω studied. To the author's knowledge, fluids with lower kinematic viscosity ν_f compared to water (acetone, ammonia or mercury for instance) would be impractical to use.
- In order to prevent sloshing, a cover could be added on the free surface.
- In view of predicting the effects of confinements induced by the finite length of the basin, the BEM code developped in Chapter III could be used on the mesh of a rotating ellipsoid and a basin.
- The use of better suited sensors would improve the quality of measurements and reduce the noise, especially at low frequencies.
- To study cases closer to the nominal operating conditions of airships, the study of a model oscillating in a wind tunnel would also be an interesting prospect.

Chapter VI

Discussion, conclusion & perspectives

VI.1 Conclusion

VI.1.1 Synthesis of the argumentation

The objective of this thesis was to model the dynamic loads of the internal and external fluids on a flexible airship.

For this purpose, chapter I has presented the potential fluid model, as well as the associated integral representation which allowed to condense the fluid problem on the fluid-structure interface. However, the equations presented in chapter I have some limitations. The Eulerian approach is not well adapted to moving interfaces, and the deformations of the domain lead to the necessity of remeshing when the problem is solved in time domain.

In chapter II, an original model of the fluid forces based on a Newtonian approach (contrary to the literature mainly focused on Lagrange equations) has been introduced. In order to take into account the moving interface in a practical way, the integral representation of the fluid velocity potential has been expressed according to an ALE formalism, inspired by Pfister (2019); Mavaleix-Marchessoux (2020). The fluid variables (velocity potential, pressure and virtual power) have then been linearized with respect to the small elastic and rigid body displacements of the interface. It includes the consideration of linearized forces due to small deformations in the context of large rotations of the structure that was cited as a scientific lock in the work of Li et al. (2009). The linearized forces have then been expressed in terms of fluid mass, gyroscopic and stiffness operators, respectively linear with the acceleration, velocity and displacements of the interface, in a manner similar to Li et al. (2009). It has been shown in the manuscript that these three operators are respectively independent, linear and quadratic with regard to the six rigid body motions of the structure, which allows to decompose the calculation of these operators associated to any rigid body motion depending on contributions from each translation and rotation. Finally, it has been shown that, contrary to the Newtonian approach introduced in this manuscript, the prediction of linear fluctuations of the fluid forces on the interface using an approach via the Lagrange equations requires the computation of the second order fluctuations of the geometric variables as well as of the velocity potential, thus justifying the use of the Newtonian approach in this study.

In chapter III, a numerical method to predict the fluid operators put into equations in chapter II has been introduced and validated. A numerical implementation of the linearized BEM based on

the theoretical model presented in chapter II has been presented. The computation of the linearized BEM operators takes into account the deformations of the structure. In order to accelerate their numerical computation, the Hierarchical Matrix Method has been implemented on the usual BEM operators, then adapted to the case of the linearized BEM operators introduced in this study. The fluid forces can thus be computed using a BEM-FEM coupling. The classical BEM operators have been validated by comparing the associated solution with analytical solutions linked to an ellipsoid. The linearized BEM operators have been validated by comparing the linear fluctuation results predicted by the model with the nonlinear fluctuation results obtained using the finite difference method with mesh deformation. The numerical solution of the potential fluid associated with a stationary flow around an airship has been compared with a RANS simulation, allowing to highlight the good prediction of the pressure distribution except for the circulation effects and the separation at the back of the hull, in coherence with the literature (Clarke, 2009). Finally, it has been numerically verified that the second order perturbations of the geometry and velocity potential play a non-negligible role in the prediction of the forces with the linearized Lagrangian equations, thus justifying the consistency of the Newtonian approach used in this study.

In chapter IV, the effects of internal and external fluids on the flexibility of an airship have been studied. For this purpose, a dynamic model of the structure has been presented, taking into account non-linear effects associated with the internal pressure as well as dynamic elastic deformations around the prestressed state. The associated operators have been calculated numerically using FEM. Using the monolithic equation thus obtained by coupling the FEM operators of the structure and BEM-FEM operators of the fluid, the associated eigenvalues have been obtained as a function of the flow velocity, which predicted the risks of instabilities of the airship by divergence or flutter. The stabilizing effects due to the fins have then been introduced numerically and the new associated eigenvalues induced a better stability of the flexible airship.

Finally, in chapter V, the added mass results obtained from potential flow theory have been compared with experimental results acquired from rotating oscillations of an ellipsoidal model in a pool of water at rest. First, a model giving the expression of the magnitude of the viscous forces of the fluid as a function of the frequency, density and viscosity of the fluid, or more generally as a function of the Stokes number, has been introduced. The experimental setup has been used to study the fluid forces as a function of the Stokes number. The experimental results gave trends consistent with the modeling. Although the Stokes numbers reached experimentally are not comparable to the nominal operating conditions of airships, the measurements obtained tended to confirm the validity of the hypothesis of potential flow for the study of flexible airships.

VI.1.2 Putting the research into perspective

This paragraph puts the work presented in this manuscript in context by comparing it with the literature associated with the subject.

First of all, the fluid forces have been taken into account in this work using a Newtonian formalism (in a similar way to Mavaleix-Marchessoux (2020) for example) on the contrary to the approaches commonly used to model the effects of potential flows on the dynamics of airships (Li et al., 2009; Azouz et al., 2012; Azinheira José et al., 2002; Thomasson and Woolsey, 2013). Indeed, it is shown in chapter II that the Newtonian approach allows to completely describe the linear fluctuations of the fluid forces using the perturbations of the potential and the geometry at order 1, while the Lagrange equations approach requires to compute the perturbations at order 2 (although the latter are not taken into account by Li et al. (2009); Azouz et al. (2012)), which has

been demonstrated in this manuscript.

The method introduced in this manuscript is based on the BEM, itself based on the use of a mesh of the fluid-structure interface. This method can take into account any type of interface whatever its geometry, contrary to the approaches of Li et al. (2009) or Azouz et al. (2012) based on analytical solutions obtained on simplified geometries, respectively an ellipsoid of revolution and an ellipsoid cone.

Contrary to the work of Li et al. (2009); Azouz et al. (2012) which only considered transverse elastic deformations of the interface, this work can be applied to any elastic deformation of the interface, thus providing a more complete description of the interface movements. Unlike Li's approach based on the slender body theory which takes into account the rotation of the normal due to transverse elastic deformations in the kinematic boundary condition of the fluid, but does not take into account the dilatation of the interface nor the rotation of the normal in the dynamic boundary condition of the fluid, the work presented in this manuscript takes into account the full effects of the fluid due to variations in the geometry.

Contrary to the approach of Mavaleix-Marchessoux (2020) who considers the effects of geometry fluctuations on the BEM operators only beyond a certain admissibility criterion based on the relative amplitude of the deformations, the linearization of the BEM operators allows to naturally take into account the above mentioned effects. In the work of Mavaleix-Marchessoux (2020), the effects of rotation of the normal in the kinematic boundary condition are taken into account directly in the second member data vector, which reduces the size of the associated BEM operator by a factor of 3, but leads to approximations because the normal is not naturally defined at the nodes of the mesh and thus requires an interpolation. In this manuscript, the chosen approach differs and is based on the values of the normal on the triangles where it is naturally defined via the BEM operator of the second member. However, a methodology similar to the first mentioned method is also possible for the approach introduced in this manuscript, as described in appendix E. Moreover, contrarily to (Mavaleix-Marchessoux, 2020; Carbone et al., 2019), the BEM methods is based on a regularized formulation of the integral equation, compatible with the geometrical singularities of the mesh.

Unlike (Li et al., 2009), the work introduced in this manuscript does not take into account the turbulence effects at the back of the airship, nor the hull-fin interaction effects. However, it is important to note that the approach introduced in this work offers the possibility to be extended in a consistent way to a model including vortex shedding at the back of the fins in order to take into account circulation effects, contrary to Li's approach which requires to add the effects of lift of the fins and of hull-fin interaction a posteriori based on the superposition of effects predicted from several distinct models.

As mentioned by Li et al. (2011), the linearized fluid forces associated with large rotational motions of an elastic interface constitute one of the scientific bottleneck in the field of airship dynamic aeroelasticity. In this manuscript, a model taking into account linearized aeroelastic dynamic forces in the framework of large rotations has been proposed in section II.2.

In the work of Li et al. (2009), the aeroelastic dynamic effects are predicted without taking into account the pre-stressing effects due to the internal gas pressure, while Bessert and Frederich (2005) took into account the pre-stressing effects but in the framework of a static model. In this manuscript, an approach is proposed to take into account the membrane pre-stressing effects associated with the dynamic aeroelasticity of airships in section IV.1.

The experimental set-up in chapter V was used to study the forces of the fluid on a model

in rotary oscillations, contrary to Sarpkaya (1977); Otter (1990); Chaplin (2000) who focused on the translational vibrations of a cylinder in a fluid. Moreover, contrary to the studies cited above where the parameter space explored was constituted by the amplitude of motion and the frequency of oscillation, this manuscript also explores the effects due to changes in the kinematic viscosity of the fluid.

Now that the work of this manuscript has been put into perspective with respect to the state of the art, the limitations associated with this study are summarized in the following section.

VI.1.3 Limitations of the research

Unlike the studies of Li et al. (2009); Chaabani (2014), the study of trajectory in response to changes in flight conditions (fin deflection, gusts) has not been studied in this manuscript. Vortex shedding effects have not yet been included in the model and numerical simulations. In addition, the stability analysis of the airship associated with large rotation movements has not yet been performed due to time constraints, although it is possible with the theoretical model of this thesis.

The potential flow model used in this manuscript is adapted to the small angles of incidence of the wind with respect to the airship, which consitutes a limitation of the model. A comparison with more realistic fluid simulations could determine up to which incidence angle the potential flow model remains efficient.

The BEM method has been implemented numerically via MATLAB, which is an interpreted language, less efficient than compiled languages.

Because of the density of the fluid operators as well as the complexity to solve eigenvalue problems of free structures, the numerical approach did not allow to solve the global fluid-structure modes, so the dynamics of the problem was solved after projection according to the airship modes *in vacuo*. The convergence of the fluid-structure modes of the reduced model has not been studied in this work due to time constraints.

It is difficult to know if the fluid-structure modes based on the reduced model are close to the global fluid-structure modes.

For practical reasons, the studied Stokes numbers in chapter V did not reach the orders of magnitude typical of airship operating conditions, not allowing to conclude frankly about the viscous effects on dynamic aeroelasticity using the principle of similarities. Moreover, contrary to the work of Sarpkaya (1977), the experiments performed did not explore the parameter space where the structure interacts with the vortex releases.

VI.2 Perspectives and closing remark

The limitations of the study listed above naturally lead to consider the associated perspectives. These perspectives are listed at the end of each chapter of the manuscript.

The work presented in this manuscript provides a new model to meet the demands of the lighter than air aircraft engineers in terms of aerodynamic characterization of rigid and flexible airships. This study constitutes a step towards less expensive realistic simulations for the growing airship industry.

Appendices

Appendix A

Detailed calculation of the linearization

We detail here how the linearization was performed.

A.1 Linearized Nanson formula

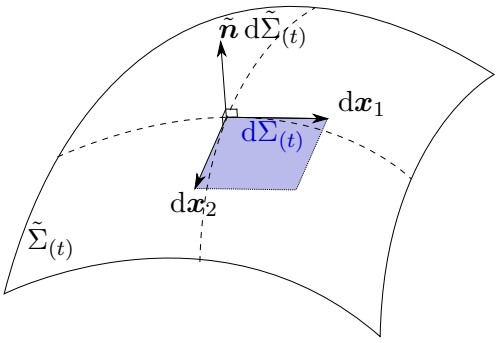

Figure A.1: Scheme of an oriented surface.

In this section, the index $_\mathrm{t}$ will refer to the surface component of a vector, hence for an arbitrary vector :

$$\boldsymbol{a}_\mathrm{t} = (\mathbb{1} - \boldsymbol{n} \otimes \boldsymbol{n})\boldsymbol{a}. \tag{A.1}$$

We define the oriented surface $\tilde{\boldsymbol{n}}\,\mathrm{d}\tilde{\Sigma}_{(t)}$ (see figure A.1) by introducing two arbitrary non colinear vectors $\mathrm{d}\boldsymbol{x}_1$ and $\mathrm{d}\boldsymbol{x}_2$ belonging to the local plane of the surface:

$$\tilde{\boldsymbol{n}}\,\mathrm{d}\tilde{\Sigma}_{(t)} = \mathrm{d}\boldsymbol{x}_1\,(t) \wedge \mathrm{d}\boldsymbol{x}_2\,(t)\,. \tag{A.2}$$

Therefore, for any vector $\boldsymbol{v} \in \mathbb{R}^3$:

$$\tilde{\boldsymbol{n}}\,\mathrm{d}\tilde{\Sigma}_{(t)} \cdot \boldsymbol{v} = [\,\mathrm{d}\boldsymbol{x}_1,\, \mathrm{d}\boldsymbol{x}_2, \boldsymbol{v}], \tag{A.3}$$

the term on the right of the equal sign being a mixed product. It is possible to explain $\mathrm{d}\boldsymbol{x}_1$ and $\mathrm{d}\boldsymbol{x}_2$ from the reference configuration with the deformation gradient $\overline{\mathbb{F}}$:

$$\tilde{\boldsymbol{n}}\,\mathrm{d}\tilde{\Sigma}_{(t)}\cdot\boldsymbol{v}=[\overline{\mathbb{F}}\,\mathrm{d}\bar{\boldsymbol{x}}_1,\overline{\mathbb{F}}\,\mathrm{d}\bar{\boldsymbol{x}}_2,\boldsymbol{v}]. \tag{A.4}$$

Recalling the surface deformation gradient $\overline{\mathbb{F}}_\mathrm{t}$ definition from equation (II.23) and noting that $\mathrm{d}\bar{\boldsymbol{x}}_1$ is tangential to the interface, we have:

$$\begin{aligned}
\overline{\mathbb{F}}\,\mathrm{d}\bar{\boldsymbol{x}}_1 &= \overline{\mathbb{F}}\,\mathrm{d}\bar{\boldsymbol{x}}_{1\mathrm{t}}\\
&= \left(\mathbb{1}+\begin{pmatrix}(\overline{\boldsymbol{\nabla}}\bar{\boldsymbol{\xi}}\cdot\boldsymbol{e}_x)^\mathrm{T}\\(\overline{\boldsymbol{\nabla}}\bar{\boldsymbol{\xi}}\cdot\boldsymbol{e}_y)^\mathrm{T}\\(\overline{\boldsymbol{\nabla}}\bar{\boldsymbol{\xi}}\cdot\boldsymbol{e}_z)^\mathrm{T}\end{pmatrix}\right)\mathrm{d}\bar{\boldsymbol{x}}_{1\mathrm{t}}\\
&= \mathrm{d}\bar{\boldsymbol{x}}_{1\mathrm{t}}+\begin{pmatrix}(\overline{\boldsymbol{\nabla}}\bar{\boldsymbol{\xi}}\cdot\boldsymbol{e}_x)\cdot\mathrm{d}\bar{\boldsymbol{x}}_{1\mathrm{t}}\\(\overline{\boldsymbol{\nabla}}\bar{\boldsymbol{\xi}}\cdot\boldsymbol{e}_y)\cdot\mathrm{d}\bar{\boldsymbol{x}}_{1\mathrm{t}}\\(\overline{\boldsymbol{\nabla}}\bar{\boldsymbol{\xi}}\cdot\boldsymbol{e}_z)\cdot\mathrm{d}\bar{\boldsymbol{x}}_{1\mathrm{t}}\end{pmatrix}\\
&= \mathrm{d}\bar{\boldsymbol{x}}_{1S}+\begin{pmatrix}(\overline{\boldsymbol{\nabla}}_\mathrm{t}\bar{\boldsymbol{\xi}}\cdot\boldsymbol{e}_x)\cdot\mathrm{d}\bar{\boldsymbol{x}}_{1\mathrm{t}}\\(\overline{\boldsymbol{\nabla}}_\mathrm{t}\bar{\boldsymbol{\xi}}\cdot\boldsymbol{e}_y)\cdot\mathrm{d}\bar{\boldsymbol{x}}_{1\mathrm{t}}\\(\overline{\boldsymbol{\nabla}}_\mathrm{t}\bar{\boldsymbol{\xi}}\cdot\boldsymbol{e}_z)\cdot\mathrm{d}\bar{\boldsymbol{x}}_{1\mathrm{t}}\end{pmatrix}\\
&= \overline{\mathbb{F}}_\mathrm{t}\,\mathrm{d}\bar{\boldsymbol{x}}_1,
\end{aligned} \tag{A.5}$$

and the same goes for

$$\overline{\mathbb{F}}\,\mathrm{d}\bar{\boldsymbol{x}}_2=\overline{\mathbb{F}}_\mathrm{t}\,\mathrm{d}\bar{\boldsymbol{x}}_2. \tag{A.6}$$

Combining the above equations, we obtain that

$$\begin{aligned}
\tilde{\boldsymbol{n}}\,\mathrm{d}\tilde{\Sigma}_{(t)}\cdot\boldsymbol{v} &= [\overline{\mathbb{F}}_\mathrm{t}\,\mathrm{d}\bar{\boldsymbol{x}}_1,\overline{\mathbb{F}}_\mathrm{t}\,\mathrm{d}\bar{\boldsymbol{x}}_2,\overline{\mathbb{F}}_\mathrm{t}{\overline{\mathbb{F}}_\mathrm{t}}^{-1}\boldsymbol{v}]\\
&= \det(\overline{\mathbb{F}}_\mathrm{t})[\,\mathrm{d}\bar{\boldsymbol{x}}_1,\,\mathrm{d}\bar{\boldsymbol{x}}_2,\overline{\mathbb{F}}_\mathrm{t}^{-1}\boldsymbol{v}]\\
&= \det(\overline{\mathbb{F}}_\mathrm{t})\bar{\boldsymbol{n}}\,\mathrm{d}\overline{\Sigma}\cdot(\overline{\mathbb{F}}_\mathrm{t}^{-1}\boldsymbol{v})\\
&= \bar{\Phi}_\mathrm{t}^\mathrm{T}\bar{\boldsymbol{n}}\,\mathrm{d}\overline{\Sigma}\cdot\boldsymbol{v},
\end{aligned} \tag{A.7}$$

where

$$\bar{\Phi}_\mathrm{t}=\det(\overline{\mathbb{F}}_\mathrm{t})\overline{\mathbb{F}}_\mathrm{t}^{-1}, \tag{A.8}$$

we can identify from equation (A.7) :

$$\tilde{\boldsymbol{n}}\,\mathrm{d}\tilde{\Sigma}_{(t)}=\bar{\Phi}_\mathrm{t}^\mathrm{T}\bar{\boldsymbol{n}}\,\mathrm{d}\overline{\Sigma}, \tag{A.9}$$

This shows how the small deformations of the interface can be formulated depending solely on the surface gradient of the infinitesimal displacements. Since for infinitesimal displacements, $\overline{\mathbb{F}}_\mathrm{t}$ is invertible with the property $\overline{\mathbb{F}}_\mathrm{t}\overline{\mathbb{F}}_\mathrm{t}^{-1}=\mathbb{1}$, one can get:

$${\overline{\mathbb{F}}_\mathrm{t}}^{-\mathrm{T}}=\mathbb{1}-\varepsilon\overline{\boldsymbol{\nabla}}_\mathrm{t}\bar{\boldsymbol{\xi}}'+\mathcal{O}\left(\varepsilon^2\right), \tag{A.10}$$

The expression (A.9) can be developed at order 1 as follows:

$$\det(\overline{\mathbb{F}}_{\mathrm{t}}) = \det(\mathbb{1} + \overline{\nabla}_{\mathrm{t}}\bar{\boldsymbol{\xi}}) = 1 + \varepsilon \mathrm{tr}\left(\overline{\nabla}_{\mathrm{t}}\bar{\boldsymbol{\xi}}'\right) + \mathcal{O}\left(\varepsilon^2\right) \tag{A.11}$$

$$\tilde{\boldsymbol{n}}\, \mathrm{d}\tilde{\Sigma}_{(t)} = (\mathbb{1} + \varepsilon\left(\mathrm{tr}\left(\overline{\nabla}_{\mathrm{t}}\bar{\boldsymbol{\xi}}'\right) - \overline{\nabla}_{\mathrm{t}}^{\mathrm{T}}\bar{\boldsymbol{\xi}}'\right))\bar{\boldsymbol{n}}\, \mathrm{d}\overline{\Sigma}. \tag{A.12}$$

It is therefore possible to calculate the linearized variation $\bar{\boldsymbol{\tau}}'$ of an oriented surface:

$$\tilde{\boldsymbol{n}}\, \mathrm{d}\tilde{\Sigma}_{(t)} = (\bar{\boldsymbol{n}} + \varepsilon\bar{\boldsymbol{\tau}}')\, \mathrm{d}\overline{\Sigma} + \mathcal{O}\left(\varepsilon^2\right), \tag{A.13}$$

$$\text{with } \bar{\boldsymbol{\tau}}' = \left(\mathrm{tr}\left(\overline{\nabla}_{\mathrm{t}}\bar{\boldsymbol{\xi}}'\right) - \overline{\nabla}_{\mathrm{t}}^{\mathrm{T}}\bar{\boldsymbol{\xi}}'\right)\bar{\boldsymbol{n}}. \tag{A.14}$$

For a further understanding of the above equation, one can isolate the elementary surface dilatation effects. Since the norms of $\boldsymbol{n}$ and $\bar{\boldsymbol{n}}$ are supposed to be unitary:

$$\begin{aligned}
\mathrm{d}\tilde{\Sigma}_{(t)} &= \left\|\tilde{\boldsymbol{n}}\, \mathrm{d}\tilde{\Sigma}_{(t)}\right\| \\
&= \left\|(\bar{\boldsymbol{n}} + \varepsilon\bar{\boldsymbol{\tau}}')\, \mathrm{d}\overline{\Sigma}\right\| + \mathcal{O}\left(\varepsilon^2\right) \\
&= \left\|(\bar{\boldsymbol{n}} + \varepsilon\bar{\boldsymbol{\tau}}')\right\|\, \mathrm{d}\overline{\Sigma} + \mathcal{O}\left(\varepsilon^2\right) \\
&= \left(\|\bar{\boldsymbol{n}}\| + \varepsilon\frac{\bar{\boldsymbol{n}}\cdot\bar{\boldsymbol{\tau}}'}{\|\bar{\boldsymbol{n}}\|}\right)\, \mathrm{d}\overline{\Sigma} + \mathcal{O}\left(\varepsilon^2\right) \\
&= \left(1 + \varepsilon\bar{\boldsymbol{n}}\cdot\left(\mathrm{tr}\left(\overline{\nabla}_{\mathrm{t}}\bar{\boldsymbol{\xi}}'\right) - \overline{\nabla}_{\mathrm{t}}^{\mathrm{T}}\bar{\boldsymbol{\xi}}'\right)\bar{\boldsymbol{n}}\right)\, \mathrm{d}\overline{\Sigma} + \mathcal{O}\left(\varepsilon^2\right).
\end{aligned} \tag{A.15}$$

The term $\mathrm{tr}\left(\overline{\nabla}_{\mathrm{t}}\bar{\boldsymbol{\xi}}'\right)$ is the surface divergence of the displacement $\bar{\boldsymbol{\xi}}'$. From the above equation, one can identify the small surface variations

$$\mathrm{d}\tilde{\Sigma}'_{(t)} = \bar{\boldsymbol{n}}\cdot\left(\mathrm{tr}\left(\overline{\nabla}_{\mathrm{t}}\bar{\boldsymbol{\xi}}'\right) - \overline{\nabla}_{\mathrm{t}}^{\mathrm{T}}\bar{\boldsymbol{\xi}}'\right)\bar{\boldsymbol{n}}\, \mathrm{d}\overline{\Sigma}. \tag{A.16}$$

Moreover, we obtain:

$$\bar{\boldsymbol{n}}\cdot\mathrm{tr}\left(\overline{\nabla}_{\mathrm{t}}\bar{\boldsymbol{\xi}}'\right)\bar{\boldsymbol{n}} = \mathrm{tr}\left(\overline{\nabla}_{\mathrm{t}}\bar{\boldsymbol{\xi}}'\right), \tag{A.17}$$

and

$$\begin{aligned}
\overline{\nabla}_{\mathrm{t}}^{\mathrm{T}}\bar{\boldsymbol{\xi}}'\bar{\boldsymbol{n}} &= \left(\overline{\boldsymbol{\nabla}}_{\mathrm{t}}(\bar{\boldsymbol{\xi}}\cdot\boldsymbol{e}_x), \overline{\boldsymbol{\nabla}}_{\mathrm{t}}(\bar{\boldsymbol{\xi}}\cdot\boldsymbol{e}_y), \overline{\boldsymbol{\nabla}}_{\mathrm{t}}(\bar{\boldsymbol{\xi}}\cdot\boldsymbol{e}_z)\right)\bar{\boldsymbol{n}} \\
&= \bar{\boldsymbol{n}}\cdot\boldsymbol{e}_x\overline{\boldsymbol{\nabla}}_{\mathrm{t}}(\bar{\boldsymbol{\xi}}\cdot\boldsymbol{e}_x) + \bar{\boldsymbol{n}}\cdot\boldsymbol{e}_y\overline{\boldsymbol{\nabla}}_{\mathrm{t}}(\bar{\boldsymbol{\xi}}\cdot\boldsymbol{e}_y) + \bar{\boldsymbol{n}}\cdot\boldsymbol{e}_z\overline{\boldsymbol{\nabla}}_{\mathrm{t}}(\bar{\boldsymbol{\xi}}\cdot\boldsymbol{e}_z).
\end{aligned} \tag{A.18}$$

From the equation above, since $\bar{\boldsymbol{n}}\cdot\overline{\boldsymbol{\nabla}}_{\mathrm{t}}(\bullet) = 0$, we deduce that

$$\bar{\boldsymbol{n}}\cdot\overline{\nabla}_{\mathrm{t}}^{\mathrm{T}}\bar{\boldsymbol{\xi}}'\bar{\boldsymbol{n}} = 0, \tag{A.19}$$

and the variations of the surface can be described only with the surface divergence $\mathrm{tr}\left(\overline{\nabla}_{\mathrm{t}}\bar{\boldsymbol{\xi}}\right)$:

$$\mathrm{d}\tilde{\Sigma}'_{(t)} = \mathrm{tr}\left(\overline{\nabla}_{\mathrm{t}}\bar{\boldsymbol{\xi}}'\right)\, \mathrm{d}\overline{\Sigma}. \tag{A.20}$$

Furthermore, it is possible to isolate the normal rotations, by noting that

$$\tilde{\boldsymbol{n}} = \frac{\boldsymbol{n}\,\mathrm{d}\Sigma_{(t)}}{\mathrm{d}\Sigma_{(t)}} = \frac{(\bar{\boldsymbol{n}} + \varepsilon\bar{\boldsymbol{\tau}}')\,\mathrm{d}\overline{\Sigma}}{\mathrm{d}\overline{\Sigma} + \varepsilon\,\mathrm{d}\tilde{\Sigma}'_{(t)}} + \mathcal{O}\left(\varepsilon^2\right) = \frac{(\bar{\boldsymbol{n}} + \varepsilon\bar{\boldsymbol{\tau}}')\,\mathrm{d}\overline{\Sigma}}{\mathrm{d}\overline{\Sigma}} - \varepsilon\frac{\bar{\boldsymbol{n}}\,\mathrm{d}\overline{\Sigma}}{\mathrm{d}\overline{\Sigma}^2}\,\mathrm{d}\tilde{\Sigma}'_{(t)} + \mathcal{O}\left(\varepsilon^2\right). \tag{A.21}$$

We deduce the linearized normal variations from the equation above:

$$\begin{aligned}\tilde{\boldsymbol{n}}' &= \bar{\boldsymbol{\tau}}' - \frac{\bar{\boldsymbol{n}}}{\mathrm{d}\overline{\Sigma}}\,\mathrm{d}\tilde{\Sigma}'_{(t)} \\ &= \left(\mathrm{tr}\left(\overline{\nabla}_{\mathrm{t}}\bar{\boldsymbol{\xi}}'\right) - \overline{\nabla}_{\mathrm{t}}^{\mathrm{T}}\bar{\boldsymbol{\xi}}'\right)\bar{\boldsymbol{n}} - \mathrm{tr}\left(\overline{\nabla}_{\mathrm{t}}\bar{\boldsymbol{\xi}}'\right)\bar{\boldsymbol{n}}.\end{aligned} \tag{A.22}$$

The surface divergence cancels out in the above equation, giving the order 1 rotation of the normal:

$$\tilde{\boldsymbol{n}}' = -\left[\overline{\nabla}_{\mathrm{t}}^{\mathrm{T}}\bar{\boldsymbol{\xi}}'\right]\bar{\boldsymbol{n}}. \tag{A.23}$$

It is noticeable that $\overline{\nabla}_{\mathrm{t}}^{\mathrm{T}}\bar{\boldsymbol{\xi}}'\bar{\boldsymbol{n}} \perp \bar{\boldsymbol{n}}$ because of equation (A.19), which is an expected property for the infinitesimal rotation of a unit vector. By doing the calculation of $(\bar{\boldsymbol{n}} + \varepsilon\tilde{\boldsymbol{n}}') \cdot (\bar{\boldsymbol{n}} + \varepsilon\tilde{\boldsymbol{n}}')$, it is possible to demonstrate the property $\|\bar{\boldsymbol{n}} + \varepsilon\tilde{\boldsymbol{n}}'\| = 1 + \mathcal{O}\left(\varepsilon^2\right)$.

A.2 Linearized Green's function

The order 1 Taylor expansion of the norm of a vector $\boldsymbol{a}$ at an arbitrary power n is:

$$\left\|\boldsymbol{a}^o + \varepsilon\boldsymbol{a}'\right\|^n = \|\boldsymbol{a}^o\|^n + \varepsilon\boldsymbol{a}^o \cdot \boldsymbol{a}'\,\|\boldsymbol{a}^o\|^{n-2} + \mathcal{O}\left(\varepsilon^2\right), \tag{A.24}$$

allowing to calculate the following formula:

$$\|\boldsymbol{x} - \boldsymbol{y}\|^n = \|\tilde{\boldsymbol{x}} - \tilde{\boldsymbol{y}}\| = \|\bar{\boldsymbol{x}} - \bar{\boldsymbol{y}}\|^n + n(\bar{\boldsymbol{x}} - \bar{\boldsymbol{y}}) \cdot \left(\bar{\boldsymbol{\xi}}'(\bar{\boldsymbol{x}}) - \bar{\boldsymbol{\xi}}'(\bar{\boldsymbol{y}})\right)\|\bar{\boldsymbol{x}} - \bar{\boldsymbol{y}}\|^{n-2} + \mathcal{O}\left(\varepsilon^2\right) \quad \text{for } \bar{\boldsymbol{x}}, \bar{\boldsymbol{y}} \quad \text{on } \overline{\Sigma}. \tag{A.25}$$

The Green's function given by (I.49) and its gradient becomes, when combined with the linearized expression (A.25):

$$\overline{\boldsymbol{G}_{\boldsymbol{n}}}^{\,o} = -\frac{1}{4\pi}\frac{\bar{\boldsymbol{n}}}{\|\bar{\boldsymbol{x}} - \bar{\boldsymbol{y}}\|} \tag{A.26a}$$

$$\overline{\boldsymbol{G}_{\boldsymbol{n}}}^{\,\prime} = \frac{1}{4\pi}\left(\frac{(\bar{\boldsymbol{x}} - \bar{\boldsymbol{y}}) \cdot \left(\bar{\boldsymbol{\xi}}'(\bar{\boldsymbol{x}}) - \bar{\boldsymbol{\xi}}'(\bar{\boldsymbol{y}})\right)\bar{\boldsymbol{n}}}{\|\bar{\boldsymbol{x}} - \bar{\boldsymbol{y}}\|^3} - \frac{\bar{\boldsymbol{\tau}}'}{\|\bar{\boldsymbol{x}} - \bar{\boldsymbol{y}}\|}\right) \tag{A.26b}$$

$$\overline{\partial_n G}^{\,o} = \frac{1}{4\pi}\frac{(\bar{\boldsymbol{x}} - \bar{\boldsymbol{y}}) \cdot \bar{\boldsymbol{n}}}{\|\bar{\boldsymbol{x}} - \bar{\boldsymbol{y}}\|^3} \tag{A.26c}$$

$$\overline{\partial_n G}^{\,\prime} = \frac{1}{4\pi}\left(\frac{(\bar{\boldsymbol{x}} - \bar{\boldsymbol{y}}) \cdot \bar{\boldsymbol{\tau}}'}{\|\boldsymbol{x} - \boldsymbol{y}\|^3} + \frac{\left(\bar{\boldsymbol{\xi}}'(\bar{\boldsymbol{x}}) - \bar{\boldsymbol{\xi}}'(\bar{\boldsymbol{y}})\right) \cdot \bar{\boldsymbol{n}}}{\|\bar{\boldsymbol{x}} - \bar{\boldsymbol{y}}\|^3}\right. \tag{A.26d}$$

$$\left. - 3\frac{(\bar{\boldsymbol{x}} - \bar{\boldsymbol{y}}) \cdot \left(\bar{\boldsymbol{\xi}}'(\bar{\boldsymbol{x}}) - \bar{\boldsymbol{\xi}}'(\bar{\boldsymbol{y}})\right)(\bar{\boldsymbol{x}} - \bar{\boldsymbol{y}}) \cdot \bar{\boldsymbol{n}}}{\|\bar{\boldsymbol{x}} - \bar{\boldsymbol{y}}\|^5}\right). \tag{A.26e}$$

A.3 Linearized flow velocity

In order to express the linear variations of the flow velocity at order ε on the interface, recalling that

$$\boldsymbol{u} = \boldsymbol{\nabla}\phi = \frac{\partial \phi}{\partial \boldsymbol{x}}, \tag{A.27}$$

one can express on the reference interface with the chain rule:

$$\begin{aligned} \bar{\boldsymbol{u}} &= \frac{\partial \bar{\boldsymbol{x}}}{\partial \boldsymbol{x}} \frac{\partial \bar{\phi}}{\partial \bar{\boldsymbol{x}}} \\ &= \left(\frac{\partial \boldsymbol{x}}{\partial \bar{\boldsymbol{x}}} \right)^{-\mathrm{T}} \overline{\boldsymbol{\nabla}} \bar{\phi} \\ &= (\mathbb{1} + \overline{\nabla} \bar{\boldsymbol{\xi}})^{-\mathrm{T}} \overline{\boldsymbol{\nabla}} \bar{\phi}. \end{aligned} \tag{A.28}$$

The linearized inversion of the terms in the parentheses of the above equation enables to write at both orders of magnitude 1 and ε:

$$\bar{\boldsymbol{u}} = \overline{\boldsymbol{\nabla}} \bar{\phi}^o + \varepsilon \left(\overline{\boldsymbol{\nabla}} \bar{\phi}' - \left[\overline{\nabla}^{\mathrm{T}} \bar{\boldsymbol{\xi}}' \right] \overline{\boldsymbol{\nabla}} \bar{\phi}^o \right) + \mathcal{O}\left(\varepsilon^2\right). \tag{A.29}$$

In order to obtain a formulation that depends on the surface gradient instead of the total gradient, the surface and normal components of the velocity are expressed. For the order zero velocity, the expression from (II.64) comes by using the boundary condition (I.35) at order zero on the reference interface:

$$\overline{\boldsymbol{\nabla}} \bar{\phi}^o \cdot \bar{\boldsymbol{n}} = \bar{\boldsymbol{v}}^o . \bar{\boldsymbol{n}}, \tag{A.30}$$

The expression of the surface velocity at order one is calculated as:

$$\bar{\boldsymbol{u}}'_{\mathrm{t}} = \overline{\boldsymbol{\nabla}}_{\mathrm{t}} \bar{\phi}' - \left(\overline{\nabla}^{\mathrm{T}} \bar{\boldsymbol{\xi}}' \bar{\boldsymbol{u}}^o \right)_{\mathrm{t}} \quad \text{on } \overline{\Sigma}. \tag{A.31}$$

By developing the term on the right of the above equation:

$$\begin{aligned} \overline{\nabla}^{\mathrm{T}} \bar{\boldsymbol{\xi}}' \bar{\boldsymbol{u}}^o &= \left(\overline{\boldsymbol{\nabla}}(\bar{\boldsymbol{\xi}}' \cdot \boldsymbol{e}_x), \overline{\boldsymbol{\nabla}}(\bar{\boldsymbol{\xi}}' \cdot \boldsymbol{e}_y), \overline{\boldsymbol{\nabla}}(\bar{\boldsymbol{\xi}}' \cdot \boldsymbol{e}_z) \right) \bar{\boldsymbol{u}}^o \\ &= \left(\overline{\boldsymbol{\nabla}}(\bar{\boldsymbol{\xi}}' \cdot \boldsymbol{e}_x) \right) (\bar{\boldsymbol{u}}^o \cdot \boldsymbol{e}_x) + \left(\overline{\boldsymbol{\nabla}}(\bar{\boldsymbol{\xi}}' \cdot \boldsymbol{e}_y) \right) (\bar{\boldsymbol{u}}^o \cdot \boldsymbol{e}_y) + \left(\overline{\boldsymbol{\nabla}}(\bar{\boldsymbol{\xi}}' \cdot \boldsymbol{e}_z) \right) (\bar{\boldsymbol{u}}^o \cdot \boldsymbol{e}_z). \end{aligned} \tag{A.32}$$

From the above equation can be deduced

$$\begin{aligned} (\overline{\nabla}^{\mathrm{T}} \bar{\boldsymbol{\xi}}' \bar{\boldsymbol{u}}^o)_{\mathrm{t}} &= \left(\overline{\boldsymbol{\nabla}}_{\mathrm{t}}(\bar{\boldsymbol{\xi}}' \cdot \boldsymbol{e}_x) \right) (\bar{\boldsymbol{u}}^o \cdot \boldsymbol{e}_x) + \left(\overline{\boldsymbol{\nabla}}_{\mathrm{t}}(\bar{\boldsymbol{\xi}}' \cdot \boldsymbol{e}_y) \right) (\bar{\boldsymbol{u}}^o \cdot \boldsymbol{e}_y) + \left(\overline{\boldsymbol{\nabla}}_{\mathrm{t}}(\bar{\boldsymbol{\xi}}' \cdot \boldsymbol{e}_z) \right) (\bar{\boldsymbol{u}}^o \cdot \boldsymbol{e}_z) \\ &= \overline{\nabla}_{\mathrm{t}}^{\mathrm{T}} \bar{\boldsymbol{\xi}}' \bar{\boldsymbol{u}}^o \quad \text{on } \overline{\Sigma}. \end{aligned} \tag{A.33}$$

By combining equations (A.31) and (A.33), one obtains the result from equation (II.65c). With a view to express the normal veocity at order one, the boundary condition (I.20) is developped at first order, recalling the expression from the normal fluctuations from (A.23):

$$\bar{\boldsymbol{u}}' \cdot \bar{\boldsymbol{n}} + \bar{\boldsymbol{u}}^o \cdot (-\overline{\nabla}_{\mathrm{t}}^{\mathrm{T}} \bar{\boldsymbol{\xi}}') \bar{\boldsymbol{n}} = \bar{\boldsymbol{v}}' \cdot \bar{\boldsymbol{n}} - \bar{\boldsymbol{v}}^o \cdot (\overline{\nabla}_{\mathrm{t}}^{\mathrm{T}} \bar{\boldsymbol{\xi}}') \bar{\boldsymbol{n}}. \tag{A.34}$$

By rearraging the terms from the equation above, the normal velocity perturbations from equation (II.65b) are obtained.

A.4 Skew-symmetry of the rotation operator perturbations

In order to show the skew-symmetry of $\mathbb{R}'\mathbb{R}^{o\mathrm{T}}$, the property $\mathbb{R}^{-1} = \mathbb{R}^{\mathrm{T}}$ of the operators is used. The first order developpment of $\mathbb{R}^{-1}$ is:

$$\mathbb{R}^{-1} = \mathbb{R}^{o-1} - \varepsilon \mathbb{R}^{o-1} \mathbb{R}' \mathbb{R}^{o-1} + \mathcal{O}\left(\varepsilon^2\right), \tag{A.35}$$

a property that can be verified by developing the product

$$(\mathbb{R}^{o-1} - \varepsilon \mathbb{R}^{o-1} \mathbb{R}' \mathbb{R}^{o-1})(\mathbb{R}^o + \varepsilon \mathbb{R}') = \mathbb{1} + \mathcal{O}\left(\varepsilon^2\right).$$

Noting that, to the contrary of $\mathbb{R}'$ which is the perturbation of a rotation operator, $\mathbb{R}^o$ is a rotation operator, we have the property $\mathbb{R}^{o-1} = \mathbb{R}^{o\mathrm{T}}$, hence:

$$\mathbb{R}^{-1} = \mathbb{R}^{o\mathrm{T}} - \varepsilon \mathbb{R}^{o\mathrm{T}} \mathbb{R}' \mathbb{R}^{o\mathrm{T}} + \mathcal{O}\left(\varepsilon^2\right). \tag{A.36}$$

Therefore, the property of the rotation operators leads to the condition:

$$\begin{aligned}
&\mathbb{R}^{-1} = \mathbb{R}^{\mathrm{T}} \\
\Leftrightarrow &\mathbb{R}^{o\mathrm{T}} - \varepsilon \mathbb{R}^{o\mathrm{T}} \mathbb{R}' \mathbb{R}^{o\mathrm{T}} + \mathcal{O}\left(\varepsilon^2\right) = \mathbb{R}^{o\mathrm{T}} + \varepsilon \mathbb{R}'^{\mathrm{T}} \\
\Rightarrow &- \mathbb{R}^{o\mathrm{T}} \mathbb{R}' \mathbb{R}^{o\mathrm{T}} + \mathcal{O}\left(\varepsilon^2\right) = \mathbb{R}'^{\mathrm{T}} \\
\Rightarrow &\mathbb{R}' \mathbb{R}^{o\mathrm{T}} = -\mathbb{R}^o \mathbb{R}'^{\mathrm{T}} \\
\Rightarrow &\mathbb{R}' \mathbb{R}^{o\mathrm{T}} = -\left(\mathbb{R}' \mathbb{R}^{o\mathrm{T}}\right)^{\mathrm{T}}.
\end{aligned} \tag{A.37}$$

The last line of the equation above shows that the perturbation $\mathbb{R}'\mathbb{R}^{o\mathrm{T}}$ is skew symmetric.

A.5 Linear perturbations of the double layer term on a triangle

This section aims to show how, for triangular elements, the double layer perturbations (see equation (A.26d)) vanish for two points $\bar{\boldsymbol{y}}$ and $\bar{\boldsymbol{y}}$ in the same triangle:

$$\overline{\partial_n G}' = \frac{1}{4\pi} \left(\frac{(\bar{\boldsymbol{x}} - \bar{\boldsymbol{y}}) \cdot \bar{\boldsymbol{\tau}}'}{\|\boldsymbol{x} - \boldsymbol{y}\|^3} + \frac{\left(\bar{\boldsymbol{\xi}}'(\bar{\boldsymbol{x}}) - \bar{\boldsymbol{\xi}}'(\bar{\boldsymbol{y}})\right) \cdot \bar{\boldsymbol{n}}}{\|\bar{\boldsymbol{x}} - \bar{\boldsymbol{y}}\|^3} - 3 \frac{(\bar{\boldsymbol{x}} - \bar{\boldsymbol{y}}) \cdot \left(\bar{\boldsymbol{\xi}}'(\bar{\boldsymbol{x}}) - \bar{\boldsymbol{\xi}}'(\bar{\boldsymbol{y}})\right) (\bar{\boldsymbol{x}} - \bar{\boldsymbol{y}}) \cdot \bar{\boldsymbol{n}}}{\|\bar{\boldsymbol{x}} - \bar{\boldsymbol{y}}\|^5} \right).$$

The most right term on the above equation vanishes since it has already been demonstrated that $(\bar{\boldsymbol{x}} - \bar{\boldsymbol{y}}) \cdot \bar{\boldsymbol{n}} = \boldsymbol{0}$ for $\bar{\boldsymbol{x}}$ and $\bar{\boldsymbol{y}}$ in the same triangle. The term on the left of the right hand side can be rewritten by combining with (A.23) and (A.13)

$$(\bar{\boldsymbol{x}} - \bar{\boldsymbol{y}}) \cdot \bar{\boldsymbol{\tau}}' = tr(\overline{\nabla}_{\mathrm{t}} \bar{\boldsymbol{\xi}}')(\bar{\boldsymbol{x}} - \bar{\boldsymbol{y}}) \cdot \bar{\boldsymbol{n}} - (\bar{\boldsymbol{x}} - \bar{\boldsymbol{y}}) \cdot (\overline{\nabla}_{\mathrm{t}}^{\mathrm{T}} \bar{\boldsymbol{\xi}}' \bar{\boldsymbol{n}}). \tag{A.38}$$

For the same reason mentioned just previously, the term $(\bar{\boldsymbol{x}} - \bar{\boldsymbol{y}}) \cdot \bar{\boldsymbol{n}}$ vanishes. Consequently, a first simplified expression of the double layer perturbations is obtained:

$$\overline{\partial_n G}' = \frac{1}{4\pi \left\| \bar{\boldsymbol{x}} - \bar{\boldsymbol{y}} \right\|^3} \left(-(\bar{\boldsymbol{x}} - \bar{\boldsymbol{y}}) \cdot \left(\overline{\nabla}_{\mathrm{t}}^{\mathrm{T}} \bar{\boldsymbol{\xi}}' \bar{\boldsymbol{n}} \right) + \left(\bar{\boldsymbol{\xi}}'(\bar{\boldsymbol{x}}) - \bar{\boldsymbol{\xi}}'(\bar{\boldsymbol{y}}) \right) \cdot \bar{\boldsymbol{n}} \right) \quad \text{for } \bar{\boldsymbol{x}}, \bar{\boldsymbol{y}} \text{ in the same triangle.} \tag{A.39}$$

The deformation fluctuation $\bar{\boldsymbol{\xi}}'(\bar{\boldsymbol{x}}) - \bar{\boldsymbol{\xi}}'(\bar{\boldsymbol{y}})$ can be expressed using the surface gradient of the deformations, which is homogeneous over the triangle for linear deformations:

$$\bar{\boldsymbol{\xi}}'(\bar{\boldsymbol{x}}) - \bar{\boldsymbol{\xi}}'(\bar{\boldsymbol{y}}) = \overline{\nabla}_{\mathrm{t}} \bar{\boldsymbol{\xi}}'(\bar{\boldsymbol{x}} - \bar{\boldsymbol{y}}) \quad \text{for } \bar{\boldsymbol{x}}, \bar{\boldsymbol{y}} \text{ in the same triangle.} \tag{A.40}$$

The equality above is only verified because the deformations are linear over the triangle. The scalar product has the following property:

$$\mathbb{A}\boldsymbol{a} \cdot \boldsymbol{b} = \boldsymbol{a} \cdot (\mathbb{A}^{\mathrm{T}} \boldsymbol{b}) \quad \forall \boldsymbol{a}, \boldsymbol{b} \in \mathbb{R}^3, \mathbb{A} \in \mathbb{R}^3 \otimes \mathbb{R}^3. \tag{A.41}$$

As a consequence, the term on the right of equation (A.39) can be expressed under a new form by combining equations (A.40) and (A.41):

$$\left(\bar{\boldsymbol{\xi}}'(\bar{\boldsymbol{x}}) - \bar{\boldsymbol{\xi}}'(\bar{\boldsymbol{y}}) \right) \cdot \bar{\boldsymbol{n}} = \overline{\nabla}_{\mathrm{t}} \bar{\boldsymbol{\xi}}'(\bar{\boldsymbol{x}} - \bar{\boldsymbol{y}}) \cdot \bar{\boldsymbol{n}} = (\bar{\boldsymbol{x}} - \bar{\boldsymbol{y}}) \cdot \left(\overline{\nabla}_{\mathrm{t}}^{\mathrm{T}} \bar{\boldsymbol{\xi}}' \bar{\boldsymbol{n}} \right) \quad \text{for } \bar{\boldsymbol{x}}, \bar{\boldsymbol{y}} \text{ in the same triangle.} \tag{A.42}$$

Thus, by combining equations (A.39) and (A.42), the double layer term perturbations vanishes:

$$\overline{\partial_n G}' = 0 \quad \text{for } \bar{\boldsymbol{x}}, \bar{\boldsymbol{y}} \text{ in the same triangle.} \tag{A.43}$$

Appendix B

Linearized fluid loads using Lagrange's equations

In this section, we consider the case of a zero order translation of the structure $\bar{\boldsymbol{v}}_{\mathrm{c}}^{o}$ with no rotations $\bar{\boldsymbol{\omega}}^{o} = \mathbf{0}$. The surrounding flow is supposed to be potential as in chapter II. In order to focus on a reasonably simple case study, gravity effects are neglected, and only the elastic perturbations $\bar{\boldsymbol{\xi}}'$: the rigid-body perturbations are supposed to be nil $\bar{\boldsymbol{v}}' = \mathbf{0}$ and $\bar{\boldsymbol{\omega}}' = \mathbf{0}$. Moreover, only the forces acting on the elastic movements are considered. For an example of application of the Lagrange equations to rigid-body motions and forces, see (Thomasson and Woolsey, 2013). Moreover, in order to keep the study case simple, only the external problem ($\mathcal{P}_{\mathrm{ext}}$) is considered, but the calculations could be extended to the internal gas problem in order to demonstrate the symmetry properties of the associated added mass operator.

In this section, the kinematic equations of the fluid ($\mathcal{F}_{\mathcal{K}}$) are solved using the BEM as proposed in this work, but could be based on any other method used to calculate the velocity potential ϕ (e.g FEM or analytical). However, the efforts associated with the kinematic solution are obtained using the Lagrange equations. Instead of calculating the fluid forces on the interface via the local Euler equation for the conservation of momentum (I.19), the minimization of the global energy of the fluid is used. First, we express the kinetic energy of the fluid (Darrozès and François, 1982)

$$\mathcal{L} = \frac{1}{2}\int_{\Omega_{f(t)}} \boldsymbol{u}^2 \,\mathrm{d}\Omega = \frac{1}{2}\int_{\Omega_{f(t)}} \boldsymbol{\nabla}\phi \cdot \boldsymbol{\nabla}\phi \,\mathrm{d}\Omega. \tag{B.1}$$

We use the following vector calculus identity, combined with the incompressibility condition (I.34):

$$\boldsymbol{\nabla} \cdot (\phi \boldsymbol{\nabla}\phi) = \boldsymbol{\nabla}\phi \cdot \boldsymbol{\nabla}\phi + \phi\Delta\phi = \boldsymbol{\nabla}\phi \cdot \boldsymbol{\nabla}\phi. \tag{B.2}$$

The integrand of the kinetic energy expression can therefore be expressed as the gradient of a scalar, enabling to use the divergence theorem:

$$\begin{aligned} \mathcal{L} &= \frac{1}{2}\int_{\Omega_{f(t)}} \boldsymbol{\nabla} \cdot (\phi \boldsymbol{\nabla}\phi) \,\mathrm{d}\Omega \\ &= \frac{1}{2}\int_{\Sigma_{(t)} \cup \partial\Omega_{\infty}} \phi \boldsymbol{\nabla}\phi \cdot \boldsymbol{n} \,\mathrm{d}\Sigma. \end{aligned} \tag{B.3}$$

Recalling how the potential and its gradient vanish at infinity in $\mathcal{O}(r^-1)$ and $\mathcal{O}(r^-2)$ respectively (Folland, 2020), the terms at infinity in the expression above vanish. Consequently, the energy above can be written by replacing the gradient of the velocity potential by the velocity:

$$\mathcal{L} = \frac{1}{2}\int_{\Sigma_{(t)}} \phi \boldsymbol{v}\cdot\boldsymbol{n}\,\mathrm{d}\Sigma \tag{B.4}$$

$$= \frac{1}{2}\int_{\overline{\Sigma}} \bar{\phi}\bar{\boldsymbol{v}}\cdot(\bar{\Phi}_{\mathrm{t}}^{\mathrm{T}}\bar{\boldsymbol{n}})\,\mathrm{d}\overline{\Sigma}. \tag{B.5}$$

As will become clear later, in order to linearize the Lagrangian equations it is necessary to predict the energy fluctuations at the second order. In order to do so, the three terms in the integral above have to be developed to zero, first and second order: $\bar{\phi}$, $\bar{\boldsymbol{v}}$ and $\bar{\Phi}_{\mathrm{t}}^{\mathrm{T}}$. The development of $\bar{\boldsymbol{v}}$ arises naturally from the hypothesis of zero order translation velocity combined with elastic perturbations:

$$\bar{\boldsymbol{v}} = \bar{\boldsymbol{v}}^o + \varepsilon\bar{\boldsymbol{\xi}}'. \tag{B.6}$$

There are no second order terms in the equation above because of how the zero and first order contributions have been introduced in chapter II. The deformation operator is developed using a Taylor expansion:

$$\bar{\Phi}_{\mathrm{t}}^{\mathrm{T}}\bar{\boldsymbol{n}} = \bar{\boldsymbol{n}} + \varepsilon\frac{\partial\bar{\Phi}_{\mathrm{t}}^{\mathrm{T}}\bar{\boldsymbol{n}}}{\partial\bar{\boldsymbol{\xi}}}\bar{\boldsymbol{\xi}}' + \frac{1}{2}\varepsilon^2\bar{\boldsymbol{\xi}}'^{\mathrm{T}}\frac{\partial^2\bar{\Phi}_{\mathrm{t}}^{\mathrm{T}}\bar{\boldsymbol{n}}}{\partial\bar{\boldsymbol{\xi}}^2}\bar{\boldsymbol{\xi}}' + \mathcal{O}\left(\varepsilon^3\right). \tag{B.7}$$

Similarly, the velocity potential might be developed with respect to both the displacements and the velocity:

$$\bar{\phi} = \bar{\phi}^o + \varepsilon\left(\frac{\partial\bar{\phi}}{\partial\bar{\boldsymbol{\xi}}}\bar{\boldsymbol{\xi}}' + \frac{\partial\bar{\phi}}{\partial\dot{\bar{\boldsymbol{\xi}}}}\dot{\bar{\boldsymbol{\xi}}}'\right) + \frac{1}{2}\varepsilon^2\left(\bar{\boldsymbol{\xi}}'^{\mathrm{T}}\frac{\partial^2\bar{\phi}}{\partial\bar{\boldsymbol{\xi}}^2}\bar{\boldsymbol{\xi}}' + \bar{\boldsymbol{\xi}}'^{\mathrm{T}}\frac{\partial^2\bar{\phi}}{\partial\bar{\boldsymbol{\xi}}\partial\dot{\bar{\boldsymbol{\xi}}}}\dot{\bar{\boldsymbol{\xi}}}'\right) + \mathcal{O}\left(\varepsilon^3\right). \tag{B.8}$$

In the equation above, there is no quadratic dependency of the potential $\bar{\phi}$ with respect to the velocity $\dot{\bar{\boldsymbol{\xi}}}'$ since the velocity potential is linear with respect to the interface velocity.

Remark

Using the equations above at order one, we expect to obtain coherent results with chapter II:

$$\left(\frac{\partial\bar{\Phi}_{\mathrm{t}}^{\mathrm{T}}\bar{\boldsymbol{n}}}{\partial\bar{\boldsymbol{\xi}}}\bar{\boldsymbol{\xi}}'\right)\bar{\boldsymbol{n}} = \bar{\boldsymbol{\tau}}'$$

$$\frac{\partial\bar{\phi}}{\partial\bar{\boldsymbol{\xi}}}\bar{\boldsymbol{\xi}}' = \Phi_d\left(\bar{\boldsymbol{\xi}}'\right)$$

$$\frac{\partial\bar{\phi}}{\partial\dot{\bar{\boldsymbol{\xi}}}}\dot{\bar{\boldsymbol{\xi}}}' = \Phi_d\left(\dot{\bar{\boldsymbol{\xi}}}'\right).$$

As a consequence, the kinetic energy can be developed as follows:

$$\mathcal{L} = \mathcal{L}^o + \varepsilon\mathcal{L}' + \frac{1}{2}\varepsilon^2\mathcal{L}'' \tag{B.9}$$

$$\mathcal{L}^o = \frac{1}{2}\int_{\overline{\Sigma}} \bar{\phi}^o \bar{\boldsymbol{v}}^o \cdot \bar{\boldsymbol{n}}\, \mathrm{d}\overline{\Sigma} \tag{B.10}$$

$$\mathcal{L}' = \frac{1}{2}\int_{\overline{\Sigma}} \left(\frac{\partial\bar{\phi}}{\partial\bar{\boldsymbol{\xi}}}\bar{\boldsymbol{\xi}}' + \frac{\partial\bar{\phi}}{\partial\dot{\bar{\boldsymbol{\xi}}}}\dot{\bar{\boldsymbol{\xi}}}'\right)\bar{\boldsymbol{v}}^o \cdot \bar{\boldsymbol{n}} + \bar{\phi}^o\dot{\bar{\boldsymbol{\xi}}}' \cdot \bar{\boldsymbol{n}} + \bar{\phi}^o\bar{\boldsymbol{v}}^o \cdot \frac{\partial\bar{\Phi}_{\mathrm{t}}^{\mathrm{T}}\bar{\boldsymbol{n}}}{\partial\bar{\boldsymbol{\xi}}}\bar{\boldsymbol{\xi}}'\, \mathrm{d}\overline{\Sigma} \tag{B.11}$$

$$\begin{aligned}\mathcal{L}'' = &\int_{\overline{\Sigma}} \bar{\boldsymbol{\xi}}'^{\mathrm{T}}\left(\frac{\partial^2\bar{\phi}}{\partial\bar{\boldsymbol{\xi}}^2}\bar{\boldsymbol{\xi}}' + \frac{\partial^2\bar{\phi}}{\partial\bar{\boldsymbol{\xi}}\partial\dot{\bar{\boldsymbol{\xi}}}}\dot{\bar{\boldsymbol{\xi}}}'\right)\bar{\boldsymbol{v}}^o \cdot \bar{\boldsymbol{n}}... \\ &+ \left(\frac{\partial\bar{\phi}}{\partial\bar{\boldsymbol{\xi}}}\bar{\boldsymbol{\xi}}' + \frac{\partial\bar{\phi}}{\partial\dot{\bar{\boldsymbol{\xi}}}}\dot{\bar{\boldsymbol{\xi}}}'\right)\left(\bar{\boldsymbol{v}}^o \cdot \frac{\partial\bar{\Phi}_{\mathrm{t}}^{\mathrm{T}}\bar{\boldsymbol{n}}}{\partial\bar{\boldsymbol{\xi}}}\bar{\boldsymbol{\xi}}' + \dot{\bar{\boldsymbol{\xi}}}' \cdot \bar{\boldsymbol{n}}\right) + \bar{\phi}^o\bar{\boldsymbol{v}}^o \cdot \bar{\boldsymbol{\xi}}'^{\mathrm{T}}\frac{\partial^2\bar{\Phi}_{\mathrm{t}}^{\mathrm{T}}\bar{\boldsymbol{n}}}{\partial\bar{\boldsymbol{\xi}}^2}\bar{\boldsymbol{\xi}}'\, \mathrm{d}\overline{\Sigma}.\end{aligned} \tag{B.12}$$

In order to simplify the expression of the second order fluctuations, the tensors $\mathbb{L}_k$, $\mathbb{L}_g$ and $\mathbb{L}_m$ are introduced, noting that $\bar{\boldsymbol{v}}^o \cdot \bar{\boldsymbol{n}} = \bar{\boldsymbol{v}}^{o\mathrm{T}}\bar{\boldsymbol{n}}$:

$$\mathcal{L}'' = \bar{\boldsymbol{\xi}}'^{\mathrm{T}}\mathbb{L}_k\bar{\boldsymbol{\xi}}' + \bar{\boldsymbol{\xi}}'^{\mathrm{T}}\mathbb{L}_g\dot{\bar{\boldsymbol{\xi}}}' + \dot{\bar{\boldsymbol{\xi}}}'^{\mathrm{T}}\mathbb{L}_m\dot{\bar{\boldsymbol{\xi}}}' \tag{B.13}$$

$$\mathbb{L}_k = \frac{1}{2}\int_{\overline{\Sigma}} \frac{\partial^2\bar{\phi}}{\partial\bar{\boldsymbol{\xi}}^2} + \left(\frac{\partial\bar{\phi}}{\partial\bar{\boldsymbol{\xi}}}\right)^{\mathrm{T}}\bar{\boldsymbol{v}}^{o\mathrm{T}}\frac{\partial\bar{\Phi}_{\mathrm{t}}\bar{\boldsymbol{n}}}{\partial\bar{\boldsymbol{\xi}}} + \bar{\phi}^o\frac{\partial^2}{\partial\bar{\boldsymbol{\xi}}^2}\left(\bar{\Phi}_{\mathrm{t}}^{\mathrm{T}}\bar{\boldsymbol{n}} \cdot \bar{\boldsymbol{v}}^o\right)\, \mathrm{d}\overline{\Sigma} \tag{B.14}$$

$$\mathbb{L}_g = \frac{1}{2}\int_{\overline{\Sigma}} \frac{\partial^2\bar{\phi}}{\partial\bar{\boldsymbol{\xi}}\partial\dot{\bar{\boldsymbol{\xi}}}}\bar{\boldsymbol{v}}^o \cdot \bar{\boldsymbol{n}} + \frac{\partial\bar{\phi}}{\partial\bar{\boldsymbol{\xi}}}^{\mathrm{T}}\bar{\boldsymbol{n}}^{\mathrm{T}} + \frac{\partial\bar{\Phi}_{\mathrm{t}}}{\partial\bar{\boldsymbol{\xi}}} \cdot \bar{\boldsymbol{v}}^o\frac{\partial\bar{\phi}}{\partial\dot{\bar{\boldsymbol{\xi}}}}\, \mathrm{d}\overline{\Sigma} \tag{B.15}$$

$$\mathbb{L}_m = \frac{1}{2}\int_{\overline{\Sigma}} \bar{\boldsymbol{n}}\frac{\partial\bar{\phi}}{\partial\dot{\bar{\boldsymbol{\xi}}}}\, \mathrm{d}\overline{\Sigma}. \tag{B.16}$$

The Lagrange equation allows to find the force F associated with a given displacement and its time derivatives with the following expression:

$$F = \delta\mathcal{P}_f(\delta\dot{\bar{\boldsymbol{\xi}}} = \bar{\boldsymbol{\xi}}) = \frac{\partial\mathcal{L}}{\partial\bar{\boldsymbol{\xi}}} - \frac{\mathrm{d}}{\mathrm{d}t}\frac{\partial\mathcal{L}}{\partial\dot{\bar{\boldsymbol{\xi}}}} = \frac{1}{\varepsilon}\left(\frac{\partial\mathcal{L}}{\partial\bar{\boldsymbol{\xi}}'} - \frac{\mathrm{d}}{\mathrm{d}t}\frac{\partial\mathcal{L}}{\partial\dot{\bar{\boldsymbol{\xi}}}'}\right). \tag{B.17}$$

Because of the factor ε^{-1} in front of the expression above, the need for second order derivatives of the energy in order to calculate the first order fluctuations of the force arises: the force has one less order of magnitude than the energy. This is a drawback of the linearized Lagrange equations as the second order derivatives of the potential from equation (B.8) are much harder to obtain than the first order derivatives which are required with the Newton formulation from chapter II. In order to calculate the force at order zero, one need to calculate the following derivatives:

$$\frac{\partial\mathcal{L}'}{\partial\bar{\boldsymbol{\xi}}} = \frac{1}{2}\int_{\overline{\Sigma}} \frac{\partial\bar{\phi}}{\partial\bar{\boldsymbol{\xi}}}\bar{\boldsymbol{v}}^o \cdot \bar{\boldsymbol{n}} + \bar{\phi}^o\bar{\boldsymbol{v}}^o \cdot \left(\bar{\boldsymbol{n}}^{\mathrm{T}}\frac{\partial\bar{\Phi}_{\mathrm{t}}}{\partial\bar{\boldsymbol{\xi}}}\right)\, \mathrm{d}\overline{\Sigma} \tag{B.18}$$

$$\frac{\partial\mathcal{L}'}{\partial\dot{\bar{\boldsymbol{\xi}}}} = \frac{1}{2}\int_{\overline{\Sigma}} \frac{\partial\bar{\phi}}{\partial\dot{\bar{\boldsymbol{\xi}}}}\bar{\boldsymbol{v}}^o \cdot \bar{\boldsymbol{n}} + \bar{\phi}^o\bar{\boldsymbol{n}}^{\mathrm{T}}\, \mathrm{d}\overline{\Sigma} \tag{B.19}$$

$$\frac{\mathrm{d}}{\mathrm{d}t}\frac{\partial\mathcal{L}'}{\partial\dot{\bar{\boldsymbol{\xi}}}} = 0 \text{ since } \frac{\partial\bar{\boldsymbol{v}}^o}{\partial t} = 0 \text{ and } \frac{\partial\bar{\phi}^o}{\partial t} = 0. \tag{B.20}$$

As a consequence, the zero order force can be written

$$F^o = \frac{1}{2}\int_{\overline{\Sigma}} \frac{\partial \bar{\phi}}{\partial \bar{\boldsymbol{\xi}}} \bar{\boldsymbol{v}}^o \cdot \bar{\boldsymbol{n}} + \bar{\phi}^o \bar{\boldsymbol{v}}^o \cdot \left(\bar{\boldsymbol{n}}^{\mathrm{T}} \frac{\partial \bar{\Phi}_{\mathrm{t}}}{\partial \bar{\boldsymbol{\xi}}} \right) \mathrm{d}\overline{\Sigma}. \tag{B.21}$$

We are interested in the perturbations of the force as well. In order to obtain its expression, the derivatives of the second order of the energy with respect to the interface elastic movements are calculated:

$$\frac{\partial \mathcal{L}''}{\partial \bar{\boldsymbol{\xi}}} = (\mathbb{L}_k + \mathbb{L}_k^{\mathrm{T}})\bar{\boldsymbol{\xi}}' + \mathbb{L}_g \dot{\bar{\boldsymbol{\xi}}} \tag{B.22}$$

$$\frac{\partial \mathcal{L}''}{\partial \dot{\bar{\boldsymbol{\xi}}}} = \mathbb{L}_g^{\mathrm{T}} \bar{\boldsymbol{\xi}}' + (\mathbb{L}_m + \mathbb{L}_m^{\mathrm{T}})\dot{\bar{\boldsymbol{\xi}}}' \Rightarrow \frac{\mathrm{d}}{\mathrm{d}t}\frac{\partial \mathcal{L}''}{\partial \dot{\bar{\boldsymbol{\xi}}}} = \mathbb{L}_g^{\mathrm{T}} \dot{\bar{\boldsymbol{\xi}}}' + (\mathbb{L}_m + \mathbb{L}_m^{\mathrm{T}})\ddot{\bar{\boldsymbol{\xi}}}', \tag{B.23}$$

and the perturbation of the forces can be obtained through added stiffness, gyroscopic and mass contributions by combining equations (B.17) and (B.22):

$$-F' = \mathbb{K}\bar{\boldsymbol{\xi}}' + \mathbb{D}\dot{\bar{\boldsymbol{\xi}}}' + \mathbb{M}\ddot{\bar{\boldsymbol{\xi}}}' \tag{B.24}$$

$$K_{f,\mathrm{dyn}}(\bar{\boldsymbol{\xi}}', \delta\dot{\bar{\boldsymbol{\xi}}}) = -\delta\dot{\bar{\boldsymbol{\xi}}}^{\mathrm{T}}(\mathbb{L}_k + \mathbb{L}_k^{\mathrm{T}})\bar{\boldsymbol{\xi}}' \tag{B.25}$$

$$\mathrm{G}^f(\dot{\bar{\boldsymbol{\xi}}}', \delta\dot{\bar{\boldsymbol{\xi}}}) = \delta\dot{\bar{\boldsymbol{\xi}}}^{\mathrm{T}}(\mathbb{L}_g^{\mathrm{T}} - \mathbb{L}_g)\dot{\bar{\boldsymbol{\xi}}}' \tag{B.26}$$

$$\mathrm{M}^f(\ddot{\bar{\boldsymbol{\xi}}}', \delta\dot{\bar{\boldsymbol{\xi}}}) = \delta\dot{\bar{\boldsymbol{\xi}}}^{\mathrm{T}}(\mathbb{L}_m + \mathbb{L}_m^{\mathrm{T}})\ddot{\bar{\boldsymbol{\xi}}}'. \tag{B.27}$$

The symmetry of the added stiffness and mass and the skew-symmetry of the gyroscopic operator arises naturally from the expressions above.

Appendix C

Analytical solution of potential flows around an ellipsoid

The aim of this section is to give the value of the added mass of an ellipsoid undergoing rigid-body translation or rotation acceleration around its center of volume. The results presented here are taken from (Lamb, 1932). The aspect ratio t (inverse of the aspect ratio $\mathcal{A}_r$) and the eccentricity e of a rotation ellipsoid of major semi-axis $a = L/2$ and minor semi-axis $b = D/2$ are

$$t = \frac{1}{\mathcal{A}_r} = \frac{D}{L} \tag{C.1a}$$

$$e = \sqrt{1 - t^2}. \tag{C.1b}$$

The variable t is used here rather than $\mathcal{A}_r$ in order to be coherent with the literature. Moreover, the following non-dimensional geometric coefficients are introduced:

$$\alpha_0 = \frac{1 - e^2}{e^3}\left(-2e + \log\left(\frac{1+e}{1-e}\right)\right) \tag{C.2a}$$

$$\beta_0 = \frac{1}{e^2} - \frac{1 - e^2}{2e^3}\log\left(\frac{1+e}{1-e}\right) \tag{C.2b}$$

$$k_1 = \frac{\alpha_0}{2 - \alpha_0} \tag{C.2c}$$

$$k_2 = \frac{\beta_0}{2 - \beta_0} \tag{C.2d}$$

$$k_3 = \frac{(1-t^2)^2(\beta_0 - \alpha_0)}{2(1-t^4) - (1+t^2)^2(\beta_0 - \alpha_0)}. \tag{C.2e}$$

We consider that the major axis is along the $\boldsymbol{e}_x$ direction. The velocity potential at the interface of an ellipsoid with a velocity translation $\boldsymbol{v}_\mathrm{c} = v_x\boldsymbol{e}_x + v_y\boldsymbol{e}_y + v_z\boldsymbol{e}_z$ is

$$\phi(\boldsymbol{x}) = -k_1 v_x\, x - k_2\,(v_y\, y + v_z\, z) \quad \text{for } \boldsymbol{x} \in \Sigma. \tag{C.3}$$

According to (Thomasson and Woolsey, 2013), the force $\boldsymbol{F}$ and moment $\boldsymbol{M}$ exerted by a potential flow at rest on a rigid structure in movement is:

$$\begin{pmatrix} \boldsymbol{F} \\ \boldsymbol{M} \end{pmatrix} = \left[\mathrm{M}^f_{\mathrm{rig}}\right] \begin{pmatrix} \dot{\boldsymbol{v}} \\ \dot{\boldsymbol{\omega}} \end{pmatrix} + \begin{bmatrix} \boldsymbol{\omega}_\wedge & (0) \\ \boldsymbol{v}_\wedge & \boldsymbol{\omega}_\wedge \end{bmatrix} \left[\mathrm{M}^f_{\mathrm{rig}}\right] \begin{pmatrix} \dot{\boldsymbol{v}} \\ \dot{\boldsymbol{\omega}} \end{pmatrix}. \tag{C.4}$$

The rigid added mass operator $\mathrm{M}^f_{\mathrm{rig}}$ writes as a diagonal matrix:

$$\left[\mathrm{M}^f_{\mathrm{rig}}\right] = \begin{bmatrix} \mathrm{M}_{xx} & & & & & \\ & \mathrm{M}_{yy} & & & (0) & \\ & & \mathrm{M}_{zz} = \mathrm{M}_{yy} & & & \\ & & & 0 & & \\ & (0) & & & \mathrm{I}_{yy} & \\ & & & & & \mathrm{I}_{zz} = \mathrm{I}_{yy} \end{bmatrix}. \tag{C.5}$$

The extra-diagonal are all nil because the movements are considered around the center of volume of the ellipsoid. Because of the symmetry axis along the major axis $\boldsymbol{e}_x$, we have $\mathrm{M}_{yy} = \mathrm{M}_{zz}$, $\mathrm{I}_{xx} = 0$ and $\mathrm{I}_{yy} = \mathrm{I}_{zz}$. According to (Lamb, 1932), the added mass coefficients write as

$$\mathrm{M}_{xx} = \frac{4\pi}{3}\rho_f a b^2 k_1 \tag{C.6a}$$

$$\mathrm{M}_{yy} = \frac{4\pi}{3}\rho_f a b^2 k_2 \tag{C.6b}$$

$$\mathrm{I}_{yy} = \frac{4\pi}{15}\rho_f a b^2 (a^2 + b^2) k_3. \tag{C.6c}$$

Moreover, one can calculate the munk momentum associated with an ellipsoid with a steady velocity V and an angle of attack α,combining the relations $\dot{\boldsymbol{v}} = \boldsymbol{0}$, $\dot{\boldsymbol{\omega}} = \boldsymbol{0}$, $\boldsymbol{\omega} = \boldsymbol{0}$ and $\boldsymbol{v} = V(\cos\alpha \boldsymbol{e}_x + \sin\alpha \boldsymbol{e}_z)$ with equations (C.4) and (C.5):

$$\boldsymbol{M} = \boldsymbol{v}_\wedge \left[\mathrm{M}^f_{\mathrm{rig}}\right] \boldsymbol{v} = V^2(\mathrm{M}_{xx} - \mathrm{M}_{zz}) \cos\alpha \sin\alpha \boldsymbol{e}_y. \tag{C.7}$$

By replacing the added mass terms in the equation above with their expression from equations (C.2a) and (C.6) and using trigonometric relationships to simplify the $\cos\alpha \sin\alpha$ product one gets:

$$\begin{aligned} \boldsymbol{M} &= \frac{1}{2}(\mathrm{M}_{xx} - \mathrm{M}_{zz}) \sin(2\alpha) V^2 \boldsymbol{e}_y = \frac{4\pi}{3}\rho_f a b^2 (k_1 - k_2) \sin(2\alpha) V^2 \boldsymbol{e}_y \\ &= \frac{\pi}{6}\rho_f \frac{L^3}{\mathcal{A}_r^2} \frac{\alpha_0 - \beta_0}{(2 - \alpha_0)(2 - \beta_0)} \sin(2\alpha) V^2 \boldsymbol{e}_y. \end{aligned} \tag{C.8}$$

Appendix D

Properties of linear systems

D.1 Superiority of numerical (skew-)symmetrized operators

Because of the newtonian approach, the fluid operators calculated by the mixed FEM-BEM approach won't be exactly (skew-)symmetric. It is however possible to prove how their (skew-)symmetrization can lead to lower error on the estimation of the fluid loads, which is the aim of this section.

Symmetrized added mass and stiffness operators

Following Rangette's developments (Rangette, 1990), we first show how the symmetrized added mass numerical operator enables to obtain lower error on the associated fluid loads because of the symmetry of the added mass operator.

We consider a symmetric mass operator M and its numerical counterpart $\mathrm{M_{num}}$, which is not symmetric because of numerical approximations. In order to quantify the error associated with the numerical approximation of the added mass, the norm of a matrix is introduced as:

$$\|\mathrm{A}\| = \sup_{\|\boldsymbol{x}\|=1} \|\mathrm{A}\boldsymbol{x}\| \text{ with } \|\boldsymbol{x}\| = \sqrt{<\boldsymbol{x},\boldsymbol{x}>}, \tag{D.1}$$

where $<,>$ is the Hermitian inner product. The operators A and B are introduced as:

$$\mathrm{A} = \mathrm{M_{num}} - \mathrm{M} \tag{D.2a}$$

$$\mathrm{B} = \frac{1}{2}(\mathrm{M_{num}} + \mathrm{M_{num}^T}) - \mathrm{M}, \tag{D.2b}$$

where B is the symmetric part of A. Therefore, our objective is to show that $\|\mathrm{B}\| \leq \|\mathrm{A}\|$. By property of symmetric matrices, we have (Rangette, 1990)

$$\|\mathrm{B}\| = \sup_{\|\boldsymbol{x}\|=1} |<\mathrm{B},\boldsymbol{x}>|. \tag{D.3}$$

We want express the right term of the expression above with A instead of B. For this purpose, we have the below expression, recalling how the scalar product between an antisymmetric matrix applied to a vector and the same vector is nil:

$$< \mathrm{A}\boldsymbol{x}, \boldsymbol{x} > =< \frac{1}{2}(\mathrm{A} + \mathrm{A}^{\mathrm{T}})\boldsymbol{x}, \boldsymbol{x} > + < \frac{1}{2}(\mathrm{A} - \mathrm{A}^{\mathrm{T}})\boldsymbol{x}, \boldsymbol{x} >=< \frac{1}{2}(\mathrm{A} + \mathrm{A}^{\mathrm{T}})\boldsymbol{x}, \boldsymbol{x} > \tag{D.4}$$

$$=< \mathrm{B}\boldsymbol{x}, \boldsymbol{x} > . \tag{D.5}$$

By combining equations (D.3) and (D.4), we get:

$$\|\mathrm{B}\| = \sup_{\|\boldsymbol{x}\|=1} | < \mathrm{A}\boldsymbol{x}, \boldsymbol{x} > |. \tag{D.6}$$

The Cauchy-Schwartz inequality provides:

$$< \mathrm{A}\boldsymbol{x}, \boldsymbol{x} >\leq \|\mathrm{A}\boldsymbol{x}\| \, \|\boldsymbol{x}\| = \|\mathrm{A}\boldsymbol{x}\| \text{ for } \|\boldsymbol{x}\| = 1. \tag{D.7}$$

Therefore, we obtain by combining equations (D.6) and (D.7)

$$\|\mathrm{B}\| \leq \sup_{\|\boldsymbol{x}\|=1} \|\mathrm{A}\boldsymbol{x}\| = \|\mathrm{A}\| . \tag{D.8}$$

The equations above proves the property we wanted to show: the symmetrized numerical added mass operator provides a lower maximum error associated with the prediction of the fluid loading than the non-symmetrized numerical added mass operator. The same demonstration holds true for the numerical stiffness operator because of the symmetry of the stiffness operator.

Skew-symmetrized gyroscopic operator

The objective of this section is to extend Rangette's result for the symmetrization of operators supposed to be symmetric to the skew-symmetrization of operators supposed to be skew-symmetric. To the author's knowledge, it constitutes an original result. We consider a skew-symmetric operator G and its numerical counterpart $\mathrm{G}_{\mathrm{num}}$. New operators A and B are introduced for this demonstration:

$$\mathrm{A} = \mathrm{i}(\mathrm{G}_{\mathrm{num}} - \mathrm{G}) \tag{D.9a}$$

$$\mathrm{B} = \mathrm{i}\left(\frac{1}{2}\left(\mathrm{G}_{\mathrm{num}} - \mathrm{G}_{\mathrm{num}}^{\mathrm{T}}\right) - \mathrm{G}\right). \tag{D.9b}$$

Since we have $\mathrm{B} = \frac{1}{2}(\mathrm{A} + \mathrm{A}^{*})$, B is the Hermitian part of A. The following property holds true for Hermitian operators (*Add citation?*):

$$\|\mathrm{B}\| = \sup_{\|\boldsymbol{x}\|=1} | < \mathrm{B}\boldsymbol{x}, \boldsymbol{x} > | \text{ if B is Hermitian.} \tag{D.10}$$

Because B is the Hermitian part of A, we have the following property as well:

$$< \mathrm{B}\boldsymbol{x}, \boldsymbol{x} >= \frac{1}{2}\left(< \mathrm{A}\boldsymbol{x}, \boldsymbol{x} > + < \mathrm{A}^{*}\boldsymbol{x}, \boldsymbol{x} >\right). \tag{D.11}$$

Using the properties of the Hermitian product, the last term can be expressed as

$$< \mathrm{A}^{*}\boldsymbol{x}, \boldsymbol{x} >=< \boldsymbol{x}, \mathrm{A}\boldsymbol{x} >= \overline{< \mathrm{A}\boldsymbol{x}, \boldsymbol{x} >}, \tag{D.12}$$

where the overline $\bar{\bullet}$ denotes here the complex conjugate of a number. Therefore, the expression (D.11) becomes when combined with (D.12):

$$< \mathrm{B}\boldsymbol{x}, \boldsymbol{x} >= \frac{1}{2}\left(< \mathrm{A}\boldsymbol{x}, \boldsymbol{x} > + \overline{< \mathrm{A}\boldsymbol{x}, \boldsymbol{x} >}\right) = \Re e(< \mathrm{A}\boldsymbol{x}, \boldsymbol{x} >). \tag{D.13}$$

We get by combining equations (D.10) and (D.13)

$$\begin{aligned} \|\mathrm{B}\| &= \sup_{\|\boldsymbol{x}\|=1} | < \mathrm{B}\boldsymbol{x}, \boldsymbol{x} > | = \sup_{\|\boldsymbol{x}\|=1} |\Re e(< \mathrm{A}\boldsymbol{x}, \boldsymbol{x} >)| \\ &\leq \sup_{\|\boldsymbol{x}\|=1} | < \mathrm{A}\boldsymbol{x}, \boldsymbol{x} > |. \end{aligned} \tag{D.14}$$

Similarly to the previous demontration for the symmetric operators, we get thanks to the Cauchy-Schwartz inequality that $| < A\boldsymbol{x}, \boldsymbol{x} > | \leq \|A\boldsymbol{x}\|$ for $\|\boldsymbol{x}\| = 1$, and consequently:

$$\begin{aligned} \|\mathrm{B}\| &\leq \sup_{\|\boldsymbol{x}\|=1} \|\mathrm{A}\boldsymbol{x}\| \\ \Leftrightarrow \|\mathrm{B}\| &\leq \|\mathrm{A}\|. \end{aligned} \tag{D.15}$$

The above equation can be rewritten as

$$\begin{aligned} \left\| \mathrm{i}\left(\frac{1}{2}(\mathrm{G}_{\mathrm{num}} - \mathrm{G}_{\mathrm{num}}^{\mathrm{T}}) - [\mathrm{G}]\right)\right\| &\leq \|\mathrm{i}\,(\mathrm{G}_{\mathrm{num}} - [\mathrm{G}])\| \\ \Leftrightarrow \left\|\frac{1}{2}(\mathrm{G}_{\mathrm{num}} - \mathrm{G}_{\mathrm{num}}^{\mathrm{T}}) - [\mathrm{G}]\right\| &\leq \|\mathrm{G}_{\mathrm{num}} - [\mathrm{G}]\|. \end{aligned} \tag{D.16}$$

The above equation shows how the skew-symmetrized numerical gyroscopic operator provides a lower maximum error associated with the prediction of the fluid loads than the non-skew-symmetrized numerical gyroscopic operator.

D.2 Gyroscopic conservative linear systems

The aim of this section is to demonstrate that, for systems with symmetric mass and stiffness operators and skew-symmetric velocity-dependent operators (or gyroscopic operators), the work of the fluid can be derived from a potential, which demonstrates the conservative nature of such systems. One should recall that the linearized work of the fluid in the case of small elastic deformations writes as:

$$\mathrm{d}W = \delta\mathcal{P}_f(\delta\dot{\boldsymbol{\xi}} = \mathrm{d}\bar{\boldsymbol{\xi}}), \tag{D.17a}$$

$$\text{hence } \frac{\mathrm{d}W}{\mathrm{d}t} = \frac{\mathrm{d}\delta\mathcal{P}_f(\delta\dot{\boldsymbol{\xi}} = \mathrm{d}\bar{\boldsymbol{\xi}})}{\mathrm{d}t} = \delta\mathcal{P}_f\left(\delta\dot{\boldsymbol{\xi}} = \dot{\bar{\boldsymbol{\xi}}}\right). \tag{D.17b}$$

By combining equations (D.17b) and (II.94):

$$\frac{\mathrm{d}W}{\mathrm{d}t} = \frac{\mathrm{d}\bar{\boldsymbol{\xi}}}{\mathrm{d}t}^{\mathrm{T}} \left(\mathrm{M}^f \frac{\mathrm{d}^2\bar{\boldsymbol{\xi}}}{\mathrm{d}t^2} + \mathrm{G}^f \frac{\mathrm{d}\bar{\boldsymbol{\xi}}}{\mathrm{d}t} + \mathrm{K}^f \bar{\boldsymbol{\xi}} \right). \tag{D.18}$$

By property of the skew-symmetry of the gyroscopic operator G^f:

$$\left(\frac{\mathrm{d}\bar{\boldsymbol{\xi}}}{\mathrm{d}t}^{\mathrm{T}} \mathrm{G}^f \frac{\mathrm{d}\bar{\boldsymbol{\xi}}}{\mathrm{d}t} \right)^{\mathrm{T}} = \frac{\mathrm{d}\bar{\boldsymbol{\xi}}}{\mathrm{d}t}^{\mathrm{T}} \mathrm{G}^{f\,\mathrm{T}} \frac{\mathrm{d}\bar{\boldsymbol{\xi}}}{\mathrm{d}t} = -\frac{\mathrm{d}\bar{\boldsymbol{\xi}}}{\mathrm{d}t}^{\mathrm{T}} \mathrm{G}^f \frac{\mathrm{d}\bar{\boldsymbol{\xi}}}{\mathrm{d}t} \tag{D.19a}$$

$$\text{hence } \frac{\mathrm{d}\bar{\boldsymbol{\xi}}}{\mathrm{d}t}^{\mathrm{T}} \mathrm{G}^f \frac{\mathrm{d}\bar{\boldsymbol{\xi}}}{\mathrm{d}t} = 0. \tag{D.19b}$$

Moreover, the symmetry of operators K^f and M^f enables to write the derivative of a kinetic energy $\mathcal{L}_{m,k}$ as:

$$\mathcal{L}_{m,k} = \frac{1}{2} \left(\frac{\mathrm{d}\bar{\boldsymbol{\xi}}}{\mathrm{d}t}^{\mathrm{T}} \mathrm{M}^f \frac{\mathrm{d}\bar{\boldsymbol{\xi}}}{\mathrm{d}t} + \bar{\boldsymbol{\xi}}^{\mathrm{T}} \mathrm{K}^f \bar{\boldsymbol{\xi}} \right) \tag{D.20a}$$

$$\begin{aligned} \frac{\mathrm{d}\mathcal{L}_{m,k}}{\mathrm{d}t} = \frac{\mathrm{d}\mathcal{L}}{\mathrm{d}t} &= \frac{1}{2} \left(\frac{\mathrm{d}^2\bar{\boldsymbol{\xi}}}{\mathrm{d}t^2}^{\mathrm{T}} \mathrm{M}^f \frac{\mathrm{d}\bar{\boldsymbol{\xi}}}{\mathrm{d}t} + \frac{\mathrm{d}\bar{\boldsymbol{\xi}}}{\mathrm{d}t}^{\mathrm{T}} \mathrm{M}^f \frac{\mathrm{d}^2\bar{\boldsymbol{\xi}}}{\mathrm{d}t^2} + \frac{\mathrm{d}\bar{\boldsymbol{\xi}}}{\mathrm{d}t}^{\mathrm{T}} \mathrm{K}^f \bar{\boldsymbol{\xi}} + \bar{\boldsymbol{\xi}} \mathrm{K}^f \frac{\mathrm{d}\bar{\boldsymbol{\xi}}}{\mathrm{d}t} \right) \\ &= \frac{\mathrm{d}\bar{\boldsymbol{\xi}}}{\mathrm{d}t}^{\mathrm{T}} \left(\mathrm{M}^f \frac{\mathrm{d}^2\bar{\boldsymbol{\xi}}}{\mathrm{d}t^2} + \mathrm{K}^f \bar{\boldsymbol{\xi}} \right). \end{aligned} \tag{D.20b}$$

Therefore, we get a new expression of the time fluctuations of the fluid's work by combining equations (D.17b), (D.19b) and (D.20b):

$$\frac{\mathrm{d}W}{\mathrm{d}t} = \frac{\mathrm{d}\mathcal{L}_{m,k}}{\mathrm{d}t} \left(\bar{\boldsymbol{\xi}}, \frac{\mathrm{d}\bar{\boldsymbol{\xi}}}{\mathrm{d}t} \right). \tag{D.21}$$

The above expression shows how the work of the fluid derives from a potential $\mathcal{L}_{m,k}$.

D.3 Numerical error on the (skew-)symmetry of the fluid operators

In Chapter II is shown the symmetry of the added mass and stiffness operators and the skew-symmetry of the gyroscopic operator using the Lagrange equations. This statement is investigated with the numerical operators introduced in this study. In order to do so, the following errors using the Frobenius norm[1] have been determined based on a longitudinal order zero translation velocity $\bar{\boldsymbol{v}}^o$ for the same mesh as in figure III.12. The operators have been projected on the arbitrary projection basis $\mathbb{Q}_{\mathrm{rb}}$ consisting in the six rigid body movements of space completed by the first flexible (banana shaped) mode of the airship, see Chapter IV for more details about the projection basis:

[1]The Frobenius norm of a matrix $\mathbb{A} \in \mathbb{R}^n \otimes \mathbb{R}^n$ with $n \in \mathbb{N}$ is defined as $\|\mathbb{A}\|_{\mathrm{fro}} = \sqrt{\mathrm{trace}(\mathbb{A}\mathbb{A}^{\mathrm{T}})}$

$$\begin{aligned}
\frac{\left\| \left[\mathrm{K}_v^f\right] - \left[\mathrm{K}_v^f\right]^{\mathrm{T}} \right\|_{\mathrm{fro}}}{\left\| \left[\mathrm{K}_v^f\right] \right\|_{\mathrm{fro}}} &= 0.12\% \\
\frac{\left\| \left[\mathrm{G}^f\right] + \left[\mathrm{G}^f\right]^{\mathrm{T}} \right\|_{\mathrm{fro}}}{\left\| \left[\mathrm{G}^f\right] \right\|_{\mathrm{fro}}} &= 0.58\% \\
\frac{\left\| \left[\mathrm{M}^f\right] - \left[\mathrm{M}^f\right]^{\mathrm{T}} \right\|_{\mathrm{fro}}}{\left\| \left[\mathrm{M}^f\right] \right\|_{\mathrm{fro}}} &= 0.02\%.
\end{aligned} \tag{D.22}$$

D.4 Eigenvalues of gyroscopic conservative systems

D.4.1 Nature of the eigenvalues

The aim of this section is first to demonstrate that the eigenvalues of the dynamic system are purely oscillatory when the stiffness operator is positive, and second that the loss of positivity of the latter might lead to unstable solutions of the dynamic system, which can be oscillatory. The discrete eigenvalue equation of the dynamic system is:

$$(\lambda^2 \mathrm{M} + \lambda \mathrm{G}^f + \mathrm{K})\boldsymbol{q} = \boldsymbol{0} \text{ with } \mathrm{M} = \mathrm{M}^f + \mathrm{M}^s, \mathrm{K} = \mathrm{K}^f + \mathrm{K}^s, \tag{D.23}$$

where λ and $\boldsymbol{q}$ are the eigenvalue and the eigenvector respectively. In order to show the properties mentioned above, the latter equation is multiplied by $\boldsymbol{q}^*$, where the * exponent is associated with the transpose conjugate of a vector:

$$\lambda^2 \boldsymbol{q}^* \mathrm{M} \boldsymbol{q} + \lambda \boldsymbol{q}^* \mathrm{G}^f \boldsymbol{q} + \boldsymbol{q}^* \mathrm{K} \boldsymbol{q} = 0. \tag{D.24}$$

For symmetric matrices, we have the following property:

$$(\boldsymbol{q}^* \mathrm{M} \boldsymbol{q})^* = \boldsymbol{q}^* \mathrm{M} \boldsymbol{q} \Rightarrow \boldsymbol{q}^* \mathrm{M} \boldsymbol{q} = m \in \mathbb{R}^{*+}, \tag{D.25}$$

and the same goes for the stiffness

$$\boldsymbol{q}^* \mathrm{K} \boldsymbol{q} = k \in \mathbb{R}. \tag{D.26}$$

The scalar m is strictly positive because the solid mass M^s is strictly positive and the fluid added mass M^f is positive. The scalar k can be negative when the fluid stiffness K^f becomes negative. Similarly, for skew-symmetric operators, we have the following property:

$$(\boldsymbol{q}^* \mathrm{G}^f \boldsymbol{q})^* = -\boldsymbol{q}^* \mathrm{G}^f \boldsymbol{q} \Rightarrow \boldsymbol{q}^* \mathrm{G}^f \boldsymbol{q} = \mathrm{i}g \in \mathrm{i}\mathbb{R}, \tag{D.27}$$

where $\mathrm{i}\mathbb{R}$ is the set of pure imaginary numbers. As a consequence, the eigenvalues λ are roots of the equation

$$m\lambda^2 + \mathrm{i}g\lambda + k = 0. \tag{D.28}$$

The roots of the quadratic equation above are:

$$\begin{cases} \lambda &= \frac{-g \pm \sqrt{g^2+4km}}{2m}\mathrm{i} & \text{for } k \geq \frac{-g^2}{2m} \\ \lambda &= \frac{\pm\sqrt{g^2+4km}}{2m} - \frac{g}{2m}\mathrm{i} & \text{for } k < \frac{-g^2}{2m} \end{cases} \tag{D.29}$$

One can deduce from the equation above that, when the rigidity parameter k becomes too negative, the eigenvalue λ can have a positive real part associated with an instability. It appears as well that the gyroscopic loads of the fluid can stabilize the system when the stiffness scalar parameter k becomes negative, as mentioned by (Ziegler, 1977). Finally, it appears that for gyroscopic linear systems, when the gyroscopic scalar isn't nil $g \neq 0$, the unstable solutions are oscillatory ($\Re e(\lambda) > 0$ and $\Im m(\lambda) \neq 0$), resulting in a flutter phenomenon such as the Paidoussis post-divergence flutter of clamped pipes conveying fluid documented in (Paidoussis, 1998).

Remark

If one were to calculate the left eigenvalues Y such that

$$Y^* A = \mu Y^* B, \tag{D.30}$$

then because of the (skew)-symmetry properties of the operators A and B, one would get that the left eigenmodes Y are equal to the right eigenmodes X but associated with an eigenvalue such that $\mu = -\lambda^*$.

D.4.2 Properties of the eigenvalues

The aim of this section is to demonstrate how the eigenvalues of linear conservative gyroscopic systems are associated four by four by symmetry around the real and the imaginary axis. First, in the case of operators K, G^f and M with real coefficients, the conjugate of equation (D.23) is:

$$\left(\bar{\lambda}^2 \mathrm{M} + \bar{\lambda}\mathrm{G}^f + \mathrm{K}\right) \bar{\boldsymbol{q}} = \mathbf{0}. \tag{D.31}$$

where the bar notation denotes here the conjugate. Consequently, the following property holds true:

if $\lambda, \boldsymbol{q}$ are associated eigenvalue and eigenvector then $\{\bar{\lambda}, \bar{\boldsymbol{q}}\}$ are associated eigenvalue and eigenvector as well. We now consider the left eigenvalues and eigenvectors $\{\mu, \boldsymbol{p}\}$ such that:

$$\boldsymbol{p}^* \left(\mu^2 \mathrm{M} + \mu\mathrm{G}^f + \mathrm{K}\right) = \mathbf{0}. \tag{D.32}$$

By taking the transpose of the above equation and noting that M, G^f and K have real coefficients, we get:

$$\left(\mu^2 \mathrm{M} + \mu\mathrm{G}^f + \mathrm{K}\right)^{\mathrm{T}} \bar{\boldsymbol{p}} = \mathbf{0}, \tag{D.33}$$

which implies by property of the eigenvalues that the following determinant is zero:

$$\det\left(\left(\mu^2 \mathrm{M} + \mu\mathrm{G}^f + \mathrm{K}\right)^{\mathrm{T}}\right) = 0. \tag{D.34}$$

Since the transposition of a matrix doesn't affect its determinant, the above equation is equivalent to

$$\det\left(\mu^2\mathrm{M}+\mu\mathrm{G}^f+\mathrm{K}\right)=0 \tag{D.35}$$

From the above equation, one can deduce that if $\{\lambda,\boldsymbol{q}\}$ is a right eigenvalue/eigenvector couple (associated with equation (D.32)), then there exists $\boldsymbol{p}$ such that $\{\lambda,\boldsymbol{p}\}$ is a left eigenvalue/eigenvector couple (associated with equation (D.23)). Moreover, by calculating the transpose conjugate of the left eigenequation (D.32) and using the λ notation instead of μ since left and right eigenvalues are the same, we get using the symmetry properties of M and K and the skew-symmetry of G^f:

$$\begin{aligned}\left(\boldsymbol{p}^*\left(\lambda^2\mathrm{M}+\lambda\mathrm{G}^f+\mathrm{K}\right)\right)&=\left(\bar{\lambda}^2\mathrm{M}-\bar{\lambda}\mathrm{G}^f+\mathrm{K}\right)\boldsymbol{p}\\&=\left((-\bar{\lambda})^2\mathrm{M}+(-\bar{\lambda})\mathrm{G}^f+\mathrm{K}\right)\boldsymbol{p}=0\end{aligned} \tag{D.36}$$

One can deduce from the above equation that $\{-\bar{\lambda},\boldsymbol{p}\}$ is a right eigenvalue/eigenvector couple. Recalling that the conjugate of an eigenvalue/eigenvector couple is an eigenvalue/eigenvector couple as well, we get by combining with equation (D.36) the following property: if λ is an eigenvalue and $\boldsymbol{p},\boldsymbol{q}$ are left and right associated eigenvectors, then $\{\lambda,\boldsymbol{q}\}$, $\{\bar{\lambda},\bar{\boldsymbol{q}}\}$, $\{-\bar{\lambda},\boldsymbol{p}\}$ and $\{-\lambda,\bar{\boldsymbol{p}}\}$ are all right eigenvalue/eigenvector couples.

D.5 Linearized rigid body gyroscopic operator

In this section, the gyroscopic operator associated with rigid body motions is developed analytically. We consider here the forces of a potential fluid on a moving rigid interface given in equation (C.4). It is assumed in this section that the added mass of the considered structure is diagonal and can thus be written as the concatenation of blocks 3×3:

$$\left[\mathrm{M}^f_{\mathrm{rig}}\right]=\begin{pmatrix}\mathrm{M}^f_{vv} & (0)\\ (0) & Mf_{\omega\omega}.\end{pmatrix} \tag{D.37}$$

The forces associated with the velocity in the equation (C.4) can be developed:

$$\begin{bmatrix}\bar{\boldsymbol{\omega}}_\wedge & (0)\\ \bar{\boldsymbol{v}}_\wedge & \bar{\boldsymbol{\omega}}_\wedge\end{bmatrix}\left[\mathrm{M}^f_{\mathrm{rig}}\right]\begin{pmatrix}\bar{\boldsymbol{v}}\\ \bar{\boldsymbol{\omega}}\end{pmatrix}=\begin{pmatrix}\bar{\boldsymbol{\omega}}_\wedge\mathrm{M}^f_{vv}\bar{\boldsymbol{v}}\\ \bar{\boldsymbol{v}}_\wedge\mathrm{M}^f_{vv}\bar{\boldsymbol{v}}+\bar{\boldsymbol{\omega}}_\wedge\mathrm{M}^f{}_{\omega\omega}\bar{\boldsymbol{\omega}}\end{pmatrix}. \tag{D.38}$$

By combining the above two equations with the equation (C.4) and retaining only the terms of order one, we then obtain the fluctuation of the forces as a function of the velocity perturbations:

$$\begin{aligned}-\begin{pmatrix}\boldsymbol{F}'\\ \boldsymbol{M}'\end{pmatrix}&=\left[\mathrm{M}^f_{\mathrm{rig}}\right]\begin{pmatrix}\dot{\bar{\boldsymbol{v}}}'\\ \dot{\bar{\boldsymbol{\omega}}}'\end{pmatrix}+\begin{pmatrix}\bar{\boldsymbol{\omega}}^o_\wedge\mathrm{M}^f_{vv}\bar{\boldsymbol{v}}'+\bar{\boldsymbol{\omega}}'_\wedge\mathrm{M}^f_{vv}\bar{\boldsymbol{v}}^o\\ \bar{\boldsymbol{v}}^o_\wedge\mathrm{M}^f_{vv}\bar{\boldsymbol{v}}'+\bar{\boldsymbol{v}}'_\wedge\mathrm{M}^f_{vv}\bar{\boldsymbol{v}}^o+\bar{\boldsymbol{\omega}}^o_\wedge\mathrm{M}^f{}_{\omega\omega}\bar{\boldsymbol{\omega}}'+\bar{\boldsymbol{\omega}}'_\wedge\mathrm{M}^f{}_{\omega\omega}\bar{\boldsymbol{\omega}}^o\end{pmatrix}\\&=\left[\mathrm{M}^f_{\mathrm{rig}}\right]\begin{pmatrix}\dot{\bar{\boldsymbol{v}}}'\\ \dot{\bar{\boldsymbol{\omega}}}'\end{pmatrix}+\begin{pmatrix}\bar{\boldsymbol{\omega}}^o_\wedge\mathrm{M}^f_{vv}\bar{\boldsymbol{v}}'-\left(\mathrm{M}^f_{vv}\bar{\boldsymbol{v}}^o\right)_\wedge\bar{\boldsymbol{\omega}}'\\ \bar{\boldsymbol{v}}^o_\wedge\mathrm{M}^f_{vv}\bar{\boldsymbol{v}}'-\left(\mathrm{M}^f_{vv}\bar{\boldsymbol{v}}^o\right)_\wedge\bar{\boldsymbol{v}}'+\bar{\boldsymbol{\omega}}^o_\wedge\mathrm{M}^f{}_{\omega\omega}\bar{\boldsymbol{\omega}}'-\left(\mathrm{M}^f{}_{\omega\omega}\bar{\boldsymbol{\omega}}^o\right)_\wedge\bar{\boldsymbol{\omega}}'\end{pmatrix}.\end{aligned} \tag{D.39}$$

One can identify the rigid body gyroscopic operator from the equation above:

$$-\begin{pmatrix} \boldsymbol{F}' \\ \boldsymbol{M}' \end{pmatrix} = \left[\mathrm{M}^f_{\mathrm{rig}}\right] \begin{pmatrix} \dot{\bar{\boldsymbol{v}}}' \\ \dot{\bar{\boldsymbol{\omega}}}' \end{pmatrix} + \left[\mathrm{G}^f_{\mathrm{rig}}\right] \begin{pmatrix} \bar{\boldsymbol{v}}' \\ \bar{\boldsymbol{\omega}}' \end{pmatrix} \tag{D.40}$$

$$\left[\mathrm{G}^f_{\mathrm{rig}}\right] = \begin{bmatrix} \bar{\boldsymbol{\omega}}^o_\wedge \mathrm{M}^f_{vv} & -\left(\mathrm{M}^f_{vv}\bar{\boldsymbol{v}}^o\right)_\wedge \\ \bar{\boldsymbol{v}}^o_\wedge \mathrm{M}^f_{vv} - \left(\mathrm{M}^f_{vv}\bar{\boldsymbol{v}}^o\right)_\wedge & \bar{\boldsymbol{\omega}}^o_\wedge \mathrm{M}^f{}_{\omega\omega} - \left(\mathrm{M}^f{}_{\omega\omega}\bar{\boldsymbol{\omega}}^o\right)_\wedge \end{bmatrix} \tag{D.41}$$

In order to determine the possible skew-symmetry properties of the operator, it can be compared to the opposite of its transpose:

$$\begin{aligned} -\left[\mathrm{G}^f_{\mathrm{rig}}\right]^{\mathrm{T}} &= \begin{bmatrix} -\mathrm{M}^f_{vv}{}^{\mathrm{T}} \left(\bar{\boldsymbol{\omega}}^o_\wedge\right)^{\mathrm{T}} & \left(\left(\mathrm{M}^f_{vv}\bar{\boldsymbol{v}}^o\right)_\wedge\right)^{\mathrm{T}} - \mathrm{M}^f_{vv}\bar{\boldsymbol{v}}^o_\wedge \\ \left(\left(\mathrm{M}^f_{vv}\bar{\boldsymbol{v}}^o\right)_\wedge\right)^{\mathrm{T}} & \left(\left(\mathrm{M}^f{}_{\omega\omega}\bar{\boldsymbol{\omega}}^o\right)_\wedge\right)^{\mathrm{T}} - \mathrm{M}^f{}_{\omega\omega}{}^{\mathrm{T}} \left(\bar{\boldsymbol{\omega}}^o_\wedge\right)^{\mathrm{T}} \end{bmatrix} \\ &= \begin{bmatrix} \mathrm{M}^f_{vv}\bar{\boldsymbol{\omega}}^o_\wedge & \mathrm{M}^f_{vv}\bar{\boldsymbol{v}}^o_\wedge - \left(\mathrm{M}^f_{vv}\bar{\boldsymbol{v}}^o\right)_\wedge \\ -\left(\mathrm{M}^f_{vv}\bar{\boldsymbol{v}}^o\right)_\wedge & \mathrm{M}^f{}_{\omega\omega}\bar{\boldsymbol{\omega}}^o_\wedge - \left(\mathrm{M}^f{}_{\omega\omega}\bar{\boldsymbol{\omega}}^o\right)_\wedge \end{bmatrix}, \end{aligned} \tag{D.42}$$

where the second line has been obtained by using the skew-symmetry properties of the cross-product operator and the symmetry properties of the added mass operator. By comparing (D.41) and (D.42), it appears that the gyroscopic operator $\mathrm{G}^f_{\mathrm{rig}}$ is not skew-symmetric when it is associated with rotations. The upper left block of the operator is not skew-symmetric contrarily to the gyroscopic operator associated with non-rotating motions. One might note how the loss of skew-symmetry is due to the coupling of $\bar{\boldsymbol{\omega}}^o$ with $\bar{\boldsymbol{v}}'$ and $\bar{\boldsymbol{\omega}}'$ and the coupling of $\bar{\boldsymbol{\omega}}'$ with $\bar{\boldsymbol{v}}^o$: therefore, the loss of skew-symmetry is due to the rotating frame.

Appendix E

Alternative simplified BEM formulation

There is also a last approach that I have implemented but which could not be compared to the method of this manuscript due to lack of time. It is an approach allowing to reduce by a factor of 3.5 the size of the BEM operators associated to the problem, limiting largely their computation cost. As explained below, this is done at the cost of approximations on the geometry (computation of a pseudonormal and its derivative with respect to the geometry at the nodes, and fluctuations of the Green's function and its gradient with respect to the neglected interface deformations, as explained below).

This method is inspired by the solution of submarine problems by Stéphanie Chaillat and Damien Mavaleix. Given the size of the problems they solve, they use two simplifying assumptions to compute the BEM operators:

1) The computation of the single layer operator does not take into account the normal. In this manuscript, we have computed the $[G]$ operator of size $N \times 3N$ which allows to obtain the single layer term thanks to a matrix-vector product of the type $[G]\{\bar{\boldsymbol{v}}\}$. Instead, it is possible to extract the normal of the operator by computing a new operator $[g]$ of size N which has 3 times less coefficients than $[G]$. We then obtain the single layer term thanks to a calculation of the type $[g]\{\bar{\boldsymbol{v}}.\bar{\boldsymbol{n}}\}$. The calculation seems simpler, however it hides behind a slight hitch: on the mesh, the normal is naturally defined on the elements but does not exist at the nodes. It is thus necessary to interpolate the normal $\bar{\boldsymbol{n}}_{tri}$ defined on the triangles at the level of the nodes $\bar{\boldsymbol{n}}_{node}$. One of the many possibilities to achieve that is to use an interpolation method using an error minimization that can be computed in a practical way with the FEM. This will allow to compute in a similar way the fluctuations of normal at the nodes by reusing the same FEM operators. Two FEM operators are introduced to interpolate the normal at the nodes (as a reminder, $[N(\bar{\boldsymbol{x}})]$ is the FEM matrix of linear interpolation according to the values at the nodes):

$$[\mathrm{A}_{node}] \quad \text{telle que } [\mathrm{A}_{node}]\{\bar{\boldsymbol{n}}_{node}\} = \int_{\overline{\Sigma}_N} [N(\bar{\boldsymbol{x}})]\{\bar{\boldsymbol{n}}_{node}\}\,\mathrm{d}\overline{\Sigma} \quad \text{de taille } N \times 3N$$

$$[\mathrm{A}_{tri}] \quad \text{telle que } [\mathrm{A}_{tri}]\{\bar{\boldsymbol{n}}_{tri}\} = \int_{\overline{\Sigma}_N} \bar{\boldsymbol{n}}_{tri}(\bar{\boldsymbol{x}})\,\mathrm{d}\overline{\Sigma} \quad \text{de taille } N \times 3N_{tri}.$$

with N_{tri} the number of triangles. We can see that the interpolated field $\bar{\boldsymbol{n}}_{node}$ is in fact associated to a linear approximation of the normal on the whole mesh. I then define this linear approximation

of the normal as the field minimizing the following square of the L^2 norm:

$$\{\bar{\boldsymbol{n}}_{node}\} = \text{argmin}_{\{\bar{\boldsymbol{n}}\}\in\mathbb{R}^{3N}} \left(\int_{\overline{\Sigma}_N} ([N(\bar{\boldsymbol{x}})]\{\bar{\boldsymbol{n}}\} - \bar{\boldsymbol{n}}_{tri}(\bar{\boldsymbol{x}}))^2 \, \mathrm{d}\overline{\Sigma} \right).$$

This can be solved quite naturally via the FEM using the following matrix equation:

$$\{\bar{\boldsymbol{n}}_{node}\} = [\mathrm{A}_{node}]^{-1} [\mathrm{A}_{tri}] \{\bar{\boldsymbol{n}}_{tri}\}.$$

We can thus obtain the normal to the nodes from the normal to the triangles of the mesh, which allows us to calculate the zero-order solution by solving the problem

$$[H]\{\phi^o\} = [g]\{\bar{\boldsymbol{v}}.\bar{\boldsymbol{n}}\},$$

whose BEM operators require storing 2 coefficients, instead of the 4 coefficients needed to store to invert the problem as in chapter IV:

$$[H]\{\phi^o\} = [G]\{\bar{\boldsymbol{v}}\}.$$

The method thus allows a storage gain of half. Due to time constraints, the results obtained with this simplified method could not be compared with the results obtained with the BEM presented in chapter III. To obtain a matrix-vector product formulation of the velocities (similar to the results of the chapter III), one can introduce the sparse matrix associated to the normal projection $[n_{scal}]$:

$$[n_{scal}] \text{ de taille } N \times 3N \text{ telle que } \{\bar{\boldsymbol{v}}\} = \{\bar{\boldsymbol{v}}.\bar{\boldsymbol{n}}\}$$
$$[H]\{\phi^o\} = ([g][n_{scal}])\{\bar{\boldsymbol{v}}^o\}.$$

2) In order to avoid costly recalculations of the BEM operators after each time iteration where the structure takes a new shape, Mavaleix-Marchessoux (2020) considers that the fluctuation of the BEM operators is negligible for small deformations (in practice, he uses a criterion of maximum deformation from which he considers that it becomes necessary to recalculate the BEM operators). Then, the only geometrical deformation taken into account in their model comes from the deformation of the normal. We can proceed in a similar way in the case of our linearized approach, but using the linearized fluctuations $\bar{\boldsymbol{\tau}}'$ of the normal ($\bar{\boldsymbol{\tau}}'$ also takes into account the dilations of the surface in addition to the rotations of the normal, which constitutes a difference between this approach and Mavaleix-Marchessoux (2020)'s):

$$[H]\{\bar{\phi}'\} = [g][\bar{\boldsymbol{n}}]\{\bar{\boldsymbol{v}}'\} + [g]\{\bar{\boldsymbol{v}}^o.\bar{\boldsymbol{\tau}}'\}. \tag{E.1}$$

Using FEM, we can compute a sparse matrix $[tau]$ of size $3N_{tri} \times 3N$ which allows us to obtain the fluctuations of normal τ_{tri} on each element of the mesh:

$$\{\tau_{tri}\} = [\tau]\{\bar{\boldsymbol{\xi}}'\}. \tag{E.2}$$

Note that the above method also works if we have several columns in the vector $\{barxip\}$ (associated with different modes for example): we then obtain several columns on $\{\tau_{tri}\}$ associated with the

deformations of the normal according to each mode. However, we need the value of $\{\tau_{node}\}$ at the nodes for the scalar product $\{\bar{\boldsymbol{v}}^o.\bar{\boldsymbol{\tau}}'\}$, so we compute the interpolation of $\{\tau_{tri}\}$ at the nodes as follows:

$$\tau_{node} = [\mathrm{A}_{node}]^{-1}\,[\mathrm{A}_{tri}]\,\{\tau_{tri}\} = [\mathrm{A}_{node}]^{-1}\,[\mathrm{A}_{tri}]\,[\tau]\,\{\bar{\boldsymbol{\xi}}'\}. \tag{E.3}$$

Finalement, on introduit la matrice associée au produit scalaire par la vitesse à l'ordre zéro telle que

$$[v^o_{scal}]\,\{\boldsymbol{a}\} = \{\boldsymbol{v}^o.\boldsymbol{a}\} \quad \forall\{\boldsymbol{a}\}, \tag{E.4}$$

and we obtain the following first-order expression of the potential:

$$[H]\,\{\bar{\phi}'\} = ([g]\,[\bar{\boldsymbol{n}}])\,\{\bar{\boldsymbol{v}}'\} + \Big([g]\,[v^o_{scal}]\,[\mathrm{A}_{node}]^{-1}\,[\mathrm{A}_{tri}]\,[\tau]\Big)\,\{\bar{\boldsymbol{\xi}}'\}. \tag{E.5}$$

We notice in particular that for the computation of the fluctuations associated to the $\bar{\boldsymbol{\xi}}'$ deformations, it is not necessary with the above formulation to recompute a new linearized BEM operator: we have simply reused the zero-order BEM operators to which are added sparse FEM operators which are not very costly in terms of computation time and storage. Thus, we can evaluate that the storage cost necessary for the resolution of the fluctuations with the above formalism is about $2N^2$, by reusing the zero-order operators. On the contrary, the method introduced in the chapter III, although more rigorous mathematically (no interpolation of the normals and especially taking into account the fluctuations of the green function and its gradient for the operators $[H]$ and $[G]$ which makes it possible to predict the effects due to the change of geometry and not only to the rotations of the normal), is much more expensive in storage:

$$[H]\,\{\bar{\phi}'\} = [G]\,\{\bar{\boldsymbol{v}}'\} + \big[J'\big]\,\{\bar{\boldsymbol{\xi}}'\}. \tag{E.6}$$

The above equation indeed has a storage cost of about $7N^2$: we always have the matrix $[H]$ of size N^2, and the matrices $[G]$ and $[J']$ are both of size $3N^2$. Another limiting factor of the above equation in terms of computation time comes from the fact that the zero-order operators $[H]$ and $[G]$ can both be constructed at the same time (in the same "for" loop) which is a significant gain in computation time. However, as the derived operator $[J']$ depends on the zero-order solution, it can only be computed in a second time in a new "for" loop, once the zero-order problem has been solved. Thus, having to compute the BEM operators in two steps increases a lot the necessary computation time. Finally, we can note that, if we wish to make a calculation based on a second velocity at order zero, $barv^o$ changes and it is then necessary to recompute a new operator $matJ'$ which is very expensive. Using the approximate method, the calculation based on a second solution at order zero only requires to recalculate a new hollow matrix $[v^o_{scal}]$ which is very cheap in computation time and storage.

Appendix F

Loads of an ambient flow on a flexible sructure

A linearized ALE Boundary Element Method for flexible 3D bluff bodies in potential flows: towards application to airship aeroelasticity

Robin Le Mestre[a,b], Jean-Sébastien Schotté[b], Olivier Doaré[a]

[a] *IMSIA, ENSTA Paris, Institut Polytechnique de Paris, 828 Boulevard des Maréchaux, 91120, Palaiseau, France*
[b] *DAAA, ONERA, Université Paris Saclay, F-92322 Châtillon, France*

Abstract

Effects of fluid-structure coupling on the dynamic behavior of flexible airships can be modeled with a potential, incompressible, inviscid flow. A new formalism to study the linear behavior of a fluid-structure interface in a time-dependent ambient flow is introduced. The fluid equations are condensed at the interface with the help of integral equations, which are expressed as a function of the structure variables defined on a time-independent reference configuration with an Arbitrary Lagrangian-Eulerian (ALE) formalism. The features of the Boundary Element Method (BEM) used to solve this problem numerically are exhibited. The approximations of this method associated with both linearization and discretization are quantified to validate the model. A simplified flexible airship test case model is studied to illustrate a practical application of the method.

Keywords: fluid-structure interaction, linear stability analysis, arbitrary-lagrangian-eulerian, boundary element method

Contents

*Corresponding author
Email address: roblm@hotmail.fr (Robin Le Mestre)

1. Introduction

With the emergence of non-rigid airship projects such as stratospheric platforms, envelopes are getting thinner and more flexible [1]. As a consequence, strong couplings between the structure deformations and the surrounding flowing fluid occur. Research works in this domain aim to predict instabilities such as flutter, that can appear at critical velocity. However, the unsteady coupling of the elastic structure with a surrounding flow remains challenging to predict numerically or experimentally because of the large scale of airships.

To tackle the complex problem of flexible airships fluid-structure interaction, Amiryants et al. [2] simplified the volume geometry as surfaces projected on vertical and horizontal planes. The resulting geometry has been modeled as a lifting surface with the panel method in order to take into account circulation effects of the fluid around the hull and fins. This study showed the possible rise of flutter at high velocities, by coupling of the first modes of the free airship with the flow. Bessert et al. [3] further carried a panel method based on a volume mesh, calculating the static deflection of the airship. Their results showed the non-linear nature of the quasi-steady deformations under certain wind conditions. The static flexible solution was determined more precisely by Liu et al. [4] and Wu et al. [5] using Reynolds-Averaged Navier-Stokes (RANS) methods. This numerical study has been validated with a flexible model in a wind tunnel. However, the cost of RANS calculations is prohibitive for large dynamic fluid-structure coupled problems such as airships [1], hence the need for simplified approaches. Li et al. and Azouz et al. [6, 7] derived analytically the added mass effects associated with the important role of the inertia of the fluid surrounding the accelerated airship. These analytic solutions were obtained by approximating the hull shape as a simpler, regular geometric shape. Moreover, Li et al. calculated the linear interaction of a potential fluid with the structure by using the slender body approximation, on which were superimposed turbulence effects at the fins and the tail of the airship, predicting also a risk of flutter at high wind velocities.

The potential flow hypothesis relies on the fact that the rotational part of the fluid can be neglected (therefore not taking into account viscous effects), enabling to express the velocity field as the gradient of a scalar potential field. This hypothesis is met in practice for airships because of their great lengths [1]. However, viscous phenomena are not negligible locally, at the tail and the fins of the airship for example. Despite the drag forces and circulation phenomena are not captured by the potential approach, these contributions might be taken into account afterwards, superimposing it to the potential solution as done by Li [6]. Potential flows are however interesting to consider as they are easier to solve than viscous flows, especially thanks to the Boundary Element Method (BEM). Riccardi & Bernardis [9] used this method to study the dynamics of rising bubbles. Van Opstal & van Brummelen [10] investigated for their part the large displacements of membranes enclosing fluids such as airbags. The level set approach, which enables to describe the boundary of the domain as the set of roots of a function, has been coupled to the BEM resolution by Tan et al and Garzon et al. [11, 12] to solve multiphase flows (respectively bubbles and waves): such methods are particularly well suited for coupled problems involving large deformations of the interface. Véron et al. [13] solved the interaction between submerged pipes with internal and external flows. All these applications imply large displacements as well as partitioned approaches, meaning that the fluid and solid equations are solved separately and on a new deformed mesh at each time step. This paper introduces a method enabling us to solve the monolithic fluid-structure problem associated with the small movements of a membrane that enables to model the strong coupling between flexible structure vibrations and a surrounding flow. It is implemented numerically using a linearized BEM approach in an ALE framework, which is, to the author's knowledge, a novelty compared to the existing literature: actually, BEM had been used with ALE, but the associated linearized formulation had not been developed, and the linearization of the BEM in the context of potential flows is an original aspect of this work. As a linearized approach, it is particularly well suited for studies in the frequency domain or for stability analysis.

The paper is organized as follows. The expression of the work of the fluid pressure on the structure depending on its movements is derived in section 2. The integral representation of the flow in an Eulerian frame is introduced in order to obtain a formulation condensed at the fluid-structure interface. These integral equations are then expressed using an Arbitrary Lagrangian Eulerian (ALE) formulation, enabling to express the pressure work of the flow with respect to time-independent spatial coordinates. The fluid loads are

linearized for small movements around the steady state. In section 3, the linear work of the fluid is determined numerically using the BEM. The aeroelastic model is then obtained by coupling those fluid loads with the structure dynamical behavior. In section 4, the error associated with the numerical approximation, the potential flow theory and the linear approximations is quantified by comparison with analytic results, more accurate numerical simulations and a mesh deformation approach. The fluid-structure coupling method in then applied to the case of an ellipsoidal inflated membrane in section 5. The aeroelastic equations are projected on the *in vacuo* modes of the membrane to reduce the computation cost. The modes of the immersed structure are then calculated, exhibiting an instability induced by the coupling of the flow with the deformations of the structure. A conclusion is given in section 6 and the article is completed by some calculation details in two appendices.

2. Derivation of the potential flow efforts on a moving interface with respect to reference spatial coordinates

The aim of this section is to introduce the mathematical fluid model that will be solved numerically using the method presented in the next section. In all the following mathematical derivations, the vectors will be in bold notation and the tensors will be double-struck.

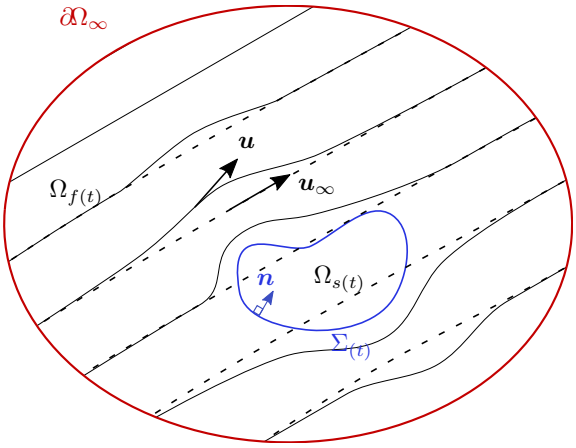

Figure 1: Schematic view of a solid defined by the volume $\Omega_{s(t)}$ that deforms in a flow defined by the volume $\Omega_{f(t)}$. The exterior boundary of the fluid, denoted Ω_∞, is supposed to be at infinity. The ambient flow in absence of solid is supposed to be a homogeneous flow $\boldsymbol{u}_\infty$.

Let us consider a solid ($\Omega_{s(t)}$ domain) that deforms in a potential flow ($\Omega_{f(t)}$ domain), as sketched in Figure 1. The time is denoted t, and the displacement field of the solid is denoted $\boldsymbol{\xi}$. We suppose that this elastic structure is characterized by a stiffness and a mass operator, respectively K_s and M_s. Using a variational approach with $\delta\boldsymbol{\xi}$ a virtual admissible displacement and f_{ext} the work of the external forces on the structure, the weak form of the fluid-structure equation can be written in this form:

$$K_s(\boldsymbol{\xi}, \delta\boldsymbol{\xi}) + M_s\left(\frac{\partial^2\boldsymbol{\xi}}{\partial t^2}, \delta\boldsymbol{\xi}\right) - f_{ext}(\delta\boldsymbol{\xi}) = 0. \tag{1}$$

Under the hypothesis that both Reynolds and Stokes [1] numbers are large:

$$\mathcal{R}_e = \frac{\rho_f U_\infty L}{\mu} \gg 1 \text{ and } \mathcal{S}_t = \frac{\rho_f \Omega L^2}{\mu} \gg 1, \tag{2}$$

[1] ratio between inertia and viscosity effects of the fluid

where L and Ω are respectively the characteristic length and circular frequency of the structure, ρ_f and μ are respectively the density and the viscosity of the fluid, and $U_\infty = \|\boldsymbol{u}_\infty\|$ is the characteristic velocity of the ambient flow. Assumption (2) enables to neglect viscosity effects and to use an inviscid fluid model. The forcing term f_{ext} applied by an inviscid fluid on the structure writes [14] :

$$f_{ext}(\delta\boldsymbol{\xi}) = \int_{\Sigma_{(t)}} p\boldsymbol{n} \cdot \delta\boldsymbol{\xi} \, \mathrm{d}\Sigma_{(t)}, \tag{3}$$

p being the pressure and $\boldsymbol{n}$ the normal of the fluid-structure interface $\Sigma_{(t)}$ oriented inward the solid. In order to calculate the dynamical solution of equations (1,3) with respect to the structure movements on a reference, stationnary interface, the fluid's and structure's dynamics have to be linearized. The objective of the next section is to obtain a set of linearized fluid equations using an Arbitrary Lagrangian Eulerian (ALE) formulation.

2.1. Eulerian description of a potential flow

A classical approach when modeling fluid dynamics is to use an Eulerian framework in order to study the velocity of particles through a fixed elementary volume contrarily to the Lagrangian framework, which is focused on the material particles. The fluid equations will first be presented in an Eulerian frame for both kinematic and dynamic equations of the potential flow. A fixed fluid domain Ω_∞ is considered, bounded by a closed surface $\partial\Omega_\infty$ which is a sphere of radius r. The ambient flow $\boldsymbol{u}_\infty$ is defined as the flow in the absence of a structure (dashed streamlines of Figure 1). The latter is supposed to be irrotational, stationary and homogeneous, enabling to express it with a potential ϕ_∞ defined up to a spatial constant by

$$\boldsymbol{u}_\infty = \boldsymbol{\nabla}\phi_\infty \quad \text{in } \Omega_\infty. \tag{4}$$

At the scale of airships, the flow velocity is much lower than that of the sound in air c, and the Mach number $\mathcal{M}_a$ verifies

$$\mathcal{M}_a = \frac{U_\infty}{c} < 0.3, \tag{5}$$

which means the flow can be considered as incompressible. For a potential flow, the incompressibility condition writes:

$$\Delta\phi_\infty = 0 \quad \text{in } \Omega_\infty. \tag{6}$$

When a moving structure is introduced, the domain Ω_∞ is divided into fluid and solid sub-domains $\Omega_{f(t)}$ and $\Omega_{s(t)}$ separated by the fluid-structure interface $\Sigma_{(t)}$. The fluid evolves in a domain $\Omega_{f(t)}$ bounded by the fluid-structure interface $\Sigma_{(t)}$ and its exterior boundary $\partial\Omega_\infty$. The effects of the turbulent boundary layer are neglected and we consider the case where no circulation is induced by the interface on the supposedly inviscid flow $\boldsymbol{u}$ (see hypothesis (2)), enabling to express it with a potential ϕ defined up to a spatial constant by

$$\boldsymbol{u} = \boldsymbol{\nabla}\phi \quad \text{in } \Omega_{f(t)} \text{ with } \phi = \phi_\infty + \phi_p \tag{7}$$

The flow $\boldsymbol{u}$ (continuous streamlines of Figure 1) in the fluid domain is decomposed into an ambient flow $\boldsymbol{u}_\infty$ and a potential perturbed flow $\boldsymbol{u}_p = \boldsymbol{\nabla}\phi_p$ such that:

$$\boldsymbol{u} = \boldsymbol{\nabla}\phi_\infty + \boldsymbol{\nabla}\phi_p \quad \text{in } \Omega_{f(t)}. \tag{8}$$

The flow incompressibility combined with (6) and (8) provides

$$\Delta\phi_p = 0 \quad \text{in } \Omega_{f(t)}. \tag{9}$$

Because of hypothesis (2), the fluid is considered inviscid, therefore the kinematic boundary condition is introduced as

$$\boldsymbol{u} \cdot \boldsymbol{n} = \frac{\partial \boldsymbol{\xi}}{\partial t} \cdot \boldsymbol{n} \quad \text{on } \Sigma_{(t)}, \tag{10}$$

$\frac{\partial \boldsymbol{\xi}}{\partial t}$ being the velocity of the interface. When combined with (8), equation (10) becomes

$$\boldsymbol{\nabla} \phi_p \cdot \boldsymbol{n} = \left(\frac{\partial \boldsymbol{\xi}}{\partial t} - \boldsymbol{u}_\infty \right) \cdot \boldsymbol{n} \quad \text{on } \Sigma_{(t)}. \tag{11}$$

Since ϕ_p is defined up to a constant, we arbitrarily impose

$$\phi_p(\boldsymbol{x}) \to 0 \quad \text{on } \partial\Omega_\infty \text{ for } r \to \infty, \tag{12}$$

to ensure the uniqueness of the solution (r is the radius of the enclosing sphere $\partial\Omega_\infty$). The exterior Laplace equation (9) associated with the Neumann condition (11) and the uniqueness condition (12) is a well-posed problem according to Folland [15], which ensures the existence and unicity of its solution ϕ_p. The latter can be written as the sum of single and double layer terms [15], meaning that its rate of decrease at infinity verifies:

$$\phi_p(\boldsymbol{x}) = \mathcal{O}\left(r^{-1}\right) \quad \text{on } \partial\Omega_\infty, \tag{13a}$$

$$\boldsymbol{\nabla} \phi_p(\boldsymbol{x}) \cdot \boldsymbol{n} = \mathcal{O}\left(r^{-2}\right) \quad \text{on } \partial\Omega_\infty, \tag{13b}$$

$$\frac{\partial \phi(\boldsymbol{x}_\infty)}{\partial t} = \mathcal{O}\left(r^{-1}\right) \quad \text{on } \partial\Omega_\infty \tag{13c}$$

$$r = \|\boldsymbol{x}\|. \tag{13d}$$

One might note that the potential solution ϕ_p might be referred to as a full potential flow as it is irrotational everywhere on the fluid domain [27], unlike quasi-potential flows which are irrotational everywhere in the fluid domain excepted on an infinitely thin vortex sheet generated behind the rear of the body [28]. Unlike quasi-potential flows, stationary full-potential flows do not generate lift on the structure. In order to obtain a well-defined fluid problem, it is necessary to add initial conditions associated with the movements of the interface, such as the Cauchy condition below:

$$\boldsymbol{\xi}(t_{\text{ini}}) = \boldsymbol{\xi}_{\text{ini}} \tag{14a}$$

$$\frac{\partial \boldsymbol{\xi}}{\partial t}(t_{\text{ini}}) = \boldsymbol{v}_{\text{ini}}. \tag{14b}$$

The pressure p, needed to compute the virtual work f_{ext} of equation (3), is calculated as a function of the kinematic variables of the fluid using the Bernoulli equation for potential flows:

$$\frac{p}{\rho_f} + \frac{\partial \phi}{\partial t} + \frac{1}{2}\boldsymbol{u}^2 + gz = C(t), \tag{15}$$

$C(t)$ being an homogeneous time-dependent parameter. The incompressibility of the fluid (5) ensures that ρ_f is homogeneous. In order to determine the constant $C(t)$, the far field condition of the ambient flow is expressed introducing the energy per unit mass Ψ_∞, far from the structure:

$$\frac{p}{\rho_f} + \frac{1}{2}\boldsymbol{u}^2 + gz = \Psi_\infty + \frac{\partial \phi(\boldsymbol{x}_\infty)}{\partial t} = \Psi_\infty \quad \text{on } \partial\Omega_\infty. \tag{16}$$

The above expression is valid at each point remote from the structure because of equations (15) and (13c). By introducing Ψ_∞ into the Bernoulli equation (15), one gets:

$$\frac{p}{\rho_f} + \frac{\partial \phi}{\partial t} + \frac{1}{2}\boldsymbol{u}^2 + gz = \Psi_\infty \quad \text{in } \Omega_{f(t)}. \tag{17}$$

It is convenient, for the sake of understanding the underlying physics behind the model, to separate the pressure in two different contributions. As with velocity potential and velocity, pressure is separated into an ambient pressure p_∞ (not to be confused with the pressure at infinity $p(\boldsymbol{x}_\infty)$), which corresponds to the pressure of the fluid in the absence of the structure, and the pressure perturbation p_p induced by the moving structure:

$$p = p_\infty + p_p \text{ with } \frac{p_\infty}{\rho_f} = \Psi_\infty - \frac{\partial \phi_\infty}{\partial t} - \frac{1}{2}U_\infty^2 - gz \tag{18a}$$

$$\frac{p_p}{\rho_f} = -\frac{1}{2}\boldsymbol{u}_p^2 - \boldsymbol{u}_\infty \cdot \boldsymbol{u}_p - \frac{\partial \phi_p}{\partial t}. \tag{18b}$$

The above expression of the pressure will be used in the numerical implementation to separate the ambient and structure perturbation contributions. Thanks to the equations above, the pressure p, which allows to determine the work of the fluid f_{ext}, can be deduced from the perturbation potential ϕ_p and its spatial derivative $\boldsymbol{u}_p$. It is therefore necessary to obtain the perturbation potential ϕ_p whose calculation with the BEM necessitates to exhibit an integral formulation, which is the aim of the next section.

2.2. Arbitrary Lagrangian Eulerian formulation of the boundary integral equations

The calculation of ϕ_p could be achieved by introducing a weak formulation [16] associated to the local equations (9) and (11) in order to use the Finite Element Method (FEM). However this approach would have inconveniences in this particular case. It would require solving the velocity potential at every node of the fluid mesh, which is very costly. Moreover, because the domain is infinite, it would have to be artificially truncated (by meshing only a part of it in practice), introducing artificial confinement effects. Finally, the ALE formulation is convenient to manage the coupling of the structure with the flow, but it requires the introduction of an unknown fluid mesh deformation when used with the FEM [17]. It is not the case with the BEM as the mesh displacement at the interface is the same as the structure displacement. Consequently, a BEM is used here, and an integral equation involving the Green's function is introduced for that purpose. In the case of Laplace's equation (9) in a three-dimension space [21], Green's function G can be defined as

$$\forall \boldsymbol{x}, \boldsymbol{y} \in \Omega_\infty \times \Omega_\infty : \ \Delta_{\boldsymbol{x}} G(\boldsymbol{x}, \boldsymbol{y}) = \delta(\boldsymbol{x} - \boldsymbol{y}) \tag{19a}$$

$$\boldsymbol{\nabla}_{\boldsymbol{x}} G(\boldsymbol{x}, \boldsymbol{y}) = \frac{\boldsymbol{x} - \boldsymbol{y}}{4\pi \left\| \boldsymbol{x} - \boldsymbol{y} \right\|^3} \tag{19b}$$

$$G(\boldsymbol{x}, \boldsymbol{y}) = -\frac{1}{4\pi(\boldsymbol{x} - \boldsymbol{y})}, \tag{19c}$$

where δ denotes the Dirac distribution. Any function written as the sum of G and a field linear with $\boldsymbol{x}$ would also be a fundamental solution of Laplace's equation, but G has the advantage of decaying to zero at infinity. Since $\partial\Omega_\infty \cup \Sigma_{(t)}$ is an enclosing boundary of the fluid volume $\Omega_{f(t)}$ and $\boldsymbol{n}$ is the outward normal of $\Omega_{f(t)}$, the Green identity can be applied as

$$\begin{aligned} \forall \boldsymbol{y} \in \Omega_\infty, \quad & \int_{\Omega_{f(t)}} \Delta_{\boldsymbol{x}} G_{(\boldsymbol{x},\boldsymbol{y})} \phi_{p(\boldsymbol{x})} - \Delta \phi_{p(\boldsymbol{x})} G_{(\boldsymbol{x},\boldsymbol{y})} \mathrm{d}\Omega_{(\boldsymbol{x})} = \dots \\ & \oint_{\Sigma_{(t)} \cup \partial\Omega_\infty} \left[\boldsymbol{\nabla}_{\boldsymbol{x}} G_{(\boldsymbol{x},\boldsymbol{y})} \cdot \boldsymbol{n}_{(\boldsymbol{x})} \phi_{p(\boldsymbol{x})} - \boldsymbol{\nabla} \phi_{p(\boldsymbol{x})} \cdot \boldsymbol{n}_{(\boldsymbol{x})} G_{(\boldsymbol{x},\boldsymbol{y})} \right] \mathrm{d}\Sigma_{(\boldsymbol{x})}. \end{aligned} \tag{20}$$

The rate of decay of the potential (13) and of the Green's function (19b), (19c) at infinity enables us to express the integral on border $\partial\Omega_\infty$ from equation (20), recalling that infinitesimal sphere surfaces (with radius r) $\mathrm{d}\Sigma_{(t)}$ are of order $\mathcal{O}\left(r^2\right)$:

$$\oint_{\partial\Omega_\infty} \left[\boldsymbol{\nabla}_{\boldsymbol{x}} G_{(\boldsymbol{x},\boldsymbol{y})} \cdot \boldsymbol{n}_{(\boldsymbol{x})} \phi_{p(\boldsymbol{x})} - \boldsymbol{\nabla} \phi_{p(\boldsymbol{x})} \cdot \boldsymbol{n}_{(\boldsymbol{x})} G_{(\boldsymbol{x},\boldsymbol{y})}\right] \mathrm{d}\Sigma_{(\boldsymbol{x})}$$
$$= \oint_{\partial\Omega_\infty} \left[\mathcal{O}\left(r^{-2}\right)\mathcal{O}\left(r^{-1}\right) + \mathcal{O}\left(r^{-1}\right)\mathcal{O}\left(r^{-2}\right)\right]\mathcal{O}\left(r^2\right) \tag{21}$$
$$= \mathcal{O}\left(r^{-1}\right) \to 0$$

The above equation enables us to neglect the integral on the border $\partial\Omega_\infty$ from equation (20). The following property, taken from [23]:

$$\int_{\Omega_{f(t)}} \Delta_{\boldsymbol{x}} G_{(\boldsymbol{x},\boldsymbol{y})} \phi_{p(\boldsymbol{x})} \mathrm{d}\Omega = \phi_p(\boldsymbol{y}) \left(1 + \oint_{\Sigma_{(t)}} \boldsymbol{\nabla}_{\boldsymbol{x}} G_{(\boldsymbol{x},\boldsymbol{y})} \cdot \boldsymbol{n}_{(\boldsymbol{x})} \mathrm{d}\Sigma_{(\boldsymbol{x})}\right) \quad \forall \boldsymbol{y} \in \Sigma_{(t)}, \tag{22}$$

combined with equations (9) and (20), gives the regularized expression og the Boundary Integral equation

$$\phi_p(\boldsymbol{y}) = \int_{\Sigma_{(t)}} \boldsymbol{\nabla}_{\boldsymbol{x}} G_{(\boldsymbol{x},\boldsymbol{y})} \cdot \boldsymbol{n}_{(\boldsymbol{x})} \left(\phi_{p(\boldsymbol{x})} - \phi_{p(\boldsymbol{y})}\right) + G_{(\boldsymbol{x},\boldsymbol{y})} \left(\boldsymbol{u}_\infty - \frac{\partial \boldsymbol{\xi}_{(\boldsymbol{x})}}{\partial t}\right) \cdot \boldsymbol{n}_{(\boldsymbol{x})} \mathrm{d}\Sigma_{(\boldsymbol{x})} \quad \forall \boldsymbol{y} \in \Sigma_{(t)}. \tag{23}$$

The solution of this equation can be approximated using the BEM. However, since the interface $\Sigma_{(t)}$ is time-dependent, solving such an equation would imply building a new mesh at each time step. In order to calculate the integral representation of the fluid problem by the means of of time-independent space coordinates, the ALE method expresses the parameters of the fluid with respect to a fixed reference interface. The linearized equations will be derived relatively to a reference position $\overline{\Sigma}$, arbitrarily set to be the fluid-structure interface in the absence of deformations: $\overline{\Sigma} = \Sigma_{(\boldsymbol{\xi}=\boldsymbol{0})}$, see Figure 2. The physical variables evolving on the time-dependent interface $\Sigma_{(t)}$ will then be expressed as a function of the reference interface $\overline{\Sigma}$, as detailed in [17] in the context of elastic structures interacting with viscous flows. The variables defined on $\overline{\Sigma}$ are written with a bar $\overline{(\bullet)}$. The displacement $\bar{\boldsymbol{\xi}}$ of the physical interface at $\boldsymbol{x} \in \Sigma_{(t)}$ is thus decomposed as

$$\bar{\boldsymbol{\xi}}(\bar{\boldsymbol{x}}, t) = \boldsymbol{x}(\bar{\boldsymbol{x}}, t) - \bar{\boldsymbol{x}} \quad \forall \bar{\boldsymbol{x}} \in \overline{\Sigma}. \tag{24}$$

It is the common definition of the displacement in solid mechanics written in a Lagrangian framework (hence inherent to a moving material point). The surface vector gradient $\overline{\boldsymbol{\nabla}}_S$, the surface gradient tensor $\overline{\nabla}_S$, the surface deformation gradient $\overline{\mathbb{F}}_S$ and the surface deformation operator $\bar{\Phi}_S$ are useful tools for the description of the geometrical evolution of the interface, defined as:

$$\overline{\boldsymbol{\nabla}}_S(\bullet) = (\mathbb{1} - \bar{\boldsymbol{n}} \otimes \bar{\boldsymbol{n}})\overline{\boldsymbol{\nabla}}(\bullet), \tag{25a}$$
$$\overline{\nabla}_S^{\mathrm{T}}(\bullet) = (\mathbb{1} - \bar{\boldsymbol{n}} \otimes \bar{\boldsymbol{n}})\overline{\nabla}^{\mathrm{T}}(\bullet), \tag{25b}$$
$$\overline{\mathbb{F}}_S(\bar{\boldsymbol{\xi}}) = \mathbb{1} + \overline{\nabla}_S \bar{\boldsymbol{\xi}}, \tag{25c}$$
$$\bar{\Phi}_S(\bar{\boldsymbol{\xi}}) = \det\left(\overline{\mathbb{F}}_S\left(\bar{\boldsymbol{\xi}}\right)\right)\ \overline{\mathbb{F}}_S(\bar{\boldsymbol{\xi}})^{-1}. \tag{25d}$$

One can express an oriented infinitesimal element of surface $\boldsymbol{n}\mathrm{d}\Sigma$ through the surface deformation operator using Nanson's formula based on the interface deformations, as shown in [21, 19, 20]:

$$\boldsymbol{n}(\boldsymbol{x})\mathrm{d}\Sigma(\boldsymbol{x}) = \bar{\Phi}_S(\bar{\boldsymbol{\xi}})^{\mathrm{T}} \bar{\boldsymbol{n}}(\bar{\boldsymbol{x}}) \mathrm{d}\overline{\Sigma}(\bar{\boldsymbol{x}}) \quad \forall \bar{\boldsymbol{x}} \in \overline{\Sigma}, \tag{26}$$

where $\bar{\boldsymbol{n}}\mathrm{d}\overline{\Sigma}$ denotes an infinitesimal oriented area on the reference surface $\overline{\Sigma}$ and superscript $(\bullet)^T$ denotes the transpose of a tensor. Let us remark that we use here the surface deformation operator $\bar{\Phi}_S$ which has the advantage of using the surface gradient of the interface displacement [21], unlike the classical expression of Nanson's formula which requires to know the normal derivative of the interface displacements. The flow velocity potential and velocity with respect to the reference interface are defined as well:

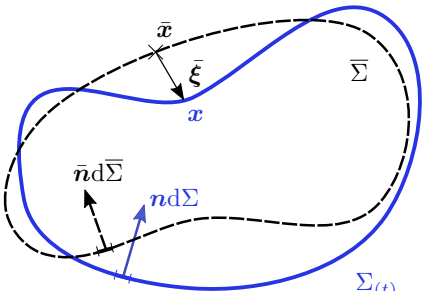

Figure 2: Reference and actual configuration of the problem.

$$\bar{\phi}_p(\bar{\boldsymbol{x}}) \equiv \phi_p(\boldsymbol{x}), \quad \bar{\boldsymbol{u}}_p(\bar{\boldsymbol{x}}) \equiv \boldsymbol{u}_p(\boldsymbol{x}) \quad \forall \bar{\boldsymbol{x}} \in \overline{\Sigma}, \tag{27}$$

where $\equiv$ stands for "is defined as". The Green's function and its normal derivative appearing in (23) are defined similarly:

$$\overline{\boldsymbol{G}_{\boldsymbol{n}}}_{(\bar{\boldsymbol{x}},\bar{\boldsymbol{y}},\bar{\boldsymbol{\xi}})}\mathrm{d}\overline{\Sigma}_{(\bar{\boldsymbol{x}})} \equiv G_{(\boldsymbol{x},\boldsymbol{y})}\boldsymbol{n}_{(x)}\mathrm{d}\Sigma_{(x)} \qquad \forall \bar{\boldsymbol{x}}, \bar{\boldsymbol{y}} \in \overline{\Sigma}, \tag{28a}$$

$$\overline{\partial_n G}_{(\bar{\boldsymbol{x}},\bar{\boldsymbol{y}},\bar{\boldsymbol{\xi}})}\mathrm{d}\overline{\Sigma}_{(\bar{\boldsymbol{x}})} \equiv \boldsymbol{\nabla}_x G_{(\boldsymbol{x},\boldsymbol{y})} \cdot \boldsymbol{n}_{(\boldsymbol{x})}\mathrm{d}\Sigma_{(\boldsymbol{x})} \qquad \forall \bar{\boldsymbol{x}}, \bar{\boldsymbol{y}} \in \overline{\Sigma}. \tag{28b}$$

It is worth noticing that equations (24), (27) and (28) differ from (26) as the former ones define an equality between the variables expressed on the physical and reference spaces whereas $\boldsymbol{n}\mathrm{d}\Sigma$ undergoes a transformation relatively to the reference configuration $\bar{\boldsymbol{n}}\mathrm{d}\overline{\Sigma}$. The way $\bar{\phi}_p$ is defined is not inherent to a moving fluid particle contrarily to a Lagrangian framework, but results from their observation on a point moving in space which also differs from the Eulerian framework that observes particles properties on a fixed point of space. This is the reason why this method is referred to as an Arbitrary Lagrangian Eulerian (ALE) approach [22]. By combining (11), (24), (26) and (27) (noting that, for an homogeneous ambient flow, the parameter $\boldsymbol{u}_\infty$ does not vary when it is expressed in the time dependant or in the reference domain), we deduce:

$$G_{(\boldsymbol{x},\boldsymbol{y})}\boldsymbol{\nabla}\phi_{p(\boldsymbol{x})} \cdot \boldsymbol{n}_{(\boldsymbol{x})}\mathrm{d}\Sigma_{(\boldsymbol{x})} = \overline{\boldsymbol{G}_{\boldsymbol{n}}}_{(\bar{\boldsymbol{x}},\bar{\boldsymbol{y}},\bar{\boldsymbol{\xi}})} \cdot \left(\frac{\partial \bar{\boldsymbol{\xi}}_{(\bar{\boldsymbol{x}})}}{\partial t} - \boldsymbol{u}_\infty\right)\mathrm{d}\overline{\Sigma} \quad \forall \bar{\boldsymbol{x}}, \bar{\boldsymbol{y}} \in \overline{\Sigma}. \tag{29}$$

The integral representation (23) written on the reference configuration is then given by:

$$\bar{\phi}_p(\bar{\boldsymbol{y}}) = \int_{\overline{\Sigma}} \overline{\partial_n G}_{(\bar{\boldsymbol{x}},\bar{\boldsymbol{y}},\bar{\boldsymbol{\xi}})} \left(\bar{\phi}_{p(\bar{\boldsymbol{x}})} - \bar{\phi}_{p(\bar{\boldsymbol{y}})}\right) + \overline{\boldsymbol{G}_{\boldsymbol{n}}}_{(\bar{\boldsymbol{x}},\bar{\boldsymbol{y}},\bar{\boldsymbol{\xi}})} \cdot \left(\boldsymbol{u}_\infty - \frac{\partial \bar{\boldsymbol{\xi}}_{(\bar{\boldsymbol{x}})}}{\partial t}\right)\mathrm{d}\overline{\Sigma} \quad \forall \bar{\boldsymbol{y}} \in \overline{\Sigma}. \tag{30}$$

Furthermore, we can introduce the time derivative of a scalar function expressed on a moving point of the interface using the chain rule:

$$\frac{\mathrm{d}\bar{\phi}(\bar{\boldsymbol{x}},t)}{\mathrm{d}t} = \frac{\mathrm{d}\phi(\boldsymbol{x},t)}{\mathrm{d}t} = \frac{\partial \phi(\boldsymbol{x})}{\partial t} + \frac{\partial \boldsymbol{x}}{\partial t} \cdot \boldsymbol{\nabla}\phi(\boldsymbol{x}) \quad \forall \bar{\boldsymbol{x}} \in \overline{\Sigma}. \tag{31}$$

By replacing the expression of $\frac{\partial \boldsymbol{x}}{\partial t} = \frac{\partial \boldsymbol{\xi}}{\partial t} = \frac{\partial \bar{\boldsymbol{\xi}}}{\partial t}$ and $\boldsymbol{\nabla}\phi = \boldsymbol{u}(\boldsymbol{x}) = \bar{\boldsymbol{u}}(\bar{\boldsymbol{x}})$, equation (31) becomes:

$$\frac{\partial \phi(\boldsymbol{x},t)}{\partial t} = \frac{\mathrm{d}\bar{\phi}(\bar{\boldsymbol{x}},t)}{\mathrm{d}t} - \frac{\partial \bar{\boldsymbol{\xi}}(\bar{\boldsymbol{x}},t)}{\partial t} \cdot \bar{\boldsymbol{u}}(\bar{\boldsymbol{x}},t) \quad \forall \boldsymbol{x} \in \Sigma. \tag{32}$$

We introduce the pressure $\bar{p}$ with respect to the reference interface:

$$\bar{p}(\bar{\boldsymbol{x}}) \equiv p(\boldsymbol{x}) \quad \forall \bar{\boldsymbol{x}} \in \overline{\Sigma}. \tag{33}$$

By combining equations (17), (32) and (33), we obtain the ALE formulation of the Bernoulli equation:

$$\frac{\bar{p}}{\rho_f} = \Psi_\infty - \frac{1}{2}\bar{\boldsymbol{u}}^2 - \frac{\mathrm{d}\bar{\phi}}{\mathrm{d}t} + \frac{\partial\bar{\boldsymbol{\xi}}}{\partial t}\cdot\bar{\boldsymbol{u}} - g\boldsymbol{e}_z\cdot(\bar{\boldsymbol{x}}+\bar{\boldsymbol{\xi}}) \quad \text{on } \overline{\Sigma}. \tag{34}$$

Finally, equation (34) can be used to express the virtual work of the pressure forces of equation (3) as:

$$f_{ext}(\boldsymbol{\xi},\delta\boldsymbol{\xi}) = \rho_f \int_{\overline{\Sigma}} \left(\Psi_\infty - \frac{1}{2}\bar{\boldsymbol{u}}^2 - \frac{\mathrm{d}\bar{\phi}}{\mathrm{d}t} + \frac{\partial\bar{\boldsymbol{\xi}}}{\partial t}\cdot\bar{\boldsymbol{u}} - g\boldsymbol{e}_z\cdot(\bar{\boldsymbol{x}}+\bar{\boldsymbol{\xi}})\right)(\bar{\Phi}_S^{\mathrm{T}}\bar{\boldsymbol{n}})\cdot\delta\boldsymbol{\xi}\,\mathrm{d}\overline{\Sigma} \tag{35}$$

In the above equation, the terms Ψ_∞, $\bar{\boldsymbol{u}}^2$ and $g\boldsymbol{e}_z\cdot(\bar{\boldsymbol{x}}+\bar{\boldsymbol{\xi}})$ come from the stationary expression of the Bernoulli equation. The time derivative of the potential results from the local acceleration of the fluid, and the scalar product between the structure and the fluid velocity is a convection term linked to the interface movement in an ALE framework. The deformation operator $\bar{\Phi}_S$ enables to take into account the fluctuations (rotation and dilatation) of the oriented interface. A numerical approximation of the set of equations (30) and (35) can be found, but requires to solve different operators at each time step, because of the time dependence of $\overline{\partial_n G}$ and $\overline{\boldsymbol{G_n}}$. In order to solve this problem with time-independent operators, a linearized formulation of the integral representation (30) under the assumption of small displacement of the fluid-structure interface $\Sigma_{(t)}$ is introduced in the next subsection.

2.3. Linearized formulation

The linearization of the equations resulting from the combined ALE and BEM approaches is now addressed, under the assumption that the following small perturbations hypotheses are satisfied:

$$\varepsilon = \frac{\max(\|\boldsymbol{\xi}\|)}{L} \ll 1 \text{ and } \|\nabla\boldsymbol{\xi}\| \ll 1. \tag{36}$$

We then develop at order 1 the fluid equations with respect to the small coefficient ε. For conditions (2.3) to be met, the reference configuration $\overline{\Sigma}$ used is the deformed state associated with the stationary flow allowing us to study small perturbations around this equilibrium state, as explained by [17]. If the stress free interface (in the absence of external fluid) was to be used as a reference interface $\overline{\Sigma}$, one would have to check that the steady state deformations induced are of small amplitude before performing the linearization, in order to prevent geometric non-linearities which are not investigated in the present approach. The lack of terms in $\mathcal{O}\left(\varepsilon^2\right)$ to describe the fluid variables leads to an approximation of the solution (quantified in section 4), but it enables to predict the apparition of instabilities [24, 25]. For the sake of conciseness, the terms in $\mathcal{O}\left(\varepsilon\right)$ of the variables (also referred to as the order 1 variables) will be denoted with a $(\bullet)^1$ superscript. The component in $\mathcal{O}\left(\varepsilon^0\right)$ of the variables will be denoted either with a superscript $(\bullet)^0$, or with no superscript when it is implicit because they do not fluctuate with the structure movements. The displacement of the structure then writes:

$$\bar{\boldsymbol{\xi}}^1(\bar{\boldsymbol{x}}) = \boldsymbol{x} - \bar{\boldsymbol{x}} \quad \forall\bar{\boldsymbol{x}}\in\overline{\Sigma}. \tag{37}$$

Because of the small perturbations hypotheses, it is implicit that $\bar{\boldsymbol{\xi}}$ is in $\mathcal{O}\left(\varepsilon\right)$, but the $\bar{\boldsymbol{\xi}}^1$ notation with a superscript is used here to help keeping in mind the condition of small displacements required for the linear formulation. The linearized Nanson's formula (26) can be expressed with $\bar{\boldsymbol{\tau}}^1$ which takes into account both the linear rotation of the normal $\boldsymbol{n}^1$ and the dilatation of the interface [18, 21, 19, 20]:

$$\boldsymbol{n} = \bar{\boldsymbol{n}} + \boldsymbol{n}^1 + \mathcal{O}\left(\varepsilon^2\right) \quad \text{on } \overline{\Sigma} \tag{38a}$$

$$\text{with } \boldsymbol{n}^1 = -\left[\overline{\nabla}_S^{\mathrm{T}}\bar{\boldsymbol{\xi}}^1\right]\bar{\boldsymbol{n}}. \tag{38b}$$

$$\boldsymbol{n}\mathrm{d}\Sigma_{(t)} = \left(\bar{\boldsymbol{n}} + \bar{\boldsymbol{\tau}}^1\right)\overline{\Sigma} + \mathcal{O}\left(\varepsilon^2\right) \quad \text{on } \overline{\Sigma} \tag{38c}$$

$$\text{with } \bar{\boldsymbol{\tau}}^1 = \left(\mathrm{tr}\left(\overline{\nabla}_S\bar{\boldsymbol{\xi}}^1\right) - \overline{\nabla}_S^{\mathrm{T}}\bar{\boldsymbol{\xi}}^1\right)\bar{\boldsymbol{n}} \tag{38d}$$

The Green's function (28), similarly to the method presented by [26], is decomposed in order 0 and 1 terms:

$$\overline{\boldsymbol{G_n}} = \overline{\boldsymbol{G_n}}^0 + \overline{\boldsymbol{G_n}}^1 + \mathcal{O}\left(\varepsilon^2\right) \qquad \text{on } \overline{\Sigma}, \tag{39a}$$

$$\overline{\partial_n G} = \overline{\partial_n G}^0 + \overline{\partial_n G}^1 + \mathcal{O}\left(\varepsilon^2\right) \qquad \text{on } \overline{\Sigma}. \tag{39b}$$

Detailed expressions of (38c) and (39) can be found in Appendix A. The assumption that the structure velocity is small (relatively to the ambient flow U_∞) is also used:

$$\frac{\partial \bar{\boldsymbol{\xi}}^1}{\partial t} = \mathcal{O}\left(\varepsilon\right). \tag{40}$$

Consequently, in the following equations, the superscript $(\bullet)^1$ will not only information on the order 1 amplitude of a variable, but will as well imply its linearity to the displacements $\bar{\boldsymbol{\xi}}^1$ or its time derivatives. Hypothesis (40) is necessary to obtain a movement-independent order 0 solution $\bar{\phi}_p^0$ as it will appear in the integral representation (42). Based on equations (30), (37), (39) and (40), a linearization of the potential $\bar{\phi}_p$ is introduced such that

$$\bar{\phi}_p(\bar{\boldsymbol{x}}) \equiv \phi_p(\boldsymbol{x}) = \bar{\phi}_p^0(\bar{\boldsymbol{x}}) + \bar{\phi}_p^1(\bar{\boldsymbol{x}}) + \mathcal{O}\left(\varepsilon^2\right) \qquad \text{on } \overline{\Sigma}. \tag{41}$$

By first keeping only the terms in $\mathcal{O}\left(1\right)$ from (30), we obtain the order 0 solution described in (42a). Afterwards, the linearization methodology consists in subtracting the order 0 equation (42a) from (30), and by neglecting the contributions in $\mathcal{O}\left(\varepsilon^2\right)$, the order 1 term is solution of (42b):

$$\bar{\phi}_p^0(\bar{\boldsymbol{y}}) = \int_{\overline{\Sigma}} \overline{\partial_n G}^0_{(\bar{\boldsymbol{x}},\bar{\boldsymbol{y}})} \left(\bar{\phi}^0_{p(\bar{\boldsymbol{x}})} - \bar{\phi}^0_{p(\bar{\boldsymbol{y}})}\right) + \overline{\boldsymbol{G_n}}^0_{(\bar{\boldsymbol{x}},\bar{\boldsymbol{y}})} \cdot \boldsymbol{u}_\infty \mathrm{d}\overline{\Sigma} \qquad \forall \bar{\boldsymbol{y}} \in \overline{\Sigma}, \tag{42a}$$

$$\begin{aligned}\bar{\phi}_p^1(\bar{\boldsymbol{y}}) = \int_{\overline{\Sigma}} & \overline{\partial_n G}^0_{(\bar{\boldsymbol{x}},\bar{\boldsymbol{y}})} \left(\bar{\phi}^1_{p(\bar{\boldsymbol{x}})} - \bar{\phi}^1_{p(\bar{\boldsymbol{y}})}\right) + \overline{\partial_n G}^1_{(\bar{\boldsymbol{x}},\bar{\boldsymbol{y}},\bar{\boldsymbol{\xi}}^1)} \left(\bar{\phi}^0_{p(\bar{\boldsymbol{x}})} - \bar{\phi}^0_{p(\bar{\boldsymbol{y}})}\right) ... \\ & - \overline{\boldsymbol{G_n}}^0_{(\bar{\boldsymbol{x}},\bar{\boldsymbol{y}})} \cdot \frac{\partial \bar{\boldsymbol{\xi}}^1_{(\bar{\boldsymbol{x}})}}{\partial t} + \overline{\boldsymbol{G_n}}^1_{(\bar{\boldsymbol{x}},\bar{\boldsymbol{y}},\bar{\boldsymbol{\xi}}^1)} \cdot \boldsymbol{u}_\infty \mathrm{d}\overline{\Sigma} \end{aligned} \qquad \forall \bar{\boldsymbol{y}} \in \overline{\Sigma}. \tag{42b}$$

The above equations express ϕ_p as a function of variables defined only on the reference configuration. The differentiability of the BEM operators appearing in these equations has already been studied in the field of acoustics [26]. It has been introduced here in the context of incompressible flows. In order to obtain the total linearized velocity potential ϕ, we need to introduce the linearized variations of the ambient potential $\bar{\phi}_\infty$ defined as

$$\bar{\phi}_\infty(\bar{\boldsymbol{x}}) \equiv \phi_\infty(\boldsymbol{x}) = \phi_\infty(\bar{\boldsymbol{x}} + \bar{\boldsymbol{\xi}}^1) \qquad \forall \bar{\boldsymbol{x}} \quad \text{on } \overline{\Sigma}. \tag{43}$$

To do so, we use a Taylor expansion at the order 1, which is valid since ϕ_∞ is defined on the whole domain Ω_∞:

$$\bar{\phi}_\infty^0(\bar{\boldsymbol{x}}) = \phi_\infty(\bar{\boldsymbol{x}}) \qquad \forall \bar{\boldsymbol{x}} \quad \text{on } \overline{\Sigma}, \tag{44a}$$

$$\bar{\phi}_\infty^1(\bar{\boldsymbol{x}}) = \boldsymbol{\nabla}\phi_\infty(\bar{\boldsymbol{x}}) \cdot \boldsymbol{\xi}^1 = \boldsymbol{u}_\infty \cdot \boldsymbol{\xi}^1 \qquad \forall \bar{\boldsymbol{x}} \quad \text{on } \overline{\Sigma}. \tag{44b}$$

The linear potential of the ambient flow perturbed by the vibrating solid can therefore be obtained from equations (42) and (44) as

$$\phi = \bar{\phi}_p^0 + \bar{\phi}_p^1 + \bar{\phi}_\infty^0 + \bar{\phi}_\infty^1 + \mathcal{O}\left(\varepsilon^2\right) \quad \text{on } \Sigma_{(t)}. \tag{45}$$

The velocity $\boldsymbol{u}$ at orders 0 and 1 is then calculated using the gradient and the potential from the reference configuration (see Appendix A for details on the calculation):

$$\bar{\boldsymbol{u}}^0 = \overline{\boldsymbol{\nabla}}\bar{\phi}^0 \quad \text{on } \overline{\Sigma}, \tag{46a}$$

$$\bar{\boldsymbol{u}}^1 = \overline{\boldsymbol{\nabla}}\bar{\phi}^1 - \left[\overline{\nabla}^{\mathrm{T}}\bar{\boldsymbol{\xi}}^1\right]\bar{\boldsymbol{u}}^0 \quad \text{on } \overline{\Sigma}. \tag{46b}$$

In a similar fashion, the pressure given by (34) can be split into order 0 and 1 terms. Knowing that for a constant ambient flow $\boldsymbol{u}_\infty$ the order 0 potential $\bar{\phi}^0$ does not vary with time (see equations (42a) and (44a)), one obtains:

$$\frac{\bar{p}^0}{\rho_f} = \Psi_\infty - \frac{1}{2}(\bar{\boldsymbol{u}}^0)^2 - g\boldsymbol{e}_z \cdot \bar{\boldsymbol{x}}, \tag{47a}$$

$$\frac{\bar{p}^1}{\rho_f} = \frac{\partial \bar{\boldsymbol{\xi}}^1}{\partial t} \cdot \bar{\boldsymbol{u}}^0 - \bar{\boldsymbol{u}}^1 \cdot \bar{\boldsymbol{u}}^0 - \frac{\mathrm{d}\bar{\phi}^1}{\mathrm{d}t} - g\boldsymbol{e}_z \cdot \bar{\boldsymbol{\xi}}^1. \tag{47b}$$

This enables to determine the virtual work on the fluid-structure interface (35) at both orders 0 and 1:

$$f^0_{ext} = \rho_f \int_{\overline{\Sigma}} \bar{p}^0 \bar{\boldsymbol{n}} \cdot \delta\boldsymbol{\xi} \, \mathrm{d}\overline{\Sigma} \tag{48a}$$

$$f^1_{ext} = \int_{\overline{\Sigma}} \left[\bar{p}^0 \bar{\boldsymbol{\tau}}^1 + \rho_f \left(\bar{\boldsymbol{u}}^0 \cdot \left(\frac{\partial \bar{\boldsymbol{\xi}}^1}{\partial t} - \bar{\boldsymbol{u}}^1 \right) - \frac{\mathrm{d}\bar{\phi}^1}{\mathrm{d}t} - g\bar{\boldsymbol{\xi}}^1 \cdot \boldsymbol{e}_z \right) \bar{\boldsymbol{n}} \right] \cdot \delta\boldsymbol{\xi} \, \mathrm{d}\overline{\Sigma}, \tag{48b}$$

It is convenient to decompose the order 0 pressure into ambient and perturbed contributions in order to isolate the different contributions of this work later (see below equation (59)):

$$\frac{\bar{p}^0_\infty}{\rho_f} = \Psi_\infty - \frac{1}{2}U^2_\infty - g\bar{\boldsymbol{x}} \cdot \boldsymbol{e}_z \tag{49a}$$

$$\frac{\bar{p}^0_p}{\rho_f} = -\frac{1}{2}(\bar{\boldsymbol{u}}^0_p)^2 - \bar{\boldsymbol{u}}^0_p \cdot \bar{\boldsymbol{u}}_\infty. \tag{49b}$$

The value of $\bar{\boldsymbol{u}}^1$ in the work expression (48) could be replaced by expression (46b). However, calculating the whole spatial gradient of a scalar field ϕ knowing only its value at the interface is inconvenient. Hence the necessity to redevelop the scalar product $\bar{\boldsymbol{u}}^0.\bar{\boldsymbol{u}}^1$ using equation (A.10) from Appendix A as well as equations (48) and (49) enables to use only the surface gradient of $\bar{\phi}$ instead of its complete gradient in the expression of the fluid forces perturbations:

$$f^1_{ext} = \int_{\overline{\Sigma}} \left[(\bar{p}^0_p + \bar{p}^0_\infty)\bar{\boldsymbol{\tau}}^1 + \rho_f \left(\bar{\boldsymbol{u}}^0 \cdot \left(\frac{\partial \bar{\boldsymbol{\xi}}^1}{\partial t} - \overline{\boldsymbol{\nabla}}_S \bar{\phi}^1 + \overline{\nabla}^{\mathrm{T}}_S \bar{\boldsymbol{\xi}}^1 \bar{\boldsymbol{u}}^0 \right) - \frac{\mathrm{d}\bar{\phi}^1}{\mathrm{d}t} - g\bar{\boldsymbol{\xi}}^1 \cdot \boldsymbol{e}_z \right) \bar{\boldsymbol{n}} \right] \cdot \delta\boldsymbol{\xi} \, \mathrm{d}\overline{\Sigma}. \tag{50}$$

It is possible to use the above expression for numerical calculation of the fluid loads on the flexible structure. The work of the fluid above can be coupled with the structure dynamics through equation (1), which is the aim of the next section.

3. Numerical calculation of the fluid mass, gyroscopic and stiffness contributions

The structure characteristics K_s and M_s are supposed to be known, and this article does not focus on their calculation. Hence, in order to obtain the dynamical solution of equation (1) associated with the fluid linearized efforts exerted on the structure, an approximation of the solution is derived through a numerical procedure based on a triangular surface mesh of the fluid-structure interface. First, the potential of the fluid will be solved using the BEM. Based on this potential solution, the resulting load of the fluid will be determined using FEM operators, allowing us to couple the flow with the structure deformations. In order to find a numerical approximation of the potential for a steady ambient flow, we used the BEM based on the integral representation (42) which approximates the integral over the fluid-structure interface [21]. The interface is discretized into triangular elements connected to N_{DOF} nodes. The variables are interpolated using linear basis functions attached to the mesh nodes. According to the collocation method [21], the evaluation points $\boldsymbol{y}_i$ are also located on the mesh nodes. BEM operators $[G]_{n\times 3n}$, $[G']_{n\times 3n}$ (single layer operators) and $[H]_{n\times n}$, $[H']_{n\times 3n}$ (double layer operators) are introduced as:

$$\sum_j [G]_{ij} \{\bar{\boldsymbol{u}}\}_j \simeq \int_{\overline{\Sigma}} -\overline{\boldsymbol{G_n}}^0_{(\bar{\boldsymbol{x}},\bar{\boldsymbol{y}}_i)} \cdot \bar{\boldsymbol{u}}_{(\bar{\boldsymbol{x}})} \mathrm{d}\overline{\Sigma}_{(\bar{\boldsymbol{x}})}, \tag{51a}$$

$$\sum_j \left[G'_{(\boldsymbol{u}_\infty)}\right]_{ij} \{\bar{\boldsymbol{\xi}}\}_j \simeq \int_{\overline{\Sigma}} -\overline{\boldsymbol{G_n}}^1_{(\bar{\boldsymbol{x}},\bar{\boldsymbol{y}}_i,\bar{\boldsymbol{\xi}})} \cdot \boldsymbol{u}_\infty \mathrm{d}\overline{\Sigma}_{(\bar{\boldsymbol{x}})}, \tag{51b}$$

$$\sum_j [H]_{ij} \{\bar{\phi}\}_j \simeq \{\bar{\phi}\}_i - \int_{\overline{\Sigma}} \overline{\partial_n G}^0_{(\bar{\boldsymbol{x}},\bar{\boldsymbol{y}}_i)} \left(\bar{\phi}_{(\bar{\boldsymbol{x}})} - \bar{\phi}_{(\bar{\boldsymbol{y}}_i)}\right) \mathrm{d}\overline{\Sigma}_{(\bar{\boldsymbol{x}})}, \tag{51c}$$

$$\sum_j \left[H'_{(\bar{\phi})}\right]_{ij} \{\bar{\boldsymbol{\xi}}\}_j \simeq \int_{\overline{\Sigma}} \overline{\partial_n G}^1_{(\bar{\boldsymbol{x}},\bar{\boldsymbol{y}}_i,\bar{\boldsymbol{\xi}})} \left(\bar{\phi}_{(\bar{\boldsymbol{x}})} - \bar{\phi}_{(\bar{\boldsymbol{y}}_i)}\right) \mathrm{d}\overline{\Sigma}_{(\bar{\boldsymbol{x}})}. \tag{51d}$$

The brackets $[\bullet]$ denote matrices and $\{\bullet\}$ denote vectors whose j^{th} component is the value of the variable at the node $\bar{\boldsymbol{y}}_j$. The reader might refer to Appendix A for the expressions of $\overline{\boldsymbol{G_n}}^0$,$\overline{\boldsymbol{G_n}}^1$,$\overline{\partial_n G}^0$ and $\overline{\partial_n G}^1$. The collocation method consists in determining each row i of the BEM operators by associating it to a reference point $\bar{\boldsymbol{y}}_i$. The integration is then calculated using Gaussian weights, the value of $\bar{\boldsymbol{x}}$ and $\bar{\phi}(\bar{\boldsymbol{x}})$ being obtained at each Gauss point from their values at the element nodes using a linear interpolation. The finer the mesh, the better the discrete expression (51) approximates their continuous counterparts. However, when $\bar{\boldsymbol{x}}$ is located in the same triangle as $\bar{\boldsymbol{y}}_i$, the norm $\|\boldsymbol{x} - \boldsymbol{y}_i\|$ is nil at $\bar{\boldsymbol{x}} = \bar{\boldsymbol{y}}_i$, which means the integral over the triangle is improper and its value has to be calculated carefully. For the double layer term

$$\overline{\partial_n G}^0 = \frac{(\bar{\boldsymbol{x}} - \bar{\boldsymbol{y}}_i).\bar{\boldsymbol{n}}}{\|\bar{\boldsymbol{x}} - \bar{\boldsymbol{y}}_i\|^3},$$

the planar shape of the triangles implies that any vector connecting two points of a same triangle is included in the triangle, and is consequently perpendicular to the triangle normal, hence:

$$(\bar{\boldsymbol{x}} - \bar{\boldsymbol{y}}_i).\bar{\boldsymbol{n}} = 0 \quad \forall \bar{\boldsymbol{x}}, \bar{\boldsymbol{y}}_i \text{ in the same triangle.} \tag{52}$$

Consequently, the term $\overline{\partial_n G}^0$ is trivial to integrate in that case. Though equation (52) simplifies the implementation of the BEM by preventing the calculation of highly singular terms, [32] mentions that this triangle mesh approximation causes a discretization error of the order of $\delta\kappa/4\pi$, where δ is the perimeter of the triangle and κ the mean curvature of the real surface $\overline{\Sigma}$. As shown in equation (A.3d), the double layer linearized term is strongly singular for $\bar{\boldsymbol{x}} \to \bar{\boldsymbol{y}}$, and, as a consequence, one might expect that difficulties could arise integrating it. However, for the same reason that the scalar product $(\bar{\boldsymbol{x}} - \bar{\boldsymbol{y}}) \cdot \bar{\boldsymbol{n}}$ is nil at order zero, the term $\overline{\partial_n G}^1$ will vanish when $\bar{\boldsymbol{x}}$ and $\bar{\boldsymbol{y}}$ are in the same triangle: the rotated normal associated with the deformed triangle will remain perpendicular to the deformed vector $\bar{\boldsymbol{x}} + \bar{\boldsymbol{\xi}}^1(\bar{\boldsymbol{x}}) - (\bar{\boldsymbol{y}} + \bar{\boldsymbol{\xi}}^1(\bar{\boldsymbol{y}}))$. This ensures that the double layer term at order one $\overline{\partial_n G}^1$ vanishes too when both $\bar{\boldsymbol{x}}$ and $\bar{\boldsymbol{y}}$ are on the same triangle. On the contrary, the term $\overline{\boldsymbol{G_n}}^0$ does not cancel for $\bar{\boldsymbol{x}} \to \bar{\boldsymbol{y}}_i$ and the integral has to be calculated carefully. In this article, their implementation was done using a Lachat-Watson transformation as detailed in [33]. Similarly, the term $\overline{\boldsymbol{G_n}}^1$ has to be calculated carefully. Its singularity for $\bar{\boldsymbol{x}} \to \bar{\boldsymbol{y}}$ is of the same order than $\overline{\boldsymbol{G_n}}^0$: more particularly, one might notice how the term $(\bar{\boldsymbol{x}} - \bar{\boldsymbol{y}}).(\bar{\boldsymbol{\xi}}^1(\bar{\boldsymbol{x}}) - \bar{\boldsymbol{\xi}}^1(\bar{\boldsymbol{y}})/\|\bar{\boldsymbol{x}} - \bar{\boldsymbol{y}}\|$ in $\overline{\boldsymbol{G_n}}^1$ is in $\mathcal{O}(\|\bar{\boldsymbol{x}} - \bar{\boldsymbol{y}}\|)$ since $\bar{\boldsymbol{\xi}}^1(\bar{\boldsymbol{x}}) - \bar{\boldsymbol{\xi}}^1(\bar{\boldsymbol{y}})$ is linear when $\bar{\boldsymbol{x}}$ and $\bar{\boldsymbol{y}}$ are in the same triangle, just like the term $\|\bar{\boldsymbol{x}} - \bar{\boldsymbol{y}}\|$ for $\overline{\boldsymbol{G_n}}^0$. As a consequence, the term $\overline{\boldsymbol{G_n}}^1$ has been implemented using the Lachat-Watson transformation, similarly to $\overline{\boldsymbol{G_n}}^0$.

Another difficulty with this approach is that the BEM operators are full. As a consequence, their storage cost is in $\mathcal{O}\left(N_{DOF}^2\right)$. The latter could be reduced by using one of the BEM acceleration methods. As explained by [41], the Hierarchical matrix method would be best suited here as it allows to calculate multiple matrix-vector products based on a single compressed matrix calculations, on the contrary to the Fast Multipole Method which would require to calculate a new approximation from scratch for each matrix-vector product.

The implementation of an accelerated BEM is however not in the scope of this article. Let us remark that, in order to reduce the required memory when computation is implemented, both linearized operators can be calculated as one:

$$[J] = [G'] + \left[H'_{(\bar{\phi}_p^0)}\right]. \tag{53}$$

Thanks to the linearization, BEM operators are calculated only once, at the cost of storing three matrix operators instead of two, enabling to take into account the variations associated with any small mesh deformation without recalculating the discretized BEM operators as done in previous studies on fluid-structure interaction such as [9, 10, 11, 12, 13]. From equation (42), the order 0 and 1 solutions of the potential can therefore be obtained by inverting the linear systems with a GMRes algorithm:

$$[H]\left\{\bar{\phi}_p^0\right\} = [G]\left\{-\boldsymbol{u}_\infty\right\}, \tag{54a}$$

$$[H]\left\{\bar{\phi}_p^1\right\} = [J]\left\{\bar{\boldsymbol{\xi}}^1\right\} + [G]\left\{\frac{\partial \bar{\boldsymbol{\xi}}^1}{\partial t}\right\}. \tag{54b}$$

Because the expression of $[J]$ depends on the field $\bar{\phi}_p^0$, this operator has to be computed once the order 0 system has been solved. The linear operators $[A]$, $[B]$ and $[U_\infty]$ are introduced as well:

$$[A] = [H]^{-1}[G], \tag{55a}$$

$$[B] = [H]^{-1}[J] + [U_\infty] \text{ with } [U_\infty]\{\bar{\boldsymbol{\xi}}\} = \{\boldsymbol{u}_\infty.\bar{\boldsymbol{\xi}}\} \tag{55b}$$

By combining (54) and (55), the linear calculation of the potential approximation at mesh nodes writes for an homogeneous ambient flow:

$$\left\{\phi^0\right\} = \{\phi_p^0\} + \{\phi_\infty^0\} = [A]\left\{-\boldsymbol{u}_\infty\right\} + [U_\infty]\left\{\bar{\boldsymbol{x}}\right\}, \tag{56a}$$

$$\left\{\phi^1\right\} = \{\phi_p^1\} + \{\phi_\infty^1\} = [A]\left\{\frac{\partial \bar{\boldsymbol{\xi}}^1}{\partial t}\right\} + [B]\left\{\bar{\boldsymbol{\xi}}^1\right\}. \tag{56b}$$

The present approach is similar to the panel method because it is based on the same integral representation of the solution of Laplace's equation. The main difference is in the way the associated integral equation is solved: we have adopted a direct resolution by looking for a polynomial field ϕ_p (linear in practice) whose values at the nodes are the unknowns of the problem (Boundary Element Method), whereas the panel method looks for ϕ_p in the form of a superposition of particular solutions associated with monopoles (source/well) or dipoles (doublet/vortex) whose intensities are the unknowns of the problem [34]. The advantage of the present approach is that one can obtain the dependence of the velocity potential solution on the movements and deformations of the immersed structure by directly differentiating the BEM operators with respect to a displacement variable of the interface. However, in the current implementation, the presence of the singularity of the solution at the wake has been omitted for simplification purposes, which does not allow imposing a Kutta condition at the trailing edge of the fins, in order to take into account the circulation effects around the body. As a consequence, the obtained solution does not allow to represent the phenomena of lift and pressure drag [34]. However, when considering the hull without fins, the pressure fluctuations seem to be relatively close to more complete RANS type simulations as shown in Figure 5, which gives confidence in the results of such a method in finless configurations. Concerning the fins, a simple aerodynamic model might be added as done by [6], or the present approach might be extended to take into account vortex sheets drawing inspiration from [3, 8, 28] as mentioned in the conclusion of this article.
Using equations (56), we can now compute the potential solution of the fluid at orders 0 and 1, and an approximation of the dynamical fluid forcing for an homogeneous stationary ambient flow from equation (50) can be computed using FEM operators. In order to do so, the following FEM bilinear operators are introduced:

$$
\begin{aligned}
\{\delta\boldsymbol{\xi}\}^{\mathrm{T}}\,[C]\,\{p\} &\simeq \int_{\overline{\Sigma}} \bar{p}\bar{\boldsymbol{n}}\cdot\delta\boldsymbol{\xi}\,\mathrm{d}\overline{\Sigma},\\
\{\delta\boldsymbol{\xi}\}^{\mathrm{T}}\left[D_{(\bar{\boldsymbol{u}}^0)}\right]\{\phi\} &\simeq \int_{\overline{\Sigma}} \bar{\boldsymbol{u}}^0\cdot\overline{\boldsymbol{\nabla}}_S\bar{\phi}\quad\bar{\boldsymbol{n}}\cdot\delta\boldsymbol{\xi}\,\mathrm{d}\overline{\Sigma},\\
\{\delta\boldsymbol{\xi}\}^{\mathrm{T}}\left[E_{(\bar{\boldsymbol{u}}^0,\bar{\boldsymbol{u}}^0)}\right]\{\bar{\boldsymbol{\xi}}\} &\simeq \int_{\overline{\Sigma}} -\bar{\boldsymbol{u}}^0\cdot\left(\left[\overline{\nabla}_S^T\bar{\boldsymbol{\xi}}\right]\bar{\boldsymbol{u}}^0\right)\quad\bar{\boldsymbol{n}}\cdot\delta\boldsymbol{\xi}\,\mathrm{d}\overline{\Sigma},\\
\{\delta\boldsymbol{\xi}\}^{\mathrm{T}}\left[F_{(\bar{\boldsymbol{u}}^0)}\right]\{\bar{\boldsymbol{\xi}}\} &\simeq \int_{\overline{\Sigma}} -\bar{\boldsymbol{\xi}}\cdot\bar{\boldsymbol{u}}^0\quad\bar{\boldsymbol{n}}\cdot\delta\boldsymbol{\xi}\,\mathrm{d}\overline{\Sigma},\\
\{\delta\boldsymbol{\xi}\}^{\mathrm{T}}\left[L_{(\bar{p}_p^0)}\right]\{\bar{\boldsymbol{\xi}}\} &\simeq \int_{\overline{\Sigma}} -\bar{p}_p^0\,\bar{\boldsymbol{\tau}}^1_{(\bar{\boldsymbol{\xi}})}\cdot\delta\boldsymbol{\xi}\,\mathrm{d}\overline{\Sigma},\\
\{\delta\boldsymbol{\xi}\}^{\mathrm{T}}\,[K_s]\,\{\bar{\boldsymbol{\xi}}\} &\simeq K_s(\bar{\boldsymbol{\xi}},\delta\boldsymbol{\xi}),\\
\{\delta\boldsymbol{\xi}\}^{\mathrm{T}}\,[M_s]\left\{\frac{\partial^2\bar{\boldsymbol{\xi}}}{\partial t^2}\right\} &\simeq M_s\left(\frac{\partial^2\bar{\boldsymbol{\xi}}}{\partial t^2},\delta\boldsymbol{\xi}\right).
\end{aligned}
\tag{57}
$$

The operators $[D]$, $[E]$, $[F]$ and $[G]$ are functions of the order 0 solutions $\bar{\boldsymbol{u}}^0$ and $\bar{p}^0$. Therefore, they should be recalculated when the stationary state changes. The operators K_s and M_s were introduced in equation (1): we consider here their FEM discretized counterparts $[K_s]$ and $[M_s]$. The dynamical equation of the fluid-structure coupled system (1) becomes:

$$
\begin{aligned}
&\left([M_s]+\rho_f\,[C]\,[A]\right)\left\{\frac{\partial^2\bar{\boldsymbol{\xi}}}{\partial t^2}\right\}+\rho_f\left([C]\,[B]+\left[D_{(\bar{\boldsymbol{u}}^0)}\right]\,[A]+\left[F_{(\bar{\boldsymbol{u}}^0)}\right]\right)\left\{\frac{\partial\bar{\boldsymbol{\xi}}}{\partial t}\right\}+\ldots\\
&\left([K_s]+\rho_f\Big[\left[D_{(\bar{\boldsymbol{u}}^0)}\right]\,[B]+\left[E_{(\bar{\boldsymbol{u}}^0,\bar{\boldsymbol{u}}^0)}\right]+\left[L_{(\bar{p}_p)}\right]+\left[L_{(\bar{p}_\infty)}\right]+\left[F_{(-g\boldsymbol{e}_z)}\right]\Big]\right)\{\bar{\boldsymbol{\xi}}\}=0.
\end{aligned}
\tag{58}
$$

One can identify from the above equation the mass $[M_f]$, gyroscopic $[G_f]$ and stiffness $[K_f]$ matrices induced by the coupling with the flow:

$$
[M_f]=\rho_f\,[C]\,[A]\,, \tag{59a}
$$

$$
[G_f]=\rho_f\left([C]\,[B]+\left[D_{(\bar{\boldsymbol{u}}^0)}\right]\,[A]+\left[F_{(\bar{\boldsymbol{u}}^0)}\right]\right), \tag{59b}
$$

$$
[K_f]=\rho_f\left(\left[D_{(\bar{\boldsymbol{u}}^0)}\right]\,[B]+\left[E_{(\bar{\boldsymbol{u}}^0,\bar{\boldsymbol{u}}^0)}\right]+\left[L_{(\bar{p}_p^0)}\right]+\left[L_{(\bar{p}_\infty)}\right]+\left[F_{(-g\boldsymbol{e}_z)}\right]\right). \tag{59c}
$$

It is important to note that the term "gyroscopic" used in this article and taken from [29] refers here to fluid forces that are conservative and linear with the velocity of the structure (as mentioned below), not to be confused with the torque associated with the rotation of a solid. By linearity of the operators in the above equation, and noticing also that $\bar{\boldsymbol{u}}^0$ is linear with respect to $\boldsymbol{u}_\infty$, one can show that the stiffness operator $\left([K_f]-\left[N_{(\bar{p}_\infty)}\right]\right)$ is quadratic to the ambient flow velocity $\boldsymbol{u}_\infty$, the gyroscopic operator $[G_f]$ is linear with $\boldsymbol{u}_\infty$, whereas the added mass operator $[M_f]$ does not vary upon $\boldsymbol{u}_\infty$, which is coherent wit [6]. This is the reason why the operator $[M_f]$ is often calculated in the case of a fluid at rest, even though it is used in the dynamical equation with a flowing fluid, as in reference [6]. In their study [6], Li showed using the Lagrange equations that the added mass and stiffness operators associated with elastic movements are symmetric while the gyroscopic operator is skew-symmetric. It is important to note that these properties are verified only with the irrotational flow hypotheses usually used for bluff bodies and are not valid for slender bodies such as wings which induce vorticity in the flow. According to Ziegler [29], such properties of the operators are expected for conservative systems, which is the case of the fluid: an incompressible, ideal, irrotational flow does not lose energy and does not transfer energy to infinity either. With a Newtonian approach, these (skew-)symmetry attributes do not appear as naturally as with the Lagrange equations, but [35] has shown the symmetry properties of the added mass operator with the former approach. It is possible as well to implement the BEM method based on a variational formulation of the integral representation [35]: this approach would ensure the symmetry of the added mass matrix at the expense of more integrations. For

this reason, the collocation method used to implement the BEM in this article seems to be an acceptable compromise between accuracy and numerical effort. However, the (skew-)symmetry of the fluid operators has been numerically evaluated in section 4.
Finally, the fluid-structure dynamical equation becomes

$$([M_s] + [M_f]) \left\{ \frac{\partial^2 \bar{\boldsymbol{\xi}}}{\partial t^2} \right\} + [G_f] \left\{ \frac{\partial \bar{\boldsymbol{\xi}}}{\partial t} \right\} + ([K_s] + [K_f]) \left\{ \bar{\boldsymbol{\xi}} \right\} = 0. \tag{60}$$

Equation (60) is a monolithic equation: because the fluid and the structure dynamics are contained in a unique equation, it allows solving both simultaneously, contrary to partitioned approaches which require an alternating resolution of the fluid and structure equations. Moreover, this monolithic equation has the advantage of not depending explicitly on the fluid variables, since they have been eliminated in favor of their expressions in $\boldsymbol{\xi}$ and its time derivatives. It is of particular interest to determine the appearance of instabilities of the structure, as well as a better prediction of the structure behavior [6]. According to Ziegler's classification [29, 30], if the loads associated with the stiffness K_s of the structure are conservative (or equivalently if K_s is symmetric), then the system described by (60) is a gyroscopic conservative linear system, as it contains non-circulatory loads (as K_s, K_f and M_f are symmetric) and gyroscopic loads (as G_f is skew-symmetric). Such systems present a risk of losing stability whenever the associated non-circulatory forces become non-positive (which might be caused only by the non-positiveness of K_f since M_f is necessarily positive), although in some cases the gyroscropic loads G_f are capable of preventing such instabilities [29]. More specifically post-divergence flutter by coupling of two divergent modes can also occur in such systems according to Paidoussis [30]. However, common unstable aeroelastic phenomena such as flutter by frequency crossing or wake flutter, caused respectively by the unsymmetry of the stiffness operator and the non-positiveness of the damping operator [31, 25] are not predicted by this equation, but could arise for instance with the addition of circulatory effects around the fins. The next section aims to quantify the errors in the fluid loads from equation (60) associated with the numerical approximation and with the order 1 approximation.

4. Quantification of the error from numerical and linear approximations

In order to quantify the error of the fluid operators associated with the fluid-structure characterization exhibited in equation (60), this section focuses on four test cases.
- With a view to validating the BEM procedure, the quasi-steady solution of a homogeneous longitudinal ambient flow past a revolution ellipsoid is studied, comparing the velocity potential analytic solution with the BEM approximation.
- The potential flow model solved with the BEM is compared with more accurate fluid simulation based on RANS in a second test-case, enabling to see the regions where the potential flow model cannot capture all the physics, but to validate as well the overall good capture of the pressure fluctuations over the interface by the BEM.
- The third test case compares the linear approximation introduced in sections 2 and 3 with a numerical non-linear solution, studying the associated error on the fluid stiffness operator in the case of elastic movements, depending on a small parameter ε.
- Finally, the fourth test case quantifies the numerical error on the fluid mass and gyroscopic operators in the case of rigid body movements of the structure, enabling to validate the FEM approach and to assess the convergence of the mixed FEM-BEM approach introduced in this document.

4.1. BEM approximation

In order to validate the implementation of the BEM procedure at order zero, a simple test case is presented below. It consists of a revolution ellipsoid (also referred to as a spheroid). Its semi axis are of length L (for *length*) and D (for *diameter*) respectively. Its aspect ratio $\mathcal{S}$ is defined as

$$\mathcal{S} = \frac{L}{D}. \tag{61}$$

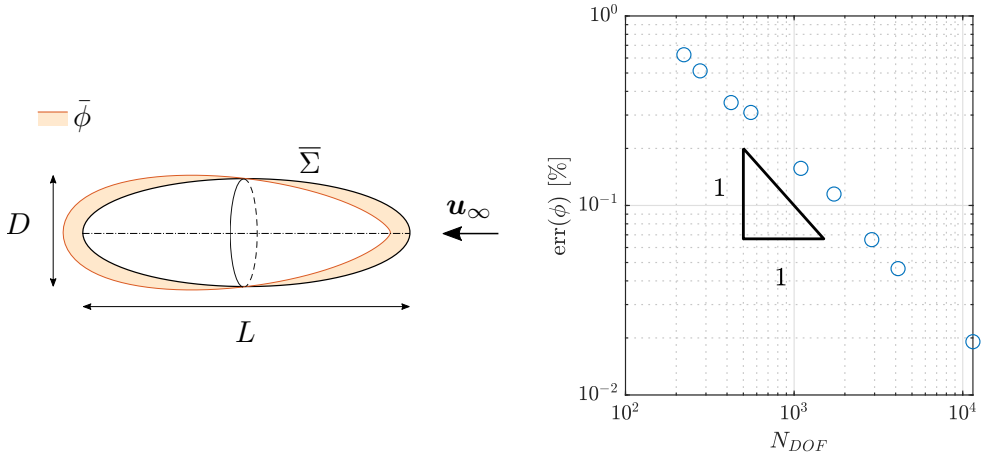

Figure 3: Left: Side view of a spheroid of aspect ratio $\mathcal{S} = 3$, with the potential solution $\bar{\phi}$ associated with a longitudinal ambient flow. Right: relative error of the numerical solution $\{\bar{\phi}_{\mathrm{BEM}}\}$ compared to its theoretical value as a function of the number of nodes. The triangle enables visualizing the $\mathcal{O}\left(N_{DOF}^{-1}\right)$ slope.

For this test case, an aspect ratio of $\mathcal{S} = 3$ is used. The ambient flow has a uniform longitudinal direction of amplitude U_∞. An analytic expression of the resulting potential at the interface can be obtained from [36], leading to the following expression:

$$\bar{\phi}(\bar{\boldsymbol{x}}) = U_\infty \bar{\boldsymbol{x}}.\boldsymbol{e}_x f(\mathcal{S}), \quad \bar{\boldsymbol{x}} \in \overline{\Sigma}, \tag{62}$$

where f is a dimensionless analytic function of the aspect ratio (see figure 3 left for an outview).
In order to validate the quasi-steady BEM procedure, the analytic potential solution is compared to numerical results. The discrete vector $\{\bar{\phi}_{\mathrm{BEM}}\}$ has been obtained with the BEM for various mesh refinements in order to study the convergence of the method. The numerical results are presented in figure 3, where the error has been defined relatively to the exact solution $\bar{\phi}$ and is defined with the $L^2(\overline{\Sigma})$ error:

$$\mathrm{err}\left(\bar{\phi}^*_{\mathrm{BEM}}\right) = \frac{\left\|\bar{\phi}^*_{\mathrm{BEM}} - \bar{\phi}^*\right\|_{L^2(\overline{\Sigma})}}{\left\|\bar{\phi}^*\right\|_{L^2(\overline{\Sigma})}} \text{ with } \|a\|_{L^2(\overline{\Sigma})} = \sqrt{\int_{\overline{\Sigma}} a(\bar{\boldsymbol{x}})^2 \mathrm{d}\overline{\Sigma}}. \tag{63}$$

The integral over $\overline{\Sigma}$ in the above equation is approximated using the values at the nodes and the FEM. As shown in Figure 3, the BEM converges toward the analytic solution in $\mathcal{O}\left(N_{DOF}^{-1}\right)$.

4.2. Comparison of RANS method and BEM

In order to further verify if the results obtained for a potential flow solved with the BEM enable to capture well the fluid forces around an interface, this section compares results of the quasi-steady order zero pressure repartition solved using the BEM with results obtained with a RANS simulation, which allows to take into account the effects of turbulence unlike the potential flow model the BEM is based on. The RANS simulations are based on a Spalart-Allmaras turbulence model, and are obtained for a compressible flow at $\mathcal{R}_e = 2.2 \times 10^6$ using the code elsA from ONERA. The comparison of the dynamic pressure repartition between the BEM and the RANS method is presented in Figure 5 on a vertical slice $y = 0$ of the interface including both the symmetry axis of the structure and the velocity vector of the ambient flow $\boldsymbol{u}_\infty$. Because the static pressure is straightforward to obtain, its value has been removed in order to compare only the dynamic pressure $p_{dyn} = -\frac{1}{2}\boldsymbol{u}^2$. which is more challenging to predict. One can see that the BEM and RANS pressure repartition are similar almost everywhere on the interface slice presented here, except for two areas.

First, on the top rear of the interface, the BEM dynamic pressure is overestimated (reminding that with the projection of p_{dyn} in Figure 5, a curve closer to the interface means a higher pressure). This means that the pressure predicted by the RANS will create a suction force on the top of the interface which is not captured by the BEM. It is due to the fact that, because of the angle of attack, the flow around the interface creates a lift toward $z > 0$. Because of the d'Alembert paradox, the potential model used for the BEM cannot predict any lift on the structure as mentioned by [1], hence this first divergence between the two methods. The second difference between these methods is that the BEM predicts a stationary point at the rear of the structure (a nil dynamic pressure associated with a nil velocity), whereas the RANS calculation does not predict a stationary point because of turbulence causing the fluid to stall locally at the rear of the structure. As turbulence is not taken into account with the potential flow hypothesis, BEM is not able to predict the stall phenomenon. Let us remark that the fluctuation spikes of pressure that appear on the blue curves apart from the symmetry axis ($[x, z] \simeq \{[-20, 5], [-15, -3], [16, 1], [16, -1]\}$ are only visualization artifacts due to the linear interpolation of the pressure field between different mesh zones, and since the RANS mesh is singular on the symmetry axis of the mesh, the fluid perceives the front and rear of the interface as a hole very locally, hence the pressure local spikes of the RANS results at an altitude $z = 0$. Further comparisons between potential flow theory and experimental measurements can be found in [38], where the pressure repartition around a non-axisymetric ellipsoid of aspect ratio $\mathcal{S} = 3.5$ obtained with an analytic potential method is compared with both RANS simulations and experimental measurements at $\mathcal{R}_e = \mathcal{O}\left(10^6\right)$. This study leads to similar conclusions: the potential pressure repartition compares well except for the rear of the body where stall occurs.

The results presented in this section confirms statements that had been made in the literature [1]: at sufficiently low angles of attack, the potential flow hypothesis enables to predict the pressure fluctuations of the flow, even thought it cannot capture the lift caused by the circulation induced on the flow in practice, and it is not able to predict turbulent effects at the rear of the body. Moreover, as the RANS simulations are associated with a compressible fluid, these results tend to validate the hypothesis that the compressibility of the fluid plays a negligible role at the scale of airships.

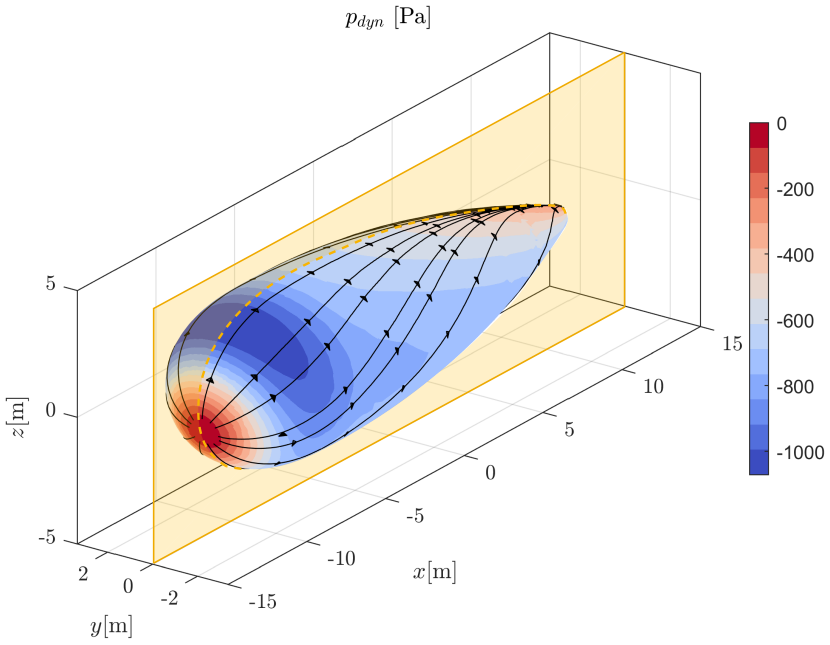

Figure 4: Dynamic pressure repartition around a generic airship shape with a symmetry axis. The orange slice is the plane $y = 0$ used to plot the pressure in Figure 5. The ambient flow has an angle of attack of 10^o and an amplitude of 34 m/s (see Figure 5 for a visualization of the ambient flow).

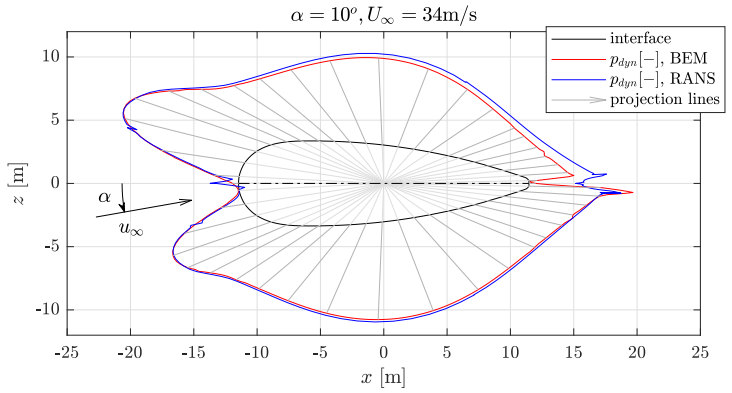

Figure 5: Comparison of the dynamic pressure associated with the steady ambient flow on a generic airship shape shown in Figure 4. The ambient flow has an angle of attack of 10^o. The pressure amplitude is projected in a radial direction represented by the light grey lines. When the pressure curve is coincident with the interface, it signifies that there is no dynamic pressure at this point. If the pressure curve is outside the airship domain, it signifies that the dynamic pressure is negative. The BEM is calculated on a $N_{DOF} = 5713$ surface mesh. The RANS method was obtained for a compressible flow with a Spalart-Allmaras turbulence model at $\mathcal{R}_e = 2, 2.10^6$. For visualization purposes, the pressure which is supposed to be constant over the elements has been interpolated linearly for both methods, hence the relative smoothness of both curves.

4.3. First order approximation

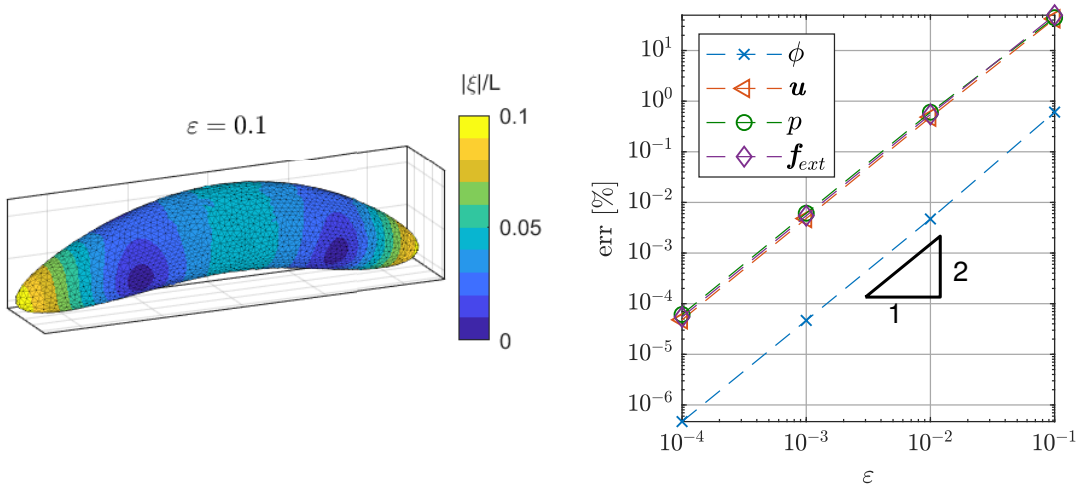

Figure 6: Left: shape of the deformed ellipsoidal fluid-structure interface for $\varepsilon = 0.1$. Right: evolution of the error in % associated with the linear prediction of the potential ϕ, the velocity $\boldsymbol{u}$, the pressure p and the force $\boldsymbol{f}_{ext}$ for a displacement $\boldsymbol{\xi}$ (as plotted on the left), as a function of ε. The triangle highlights the slope in $\mathcal{O}\left(\varepsilon^2\right)$ of the error.

In order to quantify the error associated with the linear approximation of fluid forces, the test case below compares both linear and non-linear fluid solutions with quasi-static approximation. The terms proportional to displacement $\bar{\boldsymbol{\xi}}$ in equations (54) and (60) are referred to as quasi-static: they correspond to the solution

found when deformations occur at a negligible velocity and acceleration. In order to see to which extent the associated linearized fluctuations are valid or not, the results of the order 1 solution are compared with the variations of the non-linear solution obtained by physically deforming the mesh, hence using a finite difference method by calculating new BEM operators from scratch between consecutive mesh positions. Effects of gravity are not taken into account for this test case. The generalized fluid forces $\boldsymbol{f}_{ext}$ are introduced as:

$$\boldsymbol{f}_{ext} = -\left[M_f\right]\left\{\frac{\partial^2 \bar{\boldsymbol{\xi}}}{\partial t^2}\right\} - \left[G_f\right]\left\{\frac{\partial \bar{\boldsymbol{\xi}}}{\partial t}\right\} - \left[K_f\right]\left\{\bar{\boldsymbol{\xi}}\right\}. \tag{64a}$$

In order to validate the stiffness operator $[K_f]$, one can compare the linear predictions of ϕ, p, $\boldsymbol{f}_{ext}$ and $\boldsymbol{u}$ (see Appendix A for the detailed calculation of $\boldsymbol{u}$) with their non-linear counterpart. The linear prediction for those four variables are obtained for an arbitrary displacement $\boldsymbol{\xi}$ forming a banana shape (see Figure 6) representing the lowest frequency flexible modes of airship deformations according to [6]. More details about this displacement mode are given in section 5. The errors on ϕ, $\boldsymbol{u}$, p and $\boldsymbol{f}_{ext}$ are defined as:

$$\mathrm{err}(a) = \frac{\max\left(\left\|\bar{a}^0(\bar{\boldsymbol{x}}) + \bar{a}^1(\bar{\boldsymbol{x}}, \bar{\boldsymbol{\xi}}^1) - a(\bar{\boldsymbol{x}} + \bar{\boldsymbol{\xi}}^1)\right\|\right)}{\max\left(\left\|\bar{a}^0(\bar{\boldsymbol{x}})\right\|\right)}, \tag{65}$$

and are displayed in Figure 6. If the error is related to a scalar, the norm $\|\bullet\|$ in the equation above consists of the absolute value of its argument, if it is a vector, the euclidean norm is used. Figure 6 shows that the order 1 prediction of the fluid variables all tend to their respective non-linear value when $\varepsilon \to 0$, with an error in $\mathcal{O}\left(\varepsilon^2\right)$. This is in agreement with the fact that only terms of order 2 or more have been neglected. Furthermore, this test case validates the numerical implementation of the stiffness operator $[K_f]$ and quantifies the error associated with the linearization. In a similar way, it is expected that the error prediction of the added mass and gyroscopic loads from the fluid scale as $\mathcal{O}\left(\varepsilon^2\right)$, which will be verified in the next section.

4.4. Numerical approximation

In order to quantify the error associated with the numerical approximation of section 3, the fluid numerical operators are compared with analytical values found in the literature. This analytic reference comes from the non-linear fluid equations of a structure with rigid body movements in a perfect fluid with no gravity effects [37]. We present a linearization of these equations in Appendix A. Using this linearization as an analytic reference, the fluid operators obtained numerically with our method from equation (59) are compared with those obtained from the linearized fluid equation from Thomasson [37]. For a prolate ellipsoid of aspect ratio 5:1 (major axis length over minor axis length), the analytic value of $[M_f^{\mathrm{rig}}]^{ref}$ can be found in [39] (only the non nil coefficients are displayed below, with three significant digits):

$$[M_f^{\mathrm{rig}}]_{11}^{ref} = \frac{0.0591}{150}\pi\rho_f L^3 \tag{66a}$$

$$[M_f^{\mathrm{rig}}]_{22}^{ref} = [M_f^{\mathrm{rig}}]_{33}^{ref} = \frac{0.894}{150}\pi\rho_f L^3 \tag{66b}$$

$$[M_f^{\mathrm{rig}}]_{55}^{ref} = [M_f^{\mathrm{rig}}]_{66}^{ref} = \frac{0.700}{150}\frac{13}{250}\pi\rho_f L^5, \tag{66c}$$

The superscript $[\bullet]^{ref}$ stands for the terms obtained analytically. One can deduce the values of the rigid body gyroscopic operator $[G_f^{\mathrm{rig}}]^{ref}$ from the rigid body added mass operator (see Appendix A). Its non nil coefficients for an ambient flow $\boldsymbol{u}_\infty$ with an angle of attack $\pi/6$ relatively to the axis of revolution of the ellipsoid are:

$$[G_f^{\text{rig}}]_{15}^{ref} = -[G_f^{\text{rig}}]_{51}^{ref} = -0.350\rho_f L^2 U_\infty \tag{67a}$$

$$[G_f^{\text{rig}}]_{26}^{ref} = [G_f^{\text{rig}}]_{53}^{ref} = -[G_f^{\text{rig}}]_{62}^{ref} = -[G_f^{\text{rig}}]_{35}^{ref} = 0.606\rho_f L^2 U_\infty. \tag{67b}$$

Since the stiffness operator has already been validated in the case of an elastic deformation in the previous section, we do not consider this operator in this section. The fluid operators from equation (59) can be projected on the rigid body movements of the structure to be compared with the operators $[M_f^{\text{rig}}]^{ref}$ and $[D_f^{\text{rig}}]^{ref}$. These rigid body movements can be described with the displacement $\boldsymbol{d}$ of the structure's center of volume and the rotation $\boldsymbol{\theta}$, which relate to the structure displacements with the operator $\mathbb{Q}$:

$$\bar{\boldsymbol{\xi}}^1 = \mathbb{Q} \begin{pmatrix} \bar{\boldsymbol{d}}^1 \\ \bar{\boldsymbol{\theta}}^1 \end{pmatrix}, \tag{68a}$$

$$\mathbb{Q} = [\mathbb{1}, -\bar{\boldsymbol{x}}_\times]\,. \tag{68b}$$

The reduced fluid operators on rigid body modes are computed as:

$$[M_f]^{num} = \mathbb{Q}^{\mathrm{T}}[M_f]\mathbb{Q}, \quad [G_f]^{num} = \mathbb{Q}^{\mathrm{T}}[M_f]\mathbb{Q}. \tag{69}$$

The superscript $[\bullet]^{num}$ stands for the terms obtained numerically. The comparison between the analytic operators displayed in equations (66) and (67) with our model, for meshes with a varying number of nodes N_{DOF}, gives a relative error displayed in Figure 7, calculated with respect to the Frobenius norm:

$$\text{err}([\bullet]) = \frac{\left\|[\bullet]^{num} - [\bullet]^{ref}\right\|_{\text{fro}}}{\left\|[\bullet]^{ref}\right\|_{\text{fro}}}. \tag{70}$$

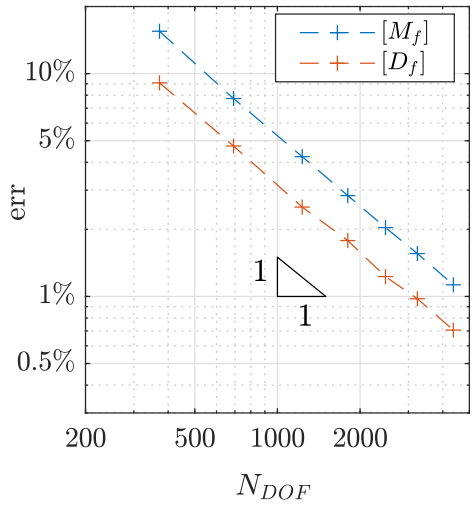

Figure 7: Numerical relative errors (in %) as a function of the number of nodes N_{DOF} associated with the Frobenius norm of the matrices $[M_f^{\text{rig}}]$ and $[G_f^{\text{rig}}]$, revealing a decreasing error in $\mathcal{O}\left(N_{DOF}^{-1}\right)$.

Figure 7 shows a convergence in $\mathcal{O}\left(N_{DOF}^{-1}\right)$, and highlights the validity of the operators written in equations (59). In order to compare with the calculations of Appendix A, the results presented in this section were computed without taking into account the gravity effects ($g = 0$). However, if gravity was to be taken into

L (ellipsoid major axis)	10 m
D (ellipsoid minor axis)	2 m
e (membrane thickness)	1 mm
ρ_f (solid density)	8000 kg.m^{-3}
ν (Poisson's ratio)	0.25
E (Young's modulus)	2$\times$ 10^9 Pa
Δp (internal overpressure)	70000 Pa
β (internal fluid compressibility)	0
N_{DOF} (number of mesh nodes)	3037
g (gravity acceleration)	0 ms^{-2}

Table 1: Parameters used for the description of the structure and its internal fluid.

account for a structure with rigid body movements in a fluid of homogeneous density ρ_f, Archimedes' force amplitude and direction would remain constant since the volume of the structure does not change. Hence, it would only add the work of Archimedes' force at order 0, and the rigid body movements would not result in any added stiffness. In order to verify this, the operator $\mathbb{Q}^{\mathrm{T}}[N_{(\bar{p}_\infty)}]\mathbb{Q}$ from equation (59) was computed for the same ellipsoid by taking into account an aerostatic pressure $p_\infty = -\rho_f g \bar{z}$, and the non-dimensional stiffness operator obtained verifies numerically:

$$\frac{\left\|\mathbb{Q}^{\mathrm{T}}[N_{(\bar{p}_\infty)}]\mathbb{Q}\right\|_{\mathrm{fro}}}{\rho_f g L} = \mathcal{O}\left(10^{-4}\right), \tag{71}$$

which seems sufficiently small. Finally, we can consider that the error associated with the numerical approximation of the fluid operators has been quantified and their convergence assessed at least in specific cases. As mentioned in section 2, [6] has shown the symmetry of the added mass and stiffness operators and the skew-symmetry of the gyroscopic operator using the Lagrange equations. This statement is investigated with the operators introduced in this study. In order to do so, the following errors using the Froebenius norm have been determined based on a longitudinal ambient flow $\boldsymbol{u}_\infty$ for the same mesh as in figure 7. The operators have been projected on the arbitrary projection basis $\mathbb{Q}_s$ consisting in the six rigid body movements of space completed by the first flexible (banana shaped) mode of the airship, see section 5 for more details about the projection basis:

$$\begin{aligned}
\frac{\left\|[K_f] - [K_f]^{\mathrm{T}}\right\|_{\mathrm{fro}}}{\|[K_f]\|_{\mathrm{fro}}} &= 0.12\% \\
\frac{\left\|[G_f] + [G_f]^{\mathrm{T}}\right\|_{\mathrm{fro}}}{\|[G_f]\|_{\mathrm{fro}}} &= 0.58\% \\
\frac{\left\|[M_f] - [M_f]^{\mathrm{T}}\right\|_{\mathrm{fro}}}{\|[M_f]\|_{\mathrm{fro}}} &= 0.02\%.
\end{aligned}$$

The results above are in agreement with the expected (skew-)symmetry of the operators shown by [6].

5. Stability analysis of a free inflated ellipsoidal membrane

Equations (60) have been developped in time domain. In the test case presented in this section, we will more specifically use the equations in the frequency domain in order to perform a stability analysis on a simple test case, which does not exclude the possibility of application in time domain such as prediction and control in the future [6]. The method introduced in this article is here applied to the particular case of

an ellipsoidal inflated membrane in a uniform flow, whose eigenvalues and eigenmodes are computed. The prolate ellipsoid has an aspect ratio of $5:1$, characterized by the slenderness number $\mathcal{S}$:

$$\mathcal{S} = \frac{L}{D} = 5. \tag{72}$$

In order to characterize the structure, operators $[K_s]$ and $[M_s]$ from equation (60) are calculated using the Finite Element analysis program NASTRAN. For that purpose, a membrane finite element linear model has been used, inflated by an incompressible fluid. Its parameters are described in table 1. The fluid operators $[K_f]$, $[G_f]$ and $[M_f]$ are calculated using the method presented in section 3. Both fluid and solid operators are calculated on the same conforming surface mesh. As mentioned in section 2, the reference interface coincides with the fluid-structure quasi-steady solution. For the sake of simplicity, we calculate in this study the dynamics of the structure as an invariant shape $\overline{\Sigma}$ assuming that the structure quasi-steady state does not drastically change with the value of U_∞. This hypothesis enables us to perform calculations based on the same reference configuration. As a consequence, the structure operators are only computed once, and are associated with a quasi-steady state with no ambient flow (homogeneous external pressure field) used as the reference configuration. The coupled model was obtained by adding the fluid and solid operators as described in equation (60). After characterizing the fluid-structure operators, the objective of this section is to calculate the associated fluid-structure coupled eigenvalues. For this purpose, the displacement $\boldsymbol{\xi}$ is looked for as the product of a function of space $\boldsymbol{q}$ and a function of time:

$$\boldsymbol{\xi}(\boldsymbol{x}, t) = \boldsymbol{q}(\boldsymbol{x}) \ \exp(\lambda t), \tag{73}$$

where λ can be complex. In the following, all the variables are written on the reference configuration and the bar notation $\overline{(\bullet)}$ is not used since there is no risk of confusion. The solution in the form of equation (73) is introduced in equation (60), which gives:

$$\Big[\left([M_s] + [M_f] \right) \lambda^2 + [G_f]\, \lambda + [K_s] + [K_f] \Big] \boldsymbol{q} \exp(\lambda t) = 0. \tag{74}$$

However, because the fluid operators are full (as a consequence of condensing the fluid equations on the interface with the integral representation [21]), solving such a problem requires a large amount of memory. To overcome this issue, the size of the problem is reduced by projecting the unknown displacements $\boldsymbol{\xi}$ of the structure on a reduced basis. The basis chosen here contains the six rigid body motions (three translations and three infinitesimal rotations), completed by two structural elastic modes $\boldsymbol{\xi}_7$ and $\boldsymbol{\xi}_8$ (computed with NASTRAN), one of which can be seen on Figure 6. These banana-shaped flexible modes are orthogonal. Both have the same *in vacuo* frequency and only differ by a $\pi/2$ rotation of their direction around the symmetry axis. According to Li et al. [6], these banana modes are expected to be the lowest frequency elastic modes emerging for high aspect ratio flexible airships. The displacement field is therefore projected on a reduced basis $\mathbb{Q}_s$:

$$\boldsymbol{\xi}(\boldsymbol{x}, t) = \mathbb{Q}_s(\boldsymbol{x}) \boldsymbol{q}_s \exp(\lambda t) \tag{75a}$$

$$\text{with } \mathbb{Q}_s = [\mathbb{Q}, \boldsymbol{\xi}_7, \boldsymbol{\xi}_8], \quad \boldsymbol{q}_s = \begin{pmatrix} \boldsymbol{d} \\ \boldsymbol{\theta} \\ q_{s7} \\ q_{s8} \end{pmatrix} \text{ and } [\bullet]_{\mathbb{Q}_s} = \mathbb{Q}_s^{\mathrm{T}} [\bullet] \mathbb{Q}_s. \tag{75b}$$

The projection basis $\mathbb{Q}_s$ is an eight-columns concatenation of the rigid body movements matrix $\mathbb{Q}$ defined in (68a) for the first six columns, and the mode shape functions of the bending modes $\boldsymbol{\xi}_7$ and $\boldsymbol{\xi}_8$ for the two last columns. The volume center displacement is given by $\boldsymbol{d}$, the structure rotation is given by $\boldsymbol{\theta}$ and the amplitudes of the elastic modes are given by the modal coefficients q_{s7} and q_{s8}. The displacements are therefore characterized by the new generalized coordinates vector $\boldsymbol{q}_s$ of the fluid-structure problem and the associated eigenvalue λ. Equation (74) is quadratic with respect to λ, however it is much more convenient to determine eigenvalues associated with linear eigen-equations. For that purpose, the equation is shifted

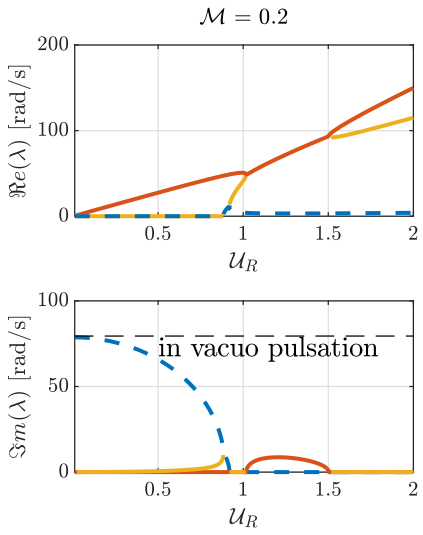

Figure 8: Evolution of the real part of the modes (top) associated with the growth rate and their imaginary part (bottom) associated with the circular frequency as a function of the reduced velocity $\mathcal{U}_R$. The mass ratio is $\mathcal{M} = 0.2$. Each color stands for an identified mode using a Modal Assurance Criterion. Only the modes with positive frequency, positive growth rate and strictly positive absolute value have been plotted. The black horizontal dashed line shows the frequency of the banana mode in the absence of fluid.

into the state space, thus reducing its order in λ from quadratic to linear, which gives by projecting on the $\mathbb{Q}_s$ basis:

$$[M_1] \begin{pmatrix} \boldsymbol{q}_s \\ \lambda \boldsymbol{q}_s \end{pmatrix} = \lambda [M_2] \begin{pmatrix} \boldsymbol{q}_s \\ \lambda \boldsymbol{q}_s \end{pmatrix}, \tag{76a}$$

$$\text{with } [M_1] = \begin{bmatrix} 0 & \mathbb{1} \\ [K_s]_{\mathbb{Q}_s} + [K_f]_{\mathbb{Q}_s} & [G_f]_{\mathbb{Q}_s} \end{bmatrix} \text{ and } [M_2]_s = \begin{bmatrix} \mathbb{1} & 0 \\ 0 & -\left([M_s]_{\mathbb{Q}_s} + [M_f]_{\mathbb{Q}_s}\right) \end{bmatrix} \tag{76b}$$

Equation (76a) consists of a system of eight equations since the dynamic equations have been projected on the modal basis with the help of a left-multiplication by $\mathbb{Q}_s^{\mathrm{T}}$. This eigenvalue equation is solved using Matlab for a flow velocity $\boldsymbol{u}_\infty$ colinear to the structure axis. A range of fluid velocities U_∞ and densities ρ_f are investigated. The results are plotted with respect to the reduced velocity $\mathcal{U}_R$ and the mass ratio $\mathcal{M}$ defined as:

$$\mathcal{U}_R = \frac{U_\infty}{\Omega L}, \tag{77a}$$

$$\mathcal{M} = \frac{\rho_f}{\rho_s \frac{e}{D}}. \tag{77b}$$

The reduced velocity $\mathcal{U}_R$ determines the ratio between the flow velocity and the velocity required for a fluid particle to travel across the structure in the time of a characteristic period. The value of the characteristic frequency Ω is chosen as the frequency *in vacuo* of the elastic modes. The mass ratio compares the order of magnitude between the added mass of the fluid and the membrane mass, D being the diameter of the ellipsoid (hence $D = L/5$ for a 5:1 prolate). The particular dependence of the operators on U_∞ is taken advantage of: they are calculated at an arbitrary velocity, and their value can be recalculated for each $\mathcal{U}_R$

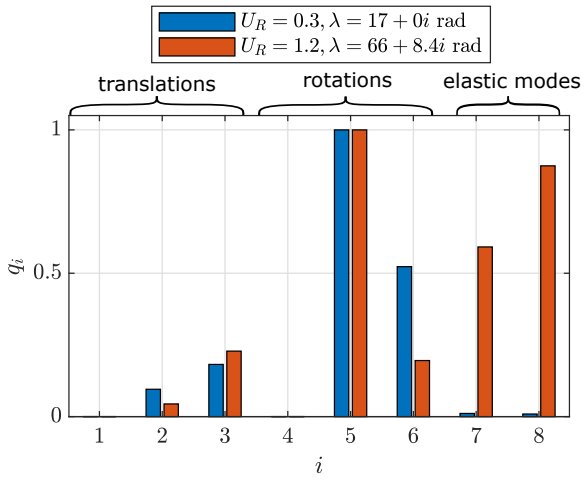

Figure 9: Generalised coordinates of a static unsteady mode (blue) and a flutter mode (orange) for two different values of $\mathcal{U}_R$, with $\mathcal{M} = 0.2$.

with a scalar multiplication, recalling that the mass operator does not vary with U_∞, the gyroscopic operator is linear with U_∞ and the stiffness operator is linear with U_∞^2, as shown in section 3. Similarly, by looking at equation (35) one can deduce that the fluid operators are linear with the fluid density ρ_f.

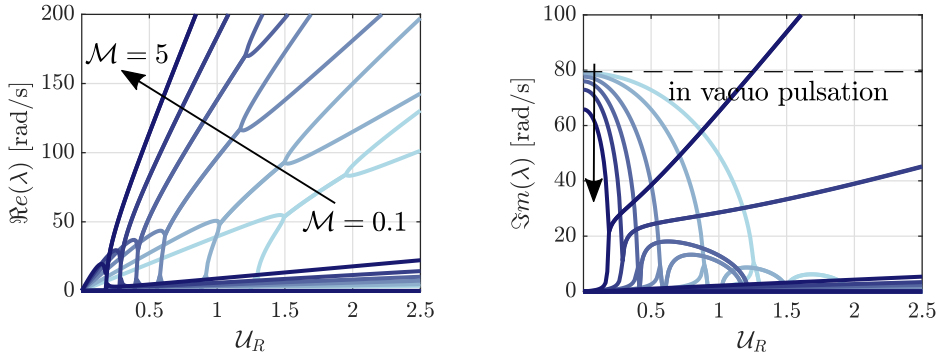

Figure 10: Real part (growth rate, top) and imaginary part (frequency, bottom) of the eigenvalues as a function of the reduced velocity $\mathcal{U}_R$. Curves are for $M = 0.1, 0.2, 0.5, 1, 2$ and 5.

The results are presented Figure 8 for a mass ratio of $\mathcal{M} = 0.2$. The order 0 solution is an unstable equilibrium position as soon as there is a flow because of the absence of fins in this simple test case. Indeed, for $\mathcal{U}_R \in]0, 1]$, the system has a mode with a nil frequency $\Im m(\lambda) = 0$ and a positive growth rate $\Re e(\lambda) > 0$ (plotted in blue in Figure 8): it is a divergence mode. At an arbitrary value $\mathcal{U}_R = 0.3$ in this region, the modal decomposition of this unstable mode $\boldsymbol{q}_s$ is shown in Figure 9 with blue bars. It appears that the generalized coordinates contributing to the instability are the rotations and translations perpendicular to the axis of $\boldsymbol{u}_\infty$, while translation and rotation in the axis of the structure and flexible deformations are not involved in the instability. The latter is triggered by the mechanical moment appearing in equation (A.30b): a small variation of $\boldsymbol{\theta}^1$ induces a moment in the same direction on the structure, leading to an exponentially growing drift. The moment responsible for this drift is known by airship engineers as the Munk moment [1].

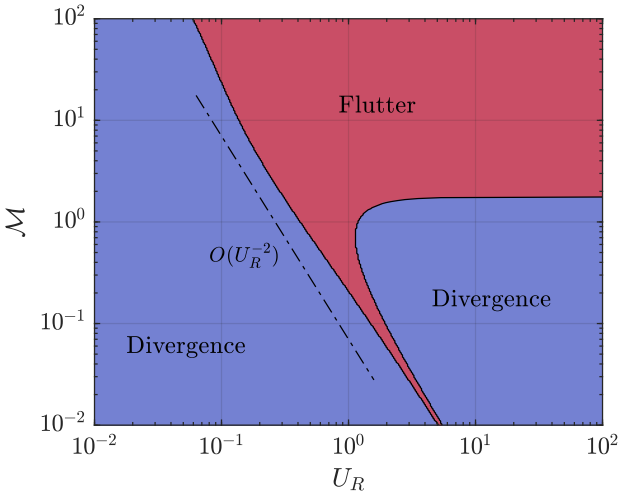

Figure 11: Instability map predicted by the linear model: divergence (static) or flutter (dynamic), for $\mathcal{M} \in [10^{-4}, 10^{6}]$ and $\mathcal{U}_R \in [10^{-2}, 10^{2}]$.

The contribution of the translations displayed in Figure 9 results from the emergence of a force perpendicular to the ambient flow when the structure rotates as predicted by equation (A.30a). In the region $\mathcal{U}_R \in]0, 1]$ of Figure 8, the frequency of the elastic mode (dashed blue line) decreases with the reduced velocity until it vanishes. If the flow velocity increases past this point, another static unstable mode appears (yellow line), with a growth rate increasing with $\mathcal{U}_R$. When the flow reaches the critical velocity $\mathcal{U}_R \simeq 1.04$, the growth rate of the two unstable modes becomes equal, and a coupled mode with a strictly positive frequency and growth rate emerges, resulting in exponentially growing oscillations of the structure. This instability is referred to as post-diverence (or Paidoussis) flutter [30], and is characteristic of conservative gyroscopic systems. This flutter phenomenon is documented in detail in section 3.4 of [30] in the context of clamped pipes conveying fluid. The orange bars from Figure 9 show the generalized coordinates of this flutter mode. It appears that, unlike the static unstable mode below the critical velocity (plotted with blue bars in the same figure), this instability results from the coupling of rigid body movements with elastic deformations of the structure, partly due to the gyroscopic effects of the fluid. Around $\mathcal{U}_R = 1.53$, the flutter mode splits into two static unstable modes. We see as well that for a mass ratio of $\mathcal{M} = 0.2$ the added mass has a low influence on the dynamics. Indeed, for $\mathcal{U}_R = 0$ (hence when fluid stiffness or gyroscopic effects vanish), the frequency of the elastic mode (dashed blue line in Figure 8) is almost the same as the frequency of the structure *in vacuo* (dashed horizontal black line). Figure 10 shows the evolution of the eigenvalues for a range of values of mass ratio $\mathcal{M}$. As expected, for larger values of the fluid density, the frequency of the immersed elastic mode in a fluid at rest decreases.
Figure 11 shows the type of instability of the system (static divergence or flutter) as a function of the parameters $\mathcal{U}_R$ and $\mathcal{M}$. It can be seen that the model presented here provides a quick way to carry out stability studies as a function of flow or structural parameters. We observe that in the absence of fins, the system is always unstable, hence the importance of adding at least a simplified model of the fins like Li [6] to apply the method to real cases.

6. Conclusion

Drawing inspiration from the work of Li et al. [6] to characterize the dynamic aeroelasticity of flexible airships, the method presented in this article aims both to enhance the precision of the prediction of the

potential flow effects and to calculate it for various shapes of airships. The approach is based on a linearization of the fluid boundary equation expressed in an ALE formalism, which leads to the numerical calculation of new BEM operators associated to the spatial derivative of the classical BEM operators for a flowing fluid with respect to the structure displacements. After quantifying the numerical and linearization errors associated to the method through test cases, some preliminary results have been presented in section 5, showcasing the advantages of the method for stability analysis of such systems. It also highlighted the high cost of the eigenvalue problem due to the density of the fluid matrices. Though the projection on the dry modal basis helped to overcome this issue, an ongoing development is the use of hierarchical matrices [41] to reduce storage space (currently in $\mathcal{O}\left({N_{DOF}}^2\right)$) and to calculate matrix vector products faster. For applications such as control of trajectory, regarding the rigid body motions, the small displacements hypothesis is a limitation: in order to expand the model to wider flight conditions such as maneuvers, an extension to large displacements coupled with small deformations would be of high interest, as done in works of Thomasson & Woolsey [37] who deal with rigid body motions in currents for example. In order to be able to represent the aspects of lift and drag with the model presented in this article, a solution could be to impose the Kutta condition at the trailing edge of the fins, thus creating a circulation in the flow. For this, it will be necessary to introduce in the integral representation a discontinuity surface (vortex sheet) representing the wake of the airship (as it is done in the panel method, cf [3, 8] for steady flight conditions or by [28] in the case of unsteady, compressible flows but without predicting the linear perturbations around a reference solution). This surface will be discretized by the BEM as it is done for the fluid-structure interface except that the associated operators are hyper-singular, as shown by [21], and their calculation requires more complex mathematical methods such as the algorithm introduced in [42]. This work will be the subject of a future article.

References

[1] Li, Y., Meyer, N. and Sharf, I., 2011, *Airship dynamics modeling: A literature review*, Progress in Aerospace Sciences, 47: 217–239.

[2] Amiryants, G.A., Grigoriev, V.D., Ishmuratov, F.Z., Franz, A., d'Henin, E. and Kaempf, B., 2002, *Investigations of airship aeroelasticity*, 23rd International Congress of Aerospace Sciences, Toronto, Canada.

[3] Bessert, N. and Frederich, O., 2005, *Nonlinear Airship Aeroelasticity*, Journal of Fluids and Structures, 21: 731–742.

[4] J.M. Liu, C.J. Lu, L.P. Xue, 2010, *Numerical investigation on the aeroelastic behavior of an airship with hull-fin configuration*, Journal of Hydrodynamics, 22: 207–213.

[5] Wu, X., Wang, Y., Huang, C., Liu, Y. and Lu, L., 2015, *Experiment and numerical simulation on the characteristics of fluid–structure interactions of non-rigid airships*, Theoretical and Applied Mechanics Letters, 5: 258–261.

[6] Li, Y., Meyer, N. and Sharf, I., 2009, *Dynamics Modeling and Simulation of Flexible Airships*, AIAA Journal, 47: 592—605.

[7] Azouz, N., Chaabani, S., Lerbet, J. and Abichou, A., 2012, *Computation of the added masses of an unconventional airship*, Journal of Applied Mathematics 2012, Article ID 714627.

[8] Lutz, T., Funk, P., Jakobi, S. and Wagner, S., 2002, *Summary of Aerodynamic Studies on the Lotte Airship*, 4th International Airship Convention and Exhibition, Cambridge, England.

[9] Riccardi, G. and De Bernardis, E., 2019, *Numerical simulations of the dynamics and the acoustics of an axisymmetric bubble rising in an inviscid liquid*, European Journal of Mechanics - B/Fluids, 79: 121–140.

[10] van Opstal, T.M., van Brummelen, E.H., de Borst, R. and Lewis, M., 2012, *A finite-element/boundary-element method for large-displacement fluid–structure interaction with potential flow*, Computer Methods in Applied Mechanics and Engineering, 50(6): 779–788.

[11] Tan, K. L., Khoo, B. C. and White, J. K., 2008, *A level set–boundary element method for the simulation of underwater bubble dynamics*, SIAM Journal on Scientific Computing, 30(2): 549–571.

[12] Garzon, M., Adalsteinsson, D., Gray, L. and Sethian, J. A., 2005, *A coupled level set–boundary integral method for moving boundary simulations*, Interfaces and Free Boundaries, 7: 277–302.

[13] Veron, E. and Bouzidi, R., 2016, *Large displacements of light thin flexible structures coupled with heavy fluids using co-simulation between finite element and fast boundary element solvers*, Proceedings of the 11th International Conference on Flow-Induced Vibration, The Hague, The Netherlands.

[14] Schotté, J.-S., Doaré, O., Le Mestre, R., 2019, *Effect of coupling with internal and external fluids on the mechanical behaviour of aerostats*, 7th International Conference on Structural Engineering, Mechanics and Computation, Cape Town, South Africa.

[15] Folland, G.B., 1995, *Introduction to partial differential equations* (Vol. 102), Princeton university press.

[16] Morand, H. J.-P., and Ohayon, R., 1995, Fluid structure interaction-Applied numerical methods, Wiley.

[17] Pfister, J.-L., Marquet, O. and Carini, M., 2019, *Linear stability analysis of strongly coupled fluid–structure problems with the Arbitrary-Lagrangian–Eulerian method*, Computer Methods in Applied Mechanics and Engineering, 355: 663—689.

[18] Ciarlet, P.G., 2005, *An introduction to differential geometry with applications to elasticity*, Journal of elasticity, 78(1): 1–215
[19] Haug, E.-J., Choi, K.-K and Komkov, V., 1986, *Design sensitivity analysis of structural systems*, Elsevier Science.
[20] Henrot, A. and Pierre, M., 2005, *Variation et optimisation de formes*, Springer.
[21] Bonnet, M., 1999, *Boundary integral equation methods for solids and fluids*, Wiley.
[22] Hughes, T., Liu, W. and Zimmermann, T., 1981, *Lagrangian-Eulerian finite element formulation for incompressible viscous flows*. Computer Methods in Applied Mechanics and Engineering, 29: 329–349.
[23] Veron, E., 2016, *Calcul numérique des grandes déformations de structures minces en contact avec des fluides lourds* (*Numerical simulation of large displacements of thin flexible structures coupled with heavy fluids*), Doctoral dissertation, Nantes.
[24] Theodorsen, T., 1949, *General theory of aerodynamic instability and the mechanism of flutter*, NACA Technical Report 496.
[25] Dowell, E. H., 1989, *A modern course in aeroelasticity*, Eds. Howard C. Curtiss, Robert H. Scanlan, and Fernando Sisto. Vol. 3. Dordrecht, The Netherlands: Kluwer academic publishers.
[26] Potthast, R., 1994, *Fréchet differentiability of boundary integral operators in inverse acoustic scattering*, Inverse Problems, 10(2): 64–84.
[27] John, D. and Anderson, D., 2003, *Modern compressible flow*, Mc Graw Hill.
[28] Gennaretti, M., Luceri, L. and Morino, L., 1997, *A unified boundary integral methodology for aerodynamics and aeroacoustics of rotors*, Journal of Sound and Vibration, 200(4): 467–489.
[29] Ziegler, H., 2013, *Principles of structural stability*, Birkhäuser.
[30] Paidoussis, M. P., 1998, *Fluid-structure interactions: slender structures and axial flow*, Volume 1, Academic press.
[31] Destuynder, P. and Santi, F. 2006, *A progressive Euler-Lagrange formulation for aeroelasticity model of quasi-axisymmetrical airship*, ECCOMAS CFD 2006: proceedings of the European Conference on Computational Fluid Dynamics.
[32] Pozrikidis, C., 2002, *A practical guide to boundary element methods with the software library BEMLIB*, CRC Press.
[33] Fischnaller, H. and Thöbin K., 2009, *Numerical integration - an introduction to the Boundary Element Method*, Masters project for Graz unitersity of technology.
[34] Katz, J. and Plotkin, A., 2001, *Low-speed aerodynamics*, Cambridge university press, Vol. 13.
[35] Rangette, A., 1990, *A boundary element method to calculate the fluid hydrodynamic mass matrix in structural analysis including free surface waves*, Engineering Computations, 7(3): 210–216.
[36] Lamb, H., 1924, *Hydrodynamics*, University Press.
[37] Thomasson, P. G. and Woolsey, C. A., 2013, *Vehicle motion in currents*, IEEE Journal of Oceanic Engineering, 38(2): 226–242.
[38] Clarke, D.B., 2009, *Experimental and computational investigation of flow about low aspect ratio ellipsoids at transcritical Reynolds numbers, Appendix C*, Doctoral dissertation, University of Tasmania.
[39] Lamb, H., 1918, *The inertia coefficients of an ellipsoid moving in fluid*, Reports and memoranda, 128–129.
[40] De Langre, E., 2008. *Effects of wind on plants*, Annual Reviews of Fluid Mechanics, 40: 141–168.
[41] Chaillat, S., Desiderio, L., Ciarlet, P., 2017, *Theory and implementation of $\mathcal{H}$-matrix based iterative and direct solvers for Helmholtz and elastodynamic oscillatory kernels*, Journal of Computational Physics, 351: 165—186.
[42] Guiggiani, M., Krishnasamy, G., Rudolphi, T. J. and Rizzo, F.J., 1992, *A general algorithm for the numerical solution of hypersingular boundary integral equations*, Journal of Applied Mechanics, 59(3): 604–614.

Appendix A. Detailed calculation of the linearization

We detail here how the linearization was performed.

Linearized Green's function

The order 1 Taylor expansion of the norm of a vector $\boldsymbol{a}$ at an arbitrary power n is:

$$\|\boldsymbol{a}\|^n = \left\|\boldsymbol{a}^0\right\|^n + \boldsymbol{a}^0 \cdot \boldsymbol{a}^1 \left\|\boldsymbol{a}^0\right\|^{n-2} + \mathcal{O}\left(\varepsilon^2\right), \tag{A.1}$$

allowing to calculate the following formula:

$$\|\boldsymbol{x}-\boldsymbol{y}\|^n = \|\bar{\boldsymbol{x}}-\bar{\boldsymbol{y}}\|^n + n(\bar{\boldsymbol{x}}-\bar{\boldsymbol{y}}) \cdot \left(\boldsymbol{\xi}^1_{(\bar{\boldsymbol{x}})} - \boldsymbol{\xi}^1_{(\bar{\boldsymbol{y}})}\right) \|\bar{\boldsymbol{x}}-\bar{\boldsymbol{y}}\|^{n-2} + \mathcal{O}\left(\varepsilon^2\right) \quad \text{on } \overline{\Sigma}. \tag{A.2}$$

The Green's function given by (19) and its gradient becomes, when combined with the linearized expression (A.2):

$$\overline{\boldsymbol{G_n}}^0 = -\frac{1}{4\pi}\frac{\bar{\boldsymbol{n}}}{\|\bar{\boldsymbol{x}}-\bar{\boldsymbol{y}}\|} \tag{A.3a}$$

$$\overline{\boldsymbol{G_n}}^1 = \frac{1}{4\pi}\left(\frac{(\bar{\boldsymbol{x}}-\bar{\boldsymbol{y}})\cdot\left(\boldsymbol{\xi}^1_{(\bar{\boldsymbol{x}})}-\boldsymbol{\xi}^1_{(\bar{\boldsymbol{y}})}\right)\bar{\boldsymbol{n}}}{\|\bar{\boldsymbol{x}}-\bar{\boldsymbol{y}}\|^3} - \frac{\bar{\boldsymbol{\tau}}^1}{\|\bar{\boldsymbol{x}}-\bar{\boldsymbol{y}}\|}\right) \tag{A.3b}$$

$$\overline{\partial_n G}^0 = \frac{1}{4\pi}\frac{(\bar{\boldsymbol{x}}-\bar{\boldsymbol{y}})\cdot\bar{\boldsymbol{n}}}{\|\boldsymbol{x}-\boldsymbol{y}\|^3} \tag{A.3c}$$

$$\overline{\partial_n G}^1 = \frac{1}{4\pi}\left(\frac{(\bar{\boldsymbol{x}}-\bar{\boldsymbol{y}})\cdot\bar{\boldsymbol{\tau}}^1}{\|\boldsymbol{x}-\boldsymbol{y}\|^3} + \frac{\left(\boldsymbol{\xi}^1_{(\bar{\boldsymbol{x}})}-\boldsymbol{\xi}^1_{(\bar{\boldsymbol{y}})}\right)\cdot\bar{\boldsymbol{n}}}{\|\bar{\boldsymbol{x}}-\bar{\boldsymbol{y}}\|^3}\right. \tag{A.3d}$$

$$\left. - 3\frac{(\bar{\boldsymbol{x}}-\bar{\boldsymbol{y}})\cdot\left(\boldsymbol{\xi}^1_{(\bar{\boldsymbol{x}})}-\boldsymbol{\xi}^1_{(\bar{\boldsymbol{y}})}\right)(\bar{\boldsymbol{x}}-\bar{\boldsymbol{y}})\cdot\bar{\boldsymbol{n}}}{\|\bar{\boldsymbol{x}}-\bar{\boldsymbol{y}}\|^5}\right). \tag{A.3e}$$

Linearized flow velocity

In order to express the linear variations of the flow velocity at order ε on the interface, recalling that

$$\boldsymbol{u} = \boldsymbol{\nabla}\phi = \frac{\partial\phi}{\partial\boldsymbol{x}}, \tag{A.4}$$

one can express on the reference interface with the chain rule:

$$\begin{aligned}\bar{\boldsymbol{u}} &= \frac{\partial\bar{\boldsymbol{x}}}{\partial\boldsymbol{x}}\frac{\partial\bar{\phi}}{\partial\bar{\boldsymbol{x}}}\\ &= \left(\frac{\partial\boldsymbol{x}}{\partial\bar{\boldsymbol{x}}}\right)^{-\mathrm{T}}\overline{\boldsymbol{\nabla}}\bar{\phi}\\ &= (\mathbb{1}+\overline{\nabla}\bar{\boldsymbol{\xi}})^{-\mathrm{T}}\overline{\boldsymbol{\nabla}}\bar{\phi}.\end{aligned} \tag{A.5}$$

The linearized inversion of the terms in the parentheses of the above equation enables to write at both orders of magnitude 0 and ε:

$$\bar{\boldsymbol{u}} = \overline{\boldsymbol{\nabla}}\bar{\phi}^0 + \overline{\boldsymbol{\nabla}}\bar{\phi}^1 - \left[\overline{\nabla}^{\mathrm{T}}\bar{\boldsymbol{\xi}}^1\right]\overline{\boldsymbol{\nabla}}\bar{\phi}^0 + \mathcal{O}\left(\varepsilon^2\right), \tag{A.6}$$

hence the demonstration of (46).

Linearized quadratic flow velocity

The linearized term $\bar{\boldsymbol{u}}^0.\bar{\boldsymbol{u}}^1$ is developed into a more useful formulation. Because of the non penetration condition (10) at order 0:

$$\bar{\boldsymbol{u}}^0\cdot\bar{\boldsymbol{n}} = 0 \quad \text{on } \overline{\Sigma}, \tag{A.7}$$

by introducing the tangential and normal components of any arbitrary vector $\bar{\boldsymbol{a}}$ on $\overline{\Sigma}$:

$$\begin{aligned}\bar{\boldsymbol{a}}_n &= (\bar{\boldsymbol{n}}\otimes\bar{\boldsymbol{n}})\bar{\boldsymbol{a}}\\ \bar{\boldsymbol{a}}_S &= \bar{\boldsymbol{a}} - \bar{\boldsymbol{a}}_n\\ \bar{\boldsymbol{a}} &= \bar{\boldsymbol{a}}_S + \bar{\boldsymbol{a}}_n,\end{aligned} \tag{A.8}$$

we obtain:

$$\bar{\boldsymbol{u}}^0 = \bar{\boldsymbol{u}}^0_S \quad \text{on } \overline{\Sigma}. \tag{A.9}$$

The scalar product becomes

$$\begin{aligned}\bar{\boldsymbol{u}}^0 \cdot \bar{\boldsymbol{u}}^1 &= \bar{\boldsymbol{u}}_S^0 \cdot (\bar{\boldsymbol{u}}_S^1 + \bar{\boldsymbol{u}}_n^1) \\ &= \bar{\boldsymbol{u}}_S^0 \cdot \bar{\boldsymbol{u}}_S^1 \quad \text{on } \overline{\Sigma}.\end{aligned} \tag{A.10}$$

Using equation (46), we obtain:

$$\bar{\boldsymbol{u}}_S^1 = (1 - \bar{\boldsymbol{n}} \otimes \bar{\boldsymbol{n}}) \left(\overline{\boldsymbol{\nabla}} \bar{\phi}^1 - \left(\overline{\nabla}^{\mathrm{T}} \bar{\boldsymbol{\xi}}^1 \bar{\boldsymbol{u}}^0 \right) \right) = \overline{\boldsymbol{\nabla}}_S \bar{\phi}^1 - (\overline{\nabla}_S^{\mathrm{T}} \bar{\boldsymbol{\xi}}^1) \bar{\boldsymbol{u}}^0 \quad \text{on } \overline{\Sigma}. \tag{A.11}$$

By combining equations (A.10) and (A.11) we obtain:

$$\bar{\boldsymbol{u}}^0 \cdot \bar{\boldsymbol{u}}^1 = \bar{\boldsymbol{u}}^0 \cdot \left(\overline{\boldsymbol{\nabla}}_S \bar{\phi}^1 - \overline{\nabla}_S^{\mathrm{T}} \bar{\boldsymbol{\xi}}^1 \bar{\boldsymbol{u}}^0 \right) \quad \text{on } \overline{\Sigma}. \tag{A.12}$$

Linearized velocity

It might be of interest, in order to validate the code for example, to be able to calculate the fluid velocity at the interface. The velocity can be decomposed into a surface and a normal component, since the surface gradient of the potential is calculated more conveniently than its total gradient since the potential is calculated only at the interface with the BEM:

$$\boldsymbol{u} = \boldsymbol{u}_S + (\boldsymbol{n} \otimes \boldsymbol{n}) \boldsymbol{u} \quad \text{on } \Sigma_{(t)} \tag{A.13}$$

where it is important to notice that $\boldsymbol{u}_S = \boldsymbol{\nabla}_S \phi$ is calculated with the surface gradient in the deformed configuration:

$$\boldsymbol{\nabla}_S \phi = (\mathbb{1} - \boldsymbol{n} \otimes \boldsymbol{n}) \boldsymbol{\nabla} \phi \quad \text{on } \Sigma_{(t)}. \tag{A.14}$$

By developing at order ε the above equation:

$$\boldsymbol{\nabla}_S \phi = (\mathbb{1} - \bar{\boldsymbol{n}} \otimes \bar{\boldsymbol{n}}) \overline{\boldsymbol{\nabla}} \bar{\phi}^0 - (\bar{\boldsymbol{n}} \otimes \boldsymbol{n}^1 + \boldsymbol{n}^1 \otimes \bar{\boldsymbol{n}}) \overline{\boldsymbol{\nabla}} \bar{\phi}^0 - \overline{\nabla}_S^{\mathrm{T}} \bar{\boldsymbol{\xi}}^1 \overline{\boldsymbol{\nabla}}_S \bar{\phi}^0 + \overline{\boldsymbol{\nabla}}_S \bar{\phi}^1 + \mathcal{O}\left(\varepsilon^2\right) \quad \text{on } \Sigma_{(t)}. \tag{A.15}$$

Therefore, we obtain the steady velocity at orders 0 and 1 by combining equations (38a) and (A.15):

$$\begin{aligned}\bar{\boldsymbol{u}}_S^0 &= (\mathbb{1} - \bar{\boldsymbol{n}} \otimes \bar{\boldsymbol{n}}) \overline{\boldsymbol{\nabla}} \bar{\phi}^0 = \overline{\boldsymbol{\nabla}}_S \bar{\phi}^0 && \text{on } \overline{\Sigma}, \\ \bar{\boldsymbol{u}}_S^1 &= \overline{\boldsymbol{\nabla}}_S \bar{\phi}^1 - \left(\left(\overline{\nabla}_S^{\mathrm{T}} \bar{\boldsymbol{\xi}}^1 \bar{\boldsymbol{n}} \right) \otimes \bar{\boldsymbol{n}} + \bar{\boldsymbol{n}} \otimes \left(\overline{\nabla}_S^{\mathrm{T}} \bar{\boldsymbol{\xi}}^1 \bar{\boldsymbol{n}} \right) - \overline{\nabla}_S^{\mathrm{T}} \bar{\boldsymbol{\xi}}^1 \right) \overline{\nabla}_S \bar{\phi}^0 && \text{on } \overline{\Sigma}.\end{aligned} \tag{A.16}$$

It has been noted that the first line had already been determined in equation (46) since the small displacements of the structure only affect the order $\mathcal{O}(\varepsilon)$ of the solution. Because the surface gradient is perpendicular to the normal, the expression at order 1 can be further simplified with:

$$\bar{\boldsymbol{u}}_S^1 = \overline{\boldsymbol{\nabla}}_S \bar{\phi}^1 - \left(\bar{\boldsymbol{n}} \otimes \left(\overline{\nabla}_S^{\mathrm{T}} \bar{\boldsymbol{\xi}}^1 \bar{\boldsymbol{n}} \right) - \overline{\nabla}_S^{\mathrm{T}} \bar{\boldsymbol{\xi}}^1 \right) \overline{\nabla}_S \bar{\phi}^0 \quad \text{on } \overline{\Sigma}. \tag{A.17}$$

By multiplying the boundary condition (10) with the normal, one gets:

$$(\boldsymbol{n} \otimes \boldsymbol{n}) \boldsymbol{u} = (\boldsymbol{n} \otimes \boldsymbol{n}) \frac{\partial \boldsymbol{\xi}}{\partial t} = (\bar{\boldsymbol{n}} \otimes \bar{\boldsymbol{n}}) \frac{\partial \bar{\boldsymbol{\xi}}^1}{\partial t} + \mathcal{O}\left(\varepsilon^2\right) \quad \text{on } \Sigma_{(t)} \tag{A.18}$$

By combining equations (A.13), (A.17) and (A.18), the order 1 fluctuations of the velocity are obtained:

$$\boldsymbol{u}^1 = \overline{\boldsymbol{\nabla}}_S \bar{\phi}^1 - \left(\bar{\boldsymbol{n}} \otimes \left(\overline{\nabla}_S^{\mathrm{T}} \bar{\boldsymbol{\xi}}^1 \bar{\boldsymbol{n}} \right) - \overline{\nabla}_S^{\mathrm{T}} \bar{\boldsymbol{\xi}}^1 \right) \overline{\nabla}_S \bar{\phi}^0 + (\bar{\boldsymbol{n}} \otimes \bar{\boldsymbol{n}}) \frac{\partial \bar{\boldsymbol{\xi}}^1}{\partial t} \quad \text{on } \overline{\Sigma}. \tag{A.19}$$

Linearized rigid-body gyroscopic loads

In order to validate the linearized equations of our model, this appendix displays here the exact nonlinear work from the pressure of an inviscid and irrotational fluid on a rigid structure. The efforts depending on the 6 rigid body movements will then be linearized in order to introduce a formulation with a fluid stiffness, damping and mass, allowing to compare the numerical results of section 4 with the analytical results displayed here. In order to parameterize the rigid body movements of the structure, the displacements are decomposed into a translation $\boldsymbol{d}$ and a rotation $\boldsymbol{\theta}$ such that:

$$\bar{\boldsymbol{\xi}}^1 = \bar{\boldsymbol{d}}^1 + \bar{\boldsymbol{\theta}}^1_\times \bar{\boldsymbol{x}}, \tag{A.20}$$

where the subscript $\times$ on a vector denotes the 3×3 matrix associated with the cross product $\times$ such that

$$\bar{\boldsymbol{\theta}}_\times \bar{\boldsymbol{x}} = \bar{\boldsymbol{\theta}} \times \bar{\boldsymbol{x}}. \tag{A.21}$$

The frame attached to the structure is noted $\tilde{\Sigma}$, which is equal to the reference frame $\overline{\Sigma}$ which has been rotated by the rotation operator $\mathbb{R}$ defined in equation (A.22a). First, literature gives the analytic expression of the 6×6 added mass matrix $[M_f^{\text{rig}}]$ of a revolution ellipsoid for any major to minor axis aspect ratio. Secondly, one can find the dynamical force and moment ($\tilde{\boldsymbol{F}}_{F/S}$ and $\tilde{\boldsymbol{M}}_{F/S}$ respectively) for a perfect stationary homogeneous ambient flow on a structure in a rigid body motion described by a velocity $\tilde{\boldsymbol{v}}$ at the center of volume and a rate of rotation $\tilde{\boldsymbol{\omega}}$. The tilde notation $(\tilde{\bullet})$ is associated with the expression of an array in the body frame, which is linked to the expression on the reference interface with the rotation operator $\mathbb{R}$ associated with a rotation angle of the structure $\boldsymbol{\theta}$:

$$\mathbb{R} = \mathbb{1} + \bar{\boldsymbol{\theta}}^1_\times + \mathcal{O}\left(\varepsilon^2\right), \tag{A.22a}$$

$$(\tilde{\bullet}) = \mathbb{R}^{-1}(\bar{\bullet}). \tag{A.22b}$$

The expression of the potential force and moment in the case of rigid body movements of a structure can be found in [37]:

$$\begin{pmatrix} \tilde{\boldsymbol{F}}_{F/S} \\ \tilde{\boldsymbol{M}}_{F/S} \end{pmatrix} = -\left[M_f^{\text{rig}}\right] \begin{pmatrix} \frac{\mathrm{d}\tilde{\boldsymbol{v}}}{\mathrm{d}t} - (\tilde{\boldsymbol{u}}_\infty)_\times \tilde{\boldsymbol{\omega}} \\ \frac{\mathrm{d}\tilde{\boldsymbol{\omega}}}{\mathrm{d}t} \end{pmatrix} - \begin{bmatrix} \tilde{\boldsymbol{\omega}}_\times & (0) \\ (\tilde{\boldsymbol{v}} - \tilde{\boldsymbol{u}}_\infty)_\times & \tilde{\boldsymbol{\omega}}_\times \end{bmatrix} \left[M_f^{\text{rig}}\right] \begin{pmatrix} \tilde{\boldsymbol{v}} - \tilde{\boldsymbol{u}}_\infty \\ \tilde{\boldsymbol{\omega}} \end{pmatrix}. \tag{A.23}$$

In the case of an ellipsoid, the added mass matrix $\left[M_f^{\text{rig}}\right]$ has only diagonal terms and can therefore be rewritten on the form:

$$\left[M_f^{\text{rig}}\right] = \begin{bmatrix} [M_{f1}] & (0) \\ (0) & [M_{f2}] \end{bmatrix}, \tag{A.24}$$

enabling to develop the expression of the force and moment:

$$\tilde{\boldsymbol{F}}_{F/S} = -\left[M_{f1}\right] \left(\frac{\mathrm{d}\tilde{\boldsymbol{v}}}{\mathrm{d}t} - (\tilde{\boldsymbol{u}}_\infty)_\times \tilde{\boldsymbol{\omega}} \right) - \tilde{\boldsymbol{\omega}}_\times \left[M_{f1}\right] (\tilde{\boldsymbol{v}} - \tilde{\boldsymbol{u}}_\infty) \tag{A.25a}$$

$$\tilde{\boldsymbol{M}}_{F/S} = -\left[M_{f2}\right] \frac{\mathrm{d}\tilde{\boldsymbol{\omega}}}{\mathrm{d}t} - (\tilde{\boldsymbol{v}} - \tilde{\boldsymbol{u}}_\infty)_\times \left[M_{f1}\right] (\tilde{\boldsymbol{v}} - \tilde{\boldsymbol{u}}_\infty) - \tilde{\boldsymbol{\omega}}_\times \left[M_{f2}\right] \tilde{\boldsymbol{\omega}} \tag{A.25b}$$

Since the structure has rotated, the relative direction of the ambient flow varies as follows:

$$\tilde{\boldsymbol{u}}_\infty = \mathbb{R}^{-1} \bar{\boldsymbol{u}}_\infty = \left(\mathbb{1} - \bar{\boldsymbol{\theta}}^1_\times\right) \bar{\boldsymbol{u}}_\infty + \mathcal{O}\left(\varepsilon^2\right), \tag{A.26}$$

and similarly for the other vectors associated with the kinematics, we have $\tilde{\boldsymbol{\omega}}^1 = \bar{\boldsymbol{\omega}}^1 + \mathcal{O}\left(\varepsilon^2\right)$, $\tilde{\boldsymbol{v}}^1 = \bar{\boldsymbol{v}}^1 + \mathcal{O}\left(\varepsilon^2\right)$, and the same goes for the time derivatives of $\tilde{\boldsymbol{v}}^1$. The linearized expression of the force and moment in the reference frame is:

$$\begin{pmatrix} \bar{\boldsymbol{F}}_{F/S} \\ \bar{\boldsymbol{M}}_{F/S} \end{pmatrix} = \left(\mathbb{1} + \bar{\boldsymbol{\theta}}^1_\times\right) \begin{pmatrix} \tilde{\boldsymbol{F}}_{F/S} \\ \tilde{\boldsymbol{M}}_{F/S} \end{pmatrix} + \mathcal{O}\left(\varepsilon^2\right). \tag{A.27}$$

we get the new expression of the fluid forces depending on the displacement of the structure and its time derivatives on the reference domain:
Therefore, by combining equations (A.25), (A.26) and (Appendix A) we obtain the expression of the fluid forces

$$\bar{\boldsymbol{F}}_{F/S} = -\left[M_{f1}\right]\left(\frac{\mathrm{d}\bar{\boldsymbol{v}}^1}{\mathrm{d}t} - \left(\left(\mathbb{1} - \bar{\boldsymbol{\theta}}^1_\times\right)\bar{\boldsymbol{u}}_\infty\right)_\times \bar{\boldsymbol{\omega}}^1\right) - \bar{\boldsymbol{\omega}}^1_\times \left[M_{f1}\right]\left(\bar{\boldsymbol{v}}^1 - \left(\mathbb{1} - \bar{\boldsymbol{\theta}}^1_\times\right)\bar{\boldsymbol{u}}_\infty\right) + \mathcal{O}\left(\varepsilon^2\right), \tag{A.28a}$$

$$\begin{aligned}\bar{\boldsymbol{M}}_{F/S} = &-\left[M_{f2}\right]\left(\frac{\mathrm{d}\bar{\boldsymbol{\omega}}^1}{\mathrm{d}t}\right) - \left(\mathbb{1} + \bar{\boldsymbol{\theta}}^1_\times\right)\left(\bar{\boldsymbol{v}}^1 - \left(\mathbb{1} - \bar{\boldsymbol{\theta}}^1_\times\right)\bar{\boldsymbol{u}}_\infty\right)_\times \left[M_{f1}\right]\left(\bar{\boldsymbol{v}}^1 - \left(\mathbb{1} - \bar{\boldsymbol{\theta}}^1_\times\right)\bar{\boldsymbol{u}}_\infty\right) + ... \\ &\bar{\boldsymbol{\omega}}^1_\times \left[M_{f1}\right]\bar{\boldsymbol{\omega}}^1 + \mathcal{O}\left(\varepsilon^2\right).\end{aligned} \tag{A.28b}$$

which becomes by expanding the terms:

$$\bar{\boldsymbol{F}}_{F/S} = -\left[M_{f1}\right]\left(\frac{\mathrm{d}\bar{\boldsymbol{v}}^1}{\mathrm{d}t} - \left(\bar{\boldsymbol{u}}_\infty\right)_\times \bar{\boldsymbol{\omega}}^1\right) + \bar{\boldsymbol{\omega}}^1_\times \left[M_{f1}\right]\bar{\boldsymbol{u}}_\infty \tag{A.29a}$$

$$\begin{aligned}\bar{\boldsymbol{M}}_{F/S} = &-\left[M_{f2}\right]\left(\frac{\mathrm{d}\bar{\boldsymbol{\omega}}^1}{\mathrm{d}t}\right) + \bar{\boldsymbol{v}}^1_\times \left[M_{f1}\right]\bar{\boldsymbol{u}}_\infty + \left(\bar{\boldsymbol{u}}_\infty\right)_\times \left[M_{f1}\right]\bar{\boldsymbol{v}}^1 + \left(\bar{\boldsymbol{\theta}}^1_\times \bar{\boldsymbol{u}}_\infty\right)_\times \left[M_{f1}\right]\bar{\boldsymbol{u}}_\infty + ... \\ &\left(\bar{\boldsymbol{u}}_\infty\right)_\times \left[M_{f1}\right]\left(\bar{\boldsymbol{\theta}}^1_\times \bar{\boldsymbol{u}}_\infty\right) - \left(\bar{\boldsymbol{u}}_\infty\right)_\times \left[M_{f1}\right]\bar{\boldsymbol{u}}_\infty - \bar{\boldsymbol{\theta}}^1_\times \left(\bar{\boldsymbol{u}}_\infty\right)_\times \left[M_{f1}\right]\bar{\boldsymbol{u}}_\infty.\end{aligned} \tag{A.29b}$$

In order to get an expression in the form of stiffness, damping and mass operators appear, we switch the position of the variables using the skew-symmetry properties of the cross product:

$$\bar{\boldsymbol{F}}_{F/S} = -\left[M_{f1}\right]\left(\frac{\mathrm{d}\bar{\boldsymbol{v}}^1}{\mathrm{d}t} - \left(\bar{\boldsymbol{u}}_\infty\right)_\times \bar{\boldsymbol{\omega}}^1\right) - \left(\left[M_{f1}\right]\bar{\boldsymbol{u}}_\infty\right)_\times \bar{\boldsymbol{\omega}}^1 \tag{A.30a}$$

$$\begin{aligned}\bar{\boldsymbol{M}}_{F/S} = &-\left[M_{f2}\right]\left(\frac{\mathrm{d}\bar{\boldsymbol{\omega}}^1}{\mathrm{d}t}\right) - \left(\left[M_{f1}\right]\bar{\boldsymbol{u}}_\infty\right)_\times \bar{\boldsymbol{v}}^1 + \left(\bar{\boldsymbol{u}}_\infty\right)_\times \left[M_{f1}\right]\bar{\boldsymbol{v}}^1 + \left(\left[M_{f1}\right]\bar{\boldsymbol{u}}_\infty\right)_\times \left(\bar{\boldsymbol{u}}_\infty\right)_\times \bar{\boldsymbol{\theta}}^1 - ... \\ &\left(\bar{\boldsymbol{u}}_\infty\right)_\times \left[M_{f1}\right]\left(\bar{\boldsymbol{u}}_\infty\right)_\times \bar{\boldsymbol{\theta}}^1 - \left(\bar{\boldsymbol{u}}_\infty\right)_\times \left[M_{f1}\right]\bar{\boldsymbol{u}}_\infty + \left(\left(\bar{\boldsymbol{u}}_\infty\right)_\times \left[M_{f1}\right]\bar{\boldsymbol{u}}_\infty\right)_\times \bar{\boldsymbol{\theta}}^1.\end{aligned} \tag{A.30b}$$

By rearranging the terms in a suitable way, the above equation can be rewritten as

$$\begin{pmatrix} \bar{\boldsymbol{F}}_{F/S} \\ \bar{\boldsymbol{M}}_{F/S} \end{pmatrix}^0 = -\begin{pmatrix} \boldsymbol{0} \\ \left(\bar{\boldsymbol{u}}_\infty\right)_\times \left[M_{f1}\right]\bar{\boldsymbol{u}}_\infty \end{pmatrix} \tag{A.31a}$$

$$\begin{pmatrix} \bar{\boldsymbol{F}}_{F/S} \\ \bar{\boldsymbol{M}}_{F/S} \end{pmatrix}^1 = -\left[M_f^{rig}\right]\begin{pmatrix} \frac{d\bar{\boldsymbol{v}}}{dt}^1 \\ \frac{d\bar{\boldsymbol{\omega}}}{dt}^1 \end{pmatrix} - \left[G_f^{rig}\right]\begin{pmatrix} \bar{\boldsymbol{v}}^1 \\ \bar{\boldsymbol{\omega}}^1 \end{pmatrix} - \left[K_f^{rig}\right]\begin{pmatrix} \bar{\boldsymbol{d}}^1 \\ \bar{\boldsymbol{\theta}}^1 \end{pmatrix}, \tag{A.31b}$$

$$\left[G_f^{rig}\right] = \begin{bmatrix} (0) & \left(\left[M_{f1}\right]\bar{\boldsymbol{u}}_\infty\right)_\times - \left[M_{f1}\right]\left(\bar{\boldsymbol{u}}_\infty\right)_\times \\ \left(\left[M_{f1}\right]\bar{\boldsymbol{u}}_\infty\right)_\times - \left(\bar{\boldsymbol{u}}_\infty\right)_\times \left[M_{f1}\right] & (0) \end{bmatrix}, \tag{A.31c}$$

$$\left[K_f^{rig}\right] = \begin{bmatrix} (0) & (0) \\ (0) & \left(\bar{\boldsymbol{u}}_\infty\right)_\times \left[M_{f1}\right]\left(\bar{\boldsymbol{u}}_\infty\right)_\times - \left(\left[M_{f1}\right]\bar{\boldsymbol{u}}_\infty\right)_\times \left(\bar{\boldsymbol{u}}_\infty\right)_\times - \left(\left(\bar{\boldsymbol{u}}_\infty\right)_\times \left[M_{f1}\right]\bar{\boldsymbol{u}}_\infty\right)_\times \end{bmatrix}, \tag{A.31d}$$

where the displacement of the structure $\bar{\boldsymbol{d}}^1$ has been artificially introduced in order to obtain arrays of variables at order ε linked with a temporal derivatives, even though the displacement does not intervene in the dynamics of the structure since the problem is invariant by translation, which is in agreement with the factors of $\bar{\boldsymbol{d}}^1$ being all nil in the above equation.

Appendix G

Complementary experimental results

G.1 Measurement of the viscosity of glucose syrup

In this appendix, the viscosity measurements of the glucose syrup are presented. These measures were obtained with a viscosimeter.

First, the viscosity μ_f has been measured for various concentrations of glucose syrup x_{syrup}, where $x_{syrup} = 0$ is associated with pure water and $x_{syrup} = 1$ with pure glucose syrup. The results are displayed in figure G.1. In order to interpolate the viscosity of the mixture for any syrup concentration, the Lederer–Roegiers equation for a binary mixture (Zhmud, 2014) has been used, with a coefficient $\alpha = 2$ which seemed to offer a good approximation as shown in figure G.1:

$$\ln(\mu) = \frac{x_{water}}{x_{water} + \alpha x_{water}} \ln\mu_{syrup} + \frac{\alpha x_{syrup}}{x_{water} + \alpha x_{syrup}} \ln\mu_{syrup}, \tag{G.1}$$

with μ_{water} and μ_{syrup} the viscosities of water and flucose syrup respectively and $x_{water} = 1 - x_{syrup}$ the water concentration.

Secondly, the viscosity of a water/syrup mixture with x_{syrup} has been measured for various temperatures, as displayed in figure G.1. In order to interpolate the viscosity of the mixture at any temperature, a linear regression as been used as shown with the dashed line.

G.2 Viscous added mass and damping uncertainties

Figure G.2 shows the same graphs as V.6 with $D^{\dagger}_{\mu_f}$ and $I^{\dagger}_{\mu_f}$ by it is completed with uncertainty bars associated with the Stokes number and the damping and mass coefficients.

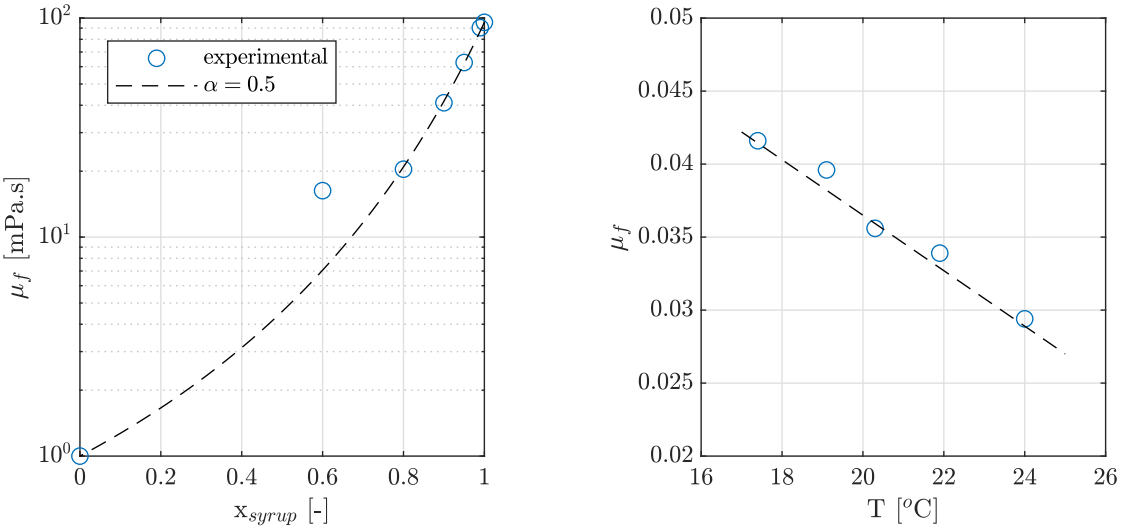

Figure G.1: Left: the blue dots show measurements of the viscosity of a mixture of water and glucose syrup for various syrup concentrations x_{syrup}. Dashed line: prediction of the viscosity using the Lederer-Roegiers equation for binary mixtures G.1 with a coefficient $\alpha = 0.5$. Right: the blue dots show the viscosity measurements of a mixture with x_{syrup} at various temperatures, while the dashed line shows the associated linear regression.

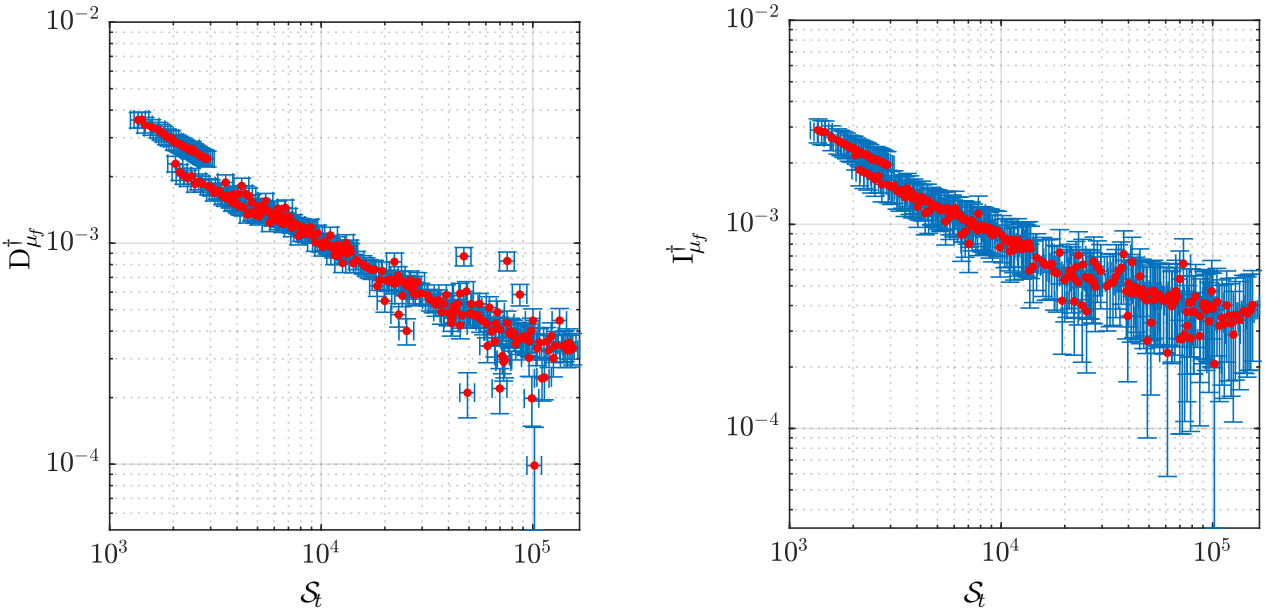

Figure G.2: Boundary layer added mass $I^\dagger_{\mu_f}$ (left) and added damping $D^\dagger_{\mu_f}$ (right) plotted against the Stokes number. Both axis are on a logarithmic scale.

Bibliography

Amiryants, G., Grigoriex, V., Ishmuratov, F. Z., Franz, A., d'Henin, E., and Kaempf, B. (2002). Investigations of airship aeroelasticity. In *23rd International Congress of Aerospace Sciences*, Toronto, Canada. 7, 8, 9

Azinheira José, R., Carneiro de Pava, E., and Sisqueira Bueno, S. (2002). Influence of wind speed on airship dynamics. *Journal of guidance, control and dynamics*, 25(6). 139

Azouz, N., Chaabani, S., Lerbet, J., and Abichou, A. (2012). Computation of the added masses of an unconventional airship. *Journal of Applied Mathematics*, 2012. 8, 42, 83, 139, 140

Bebendorf, M. and Rjasanow, S. (2003). Adaptative low-rank approximation of collocation matrices. *Computing*, 70(1):1–24. 69

Bennaceur, S. (2009). Modeling and control of flexible flying engines. *Theses, Université d'Evry-Val d'Essonne*. 8

Bennaceur, S., Azouz, N., and Boukraa, D. (2006). An efficient modelling of flexible airships. In *Engineering Systems Design and Analysis*, volume 42509, pages 573–582. 8

Bennett, A. et al. (2006). *Lagrangian fluid dynamics*. Cambridge University Press. 32

Bessert, N. and Frederich, O. (2005). Nonlinear airship aeroelasticity. *Journal of Fluids and Structures*, 21:731–742. 7, 9, 29, 30, 113, 140

Bonet, J. and Wood, R. (1997). *Nonlinear continuum mechanics for finite element analysis*. Cambridge University Press. 91

Bonnet, M. (1999). *Boundary integral equation methods for solids and fluids*. John Wiley & sons. 10, 11, 22, 44, 61, 68, 98, 101

Carbone, G. (2020). *Comportement dynamique d'un dirigeable en écoulement non homogène*. PhD thesis, Ecole nationale supérieure Mines-Télécom Lille Douai. 6

Carbone, G., Martinat, G., Farcy, D., and Harion, J.-L. (2019). Added masses of generic shape bodies interacting with external walls. *Aerospace science and technology*, 90:70–84. 6, 26, 38, 59, 140

Carbone, G., Martinat, G., Farcy, D., and Harion, J.-L. (2020). Aerodynamic investigation of a 3.5:1 prolate spheroid. In *AIAA aviation 2020 forum*. 5, 6

Chaabani, S. (2014). *Dynamique non-linéaire d'un dirigeable flexible*. PhD thesis, Evry-Val d'Essone. 8, 59, 141

Chaillat, S., Desiderio, L., and Ciarlet, P. (2017). Theory and implementation of h-matrix based iterative and direct solvers for helmholtz and elastodynamic oscillatory kernels. *Journal of Computational physics*, 351:165–186. 68, 69, 70, 71, 87

Chaplin, J. (2000). Hydrodynamic damping of a cylinder at $\beta \approx 106$. *Journal of fluids and structures*, 14(8):1101–1117. 141

Clarke, D. (2009). *Experimental and computational investigation of ow about low aspect ratio ellipsoids at transcritical Reynolds numbers.* PhD thesis, University of Tasmania. 83, 87, 139

Combescure, A. (2000). Méthodes numériques. Lecture notes at ENS Cachan. 95

Cook, M., Lipscombe, J., and Goineau, F. (2000). Analysis of the stability modes of the non-rigid airship. *The aeronautical journal*, 104(1036):279–290. 31

Costabel, M. and Le Louër, F. (2012). Shape derivatives of boundary integral operators in electromagnetic scattering. part i: Shape differentiability of pseudo-homogeneous boundary integral operators. *Integral Equations and Operator Theory*, 72(4):509–535. 10

Darrozès, J.-S. and François, C. (1982). *Mécanique des fluides incompressibles*, volume 163. Springer. 16, 17, 150

De Langre, E. (2001). *Fluides et solides.* Editions Ecole Polytechnique. 119

De Langre, E. (2008). Effects of wind on plants. *Annu. Rev. Fluid Mech.*, 40:141–168. 95, 97, 103

Destuynder, P. and Santi, F. (2006). A pgrogressive euler-lagrange formulation for aeroelasticity model of quasi-axisymmetrical airship. In *European Conference on Computational Fluid Dynamics ECCOMAS CFD.* 8, 58

Doaré, O. (2020). Interaction fluide-structure. Lecture notes at ENSTA Paris. 16, 120, 129

El Omari, K., Schall, E., Koobus, B., and Dervieux, A. (2004). Inviscid flow calculation around flexible airship. In *Mathematical Symposium Garcia De GalDeano*, volume 31, pages 535–544. 7

Fernández, M. A. and Le Tallec, P. (2003). Linear stability analysis in fluid–structure interaction with transpiration. part i: Formulation and mathematical analysis. *Computer methods in applied mechanics and engineering*, 192(43):4805–4835. 32

Fischnaller, H. and Thöbin, K. (2009). Numerical integration - an introduction to the boundary element method. Masters project for Graz university of technology. 62

Folland, G. B. (2020). *Introduction to partial differential equations.* Princeton university press. 19, 151

Freeman, H. B. and Wheatley, J. B. (1932). *Pressure-distribution Measurements on the Hull and Fins of a 1/40-scale Model of the US Airshape" Akron".* US Government Printing Office. 5

Funk, P., Lutz, T., and Wagner, S. (2003). Experimental investigations on hull-fin interferences of the lotte airship. *Aerospace Science and Technology*, 7(8):603–610. 5

Gennaretti, M., Luceri, L., and Morino, L. (1997). A unified boundary integral methodology for aerodynamics and aeroacoustics of rotors. *Journal of sound and vibration*, 200(4):467–489. 113, 117

Hackbusch, W. (1995). *Integral Equations - Theory and numerical treatment.* Springer. 11, 25

Hoareau, C. (2019). *Vibrations hydroélastiques de réservoirs élastiques couplés à un fluide interne incompressible à surface libre autour d'un état précontraint.* PhD thesis, Conservatoire National des Arts et Métiers. 116

Holmes, M. H. (2009). *Introduction to the foundations of applied mathematics.* Springer. 37

Hunt, J. D. (1982). Structural analysis of aerostat flexible structure by the finite-element method. *Journal of Aircraft*, 19(8):674–678. 7

Inamoto, Y., Saito, K., Shibasaki, K., Sasa, S., Kohno, T., and Harada, K. (2003). Flight control testing for the development of stratospheric platforrm airships. In *AIAA's 3rd annual aviation technology, integration, and operations (ATIO) forum.* 136

Jakobi, A., Funk, P., Lutz, T., and Wagner, S. (2000). Calculation of aerodynamic forces on inclined airship bodies—boundary–layer calculation method. In *3rd International Airship Convention and Exhibition, July 1–5, 2000, Friedrichshafen, Germany.* 5

Jones, R. and Bell, A. (1929). *Experiments on a Model of the Airship R. 101.* HM Stationery Office. 5

Kale, S., Joshi, P., and Pant, R. (2005). A generic methodology for determination of drag coefficient of an aerostat envelope using cfd. In *AIAA 5th ATIO and16th Lighter-Than-Air Sys Tech. and Balloon Systems Conferences*, page 7442. 5

Kanoria, A. A., Panchal, K., Dongre, R., and Damodaran, M. (2015). Computational modelling of aerodynamic characteristics of airships in arbitrary motion. In *22nd AIAA lighter-than-air systems technology conference*, page 3230. 6

Katz, J. and Plotkin, A. (2001). *Low-speed aerodynamics*, volume 13. Cambridge university press. 11, 14, 110, 111, 113, 114

Lamb, H. (1918). The inertia coefficients of an ellipsoid moving in fluid. *Advisory Committee for Aeronautics, Reports and Memoranda No. 623, London, UK.* 11, 14

Lamb, H. (1932). *Hydrodynamics.* Cambridge University Press. 64, 76, 122, 129, 133, 154, 155

Lambert, C. and Nahon, M. (2003). Stability analysis of a tethered aerostat. *Journal of Aircraft*, 40(4):705–715. 7

Le Mestre, R., Schotté, J.-S., and Doaré, O. (2022). A linearized ale boundary element method for flexible 3d bluff bodies in potential flows: Towards application to airship aeroelasticity. *Computer Methods in Applied Mechanics and Engineering*, 392:114624. 56, 59, 97

Li, Y., Meyer, N., and Sharf, I. (2009). Dynamics modeling and simulation of flexible airships. *AIAA Journal*, 47:592–605. 4, 8, 11, 28, 30, 42, 57, 58, 83, 85, 86, 87, 99, 105, 107, 108, 136, 138, 139, 140, 141

Li, Y., Meyer, N., and Sharf, I. (2011). Airship dynamics modeling: A litterature review. *Progress in aerospace sciences*, pages 217–239. 3, 5, 6, 7, 31, 42, 58, 59, 76, 81, 83, 140

Li, Y. and Nahon, M. (2007). Modeling and simulation of airship dynamics. *Journal of Guidance, Control, and Dynamics*, 30(6):1691–1700. 6, 12, 17, 28, 59

Liu, J., Lu, C., and Xue, L. (2010). Numerical investigation on the aeroelastic behavior of an airship with hull-fin configuration. *Journal of hydrodynamics*, pages 207–213. 7

Lutz, T., Funk, P., Jakobi, A., and Wagner, S. (2002). Summary of aerodynamic studies on the lotte airship. In *4th International airship Convention and Exhibition*, pages 1–12. July. 5, 17, 59

Maekawa, S. and Saito, K. (2004). The effect of ballonet slosh on an airship's longitudinal motion. *Transactions of the Japan Society for Aeronautical and Space Sciences*, 47(155):44–50. 7

Manikandan, M. and Pant, R. S. (2021). Research and advancements in hybrid airships—a review. *Progress in Aerospace Sciences*, 127:100741. 3

Mavaleix-Marchessoux, D. (2020). *Modelling the fluid-structure coupling caused by a far-field underwater explosion*. PhD thesis, Institut polytechnique de Paris. 4, 9, 11, 26, 29, 30, 32, 33, 38, 42, 61, 62, 70, 106, 138, 139, 140, 165

Miloh, T. and Galper, A. (1993). Self-propulsion of general deformable shapes in a perfect fluid. *Proceedings of the Royal Society of London. Series A: Mathematical and Physical Sciences*, 442(1915):273–299. 42

Morand, H. J.-P. and Ohayon, R. (1992). *Interactions fluides-structures*, volume 154. Masson Paris. 21, 57, 129

Morand, H. J.-P. and Ohayon, R. (1995). *Fluid-Structure Interactions : Applied Numerical Methods*. Wiley & Sons. 11, 21

Morino, L. and Gennaretti, M. (1992). Boundary integral equation methods for aerodynamics. *Progress in astronautics and aeronautics*, 146:279–320. 9, 59

Mukherjee, S. and Chandra, A. (1991). A boundary element formulation for design sensitivities in problems involving both geometric and material nonlinearities. *Mathematical and Computer Modelling*, 15(3-5):245–255. 10

Newman, J. N. (2018). *Marine hydrodynamics*, chapter 4. The MIT press. 11, 18, 19, 48

Nishimura, N. and Kobayashi, S. (1991). A boundary integral equation method for an inverse problem related to crack detection. *International Journal for numerical methods in engineering*, 32(7):1371–1387. 10

Nitikitpaiboon, C. and Bathe, K. (1993). An arbitrary lagrangian-eulerian velocity potential formulation for fluid-structure interaction. *Computers and structures*, 47(4-5):871–891. 11, 32, 33

Ohayon, R. (2004). Fluid-structure interaction problems. *Encyclopedia of computational Mechanics*. 8

Otter, A. (1990). Damping forces on a cylinder oscillating in a viscous fluid. *Applied ocean research*, 12(3):153–155. 141

Paidoussis, M. P. (1998). *Fluid-structure interactions: slender structures and axial flow*, volume 1. Academic press. 86, 102, 161

Pfister, J.-L. (2019). *Instabilities and optimization of elastic structures interacting with laminar flows*. PhD thesis, Université Paris-Saclay. 4, 138

Pfister, J.-L., Marquet, O., and Carini, M. (2019). Linear stability analysis of strongly coupled fluid–structure problems with the arbitrary–lagrangian–eulerian method. *Computer Methods in Applied Mechanics and Engineering*, 355:663–689. 22, 32, 33, 102

Posrikidis, C. (2002). *A practical guide to boundary element methods with the software library BEMLIB*. CRS Press. 11, 62

Potthast, R. (1994). Fréchet differentiability of the solution to the acoustic neumann scattering problem with respect to the domain. *Inverse problems*, 10:431. 10

Rangette, A. (1990). A boundary element method to calculate the fluid hydrodynamic mass matrix in structural analysis including free surface waves. *Engineering computations*, 7(3):210–216. 56, 58, 74, 87, 156

Rashid, F., Vartdal, M., and Grue, J. (2011). Oscillating cylinder in viscous fluid: calculation of flow patterns and forces. *Journal of engineering mathematics*, 70(1):281–295. 123

Saad, Y. and Schultz, M. H. (1986). Gmres: A generalized minimal residual algorithm for solving nonsymmetric linear systems. *SIAM Journal on scientific and statistical computing*, 7(3):856–869. 64

Sarpkaya, T. (1977). In-line and transverse forces on cylinders in oscillatory flow at high reynolds numbers. *Journal of ship Research*, 21(04):200–216. 136, 141

Schlichting, H. and Kestin, J. (1961). *Boundary layer theory*, volume 121. Springer. 17

Schobeiri, M. T. (2010). Boundary layer theory. In *Fluid Mechanics for Engineers*, pages 357–421. Springer. 16, 120

Shabana, A. A. (2003). *Dynamics of multibody systems*. Cambridge university press. 34

Shaw, J. B. (1922). *Vector Calculus: With Applications to Physics*. D. Van Nostrand Company. 18

Simoncini, V. and Gallopoulos, E. (1995). An iterative method for nonsymmetric systems with multiple right-hand sides. *SIAM journal on scientific computing*, 16:917–933. 68

Thomasson, P. G. (2000). Equations of motion of a vehicle in a moving fluid. *Journal of Aircraft*, 37(4):630–639. 6

Thomasson, P. G. and Woolsey, C. A. (2013). Vehicle motion in currents. *IEEE Journal of Oceanic Engineering*, 38(2):226–242. 6, 46, 139, 150, 154

Veron, E., Bouzidi, R., Leblond, C., Anh, L., and Sigrist, J.-F. (2016). Large displacements of light thin flexible structures coupled with heavy fluids using co-simulation between finite element and fast boundary element solvers. In *Proceedings of the 11th International Conference on Flow-Induced Vibration*, The Hague, The Netherlands. 9, 11, 26, 42, 61, 62

Wang, C.-L. (1968). On high-frequency oscillatory viscous flows. *Journal of fluid mechanics*, 32(1):55–68. 123

Wu, X., Wang, Y., Huang, C., Liu, Y., and Lu, L. (2015). Experiment and numerical simulation on the characteristics of fluid-structure interactions of non-rigid airships. *Theoretical and applied mechanics letters*, 5:258–261. 7

Zhmud, B. (2014). Viscosity blending equations. *Lube Mag*, 121(93):24–27. 199

Ziegler, H. (1977). *Principles of structural stability*. Springer. 51, 57, 161

ECOLE DOCTORALE

Titre: Modélisation des effets de fluides externes et internes sur le comportement dynamique des dirigeables flexibles

Mots clés: masse ajoutée/vibration/aérodynamique/dirigeable

Résumé: Cette thèse de doctorat porte sur la modélisation et la simulation des interactions fluide-structure entre un dirigeable souple, un écoulement externe et un gaz porteur interne. On considère que le fluide est potentiel du fait de la grande taille des dirigeables. L'écoulement potentiel est résolu sur un maillage de l'interface fluide-structure grâce à la Méthode des Éléments de Frontière, et le travail des efforts associés est obtenu par la Méthode des Eléments Finis. Les équations du fluide sont exprimées dans un formalisme Arbitrairement Lagrangien-Eulérien. Afin de se ramener à des calculs sur un maillage de référence invariant, on considère de grands mouvements d'ensemble (rotations et translations) auxquels s'ajoutent de petits mouvements de corps rigides et de petites déformations par rapport auxquels le problème fluide est linéarisé. Cela conduit en pratique à différencier les opérateurs de la Méthode des Éléments de Frontière pour caractériser la cinématique du fluide ainsi que les opérateurs de la Méthode des Eléments Finis pour déterminer les efforts associés exercés sur l'interface fluide-structure, ceci afin de prendre en compte les perturbations dans le domaine fluide liées aux mouvements de l'interface. La linéarisation permet d'exprimer les efforts du fluide à l'aide d'opérateurs de masse, gyroscopique et de raideur ajoutés, proportionnels respectivement à l'accélération, la vitesse et les déplacements de l'interface. De plus, un modèle simplifié d'ailerons basé sur la théorie de Theodorsen est utilisé afin d'ajouter leur portance au modèle. La partie structure du problème est modélisée à partir de la Méthode des Eléments Finis appliquée à une membrane. Celle-ci est précontrainte par la pression statique du fluide interne et de l'écoulement externe. Le modèle fluide-structure ainsi obtenu est utilisé pour étudier la stabilité d'un tel système couplé fluide-structure sur un cas test de dirigeable. Les opérateurs fluide-structure permettent d'obtenir les valeurs propres du système pour diverses vitesses du dirigeable. Le problème fluide-structure est coûteux à résoudre car matrices de la Méthode des Éléments de Frontière sont pleines, et pour réduire la taille du problème, celui-ci est projeté sur une base réduite des modes de la structure dans le vide. Au-delà d'une vitesse critique, on constate qu'un risque de divergence par flottement apparaît. Enfin, la masse ajoutée obtenue par le modèle d'écoulement potentiel est comparée avec des résultats expérimentaux obtenus à partir d'une maquette rigide oscillant en rotation dans une cuve de fluide au repos. En faisant varier la fréquence d'oscillation de la maquette, la densité et la viscosité du fluide, on a pu caractériser, en fonction du nombre de Stokes, l'ordre de grandeur des efforts visqueux relativement aux efforts inertiels du fluide prédits pour un fluide potentiel.

Title: Modeling of external and internal fluid effects on the dynamic behavior of a flexible airship

Keywords: added mass/ vibration/ aerodynamics/ airships

Abstract: This PhD thesis deals with the modeling and simulation of fluid-structure interactions between a flexible airship, an external flow and an internal lifting gas. The fluid is considered as potential due to the large size of the airships. The potential flow is solved on a mesh of the fluid-structure interface using the Boundary Element Method, and the work of the associated forces is obtained using the Finite Element Method. The fluid equations are expressed in an Arbitrary Lagrangian-Eulerian formalism. In order to calculate on an invariant reference mesh, we consider large rigid body motions (rotations and translations) to which are added small rigid body motions and small deformations with respect to which the fluid problem is linearized. This leads in practice to differentiate the operators of the Boundary Element Method to characterize the kinematics of the fluid and the operators of the Finite Element Method to determine the associated forces exerted on the fluid-structure interface, in order to take into account the perturbations in the fluid domain related to the movements of the interface. The linearization allows to express the fluid forces using added mass, gyroscopic and stiffness operators, proportional respectively to the acceleration, velocity and displacements of the interface. In addition, a simplified fin model based on Theodorsen theory is used to include their lift in the model.

The structural part of the problem is modeled using the Finite Element Method for a membrane. The membrane is prestressed by the static pressure of the internal fluid and the external flow. The fluid-structure model thus obtained is used to study the stability of such a coupled fluid-structure system on an airship test case. The fluid-structure operators are used to obtain the eigenvalues of the system at various speeds of the airship. The fluid-structure problem is expensive to solve since the matrices of the Boundary Element Method are full and to reduce the size of the problem, the latter is projected on a reduced basis of the structure modes in vacuum. We observe that beyond a critical velocity, a risk of divergence by flutter arises.

Finally, the added mass obtained by the potential flow model is compared with experimental results obtained with a rigid model oscillating rotationally in a fluid tank at rest. By varying the oscillation frequency of the model, the density and the viscosity of the fluid, it was possible to characterize the order of magnitude of the viscous forces compared to the inertial forces of the fluid predicted for a potential fluid as a function of the Stokes number.

Institut Polytechnique de Paris
91120 Palaiseau, France